Figure 8-16 plots the change in wave height for each potential borrow area alternative along GENESIS nearshore wave reference line landward of the borrow areas where wave information is passed from STWAVE to GENESIS. The *X*-axis of the plot goes from east on the left to west on the right. Note that change in wave height is limited to approximately plus or minus five percent for the 5.0 sec waves whereas for the 11 sec waves the wave height change approaches 10 percent for SI2, SI3, and SI4 compared to almost 20 percent for the SI1. The increase in SI5 is negligible. Of concern for SI1 is the apparent focusing of wave energy between the two borrow areas which align with the restored shoreline that will result from the closure of Camille Cut. Wave heights are reduced in the lee of the borrow areas due to refraction of waves towards each side of the pit. The combination of the two segments of SI1 causes a focusing of refracted wave energy on the restored shoreline, particularly in shore normal wave cases. For SI2, SI3, SI4 and SI5 there is also an increase in wave energy along the sides of the borrow area. Absence of the small western segment of the proposed borrow in SI1 reduces focusing of wave energy around Camille Cut for the other potential borrow area configuration, but there is still up to approximately a 10 percent increase in wave height along East Ship Island for SI1, an 8.0 percent increase for SI3, and 6.0 percent increase for SI4. SI5 shows a maximum of 2.0 percent increase in wave height over the modeling domain. For each potential borrow area alternative, wave heights are reduced in the lee of the dredged areas due to refraction of the waves towards each side of the borrow area. The more oblique angles tend to focus energy towards the northwest due to their approach angle. For longer period waves, the effects of the borrow areas are the most apparent.

8.2.3 Sediment transport and shoreline change

A GENESIS model domain was generated for examining the potential influence of the borrow areas on shoreline processes along the restored Ship Island shoreline. The model domain is 11.85 km (7.36 miles) long and the initial shoreline position was developed from the existing Gulf shorelines of East and West Ship Islands connected by the estimated post-restoration shoreline. The Camille Cut segment of shoreline is approximately 4.5 km (2.79 miles) in length and extends between approximate GENESIS alongshore positions 2800-m and 7300-m.

Wave conditions determined through STWAVE simulations for the potential borrow area alternatives and existing condition were applied as input to GENESIS to estimate longshore sand transport rates and shoreline

Figure 8-16. Percent change in wave height at nearshore reference line.

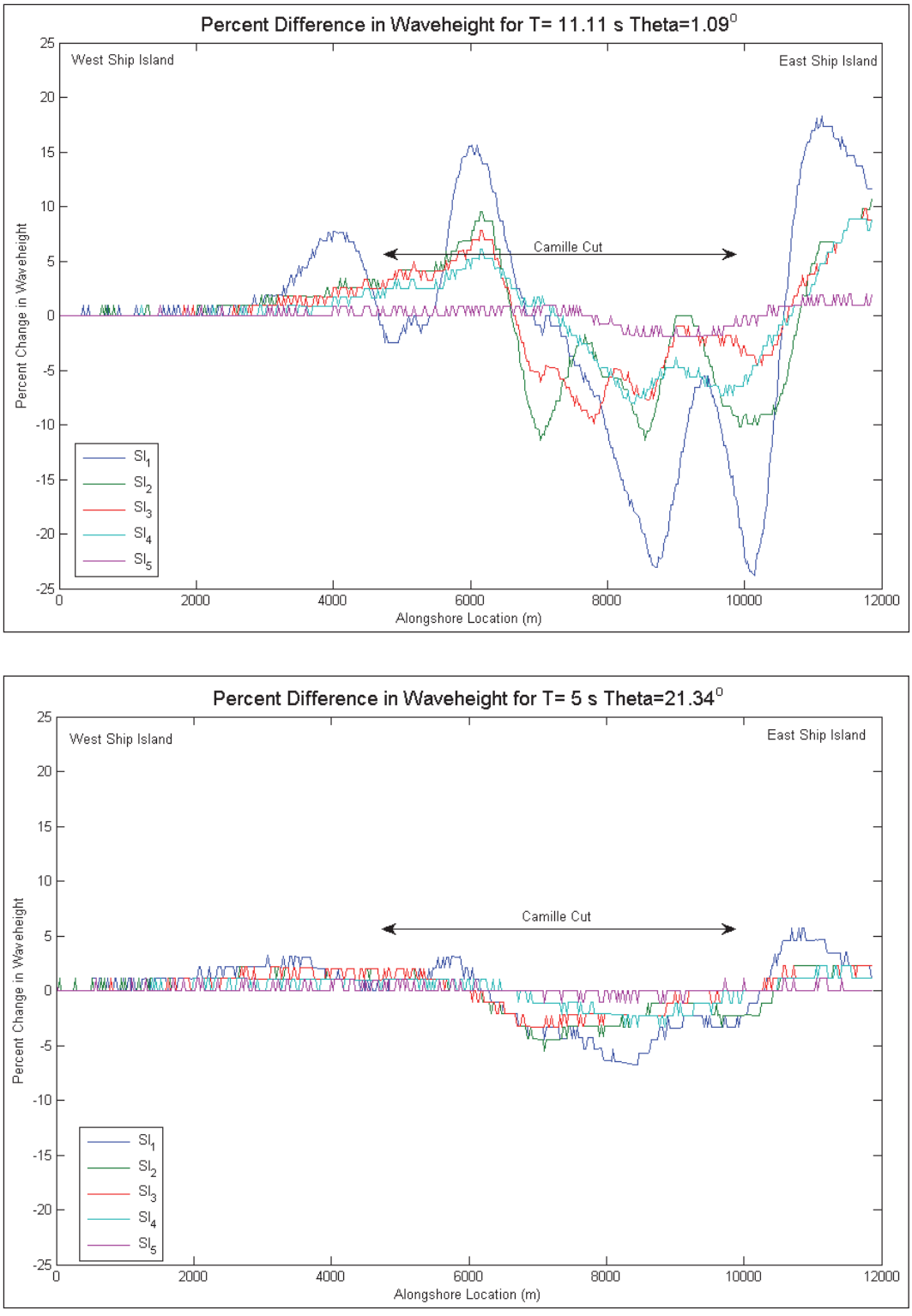

change. GENESIS simulations were run for the 20-year WIS hindcast offshore wave time-series (1980-1999). Figure 8-17 displays the estimated final shoreline position for both existing and three dredged conditions (restored condition) as well as the initial shoreline position. Potential borrow area dredged conditions show an increase in erosion over the 20-year simulation interval as compared to existing condition for borrow area SI1, SI2, SI3, SI4, and SI5 bathymetries. Increased erosion associated with the dredged bathymetries is observed primarily between GENESIS alongshore position 4500-m and 8000-m which corresponds to much of the Camille Cut restored shoreline area. The SI2, SI3, SI4, and SI5 borrow areas have a smaller impact, but still cause increased erosion. Figure 8-18 plots shoreline change rate for these conditions. Negative values indicate erosion and positive values indicate accretion. Figure 8-19 plots the difference, or change, in estimated shoreline change rates between existing and dredged conditions for each point on the GENESIS-axis. Borrow areas SI2 and SI3 decrease the erosion rate by approximately one third when compared to SI1. SI4 decreases the erosion rate by 60 percent in the vicinity of Camille Cut compared to SI1. SI5 reduces the erosion rate of SI1 by 90 percent. However, SI2 does cause a 25-m increase in erosion for Ship Island compared to the existing condition over the 20-yr period. SI3 shows a similar increase in erosion over the same period. SI4 increases the erosion by 28-m around Camille Cut. SI5 causes a minimal 5.0-m increase of erosion over 20 years. Figure 8-19 indicates that SI1 will induce accelerated shoreline erosion along eastern end of East Ship Island (alongshore positions 0- to 2000- m) and along the restored shoreline in the vicinity of Camille Cut (alongshore positions 4500- to 8000- m). Borrow area SI2 minimizes the effects on East Ship Island and reduces the induced erosion in the vicinity of Camille Cut. Borrow area SI3 slightly increases the erosion on East Ship Island compared to SI2. The increased shoreline recession rate associated with SI1 is estimated to approach 3.5-m/year in the vicinity of alongshore position 6000-m which represents an increase in shoreline erosion from approximately 2.5-m/year for the existing condition bathymetry to nearly 6.0-m/year in this region. Borrow areas SI2 and SI3 result in an increase in shoreline recession of approximately 2-m/year in the vicinity of Camille Cut. Borrow area SI4 results in an increase of shoreline recession of about 1.4-m/year in this region. Borrow area SI5 increases erosion by about 0.3-m/year in this location. Relative accretion occurs on West Ship Island for all five borrow areas. SI1, SI2, and SI4 cause accretion of about 7.0-m for East Ship Island, while SI3 causes 3.0-m and SI5 actually causes erosion of about 2.0-m over the 20 yr simulation period. West Ship Island accretes 27-m for SI1, 21-m for SI2, 24-m for SI3, 14-m for SI4, and 3.0-m for SI5.

Figure 8-17. Comparison of existing and potential Dredged borrow area condition estimated final shoreline for a 20-year simulation.

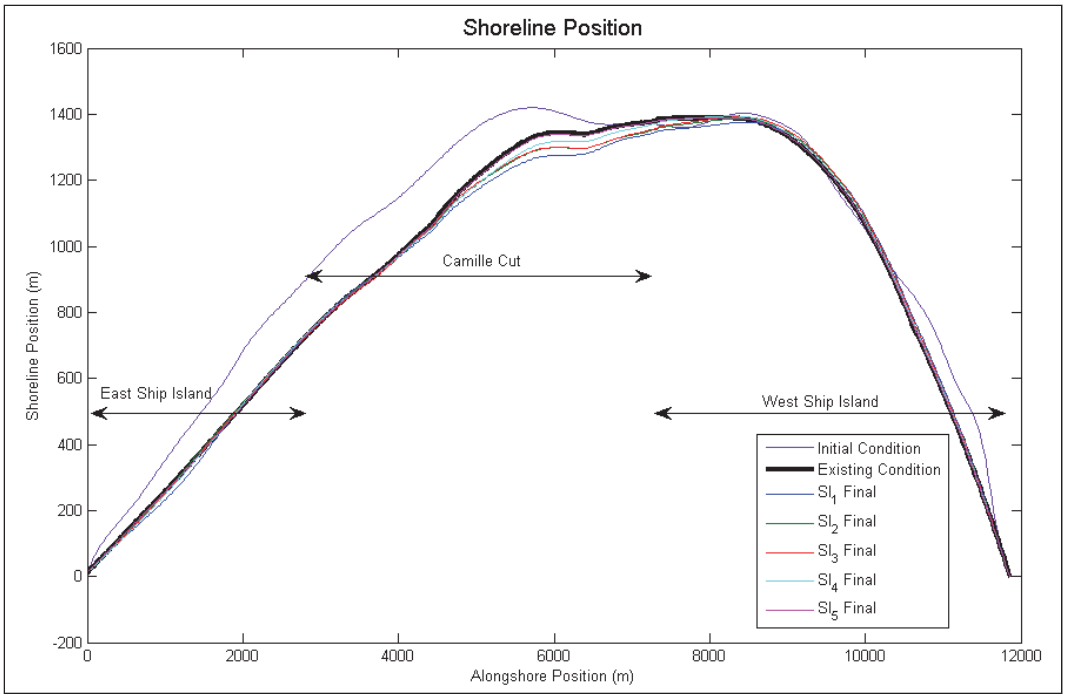

Figure 8-18. Comparison of existing and potential Dredged borrow area condition shoreline change rate.

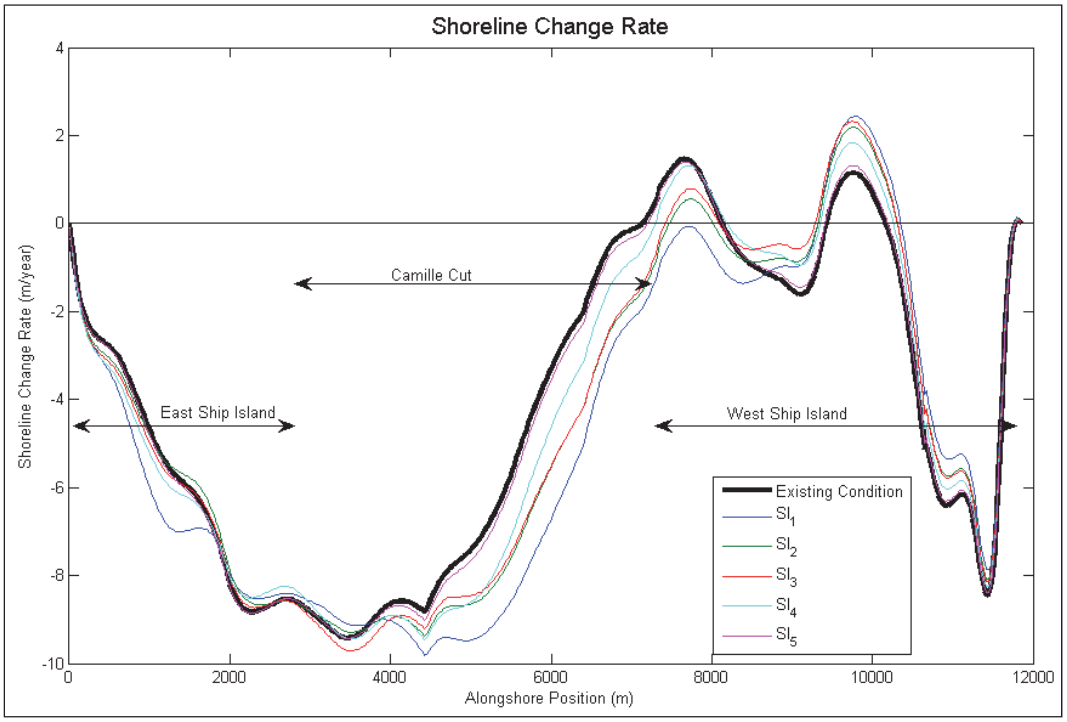

Figure 8-19. Potential borrow area dredging induced change in shoreline change rate.

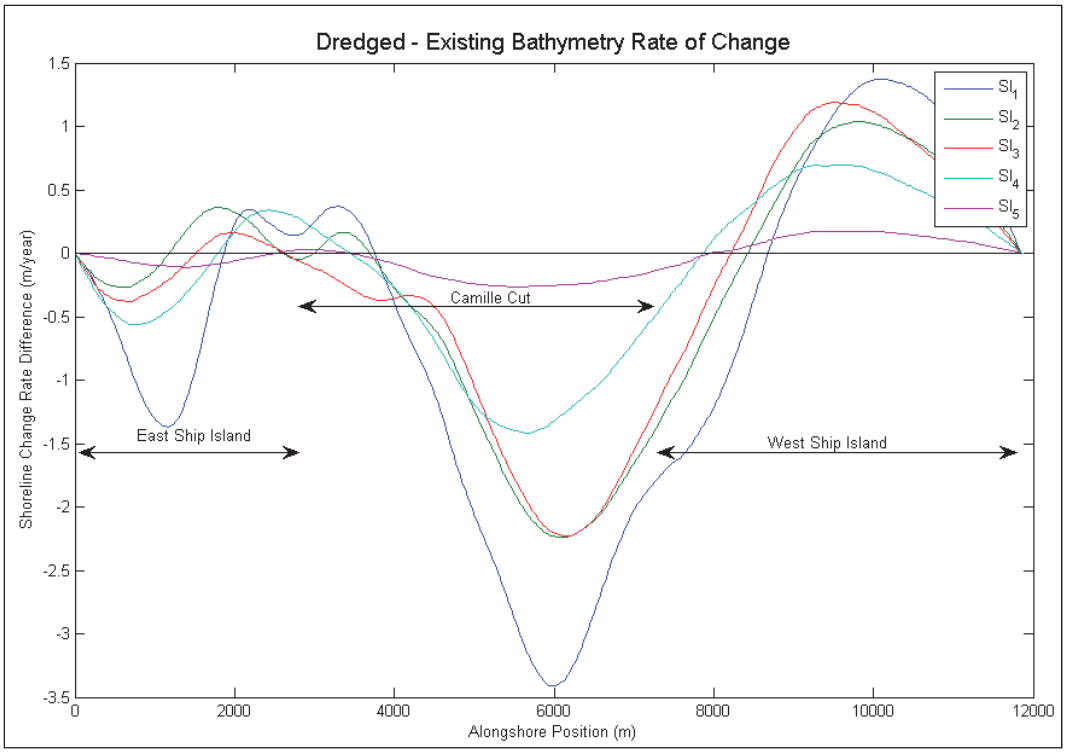

Estimated average annual longshore sand transport rate for both existing and potential borrow area Dredged conditions is plotted in Figure 8-20. Recall that positive values indicate transport to the right on the plot (east to west transport). This leads to a positive slope in the longshore sand transport rate indicating erosion; whereas, a negative slope indicates shoreline accretion. The steeper the slope the higher the predicted shoreline rate of change. A stable shoreline is associated with a constant longshore sand transport rate. Estimated average annual longshore sand transport rates for potential borrow area Dredged conditions vary from approximately -50,000 m^3/year (east-directed) at the eastern end of East Ship Island to nearly 318,000 m^3/year (west-directed) at the western end of West Ship Island for borrow area SI1 and -30,000 m^3/year to approximately 310,000 m^3/year for SI2 , SI3, and SI4. SI5 spans from approximately -20,000 m^3/year to 300,000 m^3/year. To isolate the influence of potential excavated borrow areas on longshore sand transport rates, the change in estimated transport rates between the existing and dredged condition are plotted in Figure 8-21. The change in estimated sand transport rates ranges from about -32,000 m^3/year to 33,000 m^3/year for SI1, and -15,000 m^3/year to 25,000 m^3/year for SI2 and SI3. SI4 ranges from -10,000 m^3/year to 10,000 m^3/year, while SI5 ranges from -2,000 m^3/year to 4,000 m^3/year. The transport rate difference is most significant towards the center of the island at the Camille

Cut closure area. In general, all borrow area alternatives appear to increase erosion in the area being restored, with borrow area SI5 having the least potential impact.

Figure 8-20. Mean alongshore transport rate.

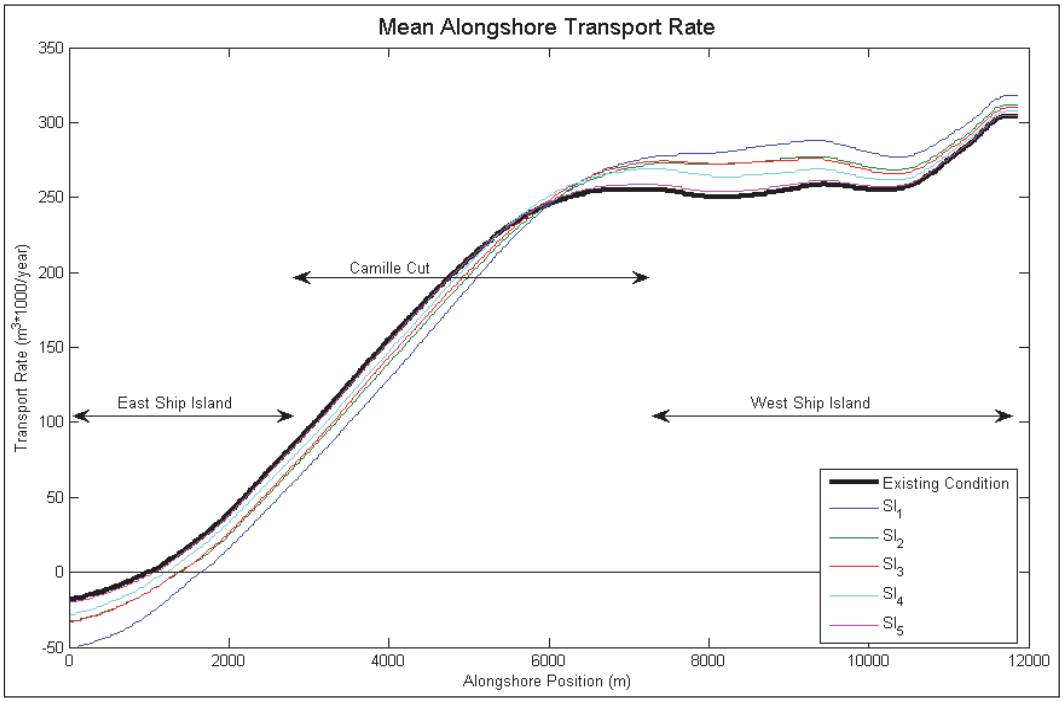

Figure 8-21. Change in average annual longshore transport.

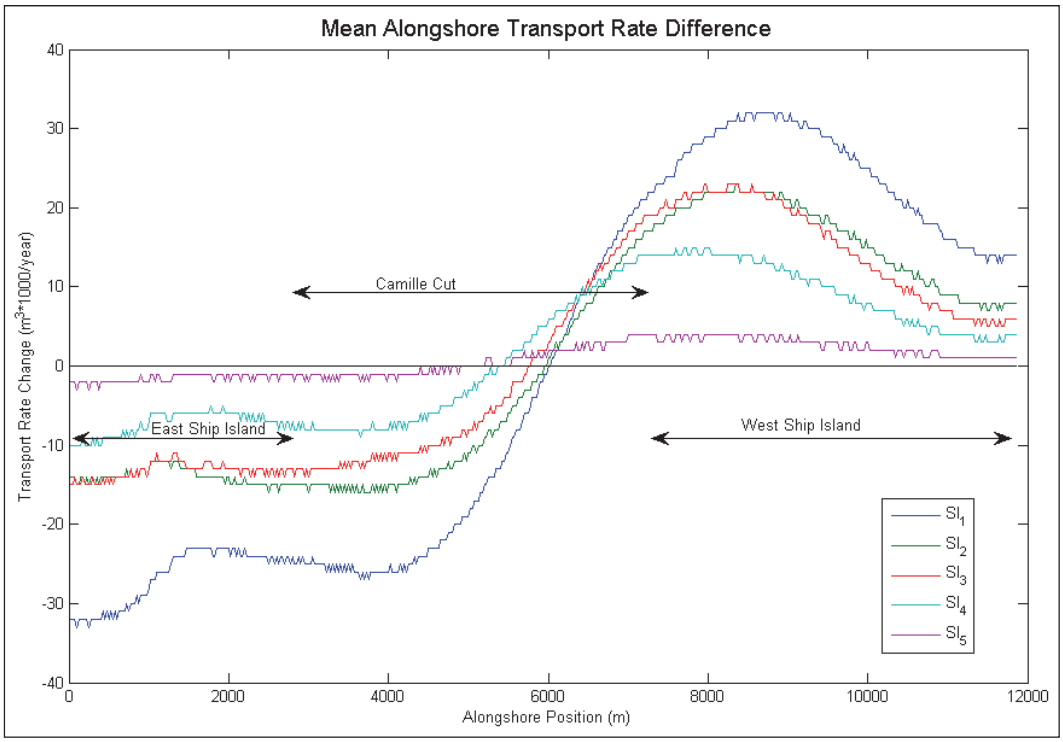

8.2.4 Summary

Potential impacts of excavation of nearshore borrow areas for the proposed restoration projects on Ship Island were assessed with spectral nearshore wave transformation model STWAVE and shoreline change model GENESIS. Wave conditions from WIS hindcast database for WIS Station GOM 144 were transformed from the 15-m contour to the 12-m contour to provide wave data for the offshore portion of the STWAVE grid using a WIS Phase III transformation. STWAVE simulations were performed for both Existing and Dredged condition to obtain estimates of nearshore wave conditions landward of the borrow areas and to enable a comparative analysis aimed at quantifying potential borrow area impacts on shoreline processes along the restored Ship Island shoreline. Potential effects of the proposed borrow areas SI1, SI2, SI3, SI4, and SI5 on nearshore wave conditions were quantified by examination of the change in nearshore wave height and direction landward of each potential borrow area alternative. STWAVE results show an increase in wave heights in the area of the Camille Cut closure due to refraction caused by the borrow areas focusing wave energy. The wave height increase was within ten percent for the short period waves but for longer period waves the focusing caused increased wave heights of over 10 percent for SI2, SI3, and SI4 compared to 20 percent for SI1. SI5 minimized the wave height increase to about 2.0 percent. The STWAVE results were applied as input to GENESIS to quantify the influence of the borrow areas on shoreline processes. Longshore sand transport rates were calibrated with typical values for K1 and K2 of 0.4 and 0.2, respectively and to produce transport rates consistent with sediment budget estimates (Byrnes et al. 2011). The borrow areas were shown to increase erosion over much of the Camille Cut closure area. The magnitude of the increased erosion reaches 68-m for SI1, 48-m around the Camille Cut over the 20-year period of analysis for the SI2 and SI3, 28-m for SI4, and 5.0-m for SI5. The western portion of West Ship Island is expected to prograde compared to the existing condition for SI1-SI4 with a maximum increase of 27-m with SI1, 21-m with SI2, 24-m with SI3, and 14-m with SI3. SI5 causes increased erosion of about 2-m.

8.3 Horn Island

A proposed borrow area for the Ship Island restoration is located to the southeast of Horn Island in an ambient water depth of 12-m. The borrow area reaches a cut depth of 10-m spanning an area 1300-m wide by 1600-m long. The proposed area's proximity to Horn Island creates potential

adverse affects on the shoreline of Horn Island due to the wave refraction over the excavated pit. This chapter details an analysis conducted to quantify the potential impacts of the borrow area excavation (for beach nourishment) on sediment transport and shoreline change at Cat Island.

8.3.1 Model setup

The STWAVE grid domain and the location of the borrow pit relative to Horn Island is shown in Figure 8-22. The analysis involved simulating the transformation of offshore wave conditions gathered from WIS Station 144 from the 16-m contour to the 14-m contour with the WISPH III transformation technique. The transformed wave information corresponds to the offshore boundary of the STWAVE grid with the *X*-axis directed onshore, and the *Y*-axis parallel with the Horn shoreline. The resolution of the STWAVE grid is 25 m in both the *x* and the *y* directions. Nearshore wave conditions generated by STWAVE along the nominal 5.0-m contour for both the Existing and Dredged condition provided necessary input to GENESIS, which estimates longshore sand transport rates and shoreline change along the shoreline of Horn Island.

Figure 8-22. STWAVE grid domain with location of borrow area.

The GENESIS *X*-axis runs parallel to the Gulf shoreline of Horn Island from east to west and is comprised of 391 shoreline cells at 25-m intervals. Because detailed calibration data are not available for this study, the calibration coefficients were assigned typical values of K1=0.10 and K2=0.05. These calibration values are typical of those applied in previous studies that employed WIS hindcast wave information as input and produced longshore sand transport rates that are in general agreement with

the Horn Island sediment budget.(Byrnes et al. 2011) Because this study is a relative analysis between with and without an excavated borrow area, aimed at estimating the potential shoreline impacts of proposed dredging of the near shore borrow area, the importance of a detailed calibration is diminished. The existing bathymetry is shown in Figure 8-23 and bathymetry change between with and without the borrow pit is plotted in Figure 8-24 to highlight the borrow pit configuration. The near shore wave reference line (where the STWAVE information is stored and transferred to the GENESIS model) is represented by a thick black line in both figures.

8.3.2 Wave transformation analysis

Near shore wave transformation simulations were performed for 162 representative wave conditions identified through analysis of WIS hindcast station GOM 144 located in 15 m water depth offshore of Cat Island. Figure 8-25 shows the distribution of the wave conditions by incident wave angle and period. The incident wave angle is measured clockwise from shore normal. The value in each block is the number of occurrences of that wave condition in the 20-yr WIS hindcast spanning the interval 1980 through 1999. For each representative wave condition an idealized TMA wave spectrum was generated and applied as the input to STWAVE.

Figure 8-23. Existing bathymetry.

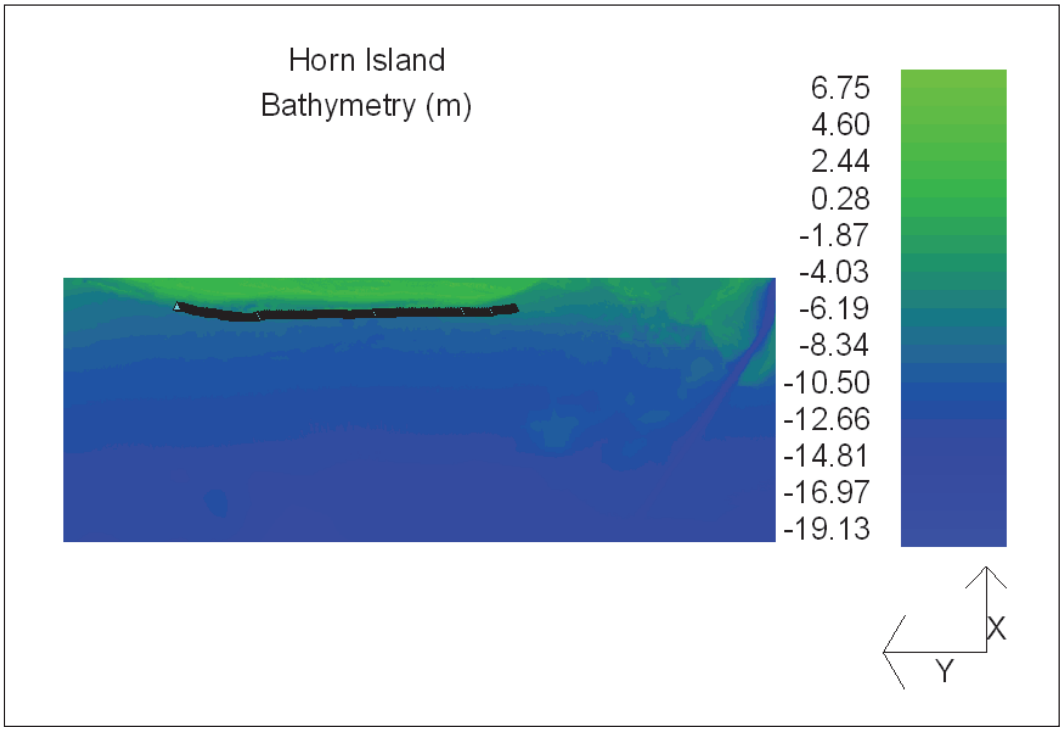

Figure 8-24. Existing condition bathymetry minus dredged condition bathymetry.

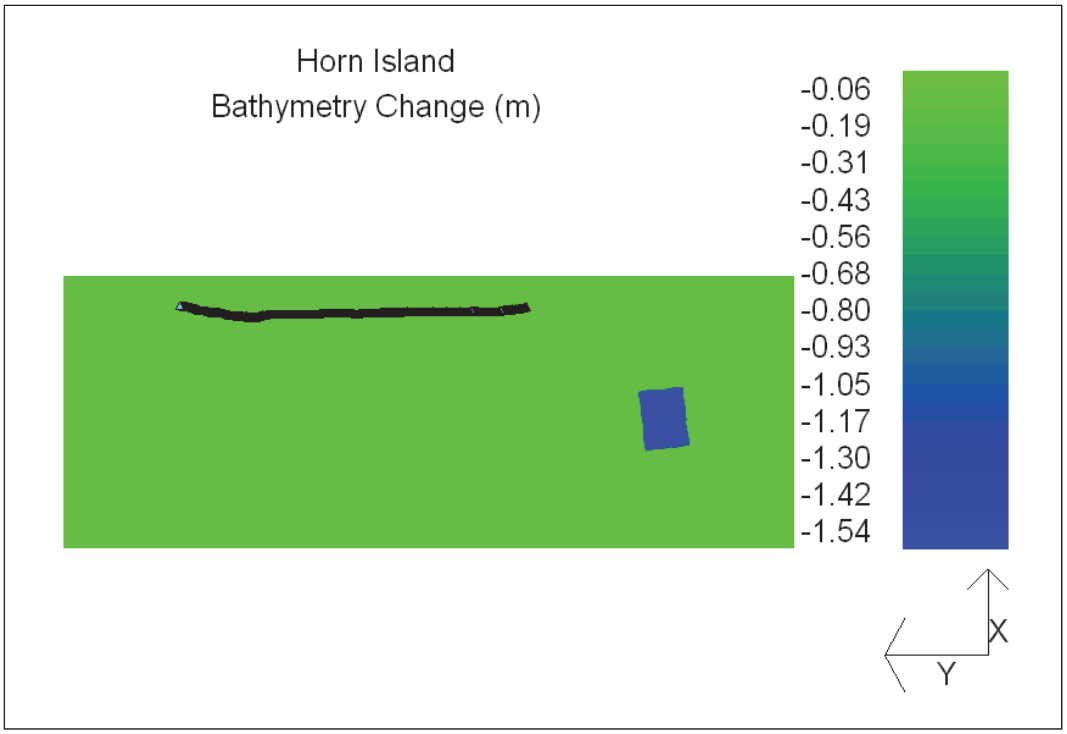

Figure 8-25. Distribution of the representative wave conditions by incident wave angle and period.

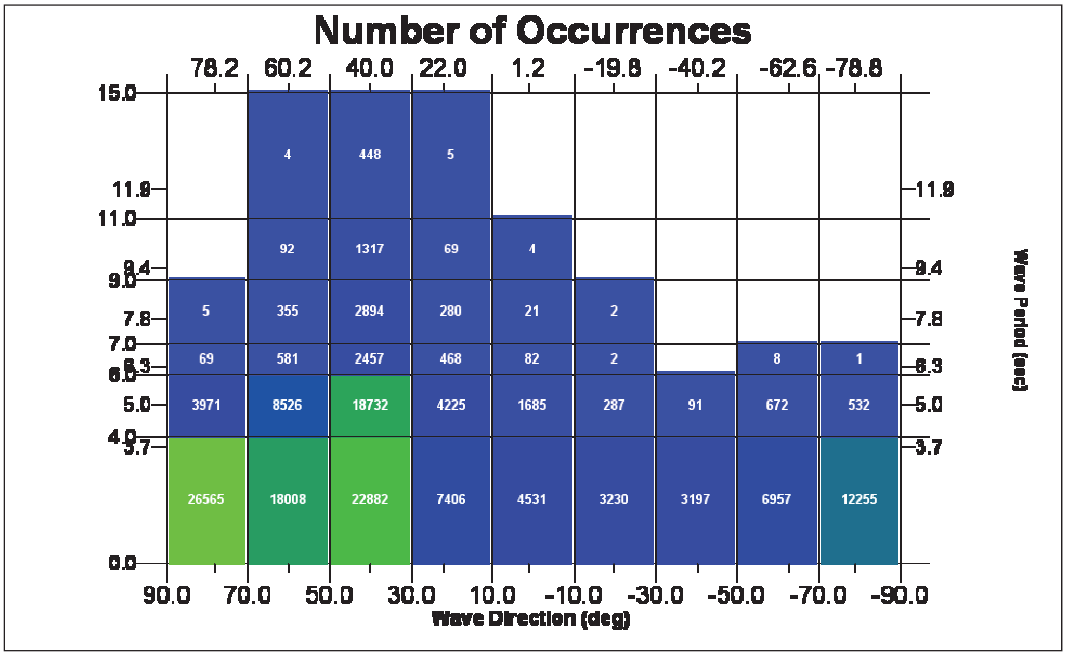

STWAVE simulations were performed to compute wave transformation across the irregular offshore bathymetry from approximately the 14-m contour to the 5.0-m contour. Two sets of STWAVE simulations were performed to estimate near shore wave conditions for both the existing and

dredged conditions. The change in significant wave height and direction resulting from excavation of the proposed borrow area was determined through subtracting the existing condition STWAVE results from the dredged condition STWAVE results. Figures 8-26 through 8-29 are the estimated significant wave height changes induced by excavation of the borrow area offshore of Horn Island for select characteristic wave conditions. These changes are calculated by subtracting the wave heights found for the existing condition from the wave heights for the dredged condition for each wave state. Figure 8-24 corresponds to typical 3.70 second waves approaching Horn Island from the southeast. Figures 8-27 through 8-29 correspond to long period waves approaching Horn Island from the south-southeast sector. For the longer period waves, wave heights decrease in the lee of the borrow area as the waves pass over the borrow areas. Wave heights tend to increase along the sides of the borrow areas in the down-wave direction for longer period wave events but breaking occurs before the waves reach the GENESIS save stations. Figure 8-30 demonstrates the percentage change in wave heights at the save stations. For both short and long period waves, minimal impact is felt along the GENESIS save stations. For short wave period events, the depth of the borrow area decreases its impact to the point that the wave conditions are virtually identical before and after dredging.

Figure 8-26. Wave height change (dredged – existing) for incident wave of *H* = 1.22 m, *T* = 3.70 sec and *Theta* = 21.92 deg.

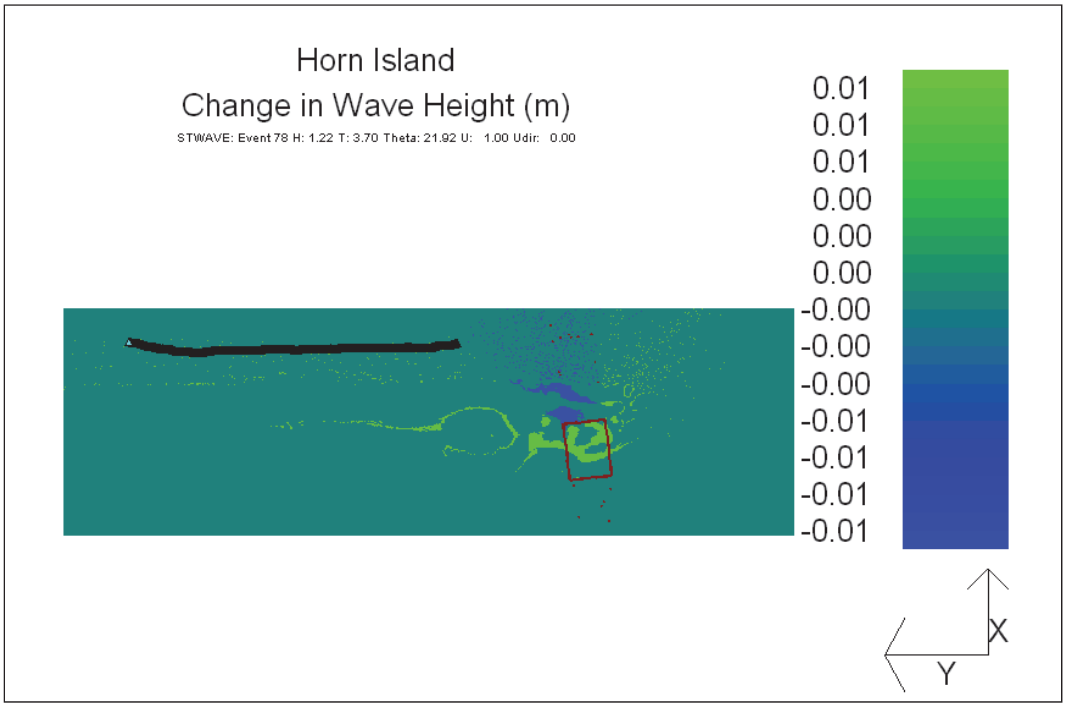

Figure 8-27. Wave height change (dredged – existing) for incident wave of *H* = 2.91 m, *T* = 7.69 ecs and *Theta* = 38.50 deg.

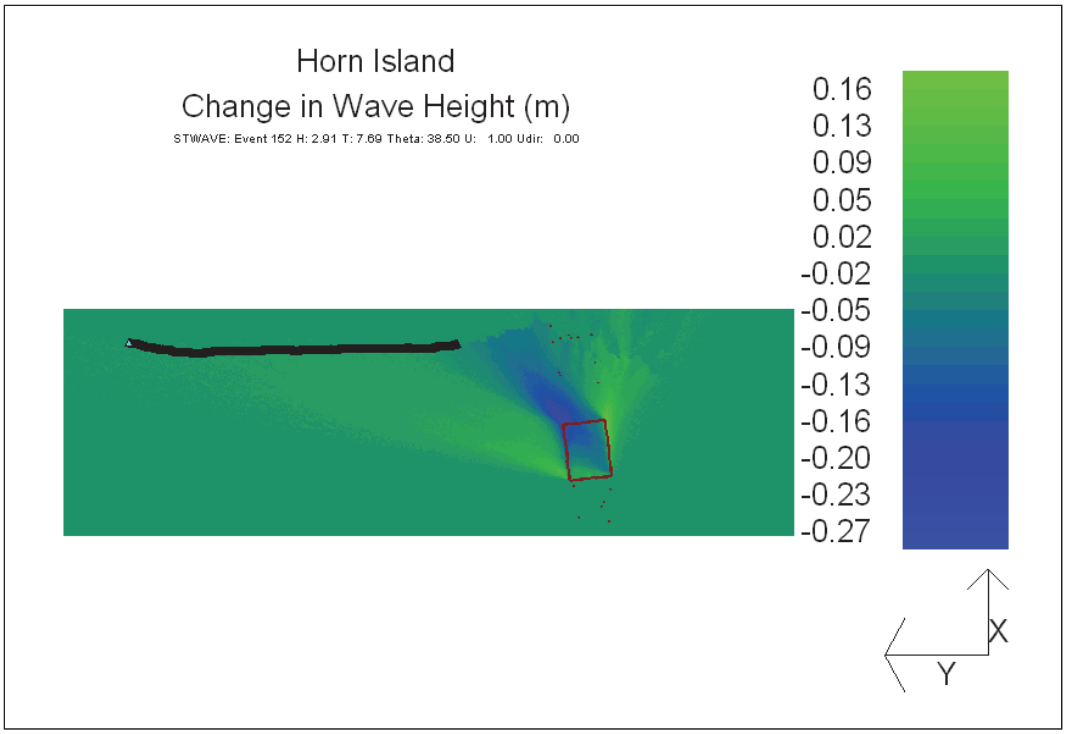

Figure 8-28. Wave height change (dredged – existing) for incident wave of *H* = 2.72 m, *T* = 9.09 sec and *Theta* = 53.43 deg.

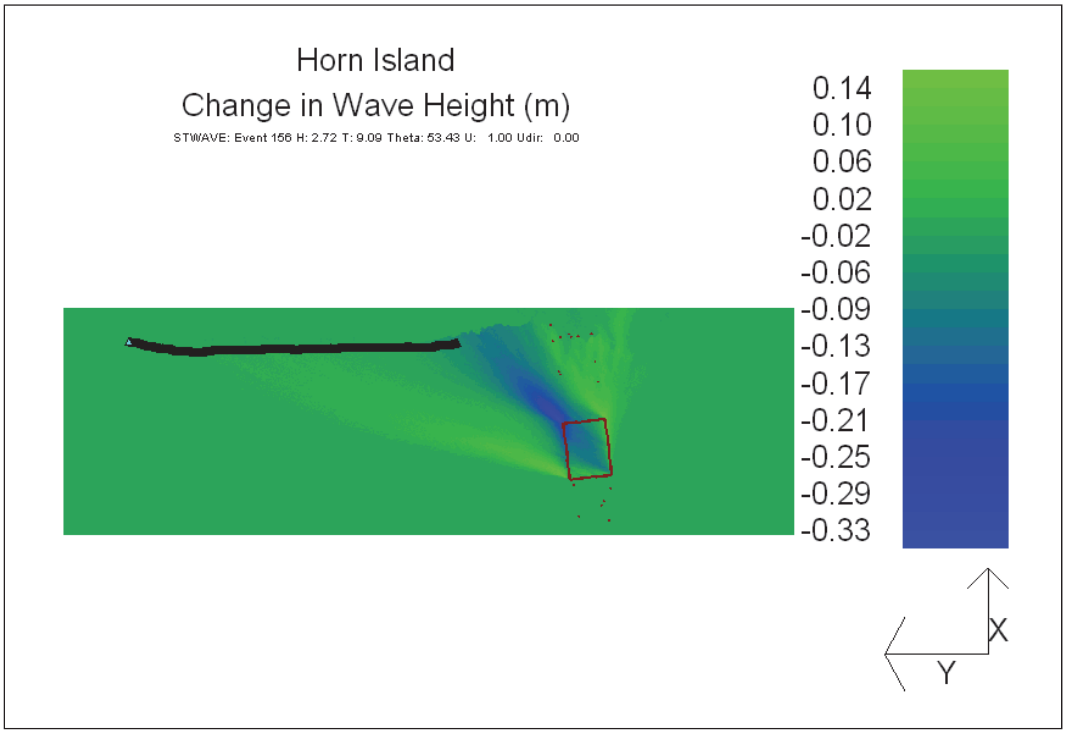

Figure 8-29. Wave height change (dredged – existing) for incident wave of *H* = 4.91 m, *T* = 11.11 sec and *Theta* = 39.94 deg.

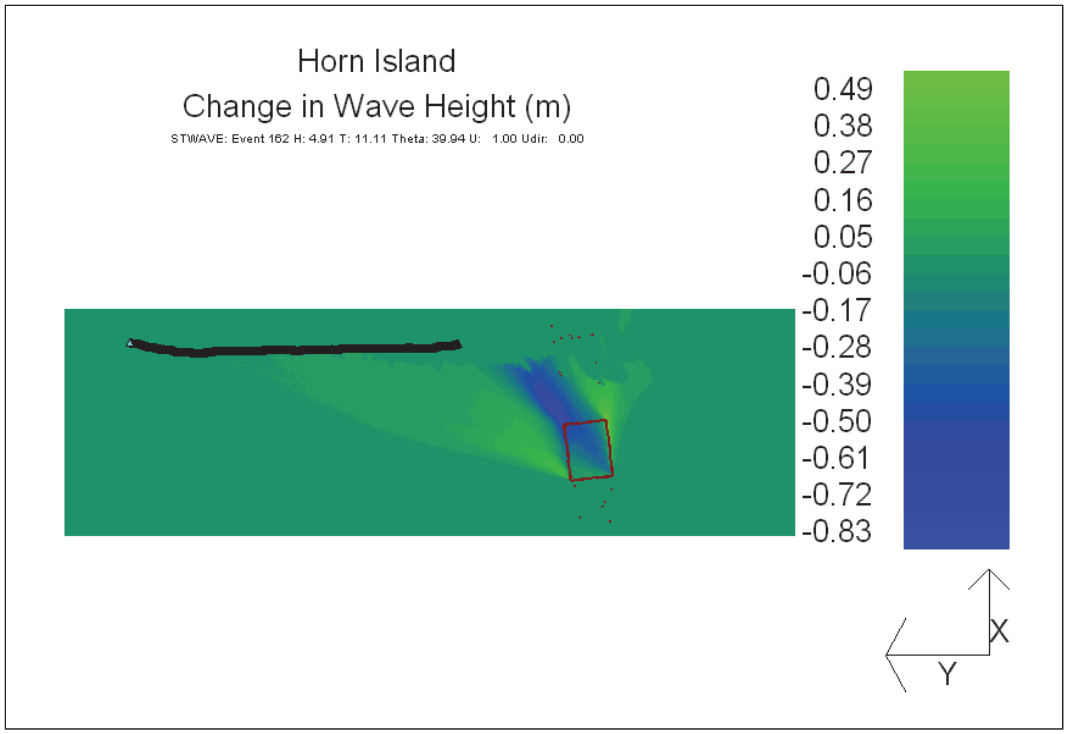

Figure 8-30. Percent wave height change at GENESIS stations.

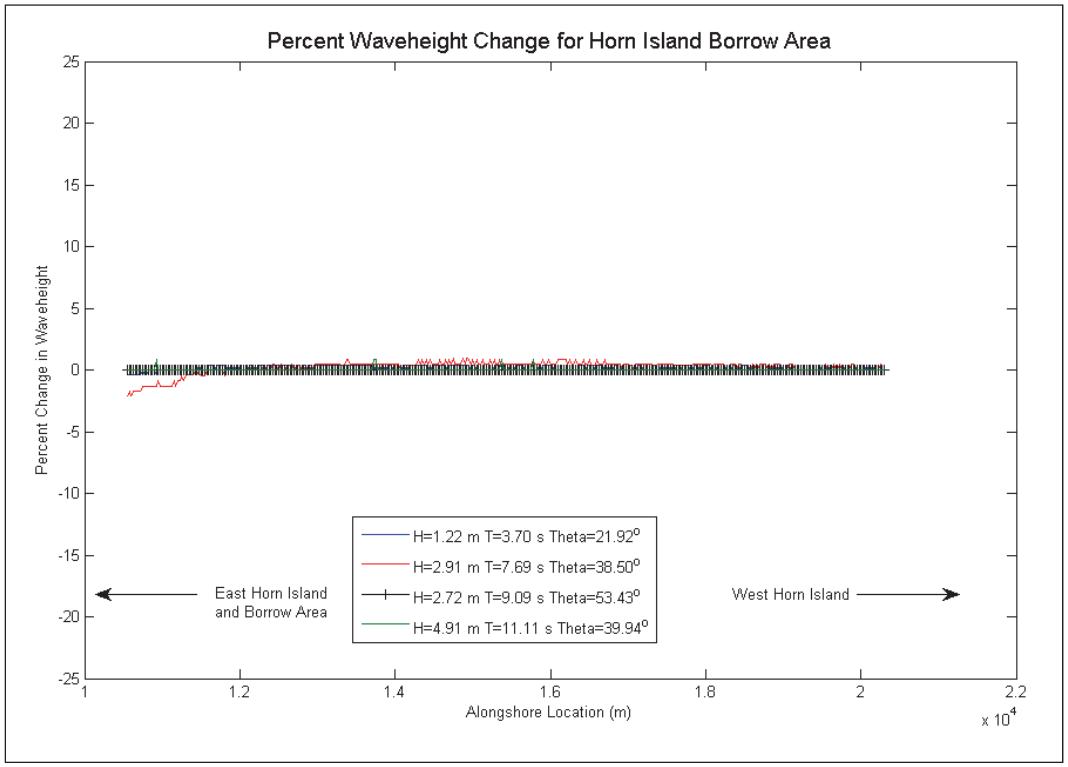

8.3.3 Sediment transport and shoreline change

A GENESIS model domain was generated for examining the influence of the borrow area on shoreline processes along the Horn Island shoreline. The model domain is 4.25 km (2.64 miles) long and the initial shoreline position was developed from the existing Gulf shorelines of Horn Island.

The wave conditions determined through the STWAVE simulations for both the dredged and existing condition were applied as input to GENESIS to estimate longshore sand transport rates and shoreline change. The GENESIS simulations were run for the 20-year WIS hindcast offshore wave time-series (1980-1999). Figure 8-30 displays the estimated final shoreline position for both the existing and dredged condition as well as the initial shoreline position. The dredged condition shows negligible change in erosion over the 20-year simulation interval as compared to the existing condition. The final shoreline show negligible difference between the dredged and existing cases. Figure 8-31 plots the shoreline change over 20 years for both conditions. Negative values indicate erosion and positive values indicate accretion. Figure 8-32 plots the difference, or change, in the estimated shoreline change rates between the existing and dredged condition for each point on the GENESIS axis. This plot indicates that the dredged bathymetry causes minimal changes in shoreline change rates over the 20 year period. The greatest difference in the shoreline change rates is a reduction in predicted shoreline advance by approximately 0.1 m per year (Figure 8-33). Estimated increases in predicted shoreline recession are less than 0.05 m per year.

8.3.4 Summary

The impacts of excavating a borrow area offshore of Horn Island for the proposed restoration project at Ship Island were assessed with the spectral near shore wave transformation model STWAVE and the shoreline change model GENESIS. Wave conditions from the WIS hindcast database for WIS Station GOM 144 were transformed from the 16 m contour to the 14 m contour to provide wave data for the offshore portion of the STWAVE grid using a WIS Phase III transformation. STWAVE simulations were performed for both the existing and dredged condition to obtain estimates of nearshore wave conditions landward of the borrow area and to enable a comparative analysis aimed at quantifying the borrow area impacts on shoreline processes along the Horn Island Gulf shoreline. The effects of the proposed borrow areas on nearshore wave conditions were quantified by

Figure 8-31. Comparison of existing and dredged condition estimated final shoreline after 20 years.

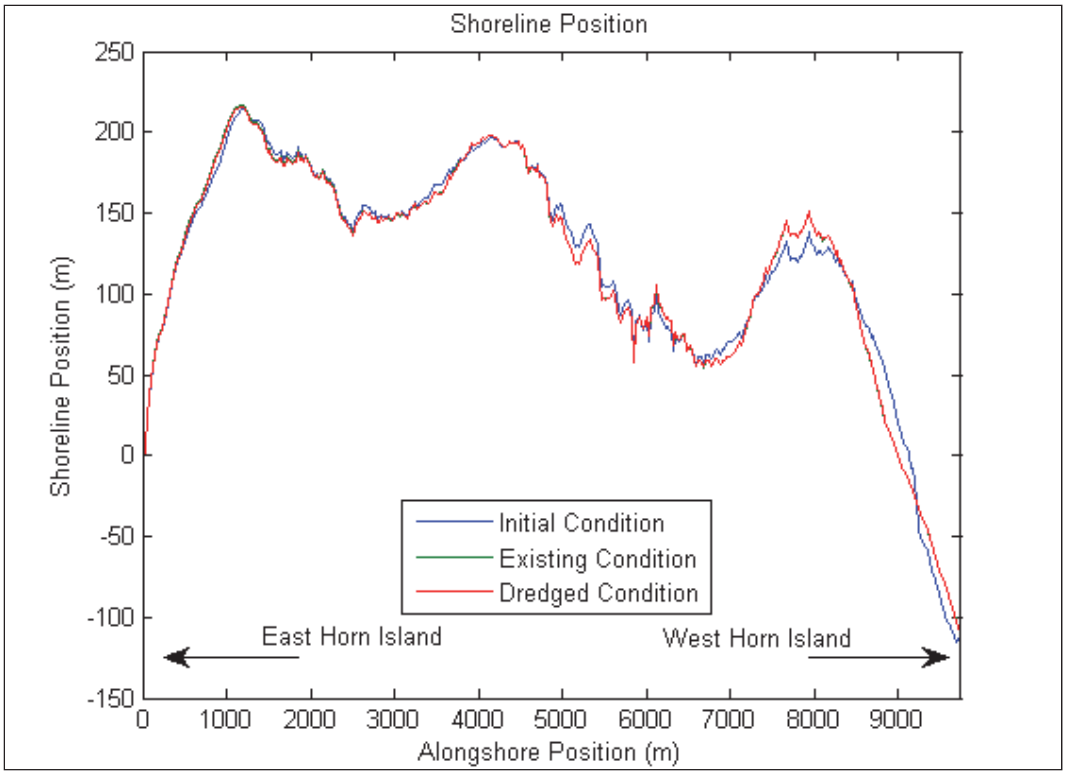

Figure 8-32. Comparison of existing and dredged condition shoreline change for the 20-year simulation period.

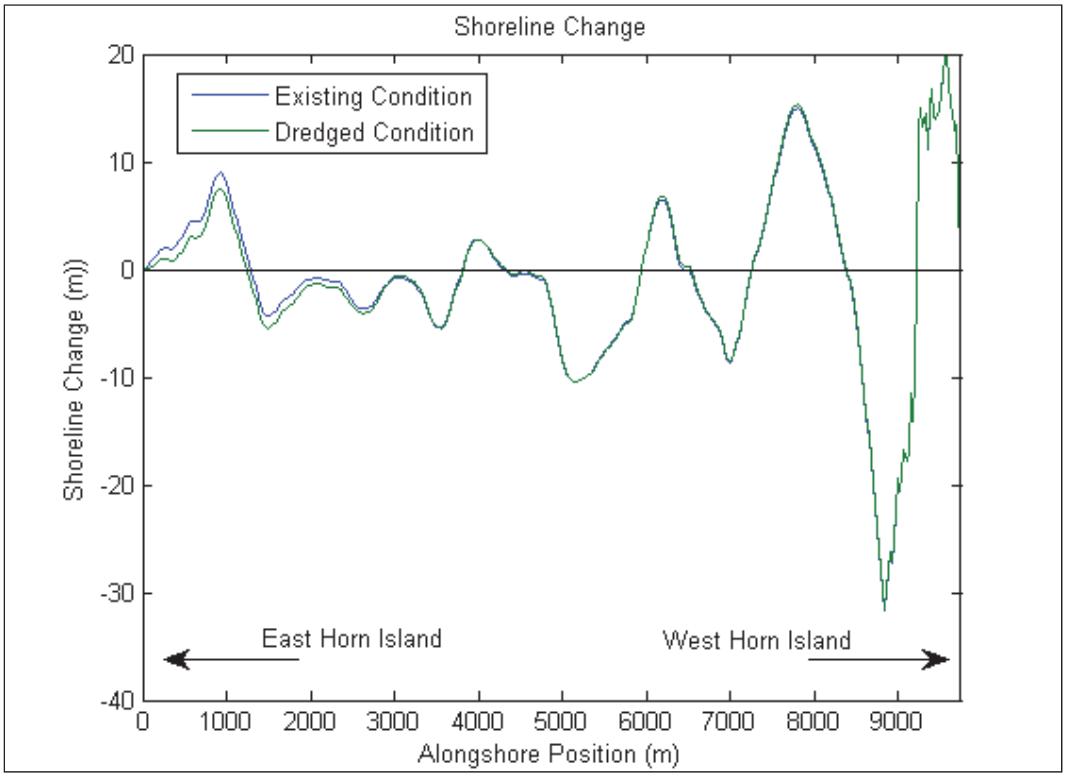

examination of the change in nearshore wave height and direction landward of the borrow area. The STWAVE results show minimal increases in wave heights surrounding the borrow area with little affect on the GENESIS save stations. The STWAVE results were applied as input to GENESIS to quantify the influence of the borrow areas on shoreline processes. A sensitivity analysis was conducted, comparing results for both the existing and dredged (restored) conditions. Longshore sand transport rates were calibrated with typical values for K1 and K2 of 0.10 and 0.05, respectively, and produced transport rates consistent with sediment budget estimates. The proposed borrow area was shown to have minimal impact on shoreline change rates over the entirety of Horn Island. The maximum magnitude of change reduces predicted shoreline advance by about 1.5 m for the 20-year period of analysis. The greatest increase in erosion is approximately 1.0 m over 20 years. The western portion of Horn Island is expected to slightly prograde as a result of the project.

Figure 8-33. Dredging induced change in shoreline change rate.

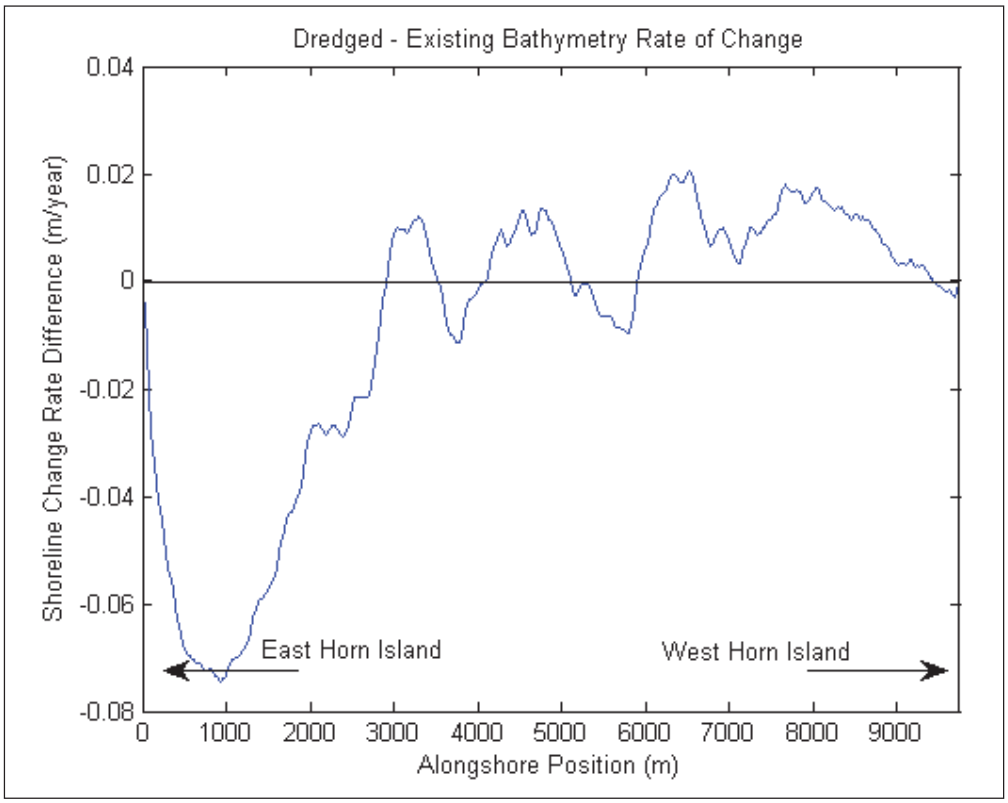

8.4 Petit Bois borrow area analysis

This chapter discusses two configurations for a proposed borrow site located on the seaward side of Petit Bois Inlet, which is between Petit Bois

Island and Dauphin Island in the northern Gulf of Mexico (Figure 8-1). The borrow site would supply sand for a shoreline restoration project on Ship Island. The two borrow site configurations broadly overlap, as shown in Figures 8-35a through 8-35c. Both are approximately 9000 ft (2700 m) southwest of West Dauphin Island in a nominal water depth of 30 ft (9.0 m).

The design for the first configuration calls for the removal of the top 8.0 feet of material from the site. The second configuration divides the site into 10 sub-areas, with each sub-area being dredged to a different depth, as shown in Table 8-34. Figure 8-35c shows how the first configuration (in brown) overlaps the second (multi-colored).

Because of the proposed borrow area's proximity to Dauphin Island, there is a potential for adverse shoreline impacts due to changes in wave refraction over the excavated pit. This chapter describes the analysis conducted to examine the impacts of the dredged borrow area on sediment transport and shoreline change along the west end of West Dauphin Island.

8.4.1 Model setup

The shoreline and littoral transport impacts induced by the excavation of proposed borrow areas were examined with the spectral near shore wave transformation model STWAVE (Smith et al. 1999) and the shoreline change model GENESIS (Hanson and Kraus 1989). The location of the STWAVE model domain, the borrow sites, and the hindcast WIS wave station are illustrated in Figures 8-35a and 8-35b. Figures 8-36a and 8-36b show a more detailed view of the bathymetry (north is approximately to the right in these figures), along with the West Dauphin Island shoreline (orange), the western portion of West Dauphin Island (yellow), the STWAVE save station line (light blue), and the line of the GENESIS grid (black) along the right edge of the figure. The borrow areas are shown incised into the bathymetry.

The analysis involved simulating the transformation of hindcast offshore wave conditions at WIS Station 73150 (Figures 8-35a and 8-35b) from the 20-m contour to the 19.5-m contour using the WIS Phase III transformation technique. The transformed wave information corresponds to the offshore boundary of the STWAVE grid. The area shown in Figures 8-36 is the model domain used for the STWAVE simulations. The STWAVE *X*-axis is directed onshore (357 deg); the *Y*-axis is directed alongshore and is aligned roughly

Figure 8-34. Location map in northern Gulf of Mexico.

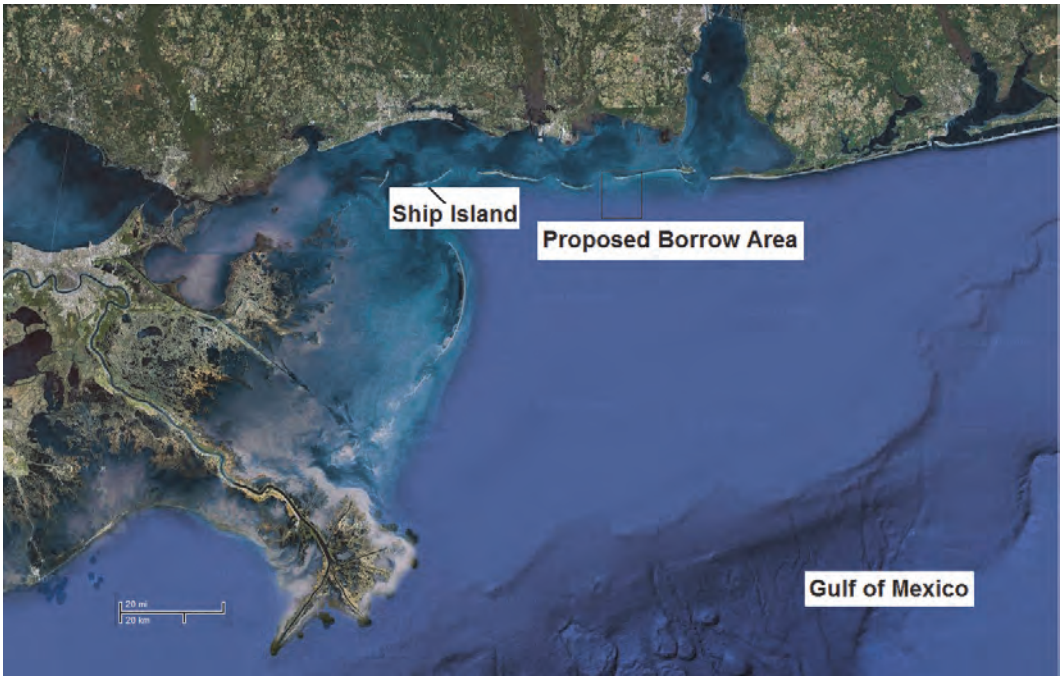

Figure 8-35a. STWAVE grid and borrow site Configuration 1.

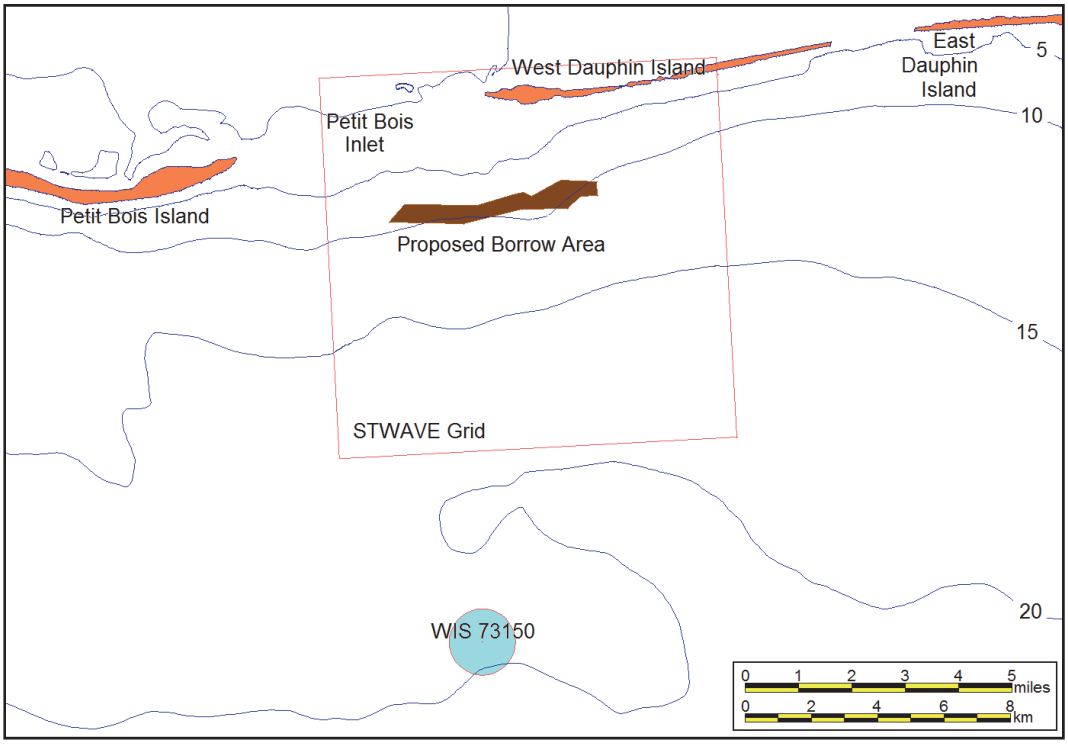

Figure 8-35b. STWAVE grid and borrow site Configuration 2.

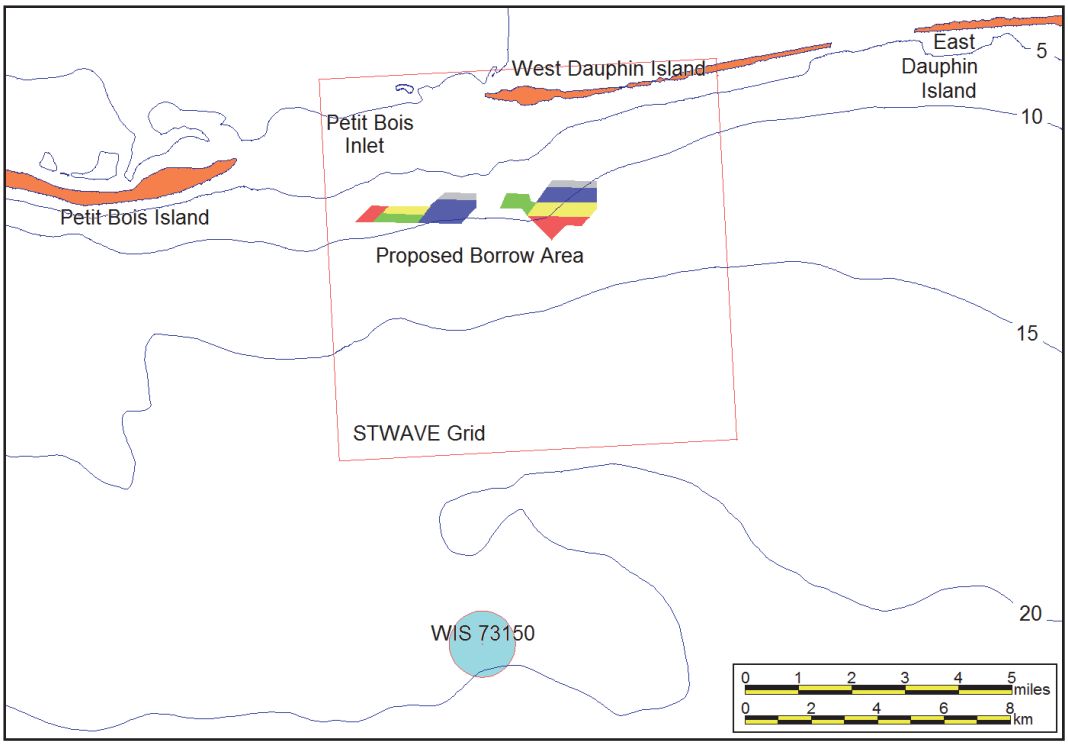

Figure 8-35c. Comparison of borrow site Configurations 1 and 2.

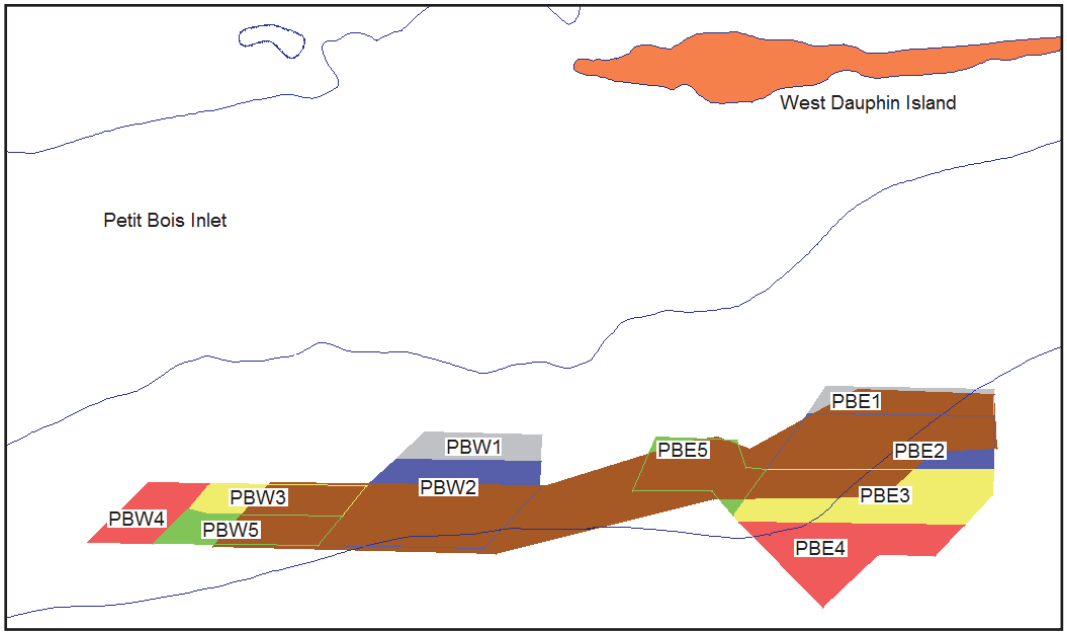

Figure 8-36a. Configuration 1 dredged bathymetry. Depth in meters.

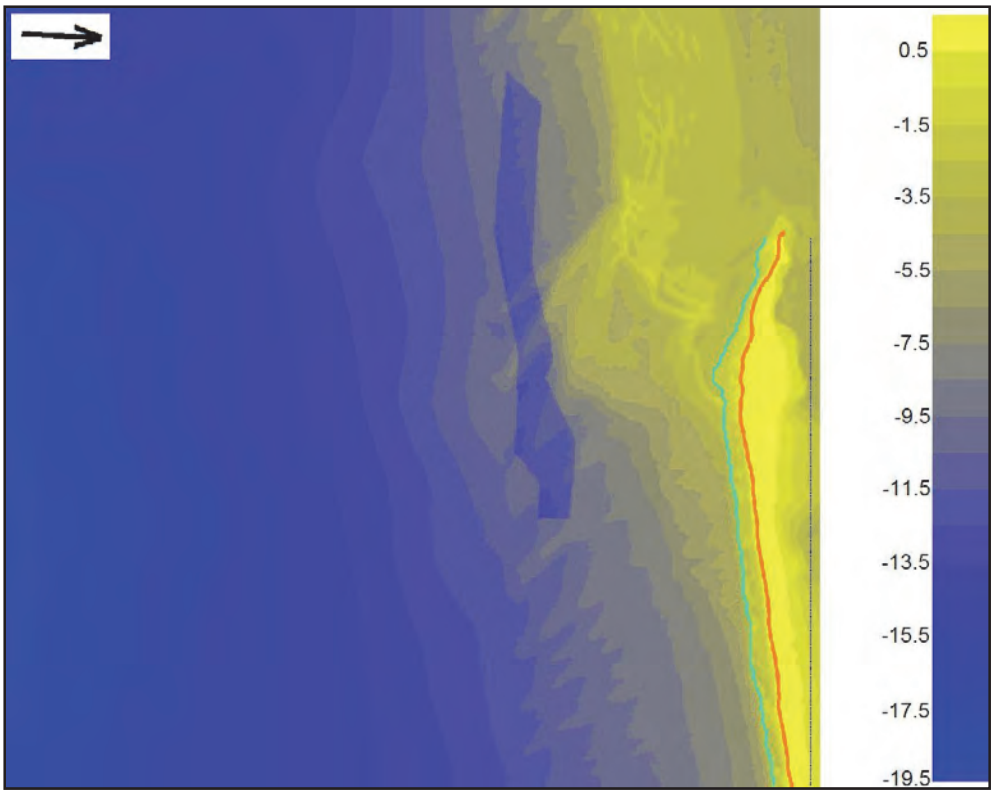

Figure 8-36b. Configuration 2 dredged bathymetry. Depth in meters.

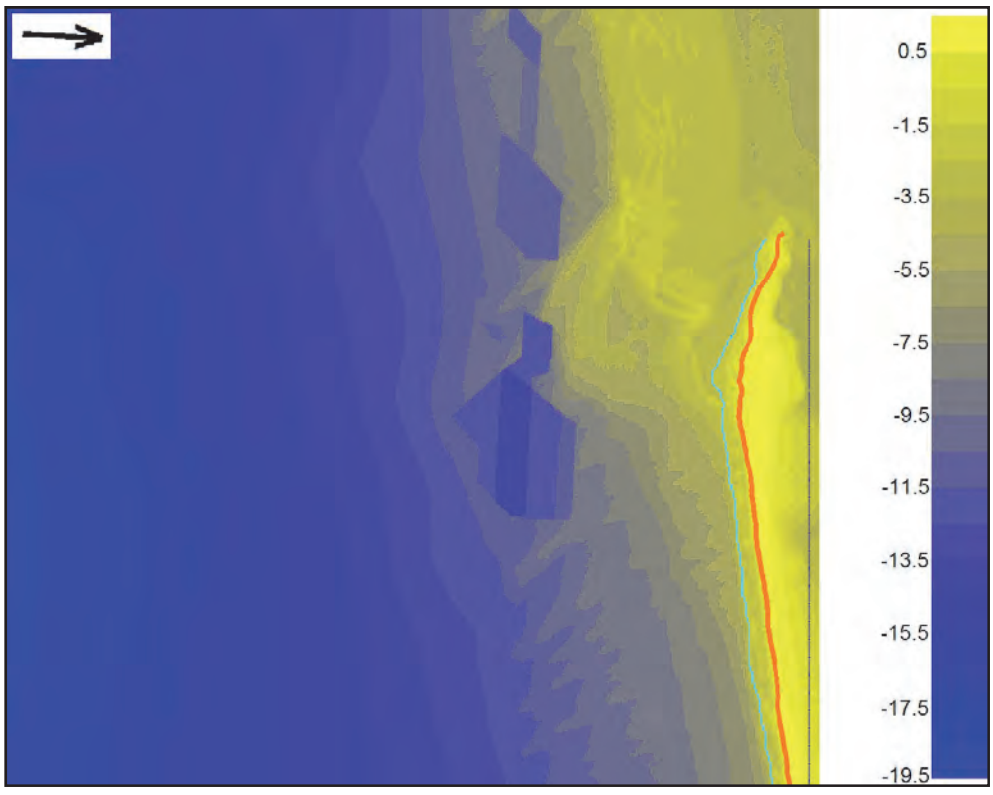

Table 8-1. Borrow site dredge depths.

Configuration 1		
Figure 8-2 color: Brown		
Dredge elevation: 8 ft below ambient.		
Configuration 2		
Sub-area	Figure 8-2 color	Dredge elevation (ft)
PBE1	Gray	-37
PB32	Blue	-42
PBE3	Yellow	-48
PBE4	Red	-42
PBE5	Green	-40
PBW1	Gray	-33
PBW2	Blue	-38
PBW3	Yellow	-34
PBW4	Red	-37
PBW5	Green	-32

parallel with the West Dauphin Island shoreline. The resolution of the STWAVE computational grid is 25 m in both the *X* and *Y* directions. Estimates of nearshore wave conditions generated by STWAVE along the nominal 3.1-m contour for both the existing and dredged condition provided necessary input to GENESIS, which estimates longshore sand transport rates and shoreline change along the western portion of the Gulf of Mexico shoreline of West Dauphin Island.

The GENESIS *X*-axis runs parallel to the West Dauphin Island shoreline and is comprised of 309 shoreline cells at 25 m intervals. Because detailed calibration data are not available for this study, the GENESIS calibration coefficients were assigned default values of K1 = 0.4 and K2 = 0.2. These calibration values are typical of those applied in other studies discussed in this report and produced longshore sand transport rates that are in general agreement with the Dauphin Island sediment budget. Because this study is a relative analysis between with and without excavated borrow areas, aimed at estimating the potential shoreline impacts of proposed dredging of the nearshore borrow area, the importance of a detailed calibration is diminished.

8.4.2 Wave transformation analysis

Wave data were obtained from WIS station 73150, whose location is shown in Figures 8-35a and 8-35b. The predominant direction of wave approach at this site is from the southeast, as seen in the Figure 8-37 wave rose. (This figure shows the compass direction that the waves are coming from.) As seen from Figure 8-34, land masses block all waves, except low energy, locally generated waves, from most other directions. Nearshore wave transformation simulations were performed for 213 representative wave conditions identified through analysis of the WIS hindcast data. Figure 8-38 shows the distribution of representative wave conditions by incident wave angle and height. The incident wave angle is measured clockwise from shore normal. Wave direction data in this figure are referenced to the local shore normal direction of 177 deg azimuth. Positive wave angles are those approaching the coast from the southeast (from the left for a person standing on the beach looking offshore). The value in each block is the number of occurrences of that wave condition in the 20-year WIS hindcast spanning the interval 1980 through 1999. Figure 8-39 shows the distribution of wave conditions by height and period, and Figure 8-40, by angle and period. Figure 8-41 shows a histogram of heights, periods, and directions. For each of the 213 representative wave conditions, an idealized TMA wave spectrum was generated and applied as the input to STWAVE.

STWAVE simulations were performed to compute wave transformation across the irregular offshore bathymetry from approximately the 19.5-m contour to the 3.1-m contour. Three simulations were run. The first employed existing bathymetry and the second and third used the bathymetry that would result from the two post-dredging configurations.

Figure 8-42 is a plot of wave heights over the STWAVE computational domain for the existing bathymetry for a 5.0 sec wave with an offshore height of 0.8 m and an angle of 40 degrees. In this figure, wave heights are shown by colors from blue to yellow and wave directions by black arrows. Also, West Dauphin Island is in gold, with its shoreline in orange, offshore contours are in brown, the STWAVE save stations are the blue-green line near the shoreline, and the GENESIS baseline is the black line across the top (right) of the figure. Note the complex changes in wave height over the large shoal area near the western tip of the island.

Figure 8-37. WIS Station 73150 wave rose.

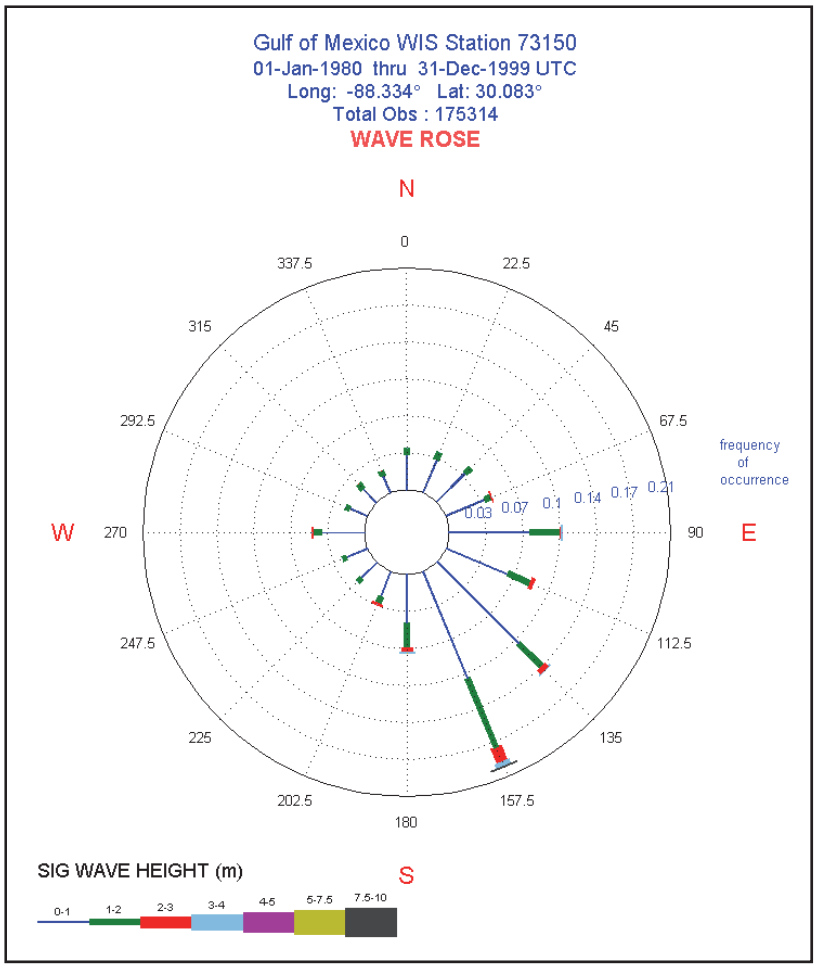

Figure 8-38. Distribution of the representative wave conditions by incident wave angle and height.

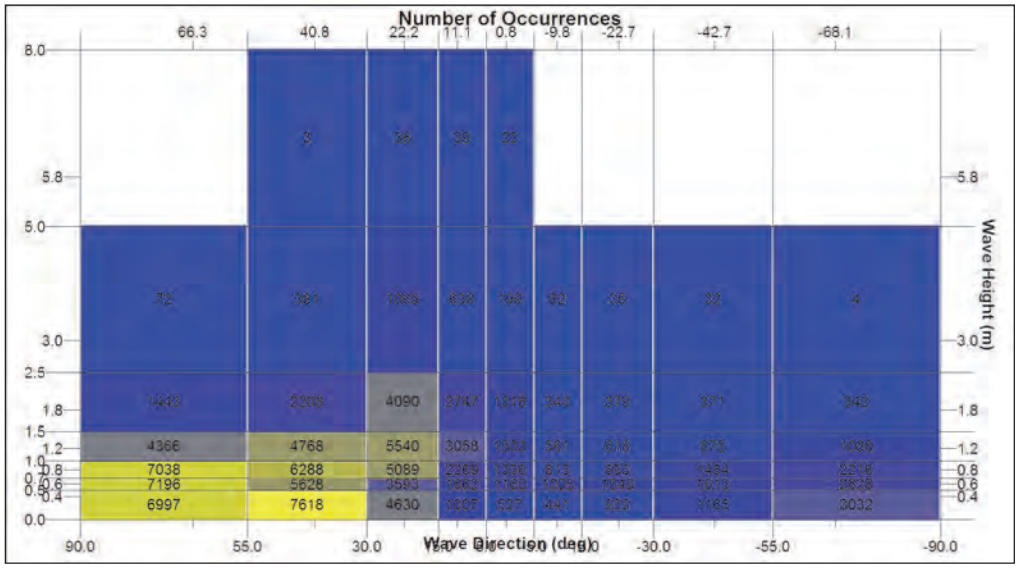

Figure 8-39. Distribution of the representative wave conditions by incident wave height and period.

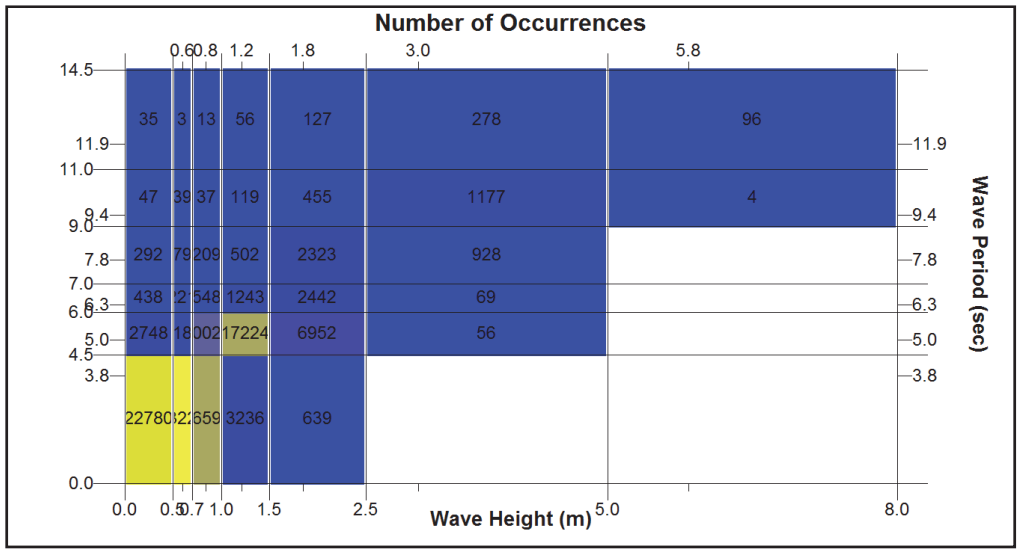

Figure 8-40. Distribution of the representative wave conditions by incident wave angle and period.

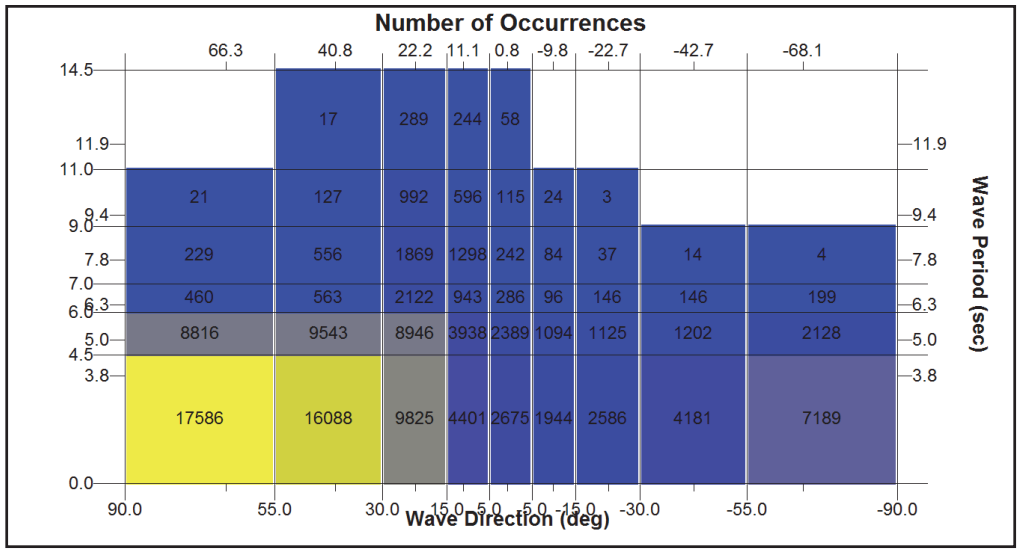

Figures 8-43 through 8-57 illustrate the effects of wave refraction over the first configuration borrow site using five example wave conditions. Figure 8-43 shows estimated significant wave height changes induced by excavation of the borrow area for a 0.8 m, 5.0 sec incident wave for three incident wave angles. The wave height changes are calculated by subtracting the existing condition wave heights from the first configuration dredged condition wave heights. The portion of the borrow area seaward of the dredged site is not shown in these figures as no differences occur there. Figure 8-43, Panel A shows height differences for the same wave condition

illustrated in Figure 8-42. As discussed above, the 20-year wave record was divided into 213 wave height-wave period-wave angle bins. The three bins shown in Figure 8-10 are representative of wave conditions that occur 1.23, 0.26, and 0.08 percent of the time, respectively.

Figure 8-41. Histogram of wave heights, periods, and directions.

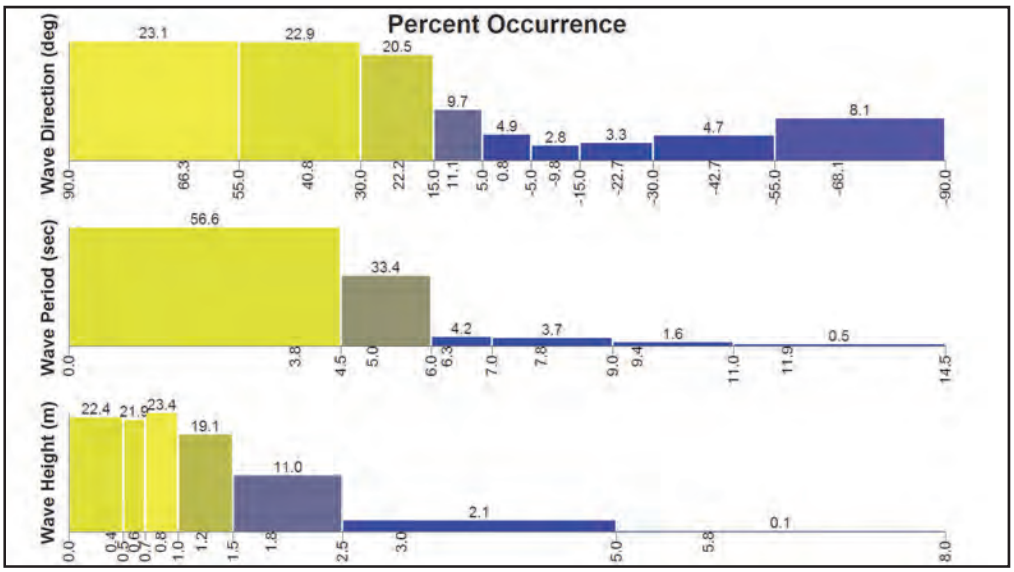

Figure 8-42. Existing condition wave heights for incident wave of *H* = 0.83 m, *T* = 5 sec and *Theta* = 40 deg.

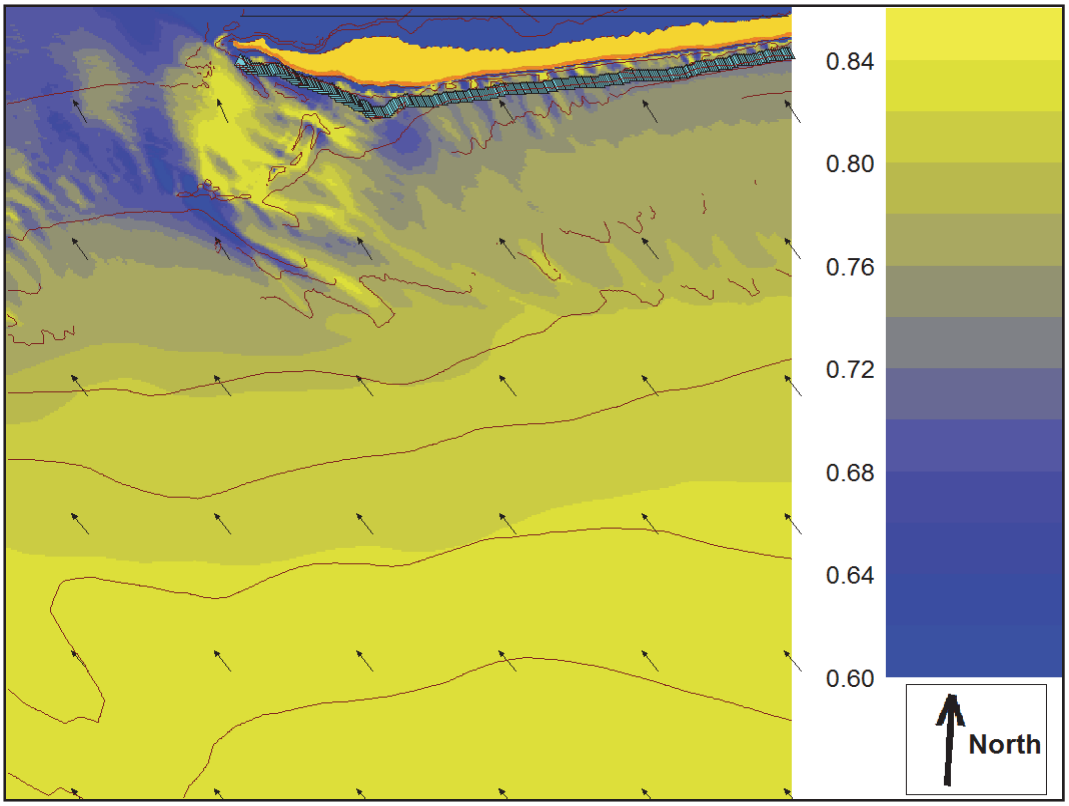

Figure 8-43. Wave height change (dredged – existing) for incident wave of H = 0.8 m, T = 5.0 sec.

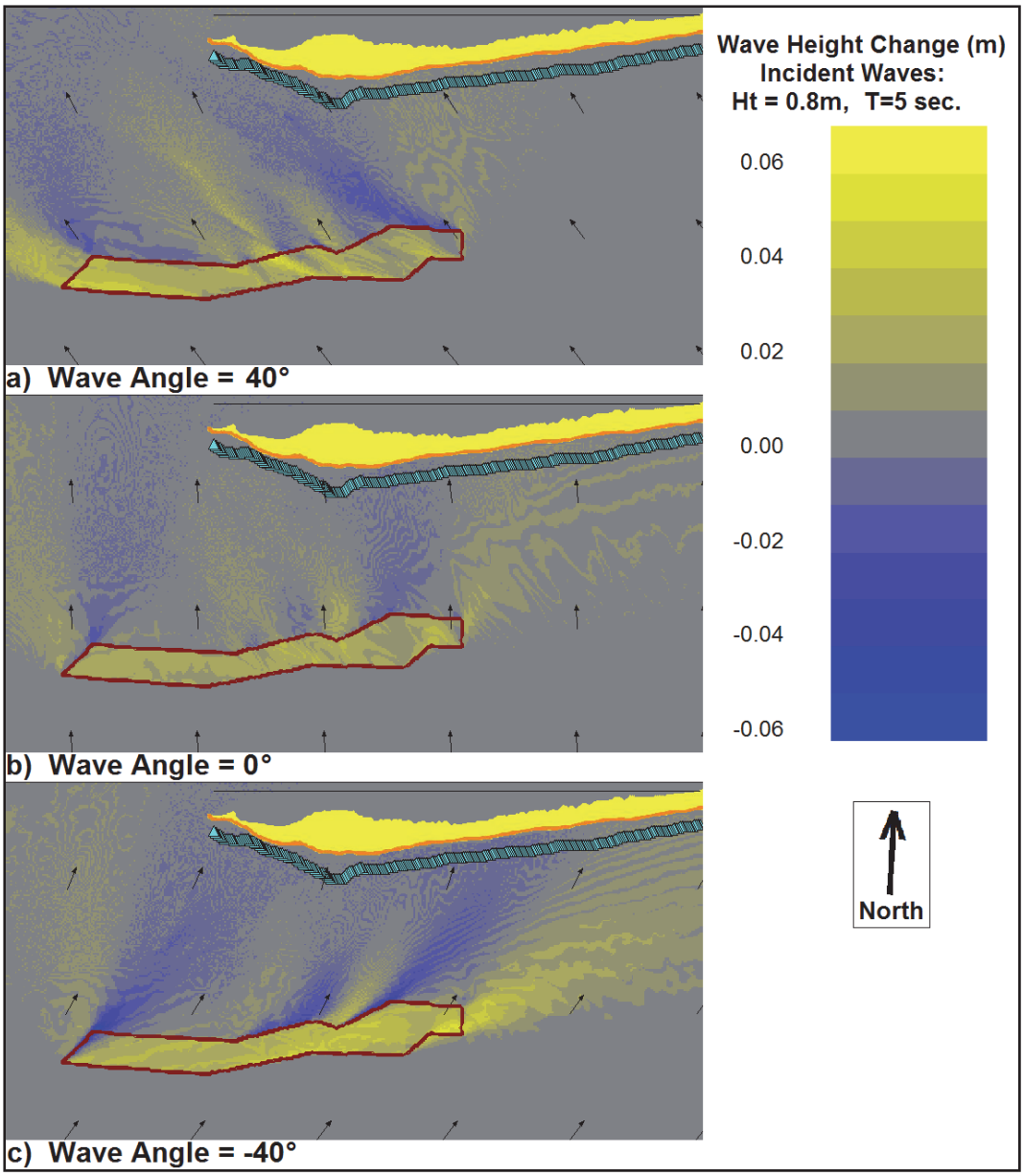

Figure 8-44 shows height differences for larger 3.0 m, 11 sec waves. These rarer conditions occurred 0.003 and 0.010 percent of the time in the wave record, respectively. The 20-year wave record contained no events for waves of this height and period approaching from a minus 40 degree angle (comparable to Figure 8-43, Panel C). Because these larger waves break on the shoal off the tip of Dauphin Island, at this location they are depth limited and their heights become equal.

Figure 8-44. Wave height change (dredged – existing) for incident wave of H = 3.0 m, T = 11 sec.

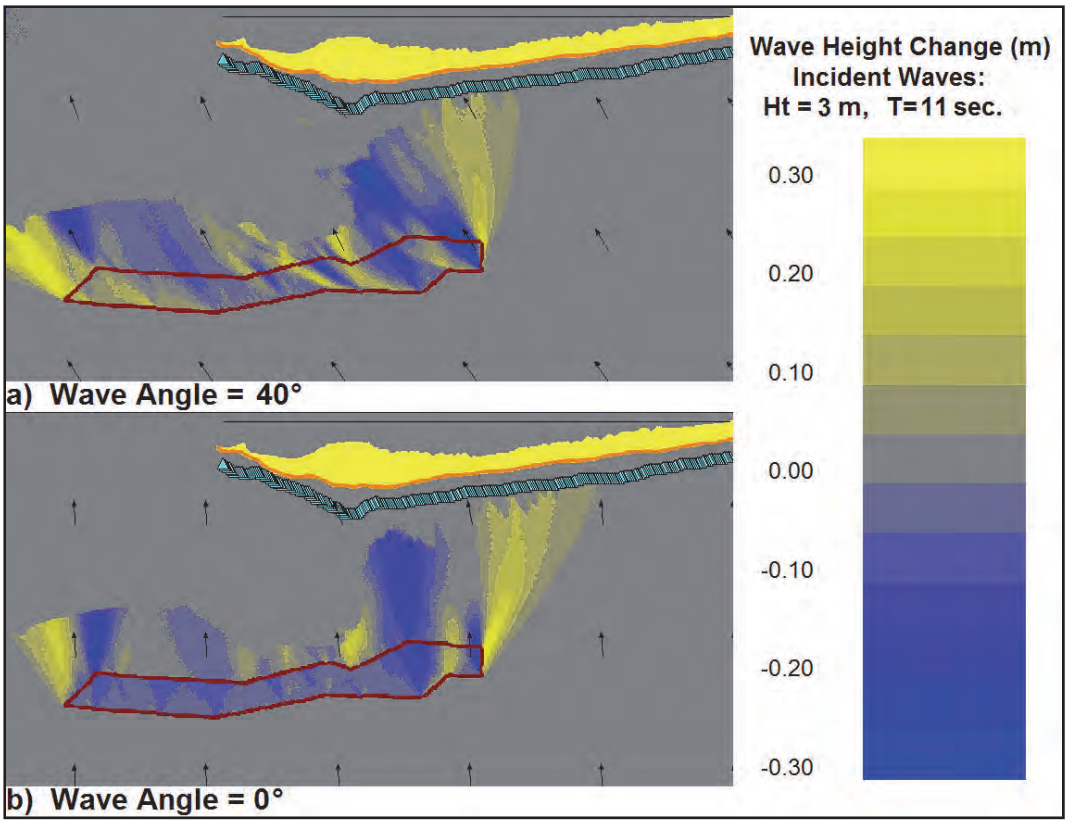

Figures 8-45 and 8-46 show wave angle differences for the same wave conditions illustrated in Figures 8-43 and 8-44. Yellow colors represent a clockwise rotation of the wave angle in the dredged condition relative to the existing condition, while blue represents a counter-clockwise rotation. The black arrows on the figures show the wave directions for the existing conditions.

Figures 8-47 through 8-50 show how the second borrow site configuration impacts the wave refraction. The explanation for these figures is the same as for Figures 8-43 through 8-46, respectively.

Figure 8-51a shows the first configuration percent difference in wave heights at the STWAVE save stations for the five wave cases shown in Figures 8-43 through 8-46. The locations of the STWAVE save stations are shown as the line of blue-green triangles offshore of Dauphin Island in Figures 8-43 through 8-50. The vertical axis in Figure 8-51a has been scaled for easy comparison with similar plots from other borrow sites. Figure 8-51b shows the same information for the second borrow site configuration. As shown in these figures, for these five cases, at no location along Dauphin Island does the wave height difference exceed 1.25 percent.

Figure 8-45. Wave angle change (dredged – existing) for incident wave of H = 0.8 m, T = 5.0 sec.

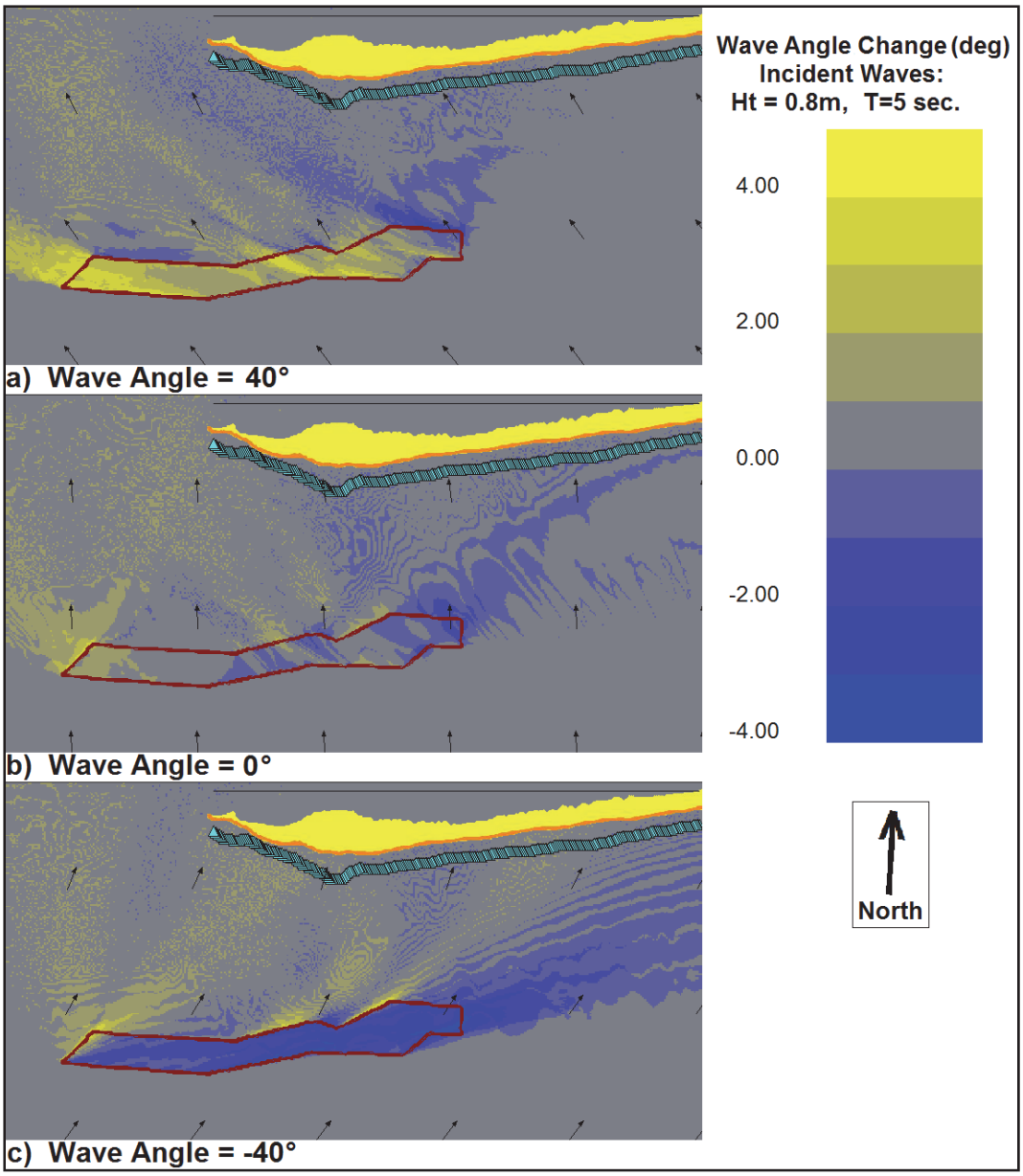

8.4.3 Sediment transport and shoreline change

A GENESIS model domain was generated for examining the influence of the borrow areas on shoreline processes along the westernmost 7700-m (4.8 miles) of West Dauphin Island. STWAVE generated near-shore wave conditions for both dredged and existing condition were applied as input to GENESIS to estimate longshore sand transport rates and shoreline change. The GENESIS simulations were run for the 20-year WIS hindcast offshore wave time-series (1980-1999).

Figure 8-46. Wave angle change (dredged – existing) for incident wave of H = 3.0 m, T = 11 sec.

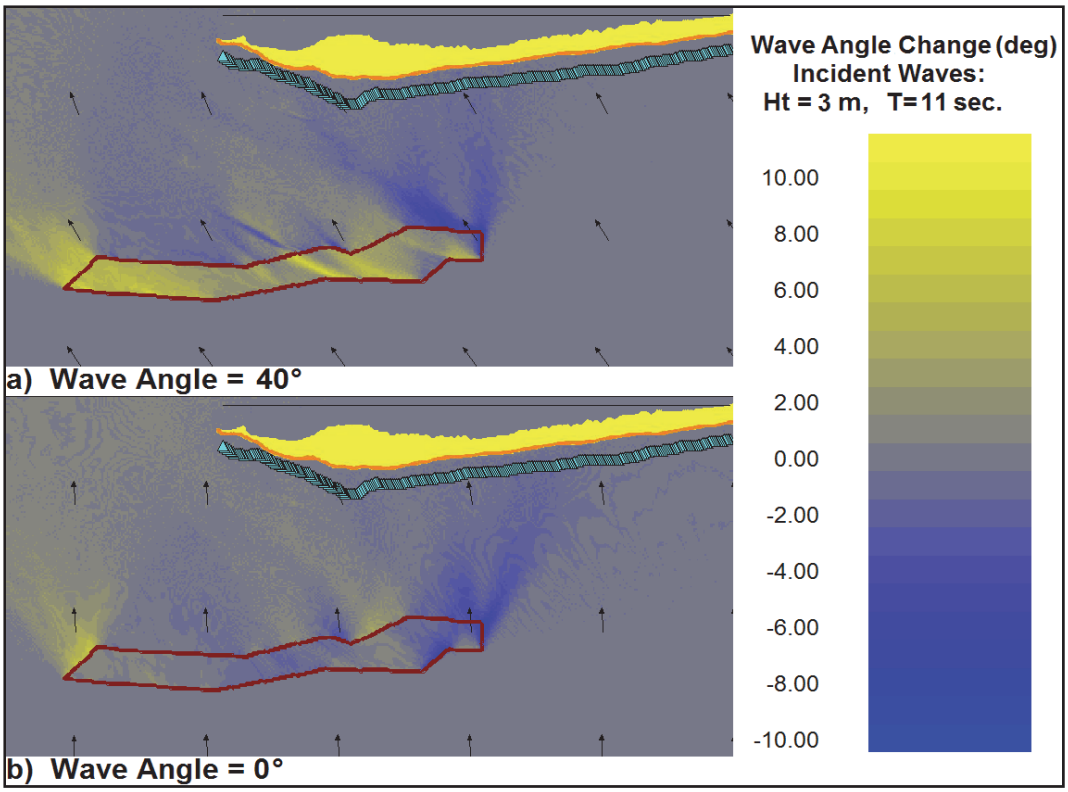

Figure 8-52 shows the GENESIS grid for the western portion of West Dauphin Island. The scale is in meters. The offshore direction in this figure is 177 degrees (nearly due south). The graphs that follow Figure 8-52 show GENESIS results referenced to this horizontal axis. That is, these graphs should be visualized as facing nearly due south, making the western tip of the island on the right. Also, in these figures, results for the first configuration are labeled BA1 (Borrow Area1), and the second, BA2.

Figure 8-53 displays the initial shoreline position along with three estimated final (20 yr) shoreline positions (existing bathymetry and both dredged configurations). In this figure there is approximately a 7:1 distortion in offshore to along shore distances.

Figure 8-54 plots the shoreline change rate for the three simulations. Negative values indicate erosion and positive values indicate accretion. Figure 8-55 plots the difference, or change, in the estimated shoreline change rates between the existing and dredged condition for each point on the GENESIS axis. Comparing Figures 8-54 and 8-55, it is seen that the dredged-induced impacts to the shoreline change rate are anticipated to be in the range of 2-4 percent of the existing rate.

Figure 8-47. Wave height change, H = 0.8 m, T = 5.0 sec, 2nd configuration.

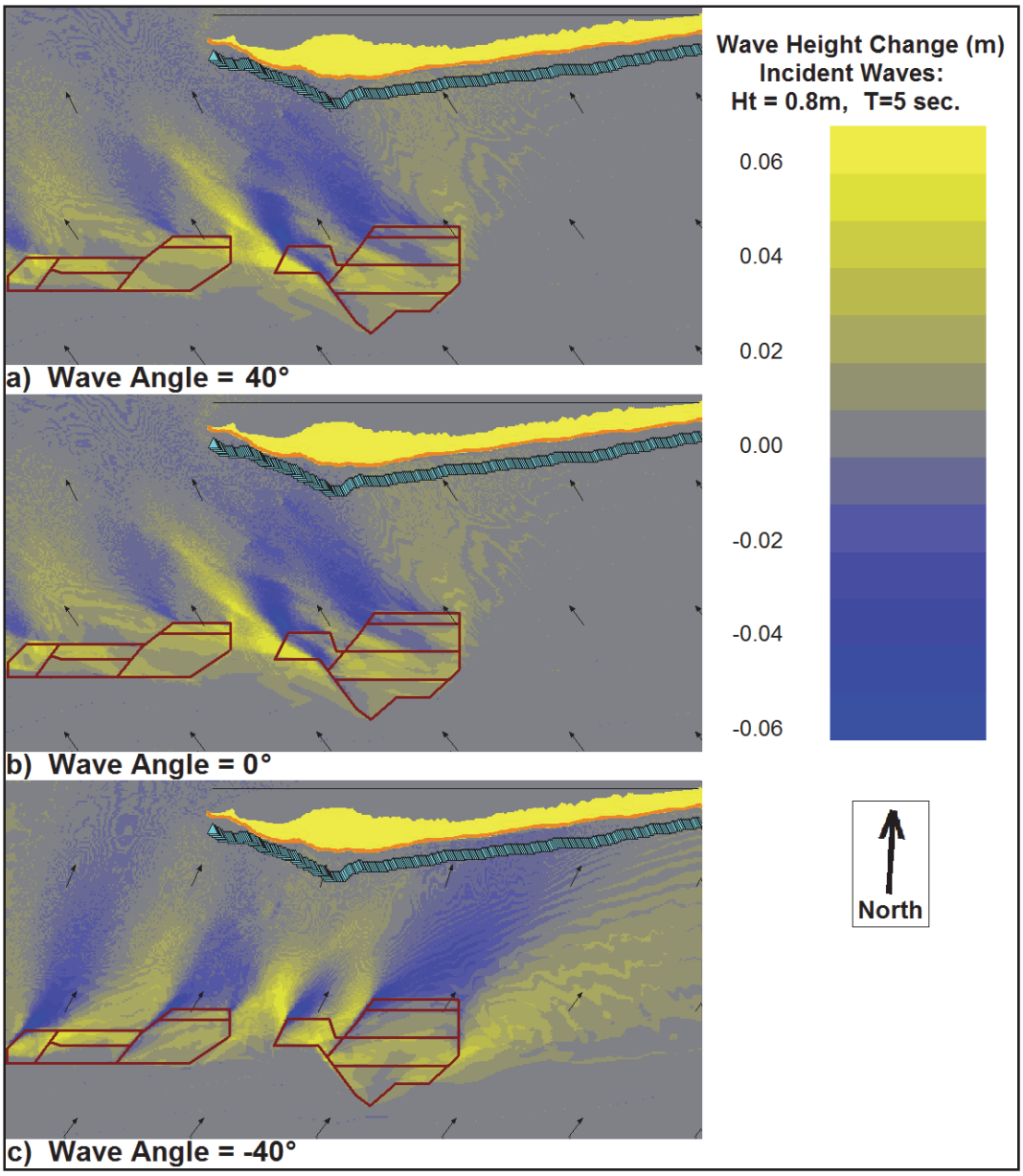

The estimated average net annual longshore sand transport rates for the existing and the two dredged conditions are plotted in Figure 8-56. Positive values indicate transport to the right on the plot (i.e., the net transport is to the west all along this portion of coastline). This leads to a positive slope in the longshore sand transport rate indicating erosion whereas a negative slope indicates shoreline accretion. The steeper the slope the higher the predicted shoreline rate of change. A stable shoreline is associated with a constant longshore sand transport rate, which would be a flat line in this figure. The estimated average annual longshore sand transport rates for the current and the two dredged conditions vary between approximately

Figure 8-48. Wave height change, H = 3.0 m, T = 11 sec, 2nd configuration.

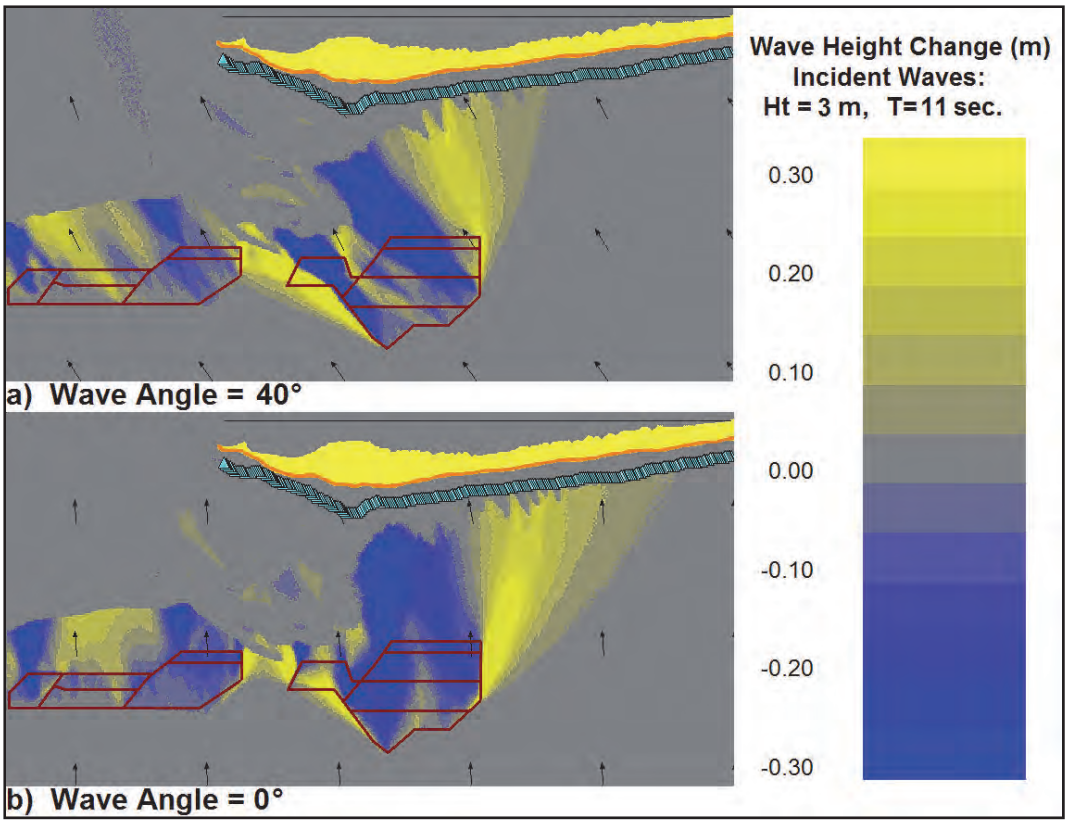

100,000 and 225,000 m³/year (west-directed). The change in estimated transport rates between the existing and dredged condition is less than 3 percent.

To isolate the influence of the excavated borrow areas on longshore sand transport rates, the change in estimated transport rates between the existing and dredged condition are plotted in Figure 8-57. The vertical axis in Figure 8-57 has been scaled for easy comparison with similar plots from other borrow sites. As shown in this figure, the modeling predicts that at no location along Dauphin Island will the net longshore sediment transport rates change by more than 4,000 m³/yr.

8.4.4 Summary

The expected refraction-induced shoreline impacts to West Dauphin Island are similar for either borrow site configuration and generally only change the naturally occurring processes by a few percent. The dredged-induced impacts to the shoreline change rate are anticipated to be in the range of 2-4 percent of the existing rate. In addition, the changes will be largely stabilizing. That is, over most of the shoreline, the small dredge

Figure 8-49. Wave angle change H = 0.8 m, T = 5.0 sec, 2nd configuration.

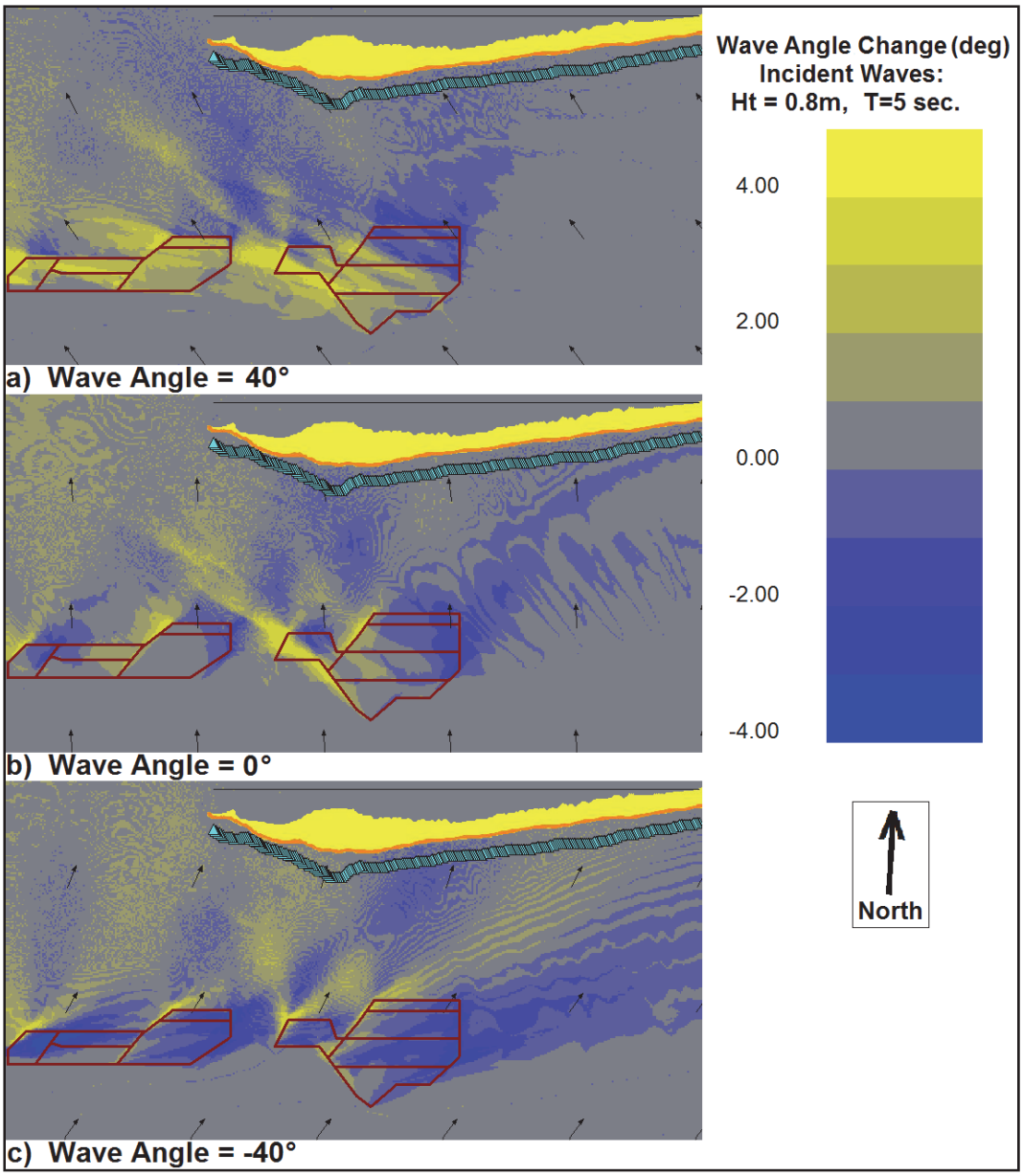

induced changes will decrease both the erosion and the accretion in the areas where they occur. A comparison of Figures 8-55 and 8-56 shows that mining either borrow area will decrease the net alongshore sediment transport rate by less than about 3 percent of its current value.

The large shallow shoal between the borrow area and Dauphin Island substantially rectifies the waves and produces wave breaking for most incident wave conditions for both the dredged and existing cases. Thus, this shoal area largely shields Dauphin Island from any bathymetry-change effects at the borrow sites. In addition, the dominant incident wave

direction is from the SSE-SE sectors (Figure 8-4) which results in down-wave impacts of the borrow area occurring generally in the region of Petit Bois Inlet rather than along the Dauphin Island shoreline. The conclusion that offshore dredging will have a minimal shoreline impact is in good general agreement with the results of Byrnes et al. (2004) who used a different procedure to analyze the potential from mining offshore sand bodies along the Alabama Gulf coast.

Figure 8-50. Wave angle change, H = 3.0 m, T = 11 sec, 2nd configuration.

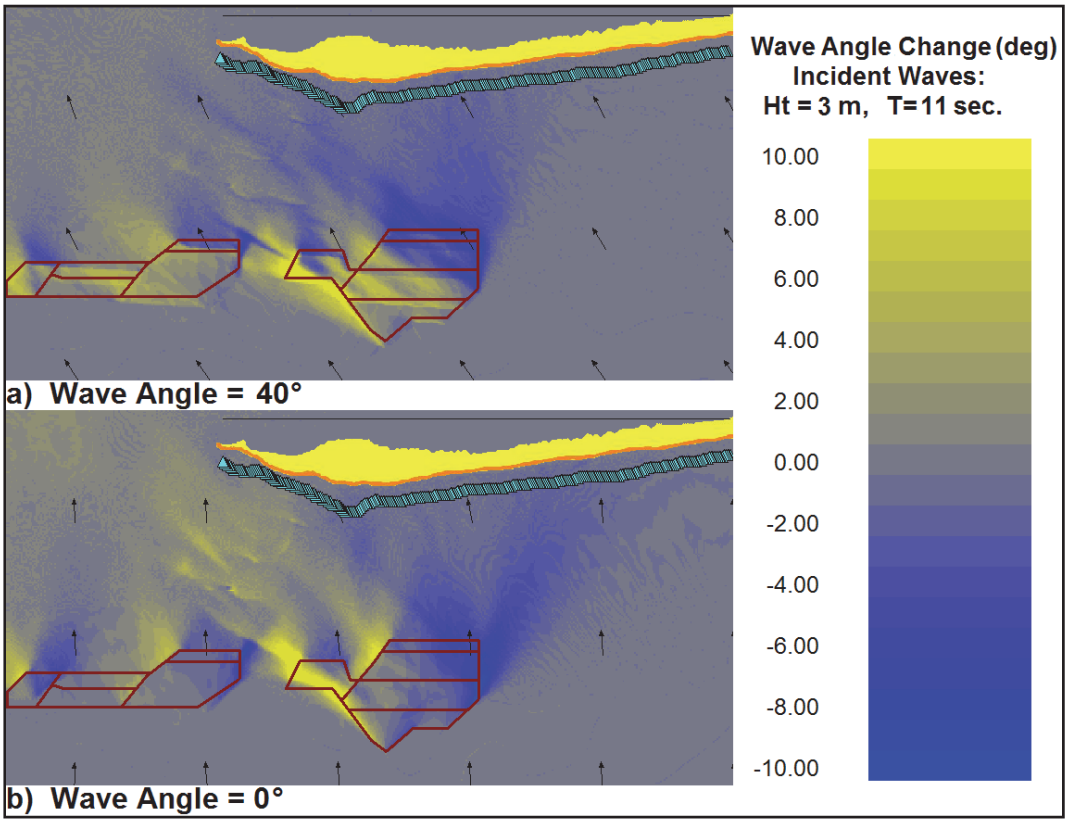

Figure 8-51a. Percent change in wave height at nearshore reference line.

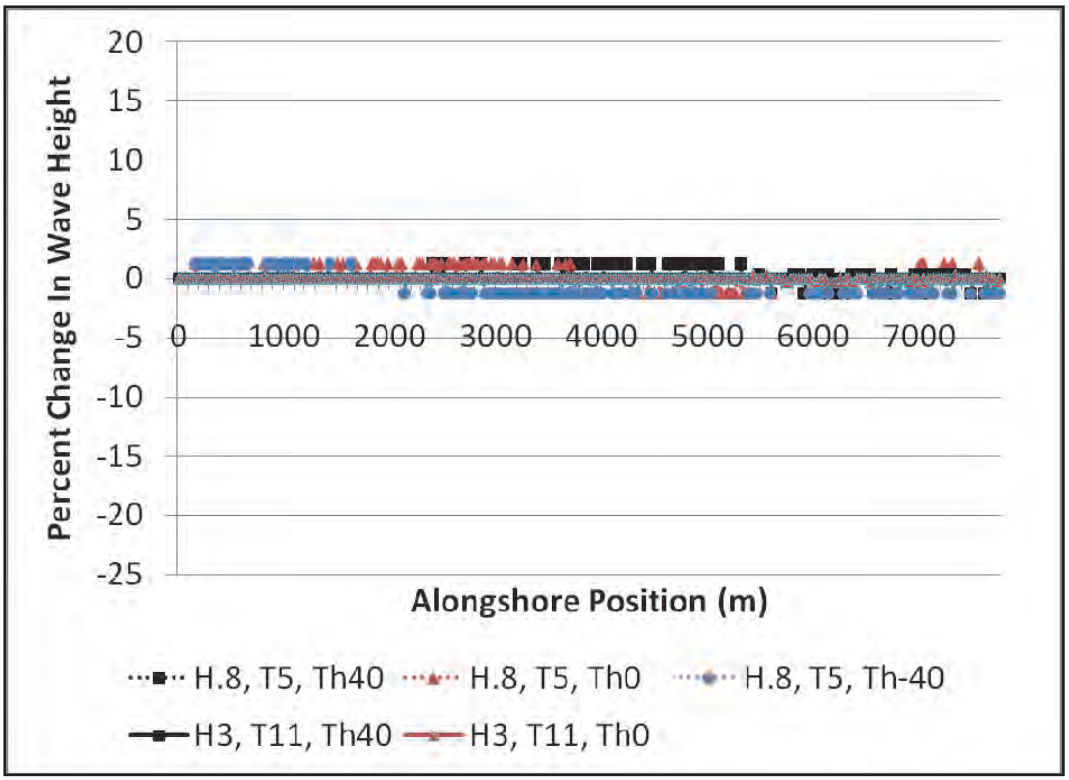

Figure 8-51b. Percent change in wave height at nearshore reference line for second borrow area configuration.

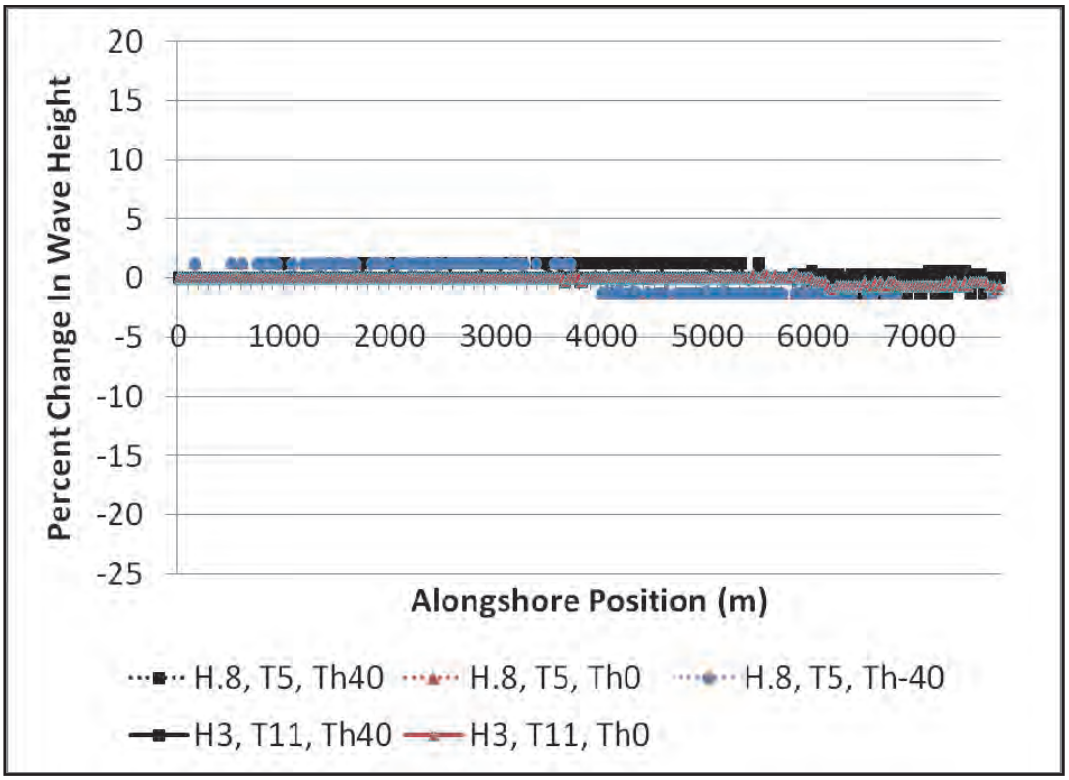

Figure 8-52. GENESIS grid for West Dauphin Island.

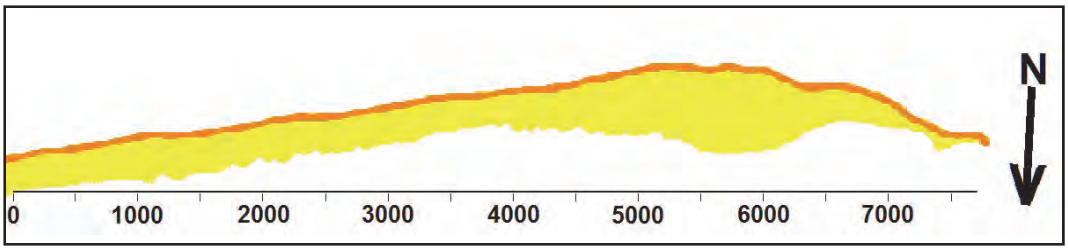

Figure 8-53. Comparison of existing and dredged condition estimated final shoreline.

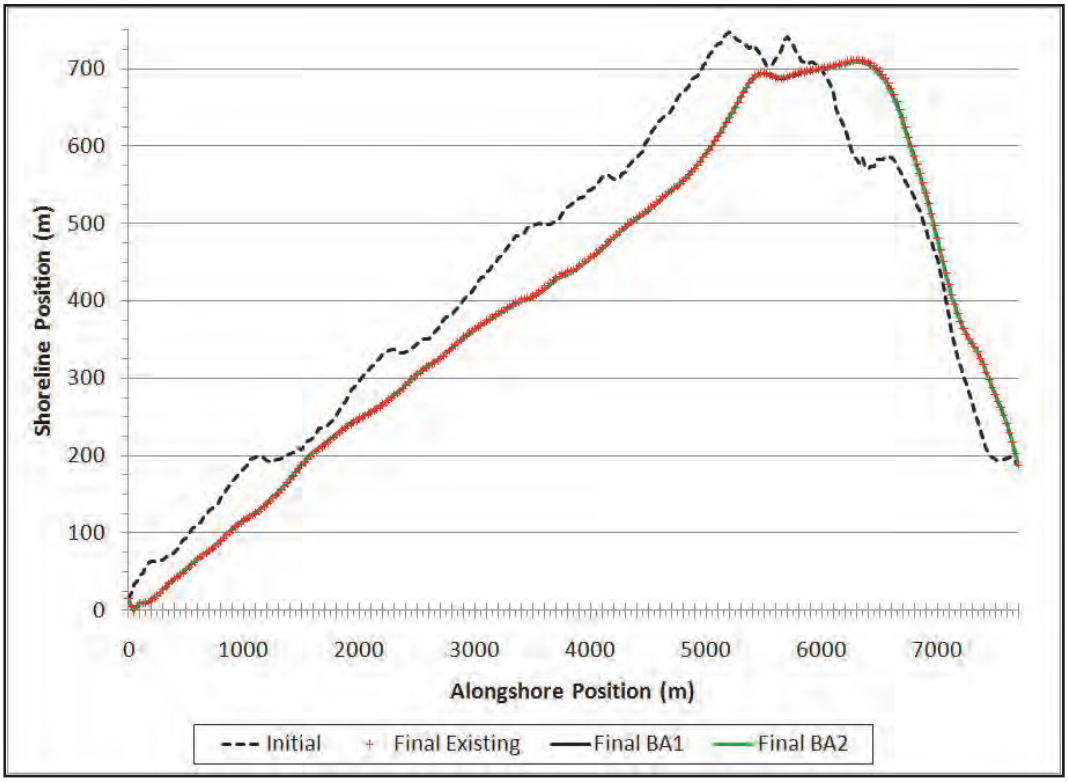

Figure 8-54. Comparison of existing and dredged condition shoreline change rate.

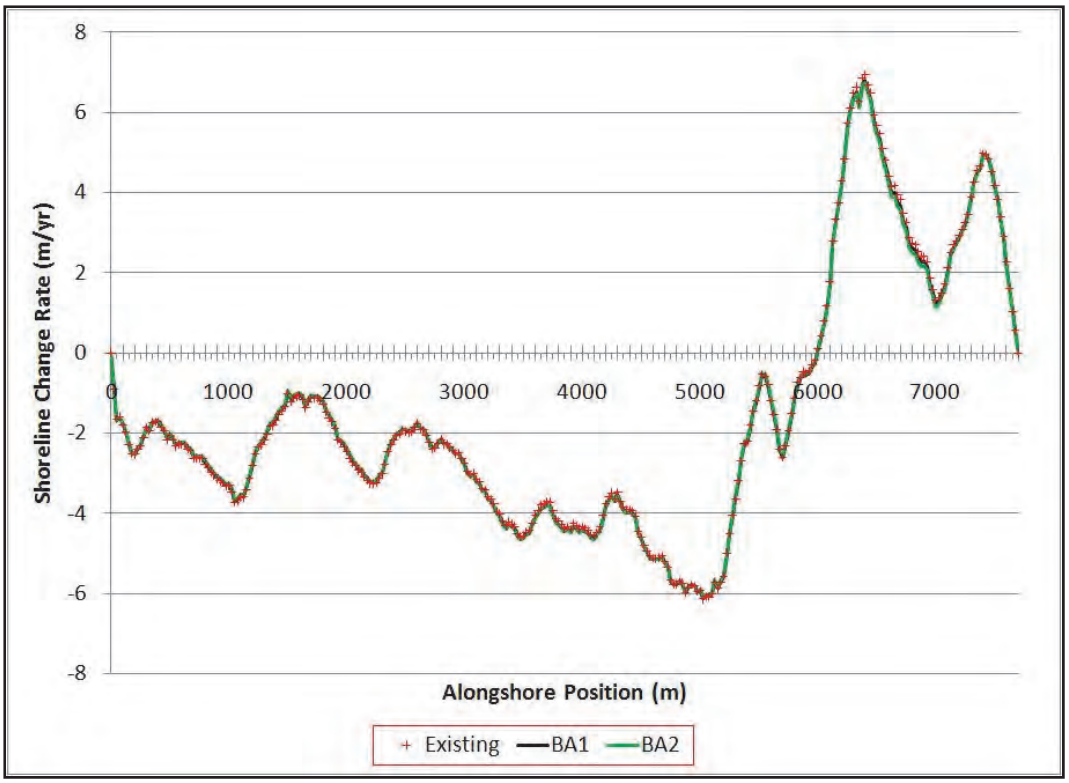

Figure 8-55. Dredging induced change in shoreline change rate.

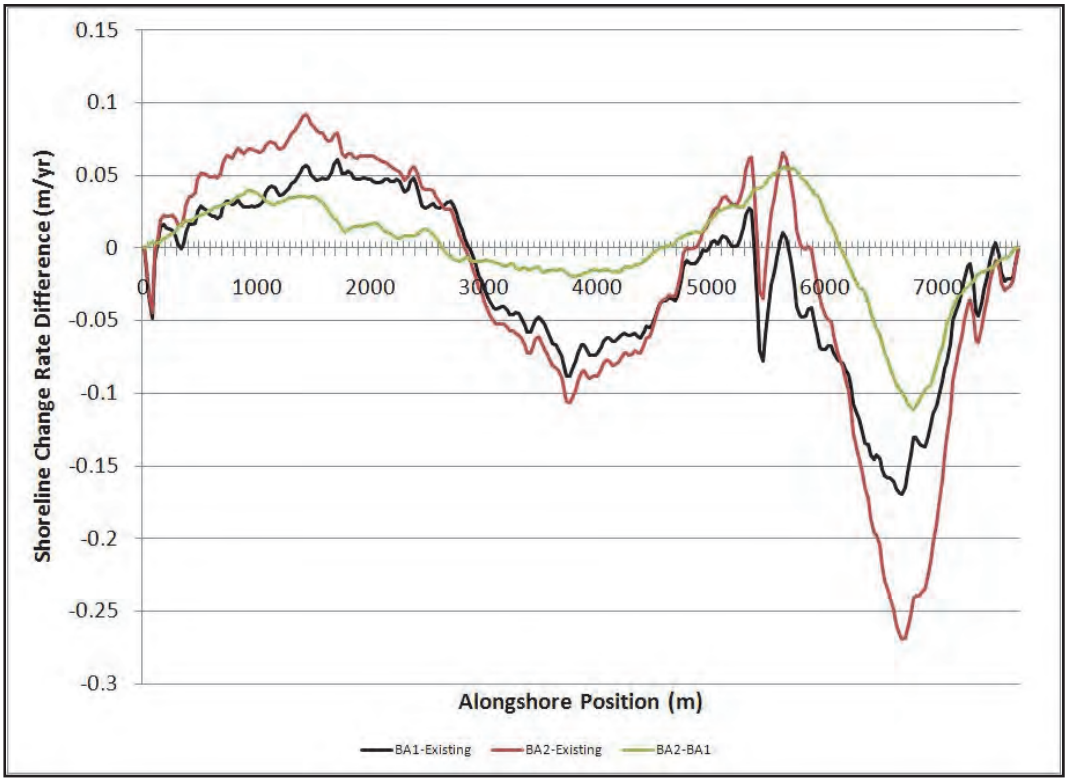

Figure 8-56. Mean alongshore transport rate.

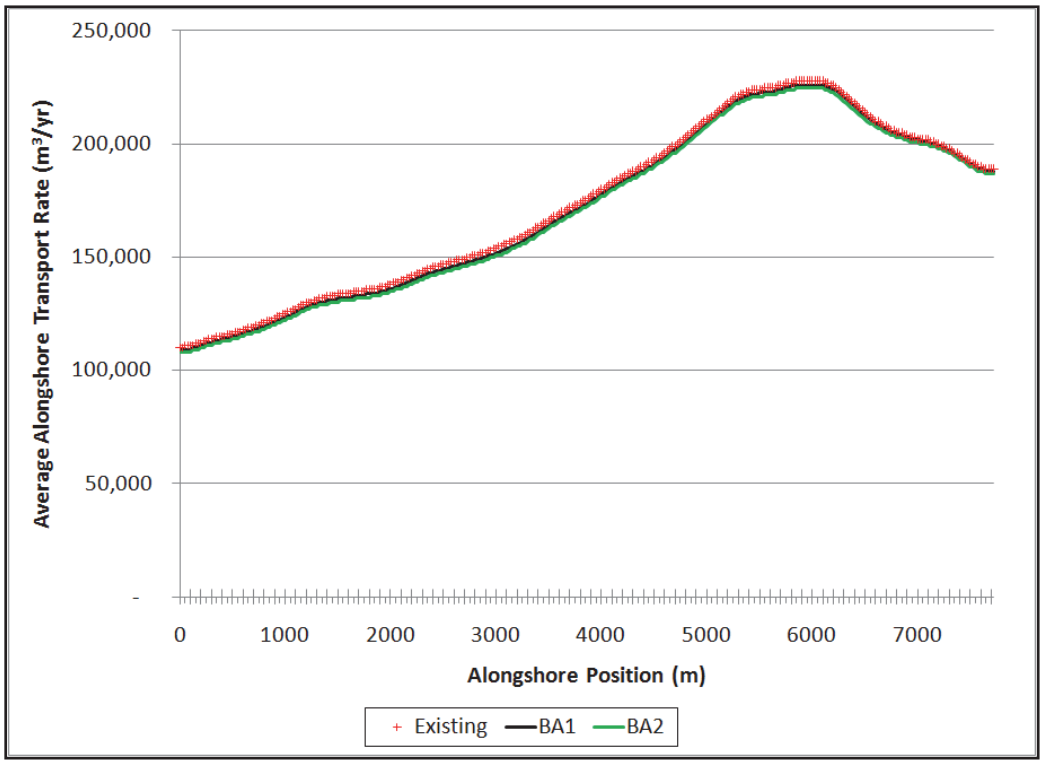

Figure 8-57. Change in the average net longshore transport rate.

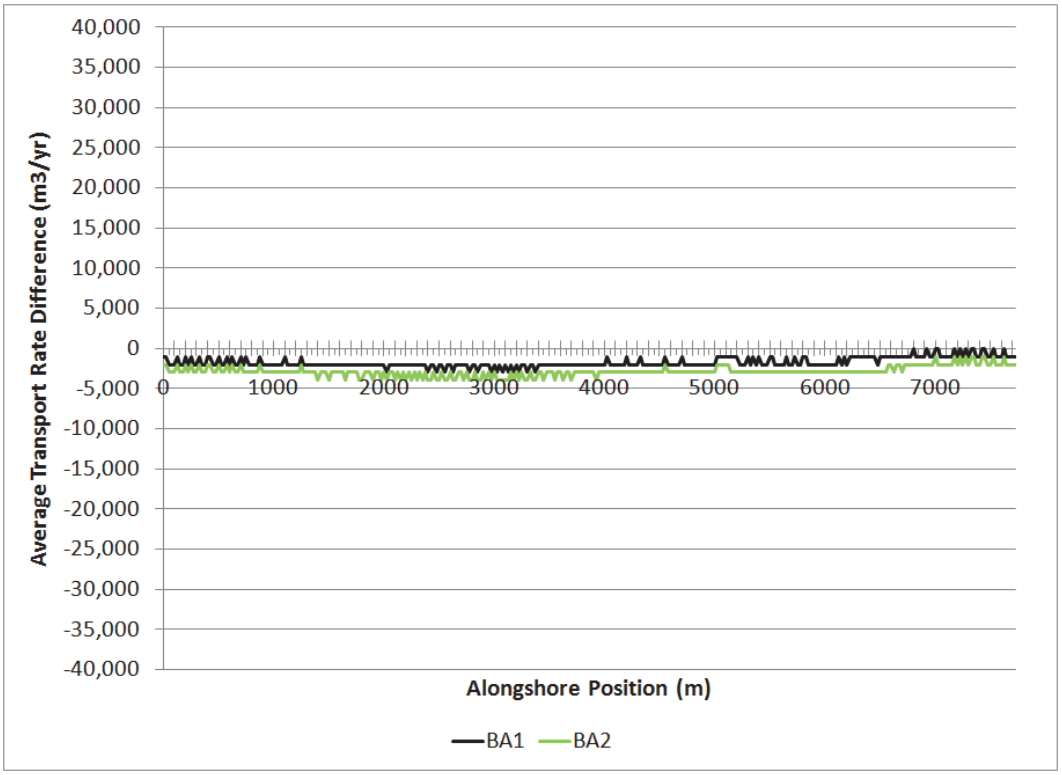

9 Summary

Hydrodynamic, wave, sediment transport, and water quality numerical modeling was conducted to support engineering and design as well as the development of a Supplemental Environmental Impact Statement for the restoration of Ship Island. The purpose of this report was to evaluate the effect of Camille Cut closure on circulation and water quality of Mississippi Sound; the combined effect of Camille Cut and Katrina Cut closures on circulation and water quality of Mississippi Sound; reduction of storm wave energy at the mainland Mississippi coast as a result of closing Camille Cut; and optimization of nearshore placement of sand in the littoral zone.

Field data was collected to support numerical modeling efforts and to provide baseline data so that changes resulting from the reconstruction of Ship Island could be quantified during project monitoring. Data collected include waves on both the seaward and sound side of Ship Island, current velocities and flow through the cuts and passes around Ship and Dauphin Islands, and water quality information at strategic locations.

The circulation, water quality, and storm wave energy was evaluated through comparison of results for four alternative conditions including a Base condition (Post-Hurricane Katrina), With-project (Camille Cut closed), Degraded (Ship Island lowered to below mean sea level across the entire island footprint), and a Cumulative condition which includes Camille Cut closed, Katrina Cut closed, and navigation channels deepened to authorized depths.

The relative changes in circulation within Mississippi Sound resulting from proposed Ship Island restoration alternative configurations were estimated through application of a combination of the two dimensional ADCIRC hydrodynamic model and the three dimensional CH3D model. These models were applied to provide hydrodynamic input to the water quality model CE-QUAL-ICM. Nearshore wave modeling was conducted with STWAVE to provide radiation stress gradients for CH3D and to estimate the reduction of storm wave energy at the mainland Mississippi coast as a result of closing Camille Cut.

STWAVE performance was evaluated through comparison to the field data collected during March-July 2010 at two stations near Ship Island, one station in the Gulf of Mexico, and one station in Mississippi Sound. In addition, STWAVE has been validated during Hurricane Gustav in 2008. Overall, the STWAVE model results compared with good agreement to the measurements. The wave model also predicted the attenuation in wave heights across Ship Island rather well, from the exposed waves at the Gulf of Mexico station to the more sheltered waves at the Mississippi Sound station. The average wave height reduction factor predicted by the model is 0.67, whereas the average wave height reduction factor observed in the measured data is 0.64, where the wave height reduction factor is defined as the ratio of wave height at the Gulf of Mexico station to the wave height at the Mississippi Sound station.

A water quality model study of Mississippi Sound was conducted to determine potential impacts from proposed actions in the Ship Island area. The focus of the water quality effort was to understand the existing water quality within the Mississippi Sound and to quantify relative changes in water quality and flushing for the four alternative configurations. CH3D and CE-QUAL-ICM were applied to the study area to simulate hydrodynamics and water quality in the Mississippi Sound. The STWAVE model was applied for the period March-September 1998 so that the resulting radiation stress gradients could be applied within CH3D. The water quality model, CE-QUAL-ICM, was calibrated for the period of April 1, 1998 - September 15, 1998, using observed data provided by the Mississippi Department of Environmental Quality and appropriate kinetic rates determined in calibration. Sediment Oxygen Demand (SOD) is specified as a constant rate in the ocean and river inflows. Final calibration results compared favorably to observed data given the limited amount of comparison and boundary data available to evaluate and drive the model, respectively.

Changes in dissolved oxygen, salinity, and chlorophyll were an indicator of changes to water quality. Comparison of Pre- and Post-Katrina results to the other alternative results showed changes in water quality for all alternatives to some degree. Although water quality changes were noted, all were within the State standard for constituents of interest for ocean waters. Total net flows show averages are two orders of magnitude less than the peak flood and ebb flows across locations analyzed in the area of Ship Island. This is an indication of two things. First, Mississippi Sound in the vicinity of Ship Island has relatively little flushing and net transport

through the system. Second, the effects of Ship Island degradation or restoration do not have major effects upon system-wide circulation and, therefore, should not have major effects on system-wide water quality conditions. The condition of Ship Island does have localized effects on circulation. Two sets of tracer simulations were performed to assess the impact of different alternatives on circulation and flushing immediately behind Ship Island. Tracer concentrations were released instantaneously and allowed to disperse. Circulation is adequate to quickly displace material and move it around but does not always completely remove it from the vicinity of Ship Island.

Overall, comparison of results from all alternative runs showed changes in circulation, but this caused only minor changes to water quality concentrations in the area of proposed restoration. It is concluded from these results that none of the alternatives simulated would likely have system-wide detrimental water quality impacts. Water quality benefits of a restored Ship Island are possible in two ways. First, water quality behind the island would be similar to Pre-Katrina conditions. This may be more desirable from a sheltered habitat standpoint than open water of a degraded island. Second, there is greater potential for submerged aquatic vegetation colonization and growth in the protected waters north of Ship Island in a restored condition.

The reduction of storm wave energy at the mainland Mississippi coast as a result of closing Camille Cut and restoring Ship Island to a Pre-Hurricane Camille condition was also evaluated. Similarly, the increase in storm wave energy at the mainland Mississippi coast as a result of Ship Island degradation was evaluated. The relative changes resulting from the barrier island restoration and degradation are quantified through the application of an integrated coastal storm modeling system. Results indicate that closure of Camille Cut and Ship Island restorations does have the potential to reduce storm waves at the mainland coast. Maximum wave height reduction at the mainland Mississippi coast ranges from 0.2 m to 1.25 m relative to the existing Post-Katrina condition. The magnitude of wave height reduction was found to be controlled by the storm characteristics, primarily minimum central pressure (maximum wind speed), radius to maximum winds, forward speed, and trajectory. Barrier island restoration reduced waves by as much as 0.2 m to 0.4 m for 4 of the 15 synthetic storms simulated, 0.4 m to 0.6 m for 5 of the 15 synthetic storms simulated, and by greater than 0.6 m for 6 of the 15 synthetic storms

simulated. The greatest decrease in wave heights observed at the mainland Mississippi coast for the storm suite simulated was 1.25 m.

The maximum wave height increase at the mainland Mississippi coast as a result of East and West Ship Island degradation ranges from 0.2 m to 0.4 m, with the majority (13 of 15) of the synthetic storms experiencing a maximum wave height increase of 0.2 m. The largest areas of wave height increase are in the leeward areas behind East and West Ship Island, which were degraded to subaqueous shoals. Maximum wave change potential at the mainland Mississippi coast is smaller for the degraded scenario than for the restored scenario because wave energy can penetrate from the Gulf of Mexico into Mississippi Sound for both the existing Post-Katrina and degraded scenarios.

The effects of the offshore borrow areas on storm waves were quantified through the cross-shore progression of significant wave heights along three parallel transects in the vicinity of the borrow areas. The borrow areas produce a local reduction in wave energy, i.e., a divergence of wave rays, for the restored (dredged) scenario when compared to the existing Post-Katrina scenario. For all of the synthetic storms simulated, de-focusing of wave energy and de-shoaling effects are observed along the transect that bisects the borrow area such that the restored (dredged) scenario results in lower significant wave heights across this transect. Because wave energy flux is conserved and the borrow areas produce a local divergence of wave rays for the restored (dredged) scenario, an increase in wave energy (i.e., a convergence of wave rays) is observed at the fringes of the borrow areas when compared to the existing Post-Katrina scenario. For all of the synthetic storms simulated, focusing of wave energy and refraction effects are observed along the fringes of the borrow areas such that the restored (dredged) scenario results in larger significant wave heights across these transects.

The borrow areas evaluated in the storm wave sensitivity represented a preliminary borrow area plan offshore of Ship Island. Additional borrow area configurations were evaluated, and further analyses were conducted to support final borrow area configuration selection. Proposed borrow areas were identified not only off the coast of Ship Island but also offshore of Dauphin and Horn Islands. Potential impacts of excavation of nearshore borrow areas for the proposed restoration projects were assessed with the spectral nearshore wave transformation model STWAVE and shoreline

change model GENESIS. STWAVE simulations were performed for both existing and restored (dredged) condition to obtain estimates of nearshore wave conditions landward of the borrow areas and to enable a comparative analysis aimed at quantifying potential borrow area impacts on shoreline processes along nearby island shorelines.

For Ship Island, potential effects of the proposed borrow areas SI1, SI2, SI3, SI4, and SI5 on nearshore wave conditions were quantified by examination of the change in nearshore wave height and direction landward of each potential borrow area alternative. STWAVE results show an increase in wave heights in the area of the Camille Cut closure due to refraction caused by the borrow areas focusing wave energy. The wave height increase was within 10 percent for the short period waves. However, for longer period waves, the focusing caused increased wave heights of over 10 percent for SI2, SI3, and SI4 compared to 20 percent for SI1. SI5 minimized the wave height increase to approximately 2 percent. The STWAVE results were applied as input conditions to GENESIS to quantify the influence of the borrow areas on shoreline processes. Longshore sand transport rates were calibrated with typical values for K1 and K2 of 0.4 and 0.2, respectively, and to produce transport rates consistent with sediment budget estimates (Byrnes et al. 2011). The borrow areas were shown to increase erosion over much of the Camille Cut closure area. The magnitude of the increased erosion over the 20-year period of analysis reaches 68 m for SI1, 48 m around the Camille Cut for SI2 and SI3, 28 m for SI4, and 5.0 m for SI5. The western portion of West Ship Island is expected to prograde compared to the existing condition for SI1-SI4 with a maximum increase of 27 m with SI1, 21 m with SI2, 24 m with SI3, and 14 m with SI3. SI5 causes increased erosion of approximately 2.0 m.

The impacts of excavating a borrow area offshore of Horn Island were also quantified by examination of the change in nearshore wave height and direction landward of the borrow area. The STWAVE results show minimal increases in wave heights surrounding the borrow area with little effect on the GENESIS save stations. The STWAVE results were applied as input conditions to GENESIS to quantify the influence of the borrow area on shoreline processes. A sensitivity analysis was conducted, comparing results for both the existing and dredged conditions. Longshore sand transport rates were calibrated with typical values for K1 and K2 of 0.10 and 0.05, respectively, and produced transport rates consistent with sediment budget estimates. The proposed borrow area was shown to have minimal impact on

shoreline change rates over the entirety of Horn Island. The maximum magnitude of change reduces predicted shoreline advance by approximately 1.5 m for the 20-year period of analysis. The greatest increase in erosion is approximately 1.0 m over 20 years. The western portion of Horn Island is expected to slightly prograde as a result of the project.

The expected refraction-induced shoreline impacts to West Dauphin Island are similar for the borrow site configurations evaluated and generally only change the naturally occurring processes by a relatively small percentage. The dredged-induced impacts to the shoreline change rate are anticipated to be in the range of 2.0-4.0 percent of the existing rate. In addition, the changes will be largely stabilizing. That is, over most of the shoreline, the small dredged-induced changes will decrease both the erosion and the accretion in the areas where they occur. The large shallow shoal between the borrow area and Dauphin Island substantially rectifies the waves and produces wave breaking for most incident wave conditions for both the dredged and existing cases. Thus, this shoal area largely shields Dauphin Island from any bathymetry-change effects at the borrow sites. In addition, the dominant incident wave direction is from the SSE-SE sectors which results in down-wave impacts of the borrow area occurring generally in the region of Petit Bois Inlet rather than along the Dauphin Island shoreline. The conclusion that offshore dredging will have a minimal shoreline impact is in good general agreement with the results of Byrnes et al. (2004) who used a different procedure to analyze the potential from mining offshore sand bodies along the Alabama Gulf Coast.

The Ship Island restoration plan includes direct sand placement in Camille Cut, increasing the island footprint, and additional sand placed into the local littoral zone. A numerical model prediction of morphological response and sand fate can assist in determining volumes and nearshore placement of sand. Beach replenishment is commonly used on long stretches of main-land coast, and these cases are well treated with a class of one-dimensional models. However, these simplified models are not appropriate for the Ship Island case with complex geometry and hydrodynamics. The C2SHORE model was applied to evaluate the performance of several restoration alternatives, including sensitivity to grain size for sediment placement and local offshore borrow sites. The C2SHORE model, with numerically intensive nearshore computations, has a relatively small domain size. The effects of basin-scale hydrodynamics such as storm surge are included in the domain through the appropriate application of boundary conditions.

Implementation of the model coupling with large scale models to C2SHORE was examined by comparing predicted hydrodynamics with the field measurements collected for this study. Because differences in the existing bathymetry and the model domain may be significant, the flow velocity averaged over Camille Cut is used as a basis for comparison. For tidally-driven flow, the model phase results were well-predicted, but the amplitude was somewhat larger than the measured values during both flood and ebb tides. To ascertain the C2SHORE performance for storm morphology change, Hurricane Katrina was modeled and compared with measured data. Unfortunately, pre-Katrina subaqueous data in the nearshore region is sparse. Therefore, a pre-storm model domain was implemented from several available data sets, including a 2008 survey. Due to these limitations in the data, model-to-measurement comparisons were limited to lidar surveys of the emergent island. The modeled evolution in a contour near mean sea level agrees well with observations, with a general loss of land and a significant widening of Camille Cut. Likewise, the comparison of details of morphology change on emergent regions is reasonably well-predicted with the exception of the west end of the island.

Three hypothetical storms were simulated, with approximate return periods of 1.0, 10, and 500 years, to examine the effect of the proposed restoration scenarios on the sediment transport environment. Initially, existing morphology is modeled to establish baseline conditions, which indicate a transport to the north around the ends of the island and a westerly long-shore transport. With restoration and the fill of Camille Cut, loss of a hydraulic pathway between the separated island results in larger flow around the east and west ends of the contiguous island. Results indicate that the Camille Cut restoration fill survives higher-frequency storms (such as the 1.0-yr and 10-yr events), but is breached during the low-frequency 500-yr event modeled herein. Gradients in transport along the island indicate a more erosive condition to the east of Camille Cut and a more stable condition to the west of Camille Cut, and these findings are in agreement with island history. To the west of Ship Island, sand infills the navigation channel, but only for the extreme event modeled (500-yrs), and the volume of infill is similar for existing conditions and the restoration scenarios. To the east of Ship Island, modeled transport values indicate that the subaqueous region off the east end (Little Dog Keys Pass) will accumulate sediment, and this is in agreement with the Mississippi sediment budget.

Several choices exist for restoration sand depending on the material source, and the grain size effect is explored by modeling storm morphology with a fine 0.2 mm, an intermediate 0.26 mm, and relatively coarse 0.3 mm sand. For smaller storms, fine-grain sand transport was 20 percent larger when compared with the 0.3 mm sand. A more dramatic difference is modeled in transport for more intense storms, where the increase in sand transport was approximately 40 percent. Additional model results indicate the effect of a possible sand borrow site located less than 1.5 km from the shoreline of the restored Ship Island. The large borrow feature modeled has the effect of redistributing wave energy along the island coast and generating localized regions of increased or decreased wave action. For the smaller events, the effect of this variation is to significantly suppress the longshore transport. An additional effect of the modeled borrow pits is revealed for the smaller two events, which shows localized regions of increased erosion along the fringes of the modeled borrow pits due to wave focusing.

References

Amante, C., and B. W. Eakins. 2009. ETOPO1 1 Arc-Minute Global Relief Model: Procedures, Data Sources and Analysis. NOAA Technical Memorandum NESDID NGDC-24, 19 pp.

Atkinson, J. H., J. J. Westerink, and J. M. Hervouet. 2004. Similarities between the Quasi-Bubble and the Generalized Wave Continuity Equation Solutions to the Shallow Water Equations. *International Journal for Numerical Methods in Fluids*, 45:689-714.

Brock, J., W. Wright, A. Nayegandhi, M. Patterson, I. Wilson, and L. Travers. 2007. EAARL Topography-Gulf Islands National Seashore-Mississippi. USGS Open File Report 2007-1377.

Bunch, B., C. Cerco, M. Dortch, B. Johnson, and K. Kim. 2000. *Hydrodynamic and water quality model study of San Juan Bay and Estuary*. ERDC TR-00-1. Vicksburg, MS: US Army Engineer Research and Development Center.

Bunch, B. W., M. Channel, W. D. Corson, B. A. Ebersole, L. Lin, D. J. Mark, J. P. McKinney, S. A. Pranger, P. R. Schroeder, S. J. Smith, D. H. Tillman, B. A. Tracy, M. W. Tubman, and T. L. Welp. 2003. *Evaluation of island and nearshore confined disposal facility alternatives, Pascagoula River Harbor Dredged Material Management Plan*. ERDC TR-03-3. Vicksburg, MS: US Army Engineer Research and Development Center.

Bunch, B. W., D. H. Tillman, and D. J. Mark. 2003a. *Sensitivity analysis of winds and bathymetry on the Port of Los Angeles (POLA) main channel*. Letter Report. Vicksburg, MS: US Army Engineer Research and Development Center.

Bunch, B. W., D. H. Tillman, and D. J. Mark. 2003b. *Sensitivity analysis of wind and bathymetry on the Port of Los Angeles Pier 300 expansion and Dominguez Channel studies*. Letter Report. Vicksburg, MS: US Army Engineer Research and Development Center.

Bunch, B. W., W. D. Corson, B. A. Ebersole, D. J. Mark, J. P. McKinney, D. H. Tillman, and M. W. Tubman. 2005. *Evaluation of Gulfport Navigation Channel Alternatives, Gulfport Reevaluation Report (GRR)*. Draft Report. Vicksburg, MS: US Army Engineer Research and Development Center, Waterways Experiment Station.

Bunya, S., J. C. Dietrich, J. J. Westerink, B. A. Ebersole, J. M. Smith, J. H. Atkinson, R. Jensen, D. T. Resio, R. A. Leuttich, C. Dawson, V. J. Cardone, A. T. Cox, M. D. Powell, H. J. Westerink, and H. J. Roberts. 2010. A high-resolution coupled riverine flow, tide, wind, wind wave, and storm surge model for southern Louisiana and Mississippi. Part I – Model development and validation. Monthly Weather Review, 138:345-377.

Buster, N. A., and R. A. Morton. 2011. Historical bathymetry and bathymetric change in the Mississippi-Alabama coastal region, 1847–2009: U.S. Geological Survey Scientific Investigations Map 3154, 13 p. pamphlet.

Byrnes, M. R., R. M. Hammer, T. D. Thibaut, and D. B. Snyder. 2004. Physical and biological effects of sand mining offshore Alabama, USA. *J. Coastal Res.*, 20(1):6–24.

Byrnes, M., J. Rosati, and S. Griffee. 2011. Sediment Budget: Mississippi Sound Barrier Islands. In *Proceedings, Coastal Sediments '11*. American Society of Civil Engineers.

Cardone, V. J., C. V. Greenwood, and J. A. Greenwood. 1992. *Unified program for the specification of hurricane boundary layer winds over surfaces of specified roughness*. Contract Report CERC-92-1. Vicksburg, MS: US Army Corps of Engineers.

Cerco, C., and T. Cole. 1994. *Three-dimensional eutrophication model of Chesapeake Bay*. Technical Report EL-94-4. Vicksburg, MS: US Army Engineer Waterways Experiment Station.

Cerco, C., B. Bunch, M. Cialone, and H. Wang. 1994. *Hydrodynamic and eutrophication model study of Indian River and Rehoboth Bay, Delaware*. Technical Report EL-94-5. Vicksburg, MS: US Army Engineer Waterways Experiment Station.

Cerco, C., and B. Bunch. 1997. *Passaic River tunnel diversion model study, Report 5, water quality modeling*. Technical Report HL-96-2. Vicksburg, MS: US Army Engineer Waterways Experiment Station.

Cerco, C. F., B. W. Bunch, A. M. Teeter, and M. S. Dortch. 2000. *Water quality model of Florida Bay*. ERDC/EL TR-00-10. Vicksburg, MS: US Army Engineer Research and Development Center.

Cerco, C., and M. Noel. 2004. The 2002 Chesapeake Bay eutrophication model. EPA 903-R-04-004. Annapolis, MD: Chesapeake Bay Program Office, US Environmental Protection Agency.

Chapman, R. S., B. H. Johnson, and S. R. Vemulakonda. 1996. *Users guide for the sigma stretched version of CH3D-WES; A three-dimensional numerical hydrodynamic, salinity and temperature model*. Technical Report HL-96-21. Vicksburg, MS: US Army EngineerWaterways Experiment Station.

Chapman, R. S., P. V. Luong, and M. W. Tubman. 2006. Mississippi sound hydrodynamic and salinity sensitivity modeling. Final Report prepared for US Army District, Mobile, Mobile, AL.

Cox, A. T., and V. J. Cardone. 2007. Workstation assisted specification of tropical cyclone parameters from archived or real time meteorological measurements. 10th International Workshop on Wave Hindcasting and Forecasting and Coastal Hazard Symposium, North Shore, Hawaii, November 11-16, 2007.

Dawson, C., J. J. Westerink, J. C. Feyen, and D. Pothina. 2006. Continuous, discontinuous and coupled discontinuous-continuous galerkin finite element methods for the shallow water equations. *International Journal for Numerical Methods in Fluids* 52:63-88.

Dietrich, J. C., S. Bunya, J. J. Westerink, B. A. Ebersole, J. M. Smith, J. H. Atkinson, R. Jensen, D. T. Resio, R. A. Leuttich, C. Dawson, V. J. Cardone, A. T. Cox, M. D. Powell, H. J. Westerink, and H. J. Roberts. 2010. A high resolution coupled riverine flow, tide, wind, wind wave and storm surge model for southern Louisiana and Mississippi. Part II - Synoptic Description and Analyses of Hurricanes Katrina and Rita. Monthly Weather Review 138:378-404.

Dortch, M. S., M. Zakikhani, M. Noel, and S. C. Kim. 2007. *Application of a water quality model to Mississippi sound to evaluate impacts of freshwater diversions*. ERDC/EL TR-07-20. Vicksburg, MS: US Army Engineer Research and Development Center.

Ebersole, B. A., J. J. Westerink, S. Bunya, J. C. Dietrich, and M. A. Cialone. 2010. Development of storm surge which led to flooding in St. Bernard Polder during Hurricane Katrina. *Ocean Engineering* 37:91-103.

Eiker, E. E. 1977. Heat exchange programs, Thermal simulation of lakes, User's manual. Baltimore, MD: US Army Engineer District, Baltimore.

Fritz, H. M., C. Blount, R. Sokoloski, J. Singleton, A. Fuggle, B. G. McAdoo, A. Moore, C. Grass, and B. Tate. 2007. Hurricane Katrina storm surge distribution and field observations on the Mississippi barrier islands, Estuarine, Coastal, and Shelf. *Science* 74:12-20.

Grzegorzewski, A. S., M. A. Cialone, and T. V. Wamsley. 2011. Interaction of barrier islands and storms: implications for flood risk reduction in Louisiana and Mississippi. *Journal of Coastal Research*.

Hanson, H., and N. C. Kraus. 1989. *GENESIS: Generalized model for simulating shoreline change, Report 1, Technical reference*. Technical Report CERC-89-19. Vicksburg, MS: US Army Engineer Waterways Experiment Station, Coastal Engineering Research Center.

Interagency Performance Evaluation Task Force (IPET). 2008. Performance evaluation of the New Orleans and southeast Louisiana hurricane protection system, Final Report of the Interagency Performance Evaluation Task Force, Volume IV, The Storm.' USACE, Washington, DC http://ipet.wes.army.mil.

Johnson, B., R. Heath, B. Hsieh, K. Kim, and L. Butler. 1991. *Development and verification of a three-dimensional numerical hydrodynamic, salinity, and temperature model of Chesapeake Bay*. HL-91-7. Vicksburg, MS: US Army Engineer Waterways Experiment Station.

Johnson, B. D., N. Kobayashi, and M. B. Gravens. 2012. *Cross-shore numerical model CSHORE for waves, currents, sediment transport and beach profile evolution*. ERDC/CHL TR-12-22. Vicksburg, MS: US Army Engineer and Research Development Center.

Kobayashi, N., and B. D. Johnson. 2001. Sand suspension, storage, advection and settling in surf and swash zones. *Journal of Geophysical Research* 106(C5): 9363-9376.

Kobayashi, N., H. Zhao, and Y. Tega. 2005. Suspended sand transport in surf zones. *J. Geophys. Res*., 110, C12009, doi:10.1029/2004JC002853.

Kobayashi, N., A. Payo, and L. Schmied. 2008. Cross-Shore Suspended Sand and Bedload Transport on Beaches. *Journal of Geophysical Research* 113,C07001, doi:10.1029/2007JC004203.

Kobayashi, N., A. Payo, and B. D. Johnson. 2009. Suspended sand and bedload transport on beaches. Handbook of Coastal and Ocean Engineering. *World Scientific*. (28):807-823.

Kolar, R. L., J. J. Westerink, M. F. Cantekin, and C. A. Blain. 1994. Aspects of nonlinear simulations using shallow water models based on the wave continuity equation. *Computers and Fluids* 23(3):523-538.

Komen, G. J., L. Cavaleri, M. Donelan, K. Hasselmann, S. Hasselmann, and P. A. E. M. Janssen. 1994. Dynamics and modelling of ocean waves. Cambridge, UK: Cambridge University Press.

Leonard, B. 1979. A stable and accurate convection modelling procedure based on quadratic upstream interpolation. *Computer Methods in Applied Mechanics and Engineering* 19:59-98

Lick, W., J. Gailani, C. Jones, E. Hayter, L. Burkhard, and J. McNeil, 2005. The 28 transport of sediments and contaminants in surface waters. short course 29 Notes, University of California, Santa Barbara.

Lillycrop, L. S., and L. Parson. 2000. The Mobile District regional sediment management demonstration program. In *Proceedings, Florida Shore and Beach Preservation Association Annual Meeting*. Captive Island, FL, 13-15 September.

Luettich, R. A., Jr., J. J. Westerink, and N. W. Scheffner. 1992. *ADCIRC: An advanced three-dimensional circulation model for shelves, coasts, and estuaries*. Technical Report DRP-92-6. Vicksburg, MS: US Army Engineer Waterways Experiment Station.

Luettich, R. A., and J. J. Westerink. 2004. Formulation and numerical implementation of the 2D/3D ADCIRC finite element model version 44.XX; http://adcirc.org/adcirc_theory_2004_12_08.pdf

Martin, K., D. H. Tillman, W. C. Seabergh, R. McAdory, B. W. Bunch, M. J. Briggs, H. Acuff, and F. C. Carson. 2008. *Port of Los Angeles: Inner Cabrillo Beach, water quality improvement project*. ERDC/CHL TR-08-3. Vicksburg, MS: US Army Engineer Research and Development Center.

Morton, R. A. 2010. First-order controls of extreme-storm impacts on the Mississippi-Alabama barrier-island chain. *Journal of Coastal Research* 26:635-648.

Mukai, A. Y., J. J. Westerink, R. A. Luettich, and D. Mark. 2002. Eastcoast 2001, *A tidal constituent database for Western North Atlantic, Gulf of Mexico, and Carribean Sea*. ERDC/CHL TR-02-24. Vicksburg, MS: US Army Corps of Engineers Engineer Research and Development Center.

National Oceanic and Atmospheric Administration (NOAA). 2008. National Geophysical Data Center, NGDC Coastal Relief Model, Retrieved 01 December 2008, http://www.ngdc.noaa.gov/mgg/coastal/coastal.html

Otvos, E., and G. Carter. 2008. Beach aggradation following hurricane landfall: Impact comparisons from two contrasting hurricanes, northern Gulf of Mexico. *Journal of Coastal Research* 24(2):463-478.

Resio, D. T. 2007. White paper on estimating hurricane inundation probabilities. Vicksburg, MS: US Army Corps of Engineers, Engineer Research and Development Center.

Ribberink, J. S. 1998. Bed-load transport for steady flows and unsteady oscillatory flows. *Journal of Coastal Engineering* 34(1-2)59-82, 1998. DOI: 10.1016/S0378-3839(98)00013-1.

Ris, R. C., L. J. Holthuijsen, and N. J. Booij. 1999. A third generation wave model for coastal regions 2. Verification. *Geophys. Res.* 104(C4)7667–7681.

Romeiser, R. 1993. Global validation of the wave model WAM over a 1-year period using Geosat wave height data. *J. Geophys. Res.* 98:4713–4726.

Schmid, K., and B. Yassin, 2004. Mississippi coastal data node and value added GIS data products [abs]: Mississippi Academy of Sciences, v. 49, 1, p. 59.

Smith, J. M., D. T. Resio, and A. K. Zundel. 1999. *STWAVE: Steady-State spectral wave model; Report 1: User's manual for STWAVE version 2.0*. Instructional Report CHL-99-1. Vicksburg, MS: US Army Engineer Research and Development Center.

Smith, J. M., A. R. Sherlock, and D. T. Resio. 2001. *STWAVE: Steady-state spectral wave model user's manual for STWAVE, Version 3.0*. ERDC/CHL SR-01-1. Vicksburg, MS: US Army Engineer Research and Development Center.

Smith, J. M. 2001. *Modeling nearshore transformation with STWAVE*. Coastal and Hydraulics Engineering Technical Note CHETN I-64. Vicksburg, MS: US Army Engineer Research and Development Center.

Smith, J. M. 2007. *Full-Plane STWAVE II: Model Overview*. ERDC CHETN-I-75. Vicksburg, MS: US Army Engineer Research and Development Center.

Smith, J. M., R. E. Jensen, A. B. Kennedy, C. J. Dietrich, and J. J. Westerink. 2010. Waves in Wetlands: Hurricane Gustav. In *Proceedings from the 32nd International Conference on Coastal Engineering*. Shanghai, China, June 30-July 5, 2010.

Sullivan, C. L. 2009. Hurricanes of the Mississippi Gulf Coast: Three centuries of destruction. Perkinston, MS: Mississippi Gulf Coast Community College Press.

Tanaka, S., S. Bunya, J. J. Westerink, C. Dawson, R. A. Luettich. 2010. Scalability of an unstructured grid continuous galerkin based hurricane storm surge model. *Journal of Scientific Computing*.

Thompson, E. F., and V. J. Cardone. 1996. Practical modeling of hurricane surface wind fields. *J. Waterway, Port, Coastal Engr.* 122(4):195-205.

Tillman, D., C. Cerco, M. Noel, J. Martin, and J. Hamrick. 2004. *Three-dimensional eutrophication model of the lower St. Johns River, Florida*. ERDC TR-04-13. Vicksburg, MS: US Army Engineer Research and Development Center.

Tillman, D. H. , R. McAdory, B. W. Bunch, S. K. Martin, M. J. Briggs, F. C. Carson, G. Savant, and N. K. Raphelt. 2008. *Circulation and water quality modeling in support of deepening the port of Los Angeles: Alternative disposal sites*. ERDC/CHL TR-08-6. Vicksburg, MS: US Army Engineer Research and Development Center.

US Army Corps of Engineers (USACE). 2009. Mississippi coastal improvements program, Hancock, Harrison, and Jackson Counties, Mississippi, comprehensive plan and integrated programmatic environmental impact statement. Mobile, AL: US Army Engineer District; Mobile.

WAMDI Group. 1988. The WAM Model – A third generation ocean wave prediction model. *Journal of Physical Oceanography* 18:1775-1810.

Wamsley, T. V., M. A. Cialone, J. M. Smith, B. A. Ebersole, and A. S. Grzegorzewski. 2009. Influence of landscape restoration and degradation on storm surge and waves in southern Louisiana. *Journal of Natural Hazards*, doi:10.1007/s11069-009-9378-z.

Westerink, J. J., C. A. Blain, R. A. Luettich, and N. W. Scheffner. 1994. *ADCIRC: an advanced three-dimensional circulation model for shelves, coasts, and estuaries*. Technical Report DRP-92-6. Vicksburg, MS: US Army Engineer Research and Development Center.

Westerink, J. J., R. A. Luettich, J. C. Feyen, J. H. Atkinson, C. Dawson, H. J. Roberts, M. D. Powell, J. P. Dunion, E. J. Kubatko, and H. Pourtaheri. 2008. A basin-to-channel-scale unstructured grid hurricane storm surge model applied to southern Louisiana. *Monthly Weather Review* 136:833-864.

Zambreski, L. 1989. A verification study of the global WAM model, December 1987–November 1988, Tech. Rep. 63, Eur. Cent. for Medium-Range Weather Forecasts, Reading, England.

Zambreski, L. 1991. An evaluation of two WAM hindcasts for LEWEX, in Directional Ocean Wave Spectra, edited by R. C. Beal, pp. 167–172. Baltimore, MD: Johns Hopkins Univ. Press.

Appendix A: Wave Measurements Results

Figure A-1. Wave direction (direction waves are coming from at the spectral peak), H_{mo}, and wave period (at the spectral peak), for the gauge in the Mississippi Sound (top) and for the gauge in the Gulf of Mexico (bottom) from March 4 through 11, 2010.

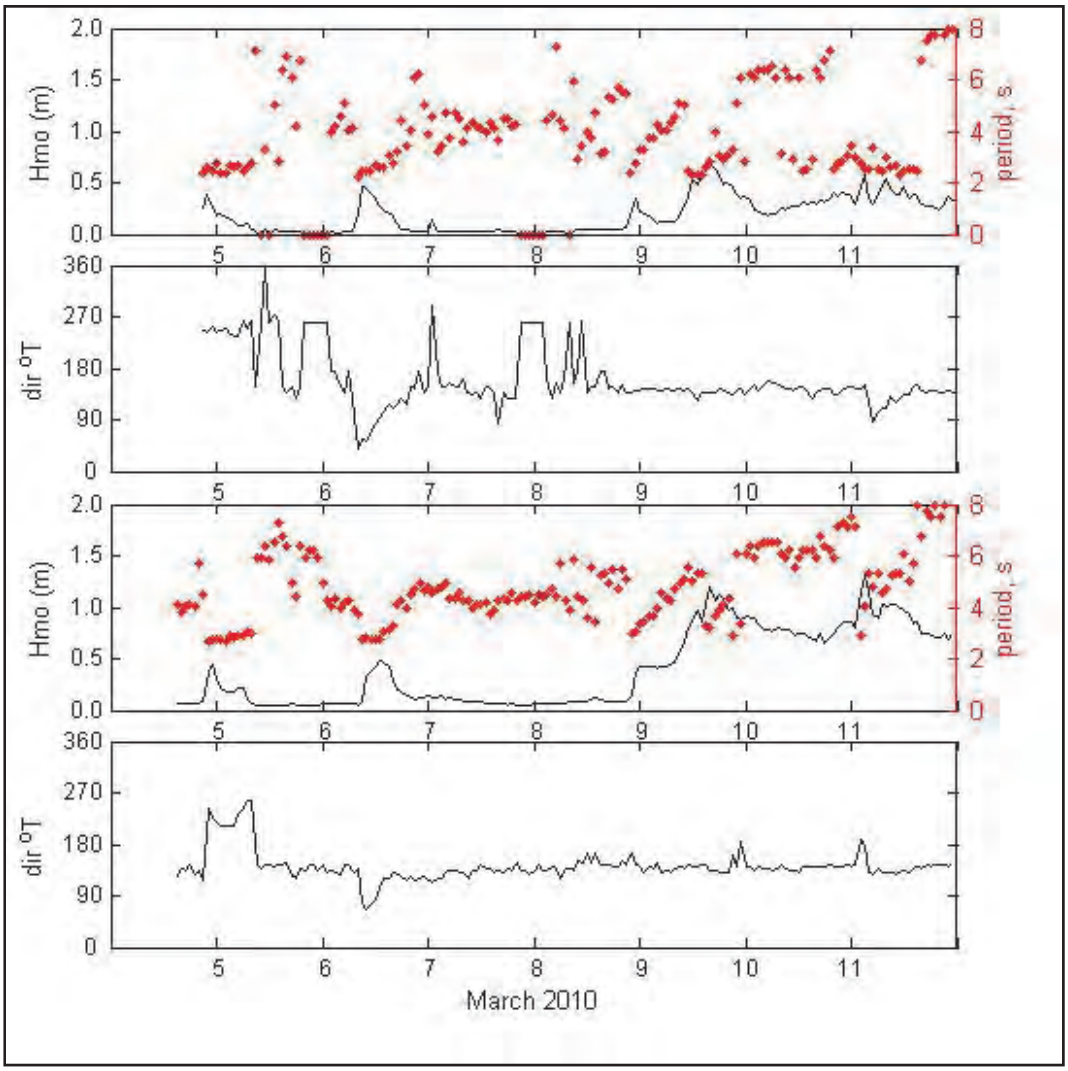

Figure A-2. Wave direction (direction waves are coming from at the spectral peak), H_{mo}, and wave period (at the spectral peak), for the gauge in the Mississippi Sound (top) and for the gauge in the Gulf of Mexico (bottom) from March 12 through 19, 2010.

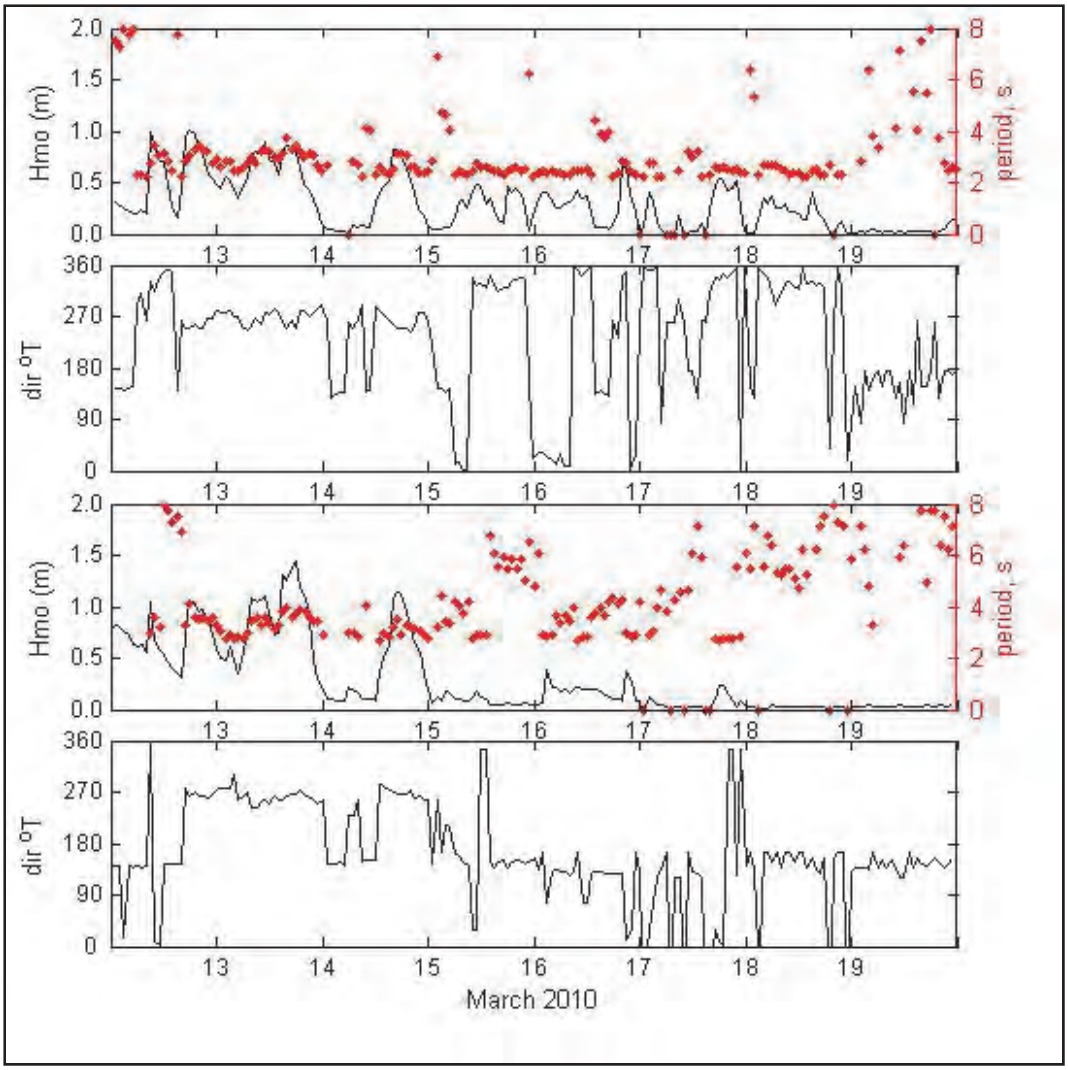

Figure A-3. Wave direction (direction waves are coming from at the spectral peak), H_{mo}, and wave period (at the spectral peak), for the gauge in the Mississippi Sound (top) and for the gauge in the Gulf of Mexico (bottom) from March 20 through 27, 2010.

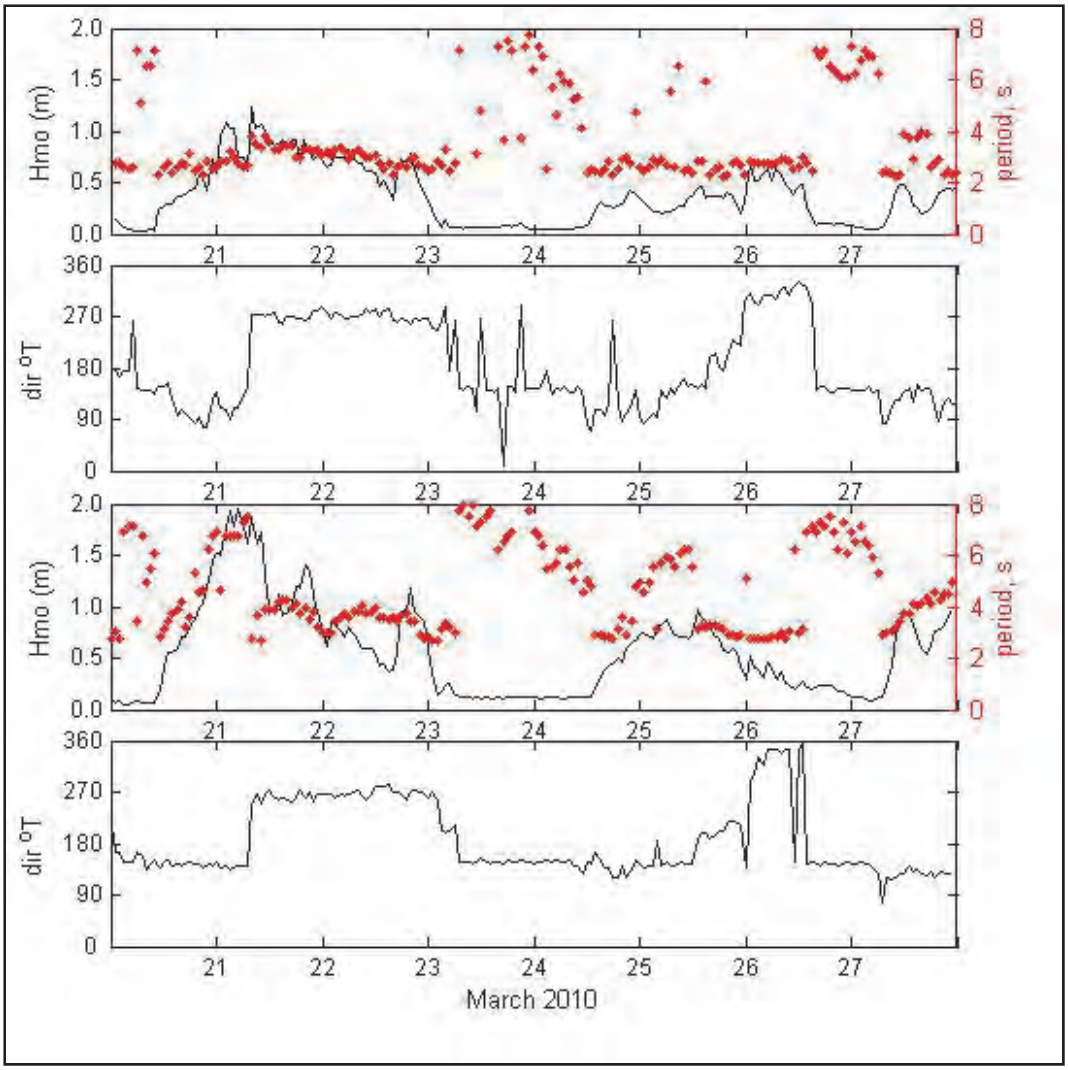

Figure A-4. Wave direction (direction waves are coming from at the spectral peak), H_{mo}, and wave period (at the spectral peak), for the gauge in the Mississippi Sound (top) and for the gauge in the Gulf of Mexico (bottom) from March 28 through April 4, 2010.

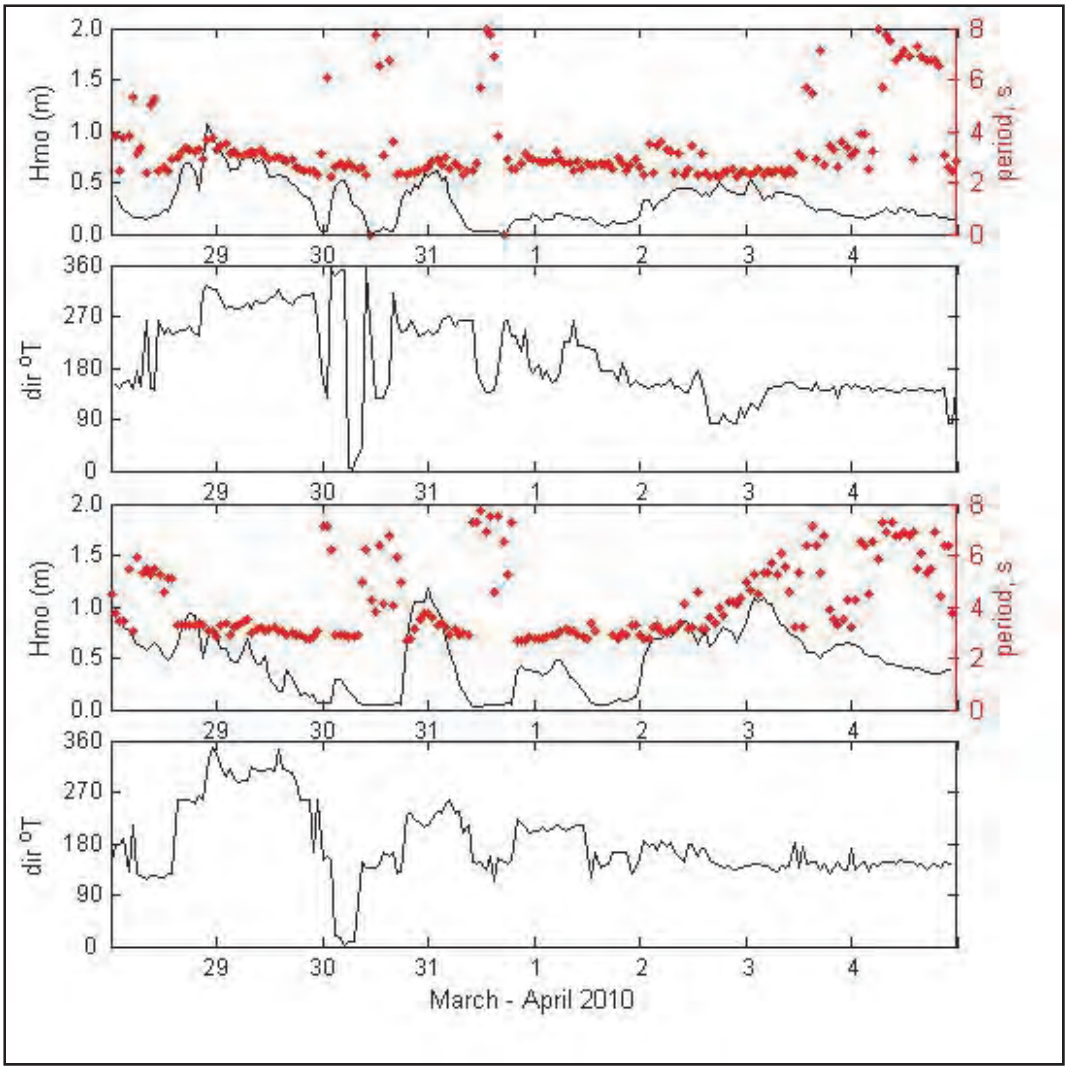

Figure A-5. Wave direction (direction waves are coming from at the spectral peak), H_{mo}, and wave period (at the spectral peak), for the gauge in the Mississippi Sound (top) and for the gauge in the Gulf of Mexico (bottom) from April 5 through 12, 2010.

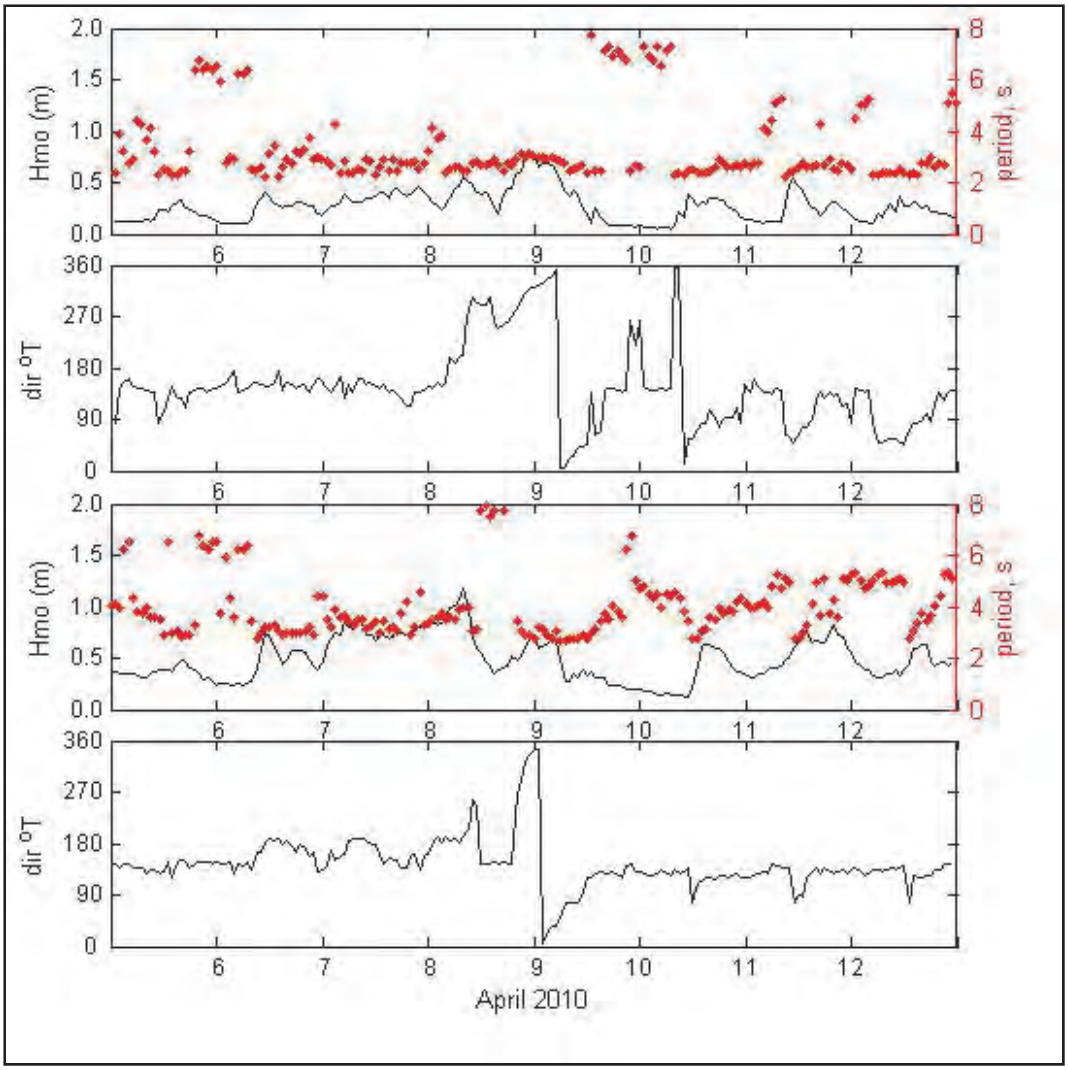

Figure A-6. Wave direction (direction waves are coming from at the spectral peak), H_{mo}, and wave period (at the spectral peak), for the gauge in the Mississippi Sound (top) and for the gauge in the Gulf of Mexico (bottom) from April 13 through 20, 2010.

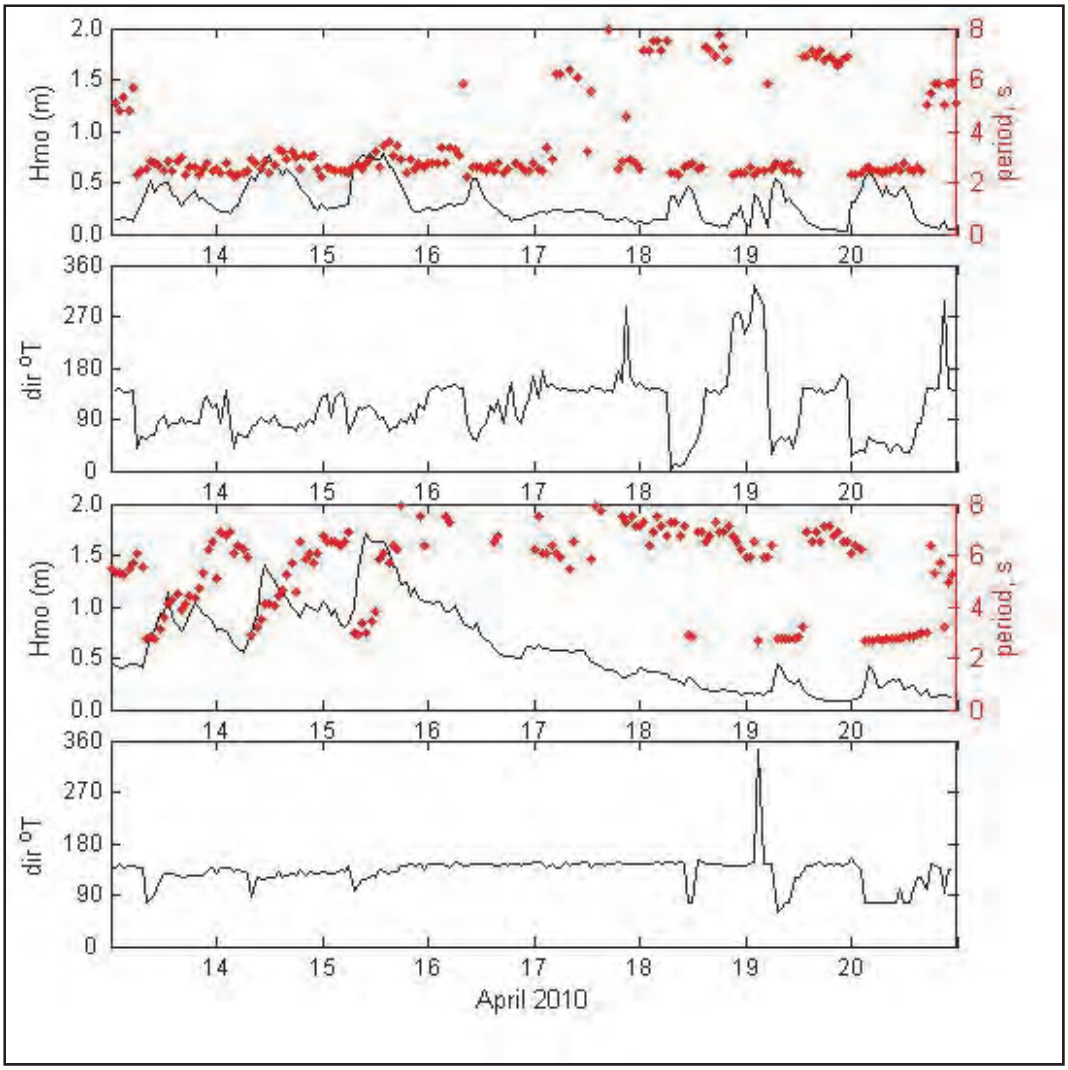

Figure A-7. Wave direction (direction waves are coming from at the spectral peak), H_{mo}, and wave period (at the spectral peak), for the gauge in the Mississippi Sound (top) and for the gauge in the Gulf of Mexico (bottom) from April 21 through 28, 2010.

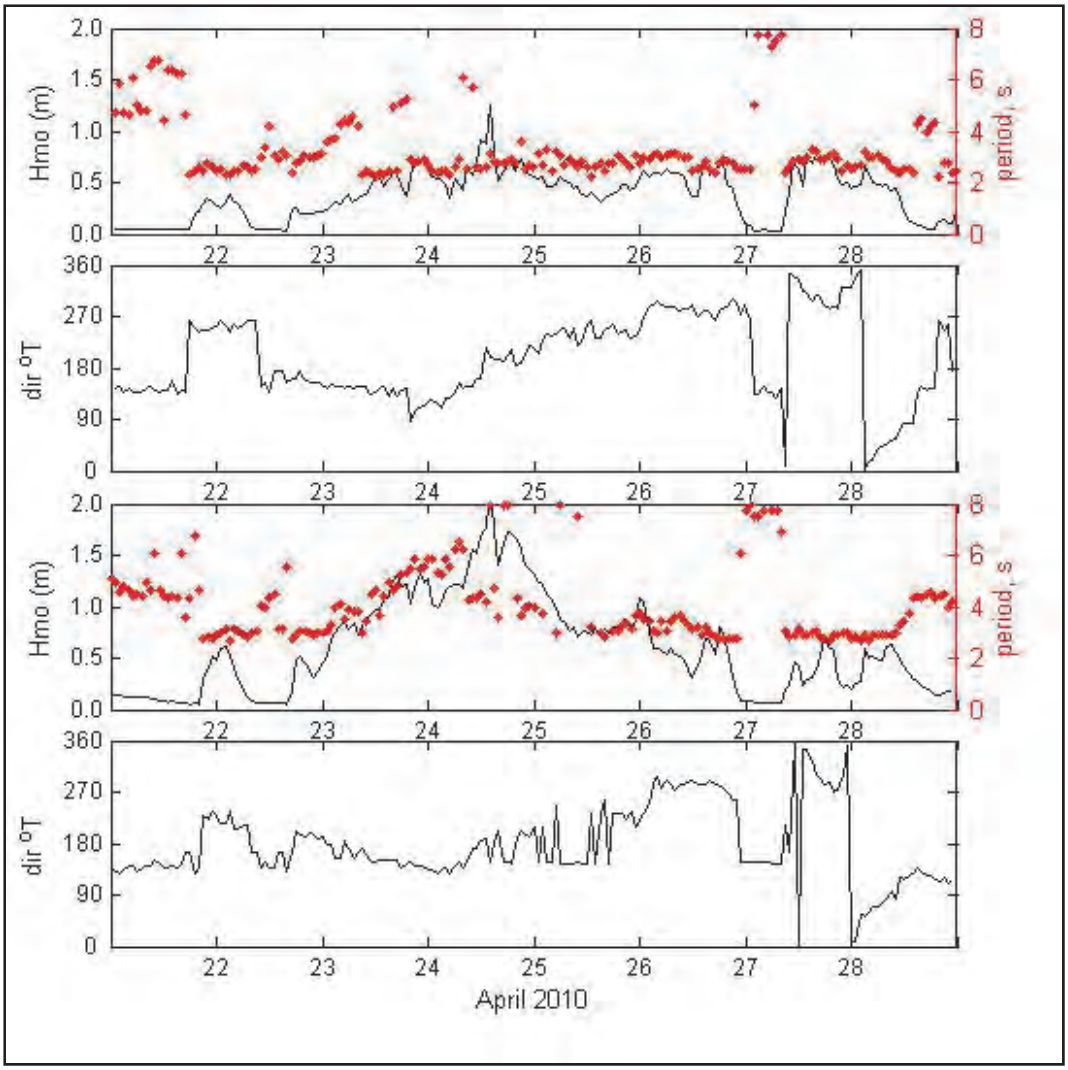

Figure A-8. Wave direction (direction waves are coming from at the spectral peak), H_{mo}, and wave period (at the spectral peak), for the gauge in the Mississippi Sound (top)) from April 29 through May 6, 2010, and for the gauge in the Gulf of Mexico (bottom) from April 29 until it stopped recording valid data on April 30, 2010.

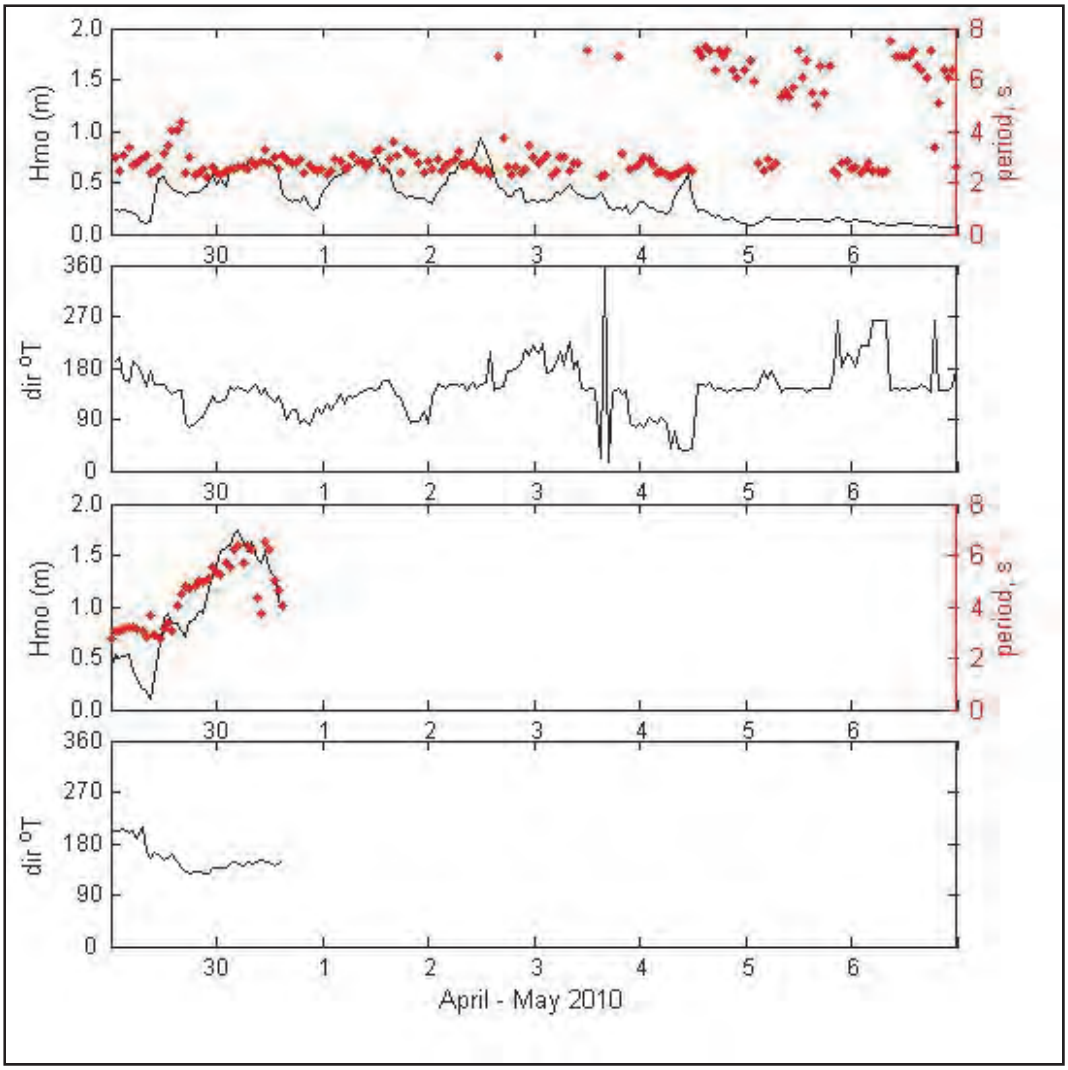

Figure A-9. Wave direction (direction waves are coming from at the spectral peak), H_{mo}, and wave period (at the spectral peak), for the gauge in the Mississippi Sound from May 7 through 22, 2010.

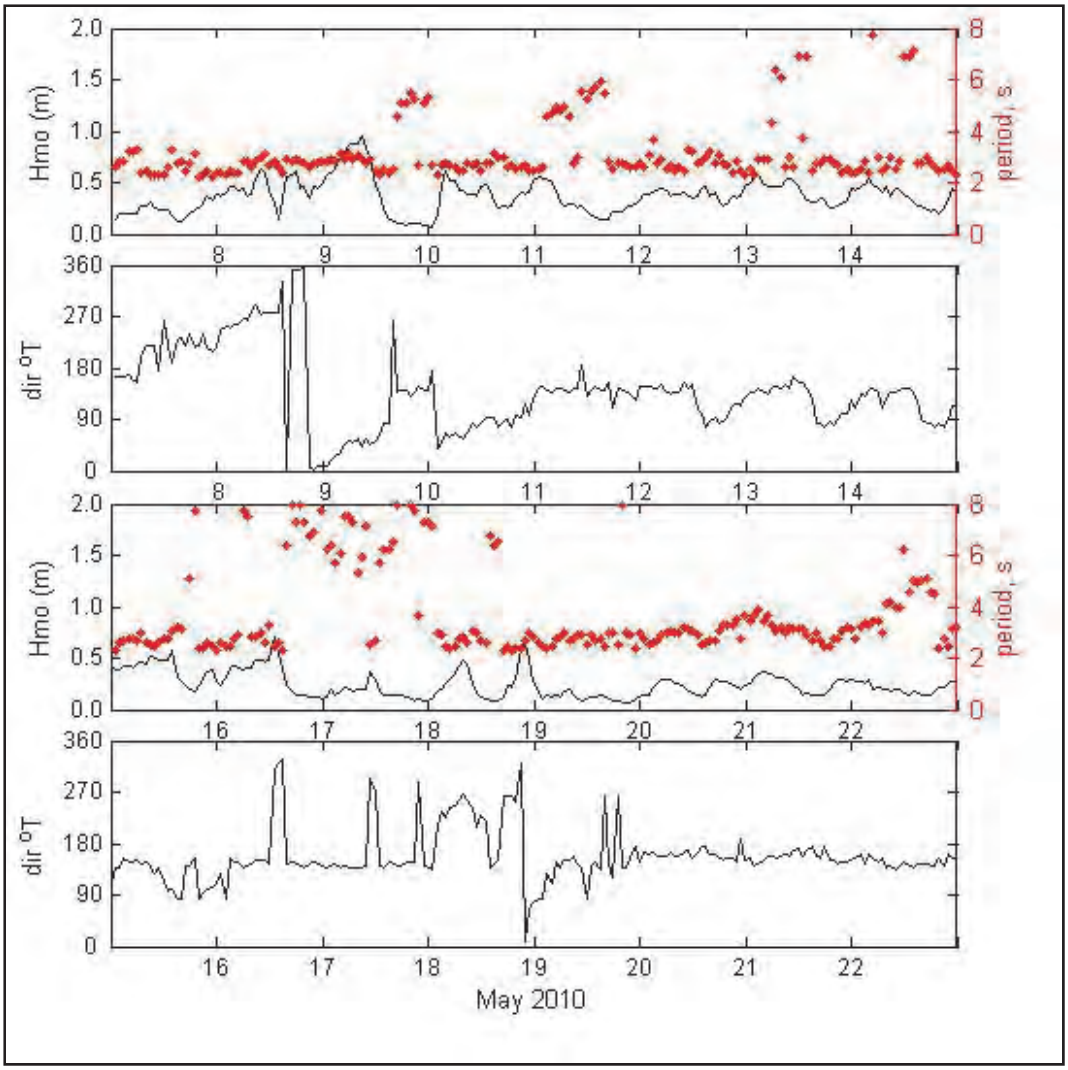

Figure A-10. Wave direction (direction waves are coming from at the spectral peak), H_{mo}, and wave period (at the spectral peak), for the gauge in the Mississippi Sound from May 23 through June 7, 2010.

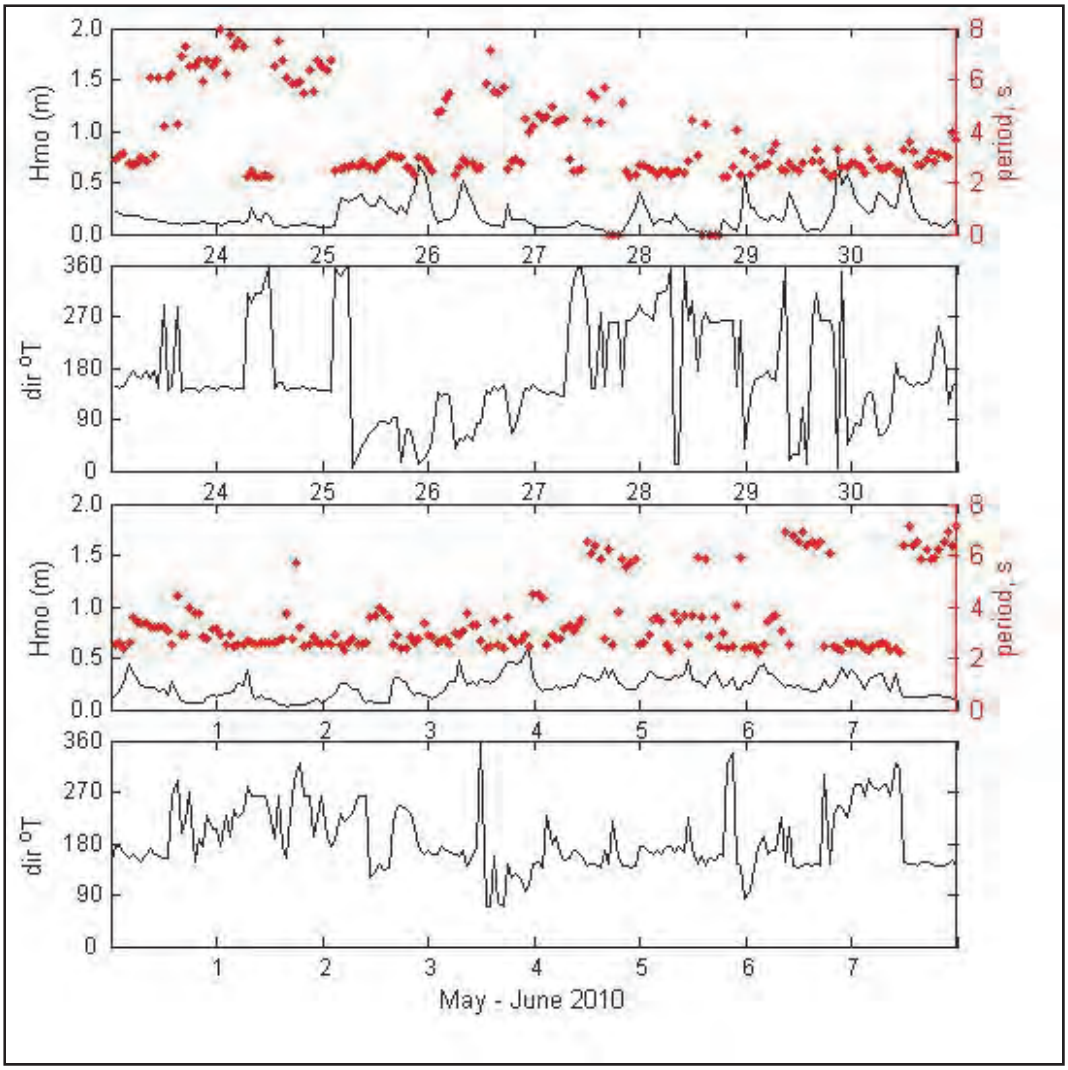

Figure A-11. Wave direction (direction waves are coming from at the spectral peak), H_{mo}, and wave period (at the spectral peak), for the gauge in the Mississippi Sound from June 8 through 23, 2010.

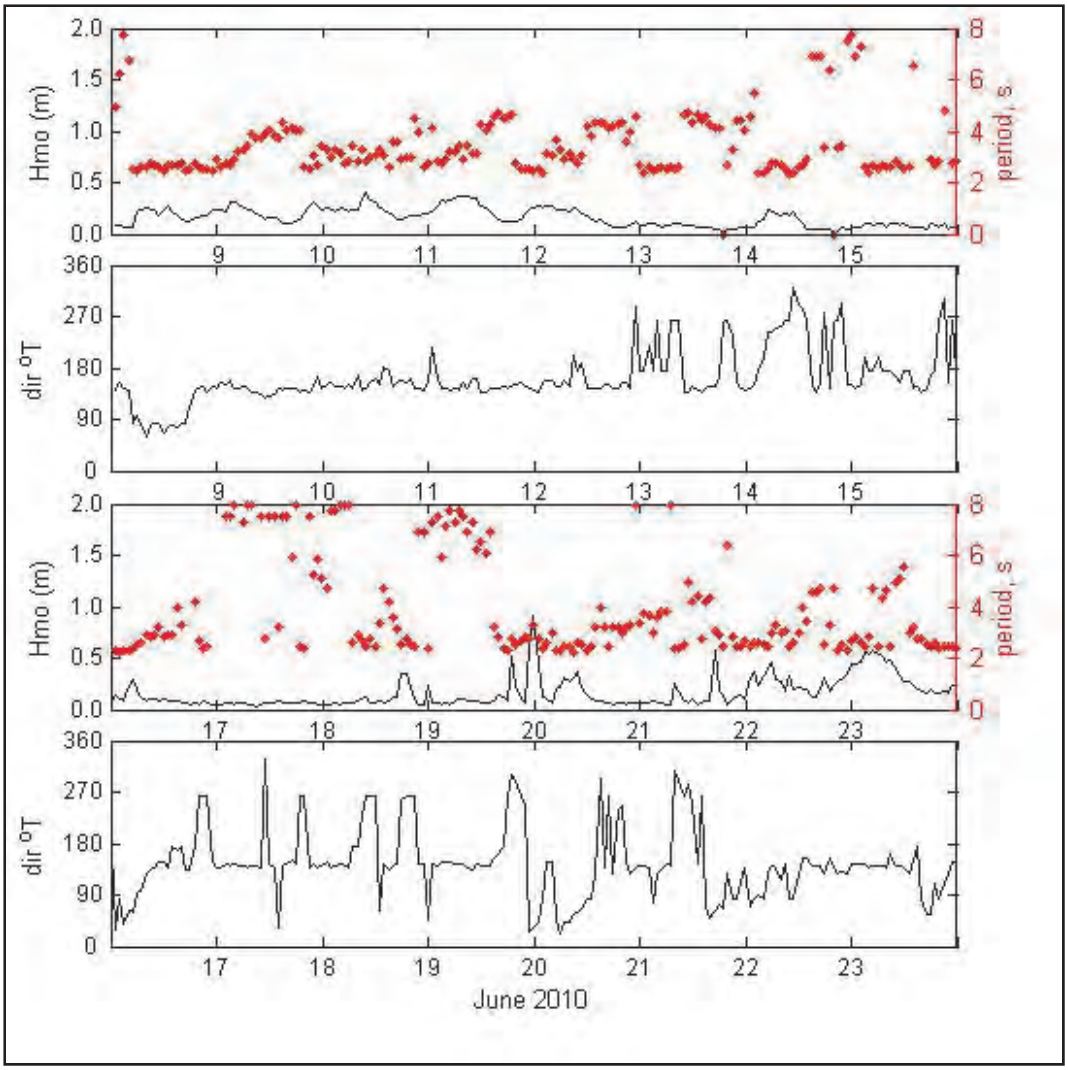

Figure A-12. Wave direction (direction waves are coming from at the spectral peak), H_{mo}, and wave period (at the spectral peak), for the gauge in the Mississippi Sound from June 24 through July 9, 2010.

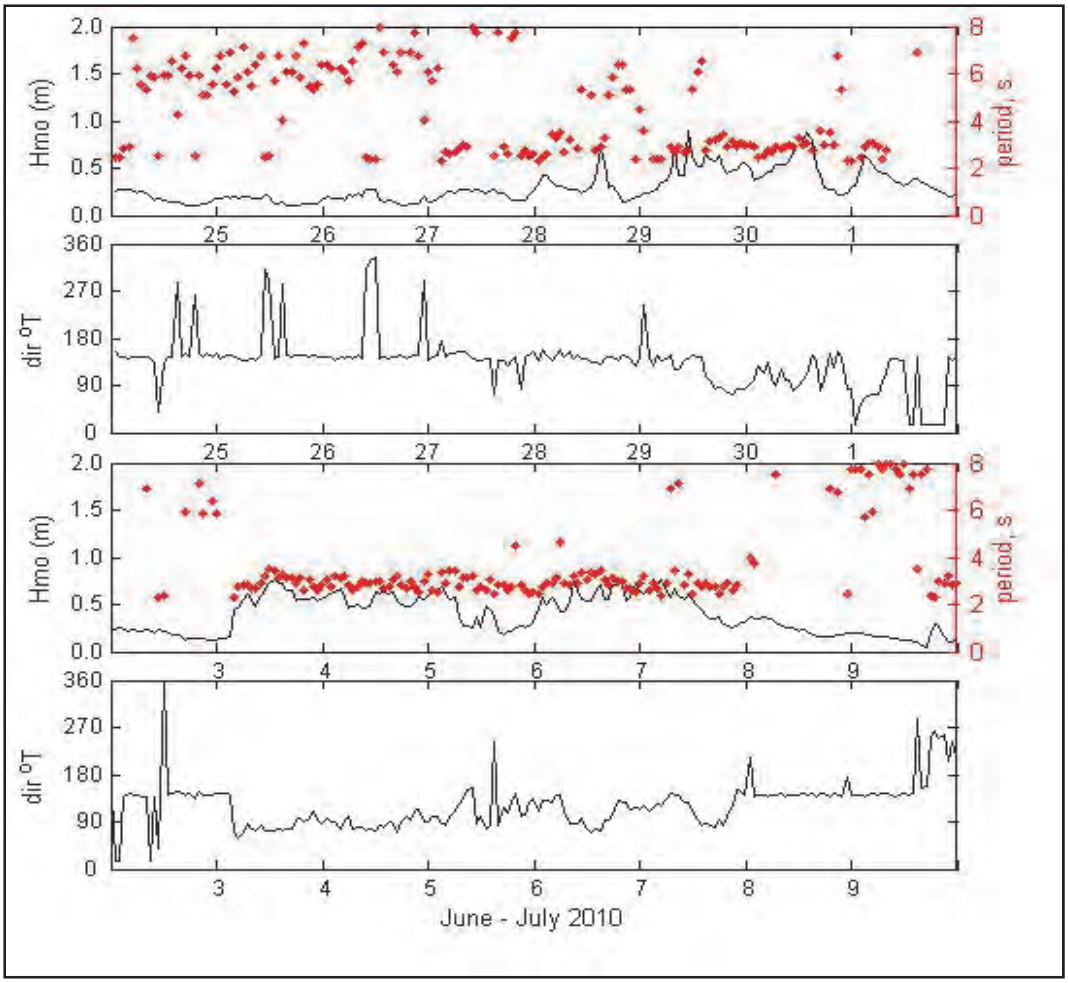

Figure A-13. Wave direction (direction waves are coming from at the spectral peak), H_{mo}, and wave period (at the spectral peak), for the gauge in the Mississippi Sound from July 10 until it was recovered on July 15, 2010.

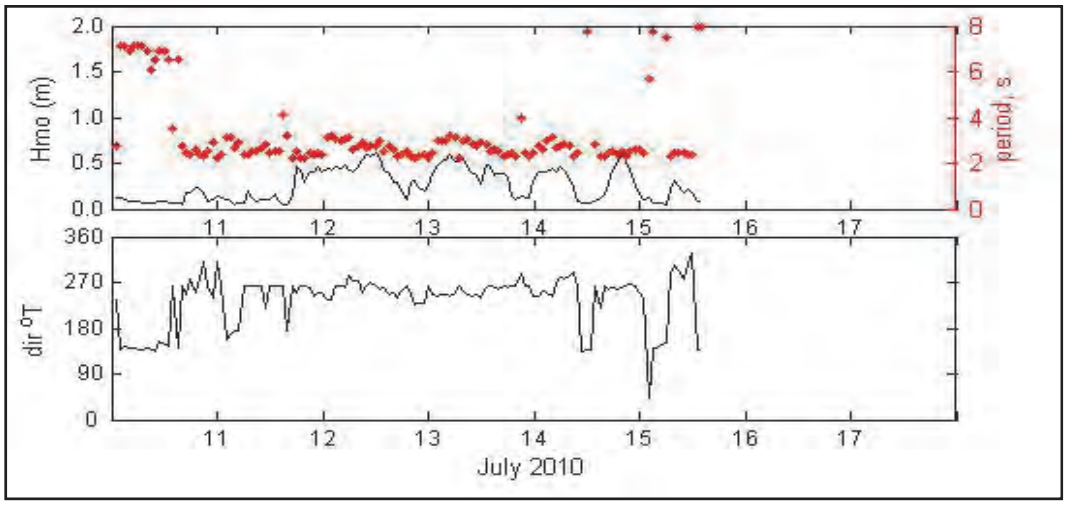

Appendix B: Water Level Measurements

Figure B-1. Mean water levels at the Sound wave gauge (black line) and at the Gulf gauge (red line) for March 4 through April 4, 2010.

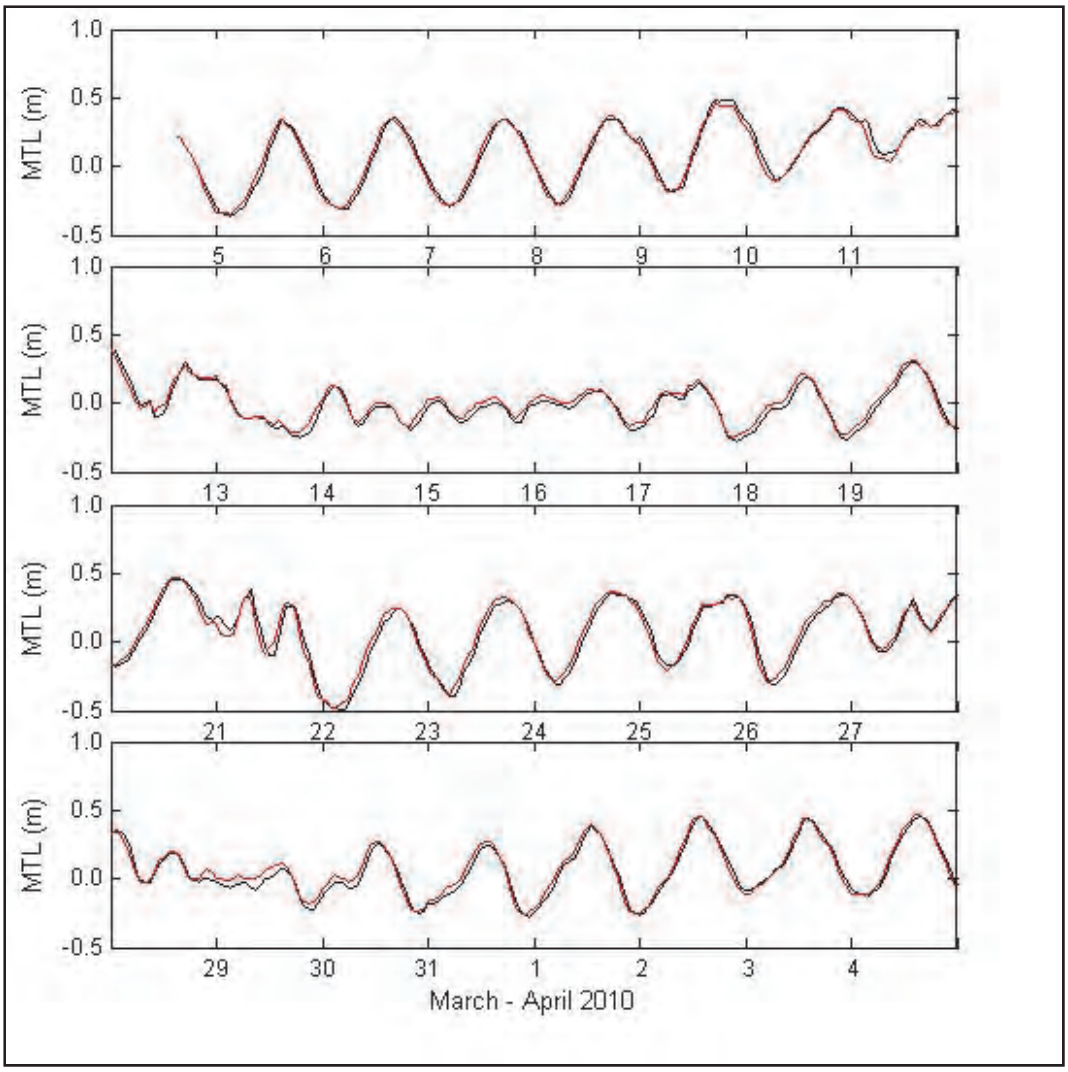

Figure B-2. Mean water levels at the Sound wave gauge (black line) for April 5 through May 6, 2010, and at the Gulf gauge (red line) for April 5 to April 30, 2010.

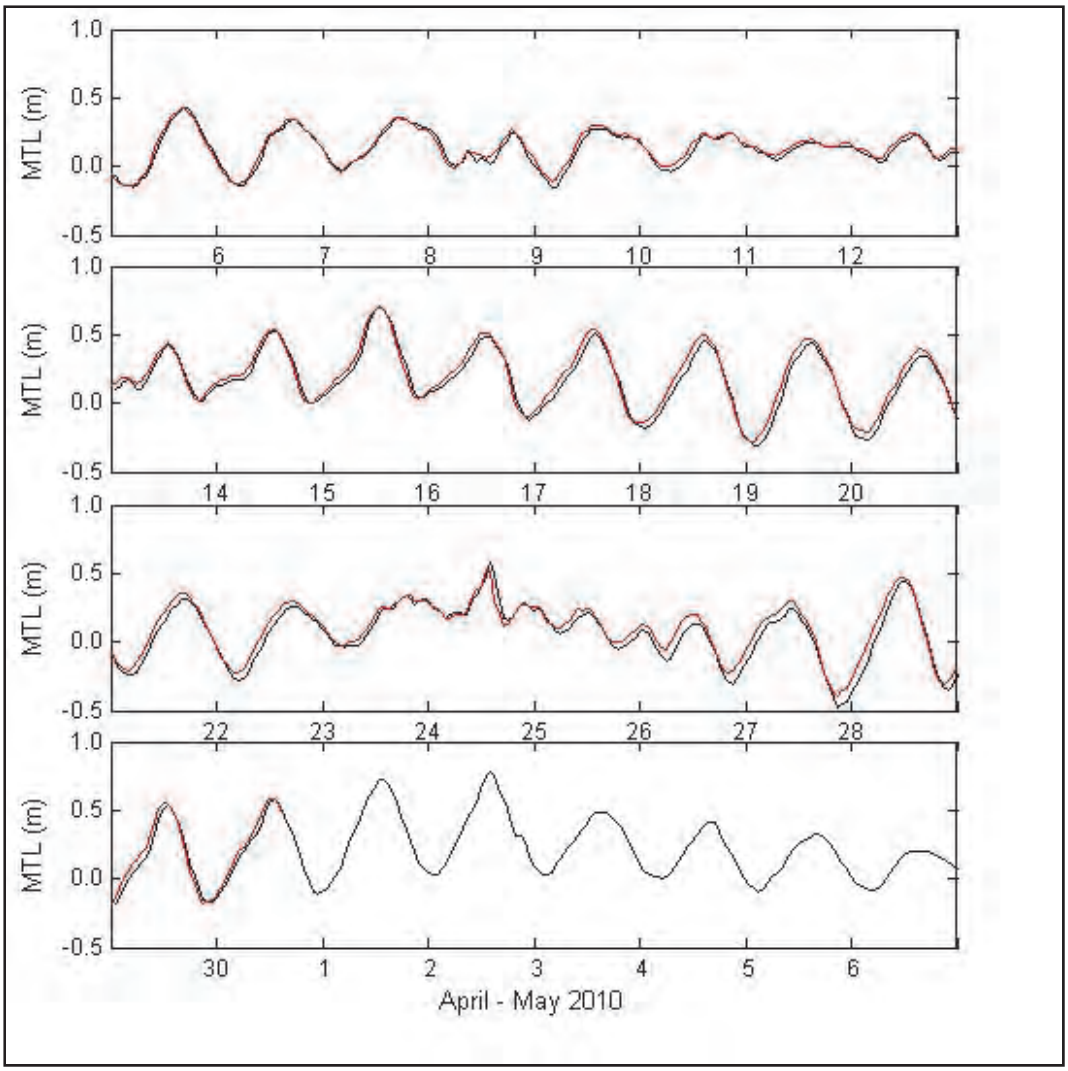

Figure B-3. Mean water levels at the Sound wave gauge for May 7 through June 7, 2010.

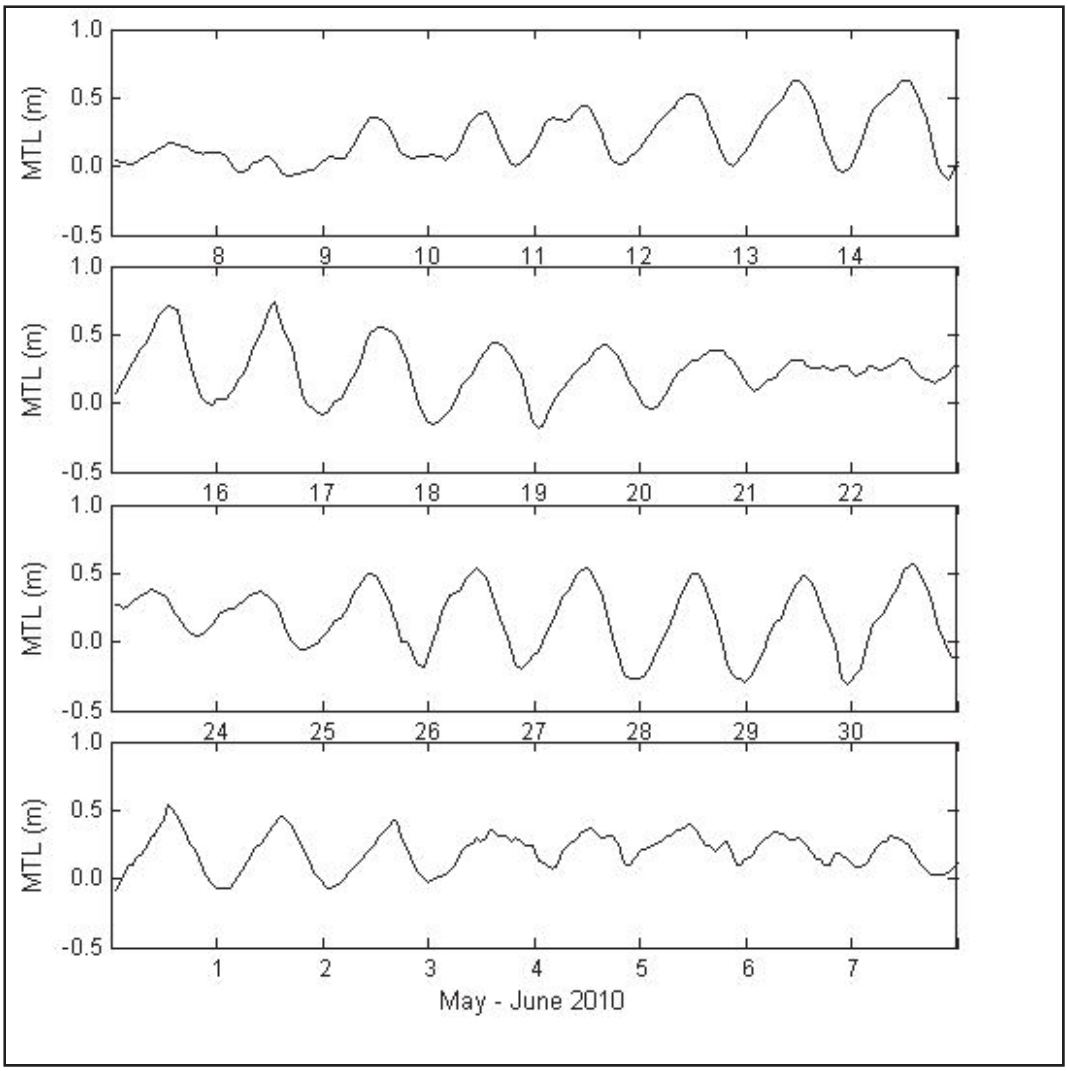

Figure B-4. Mean water levels at the Sound wave gauge for June 8 through July 9, 2010.

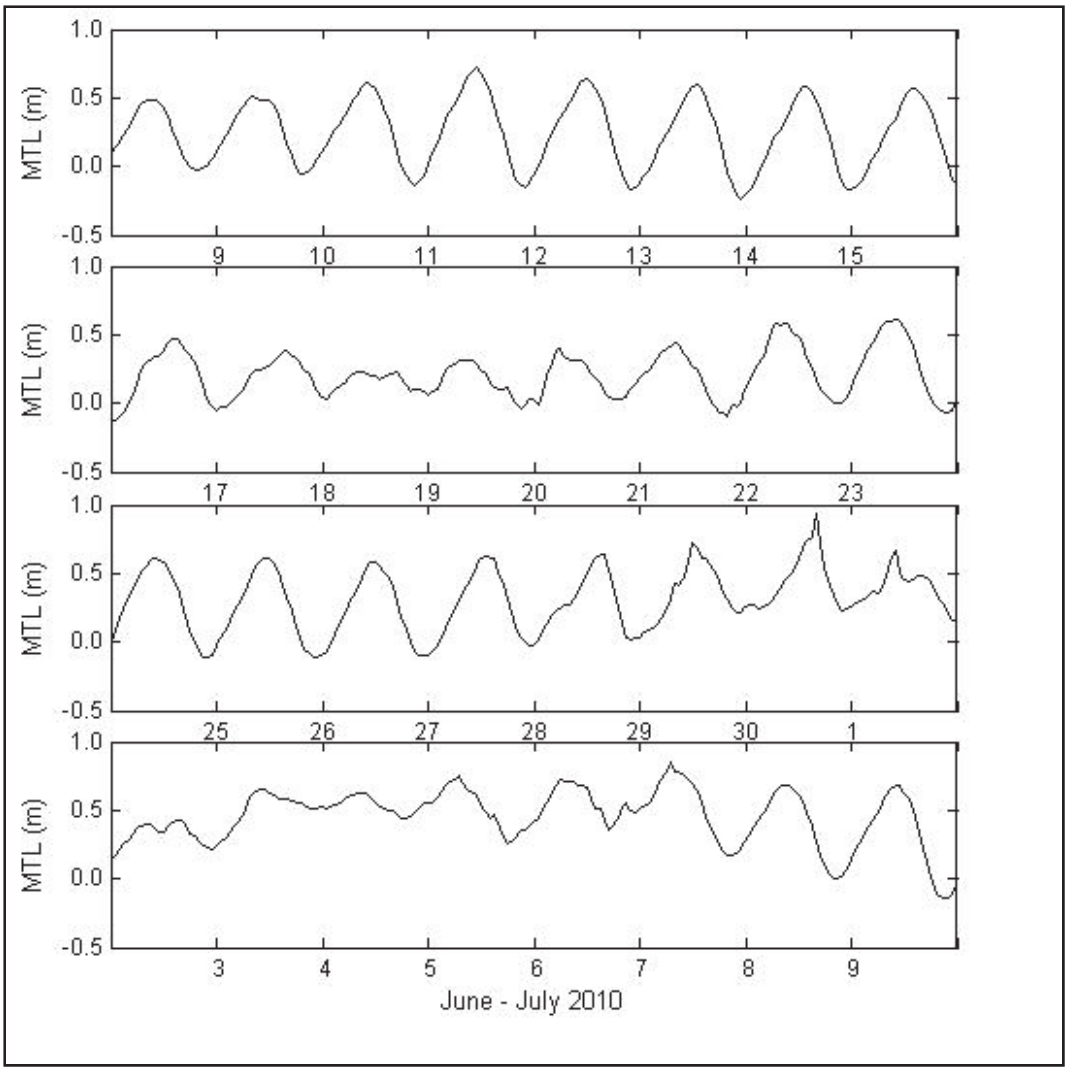

Figure B-5. Mean water levels at the Sound wave gauge for July 10 to July 15, 2010.

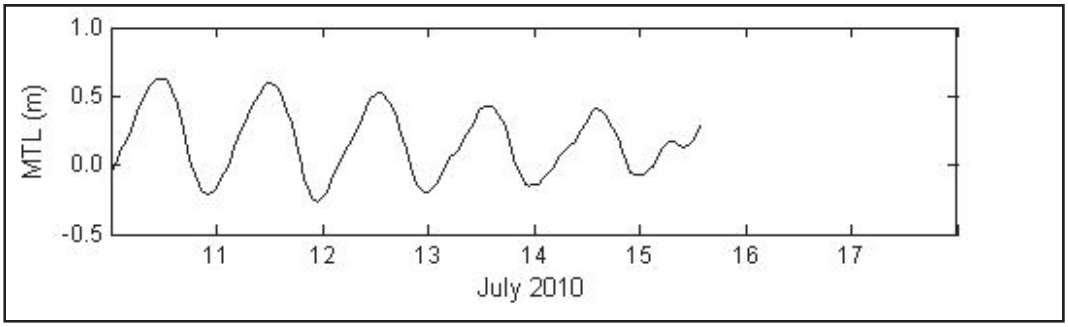

Appendix C: Current Measurements Results

Ship Island Pass

Figure C-1. Ship Island Pass Transect 1. Shown east (left side) to west (right side).

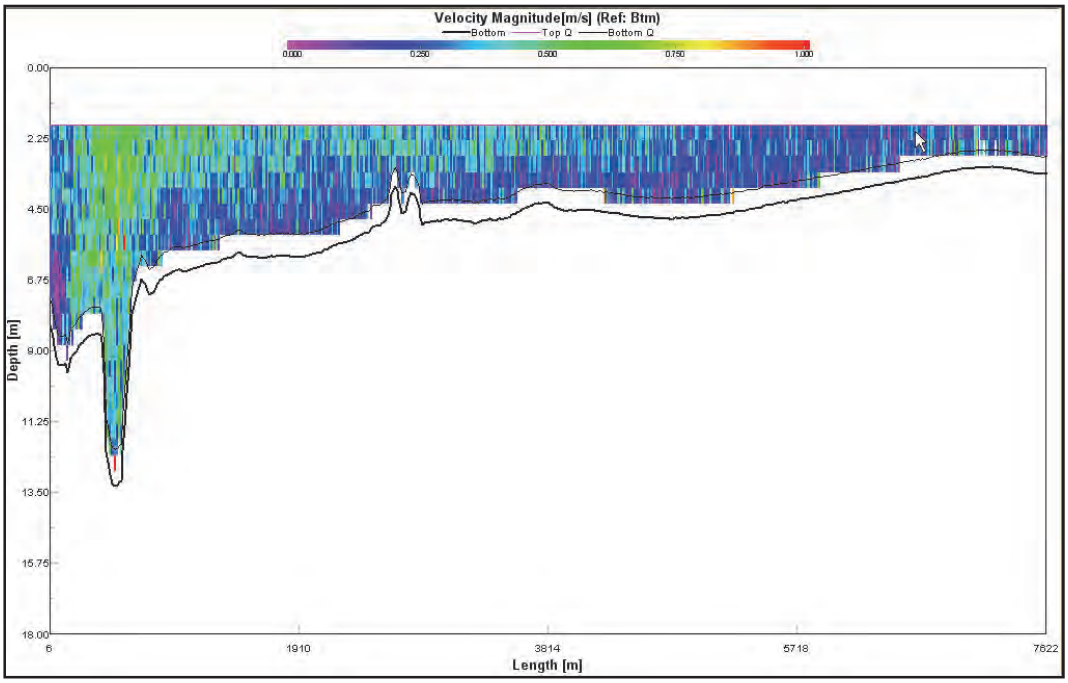

Figure C-2. Ship Island Pass Transect 2. Shown east (left side) to west (right side).

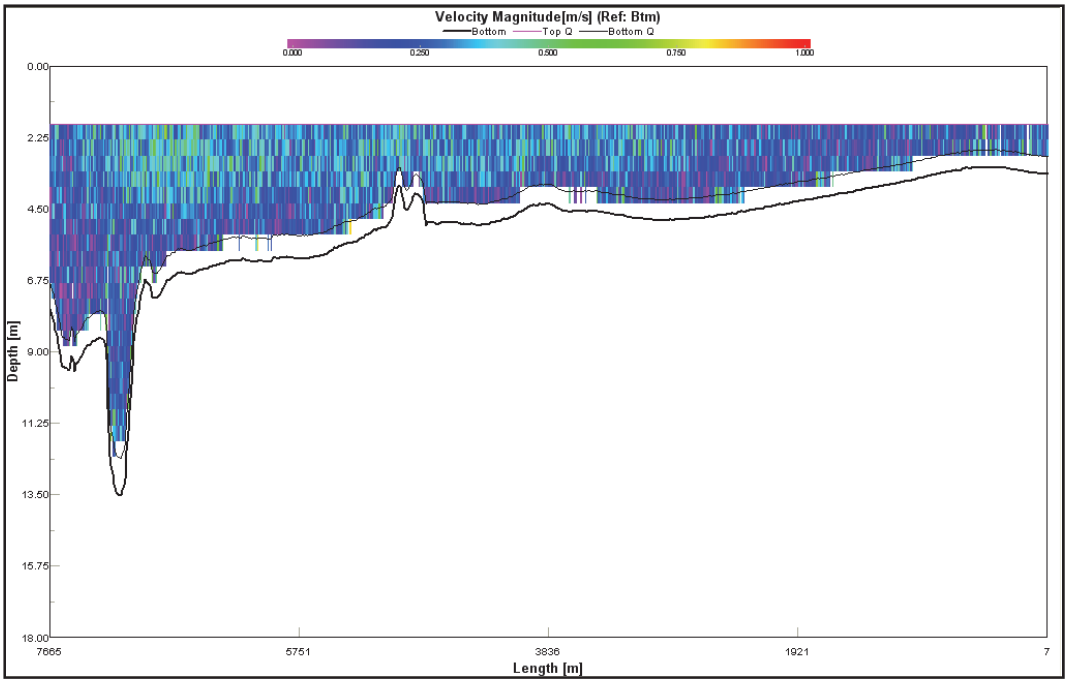

Figure C-3. Ship Island Pass Transect 3. Shown east (left side) to west (right side).

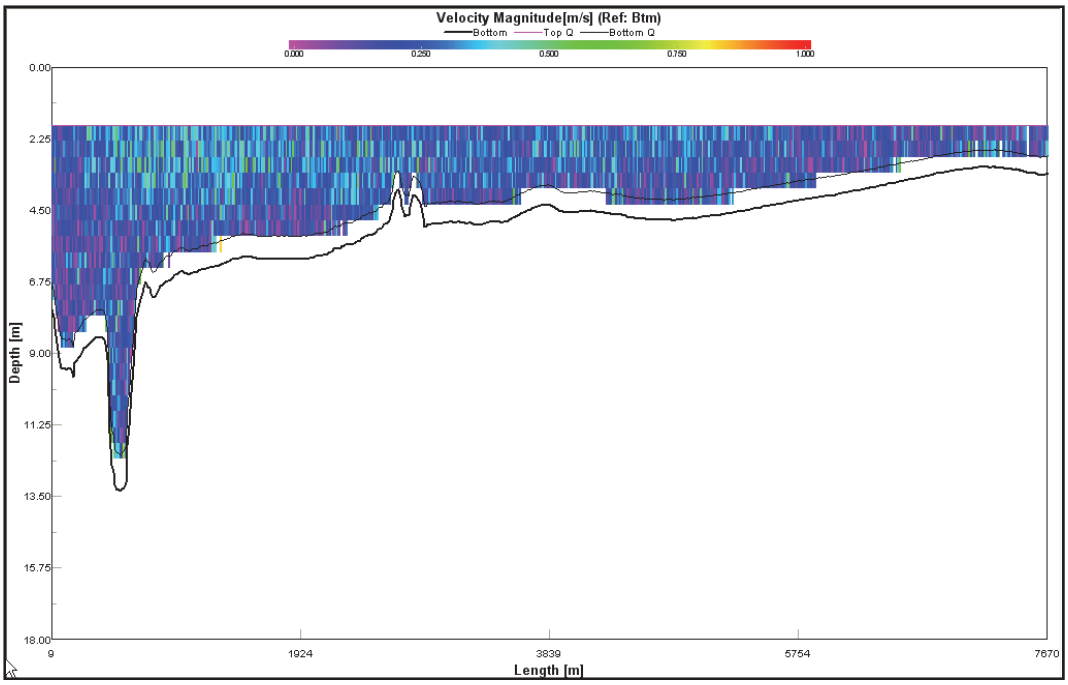

Figure C-4. Ship Island Pass Transect 4. Shown east (left side) to west (right side).

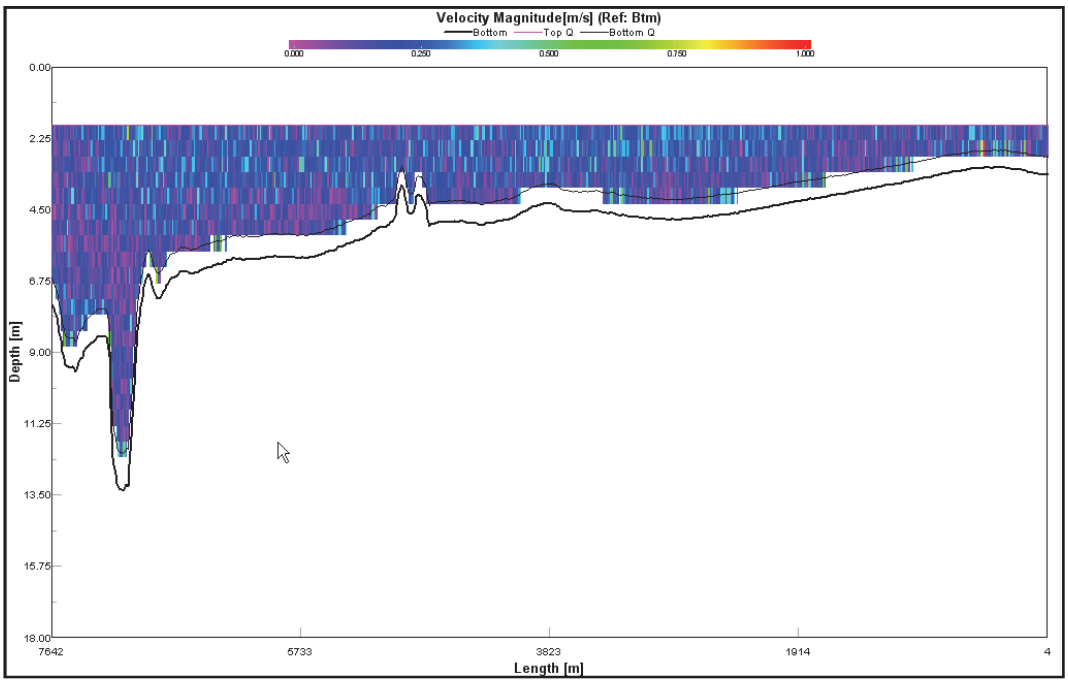

Figure C-5. Ship Island Pass Transect 5. Shown east (left side) to west (right side).

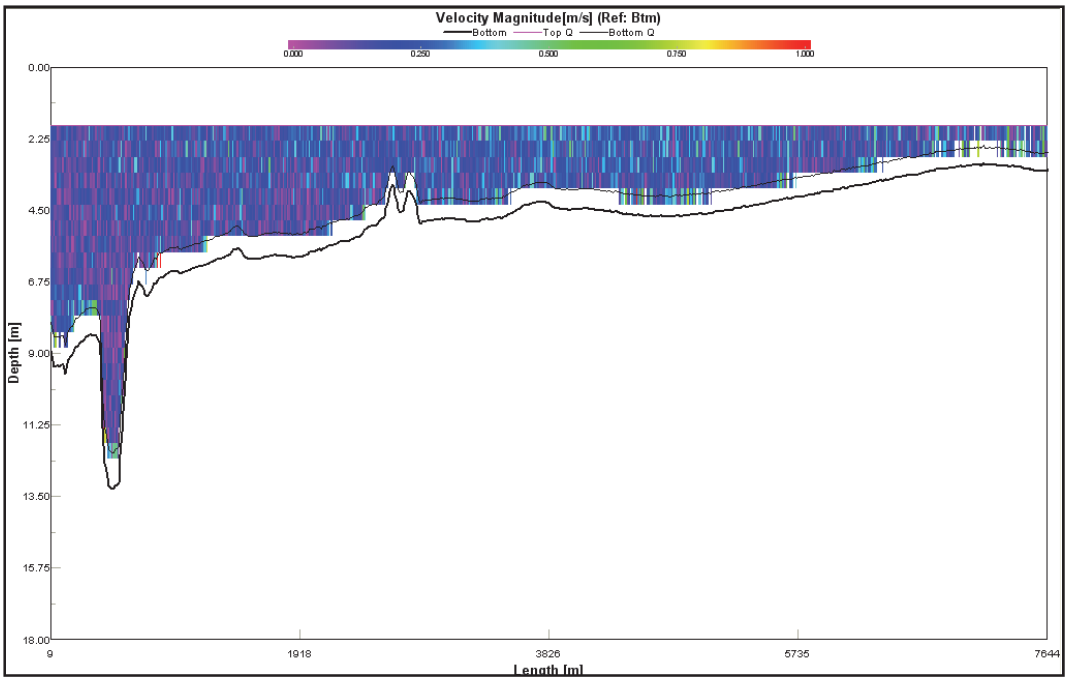

Figure C-6. Ship Island Pass Transect 6. Shown east (left side) to west (right side).

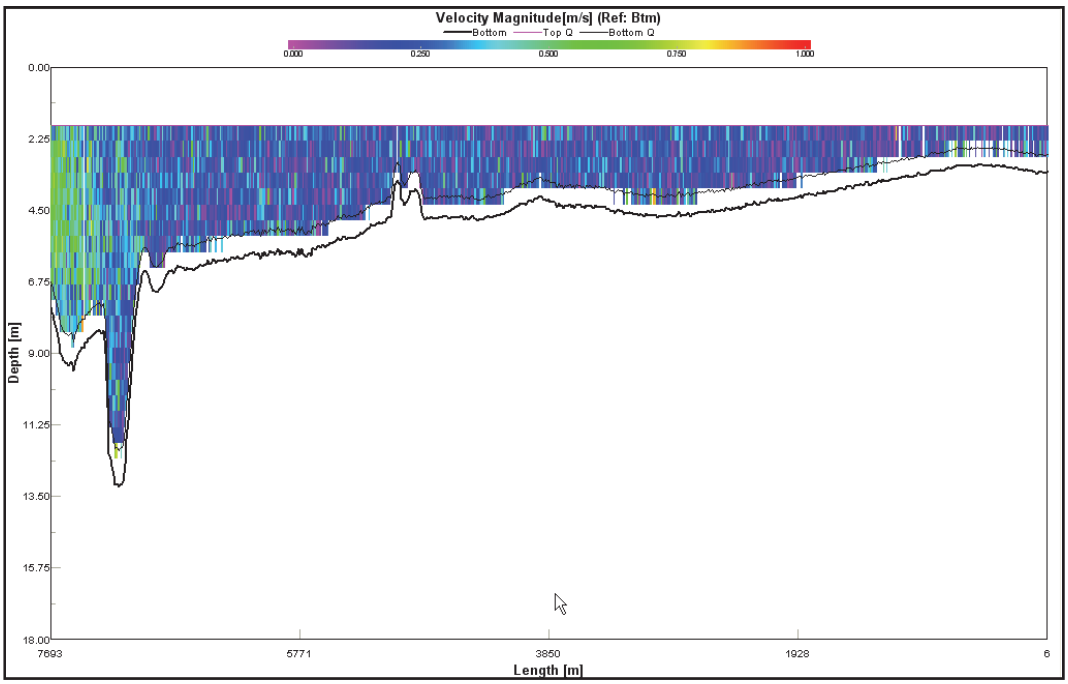

Figure C-7. Ship Island Pass Transect 7. Shown east (left side) to west (right side).

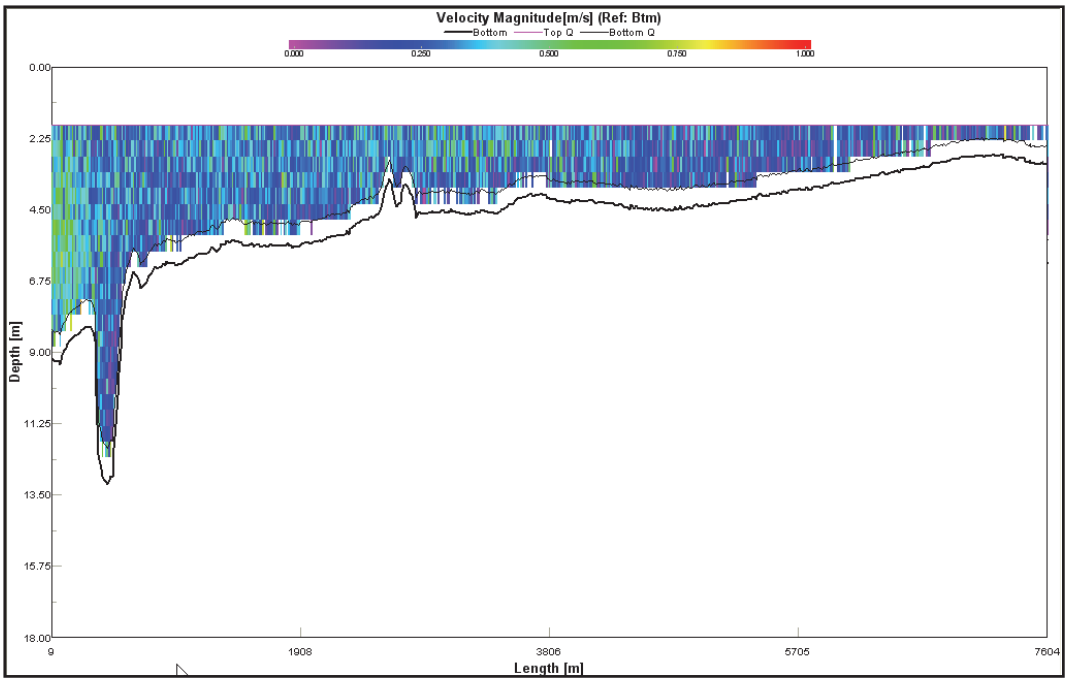

Figure C-8. Ship Island Pass Transect 8. Shown east (left side) to west (right side).

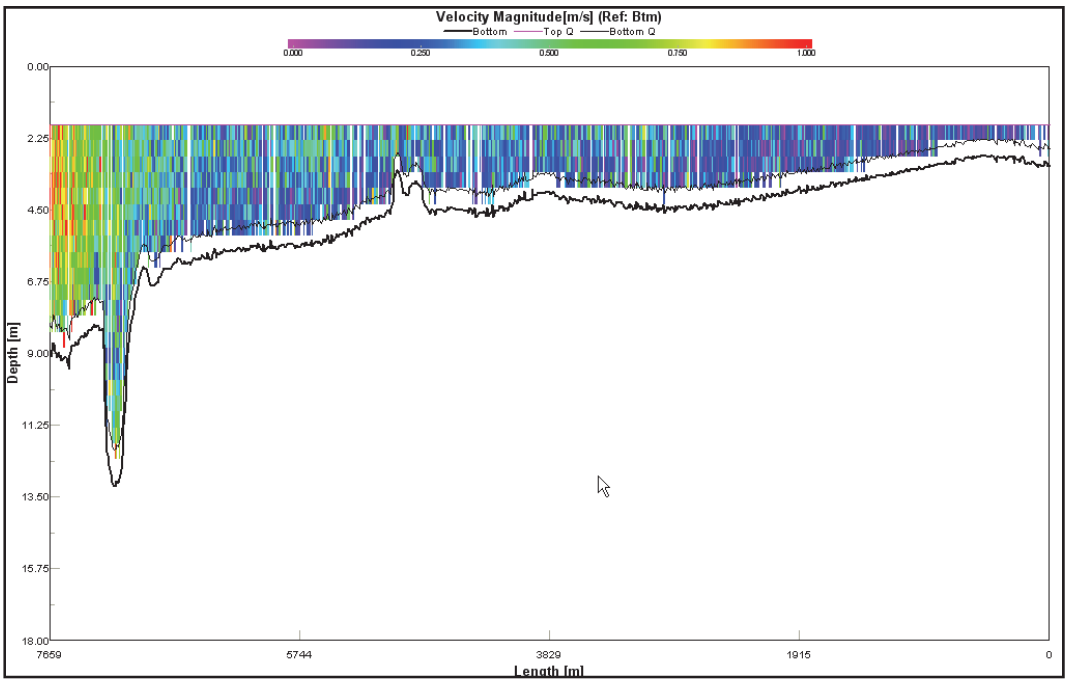

Dog Keys Passes

Figure C-9. Dog Keys Passes Transect 1. Shown west (left side) to east (right side).

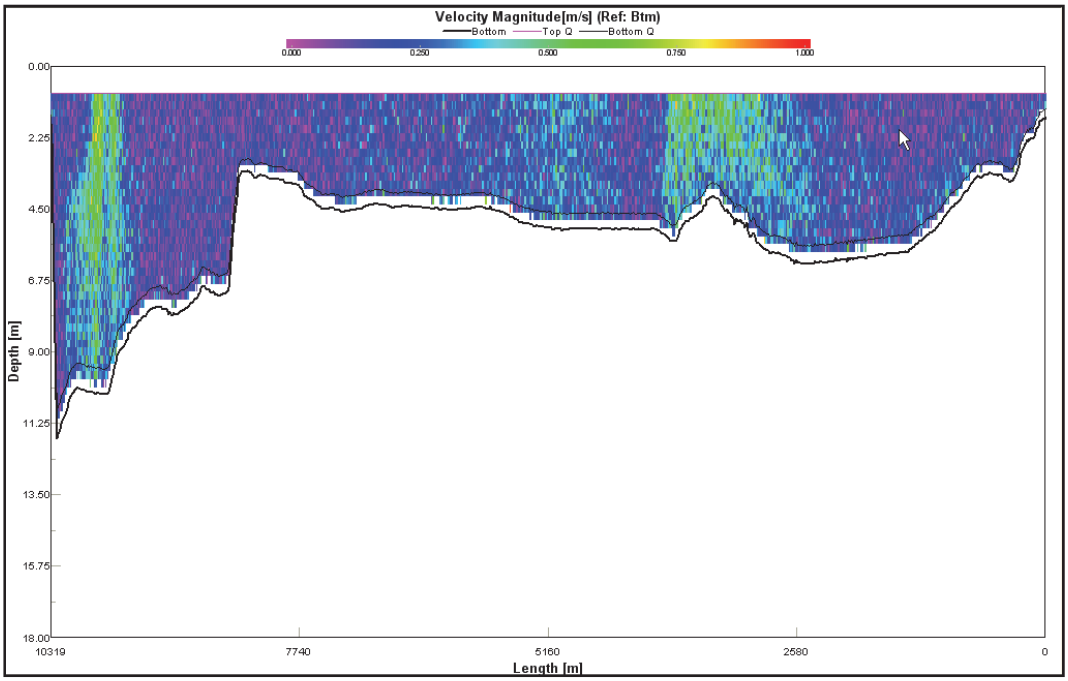

Figure C-10. Dog Keys Passes Transect 2. Shown west (left side) to east (right side).

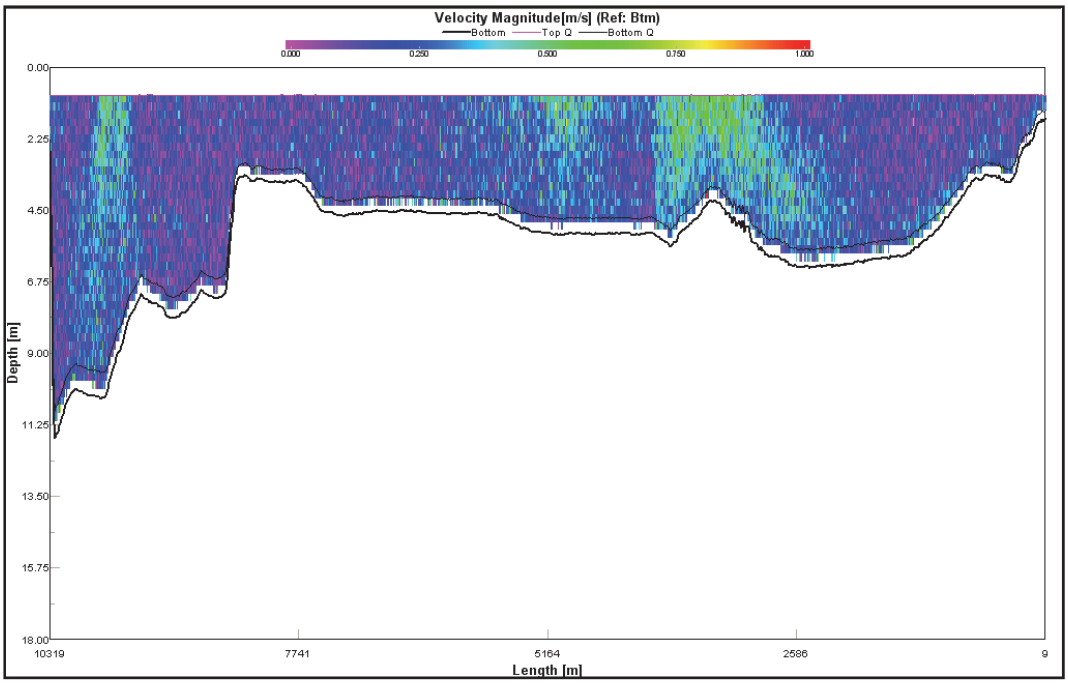

Figure C-11. Dog Keys Passes Transect 3. Shown west (left side) to east (right side).

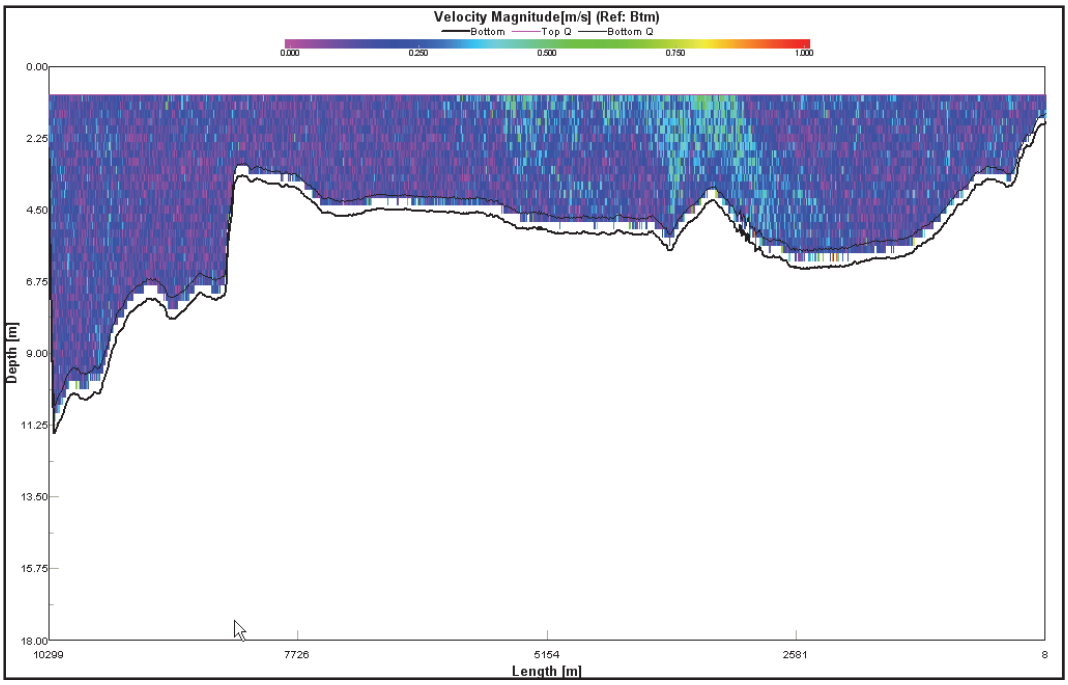

Figure C-12. Dog Keys Passes Transect 4. Shown west (left side) to east (right side).

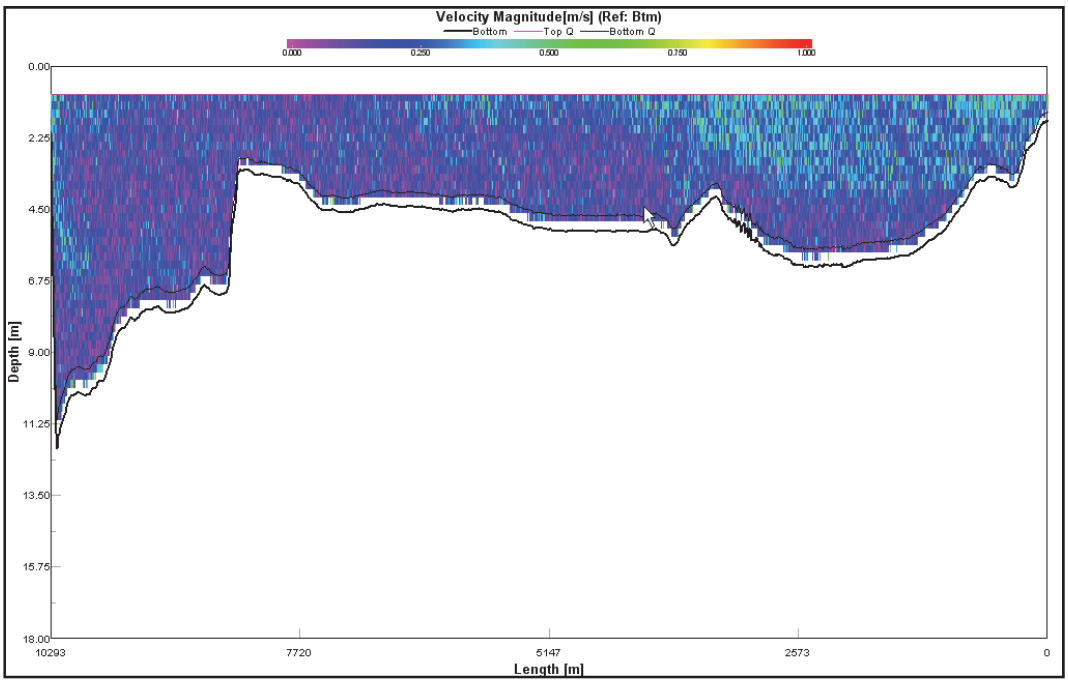

Figure C-13. Dog Keys Passes Transect 5. Shown west (left side) to east (right side).

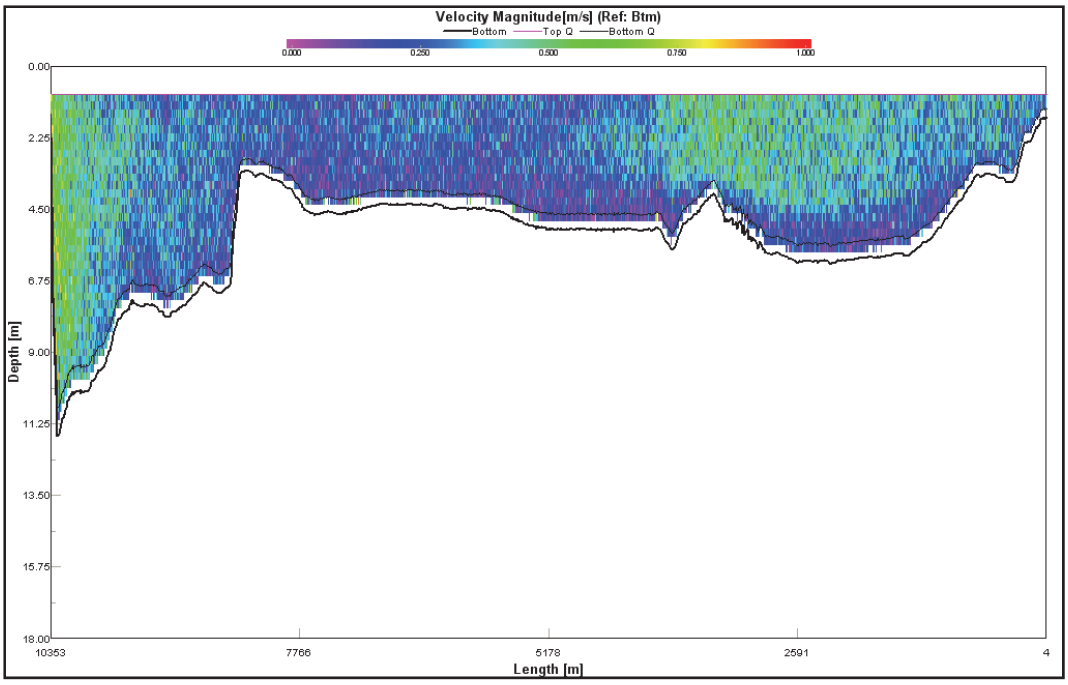

Figure C-14. Dog Keys Passes Transect 6. Shown west (left side) to east (right side).

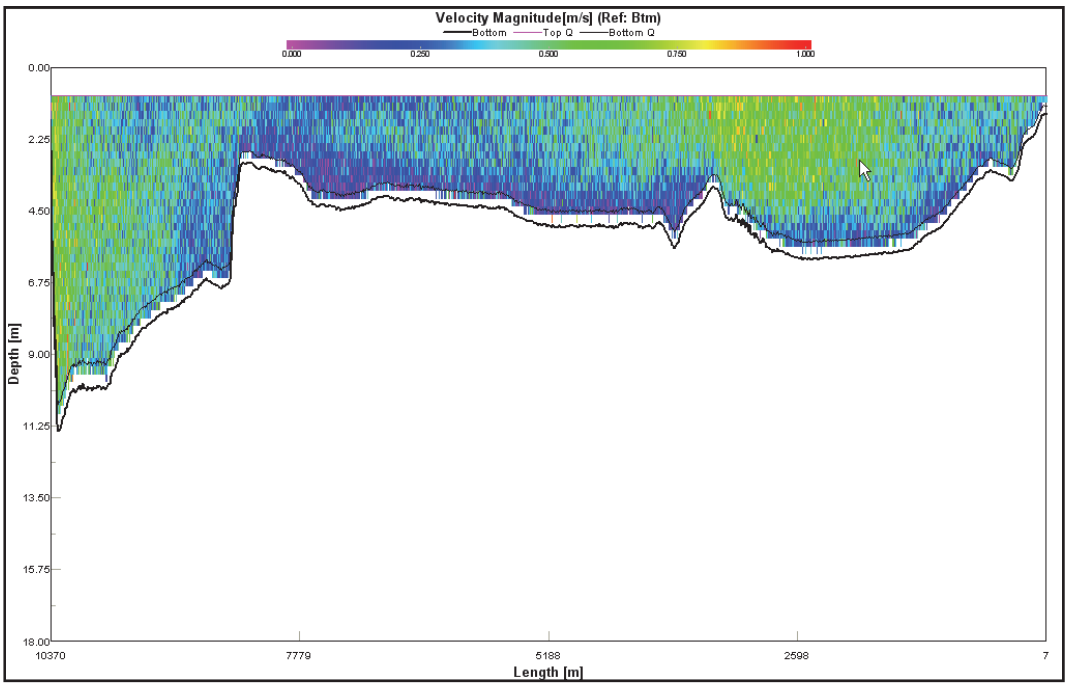

Figure C-15. Dog Keys Passes Transect 7. Shown west (left side) to east (right side).

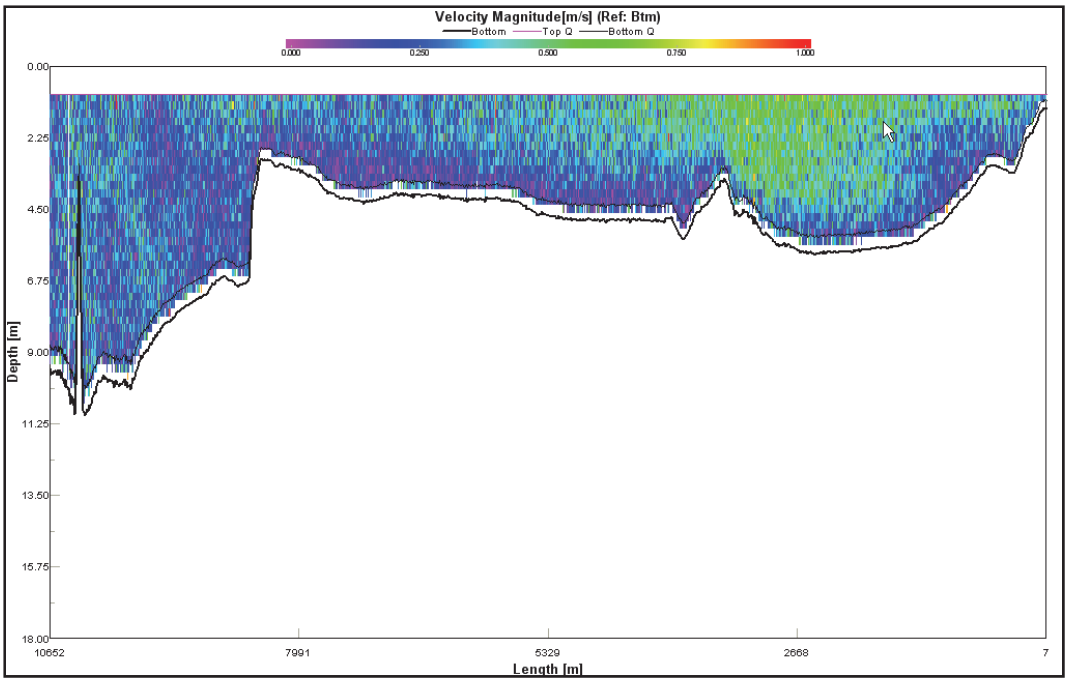

Petit Bois Pass

Figure C-16. Petit Bois Pass Transect 1. Shown west (left side) to east (right side).

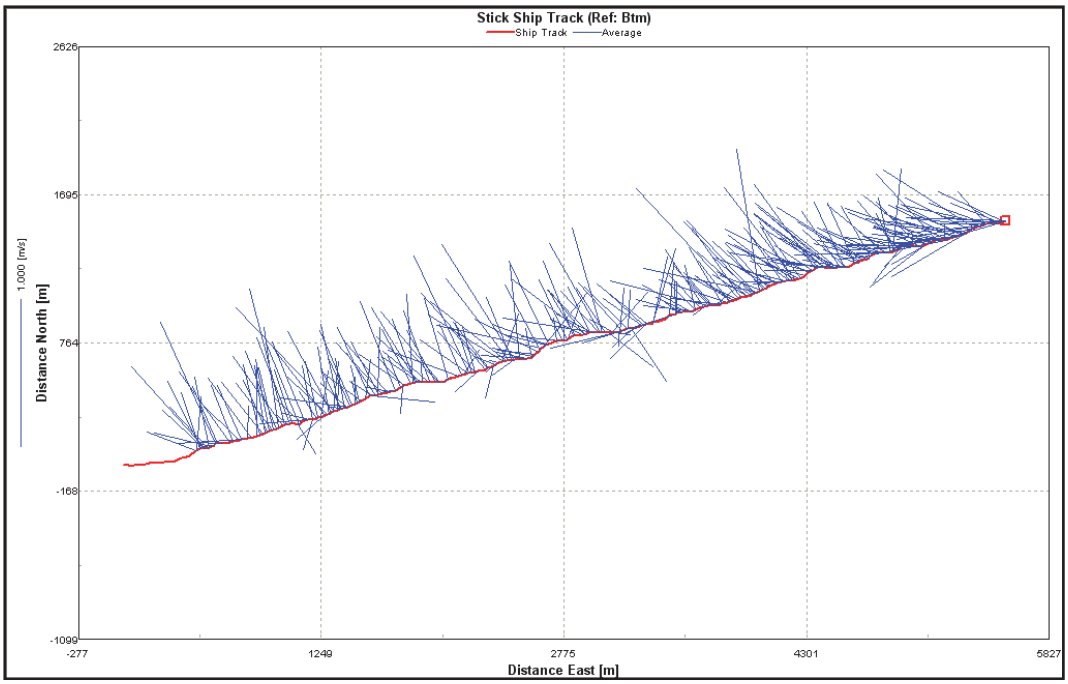

Figure C-17. Petit Bois Pass Transect 2. Shown west (left side) to east (right side).

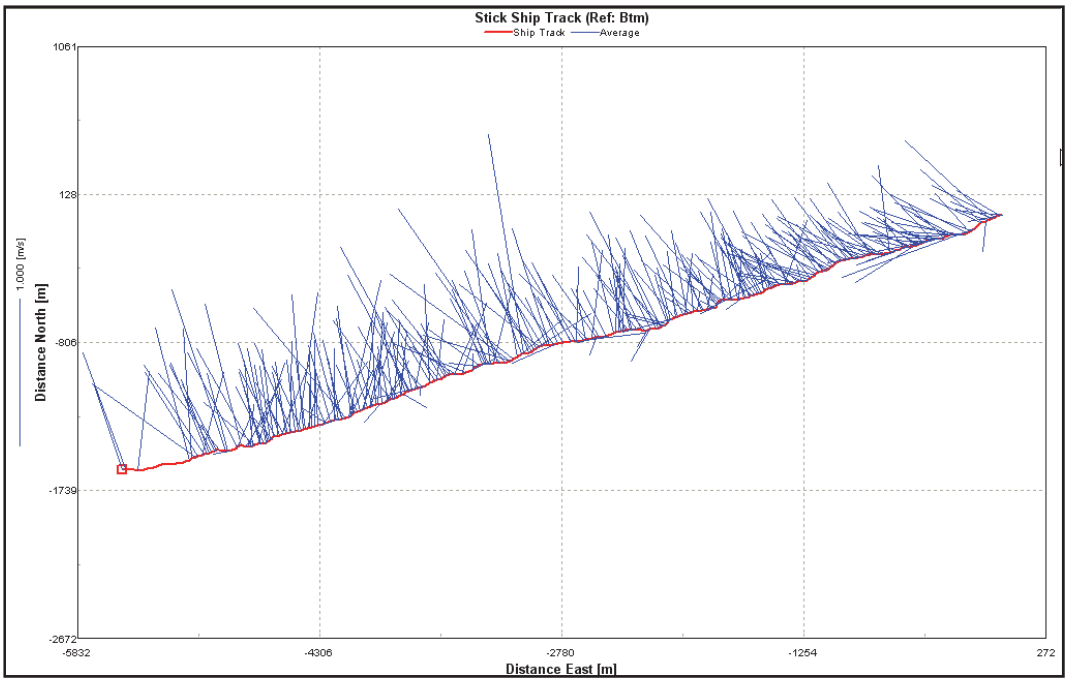

Figure C-18. Petit Bois Pass Transect 3. Shown west (left side) to east (right side).

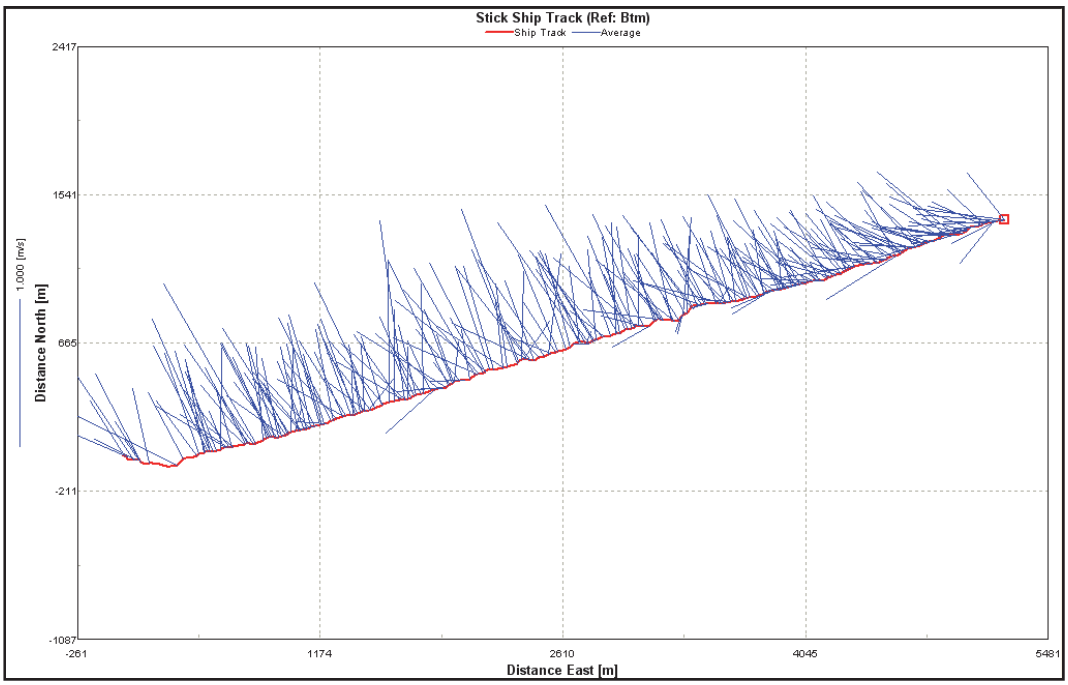

Figure C-19. Petit Bois Pass Transect 4. Shown west (left side) to east (right side).

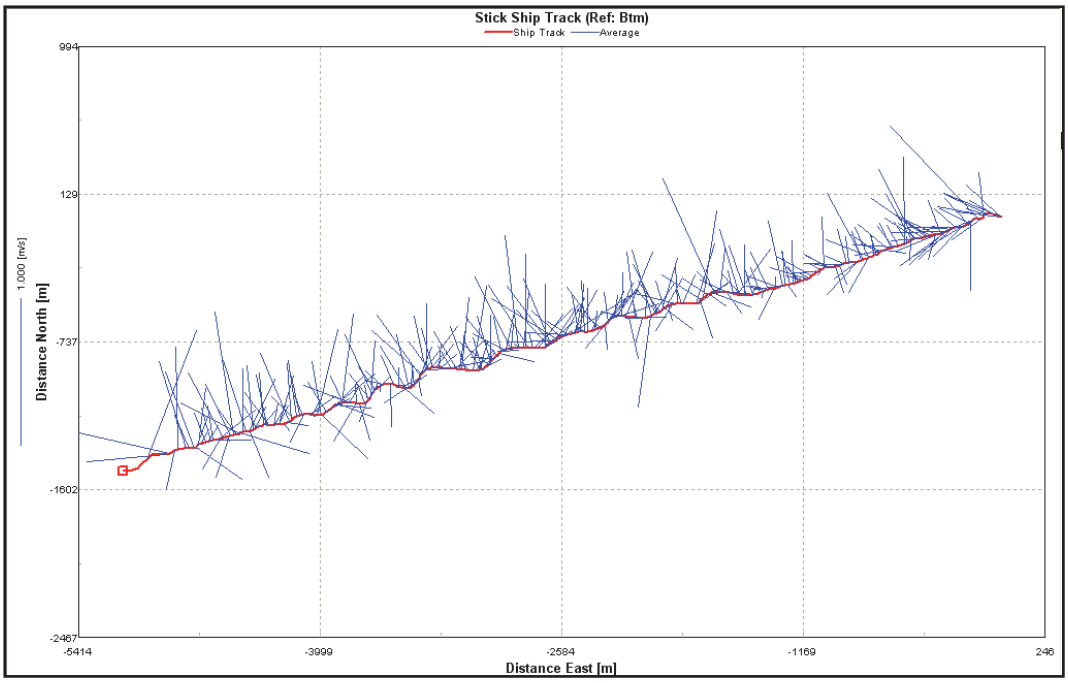

Figure C-20. Petit Bois Pass Transect 5. Shown west (left side) to east (right side).

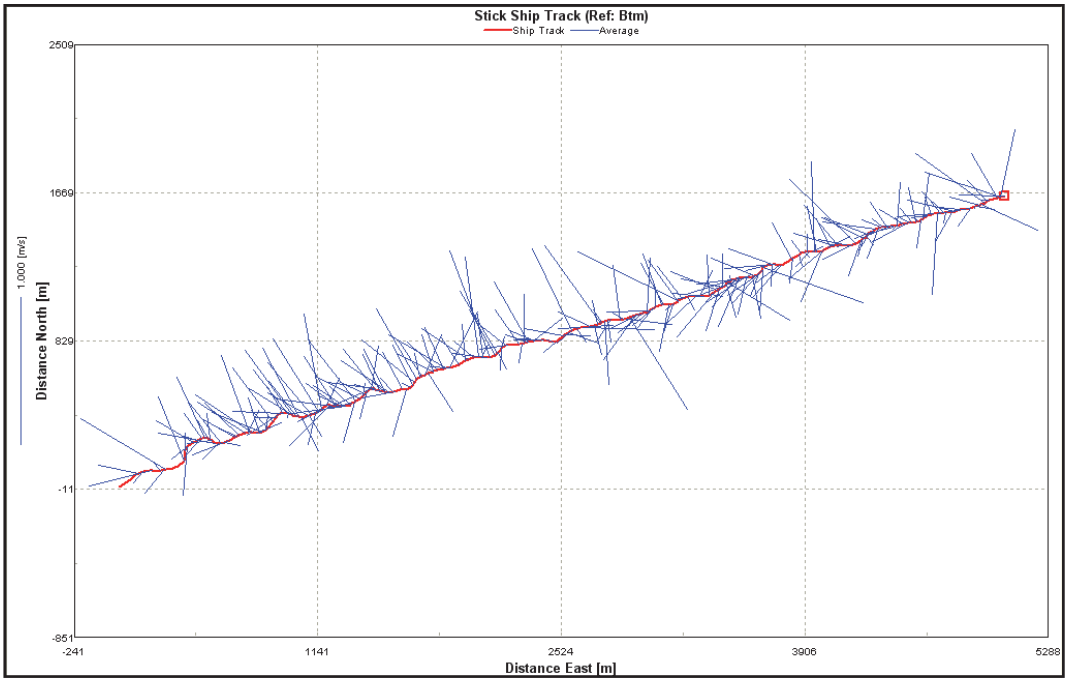

Figure C-21. Petit Bois Pass Transect 6. Shown west (left side) to east (right side).

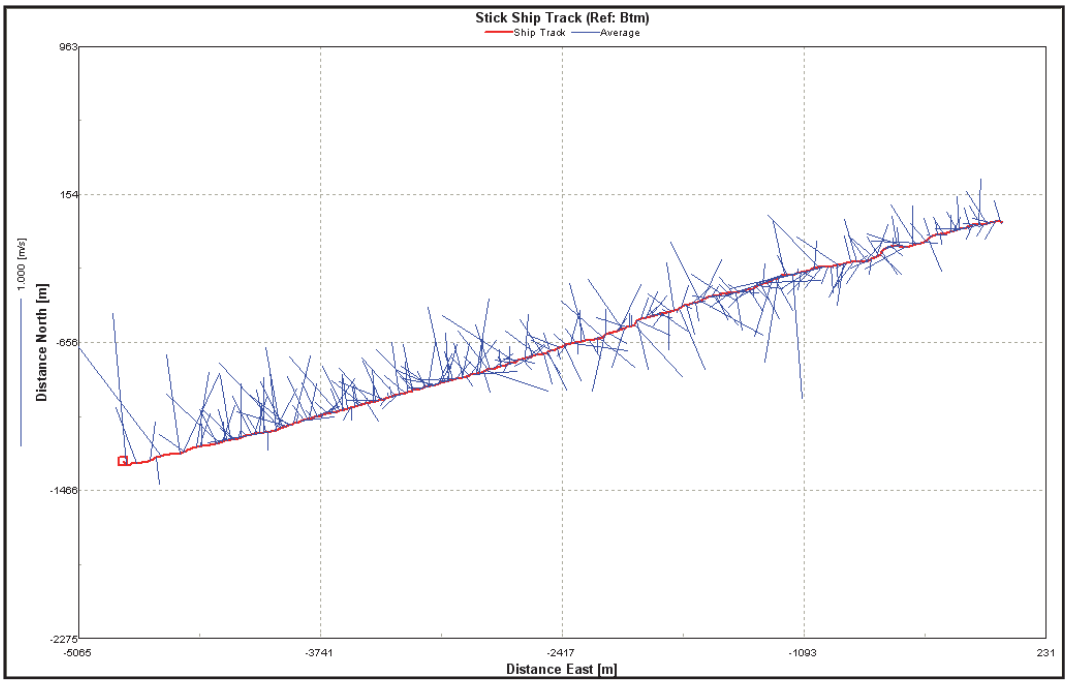

Figure C-22. Petit Bois Pass Transect 7. Shown west (left side) to east (right side).

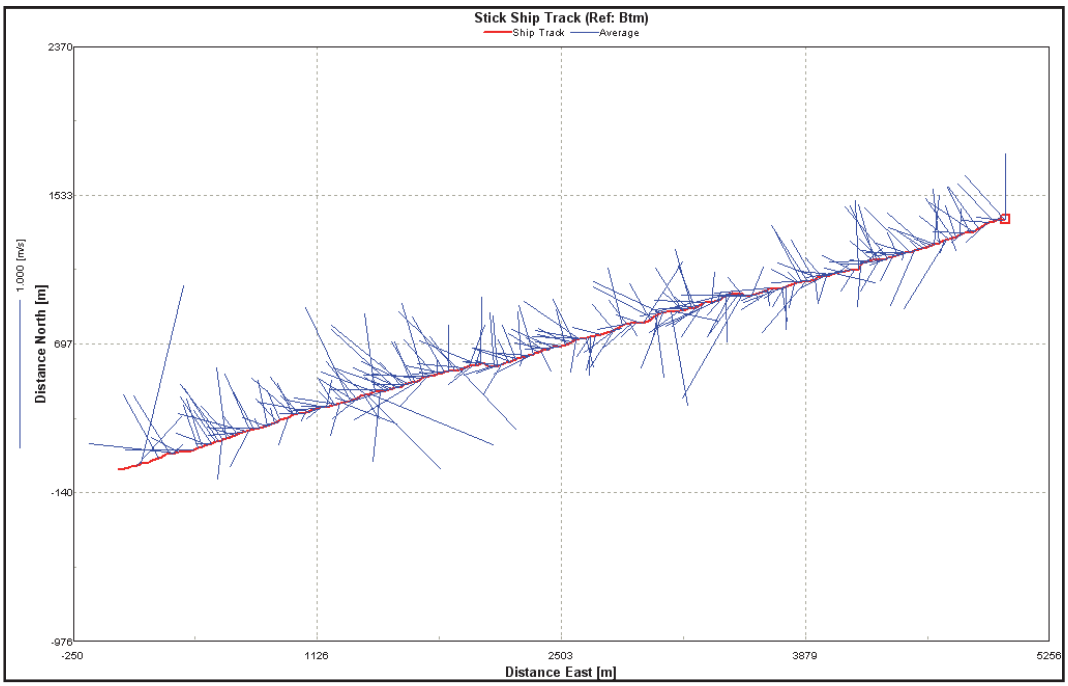

Figure C-23. Petit Bois Pass Transect 8. Shown west (left side) to east (right side).

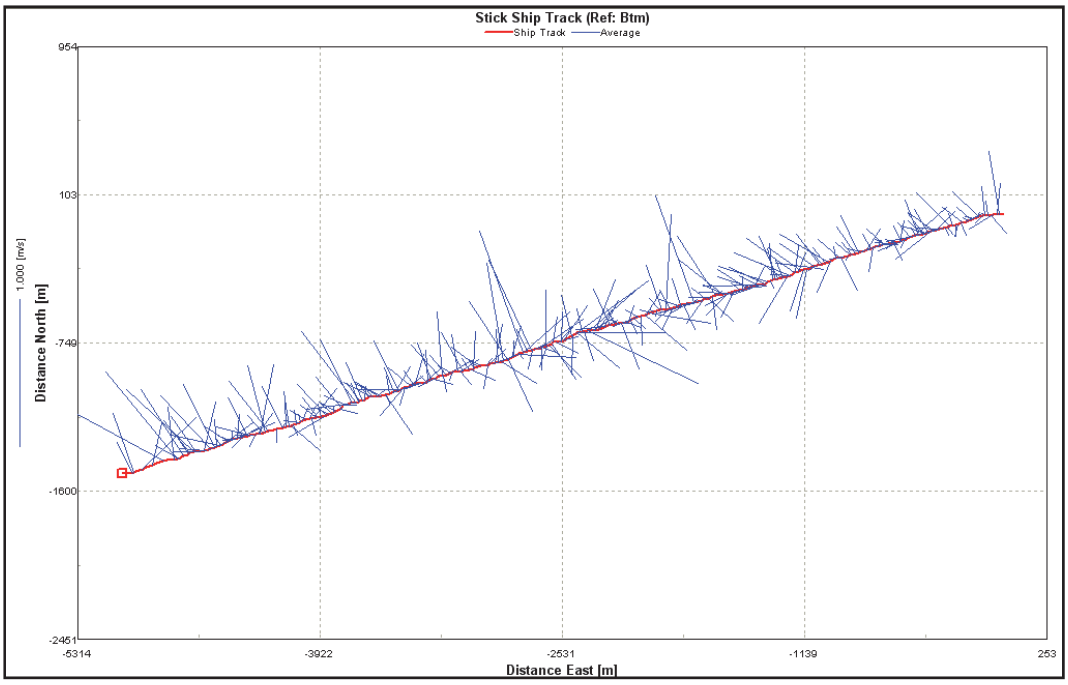

Figure C-24. Petit Bois Pass Transect 9. Shown west (left side) to east (right side).

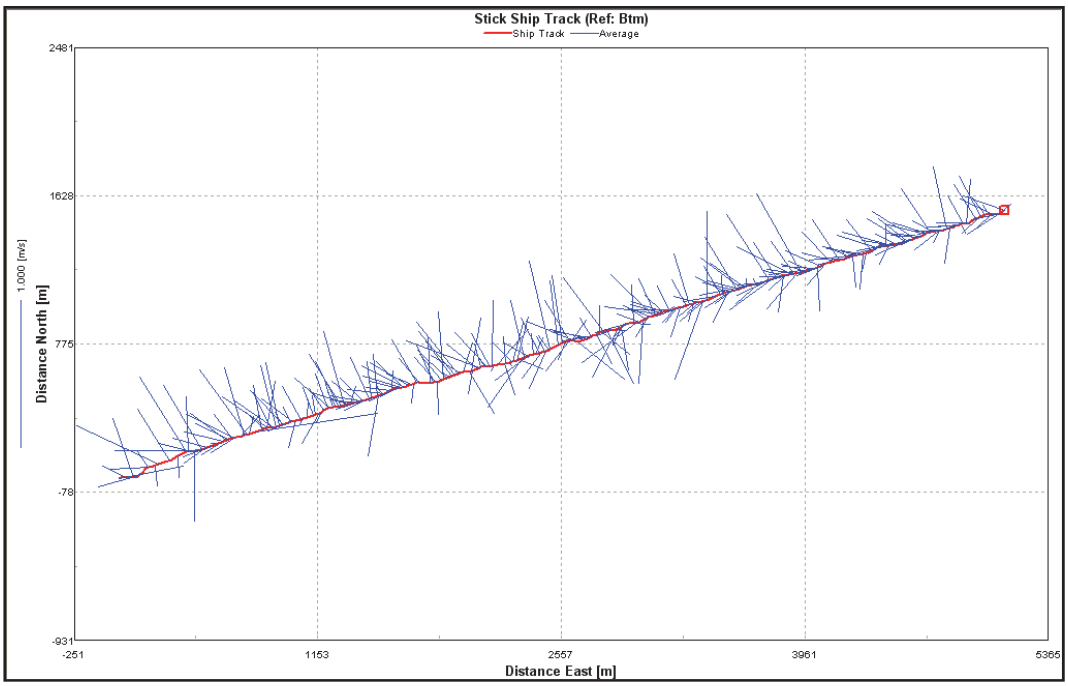

Figure C-25. Petit Bois Pass Transect 10. Shown west (left side) to east (right side).

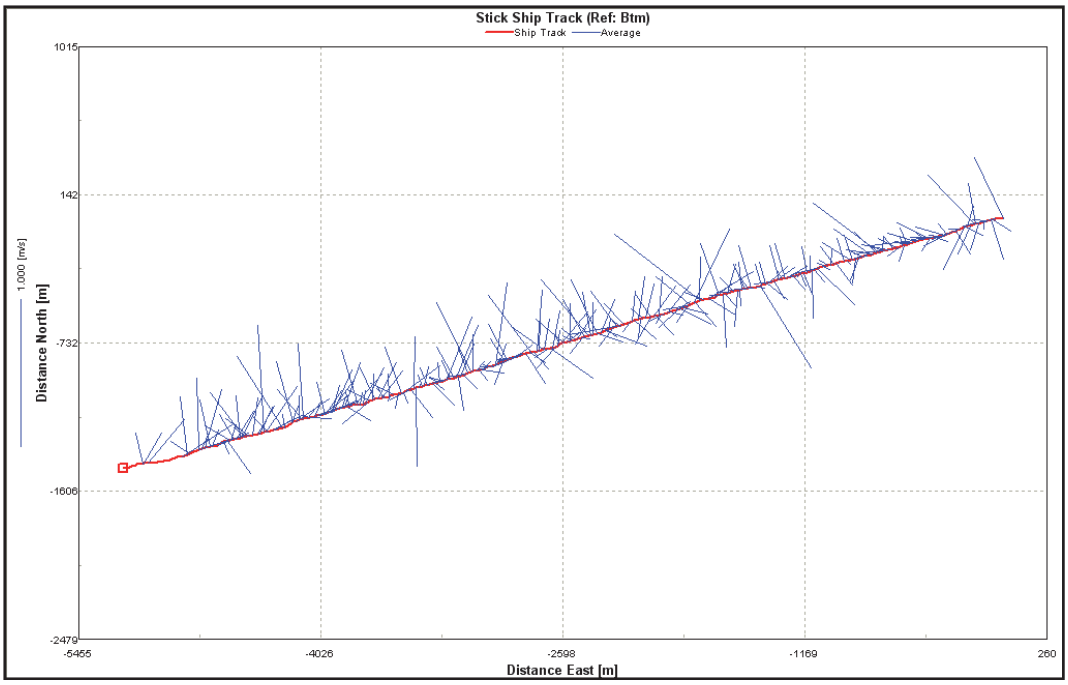

Figure C-26. Petit Bois Pass Transect 11. Shown west (left side) to east (right side).

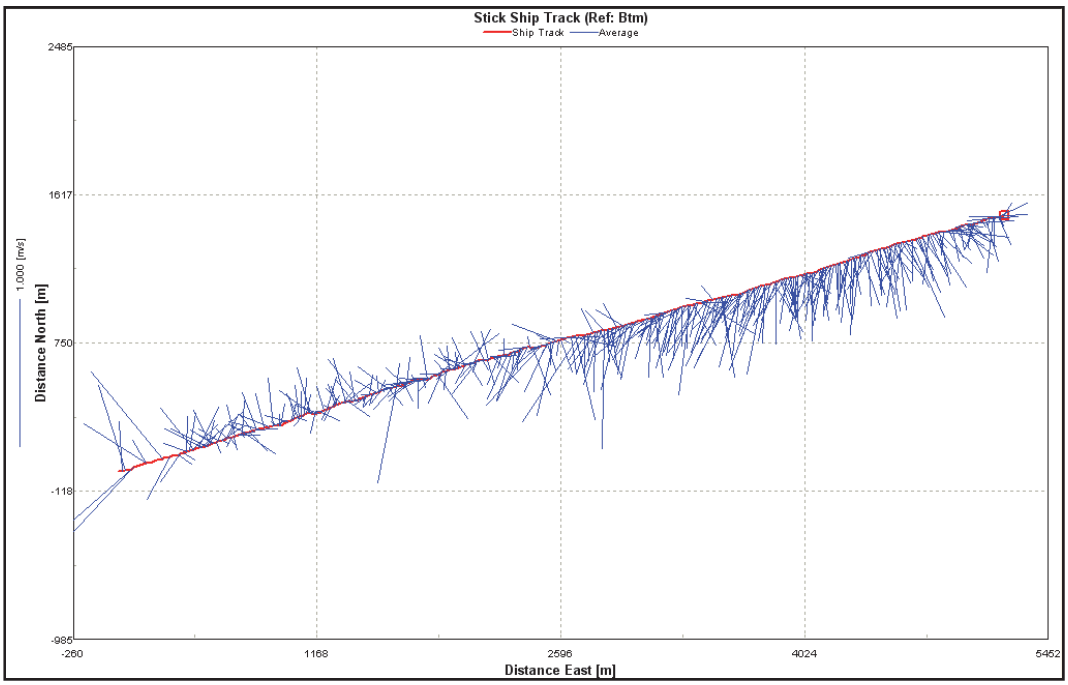

Pass Aux Herons

Figure C-27. Pass Aux Herons Transect 1. Shown northwest (top) to southeast (bottom).

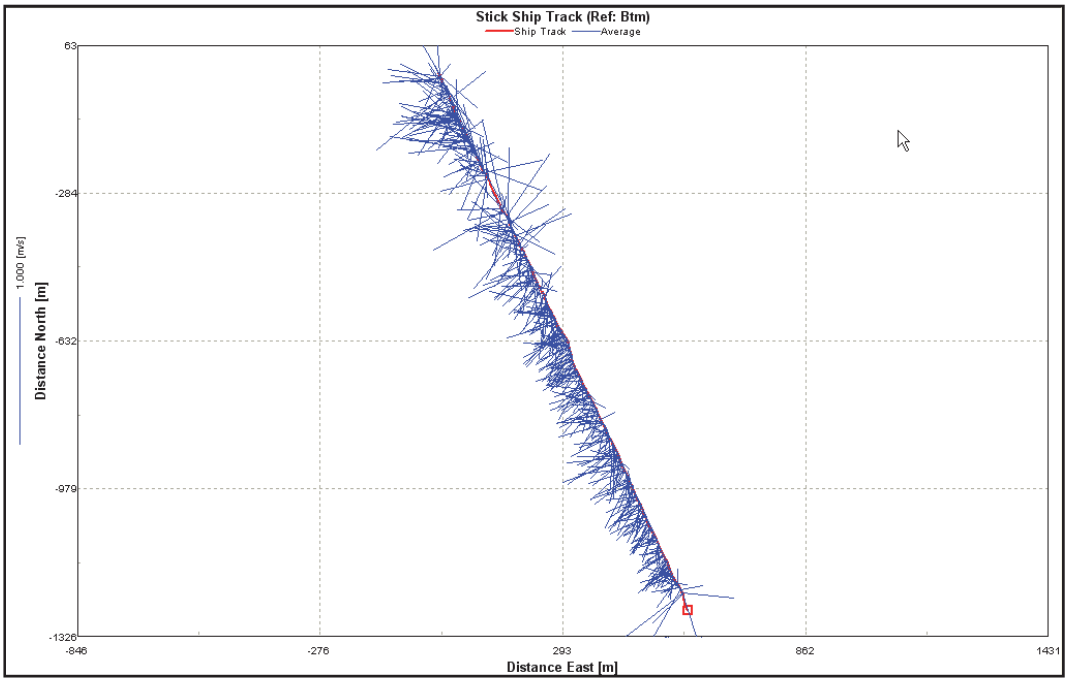

Figure C-28. Pass Aux Herons Transect 2. Shown northwest (top) to southeast (bottom).

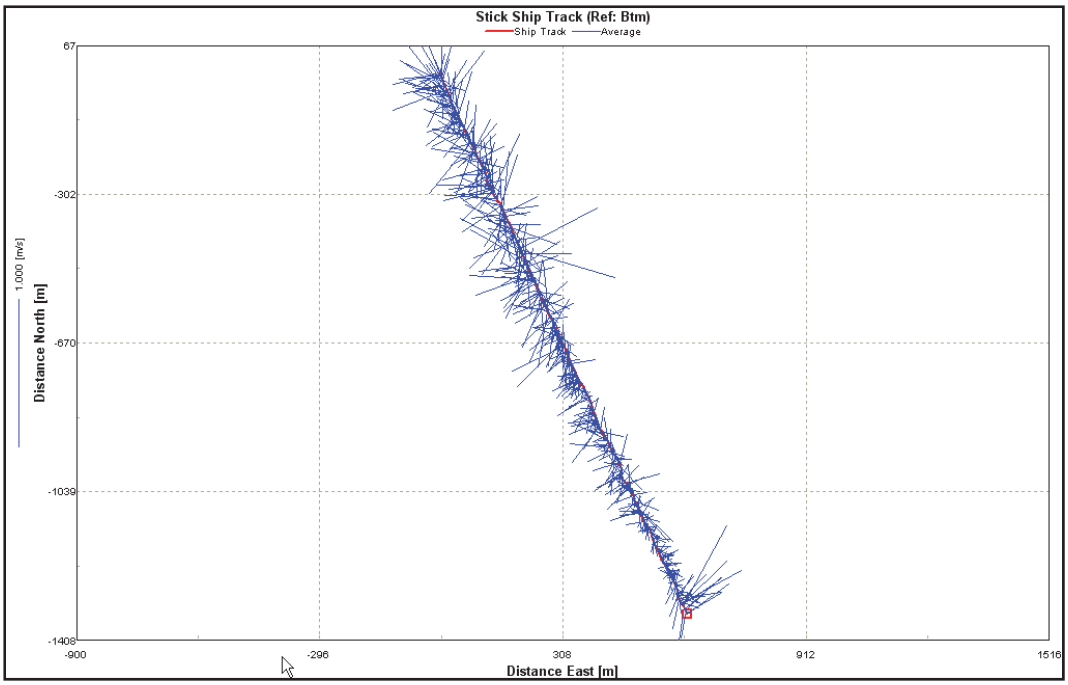

Figure C-29. Pass Aux Herons Transect 3. Shown northwest (top) to southeast (bottom).

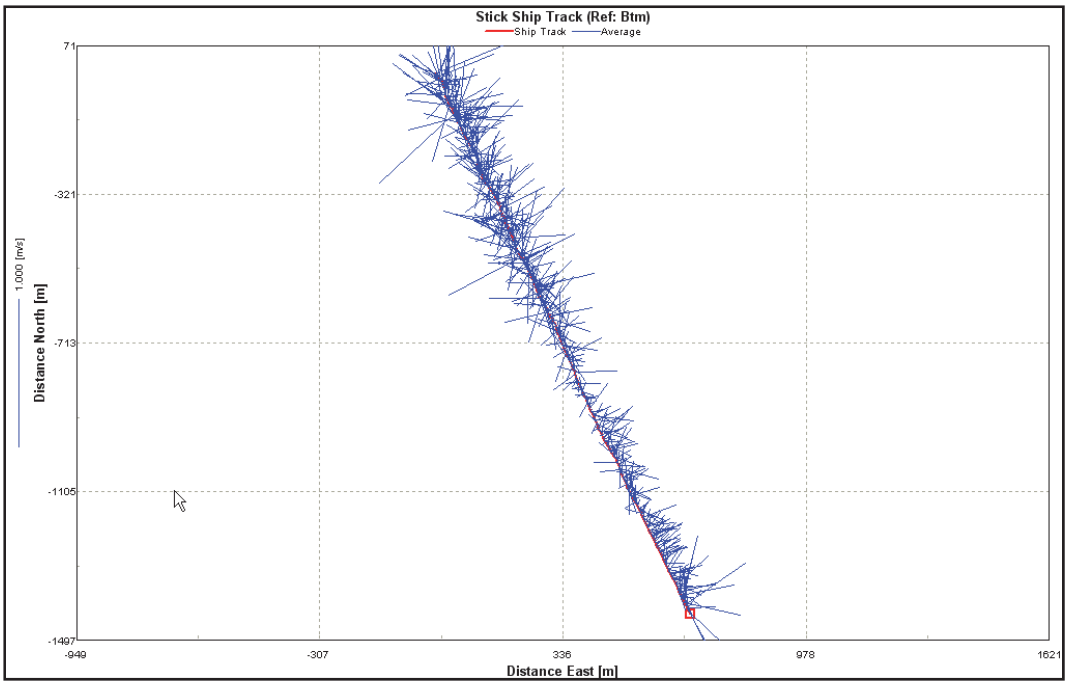

Figure C-30. Pass Aux Herons Transect 4. Shown northwest (top) to southeast (bottom).

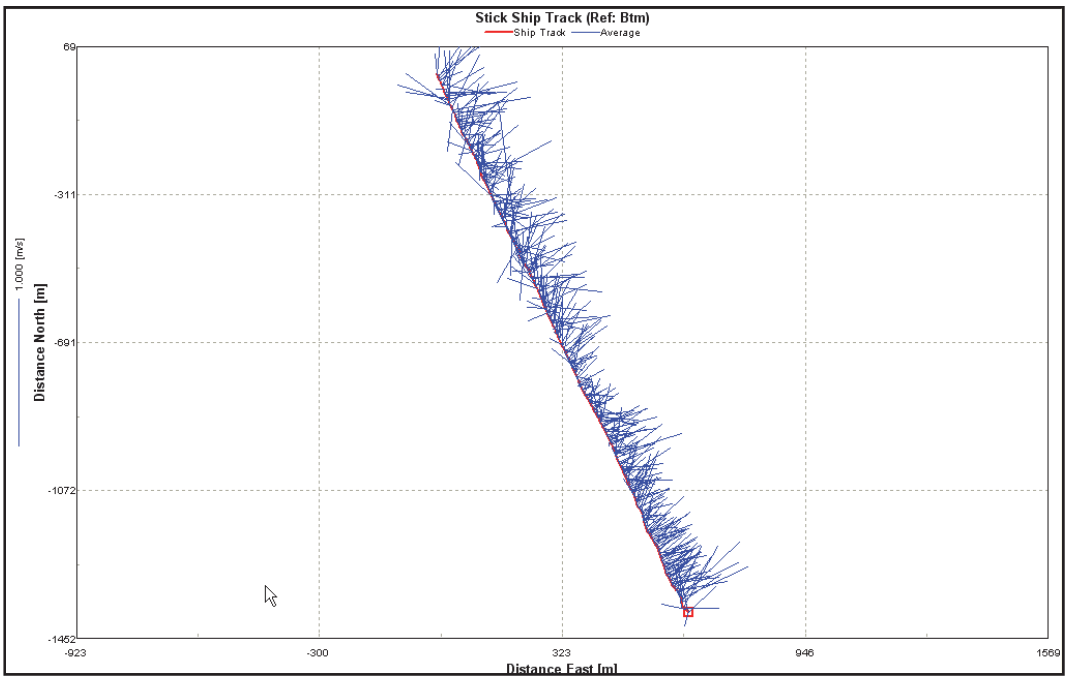

Figure C-31. Pass Aux Herons Transect 5. Shown northwest (top) to southeast (bottom).

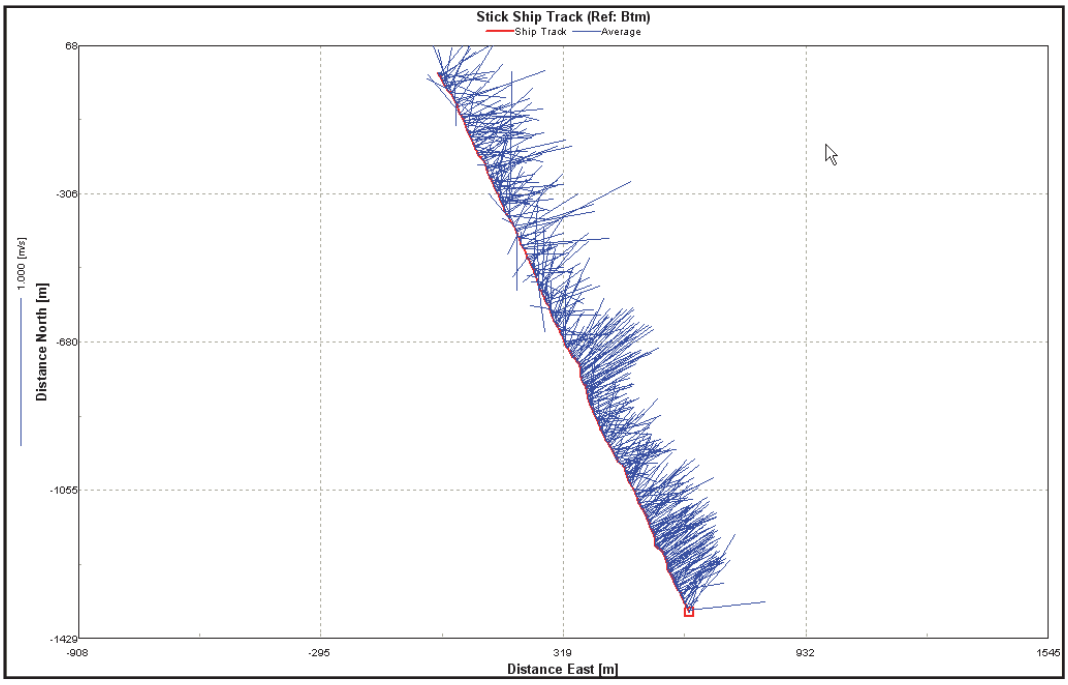

Figure C-32. Pass Aux Herons Transect 6. Shown northwest (top) to southeast (bottom).

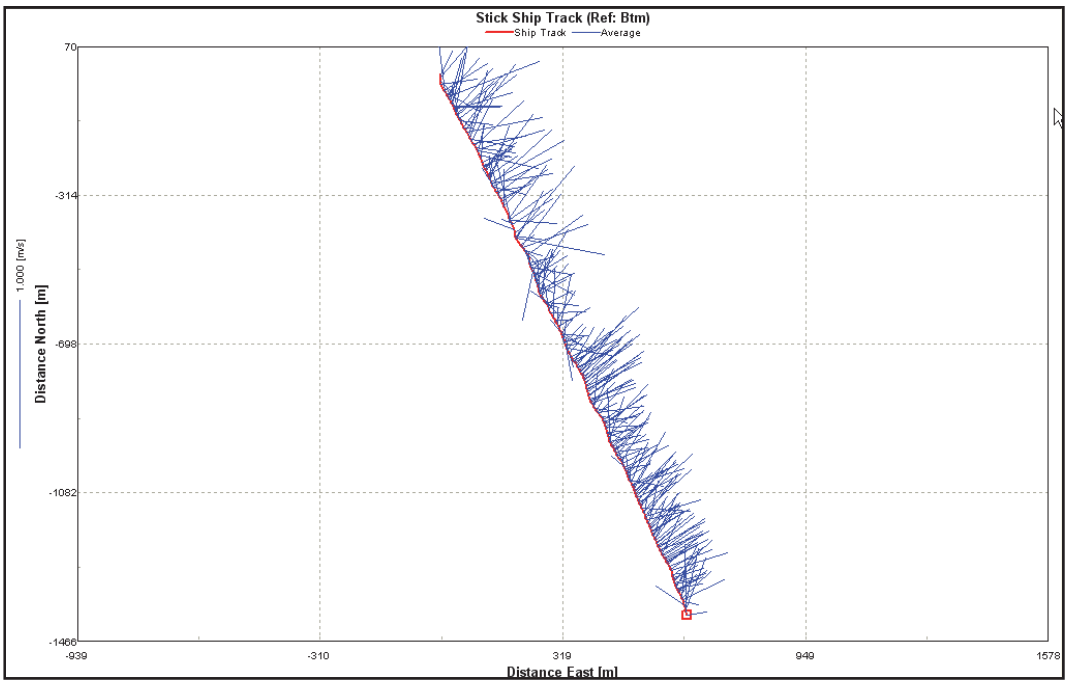

Figure C-33. Pass Aux Herons Transect 7. Shown northwest (top) to southeast (bottom).

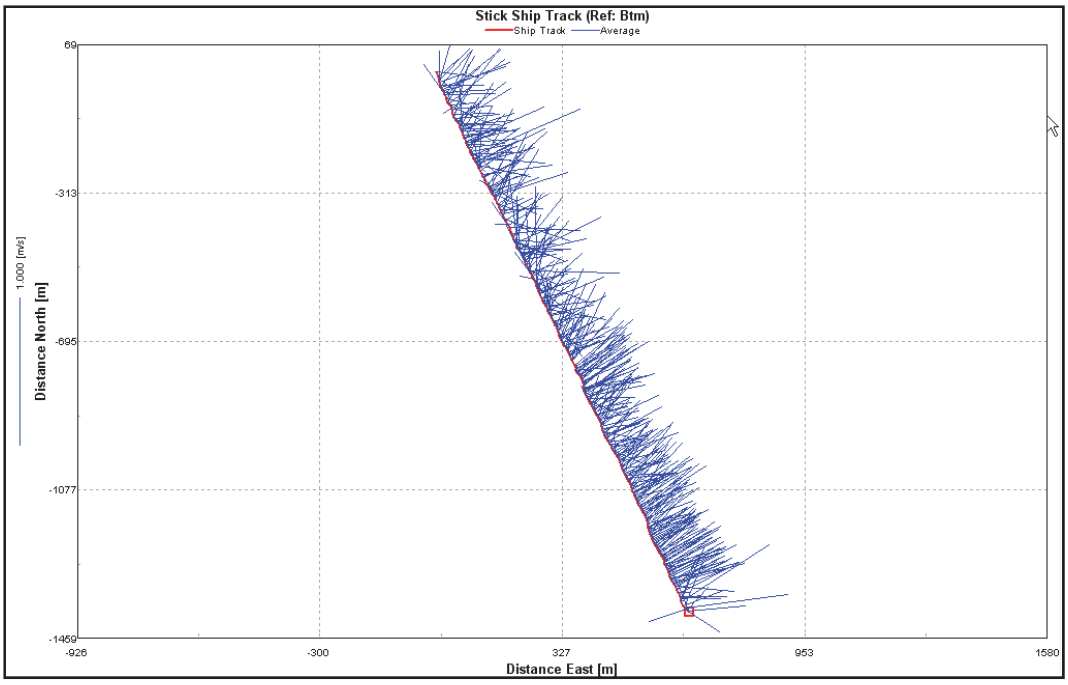

Figure C-34. Pass Aux Herons Transect 8. Shown northwest (top) to southeast (bottom).

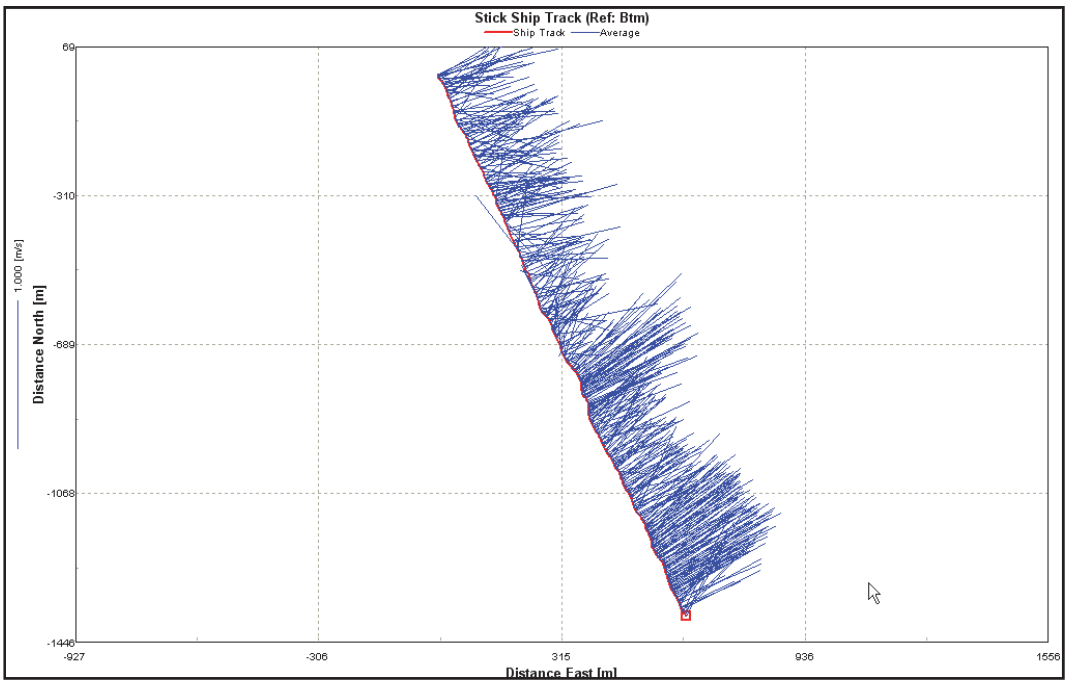

Figure C-35. Pass Aux Herons Transect 9. Shown northwest (top) to southeast (bottom).

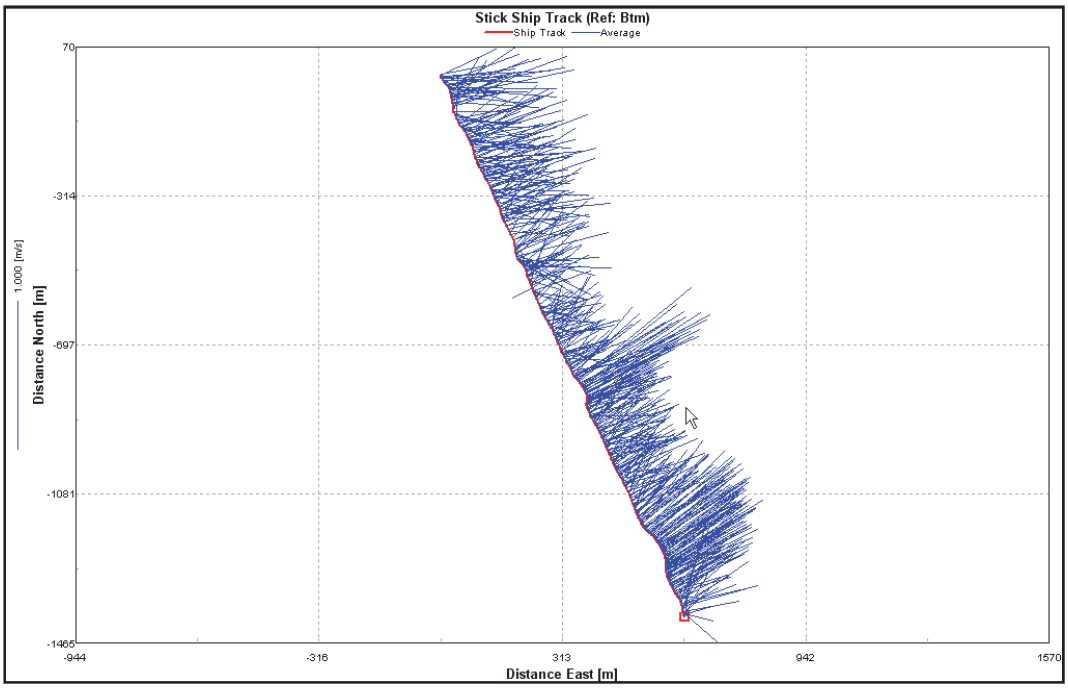

Figure C-36. Pass Aux Herons Transect 10. Shown northwest (top) to southeast (bottom).

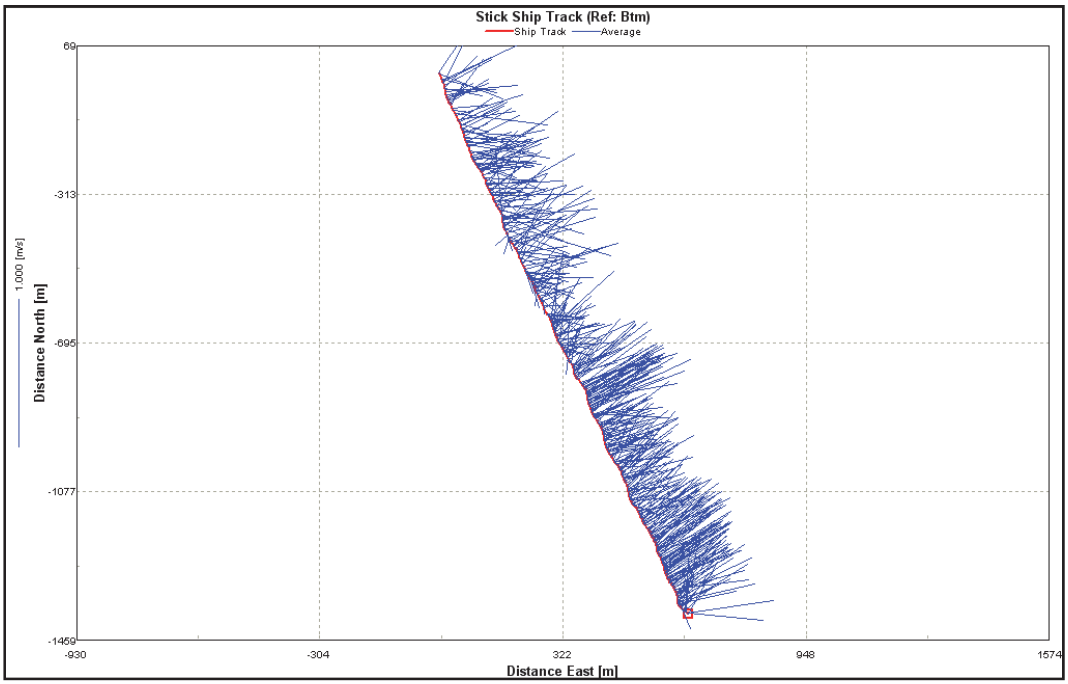

Figure C-37. Pass Aux Herons Transect 11. Shown northwest (top) to southeast (bottom).

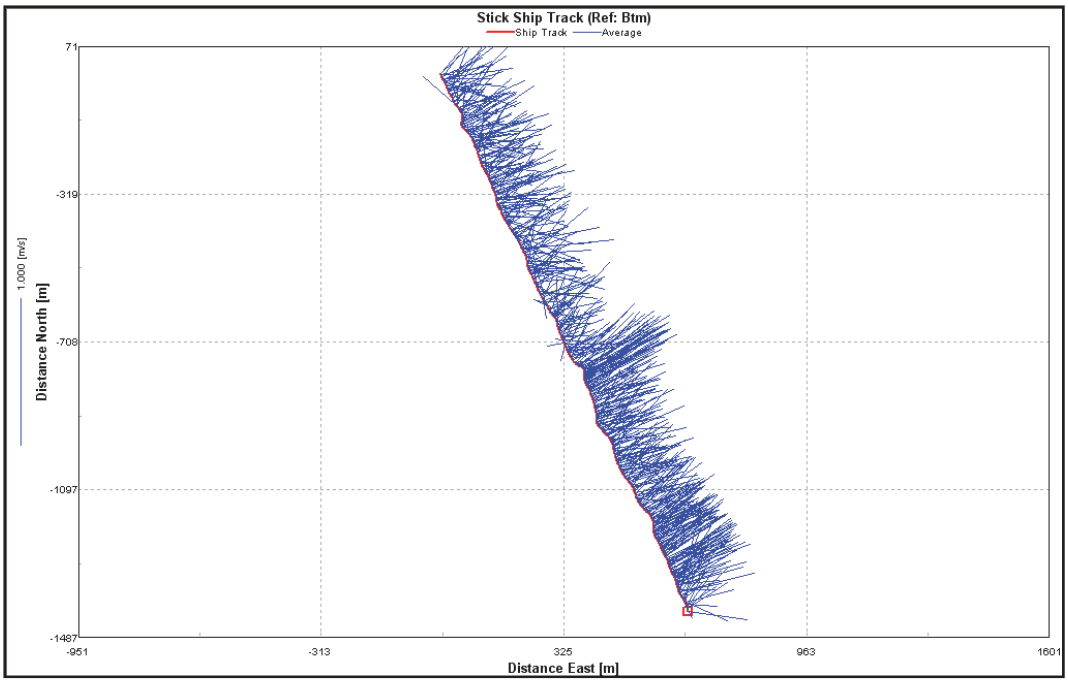

Figure C-38. Pass Aux Herons Transect 12. Shown northwest (top) to southeast (bottom).

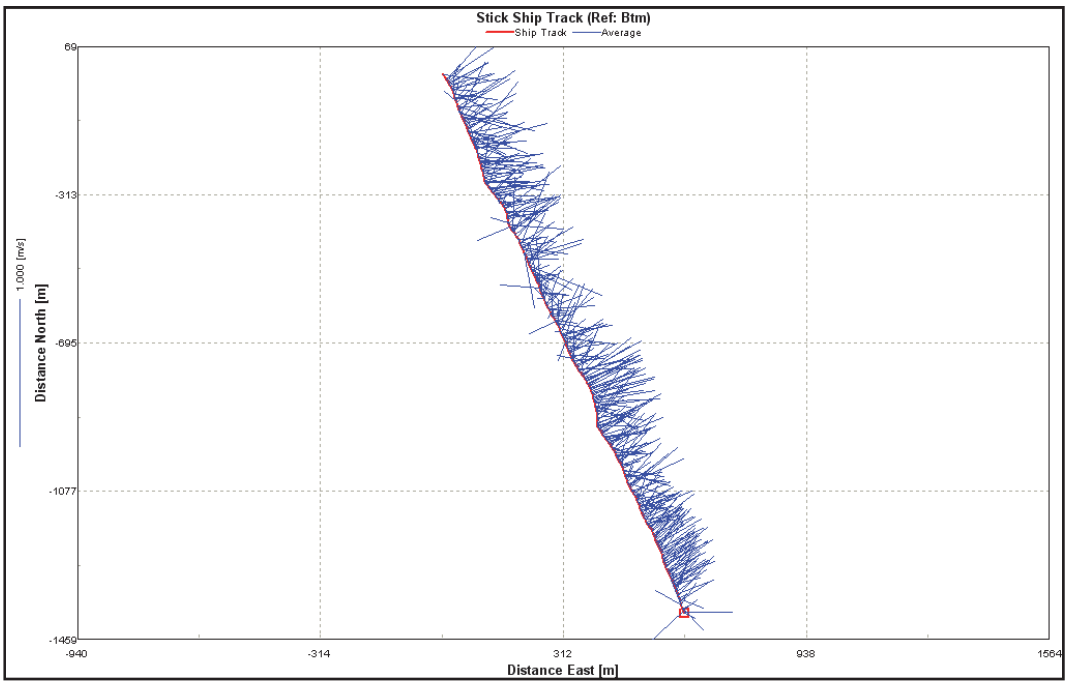

Figure C-39. Pass Aux Herons Transect 13. Shown northwest (top) to southeast (bottom).

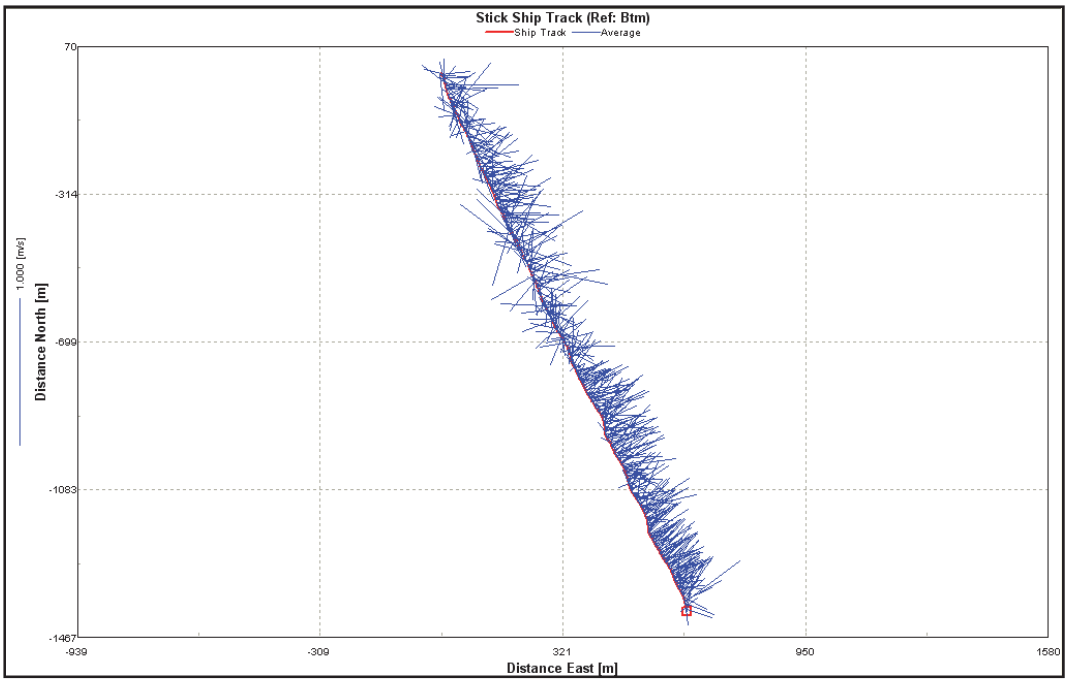

Figure C-40. Pass Aux Herons Transect 14. Shown northwest (top) to southeast (bottom).

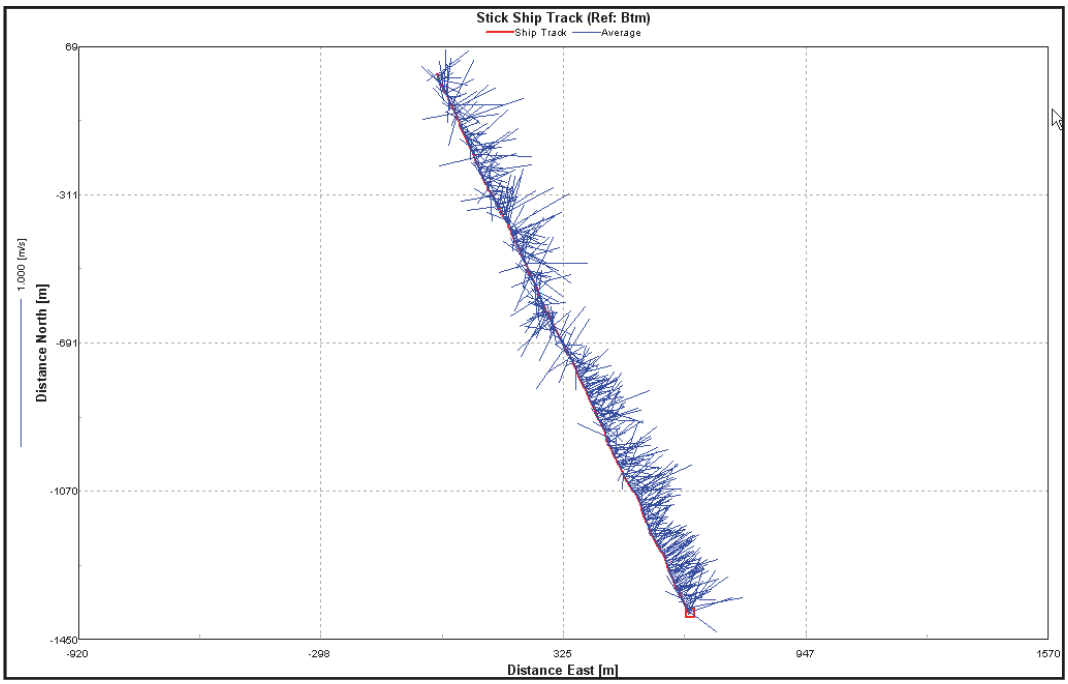

Figure C-41. Pass Aux Herons Transect 15. Shown northwest (top) to southeast (bottom).

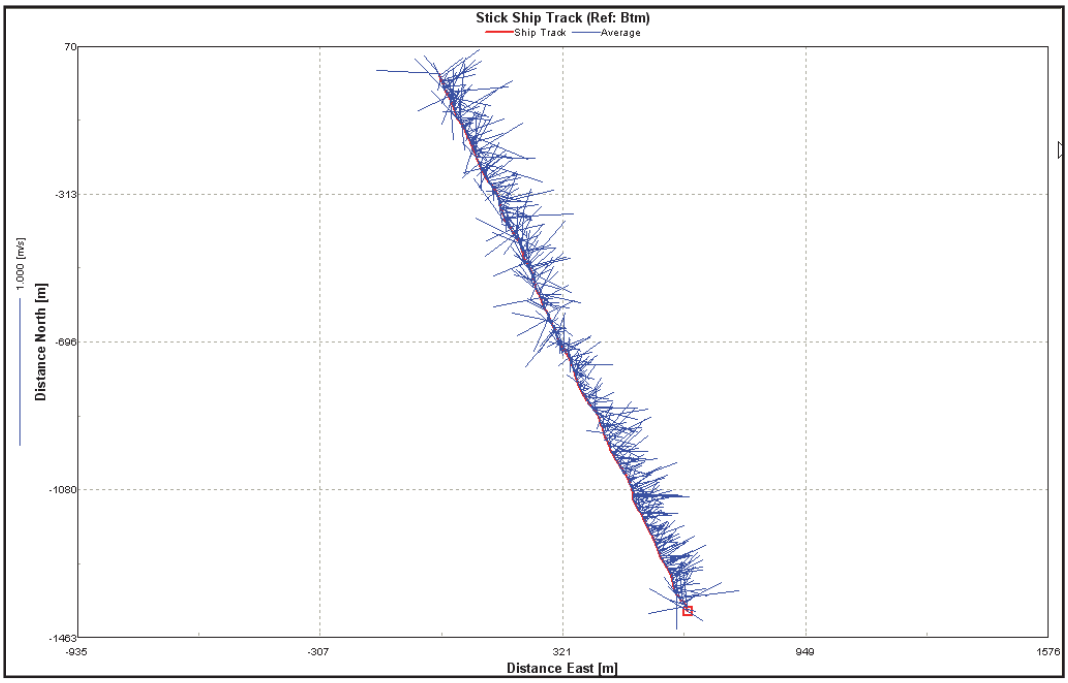

Figure C-42. Pass Aux Herons Transect 16. Shown northwest (top) to southeast (bottom).

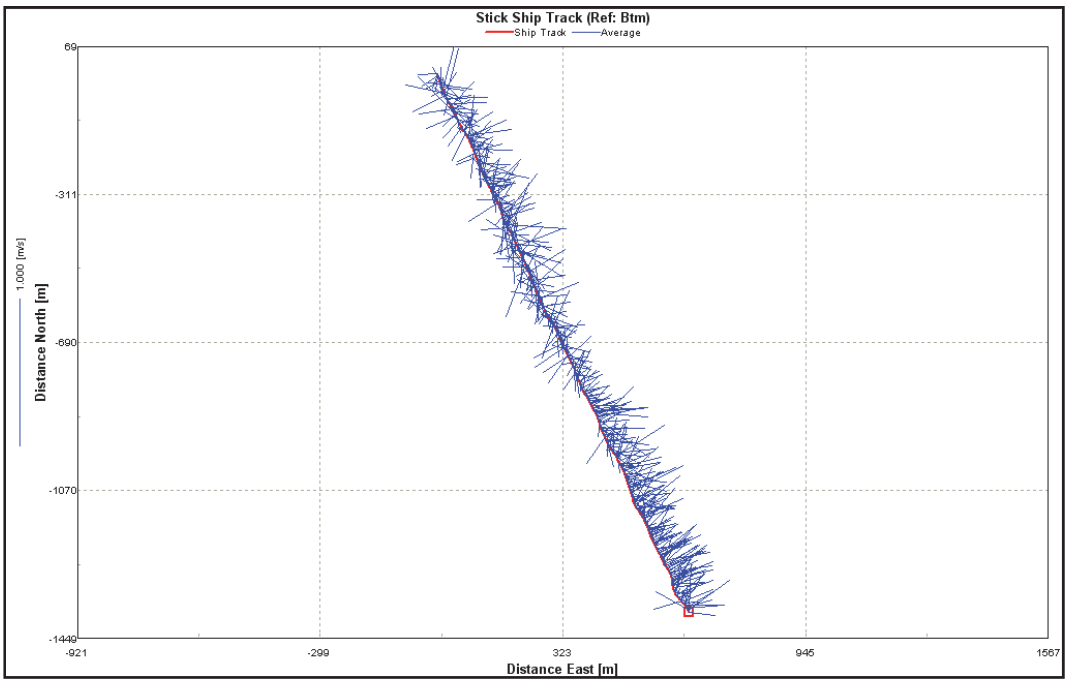

Figure C-43. Pass Aux Herons Transect 17. Shown northwest (top) to southeast (bottom).

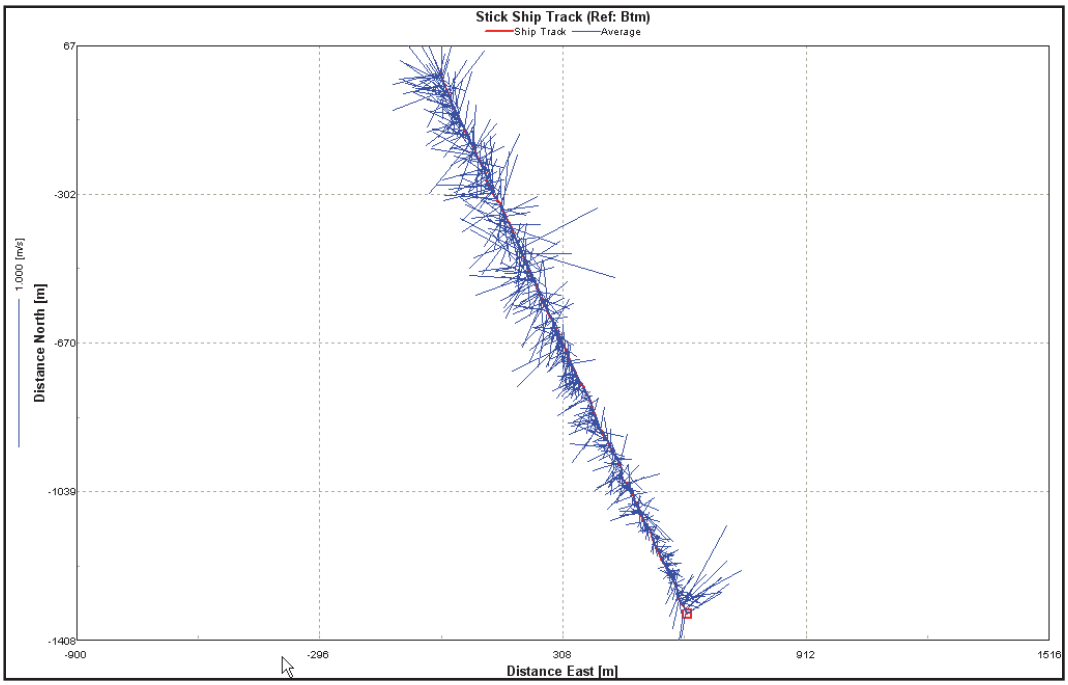

Figure C-44. Pass Aux Herons Transect 18. Shown northwest (top) to southeast (bottom).

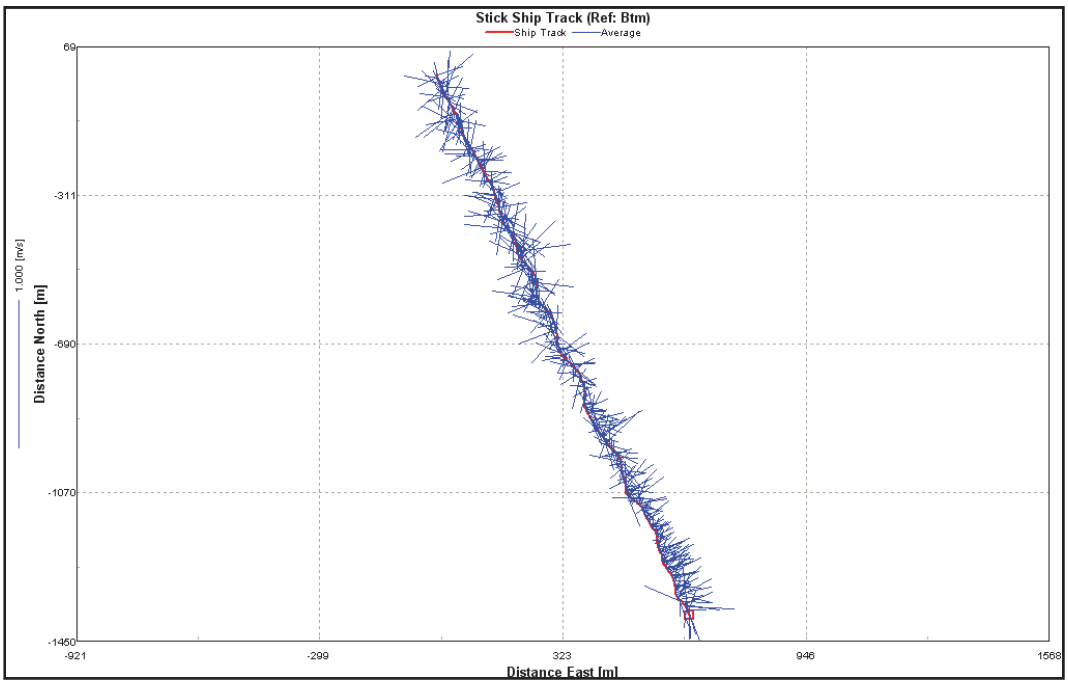

Appendix D: ICM Control and Input Files for Calibration

Control file for WQM

```
TITLE C ……TITLE……
Apply St. John's parallel code to Ship Island pre- Katrina
Code provided by MN in GOLD_STANDARD Jan 17, 2010
Terry's vertical code installed by CFC in terrys_code_FGS Jan 23, 2006
This code brought up from aquarius /disk2/new_ches_bay/Jan_27_06
Run on Jade: Run102910 052610 hydro - added atm loads : Pre-Katrina
102910; SEDNO3 = .05

GEOM DEFINE NB NSB NQF NHQF NSHQF NL
 196820 39364 544951 387495 77499 5

TIME CON TMSTRT TMEND
 0.0 163.5

# DLT NDLT
 1

DLT DAY DLTD DLTD DLTD DLTD DLTD DLTD DLTD DLTD DLTD
 0.0

DLT VAL DLTVAL DLTVAL DLTVAL DLTVAL DLTVAL DLTVAL DLTVAL DLTVAL
 3600.

DLT MAX DLTMAX DLTMAX DLTMAX DLTMAX DLTMAX DLTMAX DLTMAX DLTMAX
 3600.

DLT FTN DLTFTN DLTFTN DLTFTN DLTFTN DLTFTN DLTFTN DLTFTN DLTFTN
 0.70

HM DLT AHMDLT FILGTH
 3600.0 30.0

SNAPSHOT SNPC NSNP
 ON 1

SNAP DAY SNPD SNPD SNPD SNPD SNPD SNPD SNPD SNPD SNPD
 0.0

SNAP FRQ SNPF SNPF SNPF SNPF SNPF SNPF SNPF SNPF SNPF
 5.0

PLOT PLTC QPLTC SPLTC SAVPLTC NPLT
 ON ON OFF OFF 1

PLOT DAY PLTD PLTD PLTD PLTD PLTD PLTD PLTD PLTD PLTD
 0.5

PLOT FREQ PLTF PLTF PLTF PLTF PLTF PLTF PLTF PLTF PLTF
 1.0

AV PLOT APLTC NAPL
 ON 1
```

```
AVPLT DAY APLTD APLTD APLTD APLTD APLTD APLTD APLTD APLTD
 0.0

AVPLT FREQ APLF APLF APLF APLF APLF APLF APLF APLF APLF
 0.125

TRAN FLUX HTFLC VTFLC STFLC NTFL
 OFF OFF OFF 1

FLUX DAY TFLD TFLD TFLD TFLD TFLD TFLD TFLD TFLD TFLD
 0.0

FLUX FREQ TFLF TFLF TFLF TFLF TFLF TFLF TFLF TFLF TFLF
 30.41

KIN FLUX KFLC NKFL
 ON 7

FLUX DAY KFLD KFLD KFLD KFLD KFLD KFLD KFLD KFLD KFLD
 0.0 30.0 60.0 90.0 120.0 150.0 170.0

FLUX FREQ KFLF KFLF KFLF KFLF KFLF KFLF KFLF KFLF KFLF
 365.25 365.25 365.25 365.25 365.25 365.25 365.25

OXY PLOT OPLC NOPL NOINT
 ON 1 4

OXY INT OINT OINT OINT OINT OINT OINT OINT OINT OINT
 -10.0 0.211 2.11 5.11

OXY DAY OPLD OPLD OPLD OPLD OPLD OPLD OPLD OPLD OPLD
 .0208333

OXY FREQ OPLF OPLF OPLF OPLF OPLF OPLF OPLF OPLF OPLF
 .0416667

MASS BAL MBLC NMBL
 OFF 1

MBL DAY MBLD MBLD MBLD MBLD MBLD MBLD MBLD MBLD MBLD
 0.0

MBL FREQ MBLF MBLF MBLF MBLF MBLF MBLF MBLF MBLF MBLF
 365.0

DIAGNSTCS DIAC NDIA
 ON 1

DIA DAY DIAD DIAD DIAD DIAD DIAD DIAD DIAD DIAD DIAD
 0.

DIA FREQ DIAF DIAF DIAF DIAF DIAF DIAF DIAF DIAF DIAF
 1.00

RESTART RSOC NRSO RSIC
 OFF 1 OFF

RST DAY RSOD RSOD RSOD RSOD RSOD RSOD RSOD RSOD RSOD
 360.0

HYD MODEL HYDC
 BINARY
```

```
HYD SOLTN SLC CONSC TH MINSTEP
 QUICKEST MASS 0.55 5.0

CONTROLS SEDC AUTOC VBC BFOC STLC ICIC ICOC SAVMC
 OFF ON ON OFF ON UNIFORM ON OFF

CONTROLS SUSFDC DEPFDC KEIMC SEDKIN
 OFF OFF P_ABS SSI

DEAD SEA FLC XYDFC ZDFC
 ON ON ON

HDIFF XYDF ZDFMUL
 1.0 1.00

CST INPUT S1C S2C S3C BFC ATMC SAVLC SEDTR ROMS
 OFF OFF OFF ON ON OFF OFF OFF

NUTR RED REDS1C REDS1N REDS1P REDS2C REDS2N REDS2P REDS3C REDS3N REDS3P
 1.0 1.0 1.0 1.0 1.0 1.0 1.0 1.0 1.0

NUTR RED REDCBC REDCBN REDCBP
 1.0 1.0 1.0

BOUNDARY BNDTC
 INTERP

ACT CST ACC ACC ACC ACC ACC ACC ACC ACC ACC
 ON ON ON OFF OFF ON OFF OFF ON
 OFF ON OFF ON ON OFF ON OFF ON
 OFF ON ON OFF ON OFF OFF OFF ON
 OFF ON OFF OFF OFF OFF OFF OFF OFF

# FILES NHYDF NTVDF
 7 2

MAP FILE.....MAPFN.....
 map_pre_shipisland10.npt

GEO FILE.....GEOFN.....
 wqmgeo_pre_shipisland10.npt

ICI FILE.....ICIFN.....
 wqm_ici_shipisland10.uni

AGR FILE.....AGRFN.....
 wqm_agr_shipisland10.npt

ZOO FILE.....ZOOFN.....
 wqm_zoo.run156

SUS FILE.....SUSFN.....
 wqm_sfi.run367

STL FILE.....STLFN.....
 wqm_stl_shipisland10.npt

MRL FILE.....MRLFN.....
 wqm_mrl_shipisland.npt

EXT FILE.....EXTFN.....
 wqm_kei_shipisland10.npt
```

HYD FILE.....HYDFN.....
hydro.dat-0498Pre
hydro.dat-0598Pre
hydro.dat-0698Pre
hydro.dat-0798Pre
hydro.dat-0898Pre
hydro.dat-0998Pre
hydro.dat-0998Pre

MET FILE.....METFN.....
mobile_98_shipisland10.npt
mobile_98_shipisland10.npt

S1 FILE.....S1FN.....
wqm_ptsrc.91_Phase51
wqm_ptsrc.92_Phase51

S2 FILE.....S2FN.....
wqm_nps.91_run341
wqm_nps.92_run341

S3 FILE.....S3FN.....
wqm_atm_s3.npt
wqm_atm_s3.npt

ATM FILE.....ATMFN.....
wqm_atm.npt
wqm_atm.npt

SVI FILE.....ATMFN.....
wqm_sav.run399
wqm_sav.run399

CBC FILE.....CBCFN.....
wq_shipisland10_bc_090710.npt
wq_shipisland10_bc_090710.npt

BFI FILE.....BFIFN.....
wqm_bfi_shipisland10_pre_101510.npt
wqm_bfi_shipisland10_pre_101510.npt

ICO FILE.....ICOFN.....
wqm_ico_shipisland10_090210.npt

SNP FILE.....SNPFN.....
wqm_snp_shipisland10_pre_run102910_f.opt

RSO FILE.....RSOFN.....
wqm_rso_shipisland10_pre_run102910_f.opt

PLT FILE.....PLTFN.....
wqm_plt_shipisland10_pre_run102910_f.opt

APL FILE.....APLFN.....
wqm_apl_shipisland10_pre_run102910_f.opt

DIA FILE.....DIAFN.....
wqm_dia_shipisland10_pre_run102910_f.opt

TFL FILE.....TFLFN.....
wqm_tfl_shipisland10_pre_run102910_f.opt

KFL FILE.....KFLFN.....
wqm_kfl_shipisland10_pre_run102910_f.opt

OPL FILE.....OPLFN.....
wqm_opl_shipisland10_pre_run102910_f.opt

MBL FILE.....MBLFN.....
wqm_mbl_shipisland10_pre_run102910_f.opt

ALO FILE.....ALOFN.....
wqm_alo_shipisland10_pre_run102910_f.opt

ZFO FILE.....ZFOFN.....
wqm_zfo_shipisland10_pre_run102910_f.opt

BFO FILE.....BFOFN.....
wqm_bfo_shipisland10_pre_run102910_f.opt

SVO FILE.....BFOFN.....
wqm_svo_shipisland10_pre_run102910_f.opt

SUD FILE.....BFOFN.....
wqm_sfo_shipisland10_pre_run102910_f.opt

Nov 3, 2010.
Ship Island Algal parameters from Gulfport study.
Title line
Title line
Title line
Title line

PREDATN TRPR KTPR
20.0 0.0320

FRACTN N FNIP FNUP FLNDP FNRDP FNLP FNRP
0.40 0.30 0.30 0.00 0.300 0.000

FRACTN P FPIP FPLDP FPRDP FPLP FPRP
0.50 0.00 0.00 0.200 0.000

FRACTN C FDOP FCLDP FCRDP FCLP FCRP
0.00 0.000 0.00 0.750 0.000

FRACTN SI FSAP
0.0

GROUP 1 1 ANC1 APC1 ASC1 STF1
0.167 0.0125 0.000 0.30

GROUP 1 CCHLC1
30.

GROUP 1 2 KHN1 KHNH41 KHP1 KHS1 KHR1 KHST1
0.01 0.001 0.00250 0.00 0.50 0.5

GROUP 1 3 ALPHMN PRSP1 PRPWR
3.15 0.25 2.0

GROUP 1 4 TMP1 TR1
29.0 20.00

GROUP 1 5 KTG11 KTG12 KTB1

```
 0.0050 0.0040 0.0322

GROUP 1 6 FNI1 FNLD1 FNRD1 FNLP1 FNRP1
 0.55 0.20 0.00 0.200 0.050

GROUP 1 7 FPI1 FPLD1 FPRD1 FPLP1 FPRP1
 0.75 0.25 0.00 0.000 0.000

GROUP 1 8 FCLD1 FCRD1 FCLP1 FCRP1
 0.000 0.000 0.000 0.00

GROUP 2 1 ANC2 APC2 ASC2 STF2
 0.167 0.0125 0.300 0.1

GROUP 2 CCHLC2
 75.0

GROUP 2 2 KHN2 KHNH42 KHP2 KHS2 KHR2 KHST2
 0.025 0.001 0.0025 0.03 0.5 2.0

GROUP 2 3 ALPHMN PRSP2 PRPWR
 8.00 0.25 2.0

GROUP 2 4 TMP2 TR2
 16.0 20.00

GROUP 2 5 KTG21 KTG22 KTB2
 0.0018 0.0060 0.0322

GROUP 2 6 FNI2 FNLD2 FNRD2 FNLP2 FNRP2
 0.55 0.20 0.00 0.200 0.050

GROUP 2 7 FPI2 FPLD2 FPRD2 FPLP2 FPRP2
 0.75 0.25 0.00 0.000 0.000

GROUP 2 8 FCLD2 FCRD2 FCLP2 FCRP2
 0.100 0.00 0.100 0.000

GROUP 3 1 ANC3 APC3 ASC3 STF3
 0.175 0.0175 0.100 0.00

GROUP 3 CCHLC3
 100.

GROUP 3 2 KHN3 KHNH43 KHP3 KHS3 KHR3 KHST3
 0.050 0.100 0.0050 0.001 0.50 35.0

GROUP 3 3 ALPHMN PRSP3 PRPWR
 8.00 0.25 2.0

GROUP 3 4 TMP3 TR3
 30.0 20.00

GROUP 3 5 KTG31 KTG32 KTB3
 0.00350 0.01000 0.0320

GROUP 3 6 FNI3 FNLD3 FNRD3 FNLP3 FNRP3
 0.70 0.20 0.00 0.300 0.000

GROUP 3 7 FPI3 FPLD3 FPRD3 FPLP3 FPRP3
 0.60 0.20 0.00 0.200 0.000

GROUP 3 8 FCLD3 FCRD3 FCLP3 FCRP3
```

```
 0.000 0.000 0.000 0.00

GROUP 1 SPVAR1 PRINT1
 CONSTANT NO

 BOX PM1 BMR1 BPR1
 1 0.0 0.030 0.000

GROUP 2 SPVAR2 PRINT2
 CONSTANT NO

 BOX PM2 BMR2 BPR2
 1 0.0 0.010 0.215

GROUP 3 SPVAR3 PRINT3
 CONSTANT NO

 BOX PM3 BMR3 BPR3
 1 150.0 0.030 0.220

PREDATN TPVAR PRINT
 CONSTANT ALL

 DAY TVPR
 1 1.000

GROUP 2 TB2GR PRINT
 CONSTANT ALL

 DAY TB2G2
 1 1.00


Ship Island Uniform Initial Conditions for Large grid
No sediment model 11-04-10

INIT CONC CIC CIC CIC CIC CIC CIC CIC CIC CIC
 18.4 10.0 0.0 0.0 0.0 0.02 0.00 0.0 7.00
 0.0 0.0 0.00 0.12 0.02 0.0 0.0 .0000 0.0
 0.0 0.16 0.0045 0.0005 0.0 0.0 0.0050 0.0 8.3
 0.0 0.0 0.0 0.0 0.0 0.0 0.0 0.0 0.0


Linear model ke = a + b TSS. March 7, 2002
KE a linear function of chlorophyll

 INTKE INITKE KECHL
 0.5 0.1 0.02

 SPVARKE PRINTKE
 CONSTANT NO

 CELL KE KEISS KEDOC
 1 1.0000 0.0800 0.0000


Ship Island using Gulfport values
Direct PO4 settling 1 m/d.

HALF SAT KHONT KHNNT KHOCOD KHODOC KHNDN
 3.0 1.0 0.500 0.5 0.1
```

```
RATIOS AOCR AONT
 2.67 4.33

REF T RESP TRCOD TRMNL TRHDR TRSUA
 23.0 20.0 20.0 20.0

TEMP EFF KTCOD KTMNL KTHDR KTSUA
 0.041 0.069 0.069 0.092

NITRIF T KTNT1 KTNT2 TMNT
 0.090 0.090 30.0

SORPTION KADPO4 KADSA JBSPO4 JESPO4
 0.0 0.0 255.0 285.0

MISC AANOX ANDC
 0.5 0.933

REAER AREAR BREAR CREAR
 0.156 1.5 1.5

 SPVAR PRINT
 CONSTANT NO

 KLDC
 0.0100

 SPVAR PRINT
 CONSTANT NO

 KRDC
 0.000

 SPVAR PRINT
 CONSTANT NO

 KLPC
 0.020

 SPVAR PRINT
 CONSTANT NO

 KRPC
 0.005

 SPVAR PRINT
 CONSTANT NO

 KLDN
 0.052

 SPVAR PRINT
 CONSTANT NO

 KRDN
 0.000

 SPVAR PRINT
 CONSTANT NO

 KLPN
 0.150
```

SPVAR PRINT
CONSTANT NO

KRPN
0.000

SPVAR PRINT
CONSTANT NO

KLDP
0.100

SPVAR PRINT
CONSTANT NO

KRDP
0.000

SPVAR PRINT
CONSTANT NO

KLPP
0.100

SPVAR PRINT
CONSTANT NO

KRPP
0.000 0.000 0.005 0.000 0.000 0.000 0.000 0.000 0.000

SPVAR PRINT
CONSTANT NO

KSUA
0.030 0.100 0.100 0.000 0.000 0.000 0.000 0.000 0.000

SPVAR PRINT
CONSTANT NO

KCOD
20.000 20.000 20.000 0.000 0.000 0.000 0.000 0.000 0.000

SPVAR PRINT
CONSTANT NO

KDCALG
0.000

SPVAR PRINT
CONSTANT NO

KLCALG
0.000

SPVAR PRINT
CONSTANT NO

KDNALG
0.000

SPVAR PRINT
CONSTANT NO

KLNALG
0.000

SPVAR PRINT
CONSTANT NO

KDPALG
0.400 0.400 0.400 0.000 0.000 0.000 0.000 0.000 0.000

SPVAR PRINT
CONSTANT NO

KLPALG
0.000 0.000 0.000 0.000 0.000 0.000 0.000 0.000 0.000

SPVAR PRINT
CONSTANT NO

NTMAX
0.040 0.040 0.040 0.000 0.000 0.000 0.000 0.000 0.000

Settling Rates
Ship Island values are from Gulfport study (2004)

SPVARM PRINTM
CONSTANT NO

BOX WSS WSLAB WSREF WSC WSD WSG WSPBS WSPO4
1 0.100 0.050 0.000 0.000 0.000 0.050 1.000 0.000

Mobile-Keesler meteorological data comparison

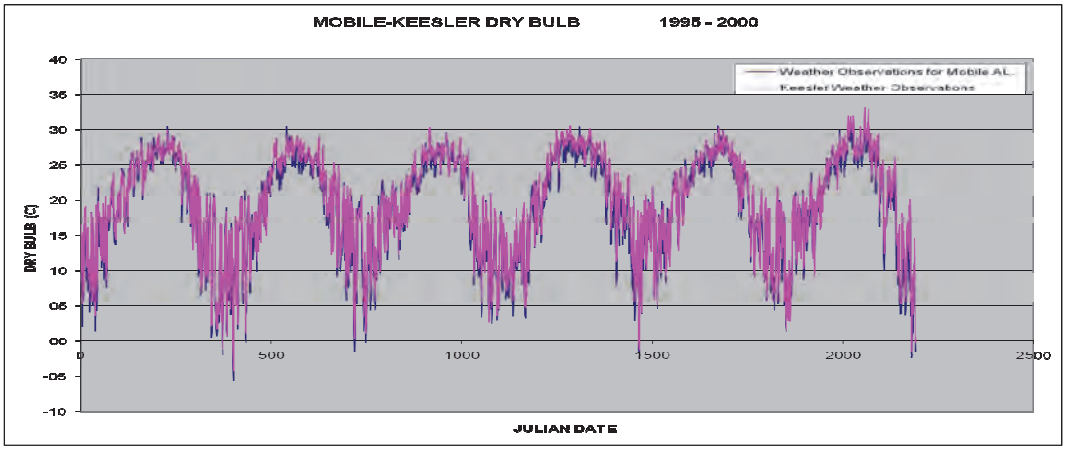

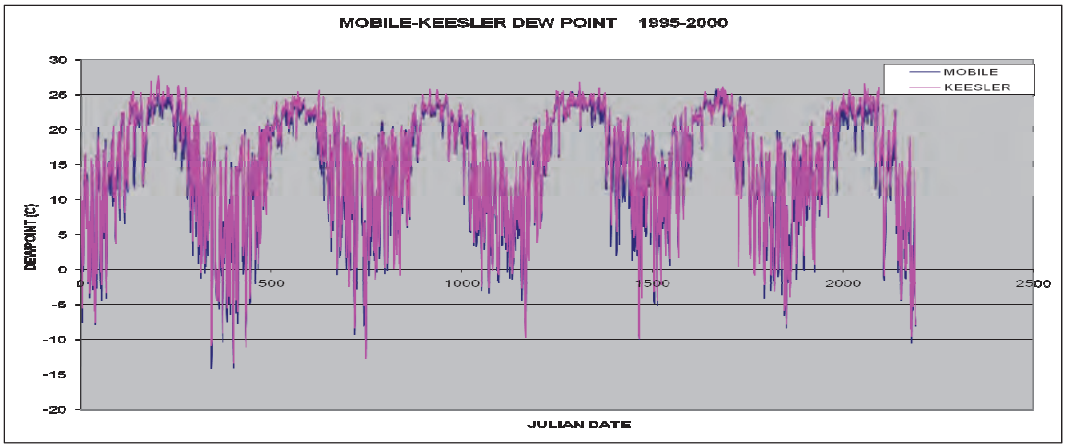

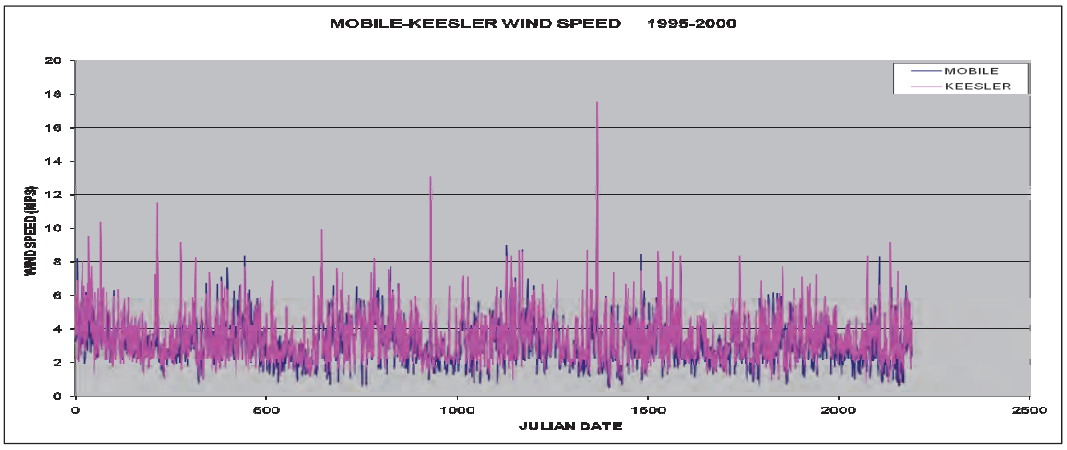

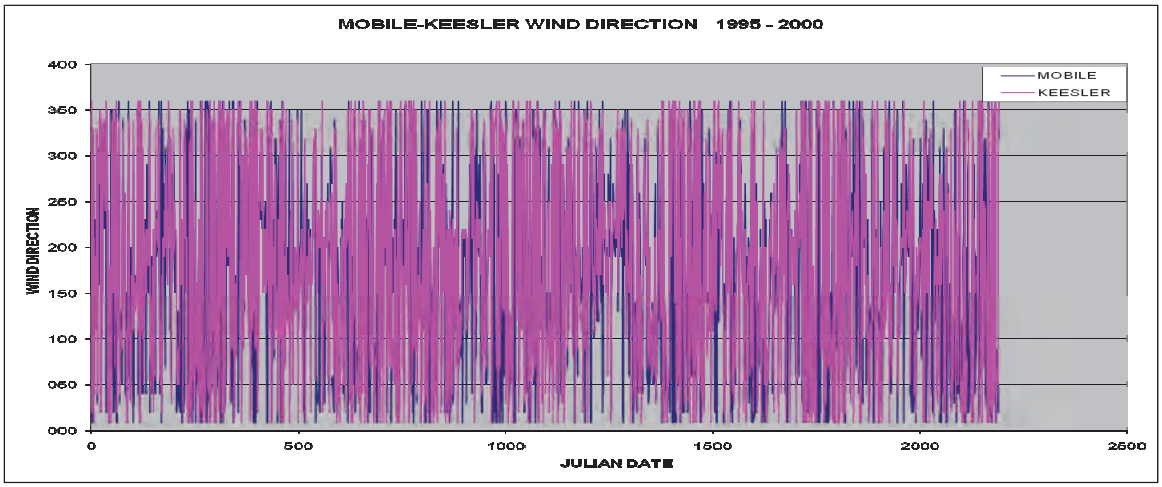
MOBILE-KEESLER WIND DIRECTION 1995 - 2000
MOBILE
KEESLER
WIND DIRECTION
400
350
300
250
200
150
100
050
000
0
500
1000
1500
2000
2500
JULIAN DATE

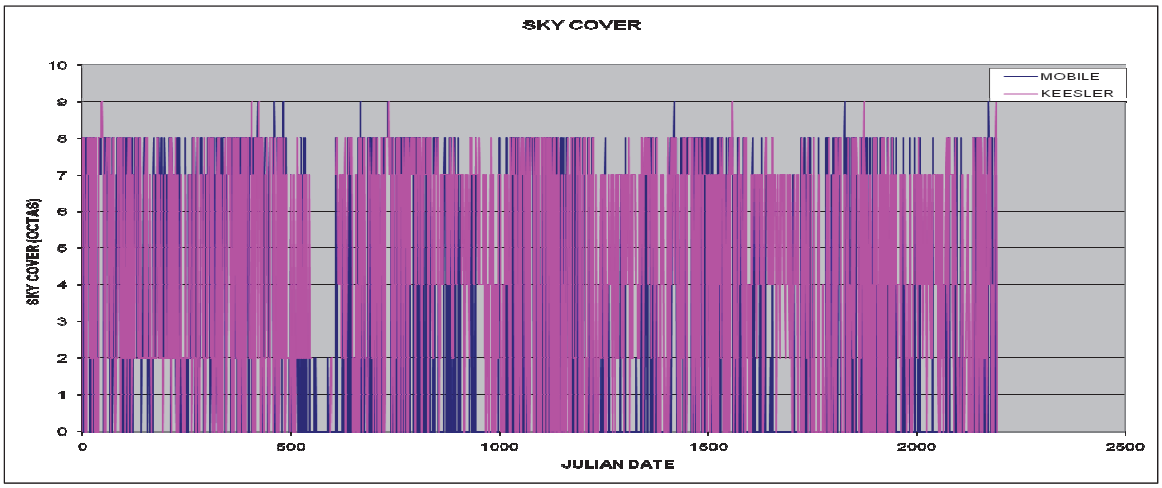
SKY COVER
MOBILE
KEESLER
SKY COVER (OCTAS)
10
9
8
7
6
5
4
3
2
1
0
0
500
1000
1500
2000
2500
JULIAN DATE

Appendix E: Calibration and Scenario Time-Series Results

Figure E-1. Calibration results for temperature at Station 1 for surface layer (upper) and bottom layer (lower).

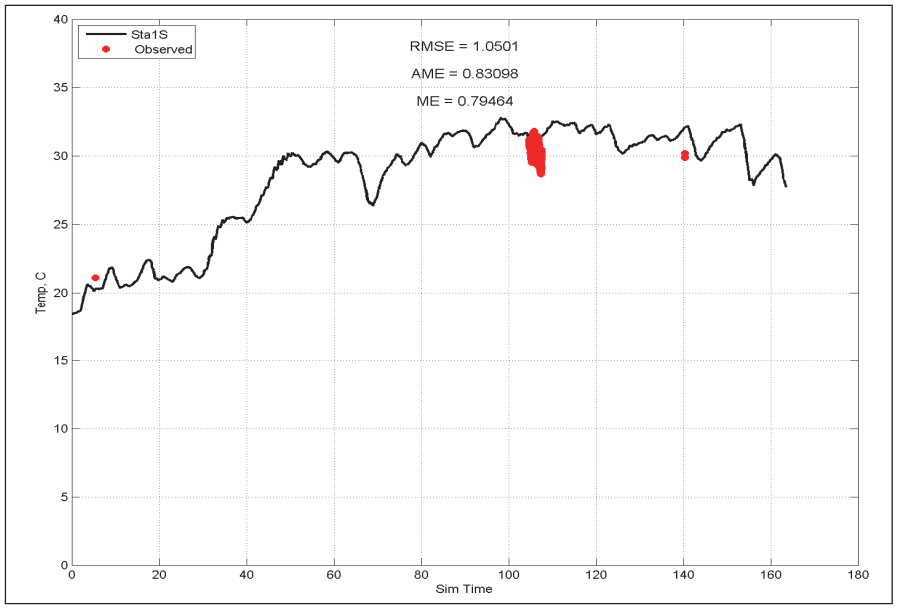

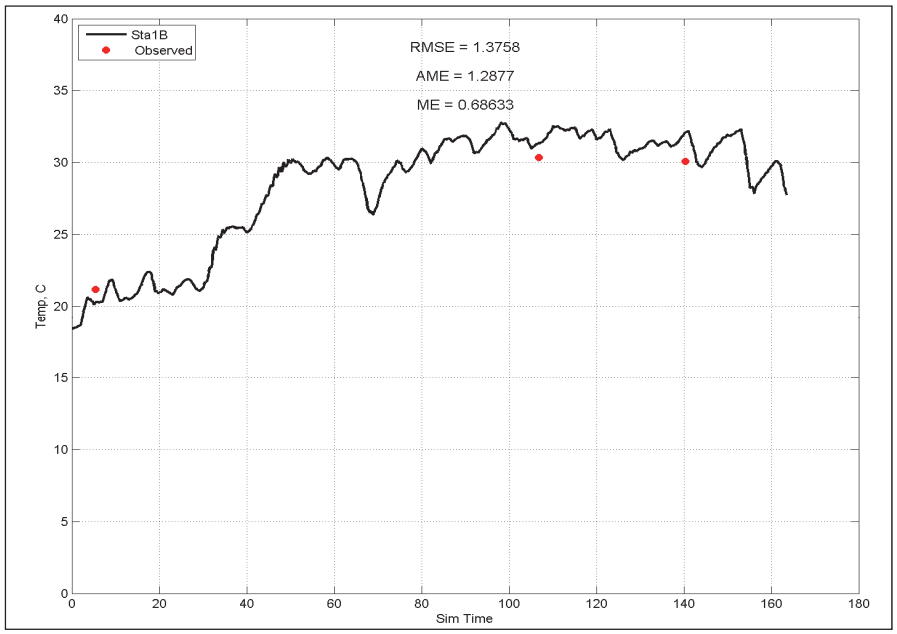

Figure E-2. Calibration results for salinity at Station 1 for surface layer upper) and bottom layer (lower).

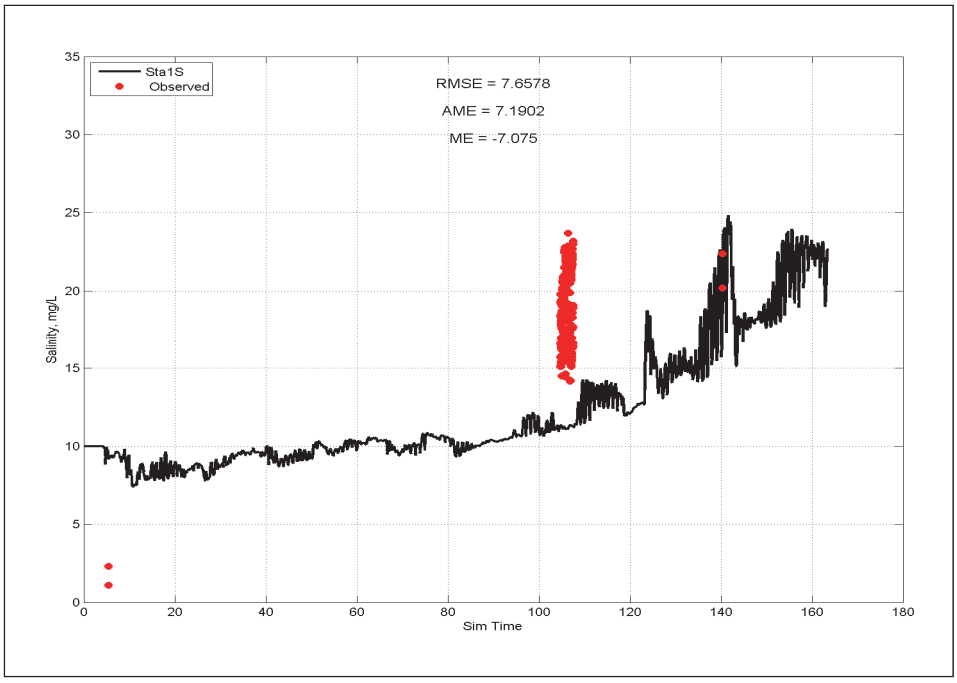

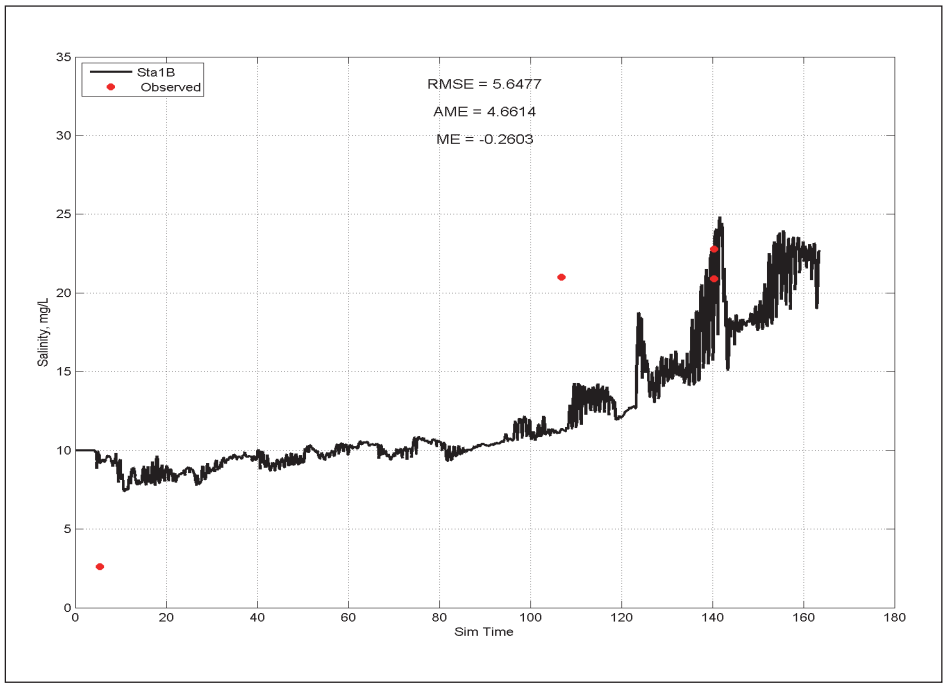

Figure E-3. Calibration results for DO at Station 1 for surface layer (upper) and bottom layer (lower).

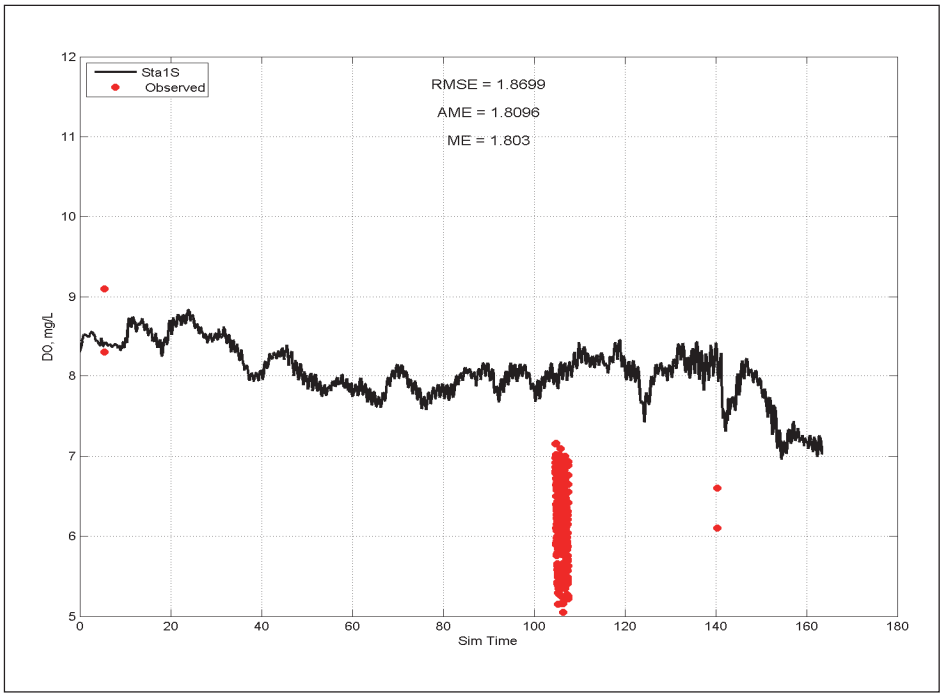

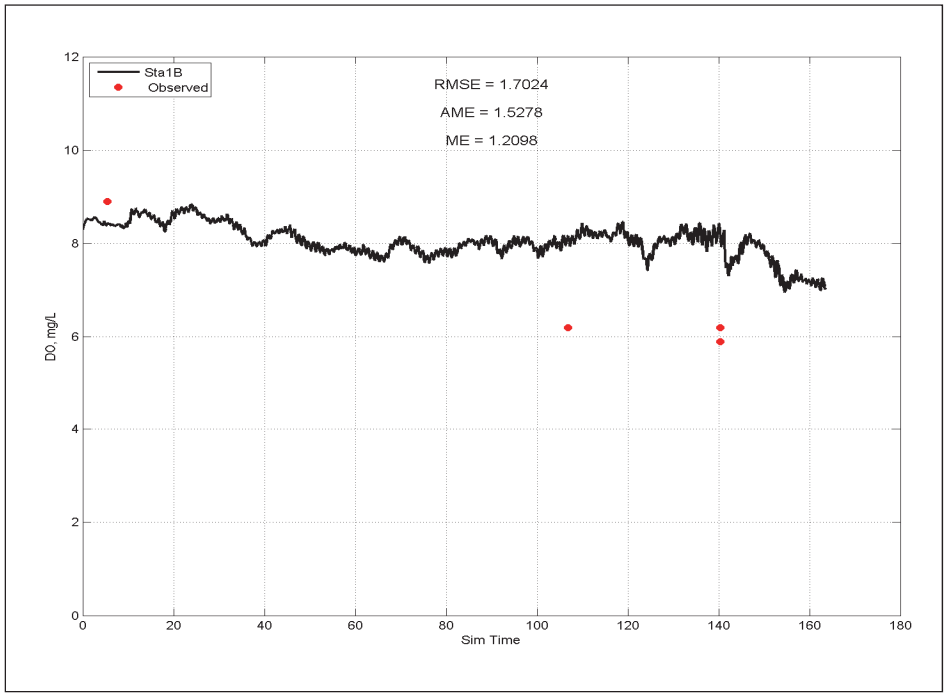

Figure E-4. Calibration results for NH_4 at Station 1 for surface layer upper) and bottom layer (lower).

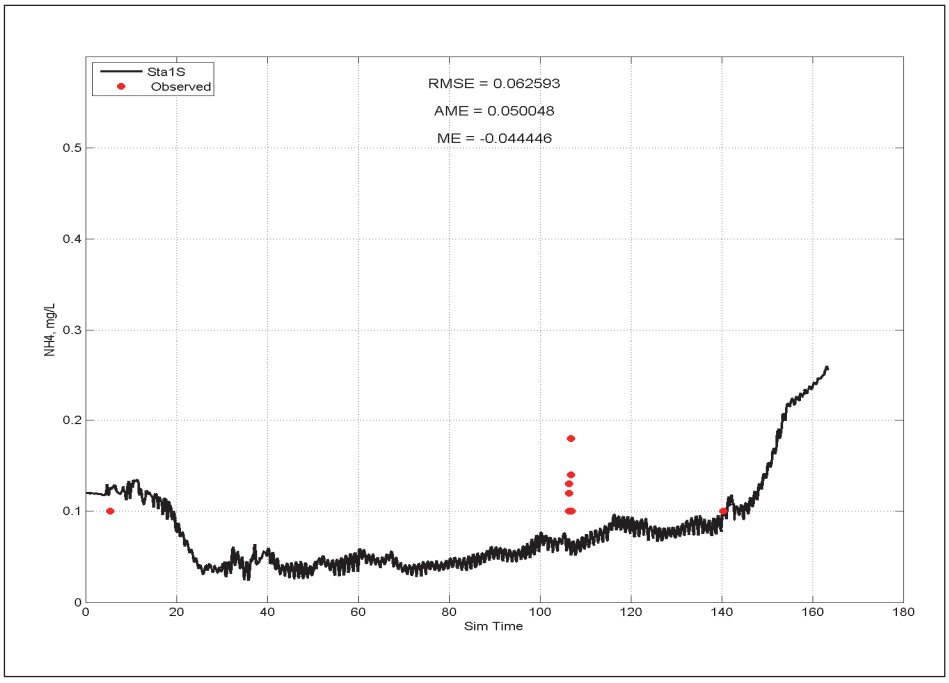

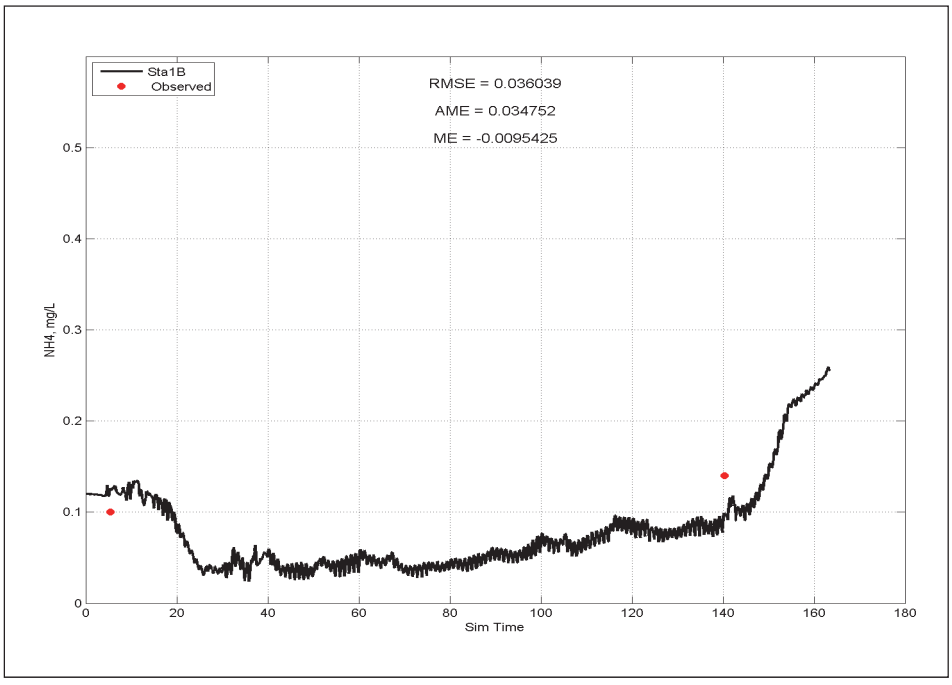

Figure E-5. Calibration results for NO_3 at Station 1 for surface layer (upper) and bottom layer (lower).

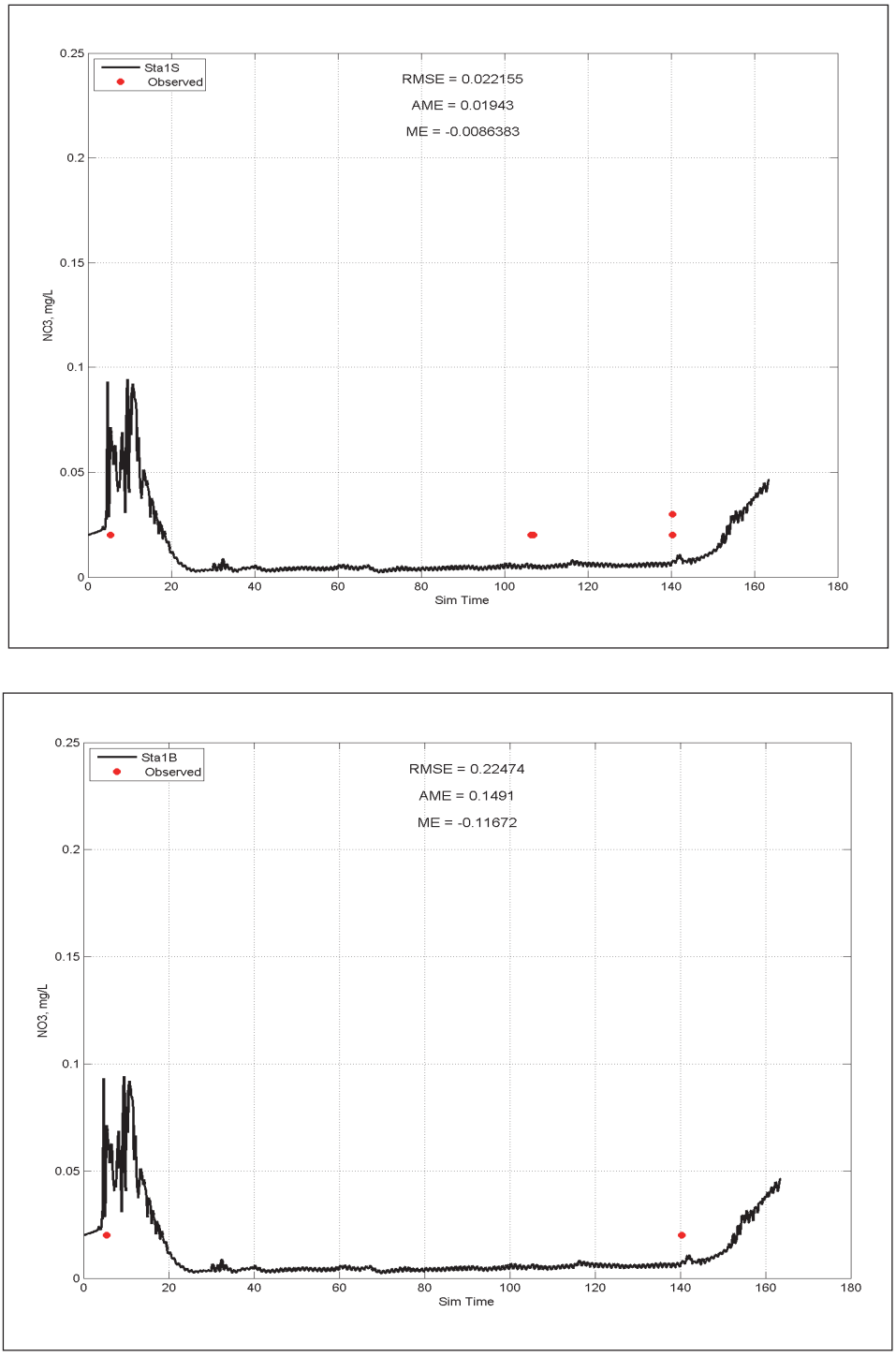

Figure E-6. Calibration results for *Tp* at Station 1 for surface layer (upper) and bottom layer (lower).

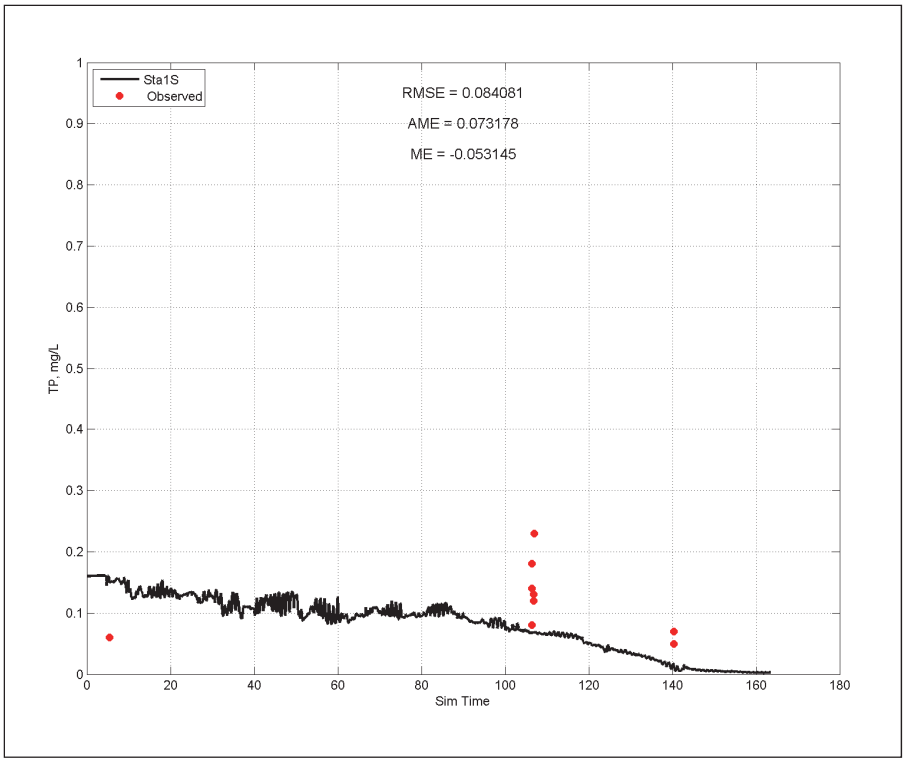

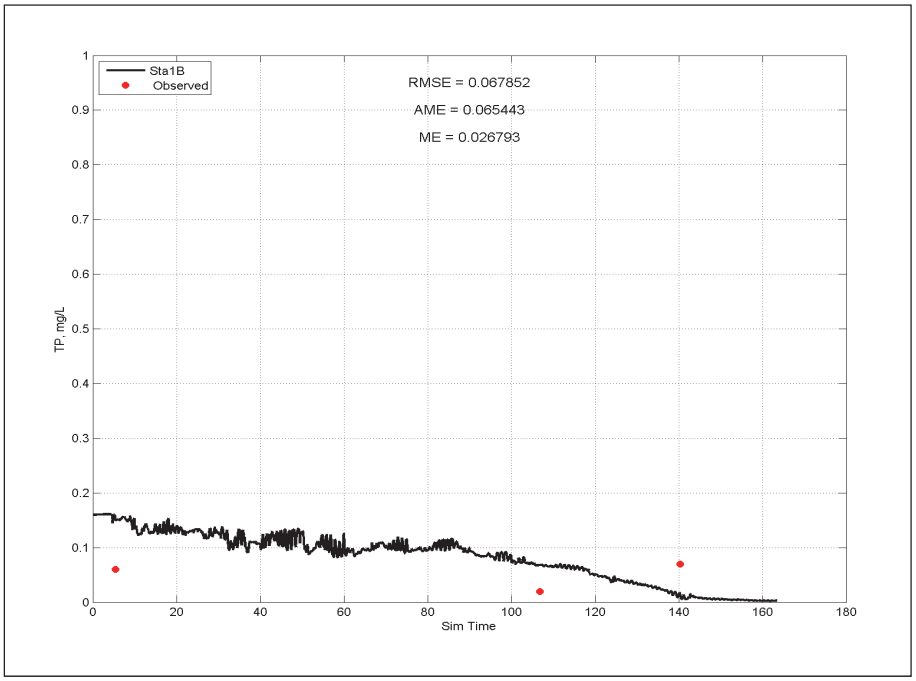

Figure E-7. Calibration results for temperature at Station 2 for surface layer (upper) and bottom layer (lower).

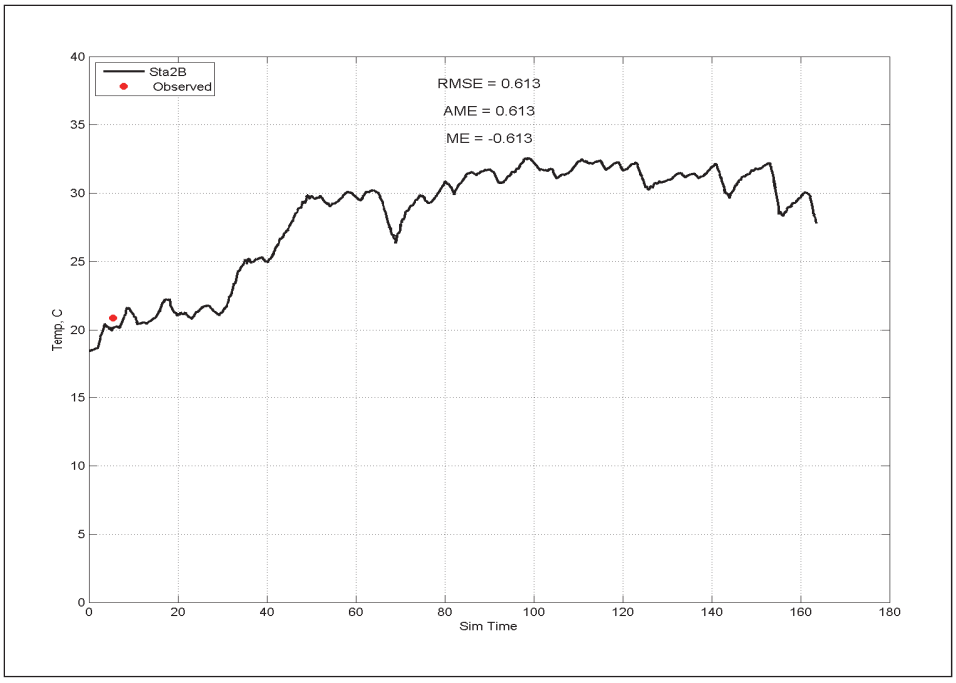

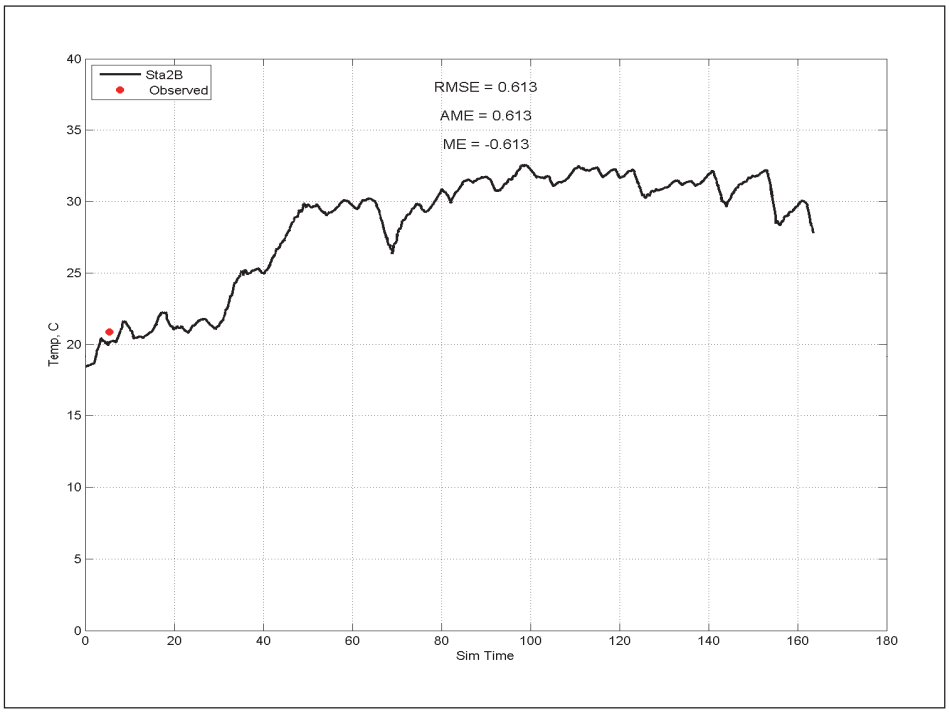

Figure E-8. Calibration results for salinity at Station 2 for surface layer (upper) and bottom layer (lower).

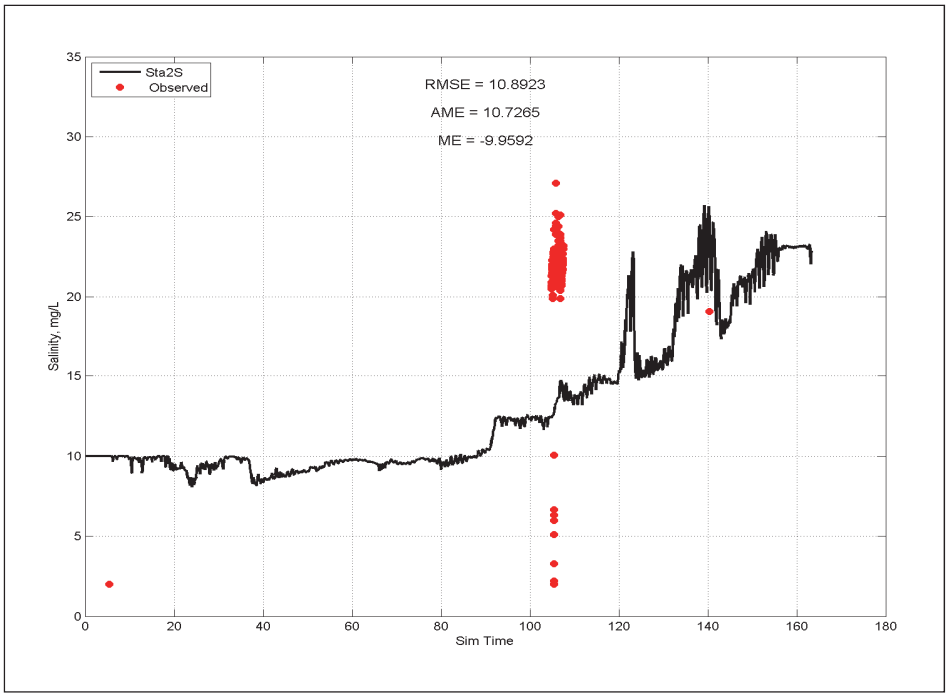

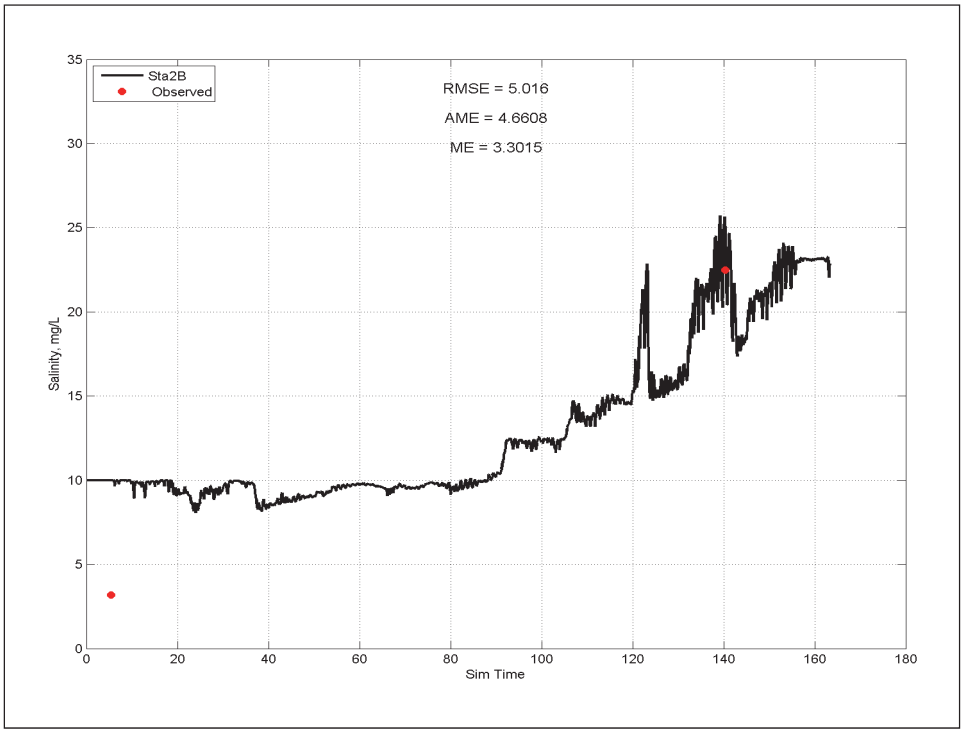

Figure E-9. Calibration results for DO at Station 2 for surface layer (upper) and bottom layer (lower).

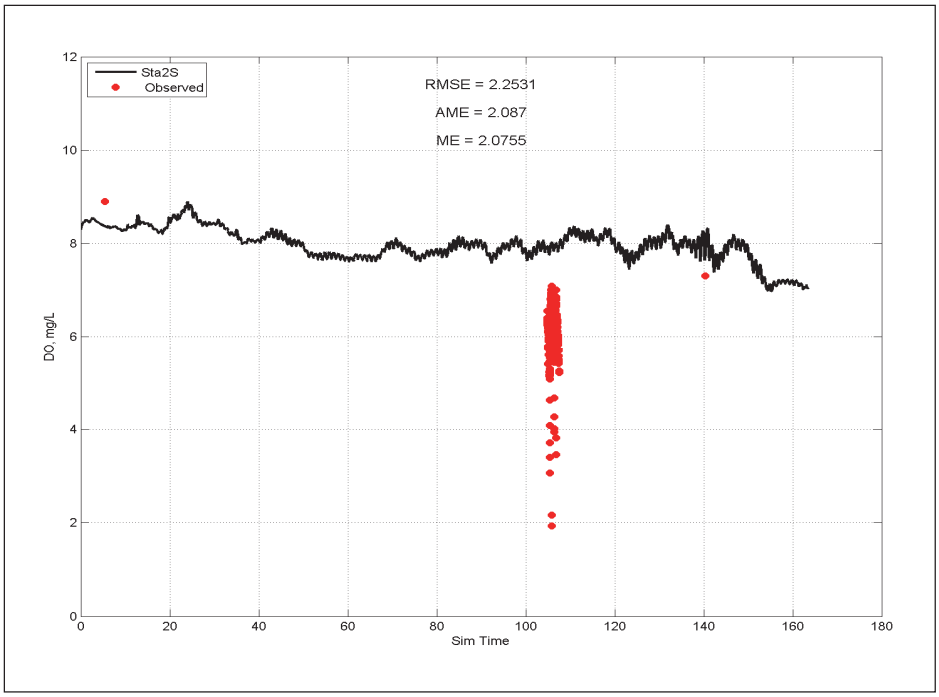

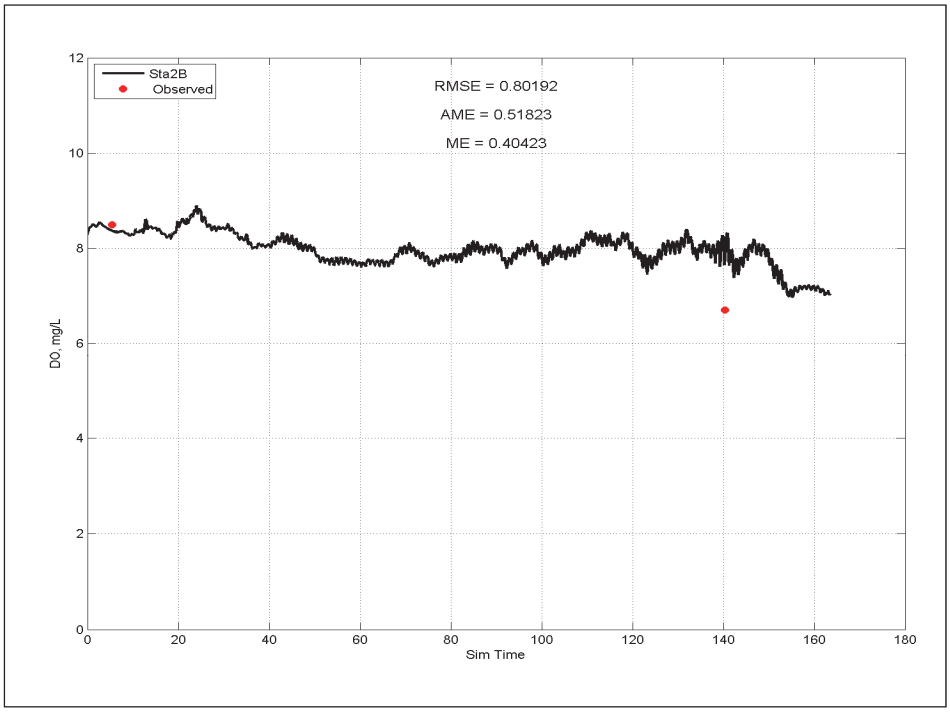

Figure E-10. Calibration results for NH_4 at Station 2 for surface layer (upper) and bottom layer (lower).

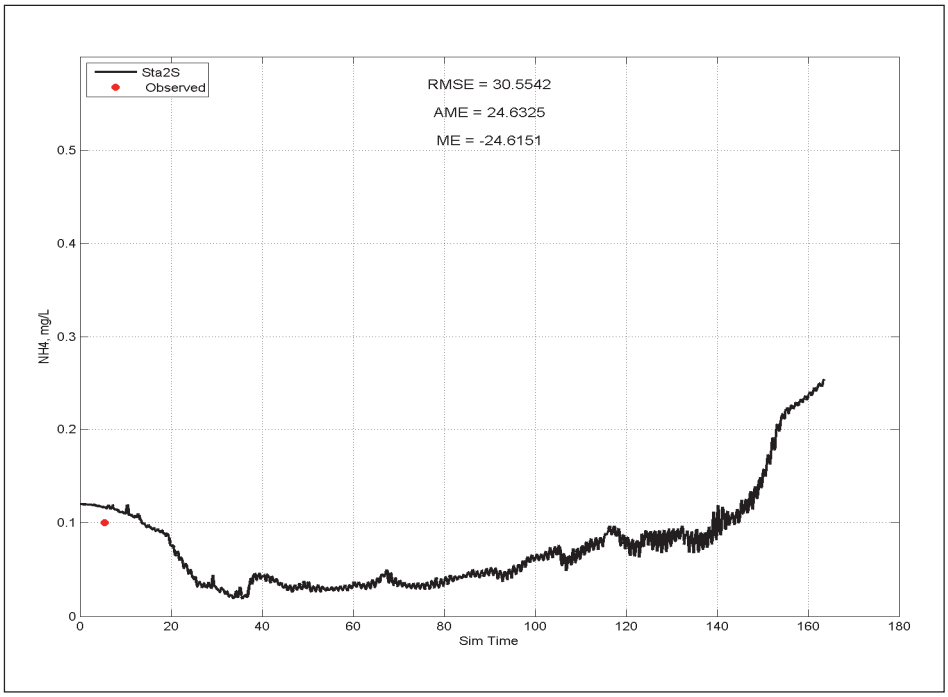

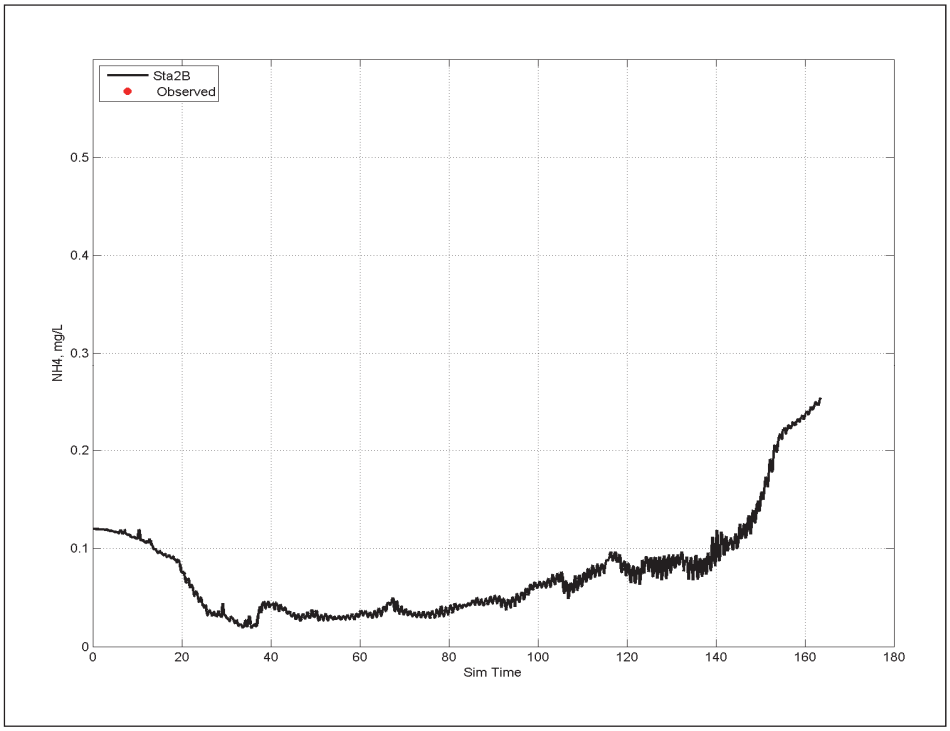

Figure E-11 Calibration results for NO_3 at Station 2 for surface layer (upper) and bottom layer (lower).

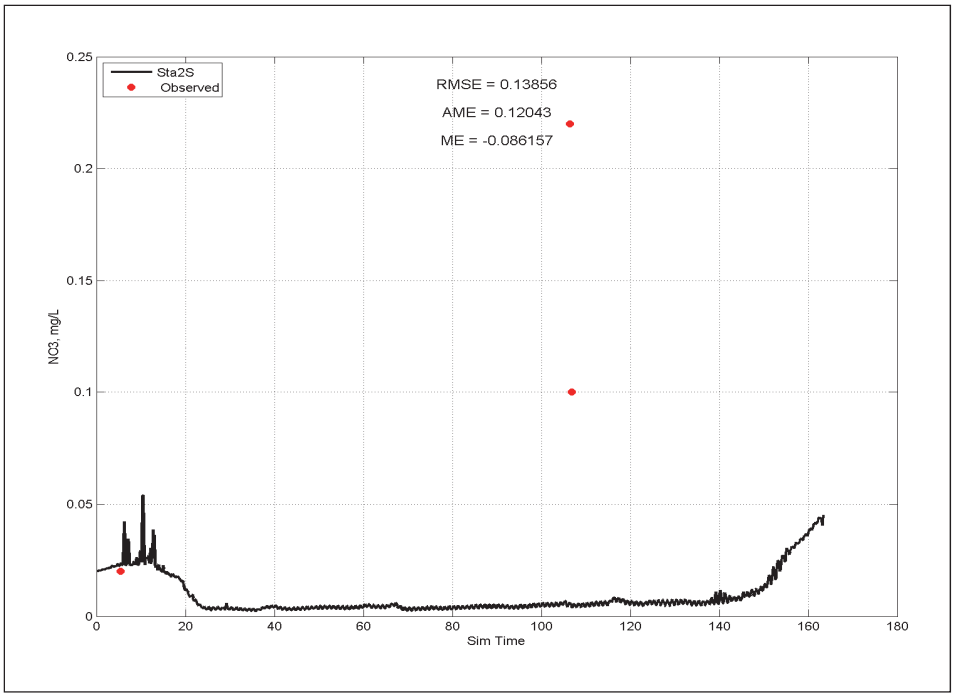

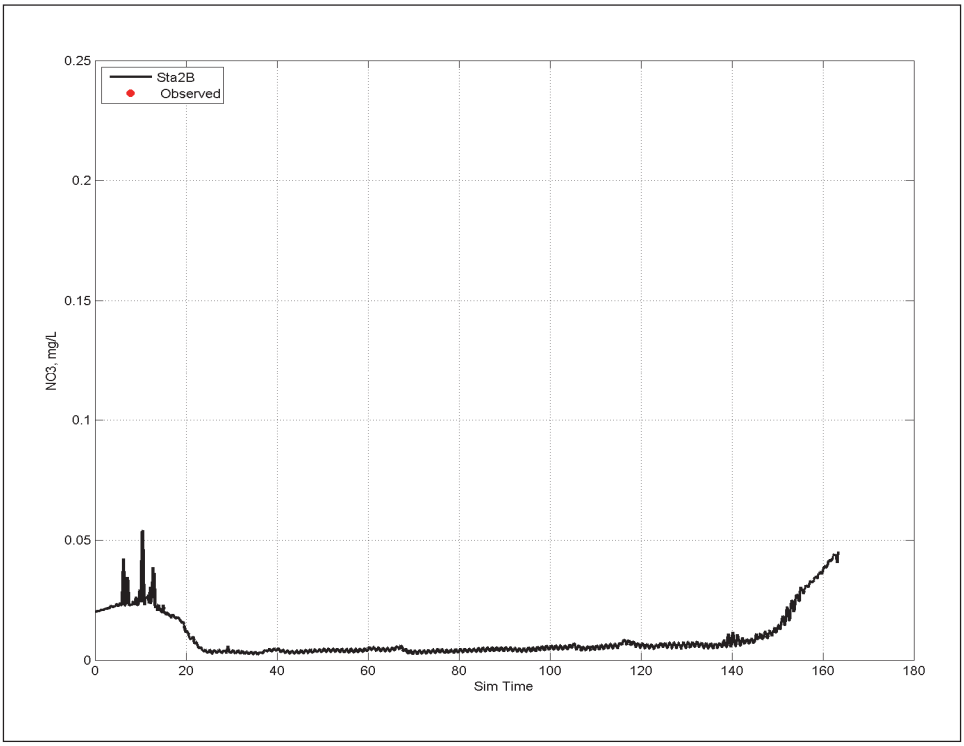

Figure E-12. Calibration results for *Tp* at Station 2 for surface layer (upper) and bottom layer (lower).

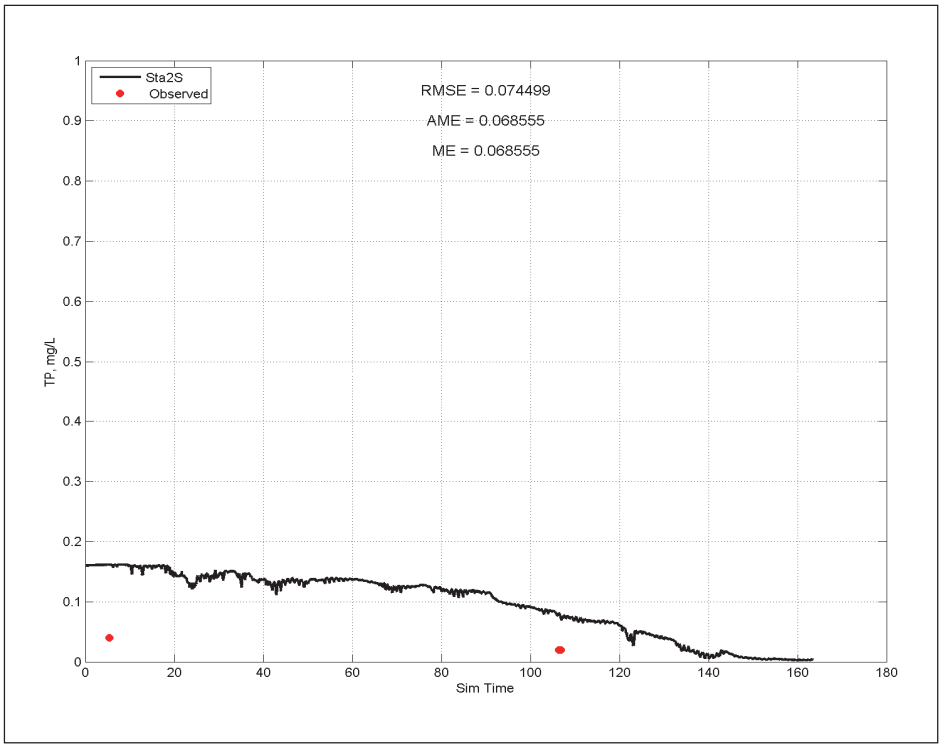

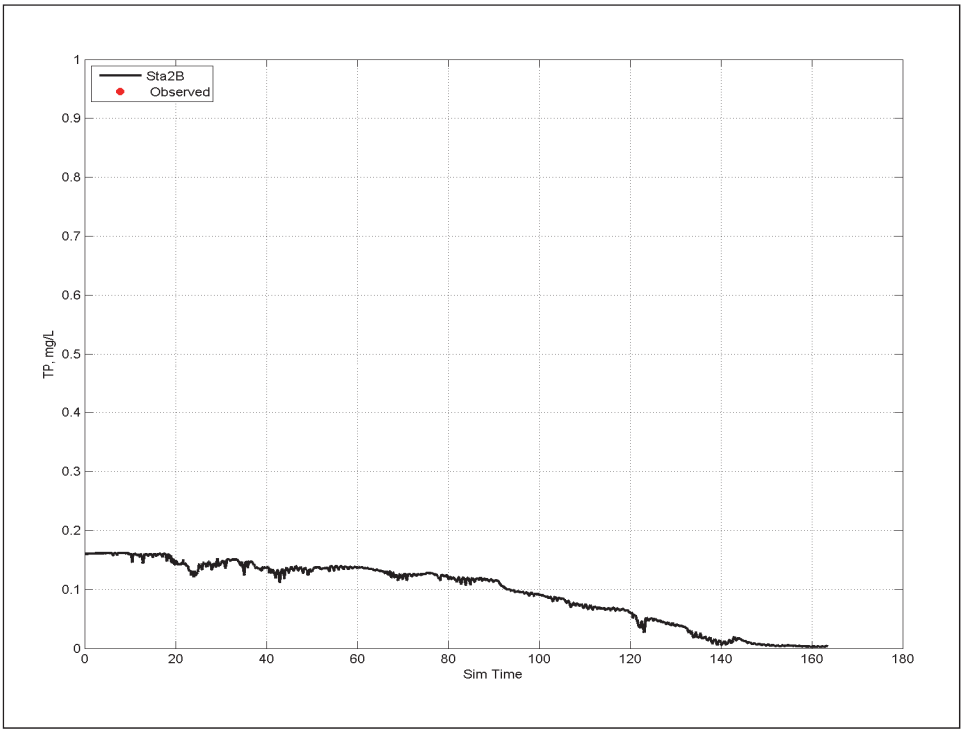

Figure E-13. Calibration results for temperature at Station 3 for surface layer (upper) and bottom layer (lower).

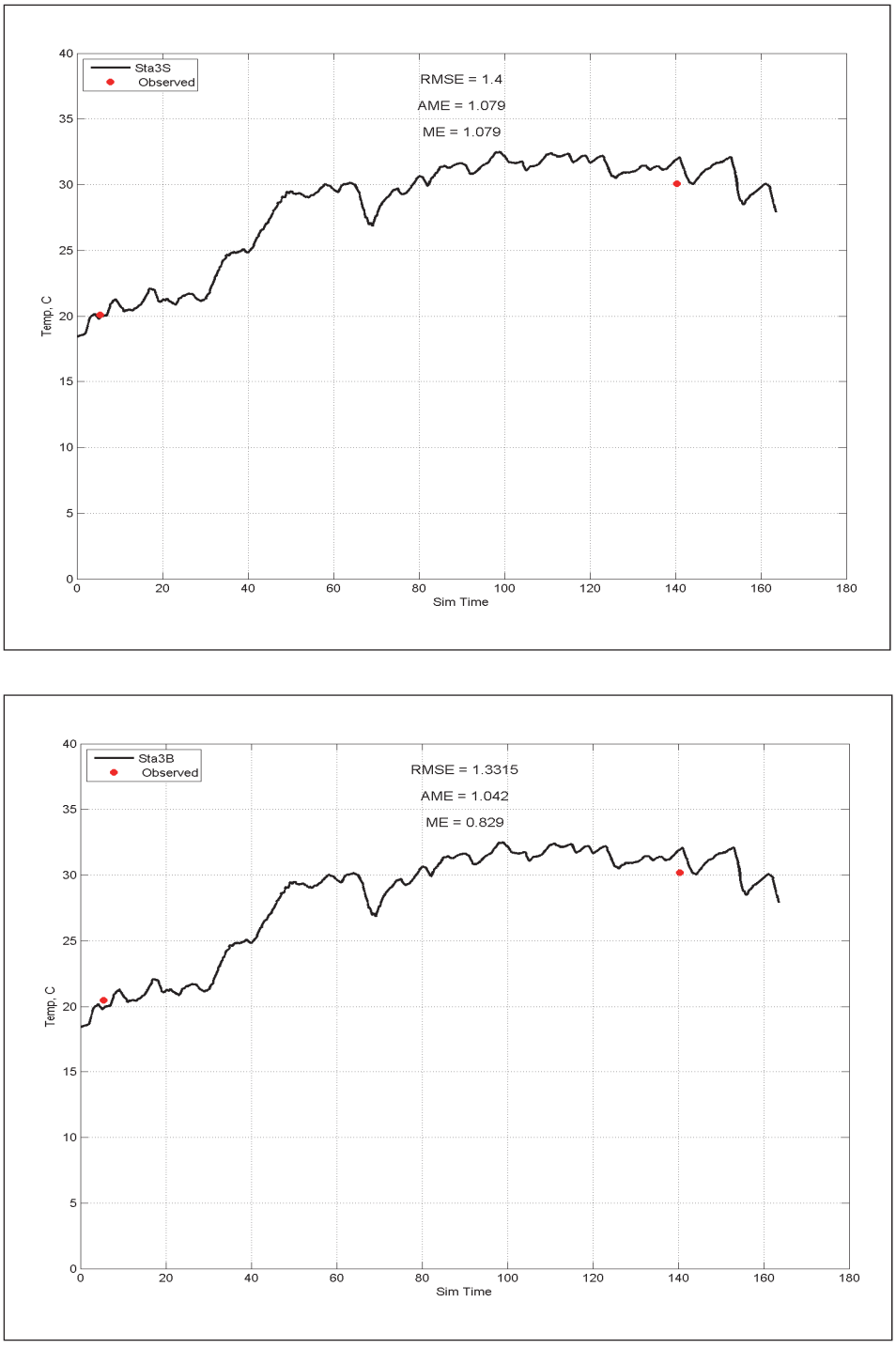

Figure E-14. Calibration results for salinity at Station 3 for surface layer (upper) and bottom layer (lower).

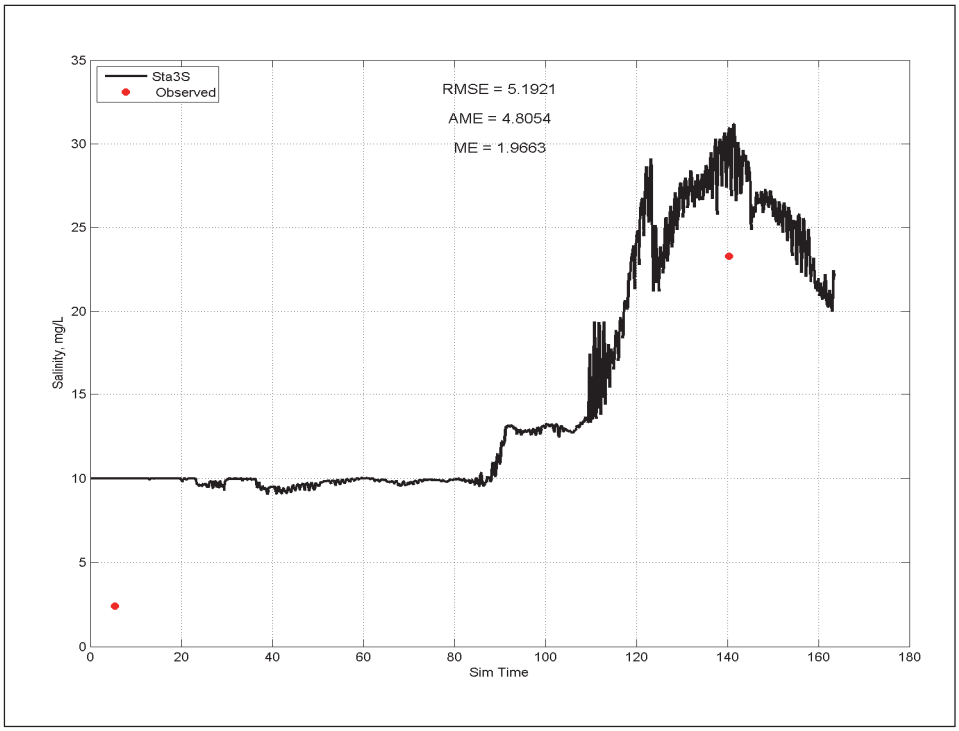

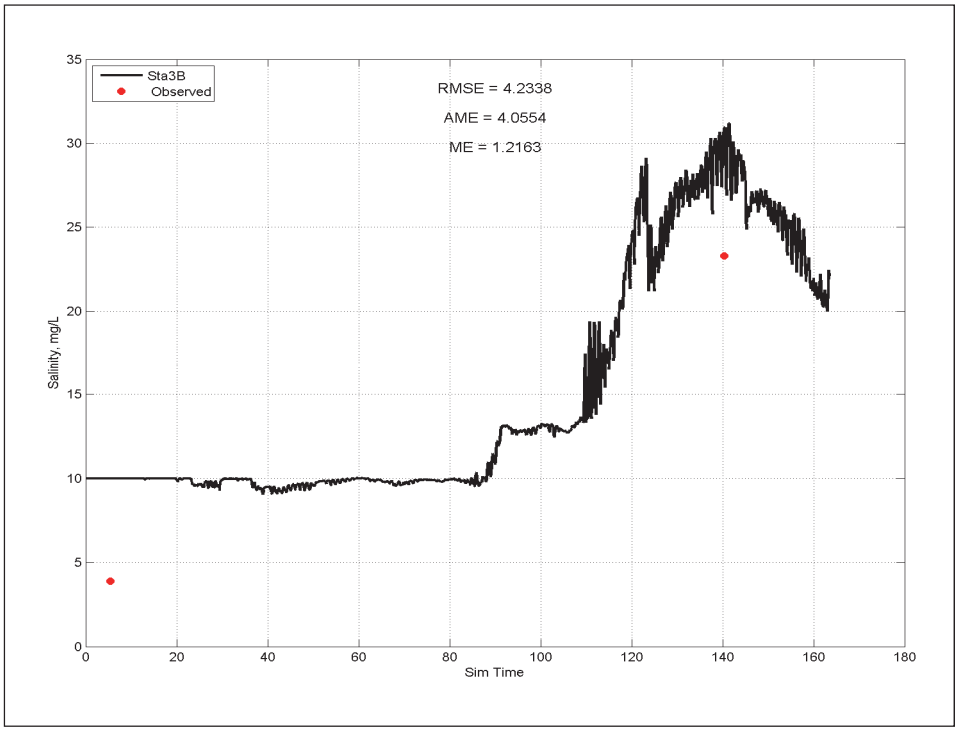

Figure E-15. Calibration results for DO at Station 3 for surface layer (upper) and bottom layer (lower).

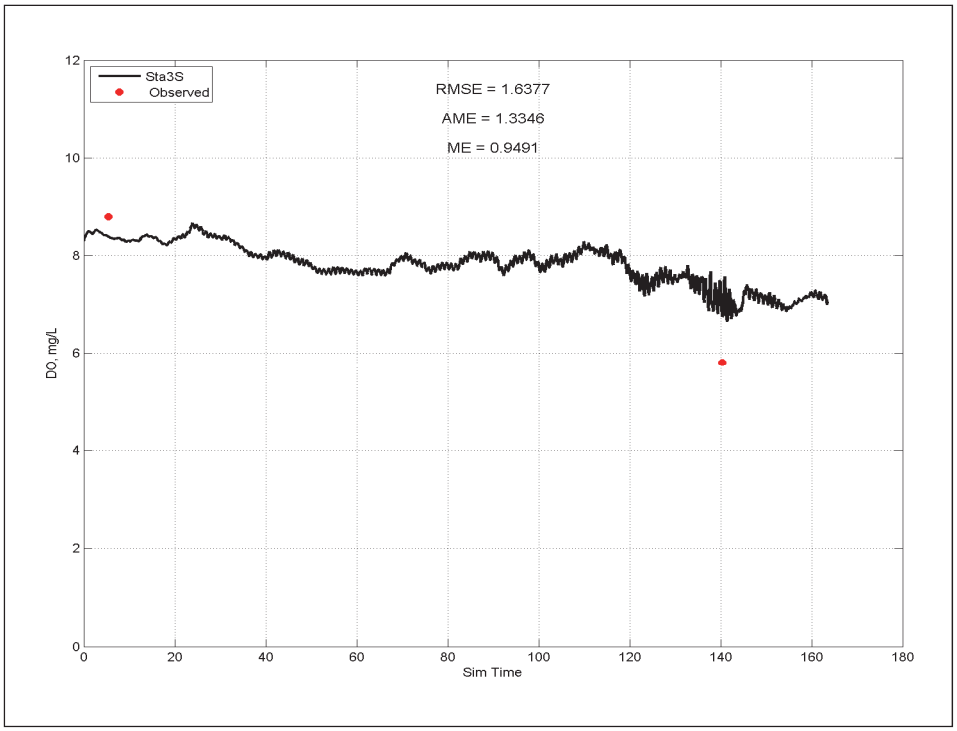

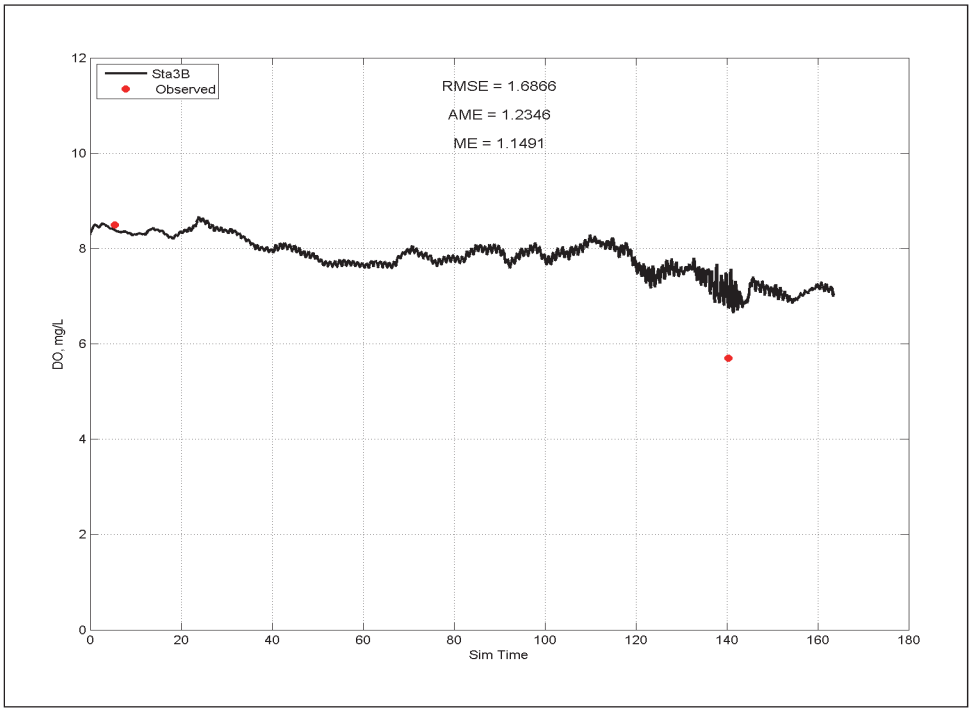

Figure E-16. Calibration results for NH_4 at Station 3 for surface layer (upper) and bottom layer (lower).

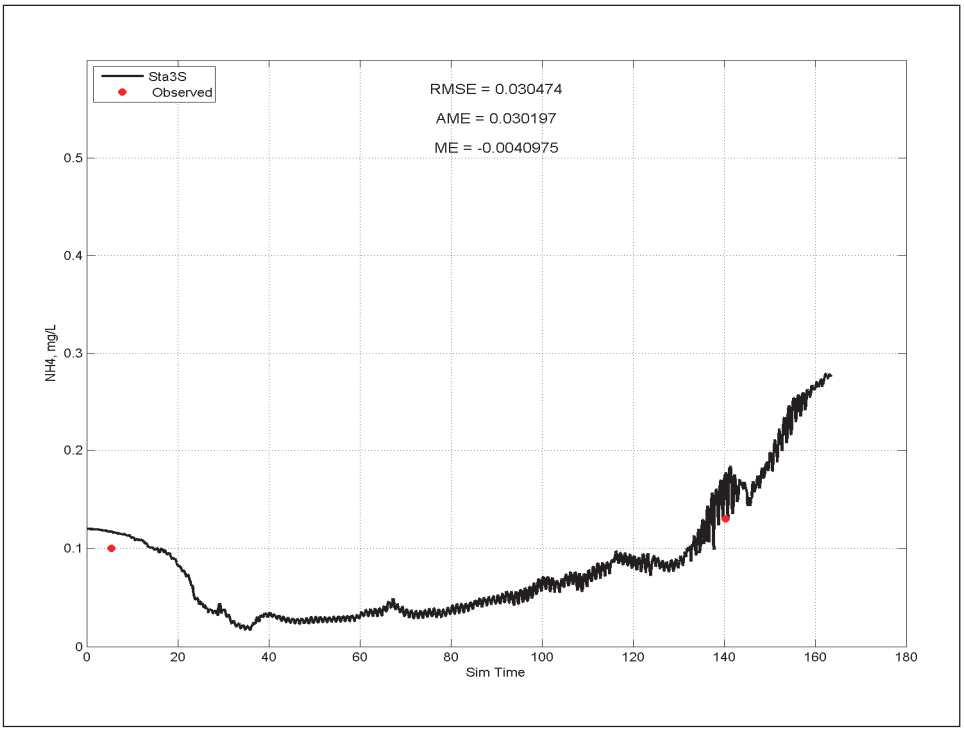

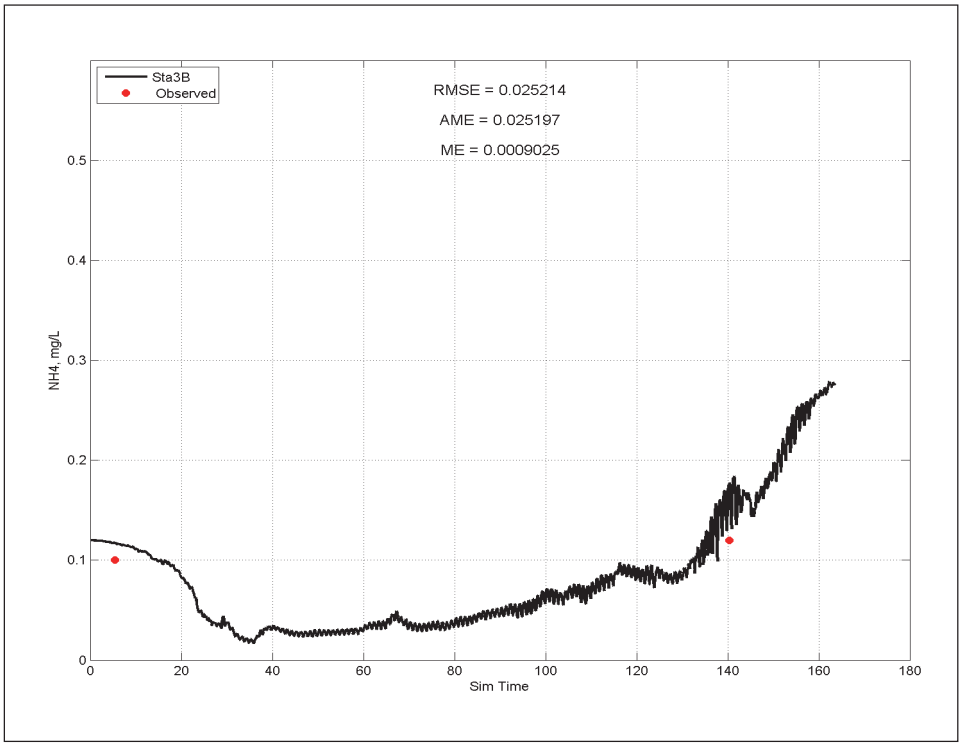

Figure E-17 Calibration results for NO_3 at Station 3 for surface layer (upper) and bottom layer (lower).

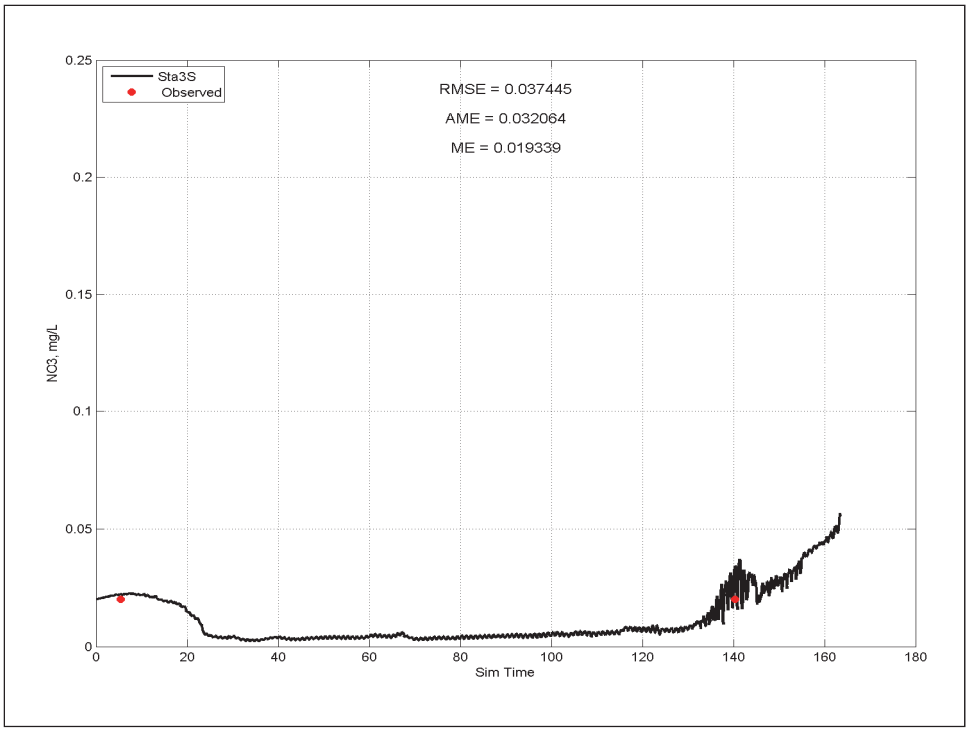

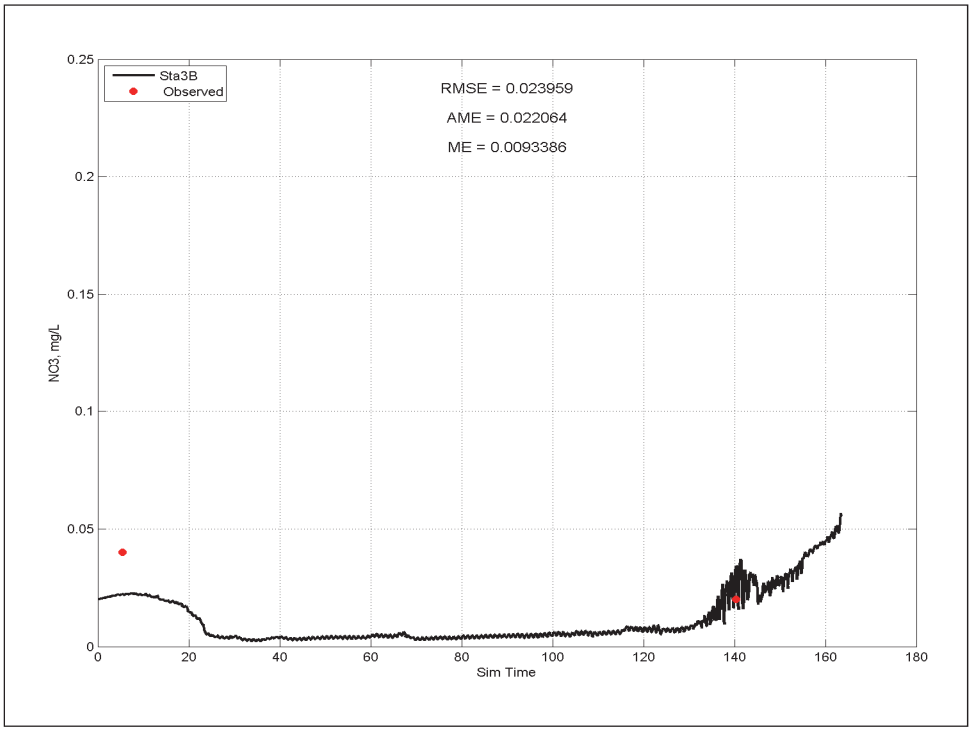

Figure E-18. Calibration results for *Tp* at Station 3 for surface layer (upper) and bottom layer (lower).

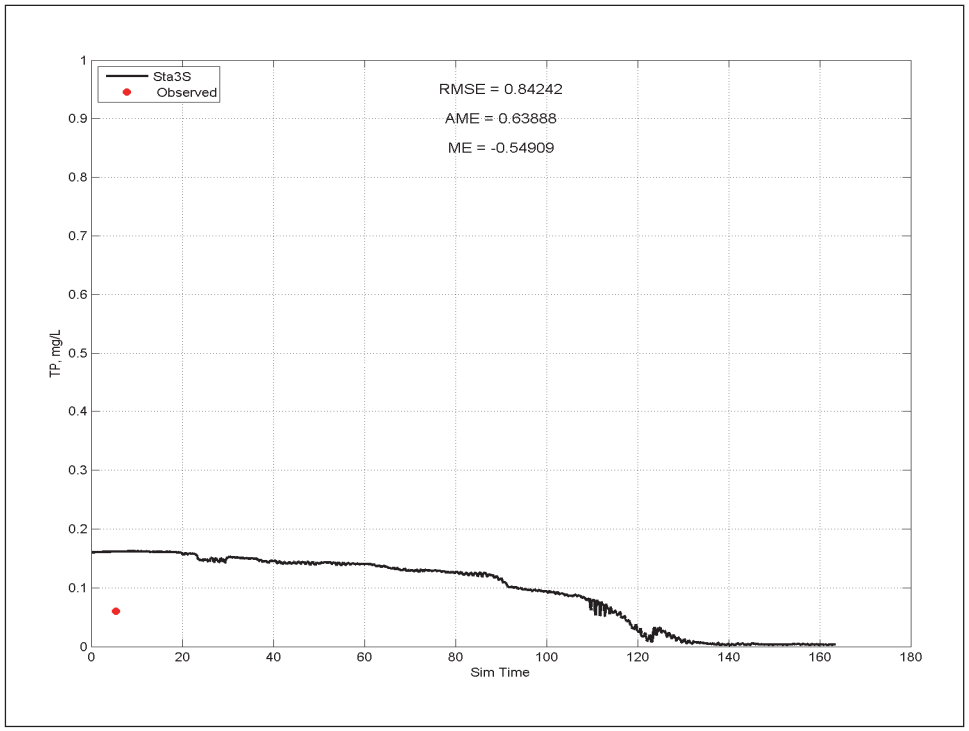

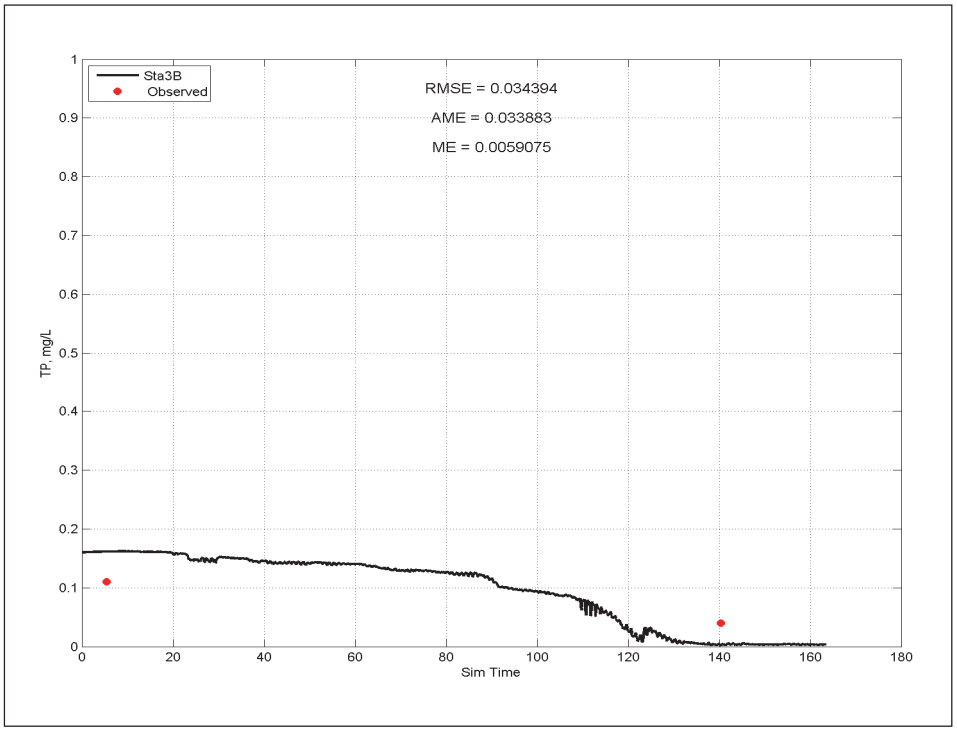

Figure E-19. Calibration results for temperature at Station 4 for surface layer (upper) and bottom layer (lower).

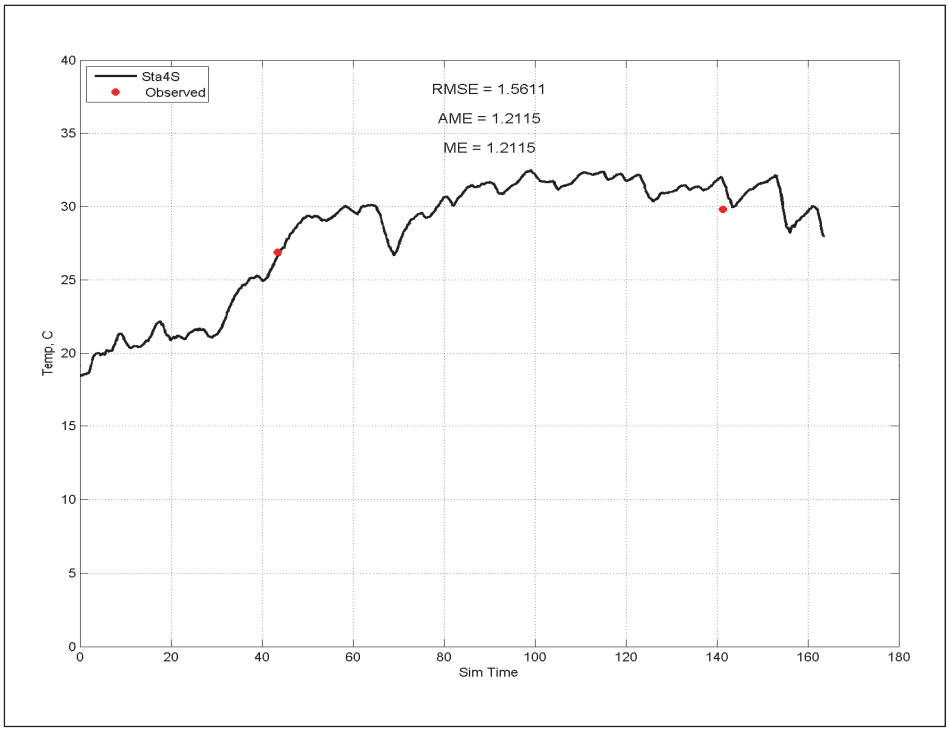

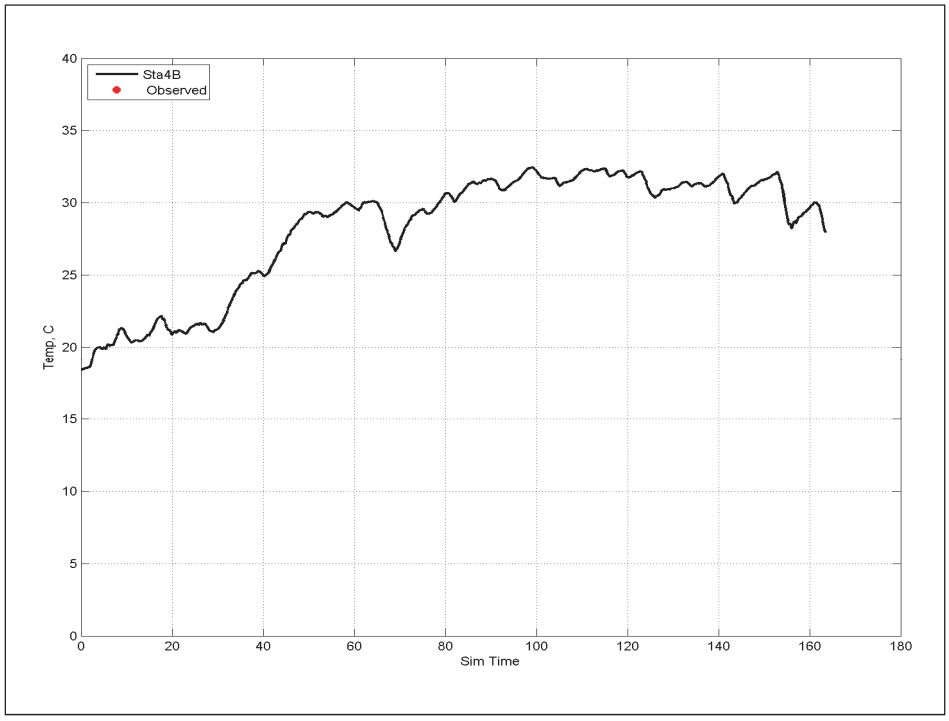

Figure E-20. Calibration results for salinity at Station 4 for surface layer (upper) and bottom layer (lower).

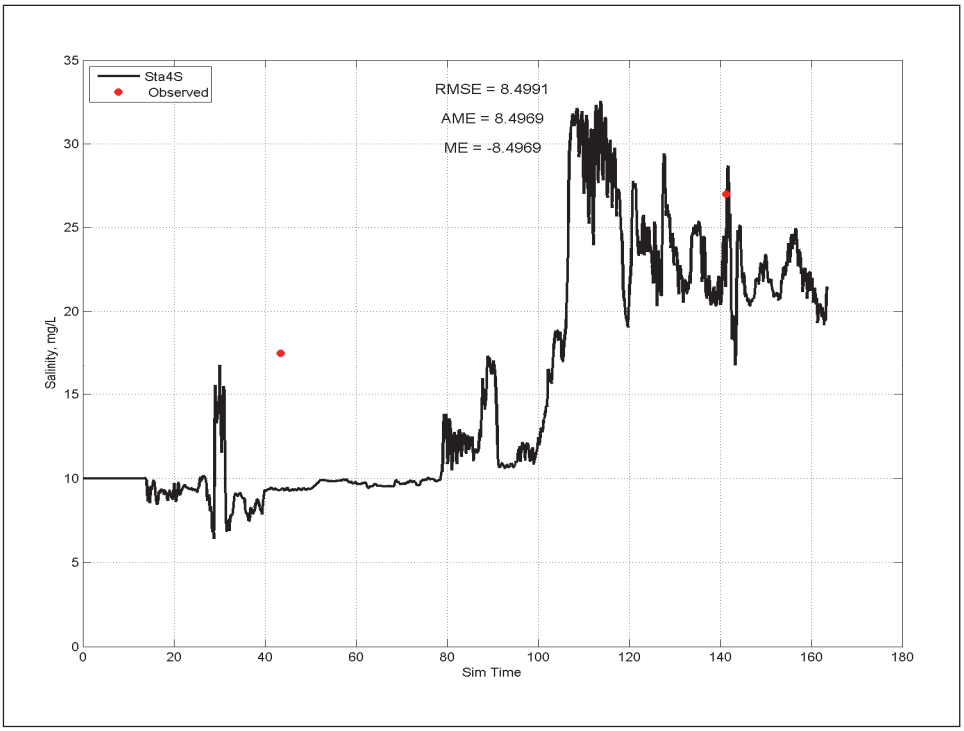

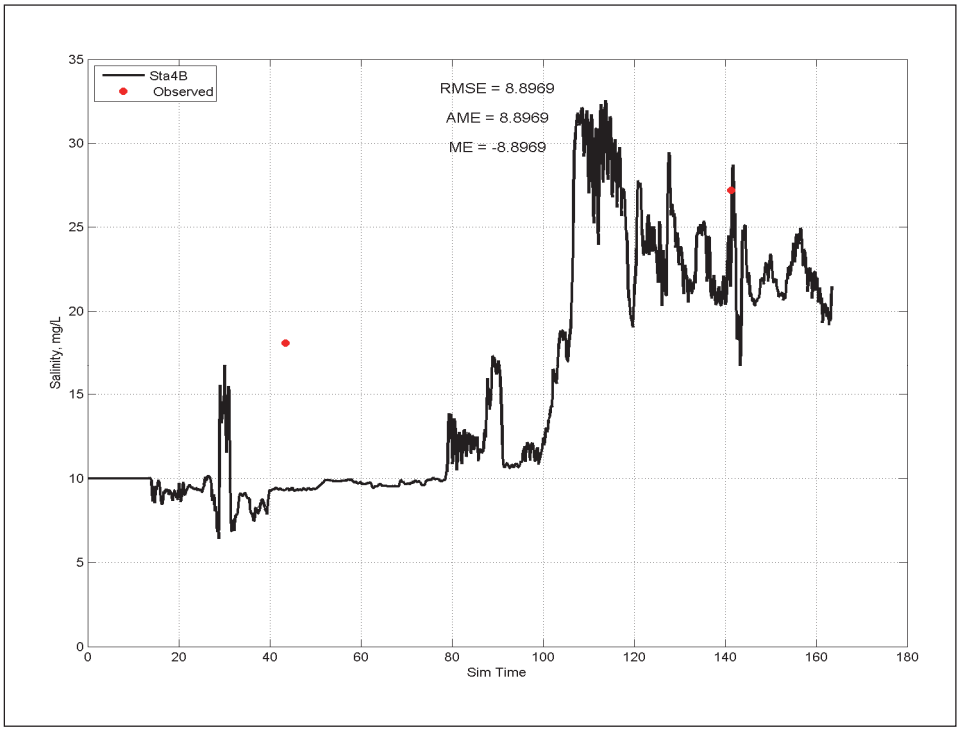

Figure E-21. Calibration results for DO at Station 4 for surface layer (upper) and bottom layer (lower).

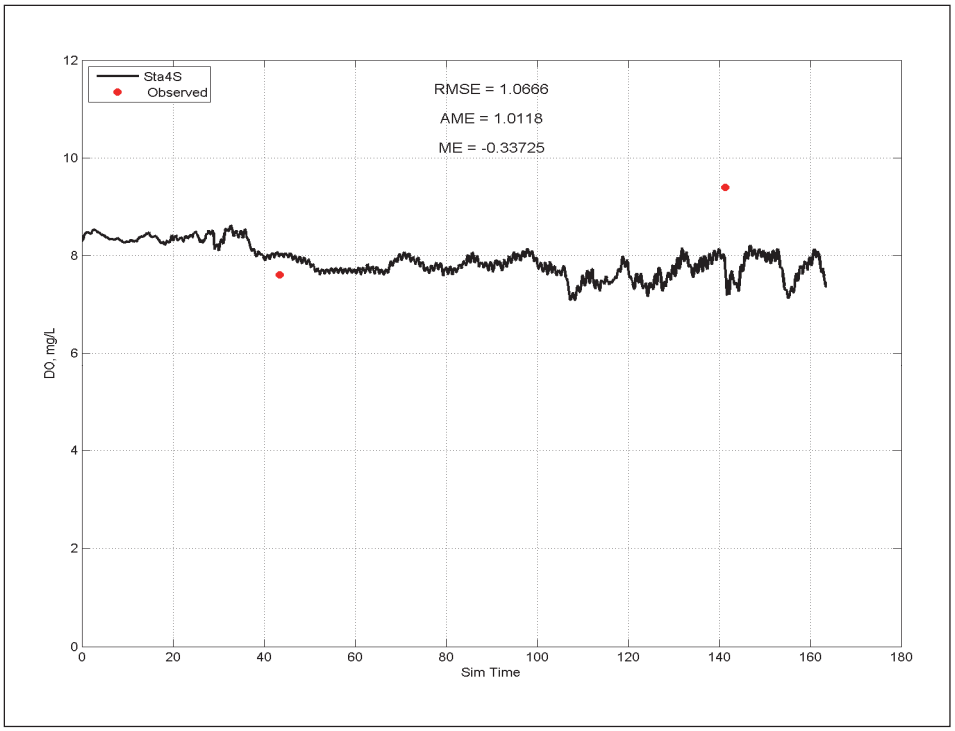

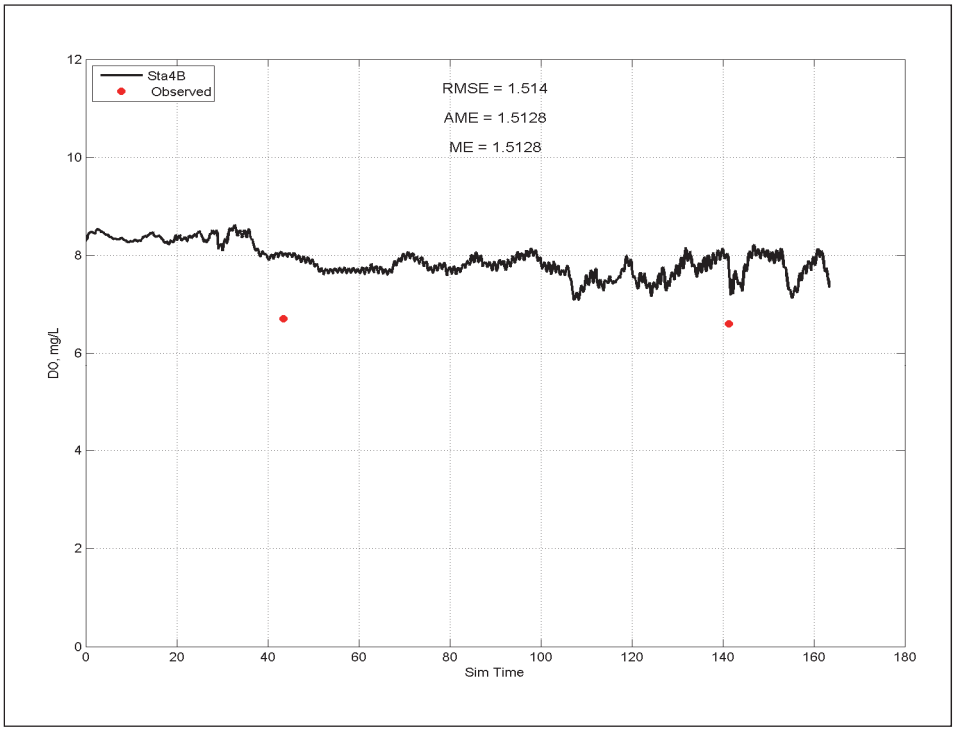

Figure E-22. Calibration results for NH_4 at Station 4 for surface layer (upper) and bottom layer (lower).

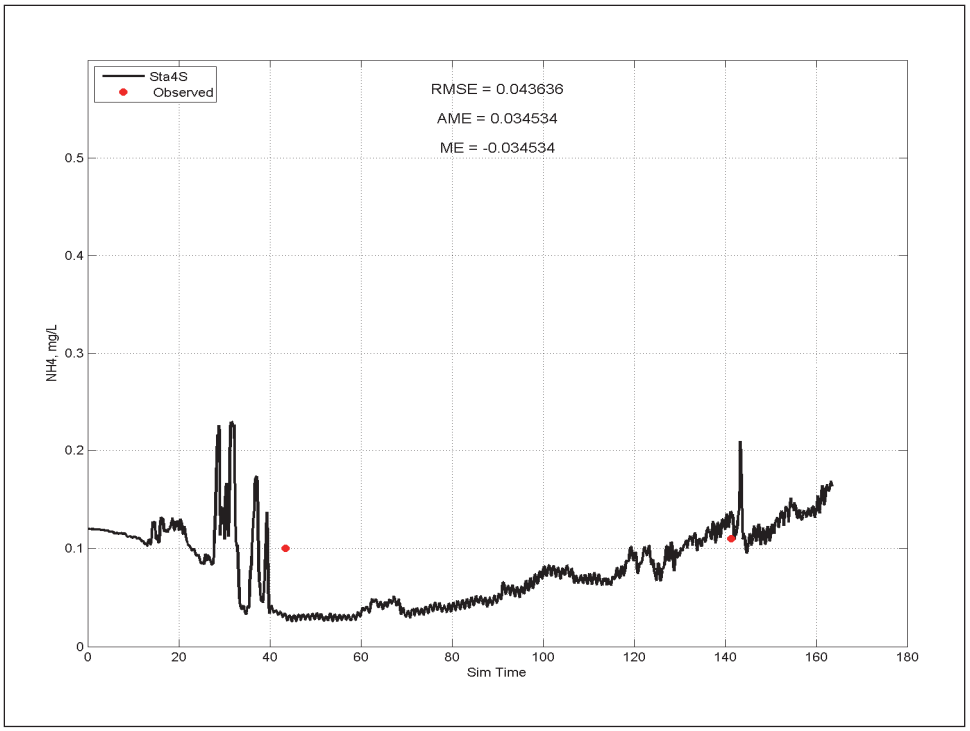

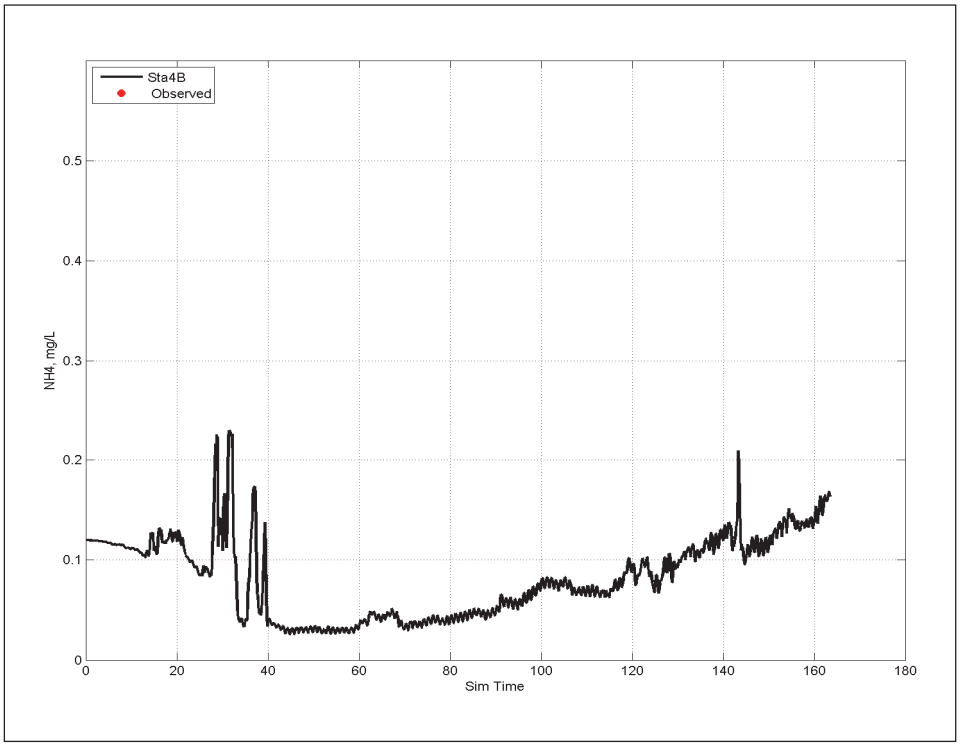

Figure E-23 Calibration results for NO_3 at Station 4 for surface layer (upper) and bottom layer (lower).

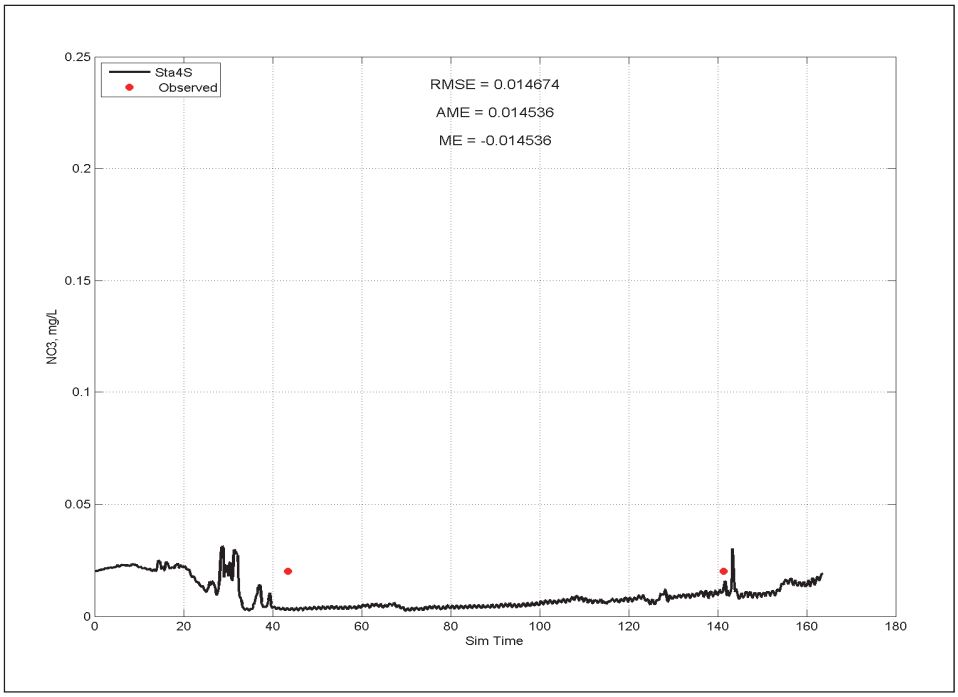

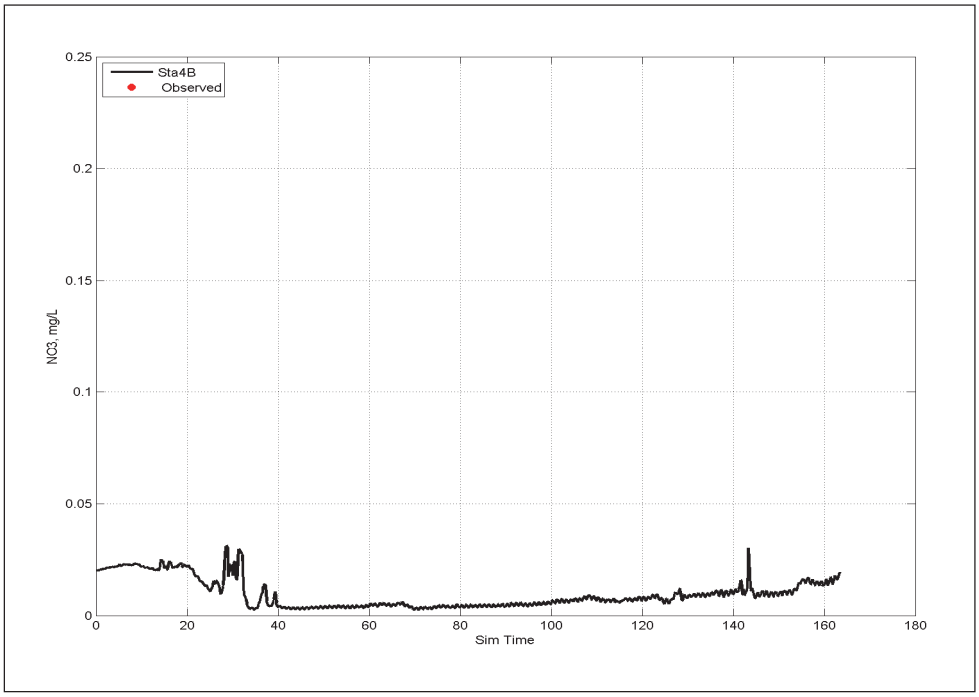

Figure E-24. Calibration results for *Tp* at Station 4 for surface layer (upper) and bottom layer (lower).

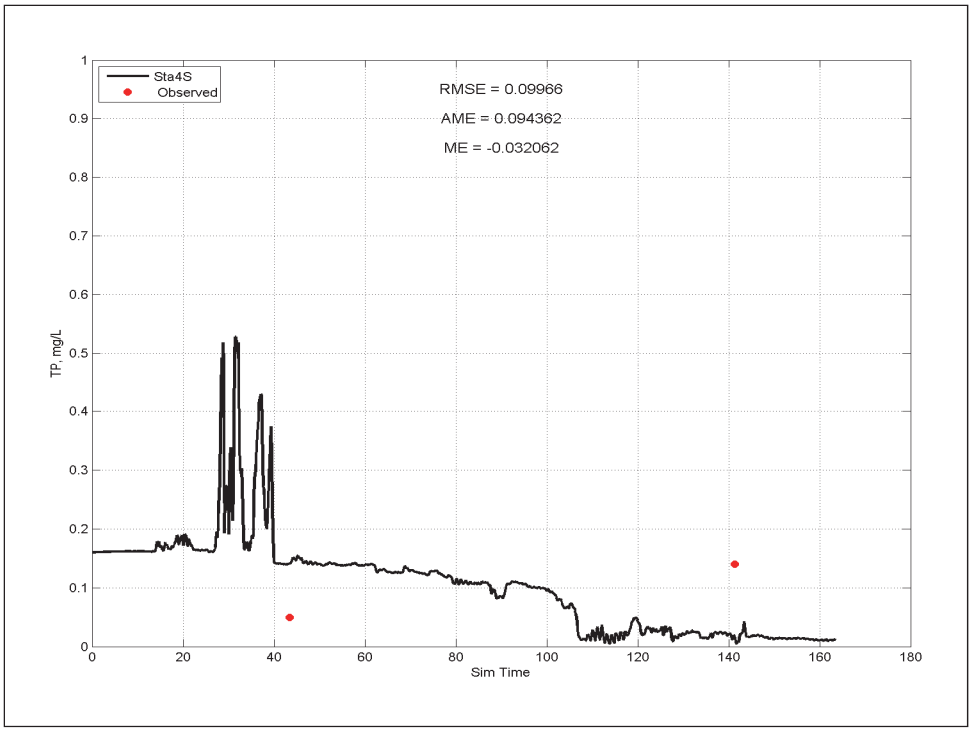

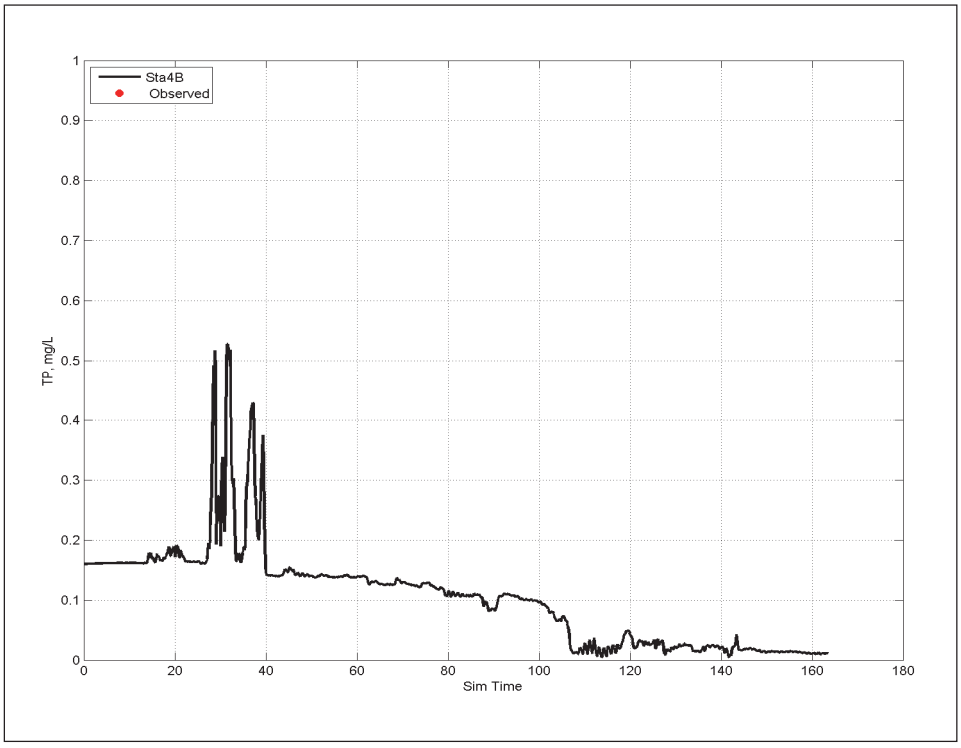

Figure E-25. Calibration results for temperature at Station 5 for surface layer (upper) and bottom layer (lower).

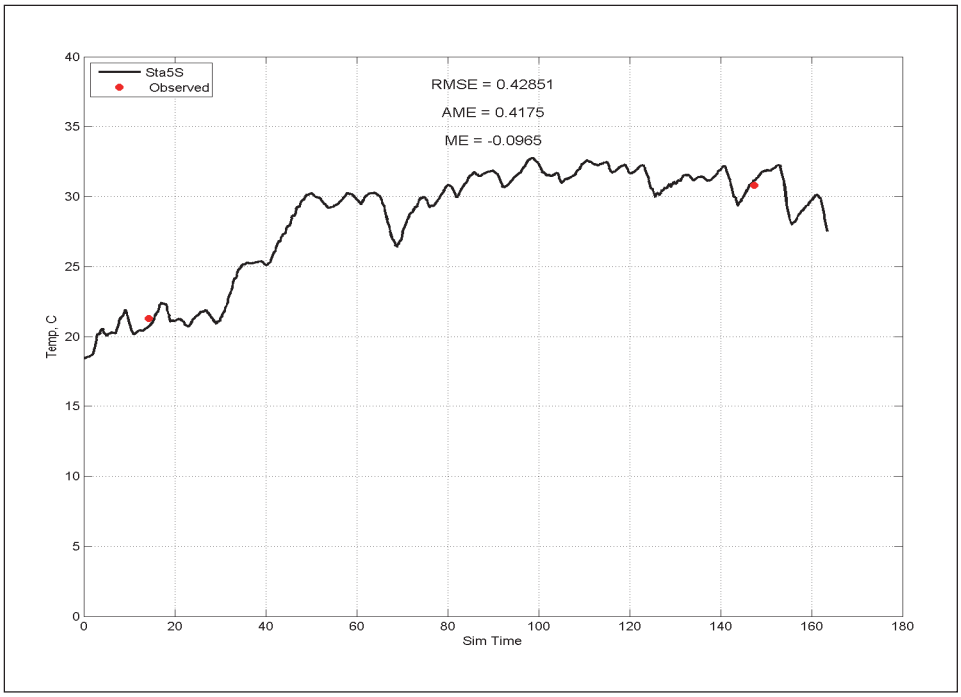

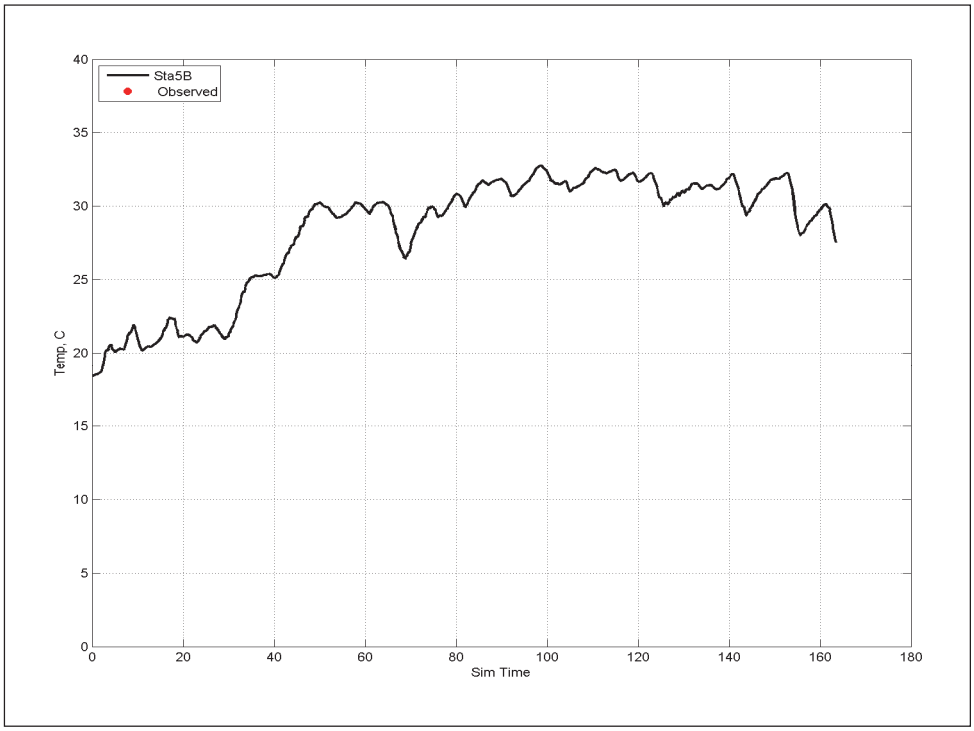

Figure E-26. Calibration results for salinity at Station 5 for surface layer (upper) and bottom layer (lower).

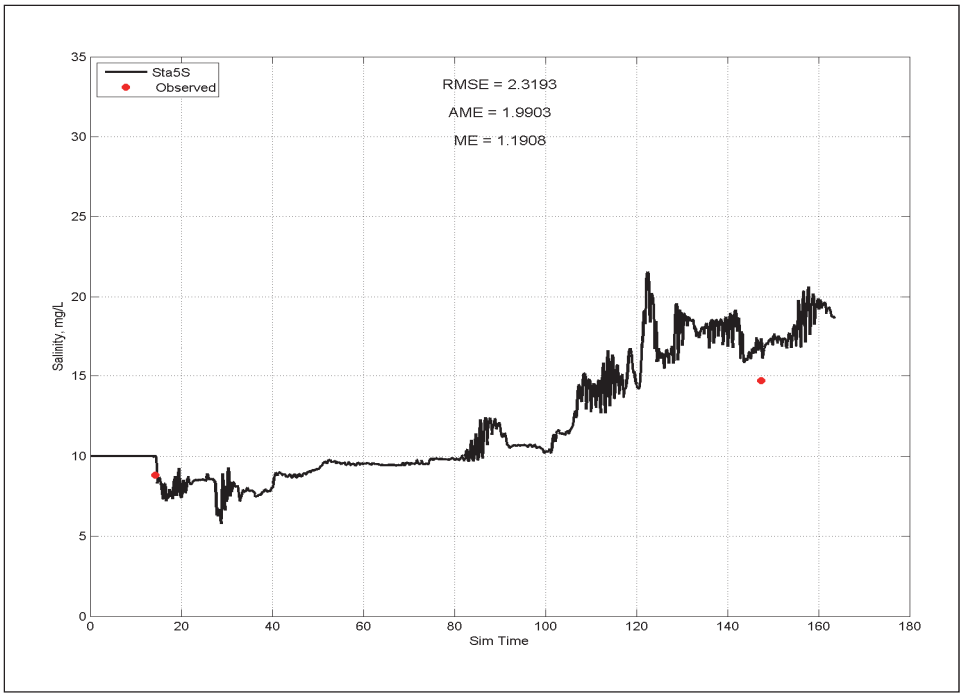

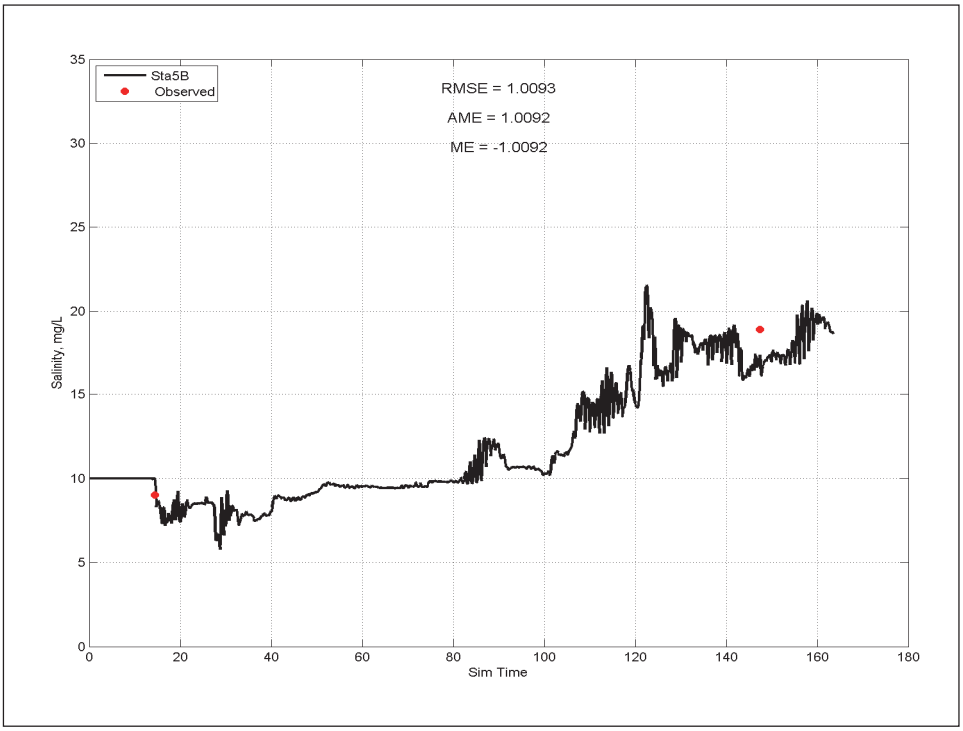

Figure E-27. Calibration results for DO at Station 5 for surface layer (upper) and bottom layer (lower).

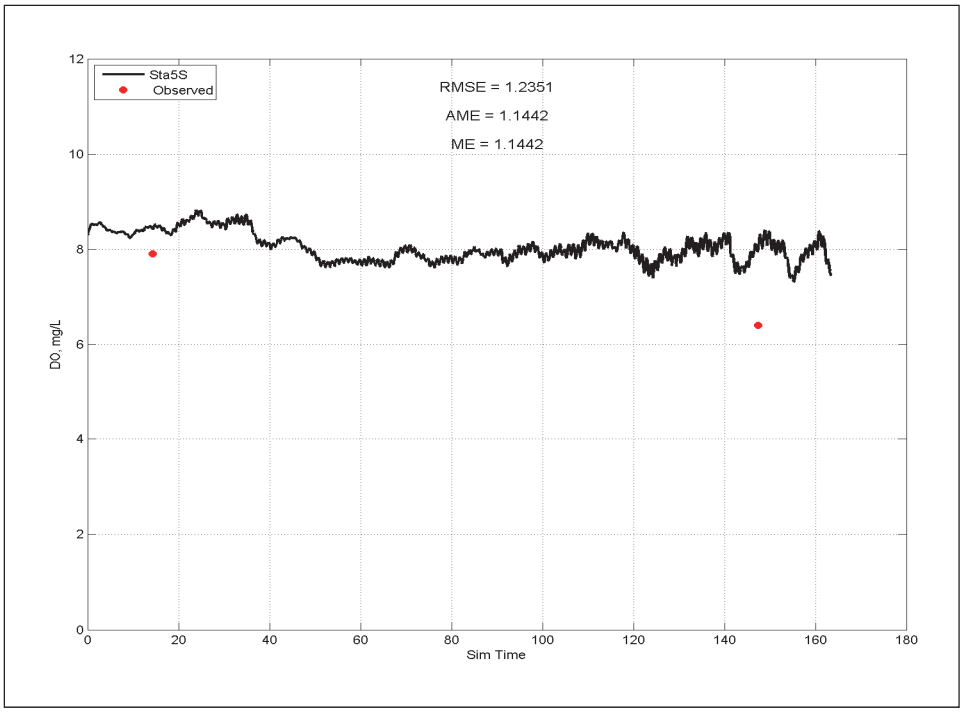

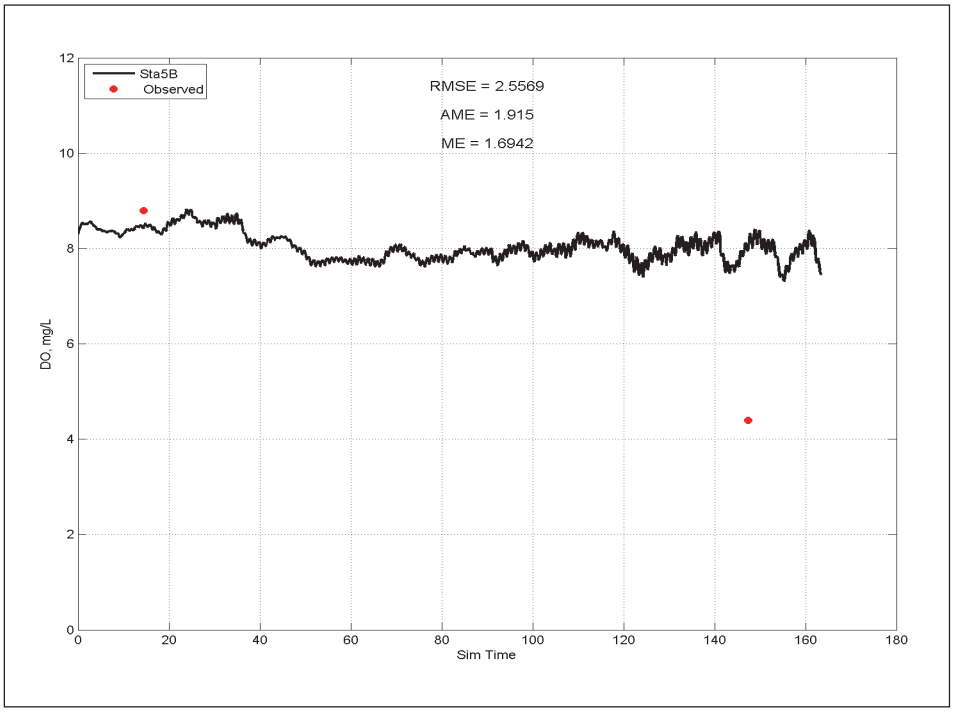

Figure E-28. Calibration results for NH_4 at Station 5 for surface layer (upper) and bottom layer (lower).

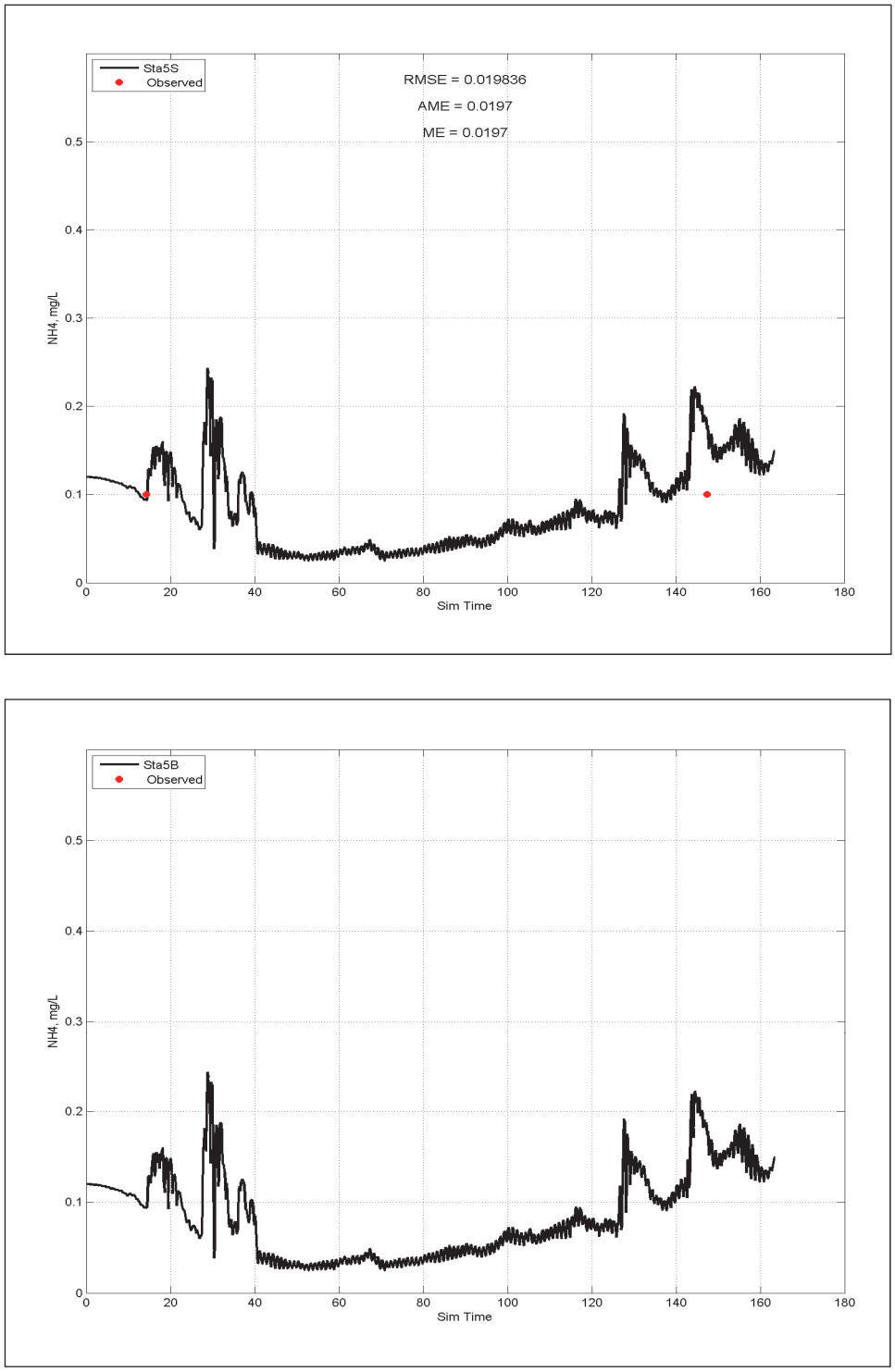

Figure E-29 Calibration results for NO_3 at Station 5 for surface layer (upper) and bottom layer (lower).

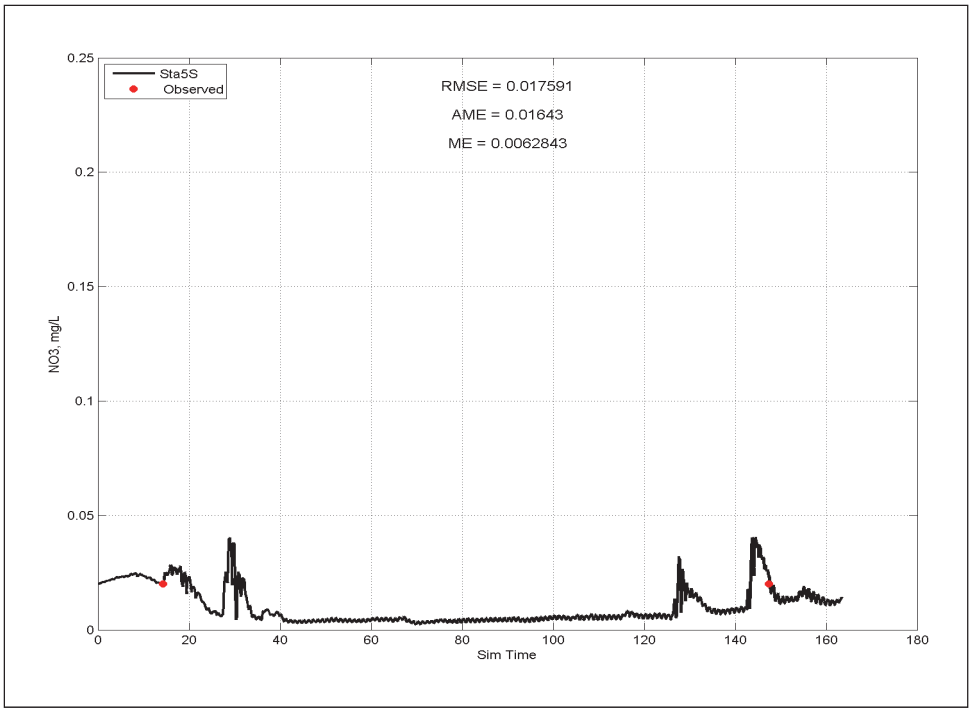

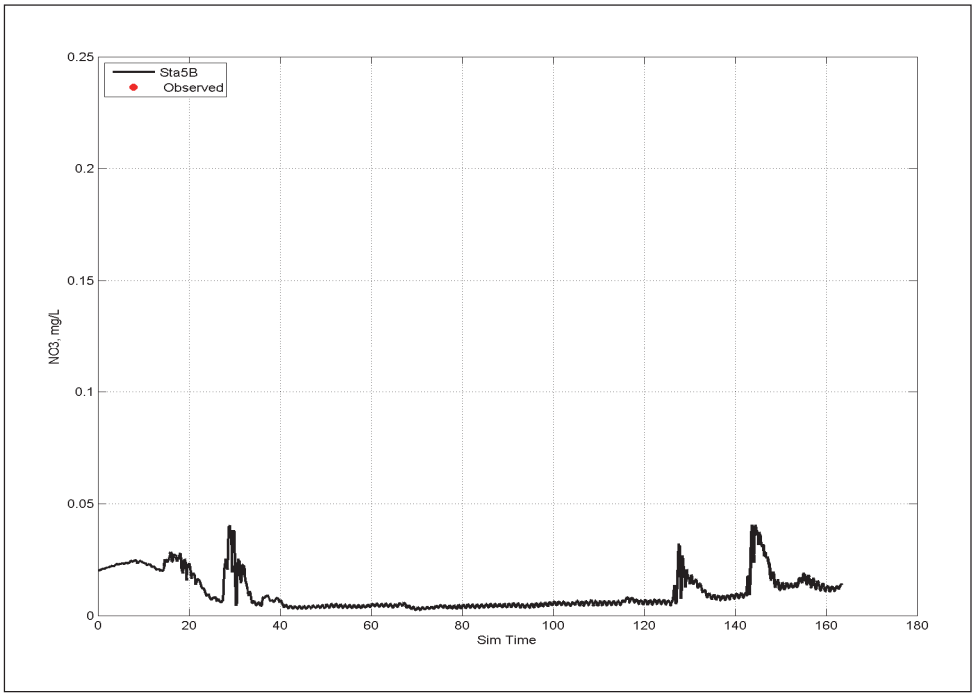

Figure E-30. Calibration results for *Tp* at Station 5 for surface layer (upper) and bottom layer (lower).

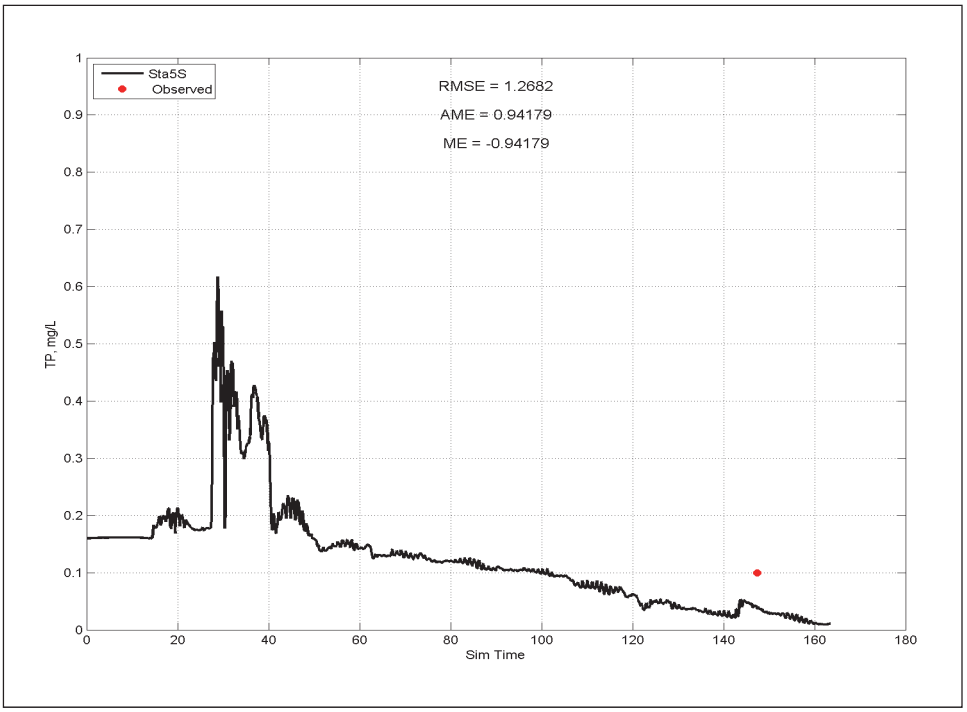

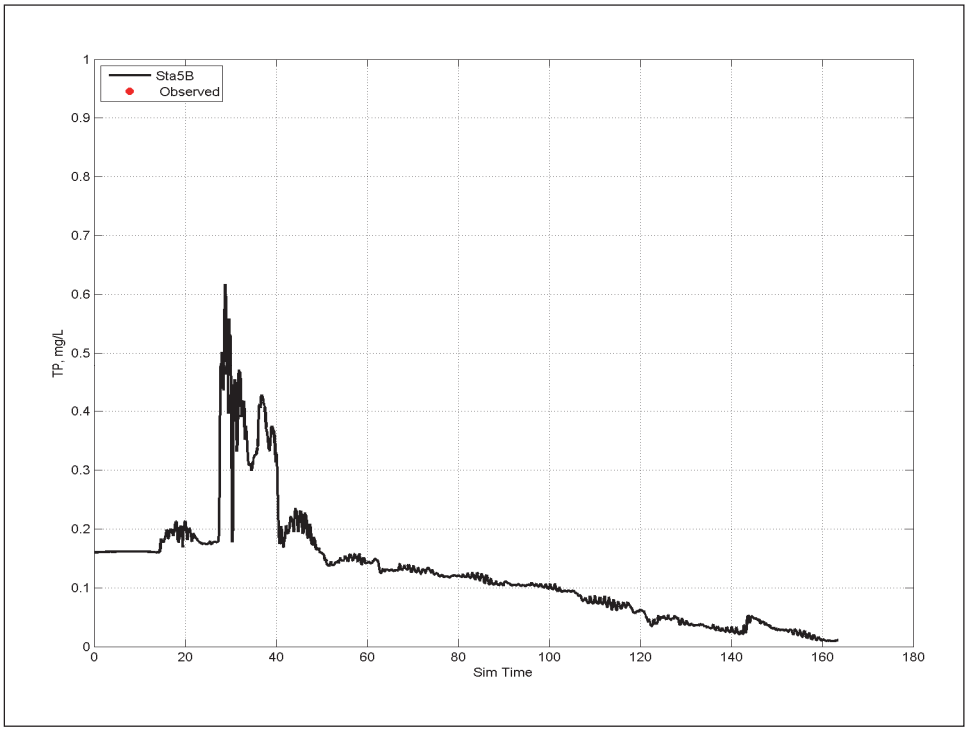

Figure E-31. Calibration results for temperature at Station 6 for surface layer (upper) and bottom layer (lower).

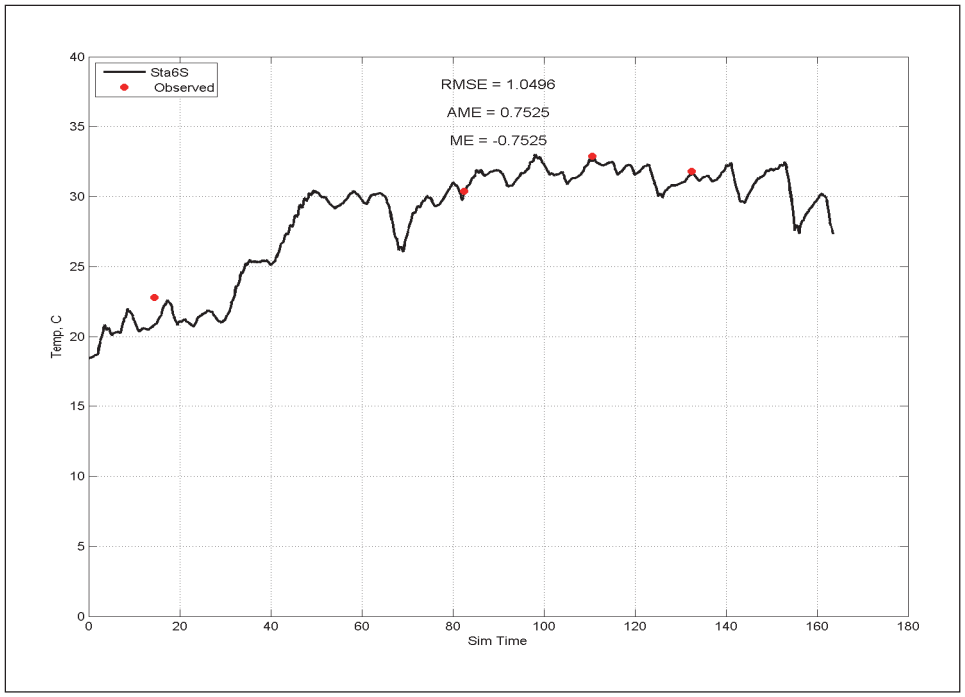

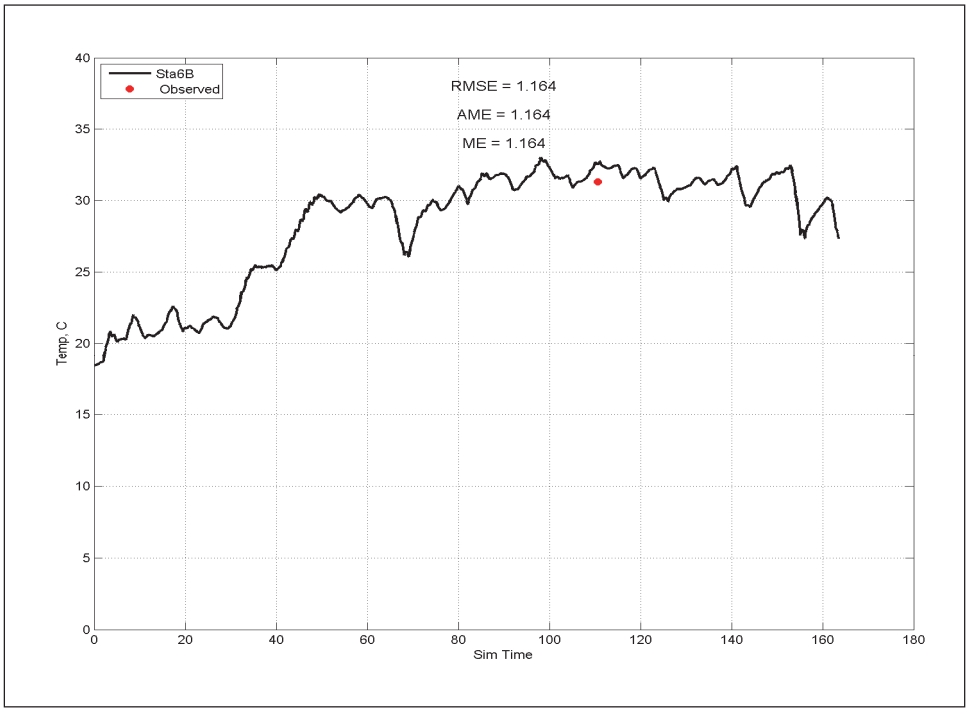

Figure E-32. Calibration results for salinity at Station 6 for surface layer (upper) and bottom layer (lower).

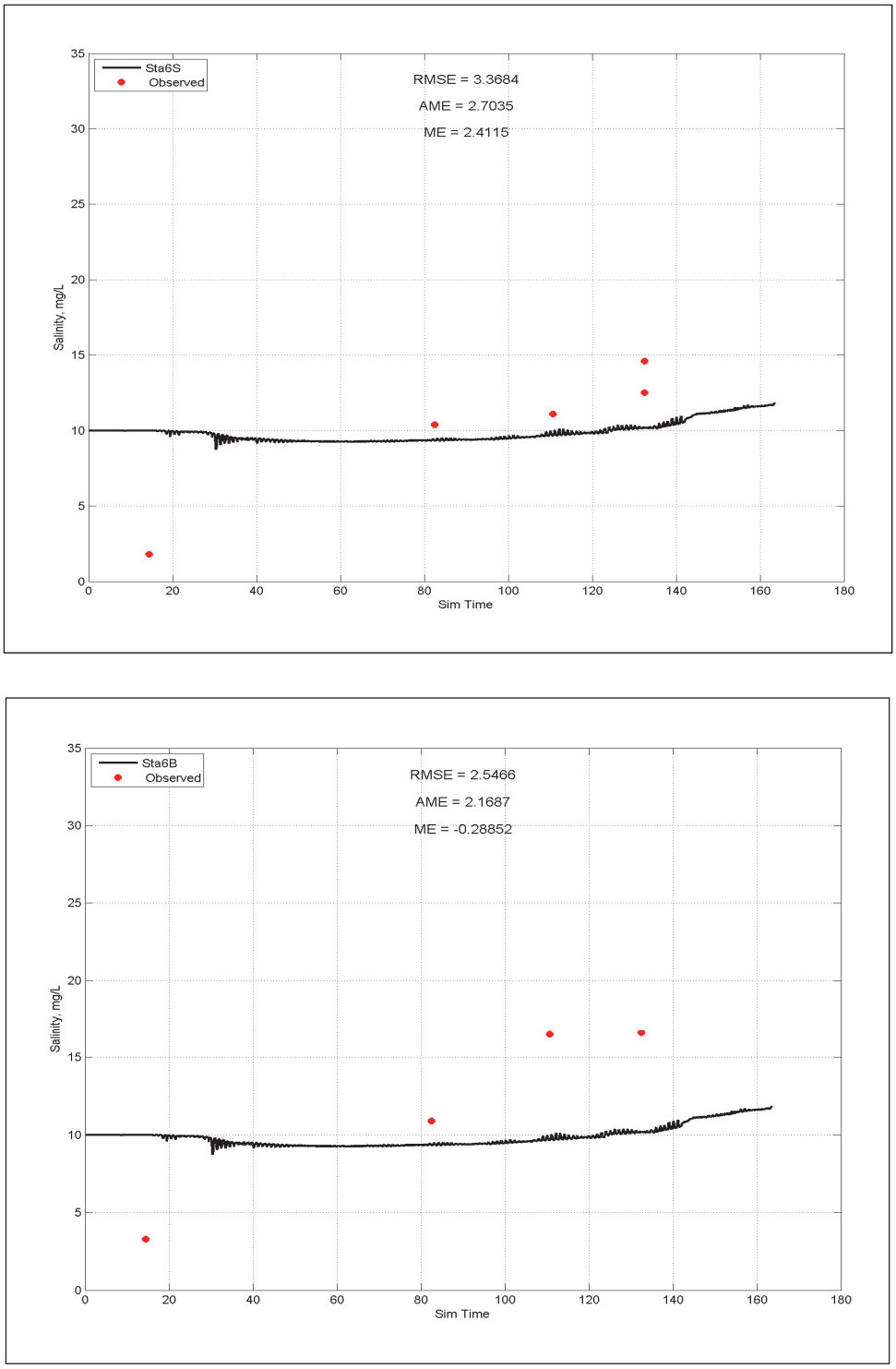

Figure E-33. Calibration results for DO at Station 6 for surface layer (upper) and bottom layer (lower).

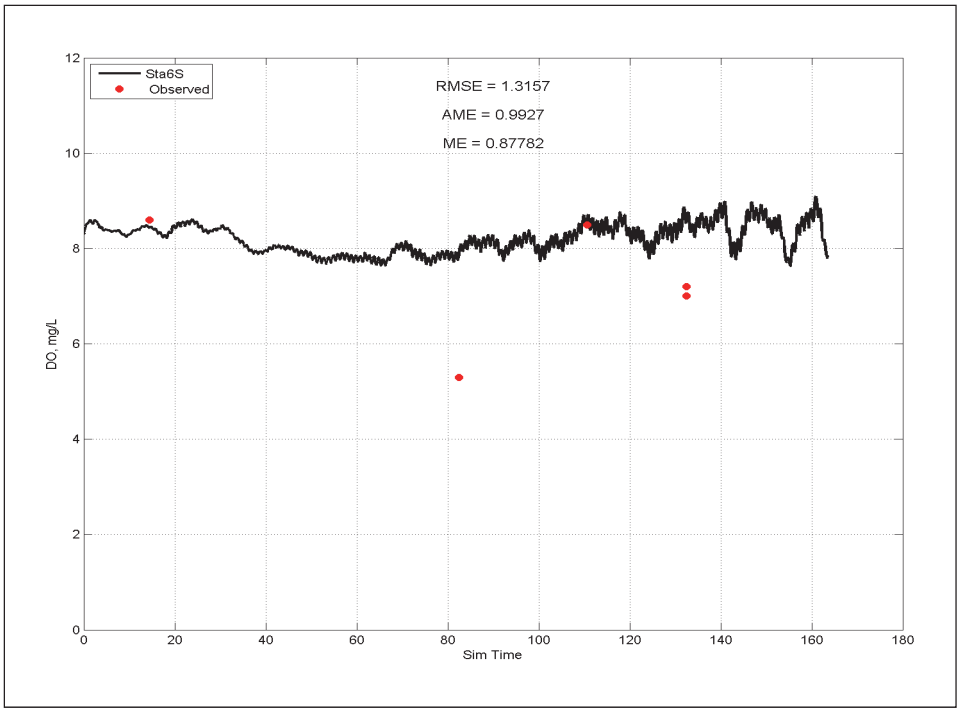

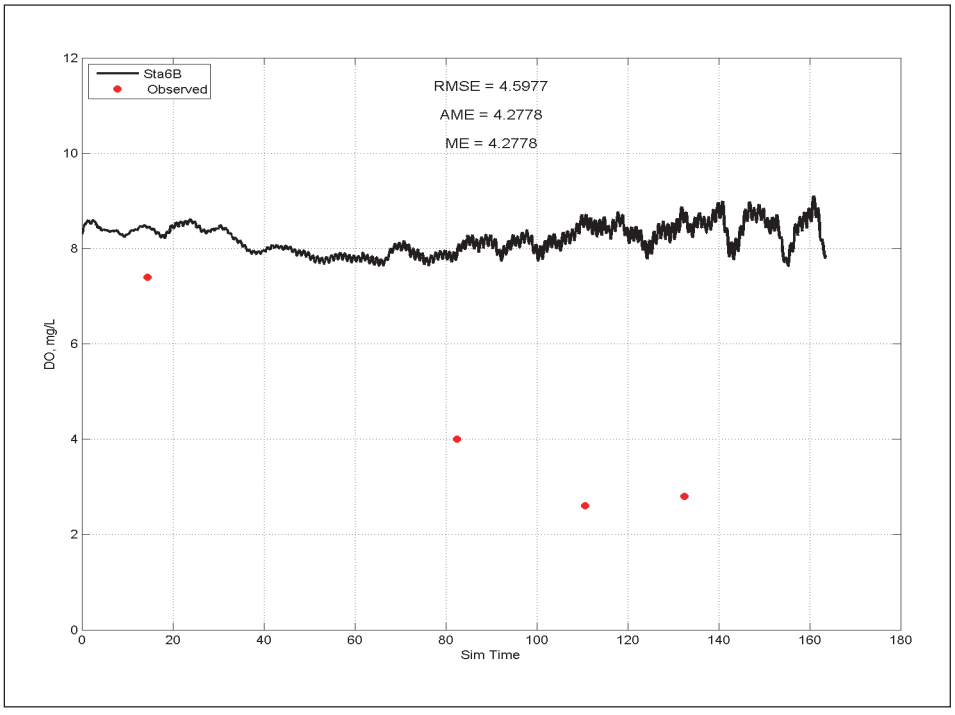

Figure E-34. Calibration results for NH_4 at Station 6 for surface layer (upper) and bottom layer (lower).

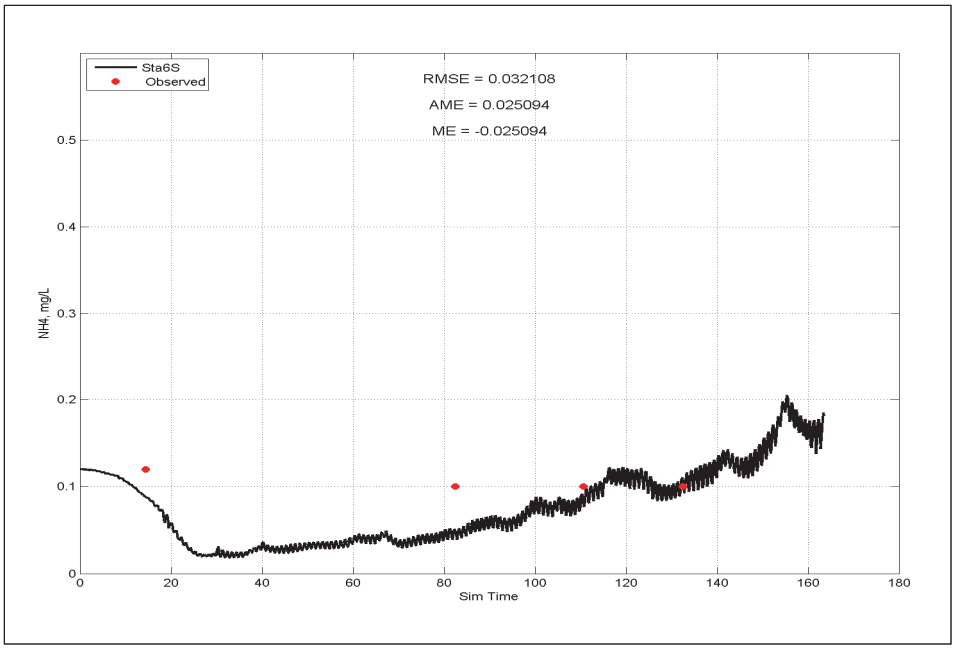

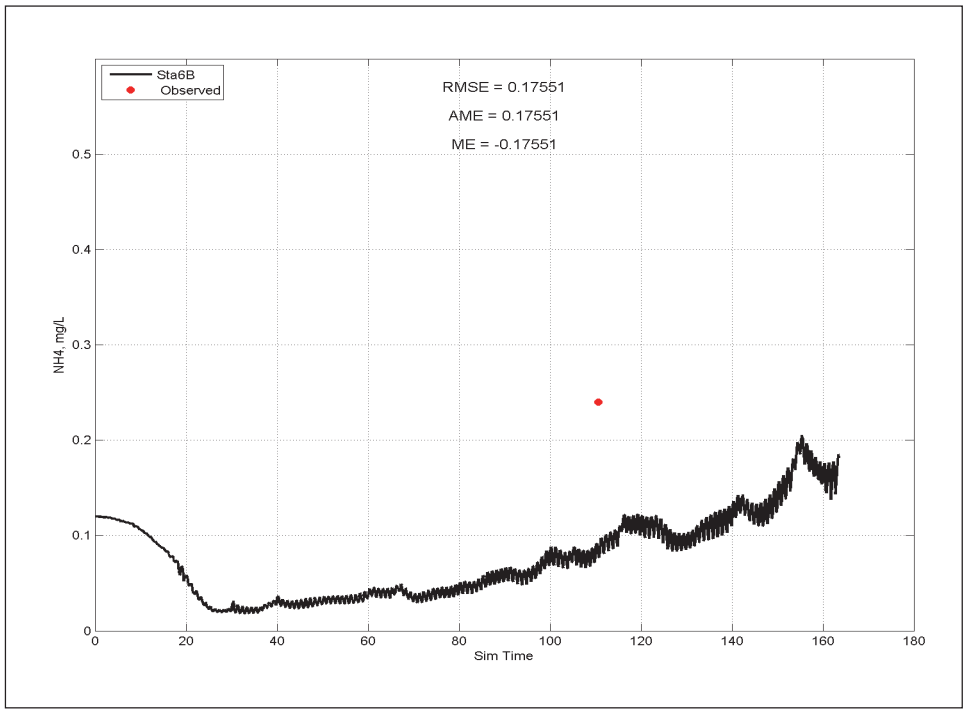

Figure E-35. Calibration results for NO_3 at Station 6 for surface layer (upper) and bottom layer (lower).

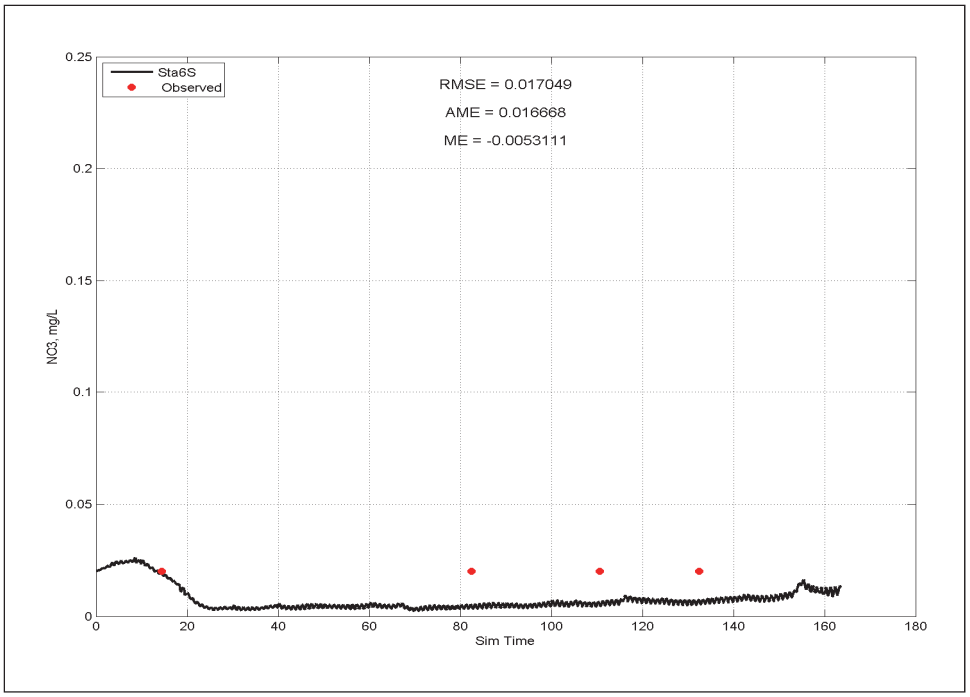

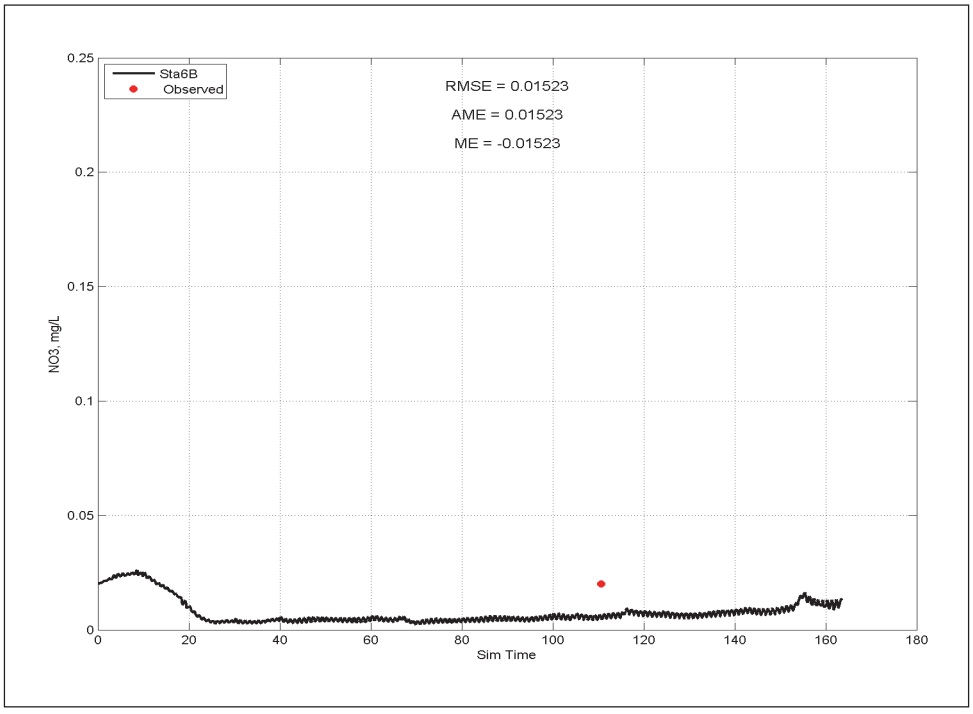

Figure E-36. Calibration results for *Tp* at Station 6 for surface layer (upper) and bottom layer (lower).

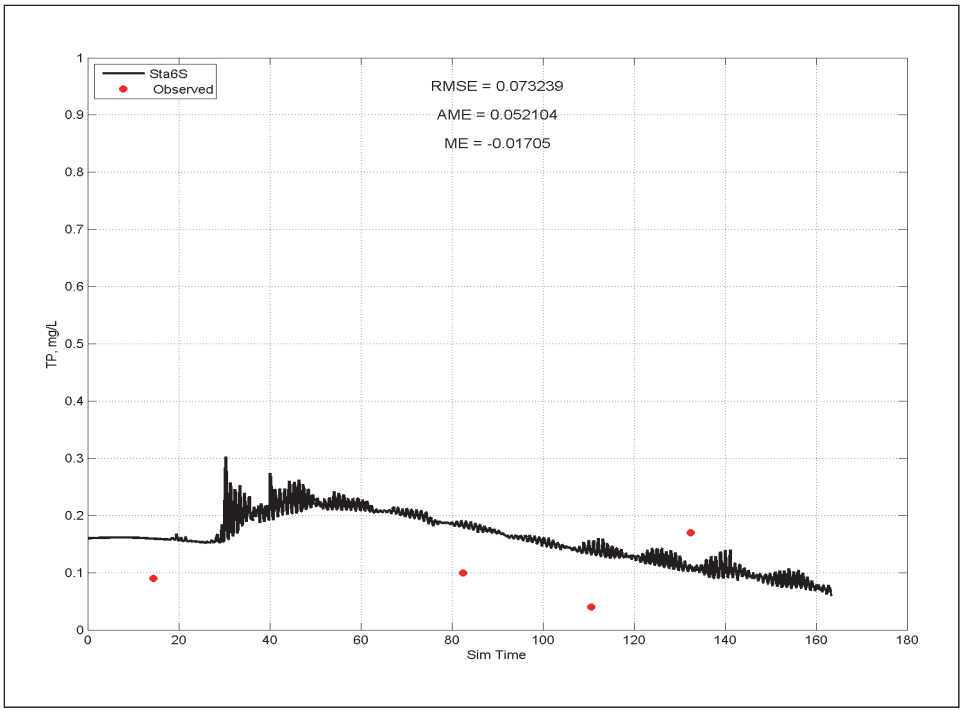

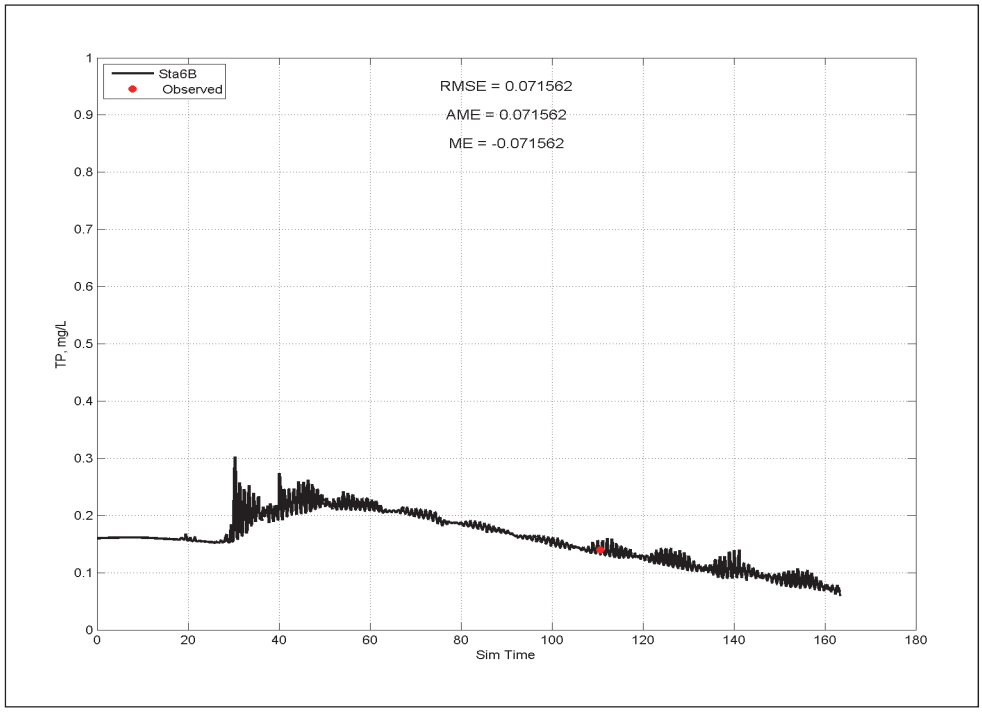

Figure E-37. Calibration results for temperature at Station 7 for surface layer (upper) and bottom layer (lower).

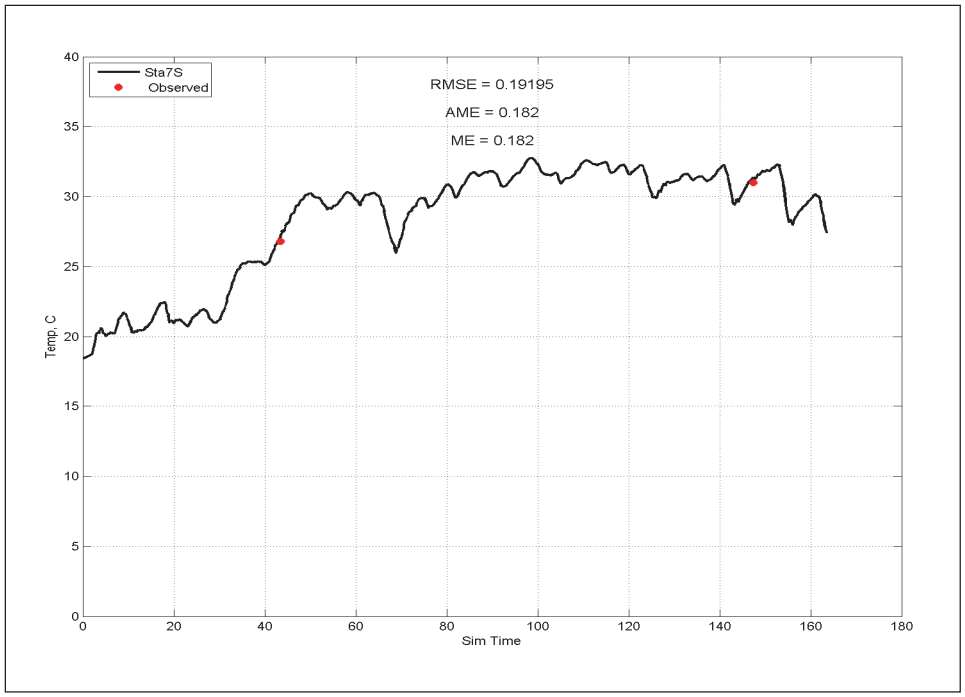

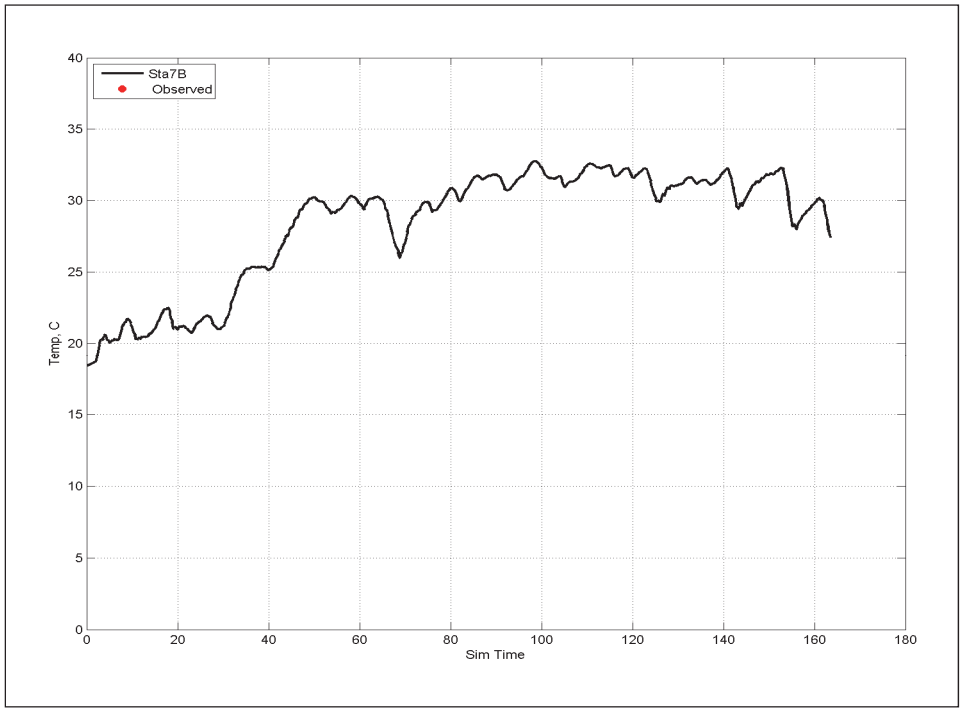

Figure E-38. Calibration results for salinity at Station 7 for surface layer (upper) and bottom layer (lower).

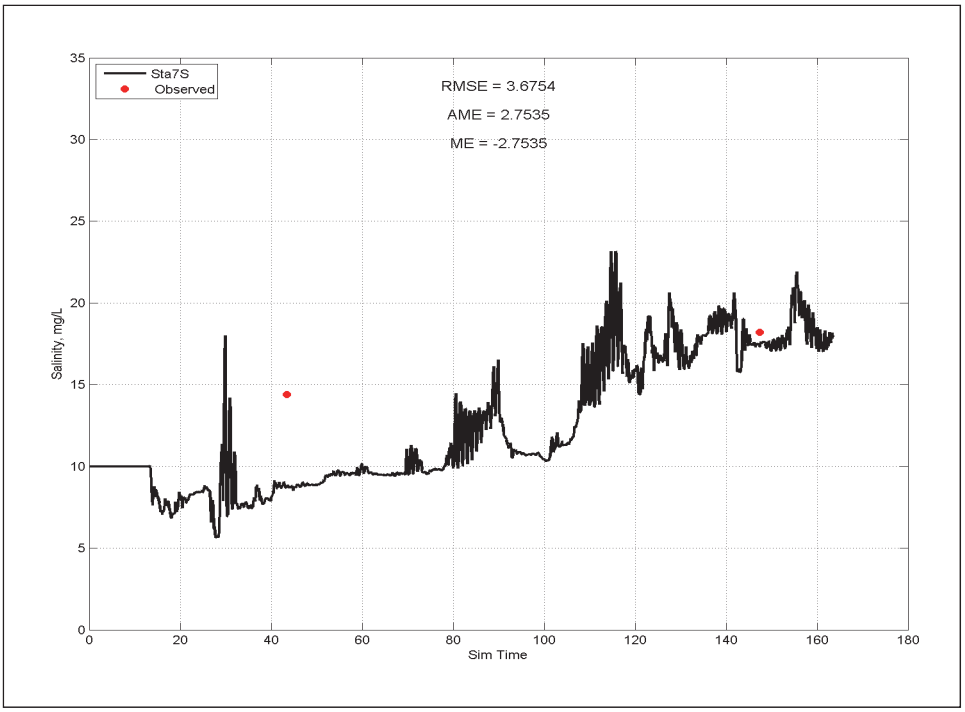

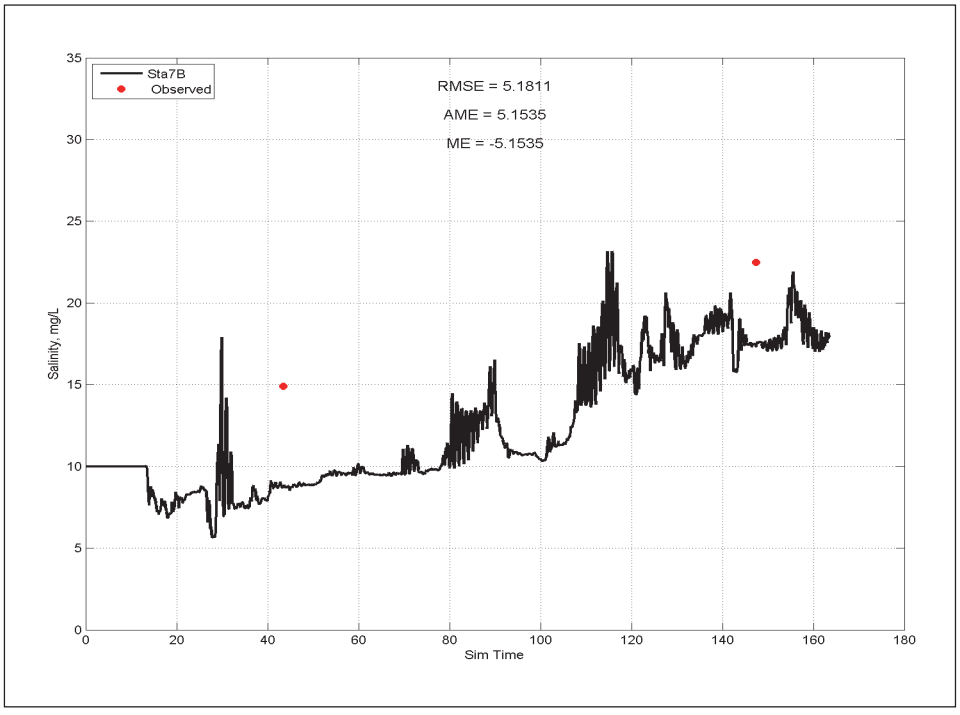

Figure E-39. Calibration results for DO at Station 7 for surface layer (upper) and bottom layer (lower).

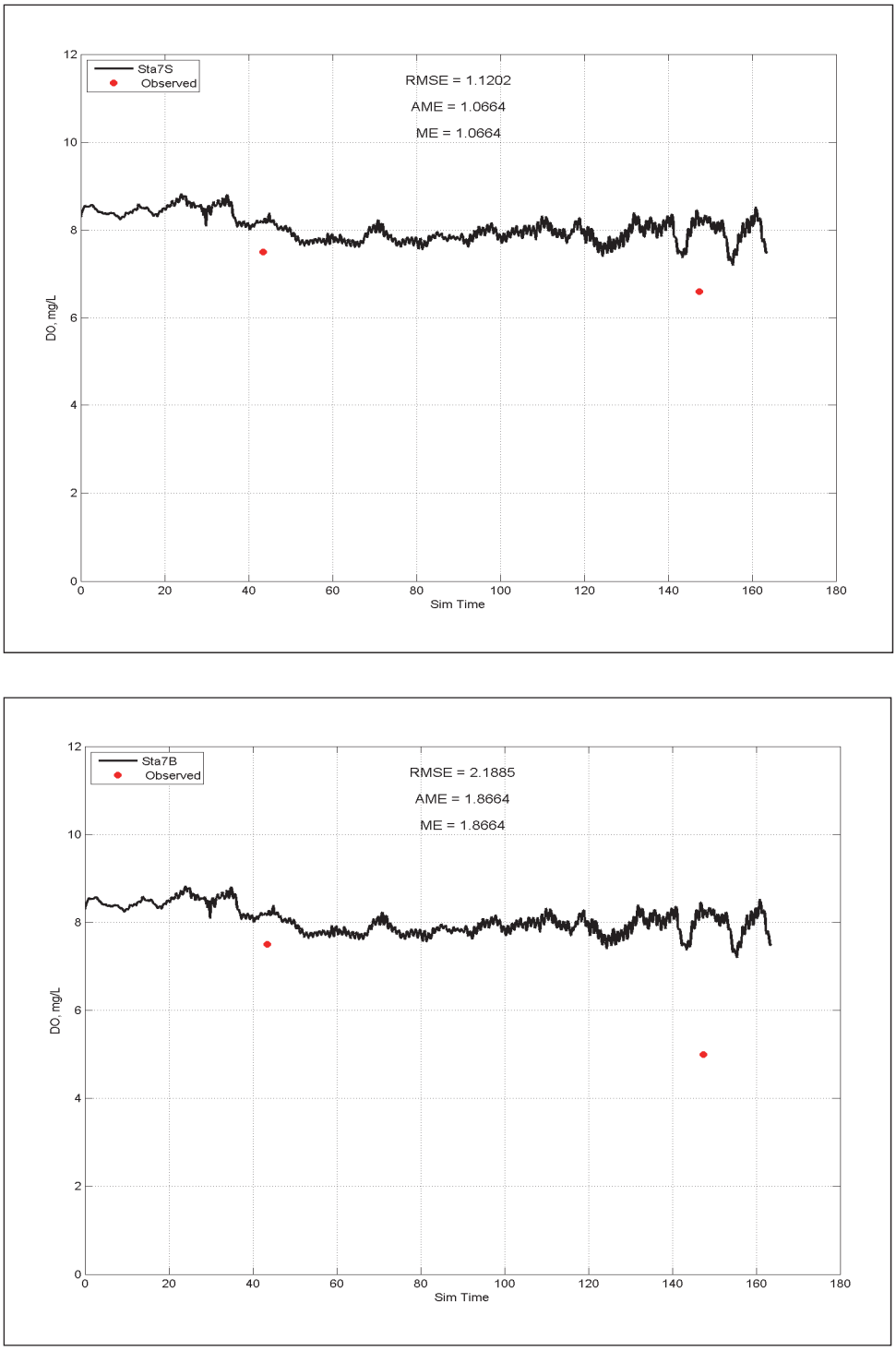

Figure E-40. Calibration results for NH_4 at Station 7 for surface layer (upper) and bottom layer (lower).

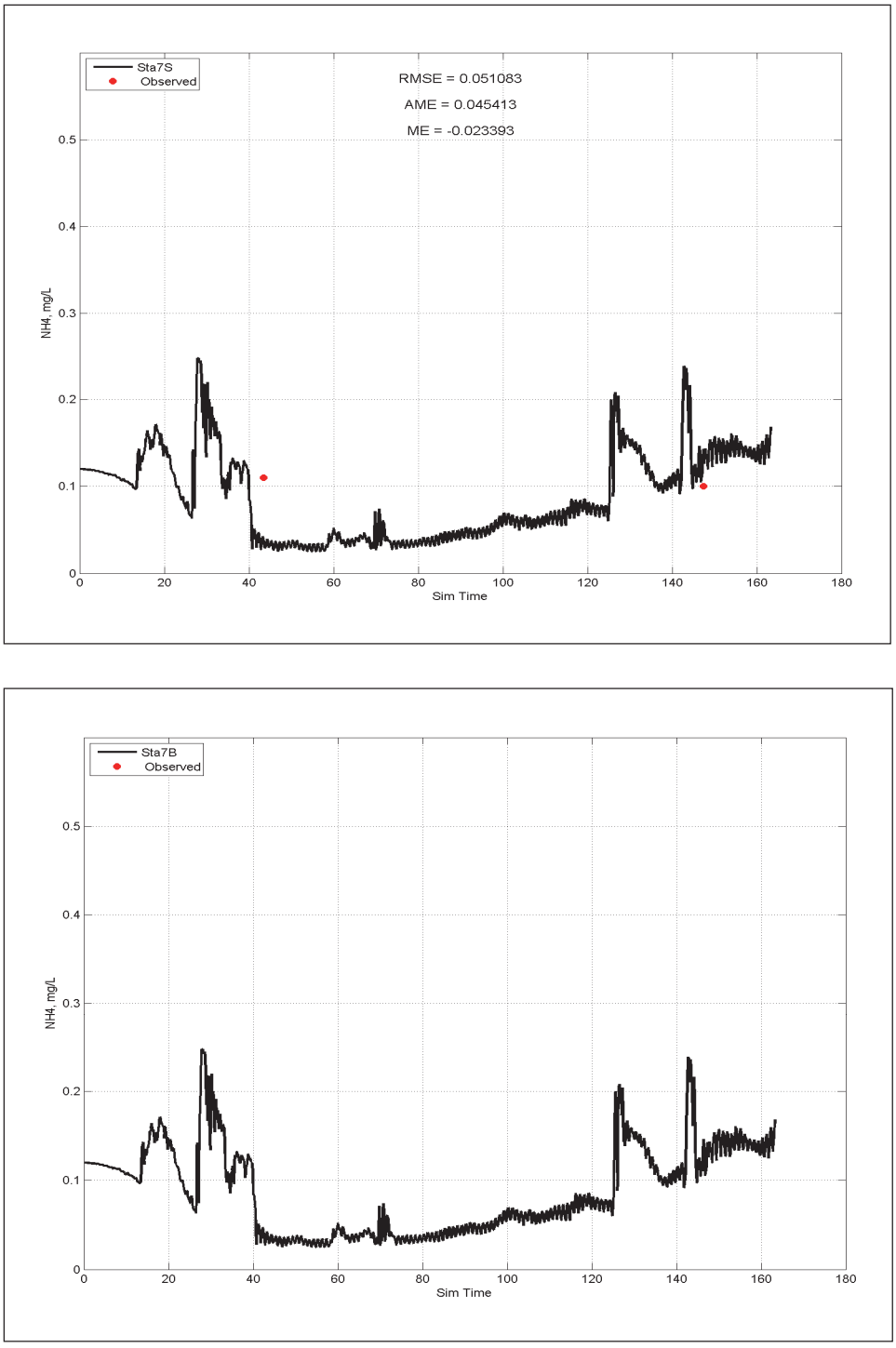

Figure E-41 Calibration results for NO_3 at Station 7 for surface layer (upper) and bottom layer (lower).

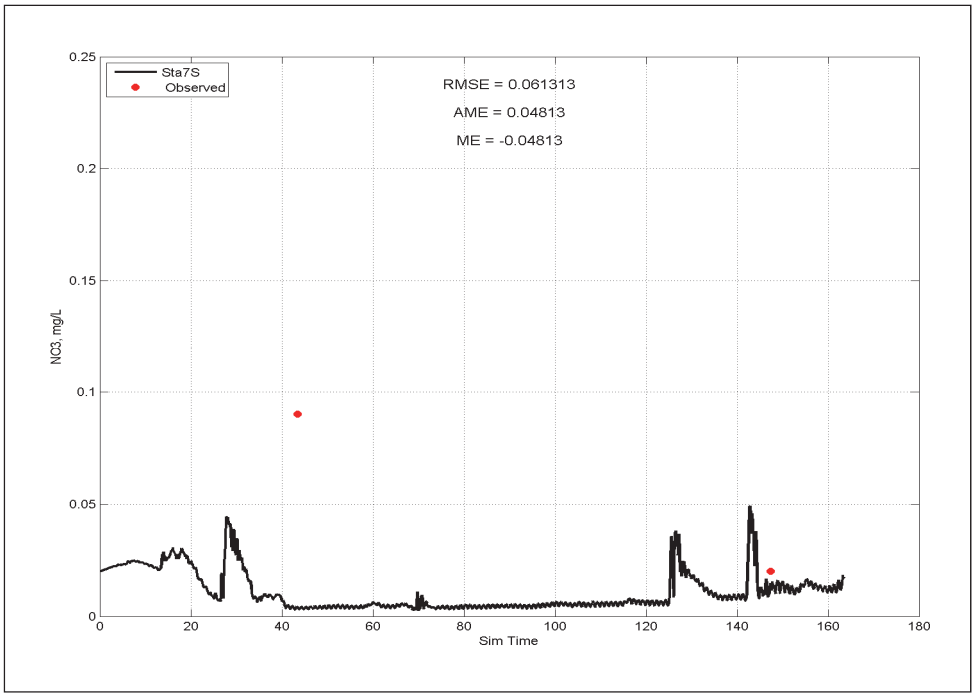

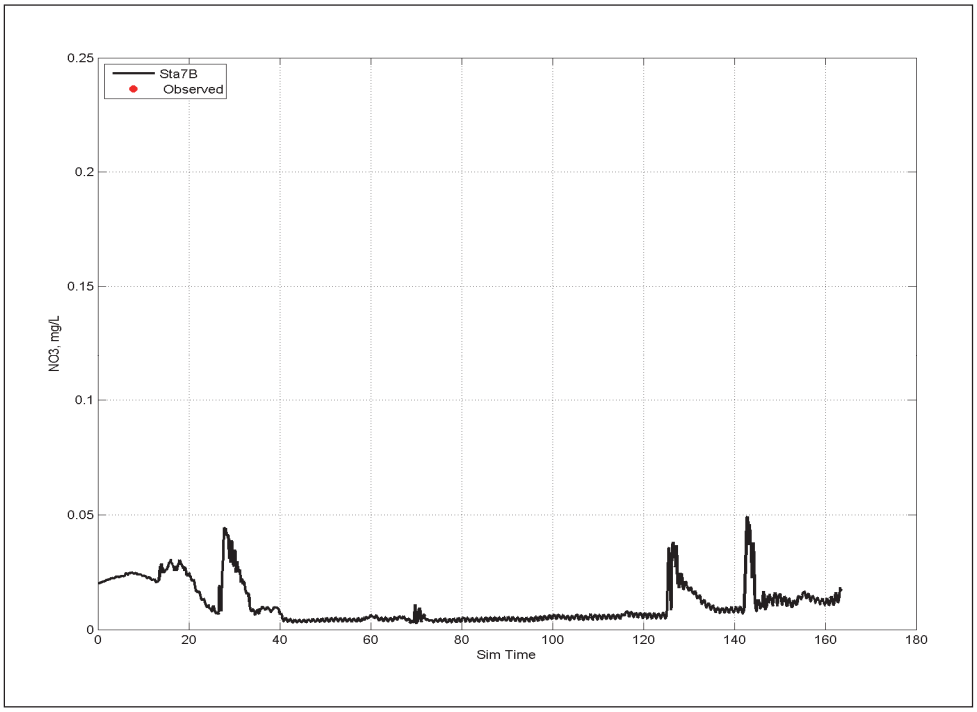

Figure E-42. Calibration results for *Tp* at Station 7 for surface layer (upper) and bottom layer (lower).

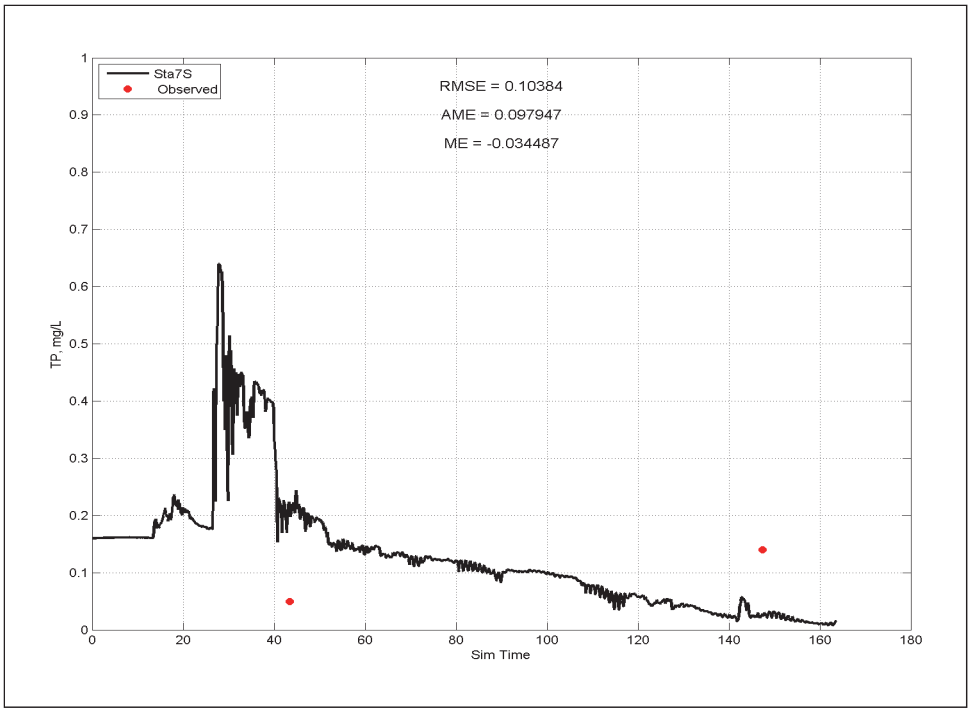

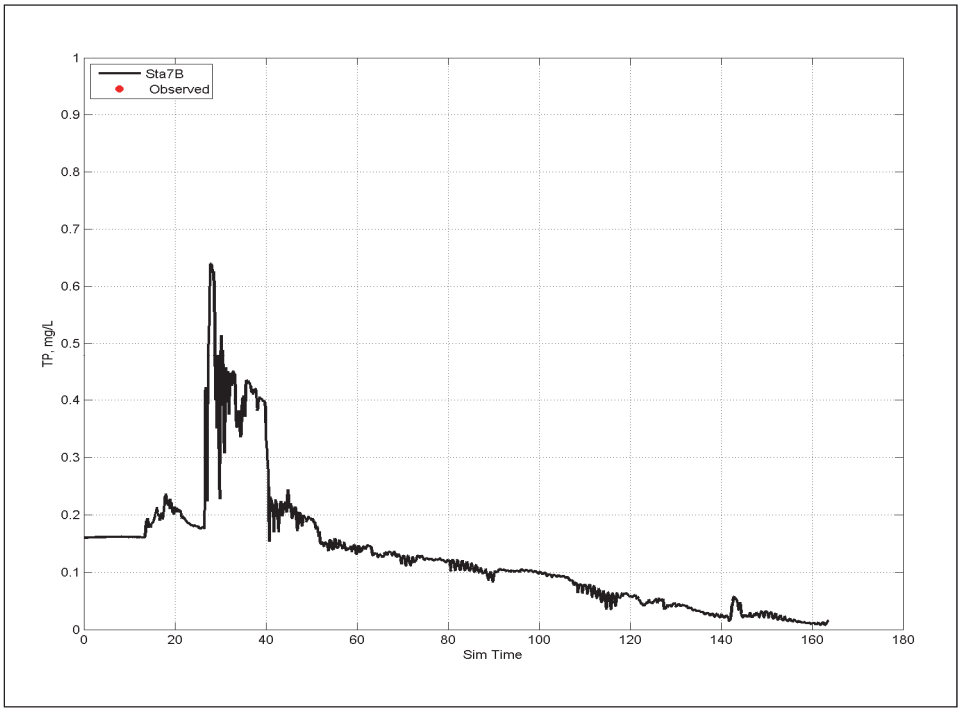

Figure E-43. Calibration results for temperature at Station 8 for surface layer (upper) and bottom layer (lower).

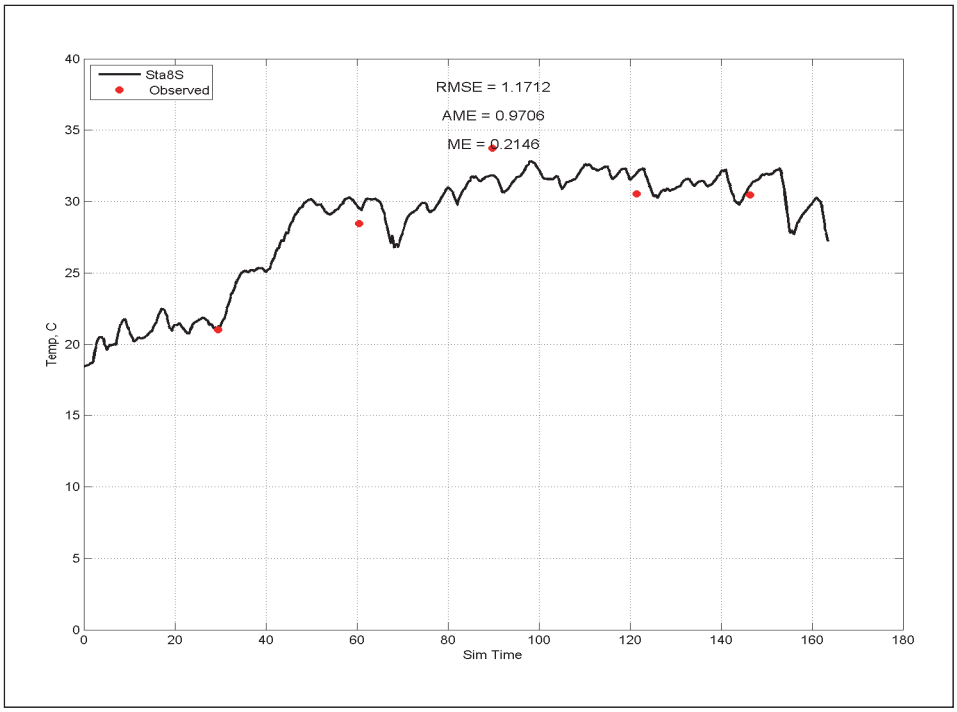

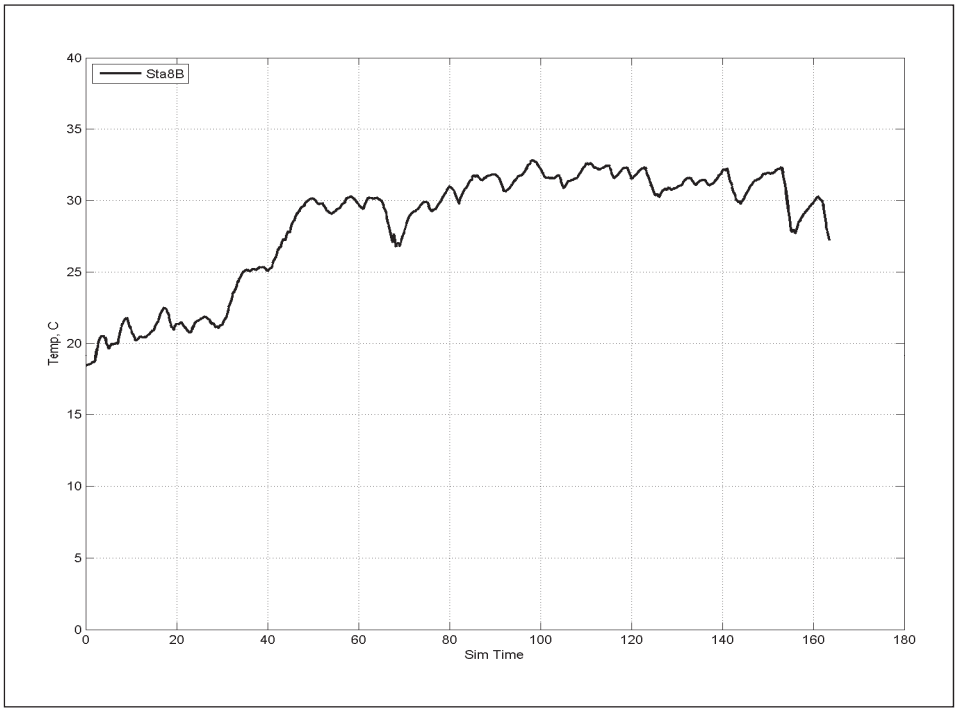

Figure E-44. Calibration results for salinity at Station 8 for surface layer (upper) and bottom layer (lower).

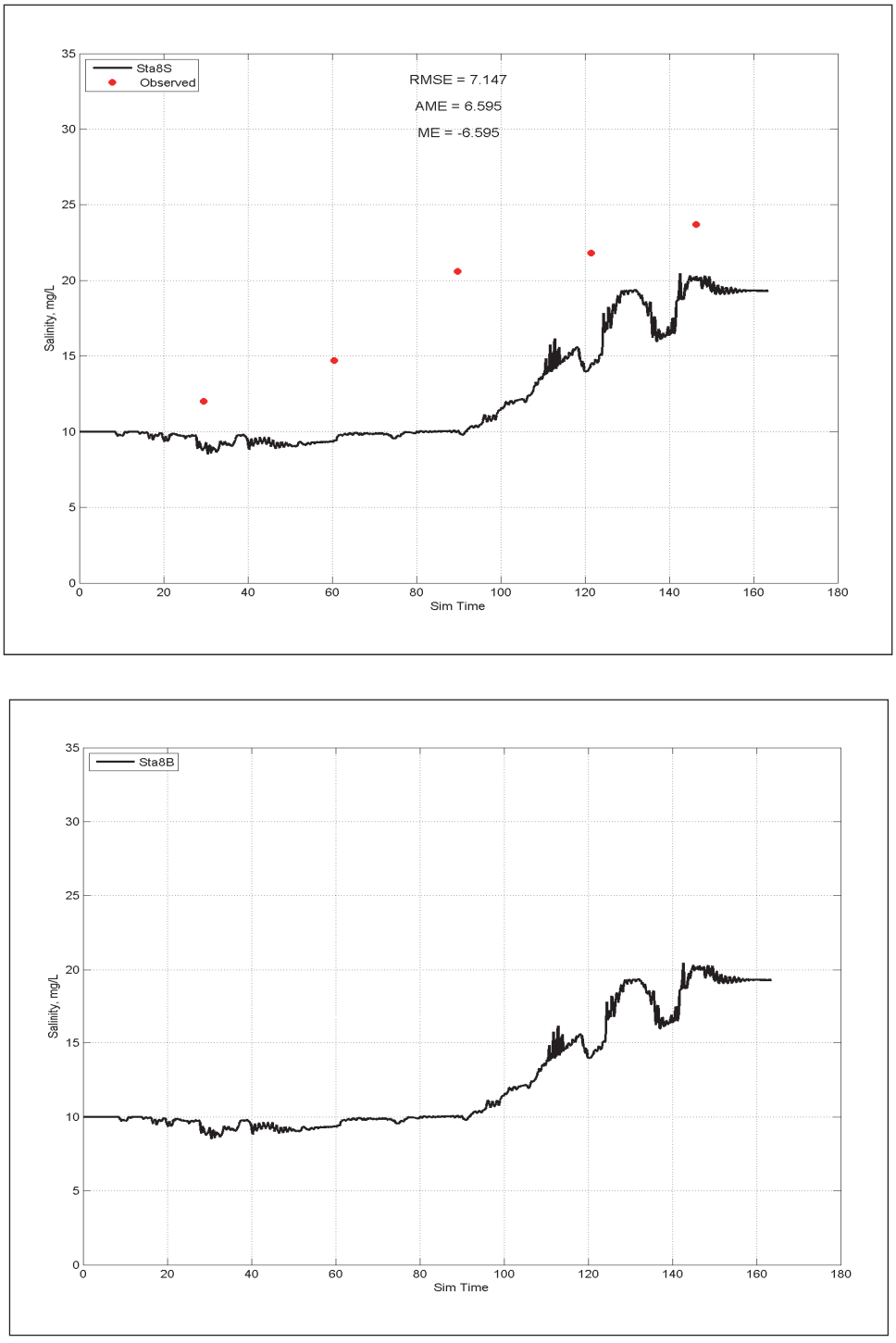

Figure E-45. Calibration results for DO at Station 8 for surface layer (upper) and bottom layer lower).

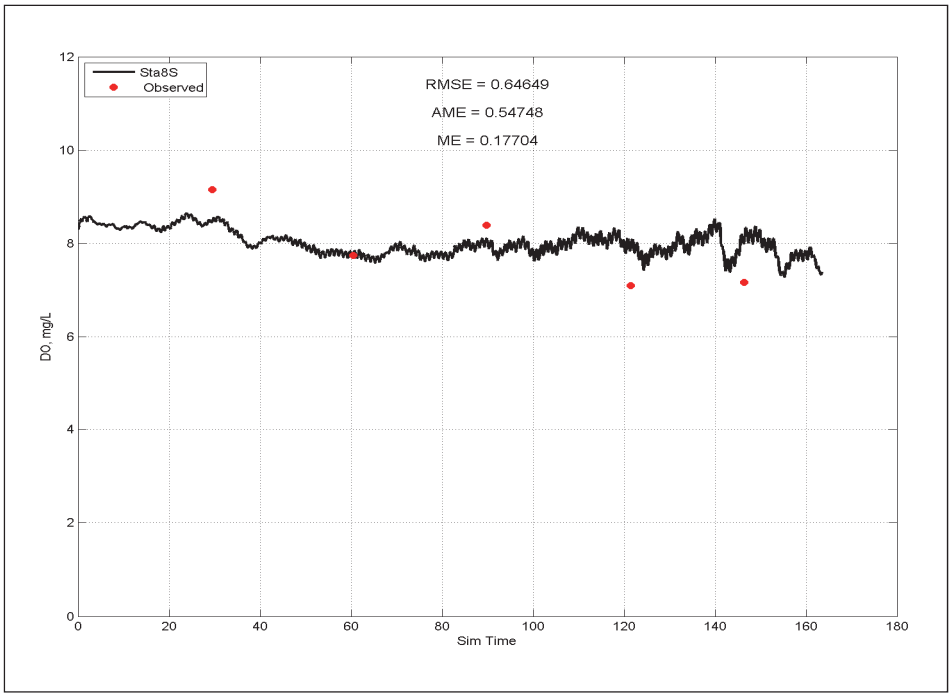

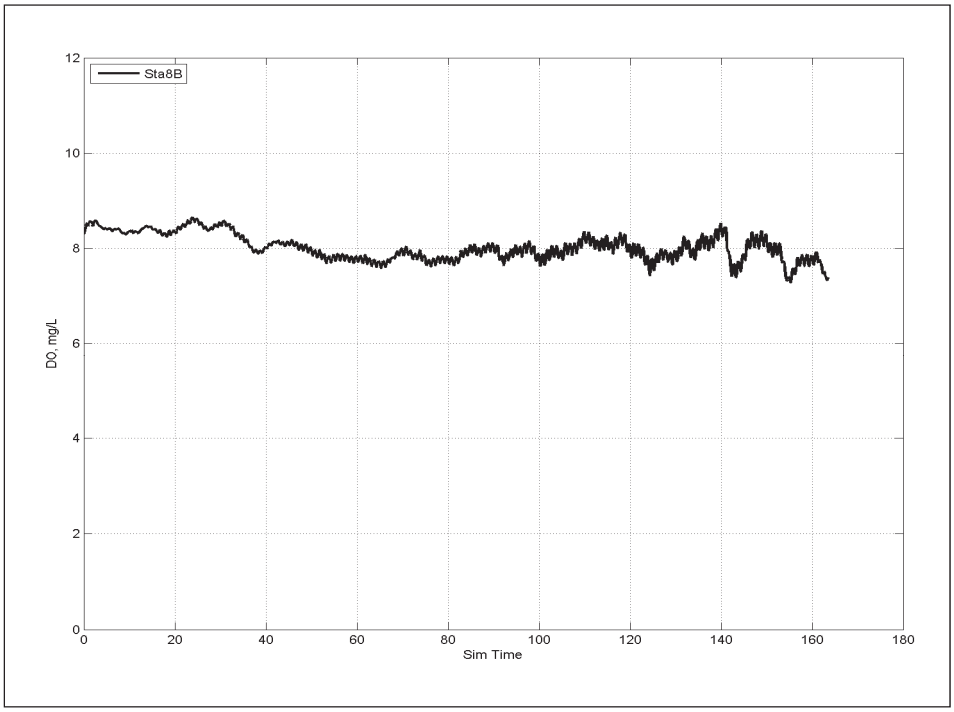

Figure E-46. Calibration results for NH_4 at Station 8 for surface layer (upper) and bottom layer (lower).

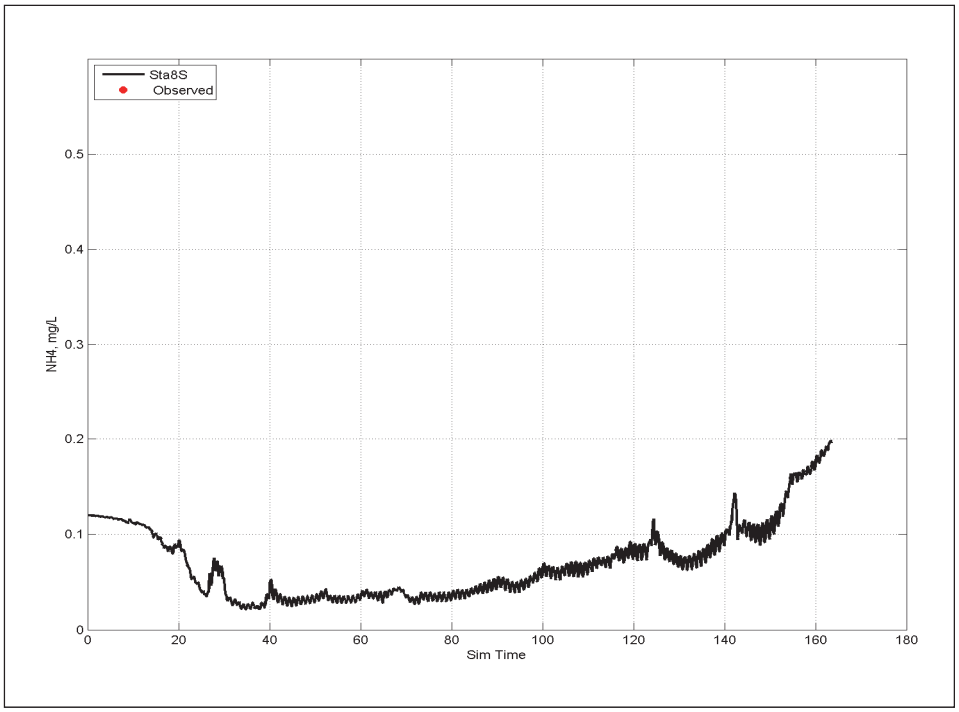

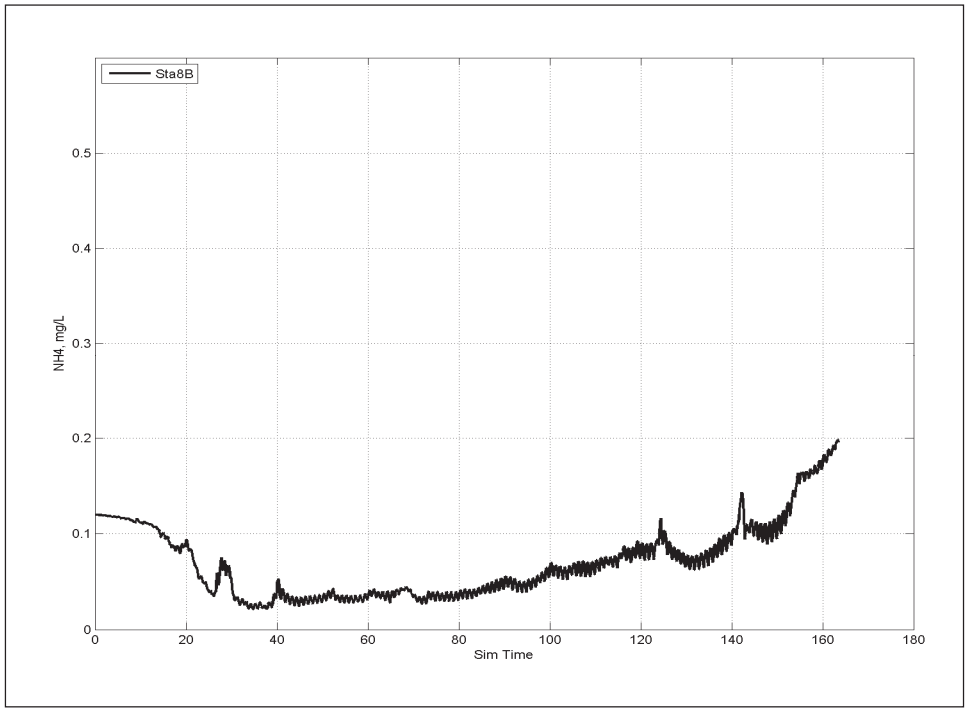

Figure E-47 Calibration results for NO_3 at Station 8 for surface layer (upper) and bottom layer (lower).

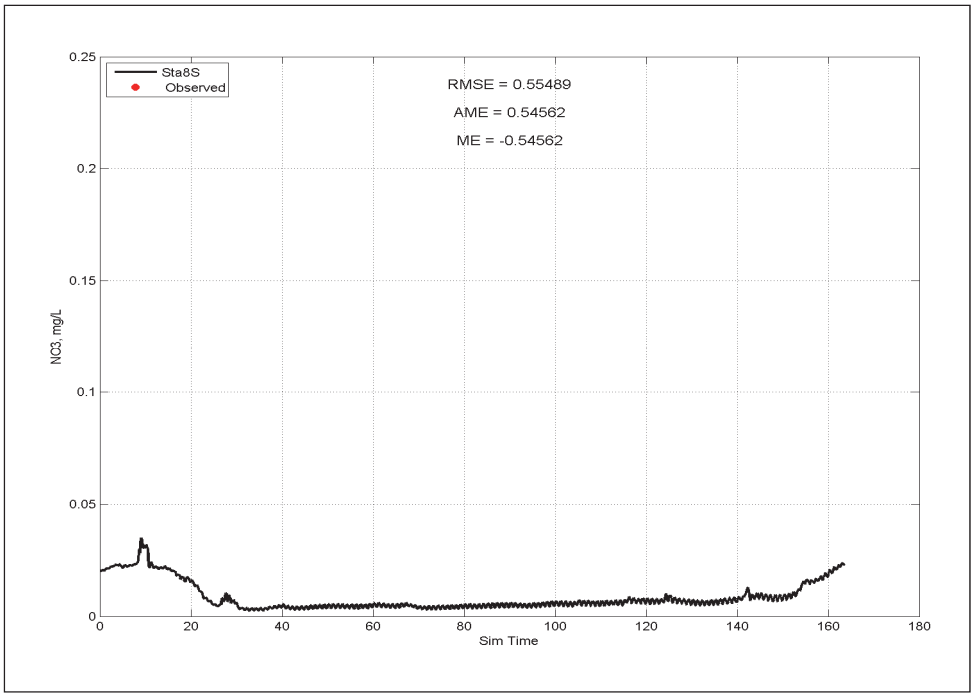

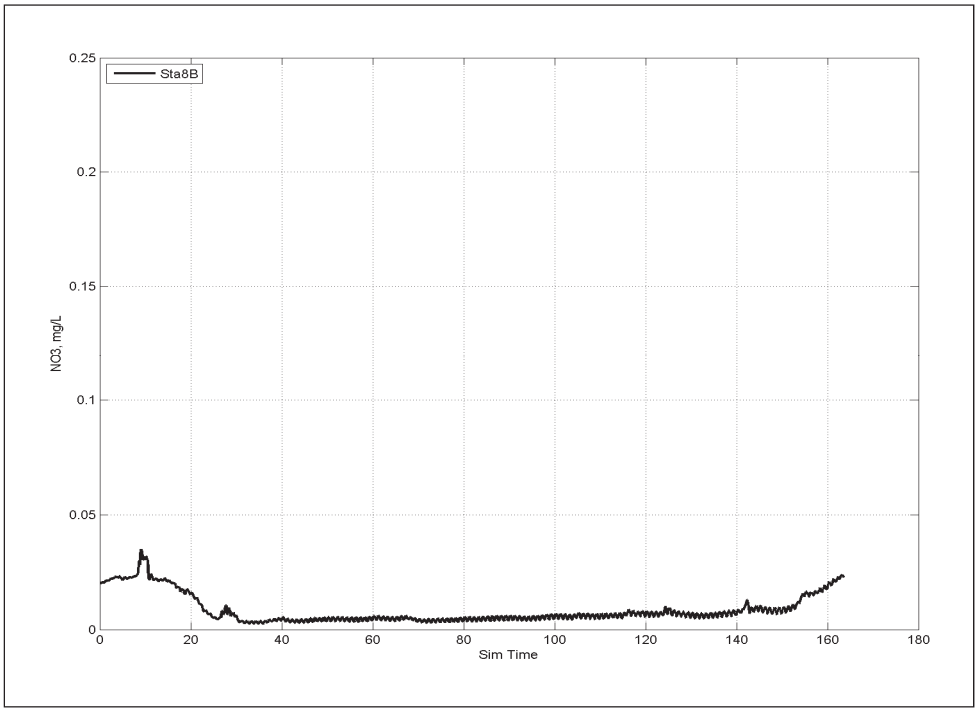

Figure E-48. Calibration results for *Tp* at Station 8 for surface layer (upper) and bottom layer lower).

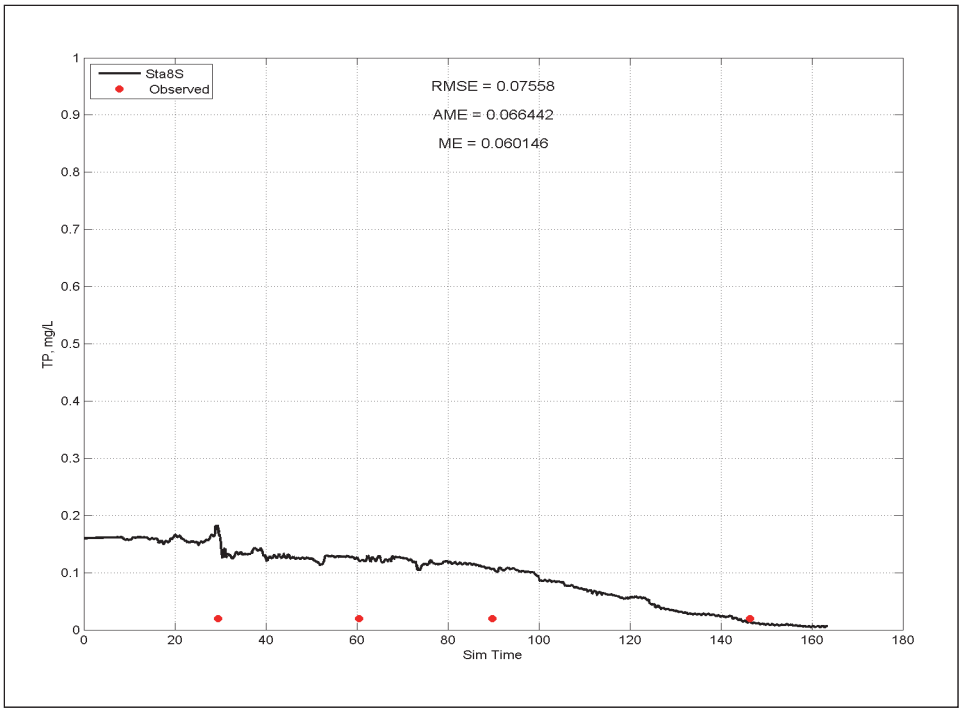

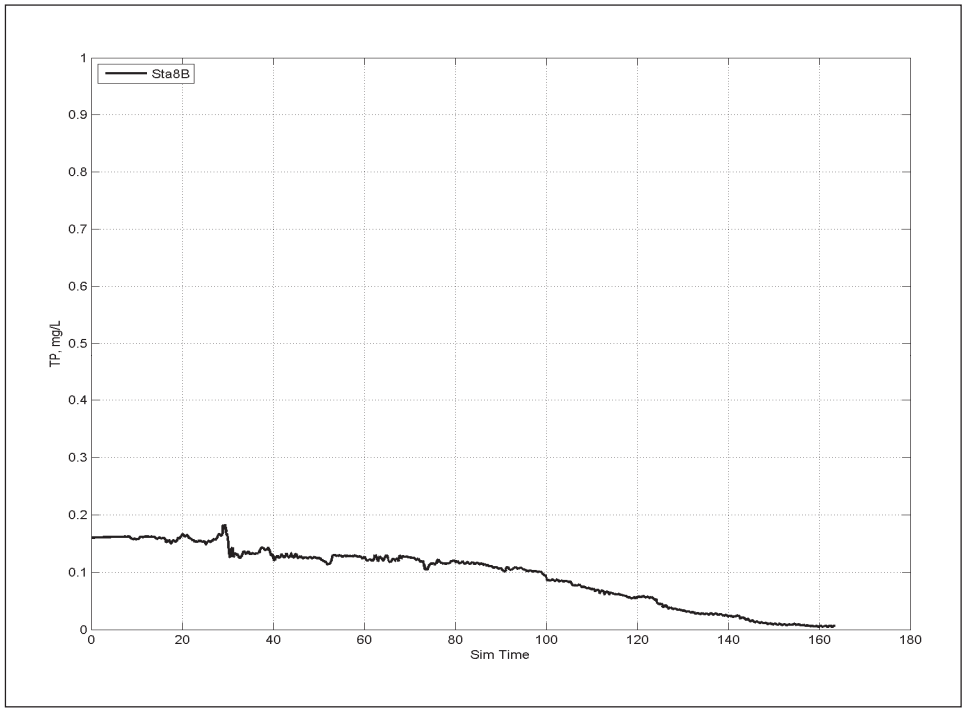

Figure E-49. Calibration results for temperature at Station 9 for surface layer (upper) and layer (lower).

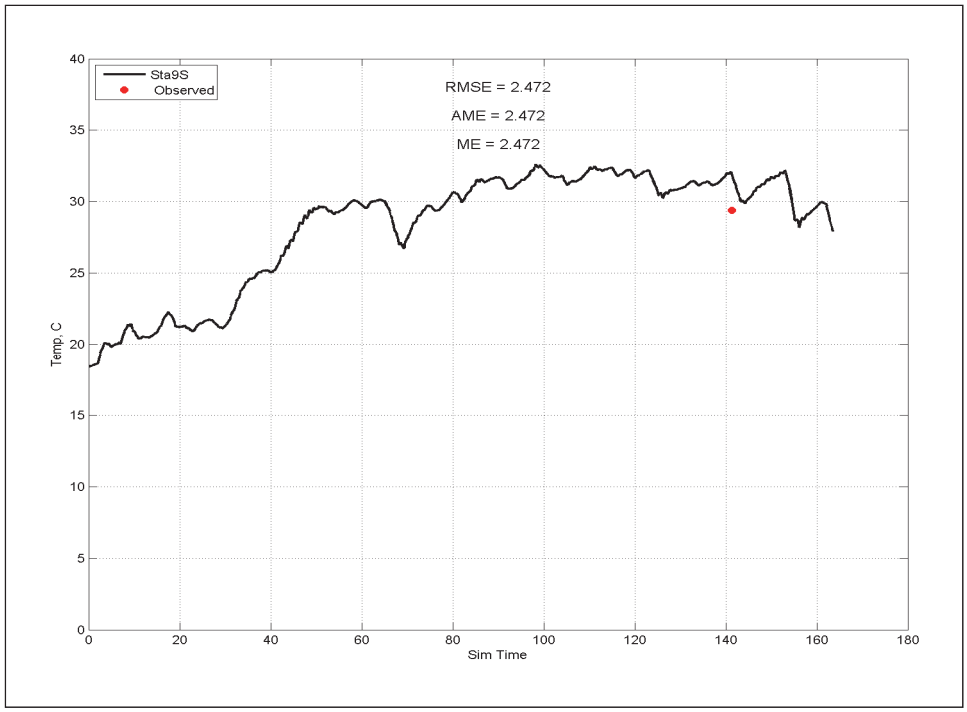

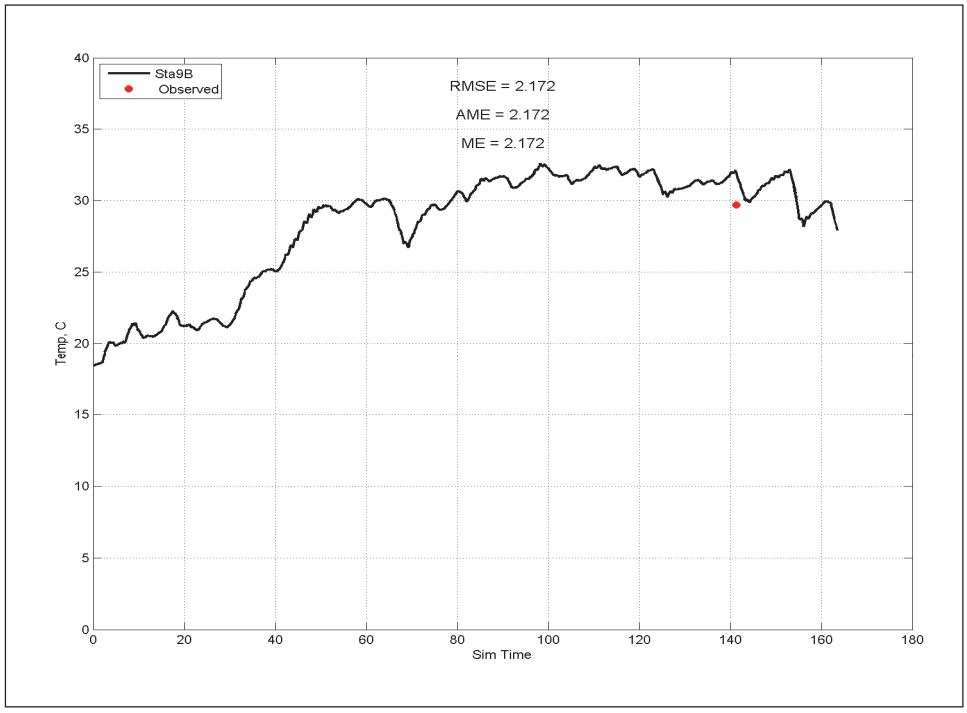

Figure E-50. Calibration results for salinity at Station 9 for surface layer (upper) and bottom layer (lower).

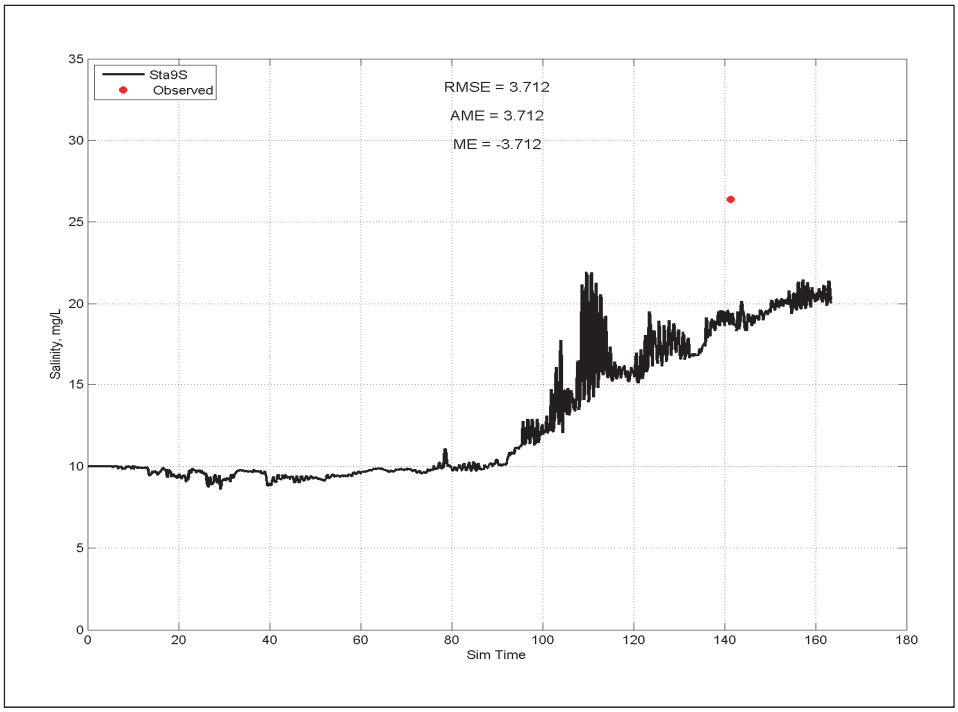

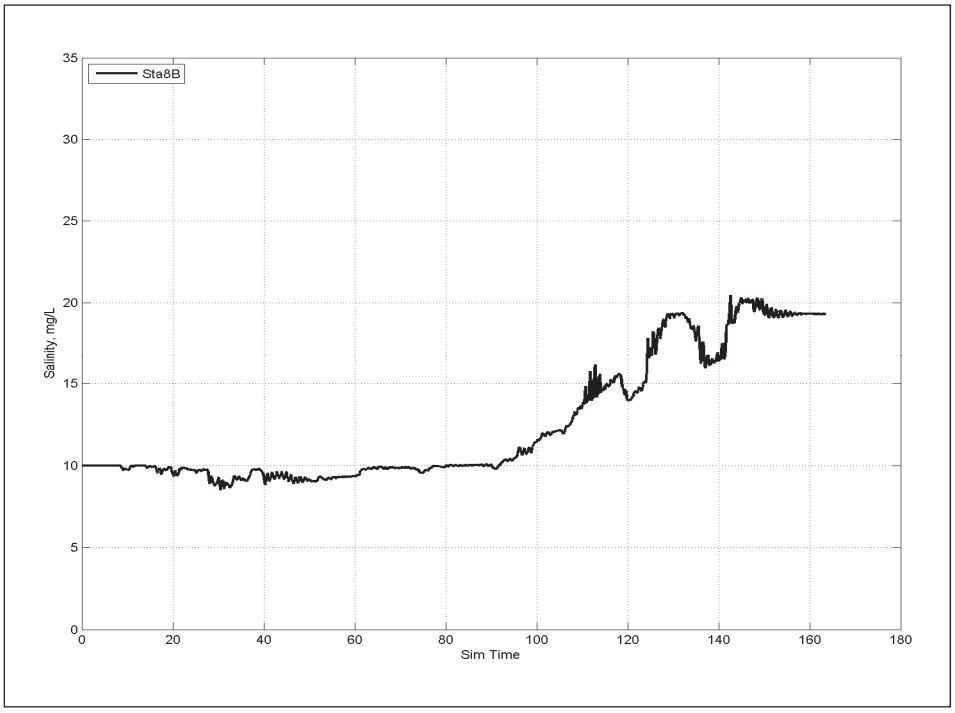

Figure E-51. Calibration results for DO at Station 9 for surface layer (upper) and bottom layer lower).

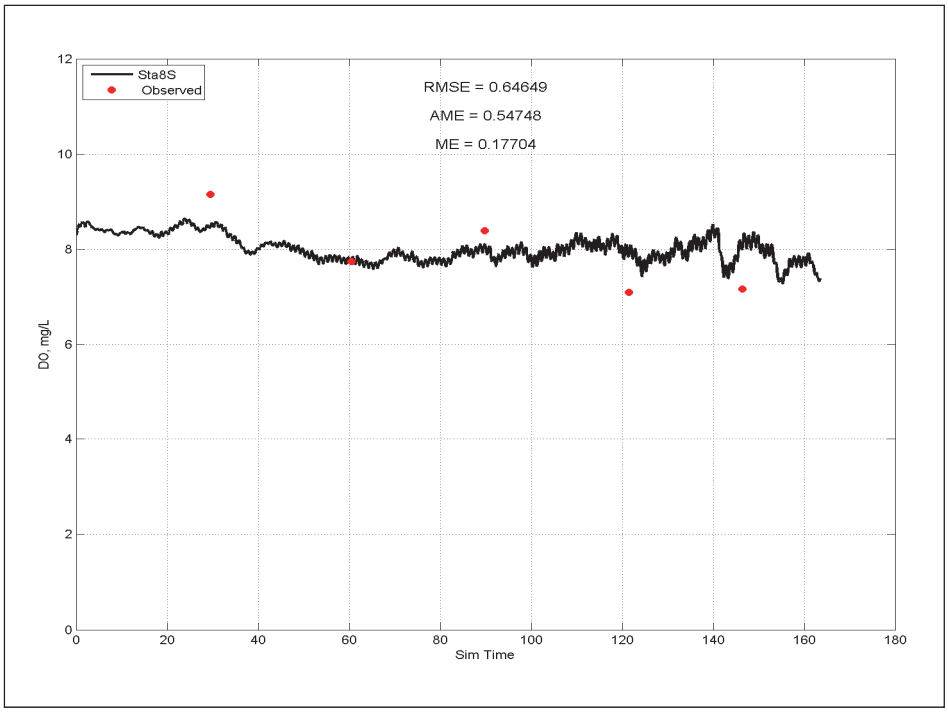

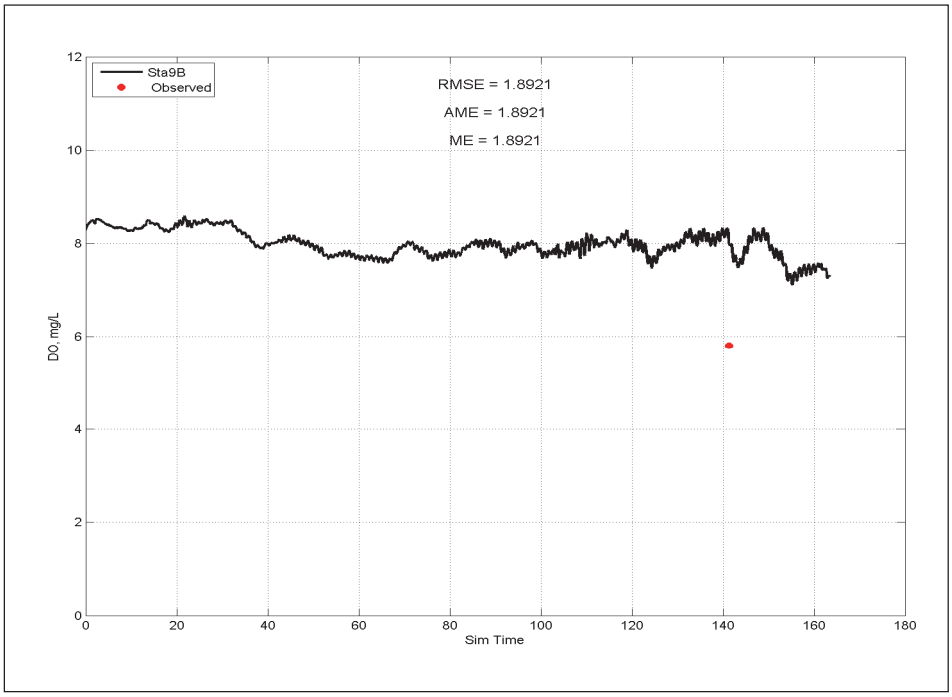

Figure E-52. Calibration results for NH_4 at Station 9 for surface layer (upper) and bottom layer (lower).

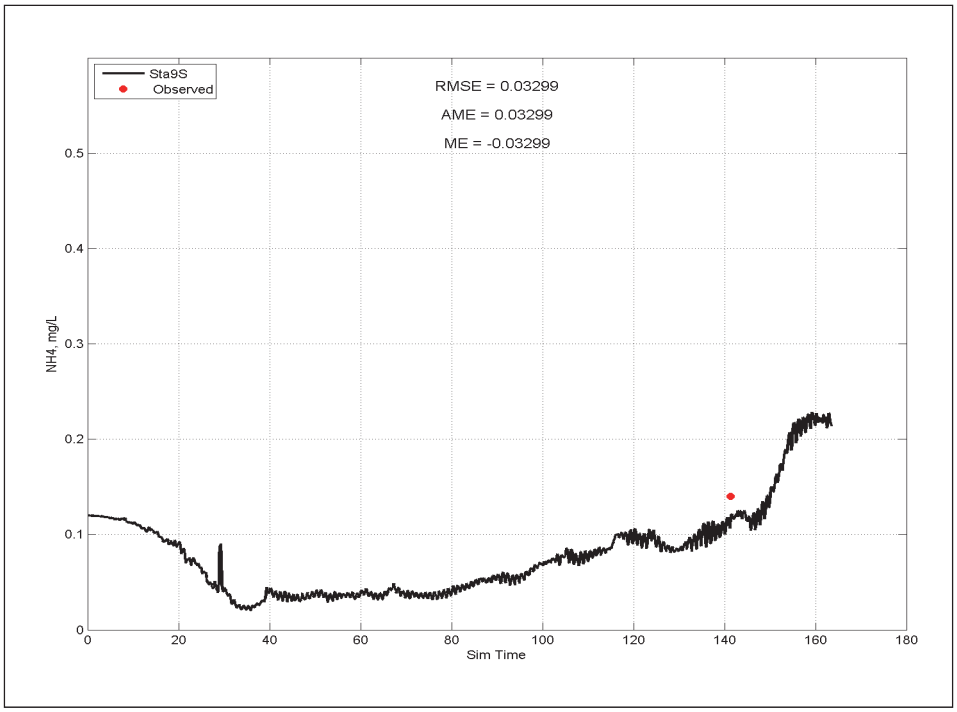

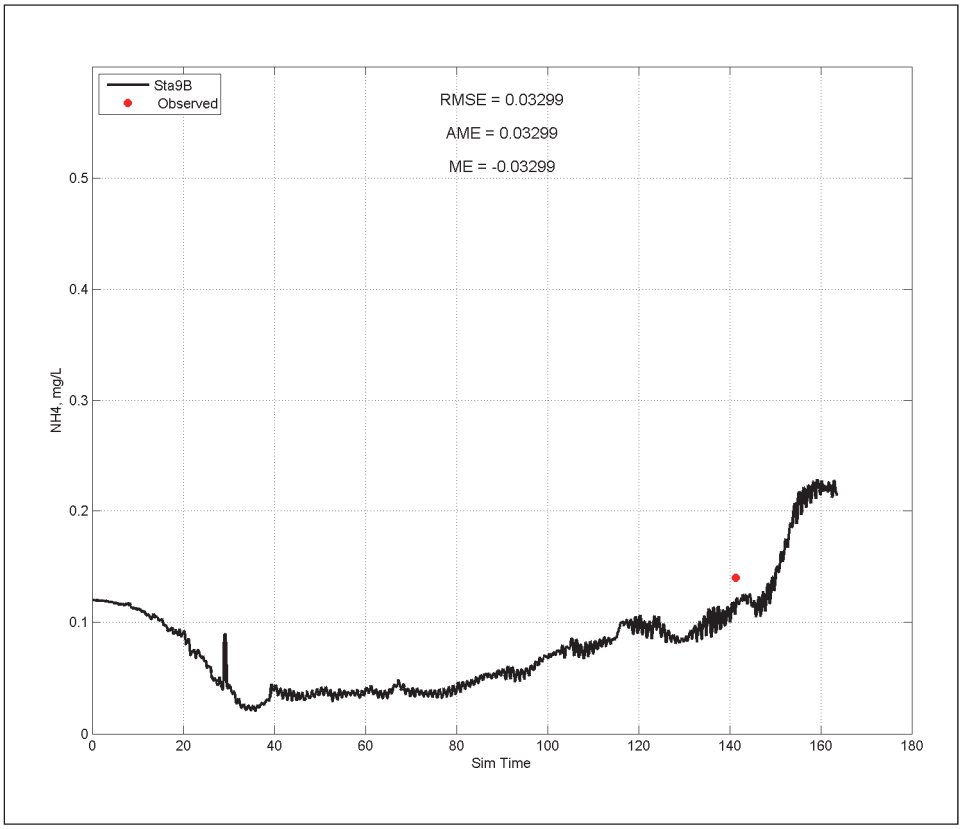

Figure E-53. Calibration results for NO_3 at Station 9 for surface layer (upper) and bottom layer (lower).

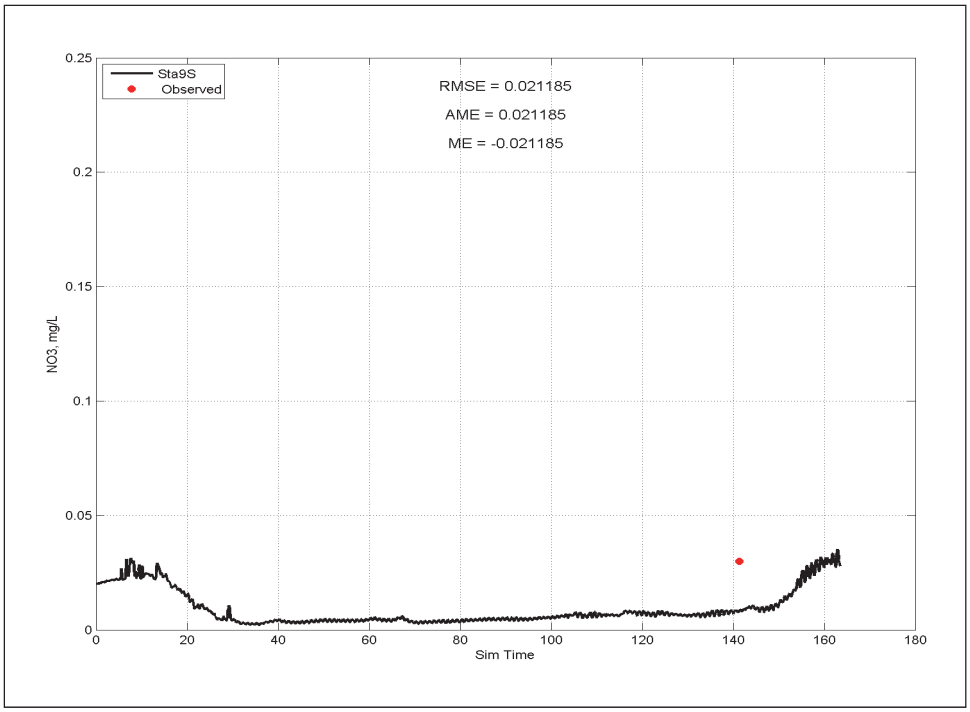

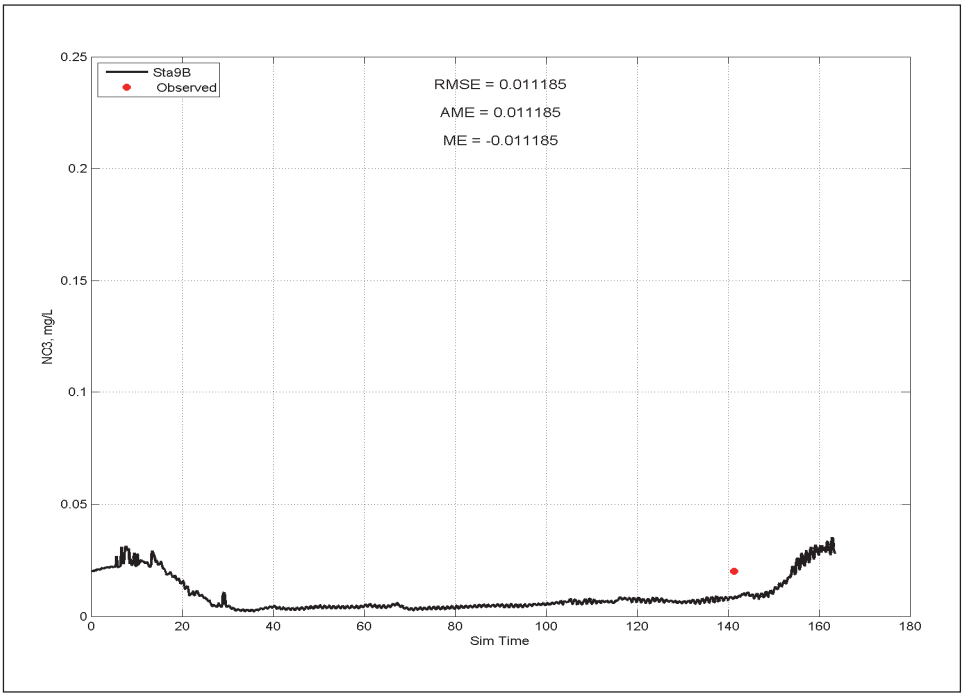

Figure E-54. Calibration results for *Tp* at Station 9 for surface layer (upper) and bottom layer (lower).

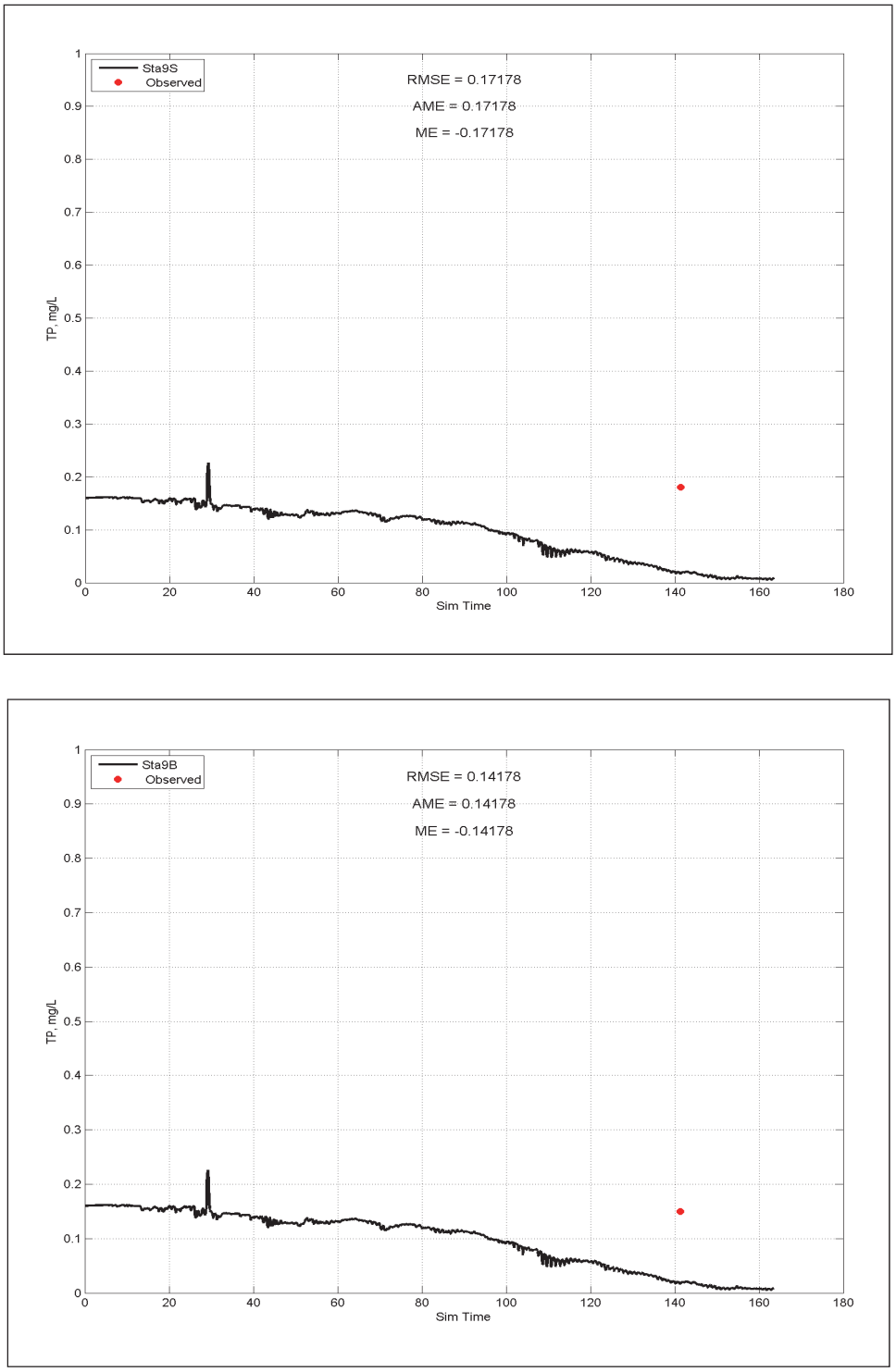

Figure E-55. Calibration results for temperature at Station 10 for surface layer (upper) and bottom layer (lower).

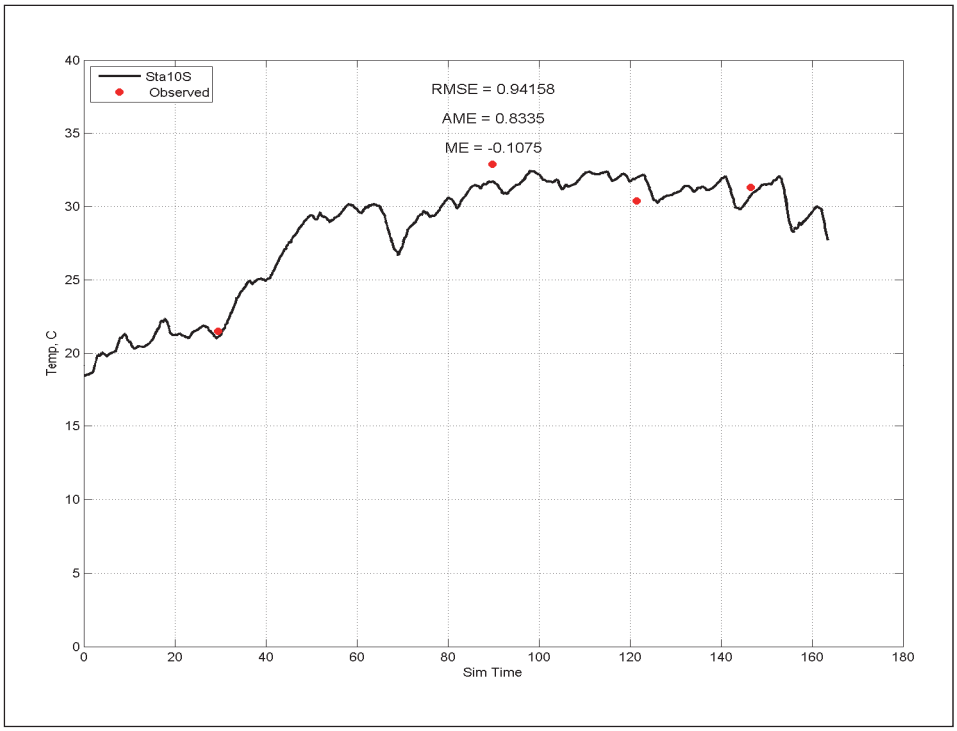

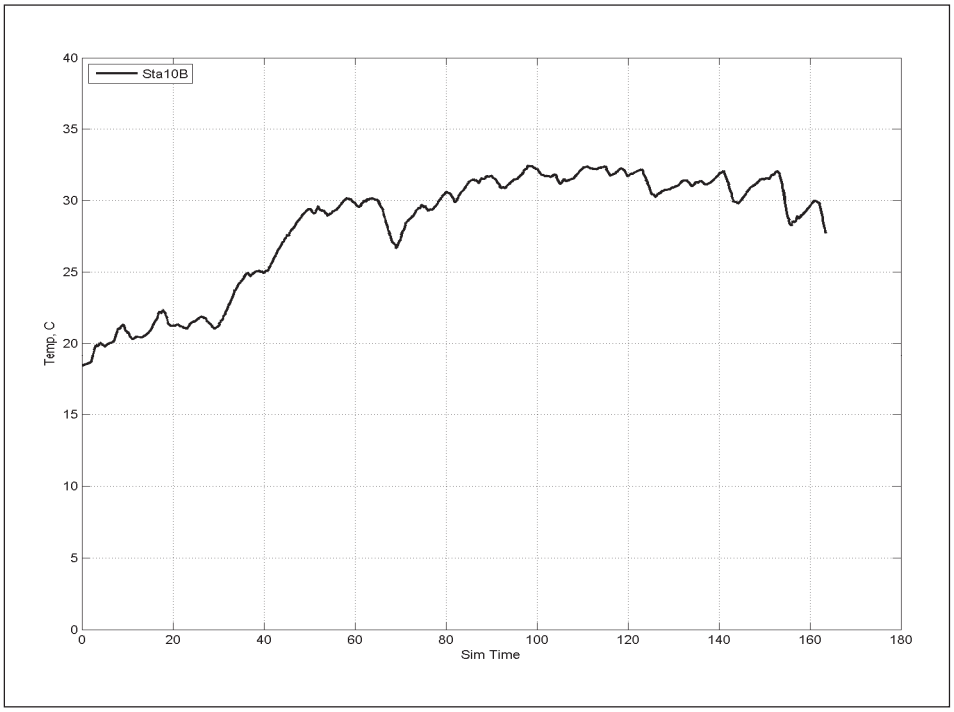

Figure E-56 Calibration results for salinity at Station 10 for surface layer (upper) and bottom layer (lower).

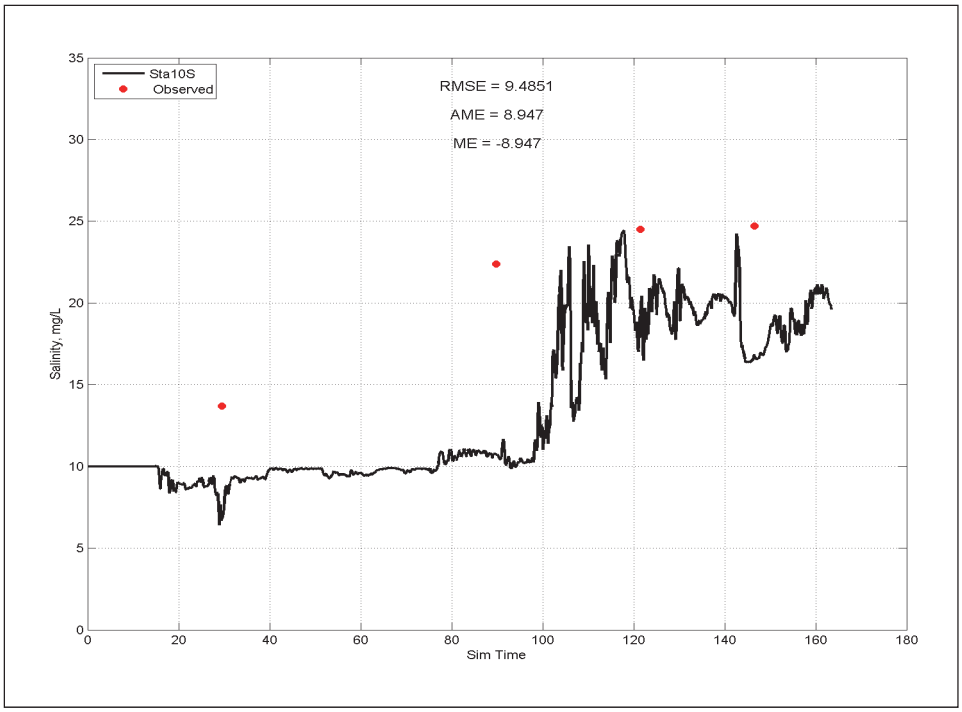

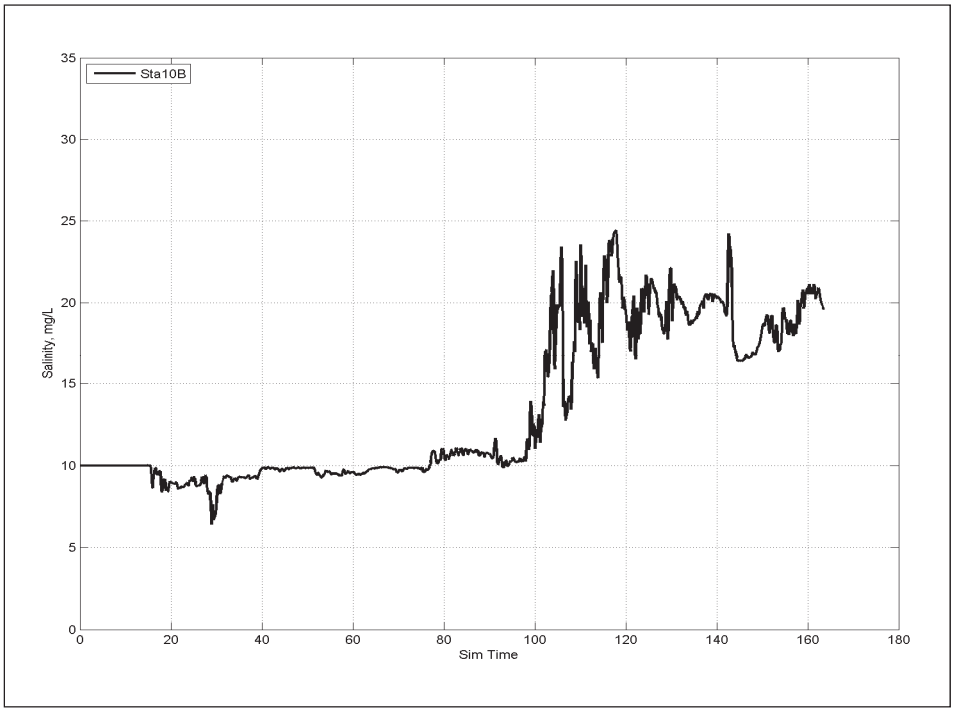

Figure E-57. Calibration results for DO at Station 10 for surface layer (upper) and bottom layer (lower).

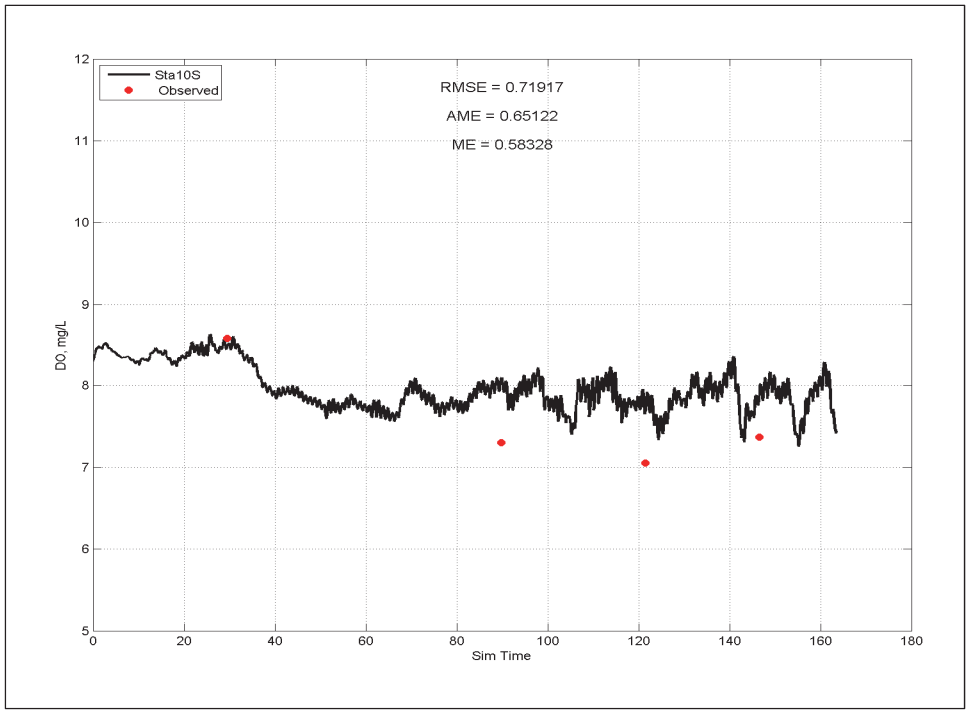

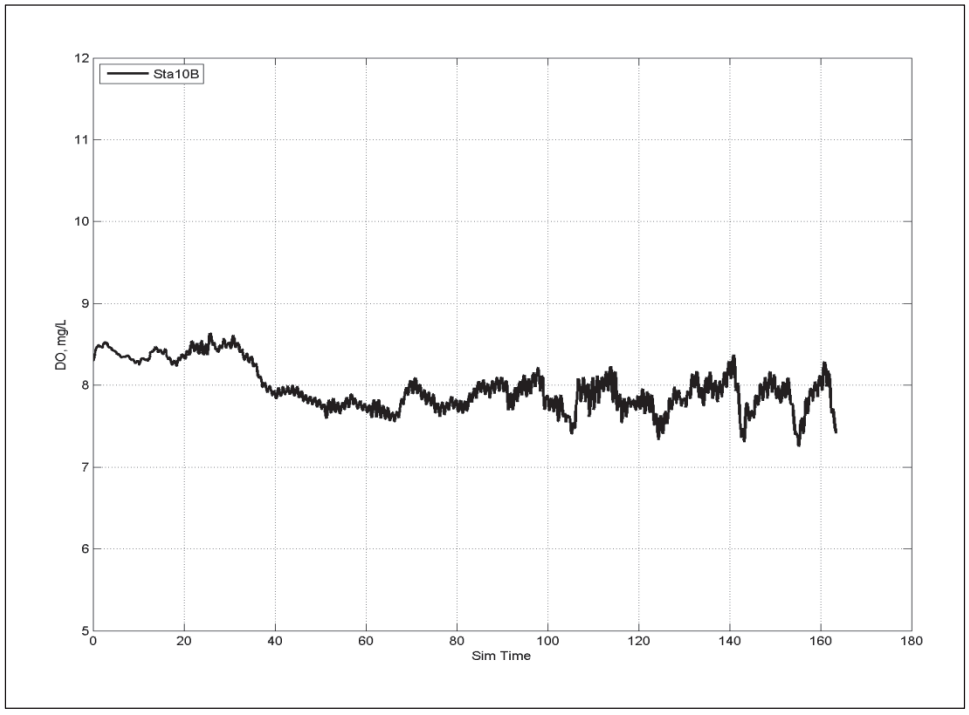

Figure E-58. Calibration results for NH_4 at Station 10 for surface layer (upper) and bottom layer (lower).

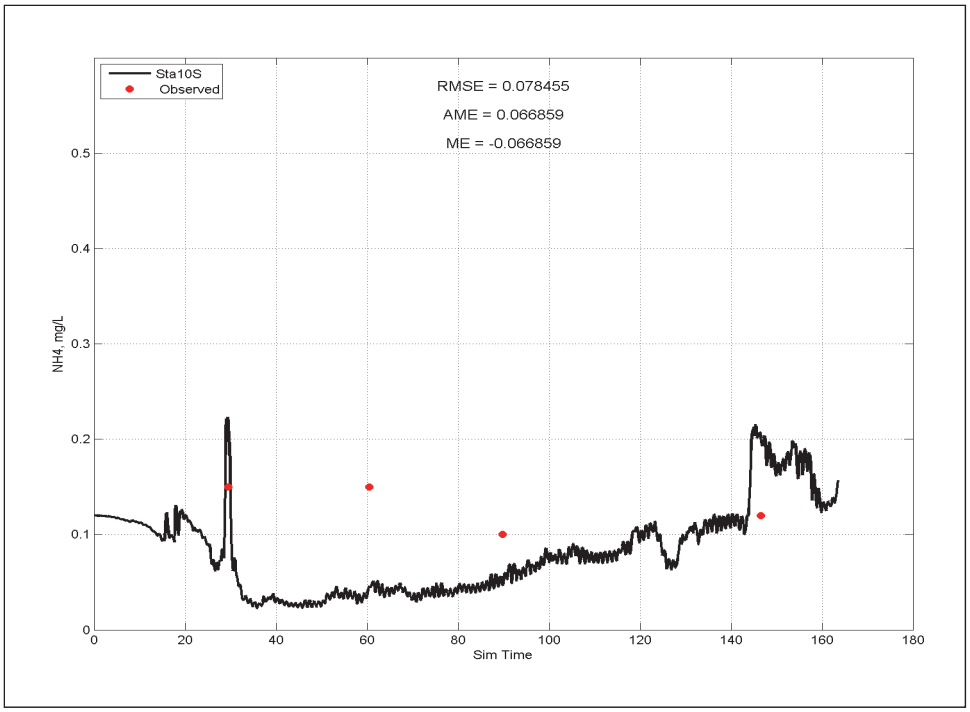

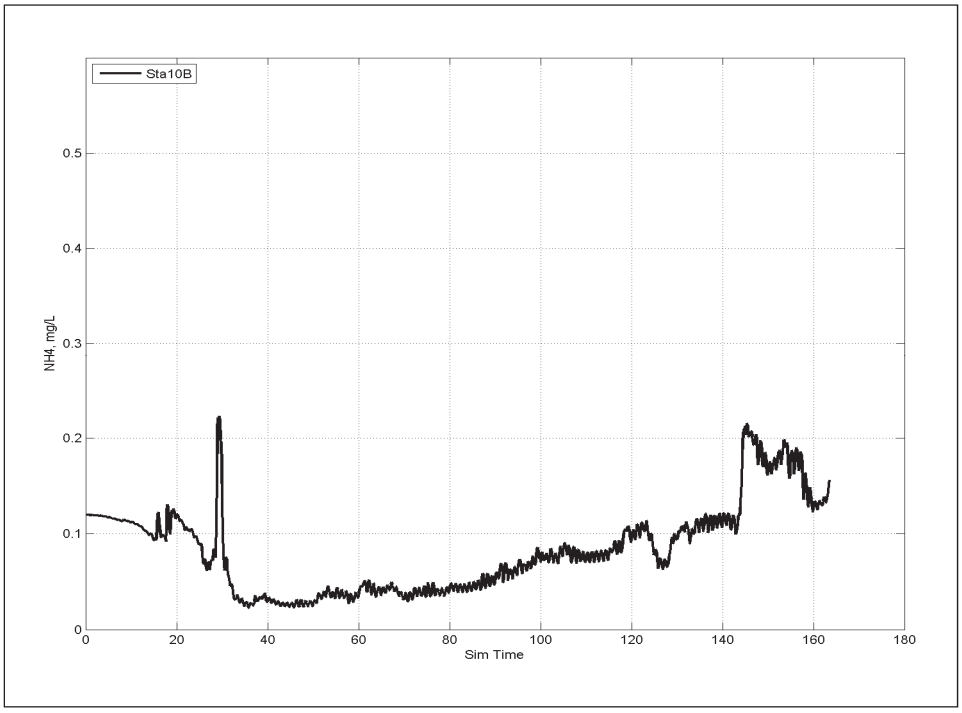

Figure E-59. Calibration results for NO_3 at Station 10 for surface layer (upper) and bottom layer (lower).

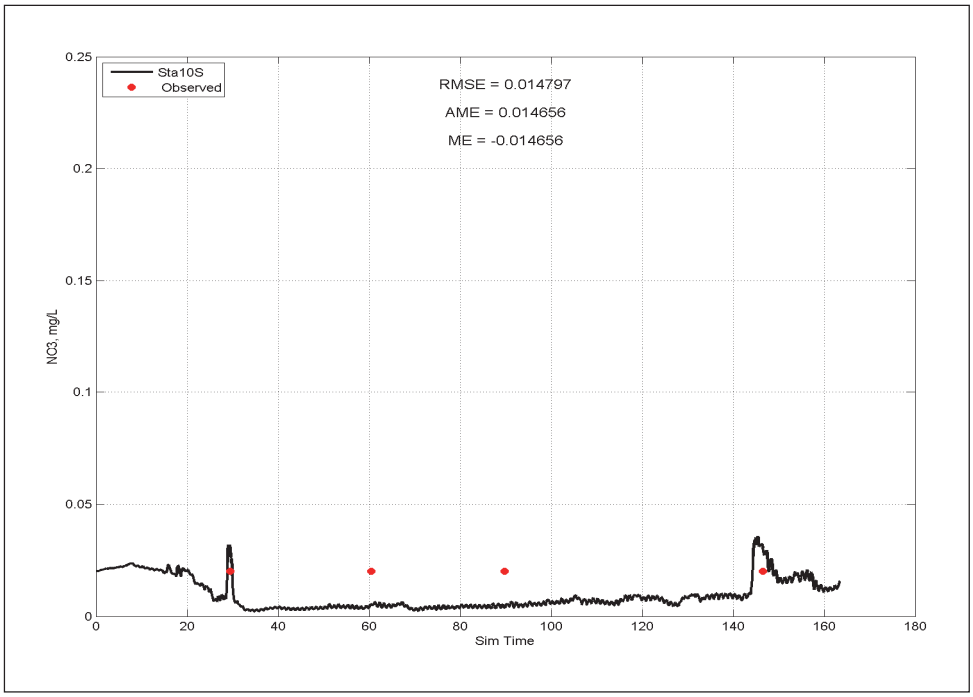

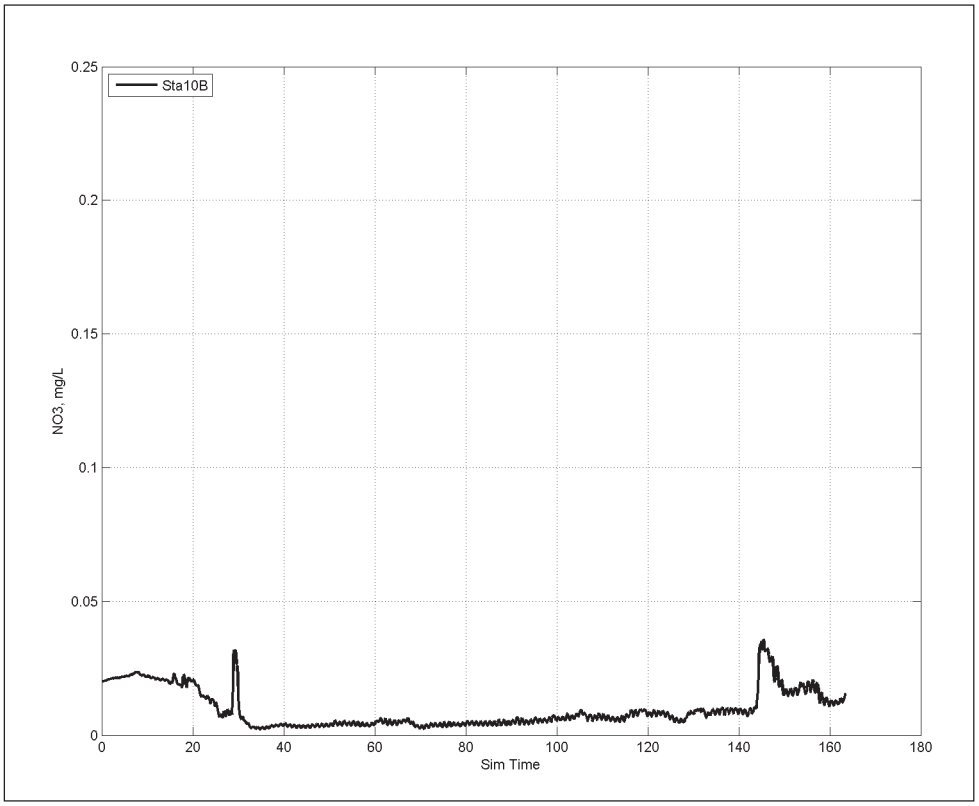

Figure E-60. Calibration results for *Tp* at Station 10 for surface layer (upper) and bottom layer (lower).

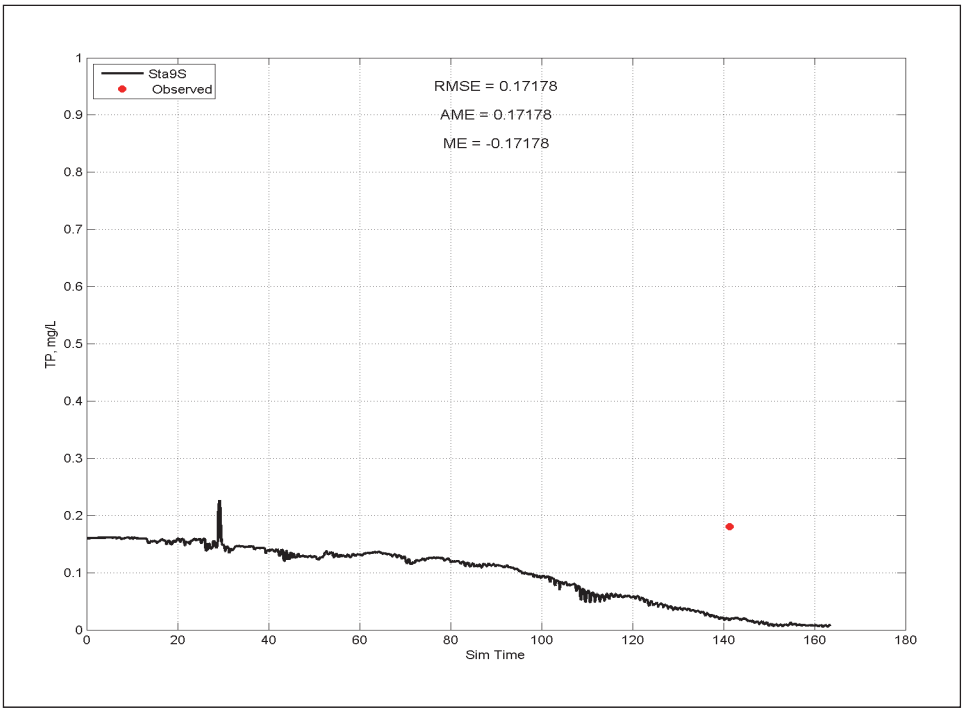

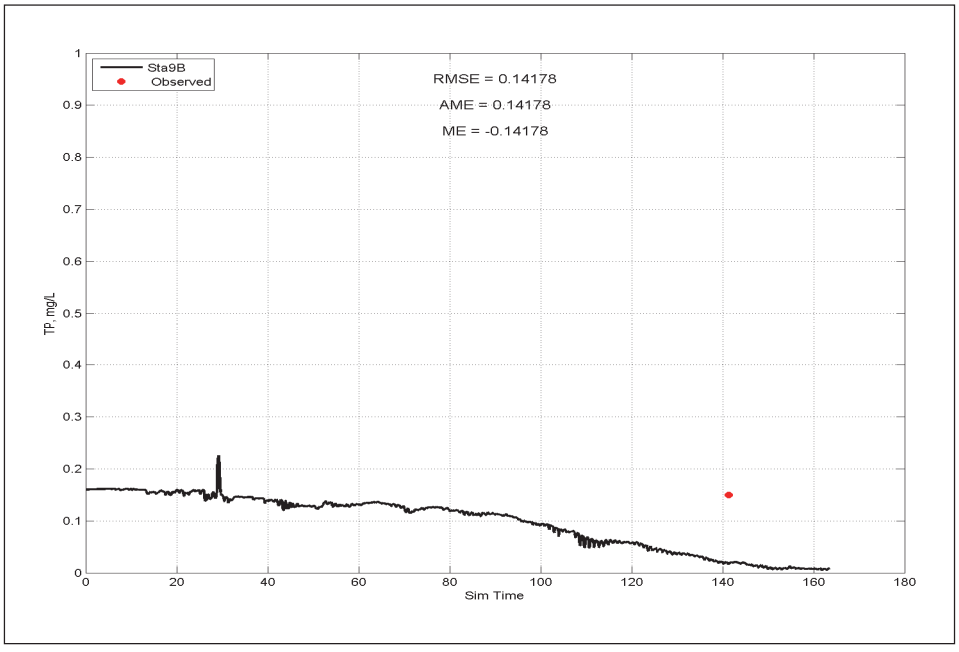

Figure E-61. Comparison of DO, Chlororphyll, and Salinity at Station 1 (Figure 5-2) for results from simulations representing Pre, Post, Restored, Degraded, and Cumulative conditions (continued).

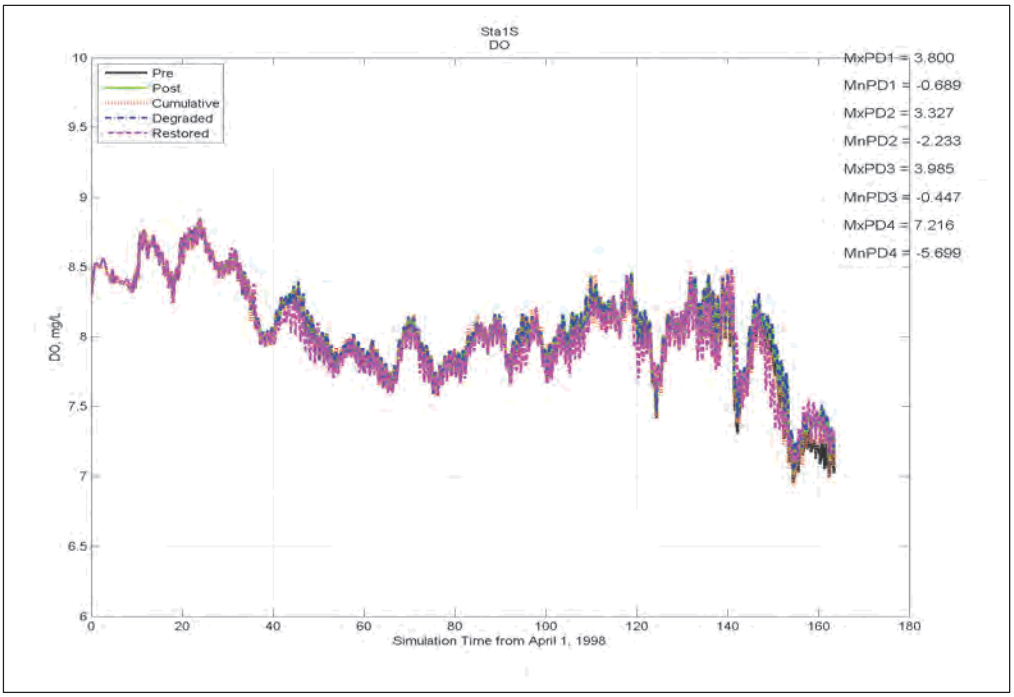

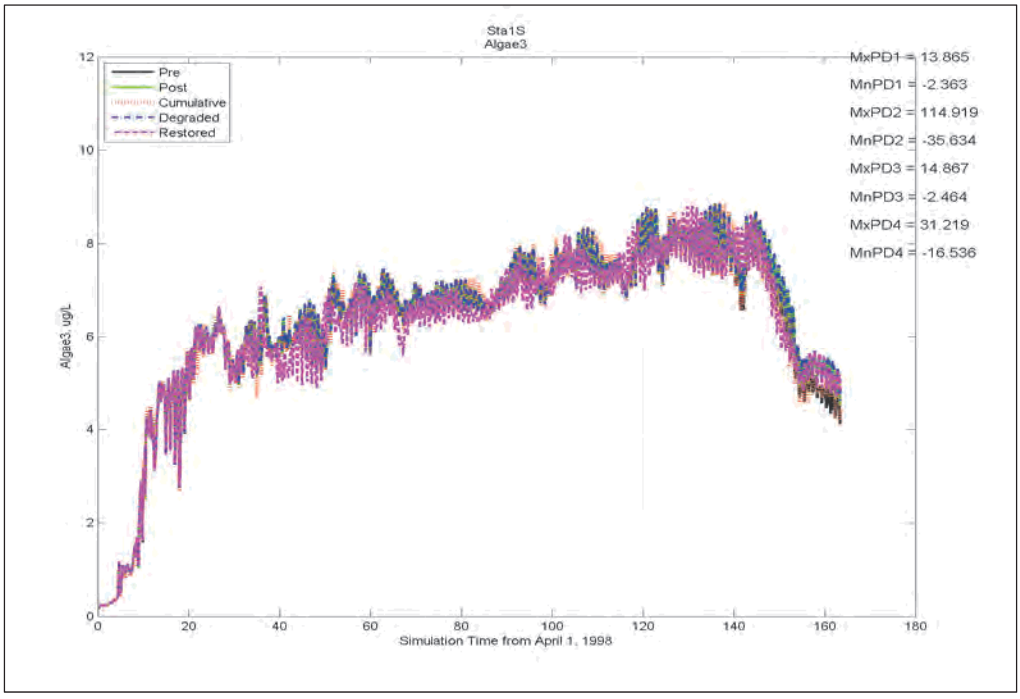

Figure B-61. Concluded.

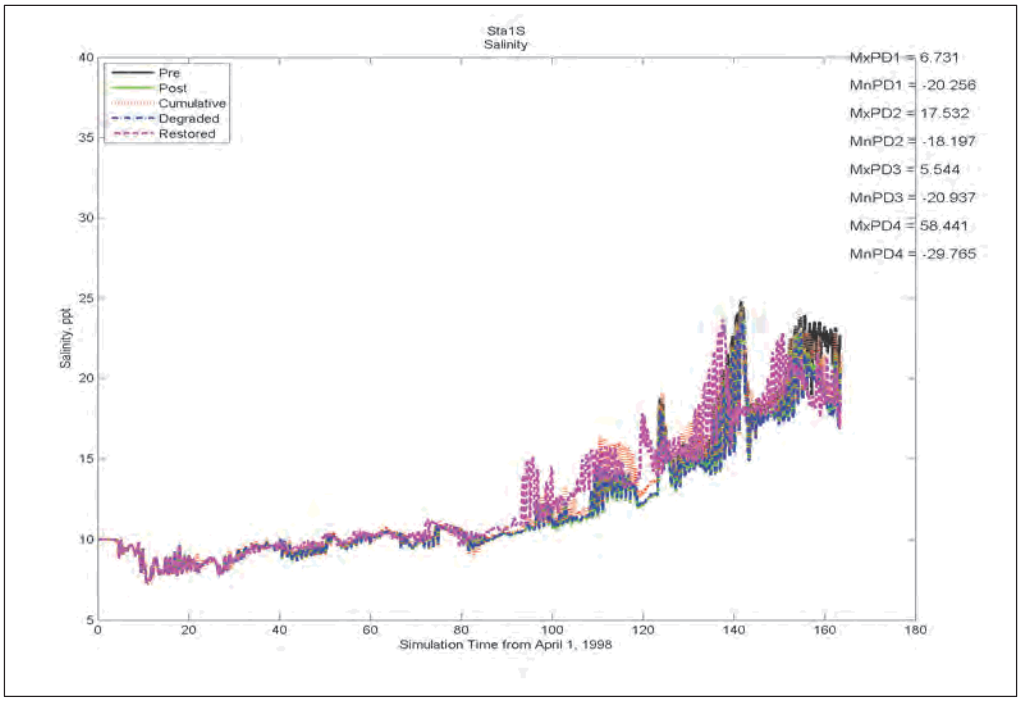

Figure E-62. Comparison of DO, Chlororphyll, and Salinity at Station 3 (Figure 5-2) for results from simulations representing Pre, Post, Restored, Degraded, and Cumulative conditions (continued).

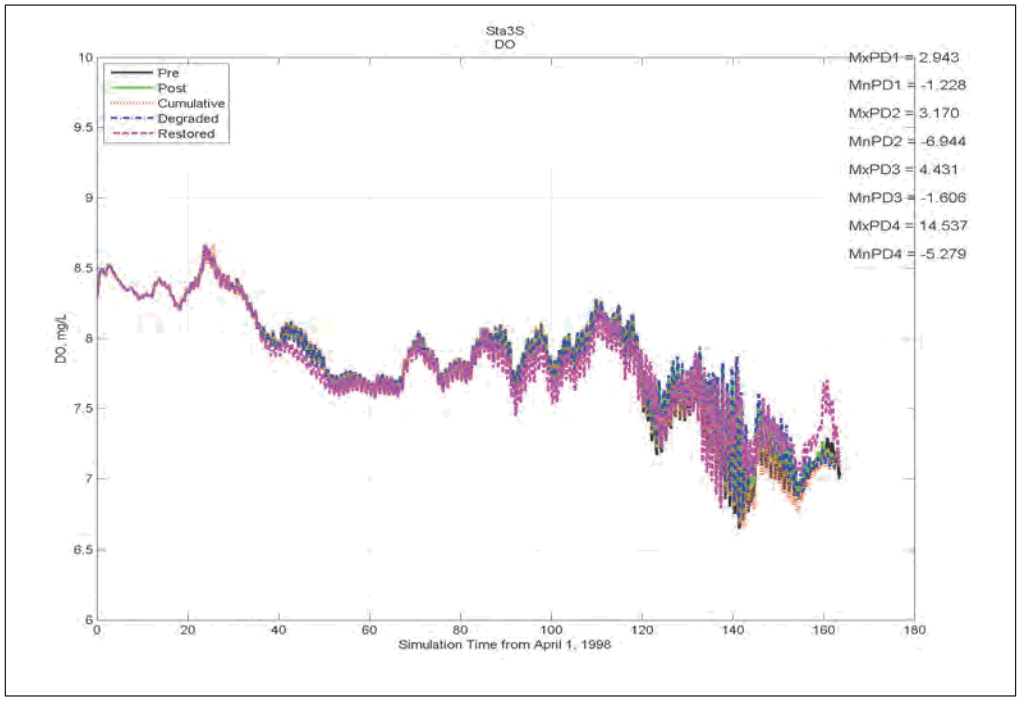

Figure E-62. Concluded.

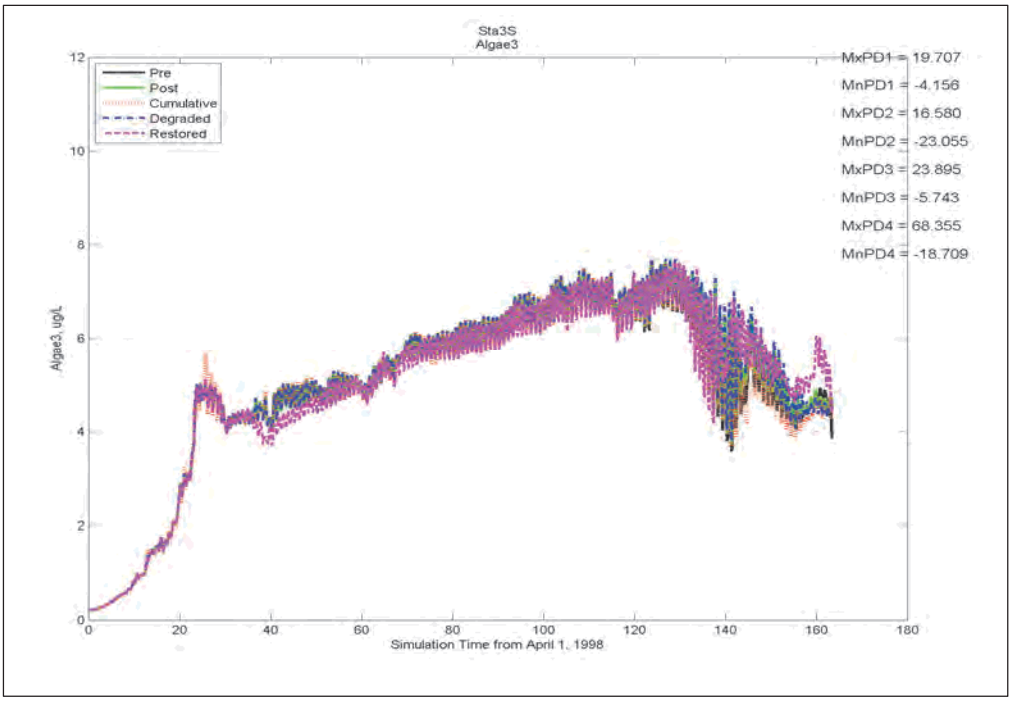

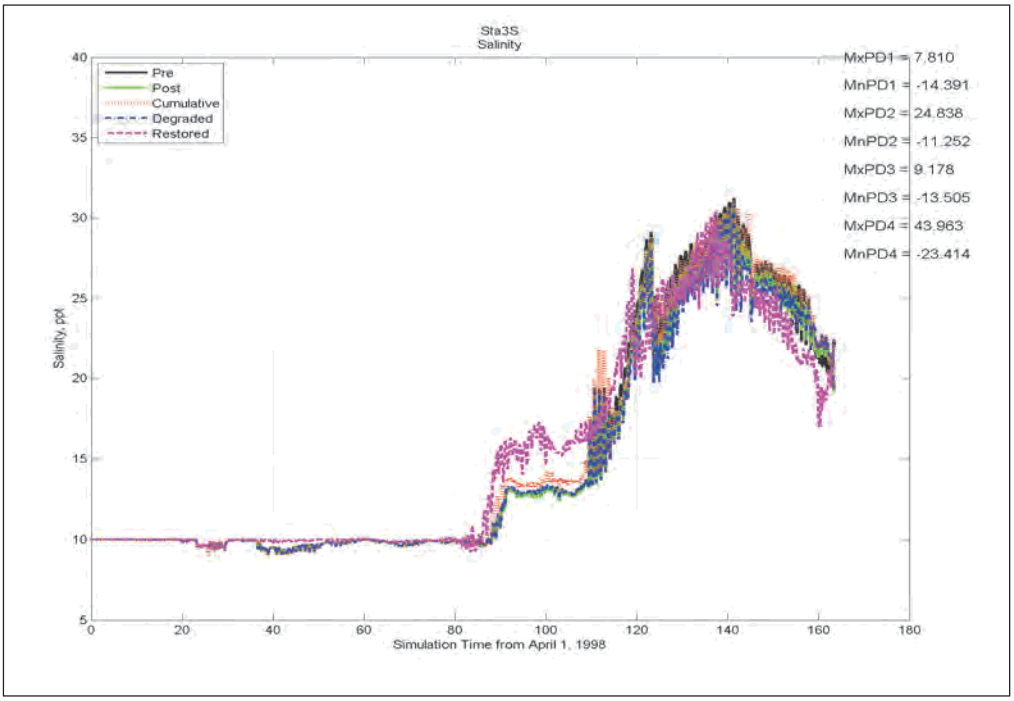

Figure E-63. Comparison of DO, Chlororphyll, and Salinity at Station 4 (Figure 5-2) for results from simulations representing Pre, Post, Restored, Degraded, and Cumulative conditions (continued).

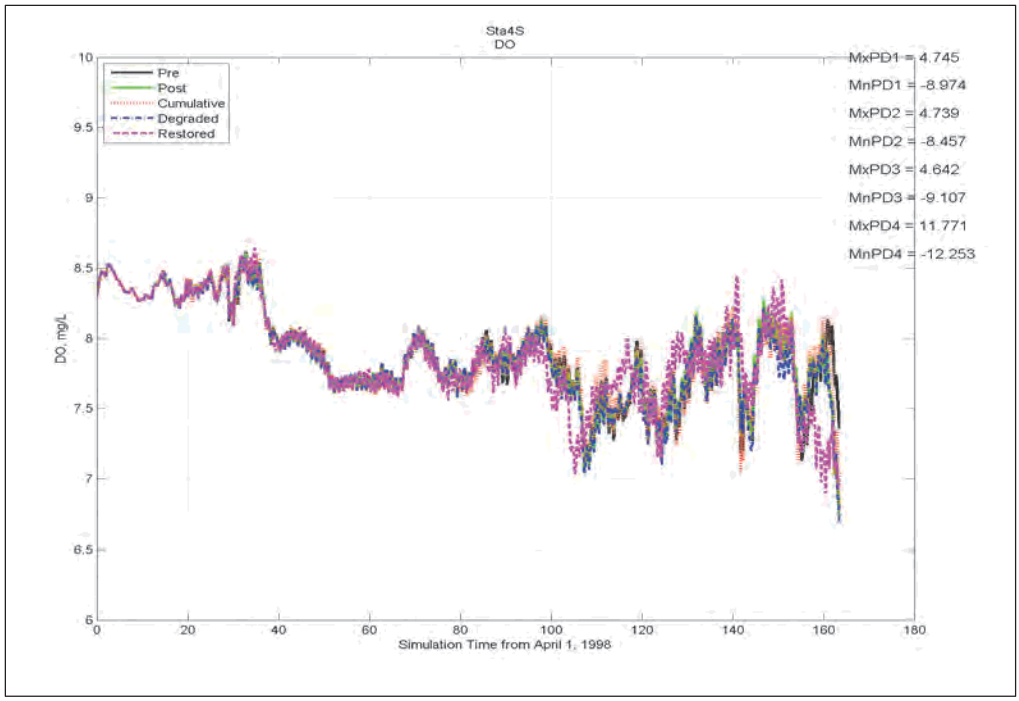

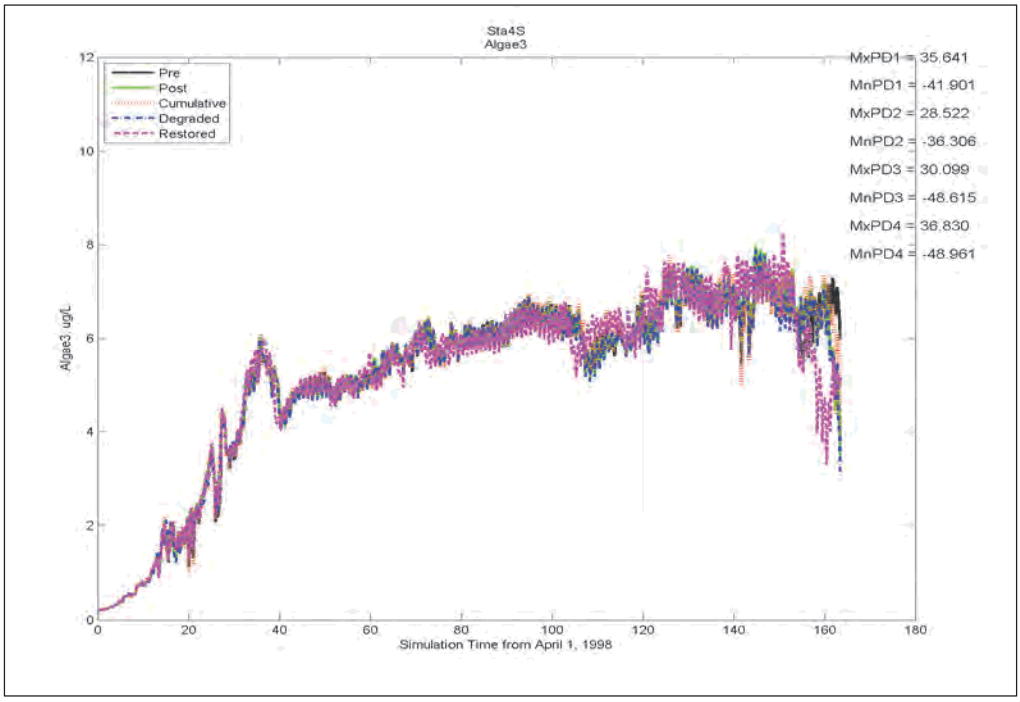

Figure E-63. Concluded.

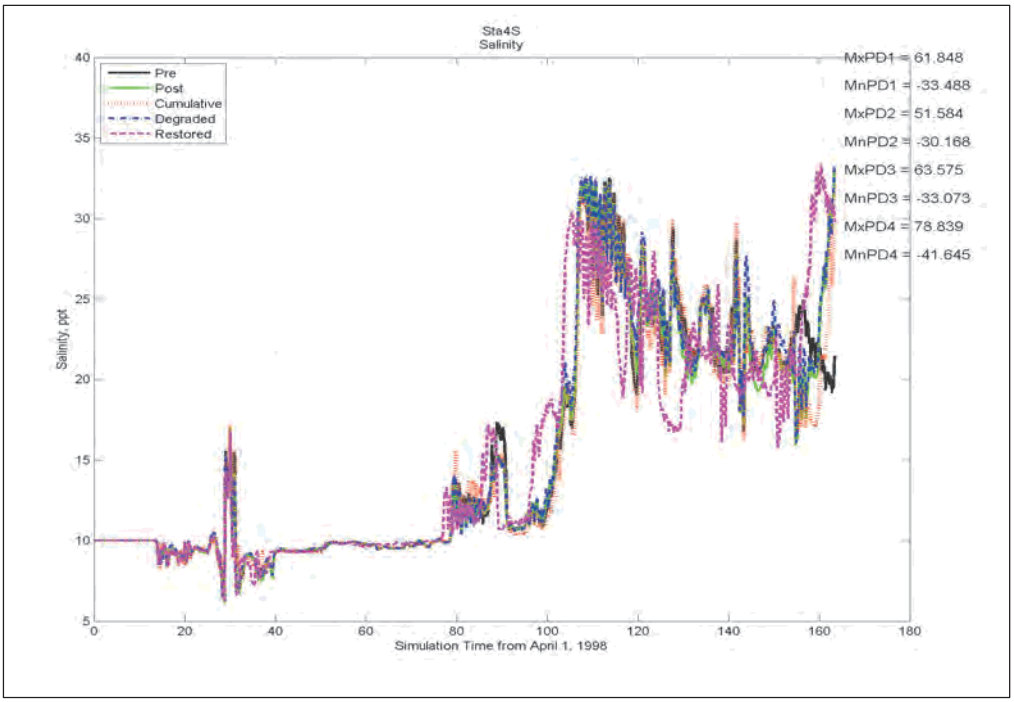

Figure E-64. Comparison of DO, Chlororphyll, and Salinity at Station 6 (Figure 5-2) for results from simulations representing Pre, Post, Restored, Degraded, and Cumulative conditions (continued).

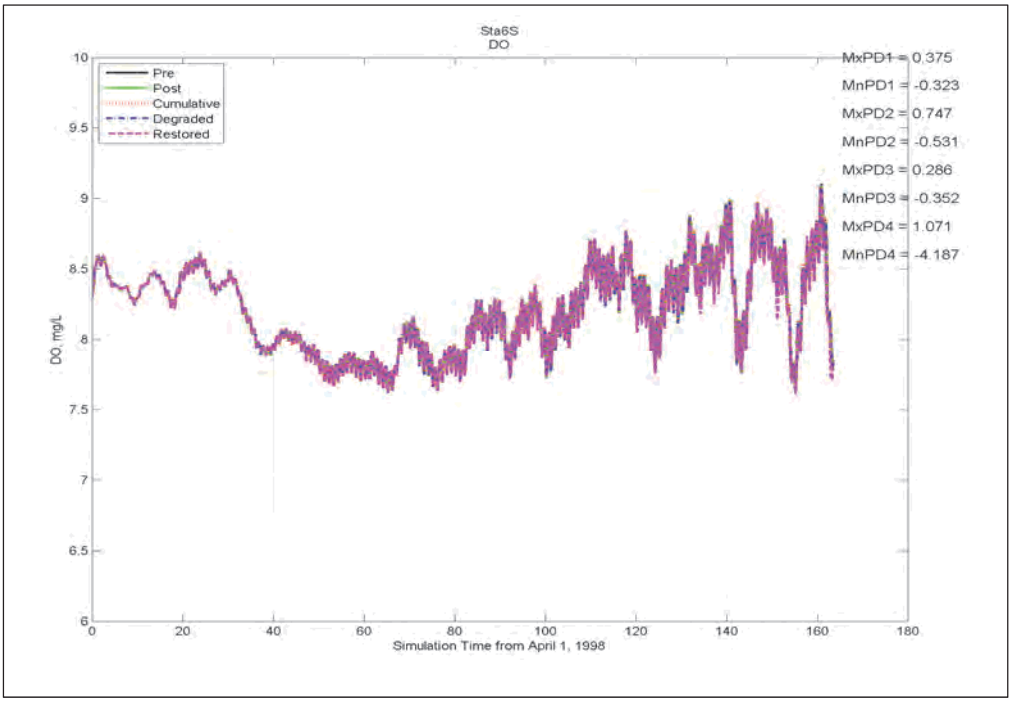

Figure E-64. Concluded.

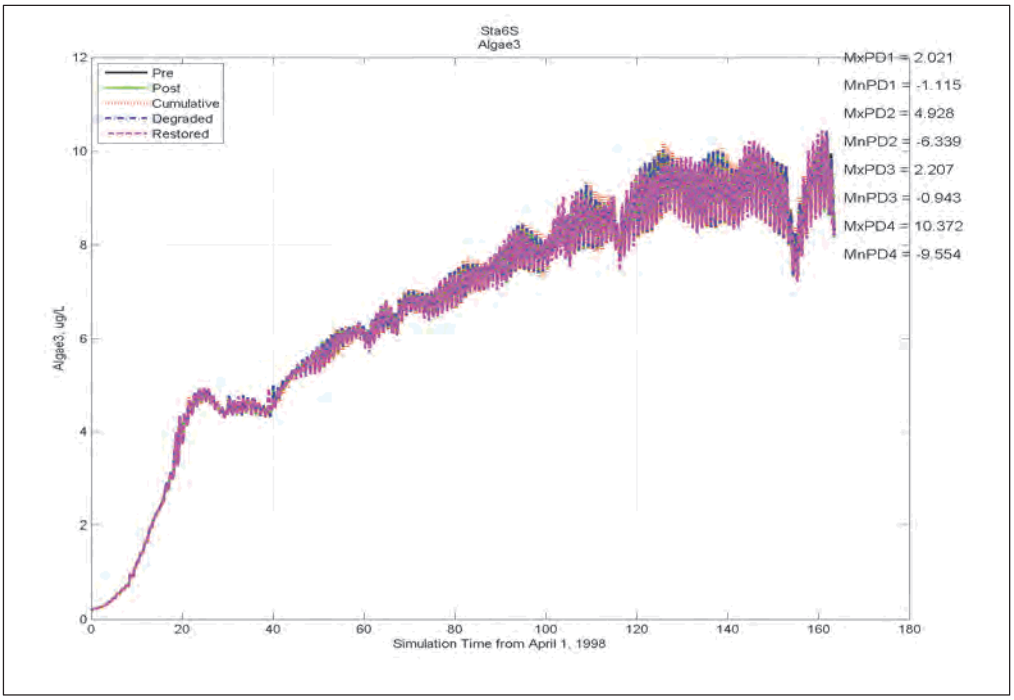

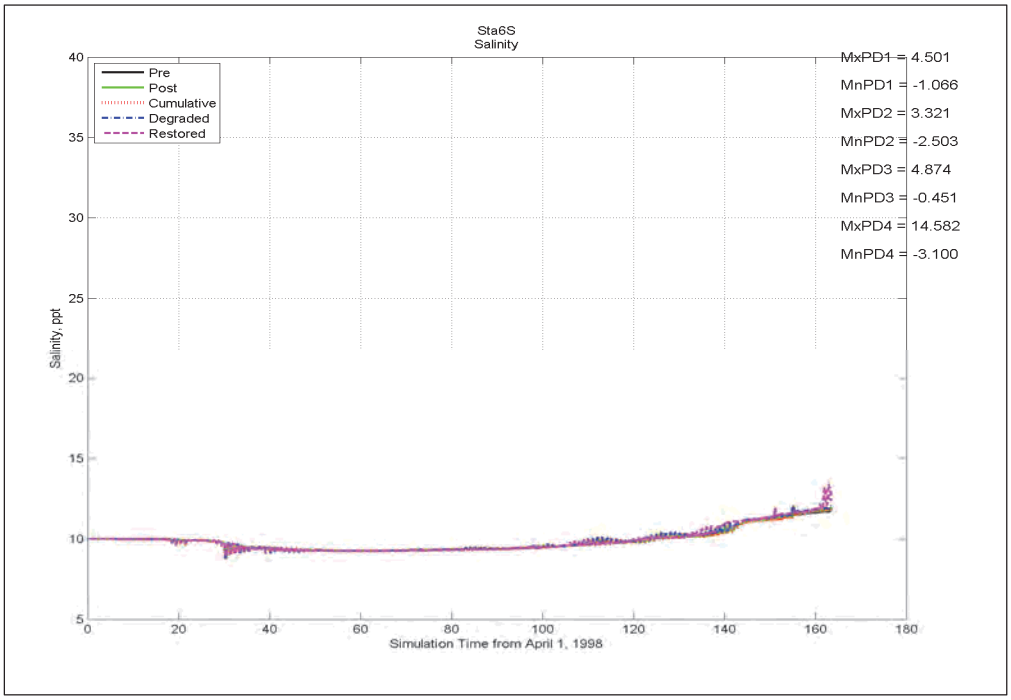

Figure E-65. Comparison of DO, Chlororphyll, and Salinity at Station 7 (Figure 5-2) for results from simulations representing Pre, Post, Restored, Degraded, and Cumulative conditions (continued).

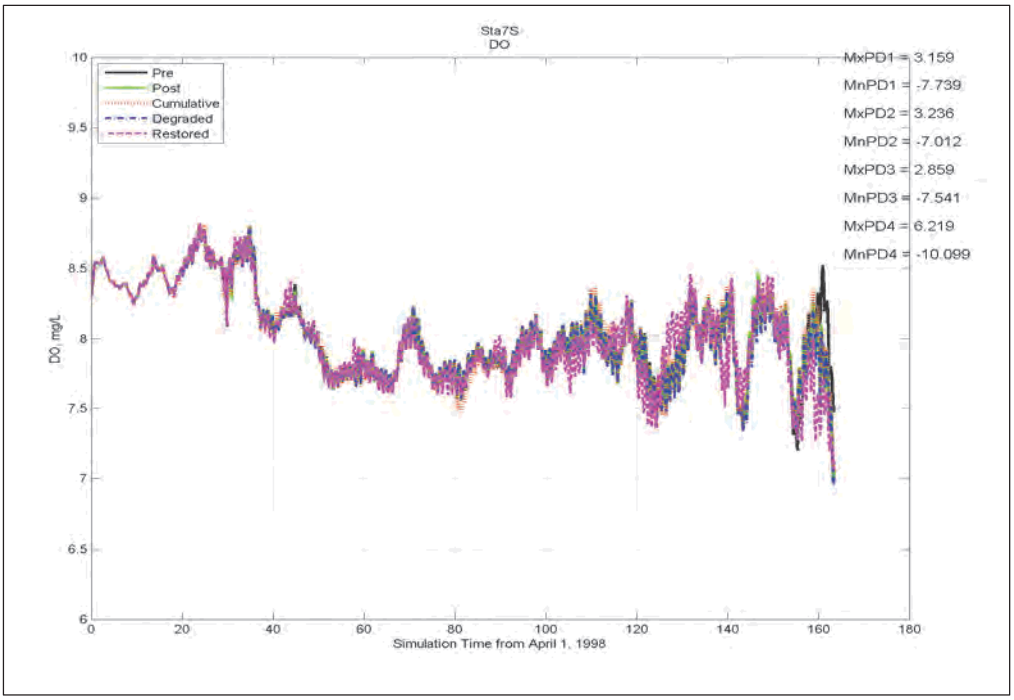

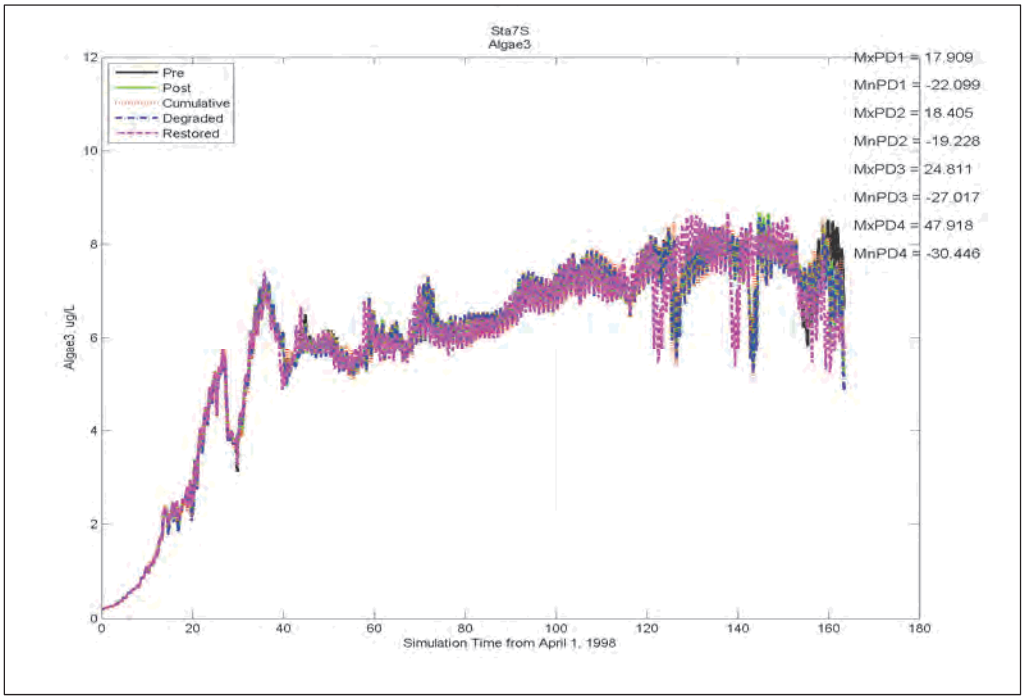

Figure E-65. Concluded.

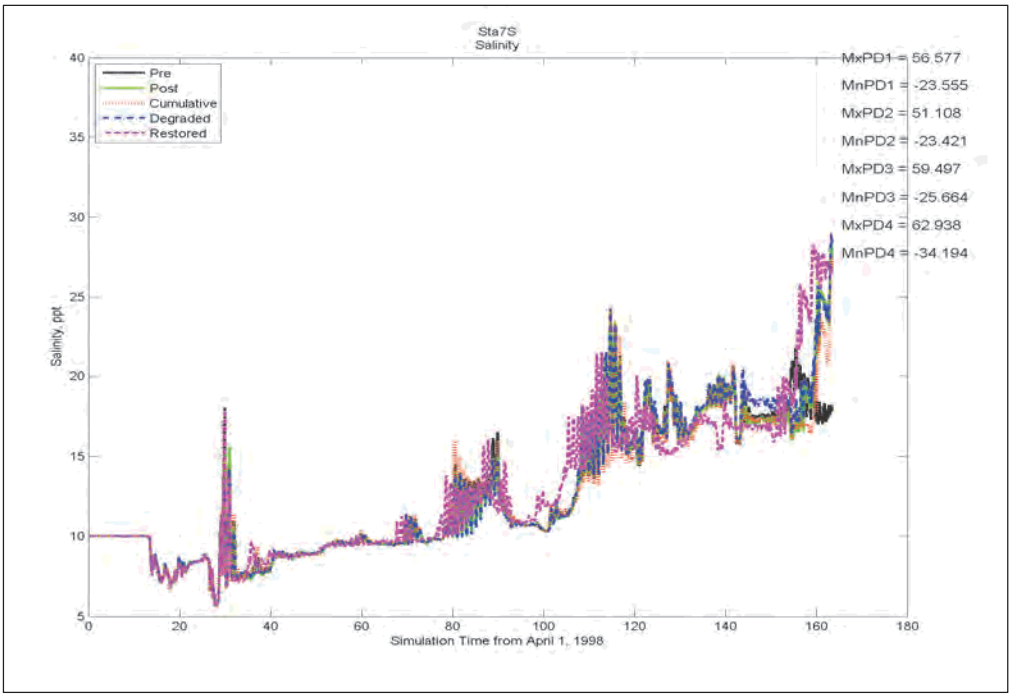

Figure E-66. Comparison of DO, Chlororphyll, and Salinity at Station 8 (Figure 5-2) for results from simulations representing Pre, Post, Restored, Degraded, and Cumulative conditions (continued).

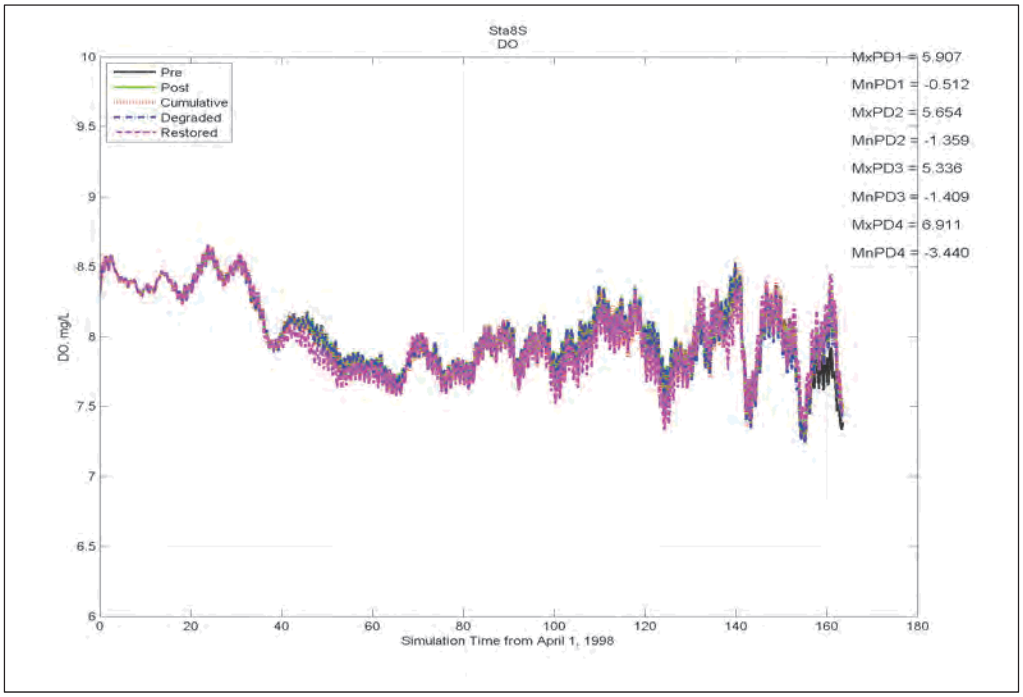

Figure E-66. Concluded.

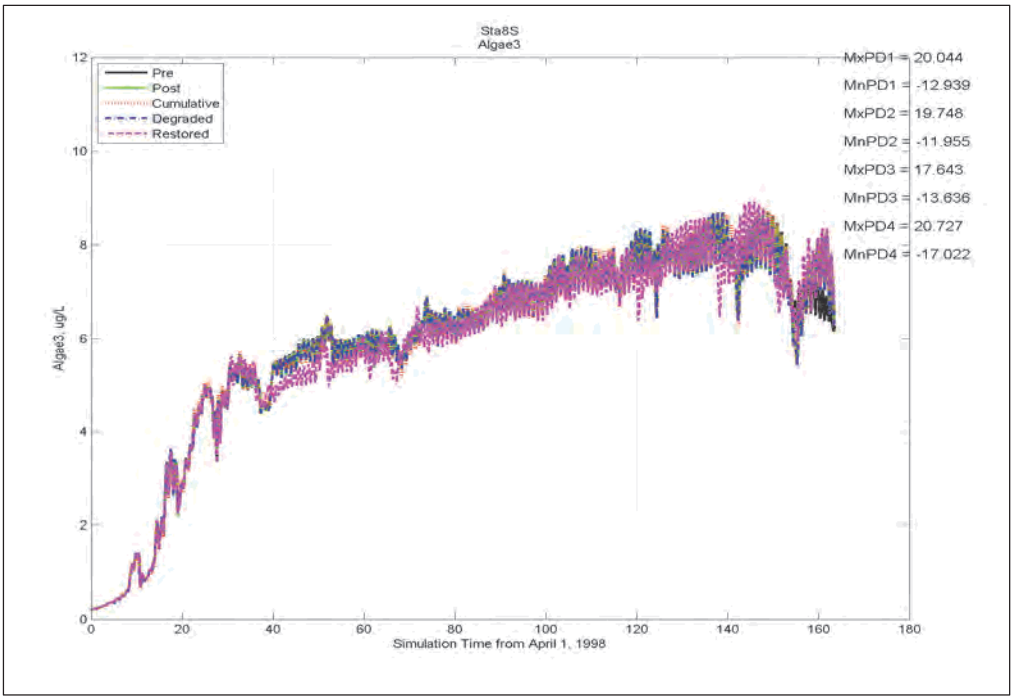

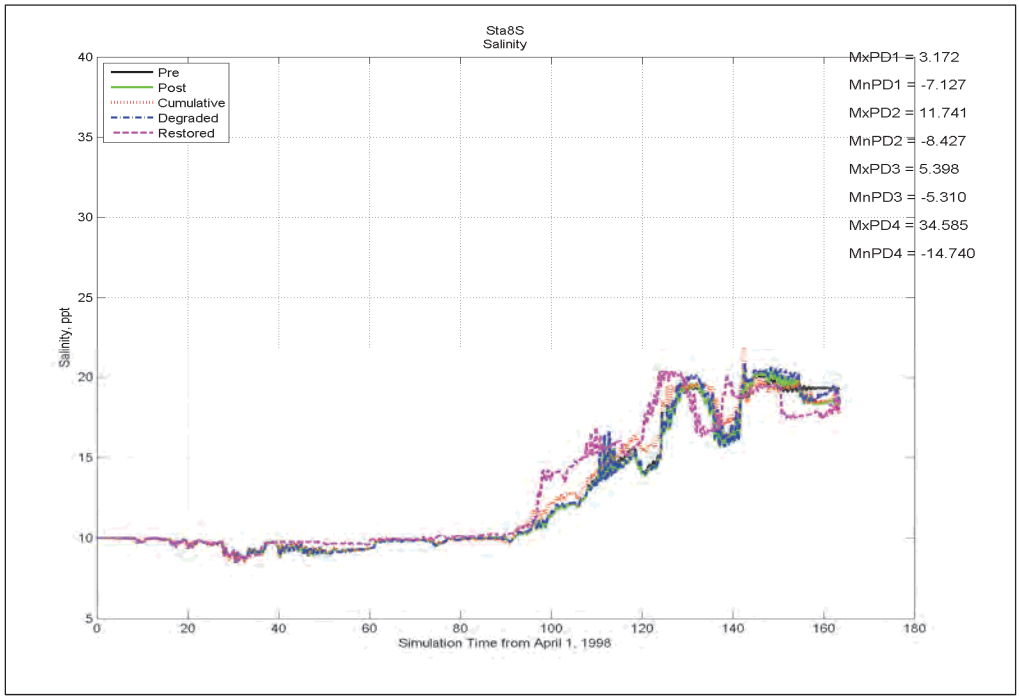

Figure E-67. Comparison of DO, Chlororphyll, and Salinity at Station 9 (Figure 5-2) for results from simulations representing Pre, Post, Restored, Degraded, and Cumulative conditions (continued).

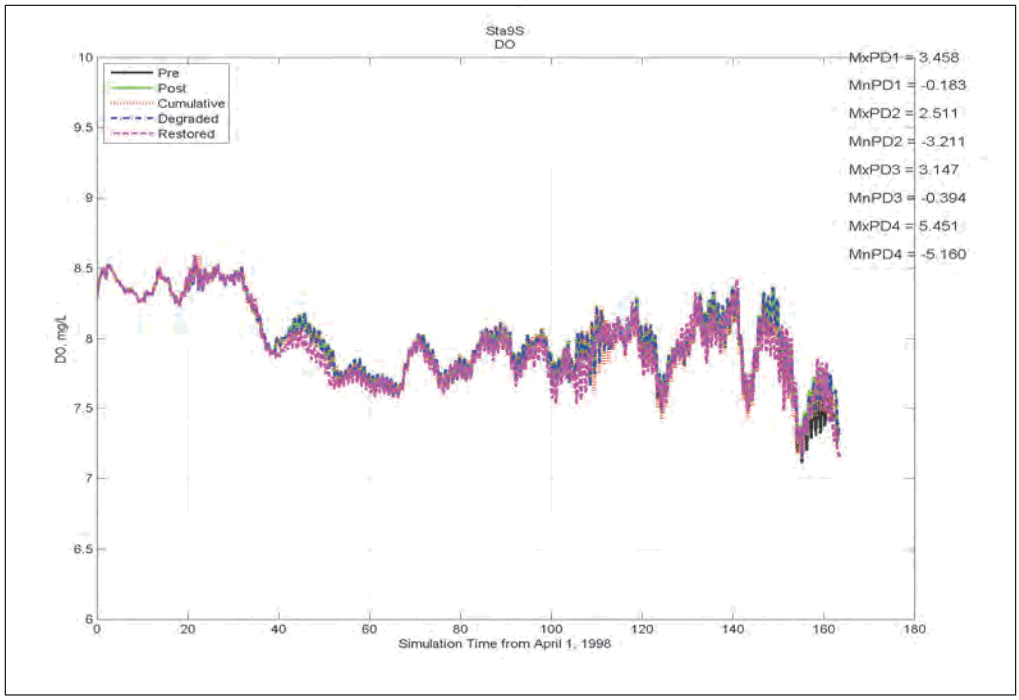

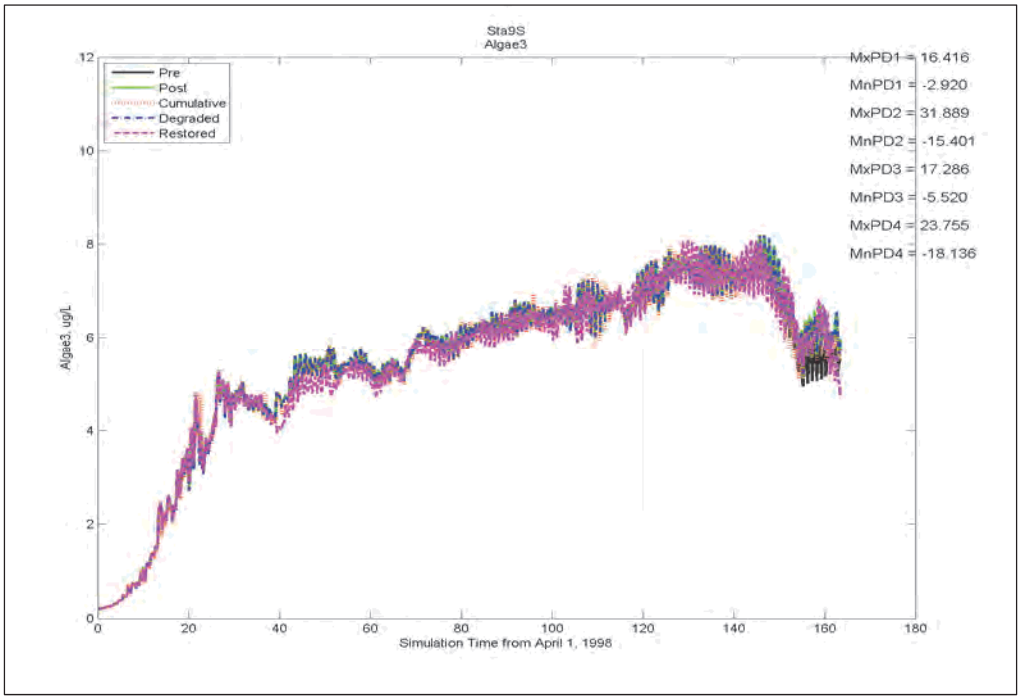

Figure E-67. Concluded.

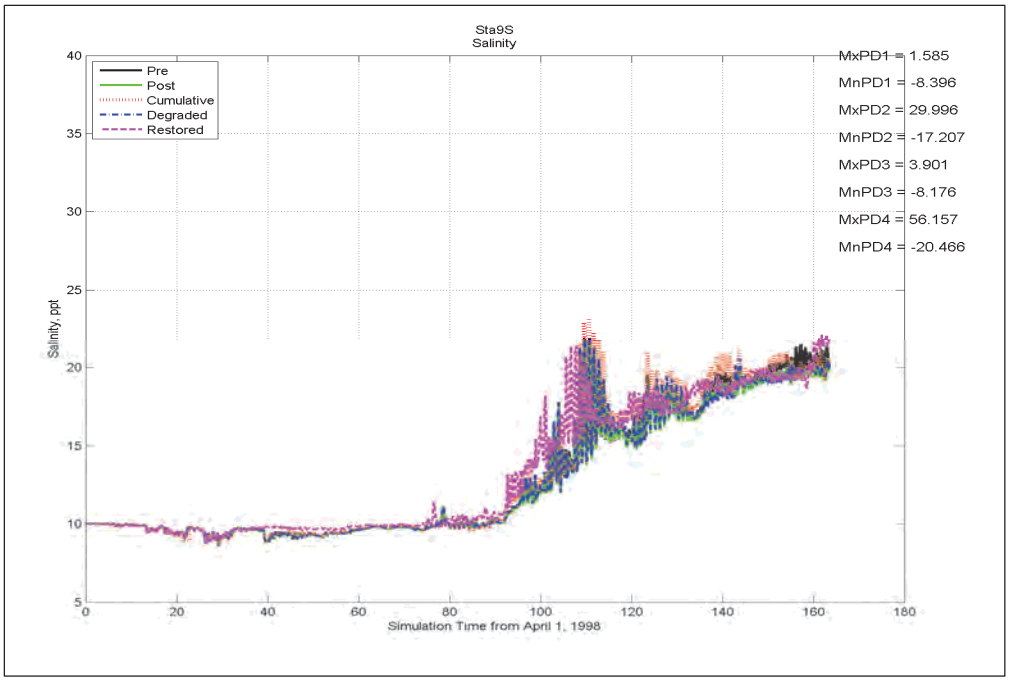

Figure E-68. Comparison of DO, Chlororphyll, and Salinity at Station 11 (Figure 5-8) for results from simulations representing Pre, Post, Restored, Degraded, and Cumulative conditions (continued).

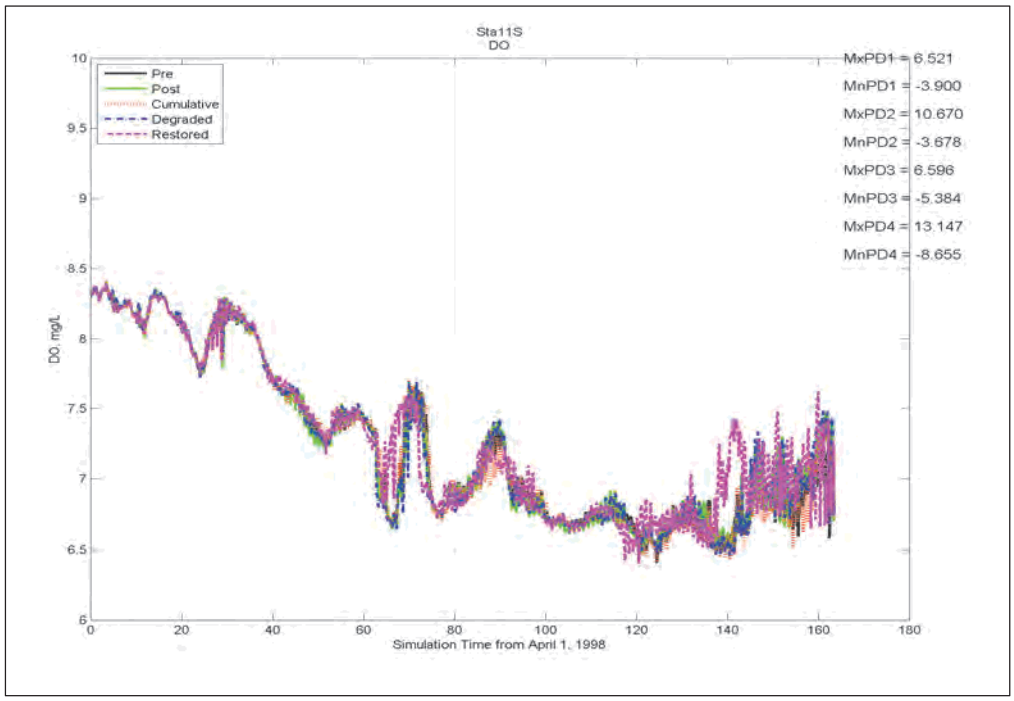

Figure E-68 Concluded.

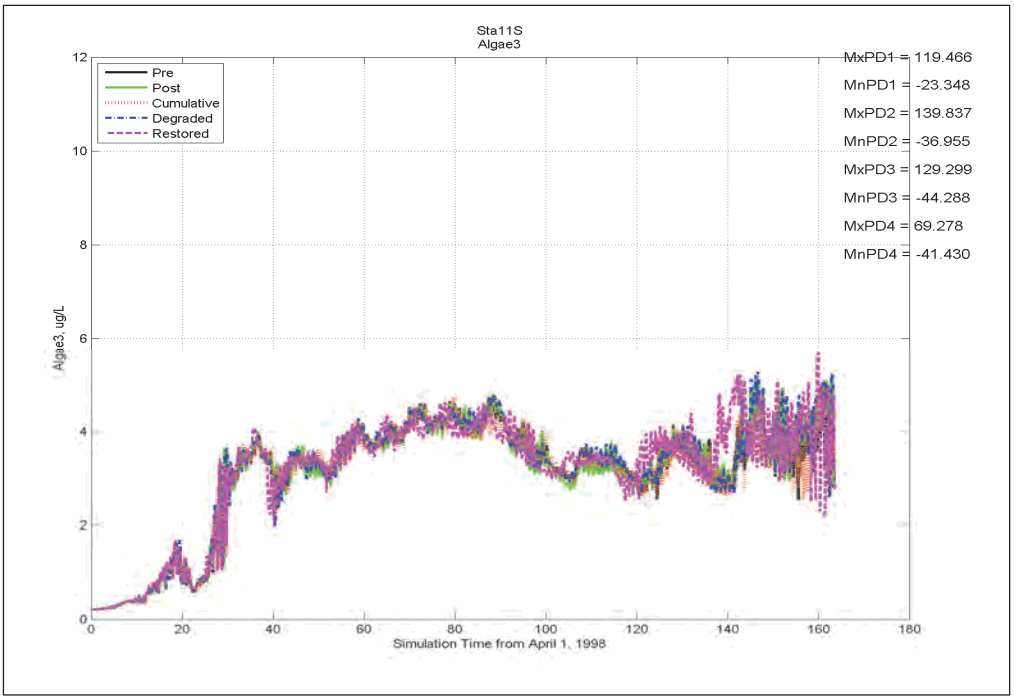

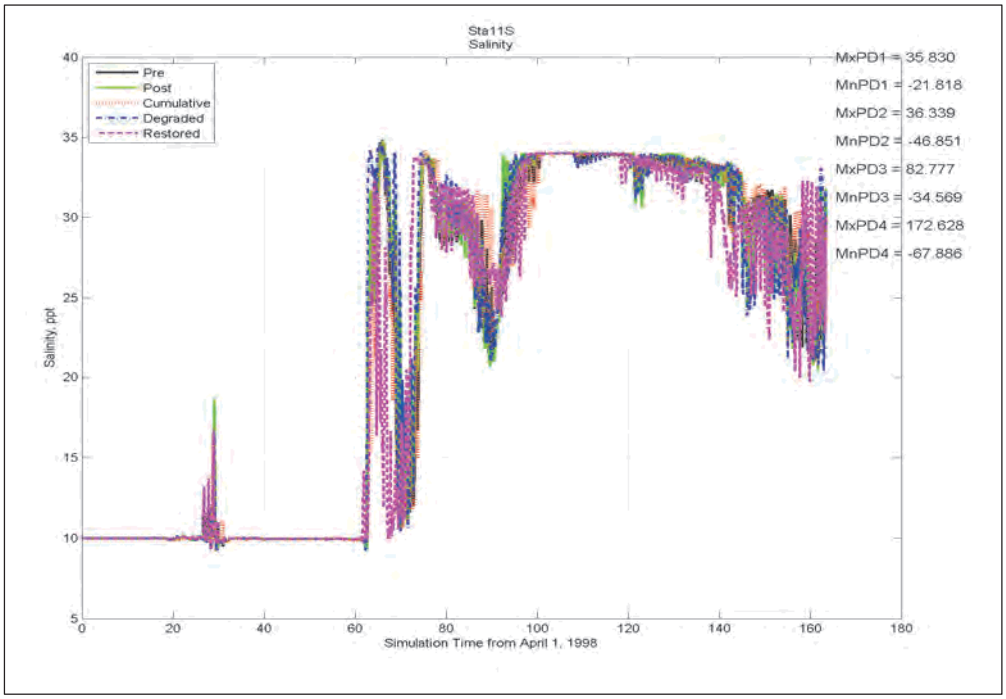

Figure E-69. Comparison of DO, Chlorophyll, and Salinity at Station 12 (Figure 5-8) for results from simulations representing Pre, Post, Restored, Degraded, and Cumulative conditions (continued).

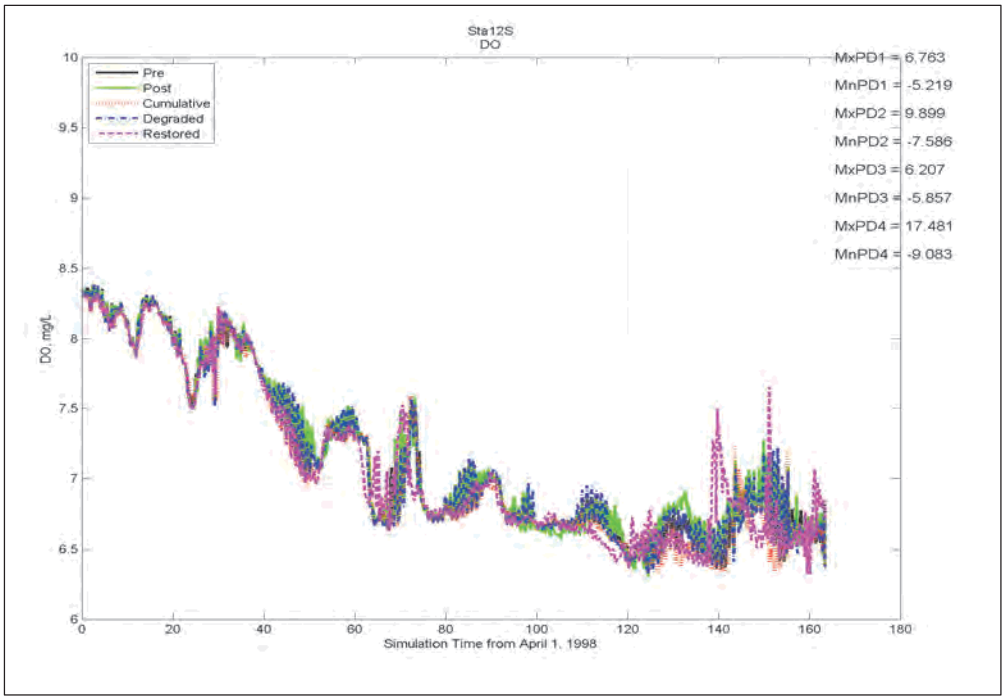

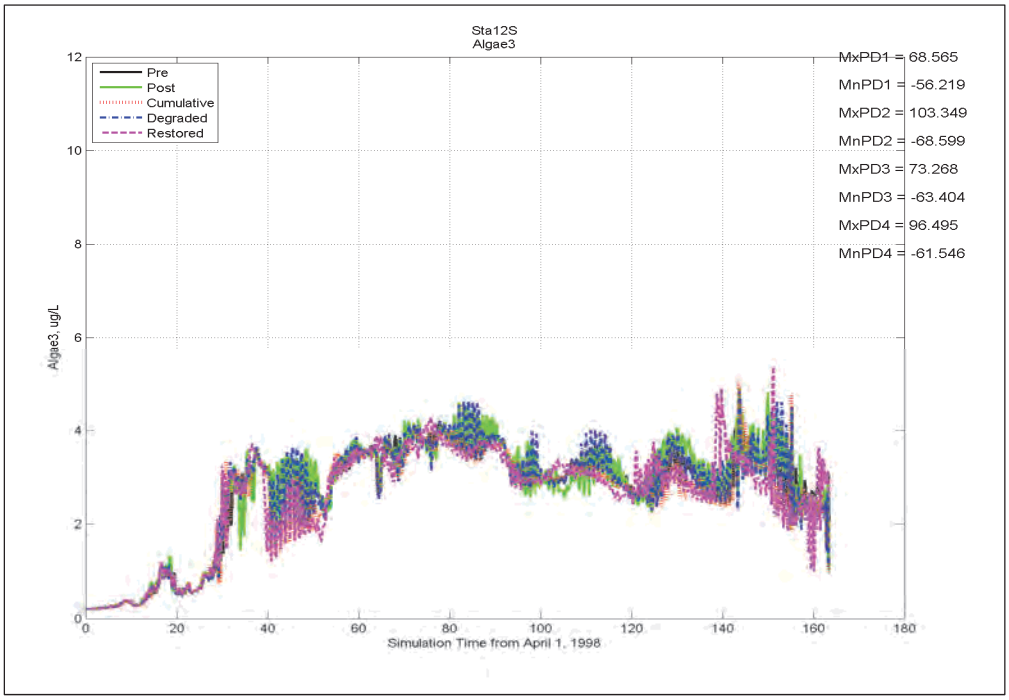

Figure E-69. Concluded.

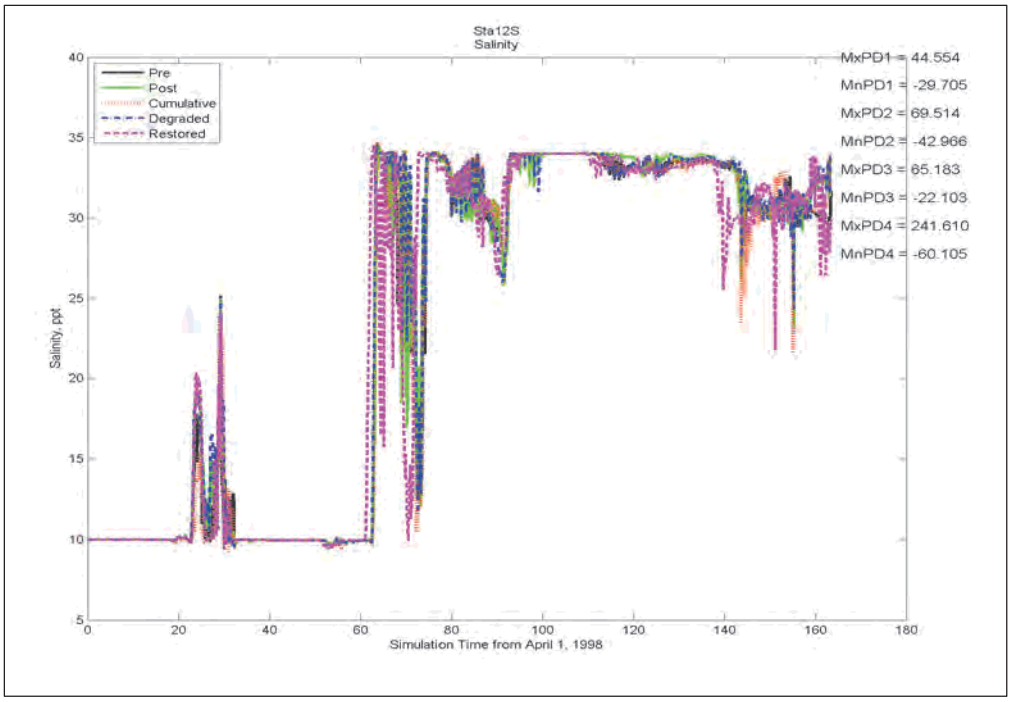

Figure E-70. Comparison of DO, Chlororphyll, and Salinity at Station 13 (Figure 5-8) for results from simulations representing Pre, Post, Restored, Degraded, and Cumulative conditions (continued).

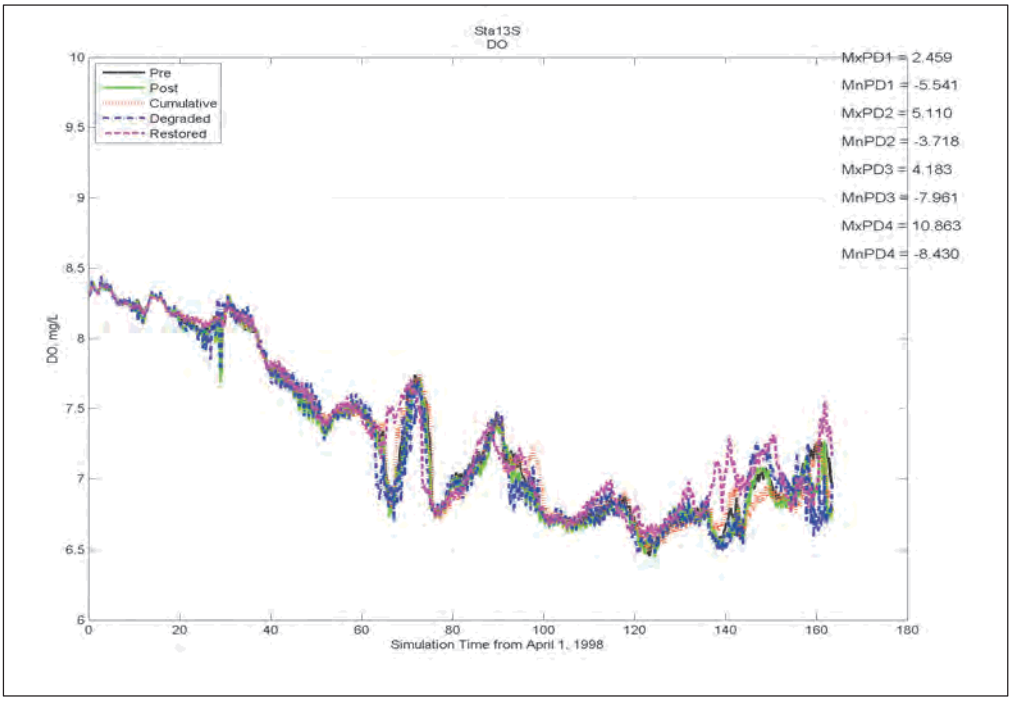

Figure E-70 Concluded.

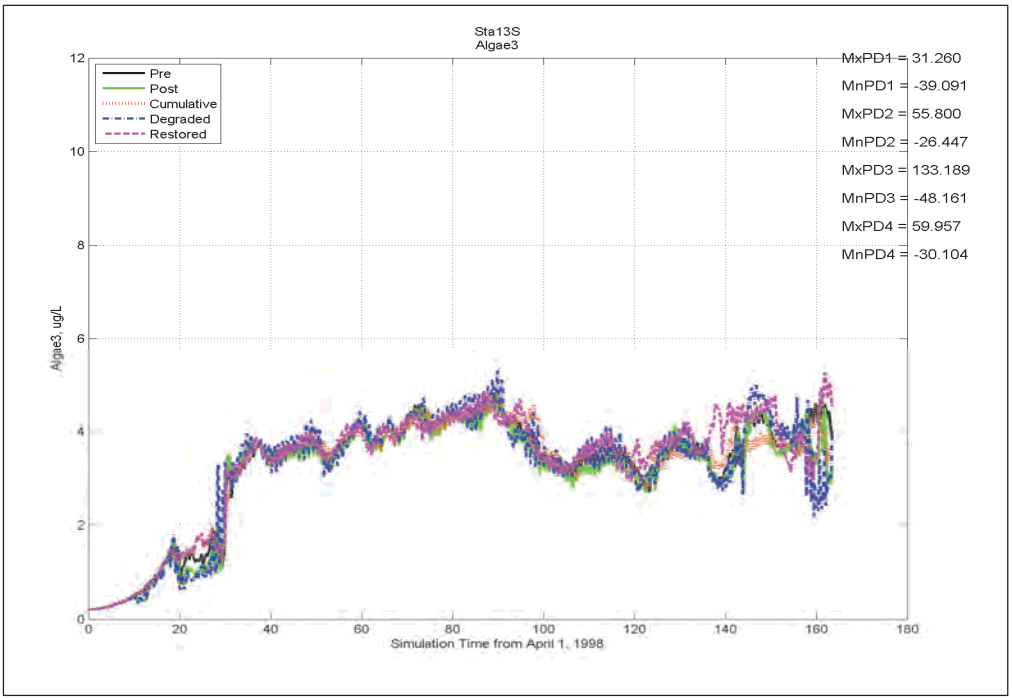

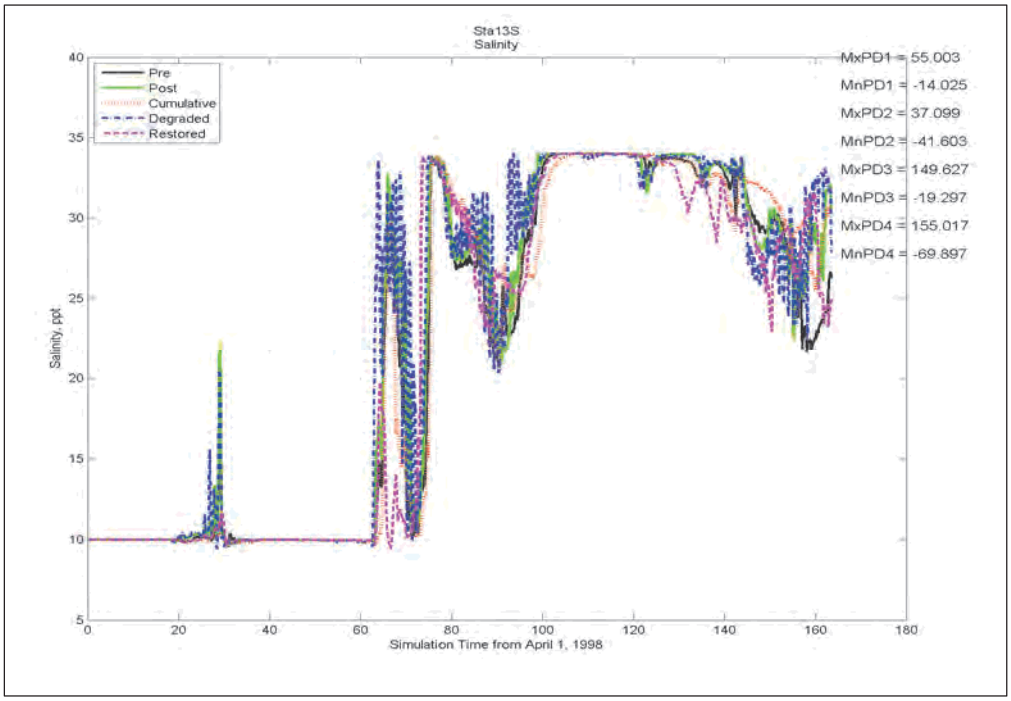

Figure E-71. Comparison of DO, Chlororphyll, and Salinity at Station 14 (Figure 5-8) for results from simulations representing Pre, Post, Restored, Degraded, and Cumulative conditions (continued).

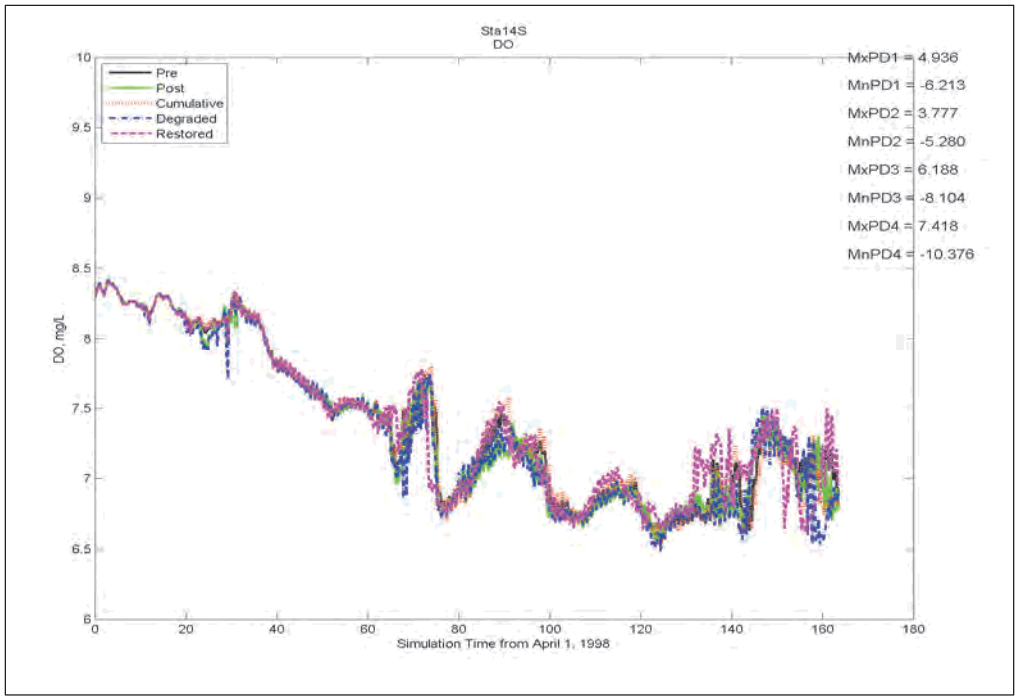

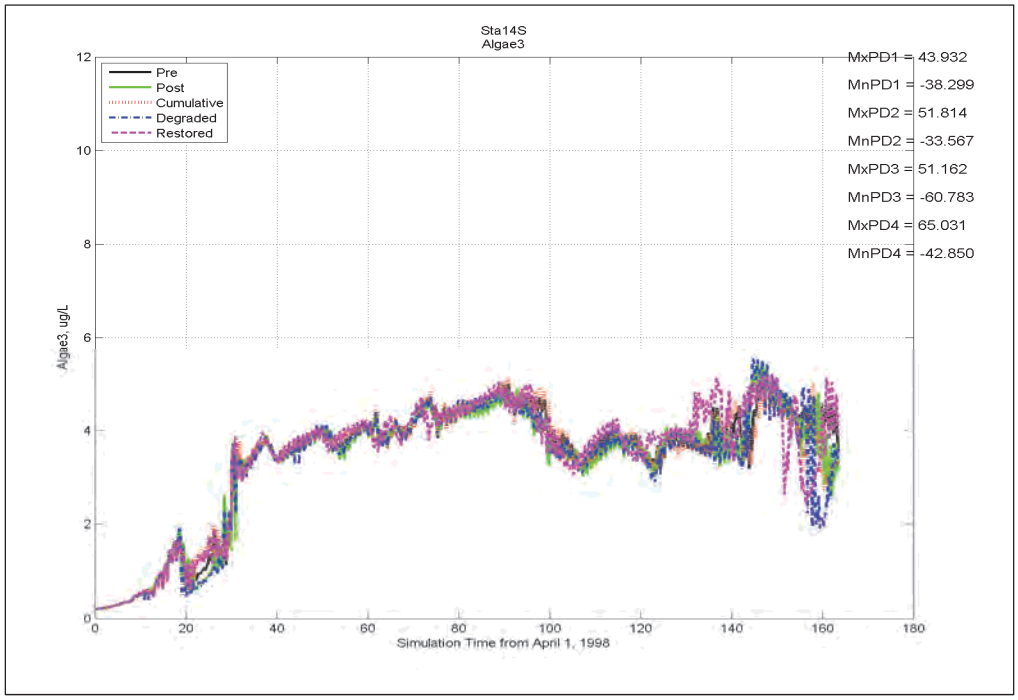

Figure E-71. Concluded.

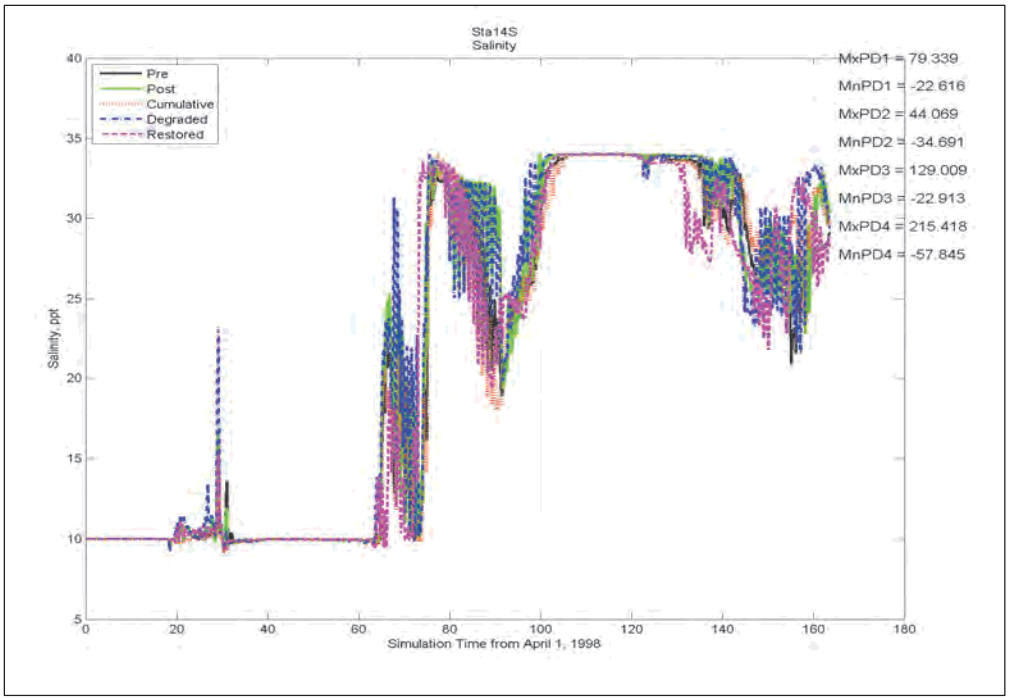

Figure E-72. Comparison of DO, Chlororphyll, and Salinity at Station 15 (Figure 5-8) for results from simulations representing Pre, Post, Restored, Degraded, and Cumulative conditions (continued).

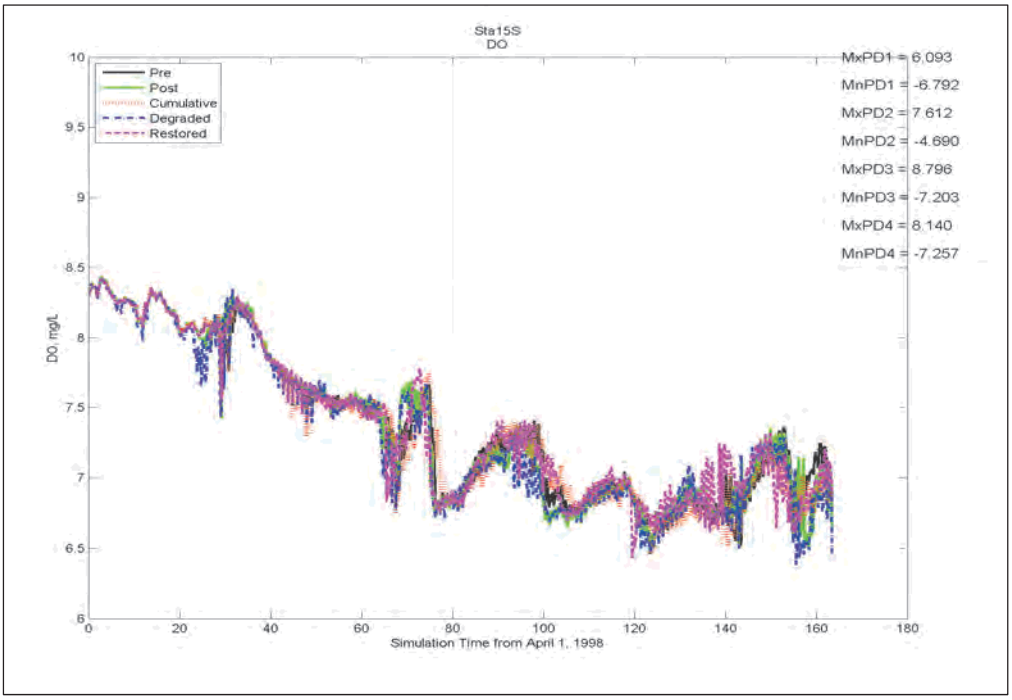

Figure E-72. Concluded.

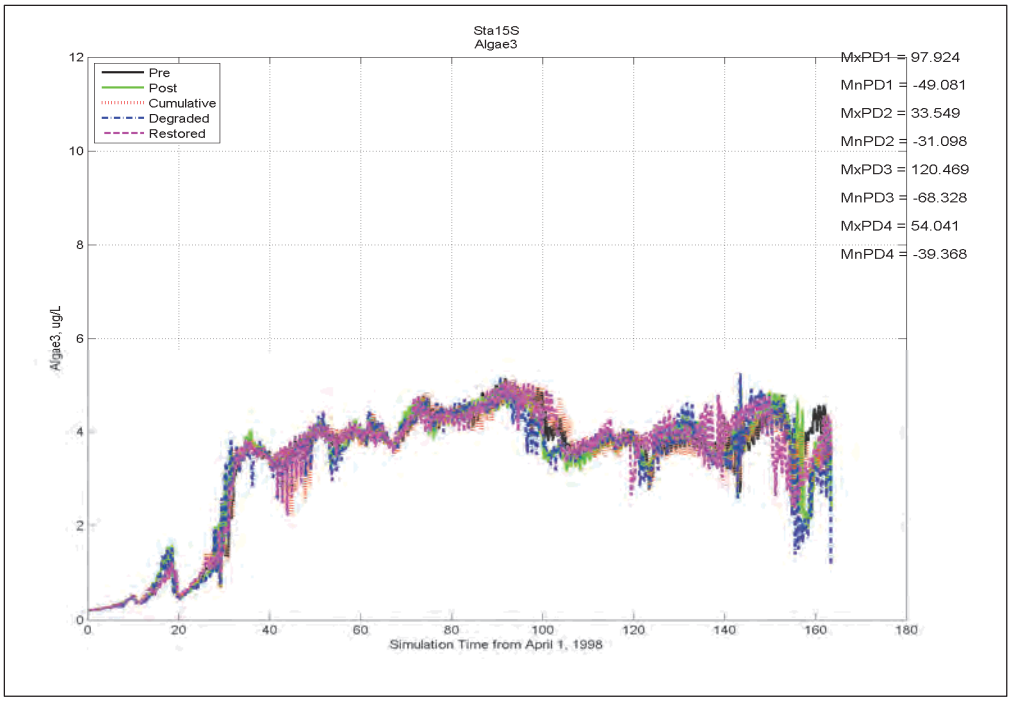

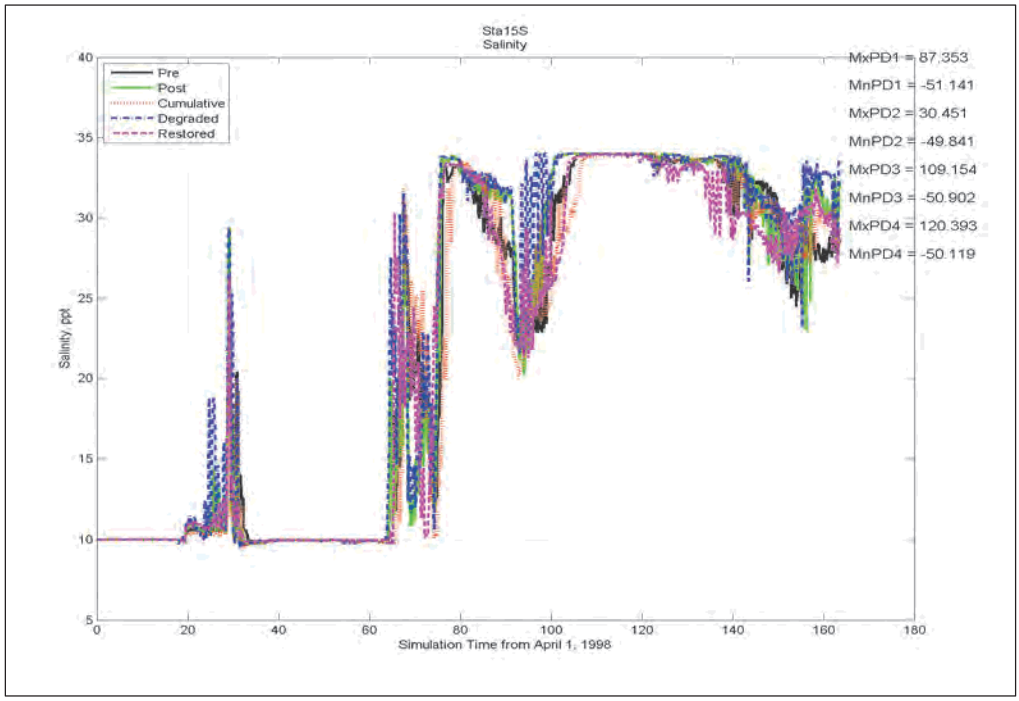

Figure E-73. Comparison of DO, Chlorophyll, and Salinity at Station 16 (Figure 5-8) for results from simulations representing Pre, Post, Restored, Degraded, and Cumulative conditions (continued).

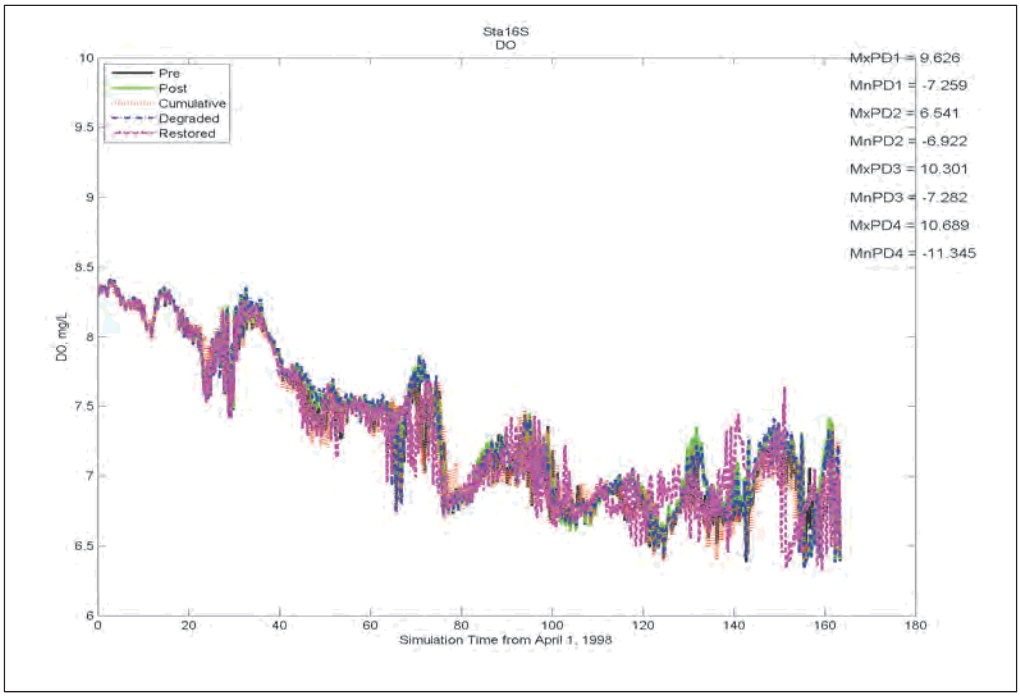

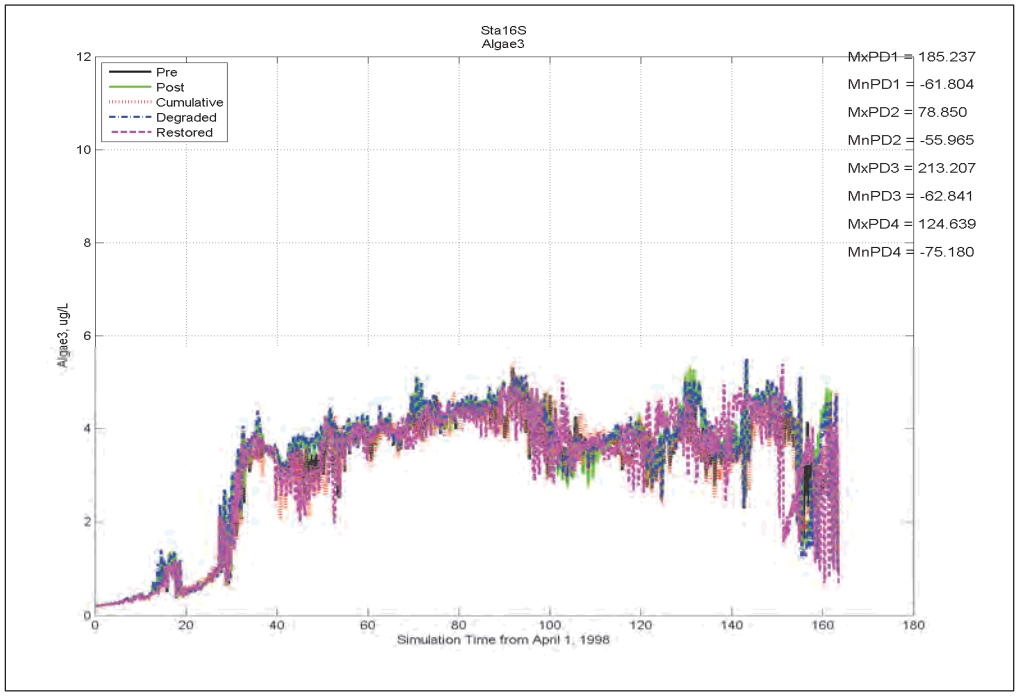

Figure E-73. Concluded.

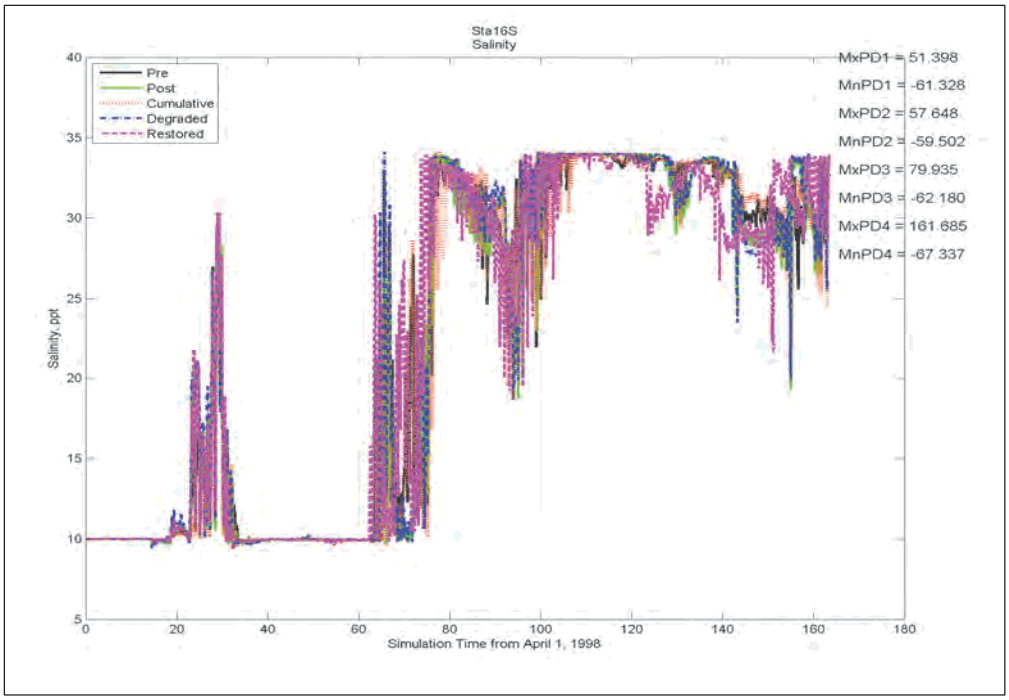

Appendix F: ADCIRC-Simulated Maximum Surge Envelopes

Figure F-1. Maximum surge envelope for Storm 028, Post-Katrina condition.

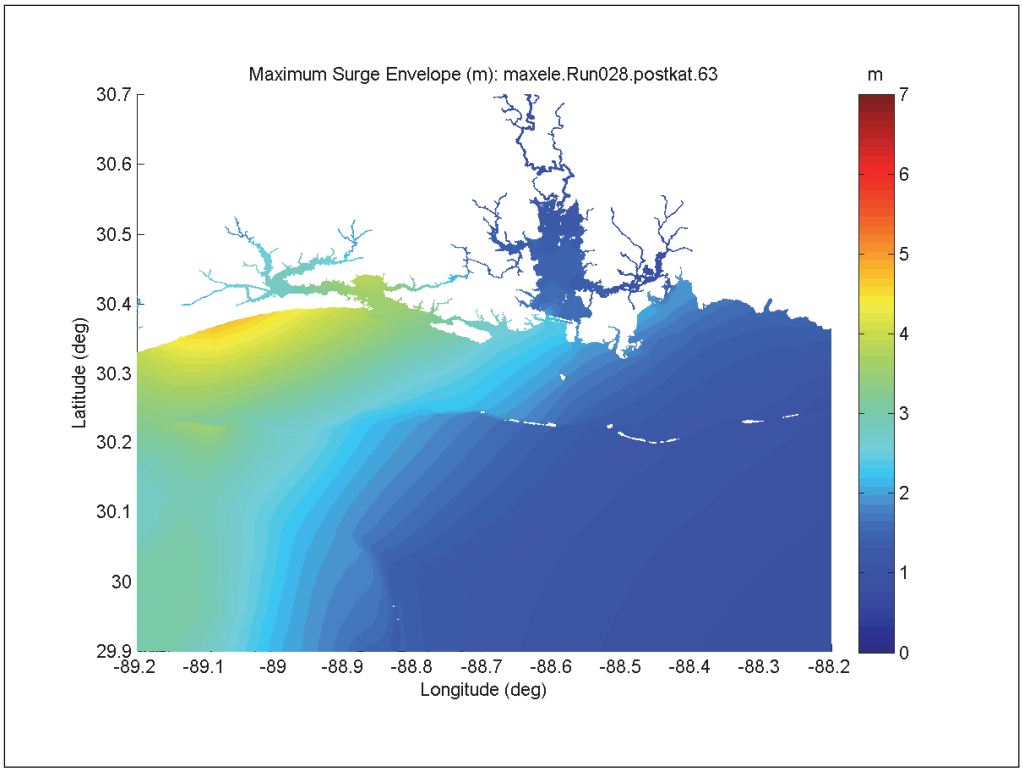

Figure F-2. Maximum surge envelope for Storm 028, Degraded condition.

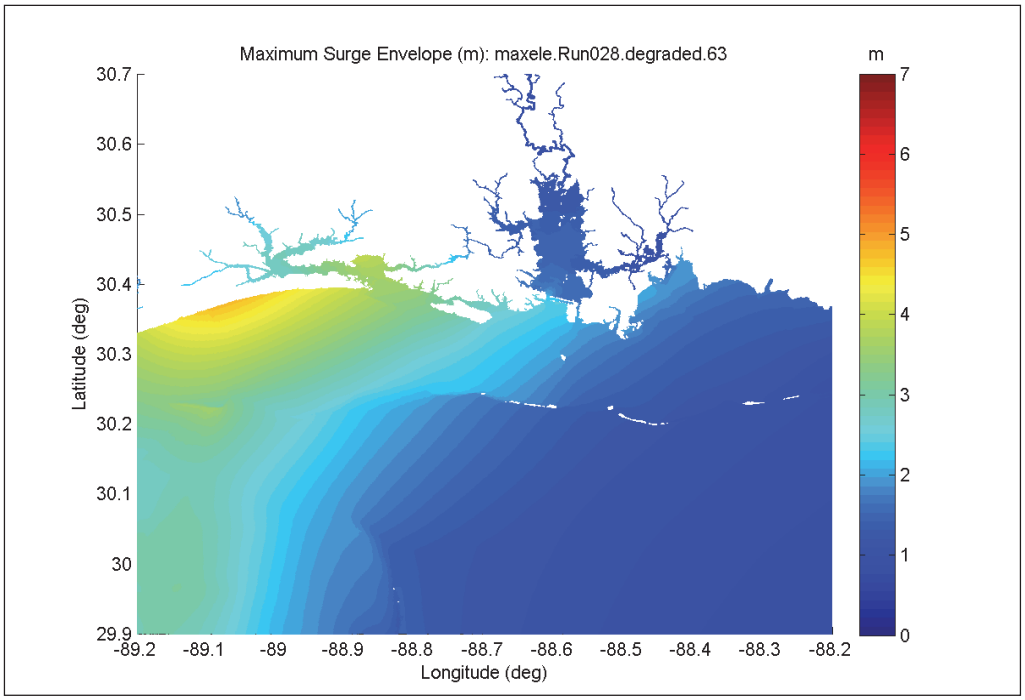

Figure F-3. Maximum surge envelope for Storm 028, Restored condition.

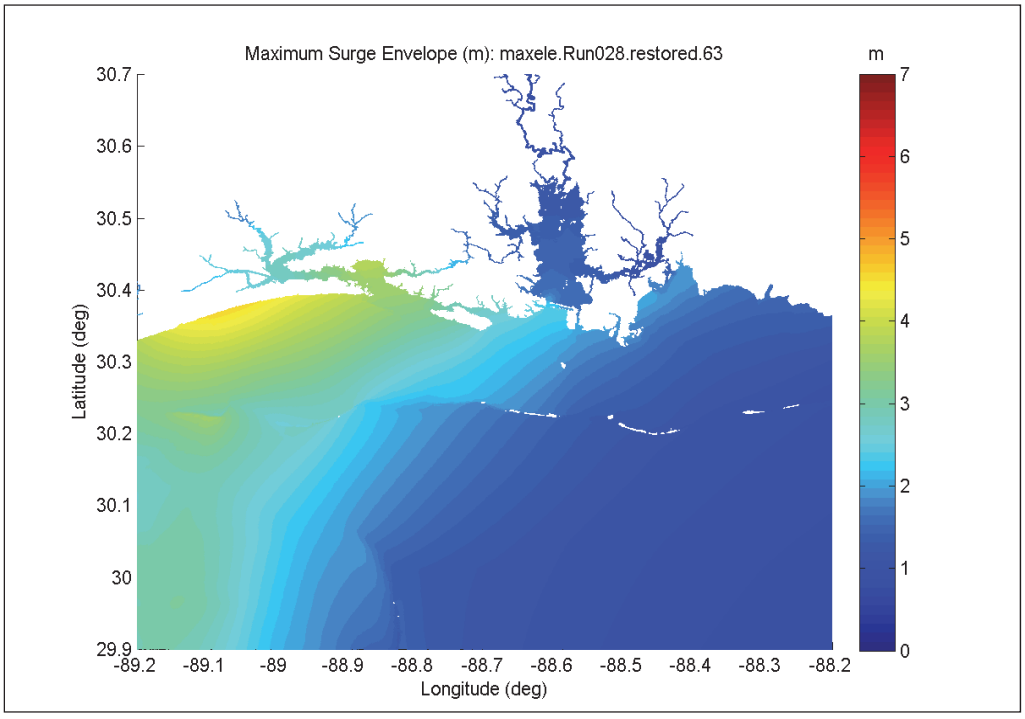

Figure F-4. Maximum surge envelope for Storm 028, Cumulative condition.

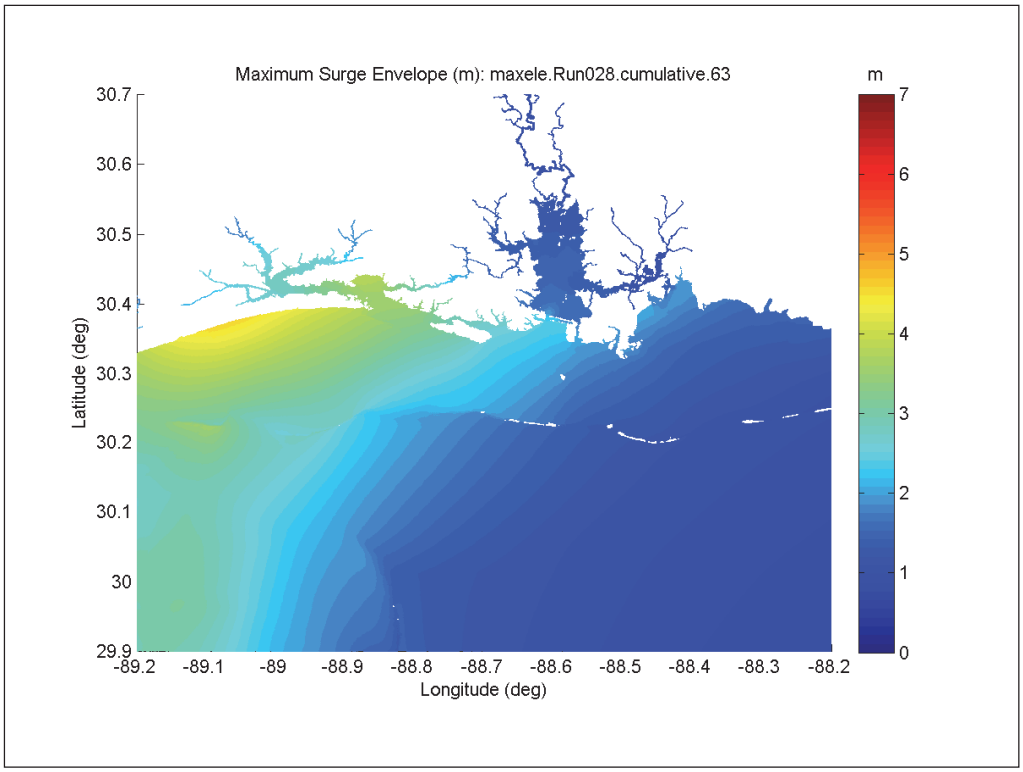

Figure F-5. Maximum surge envelope for Storm 032, Post-Katrina condition.

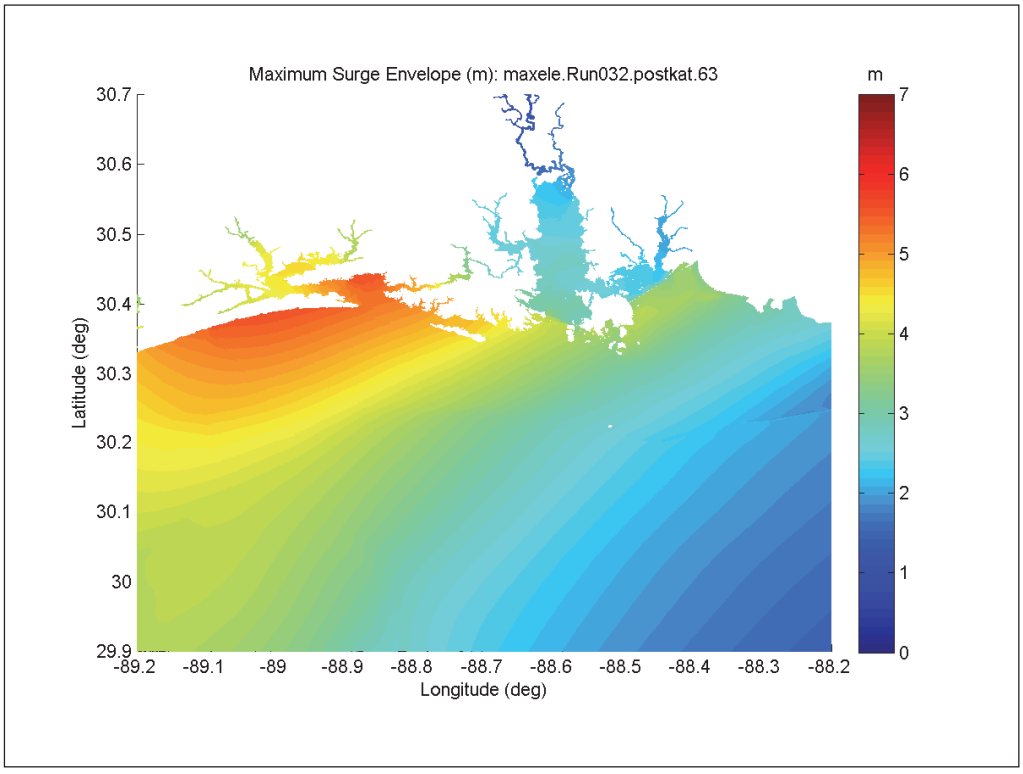

Figure F-6. Maximum surge envelope for Storm 032, Degraded condition.

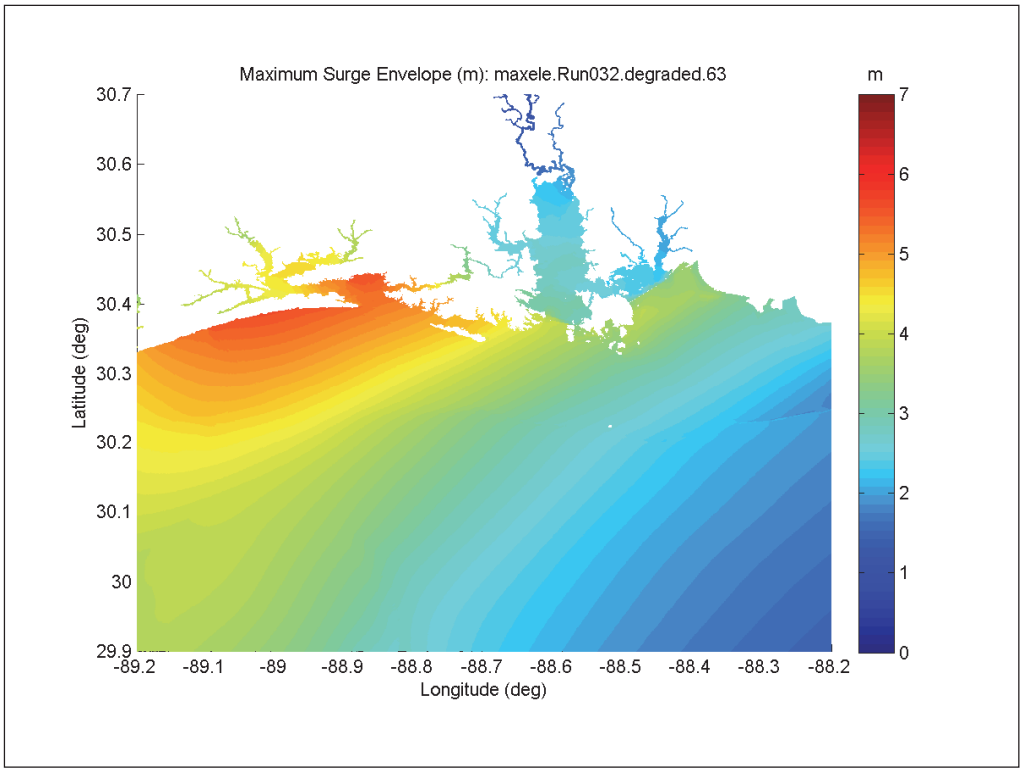

Figure F-7. Maximum surge envelope for Storm 032, Restored condition.

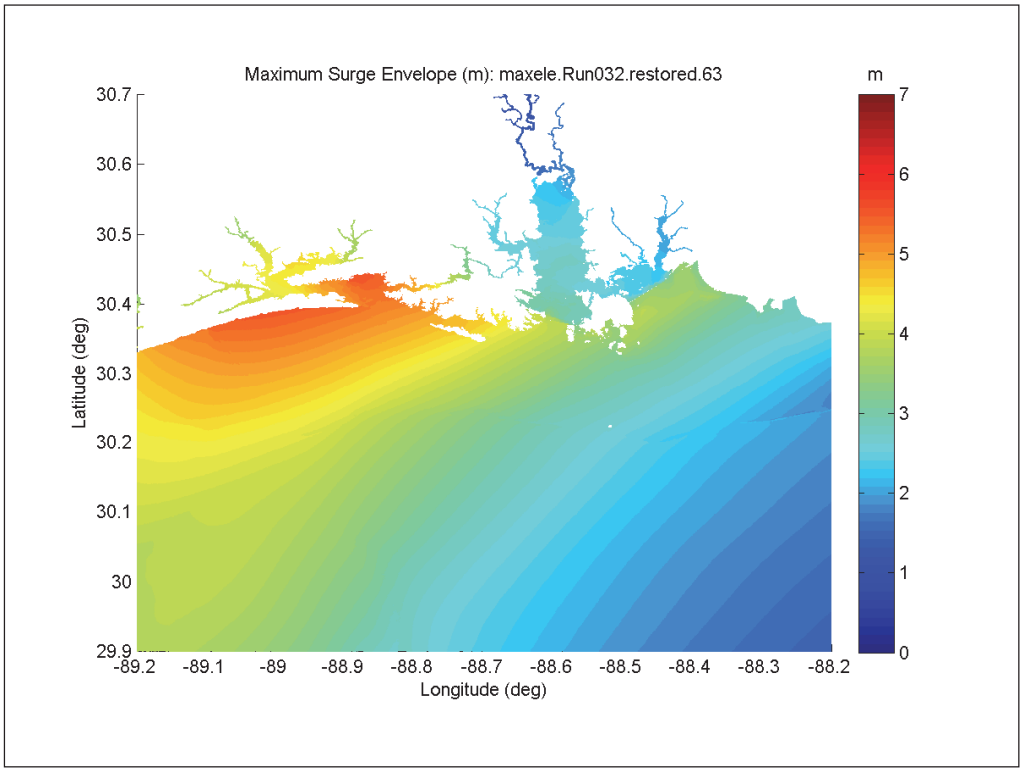

Figure F-8. Maximum surge envelope for Storm 032, Cumulative condition.

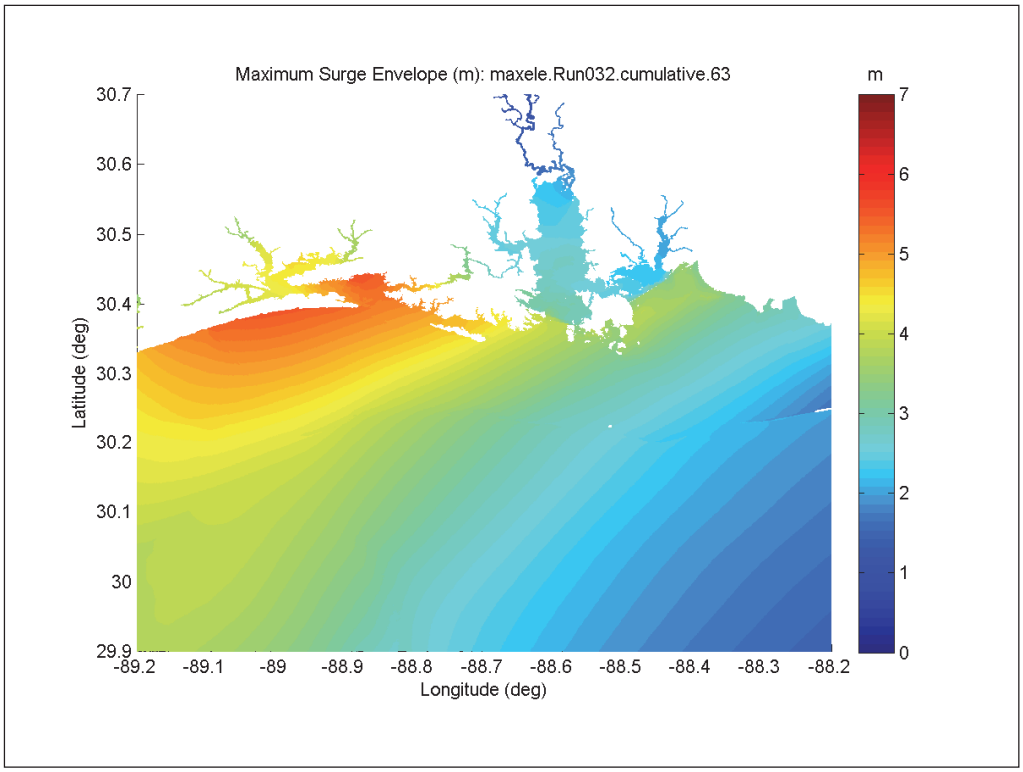

Figure F-9. Maximum surge envelope for Storm 034, Post-Katrina condition.

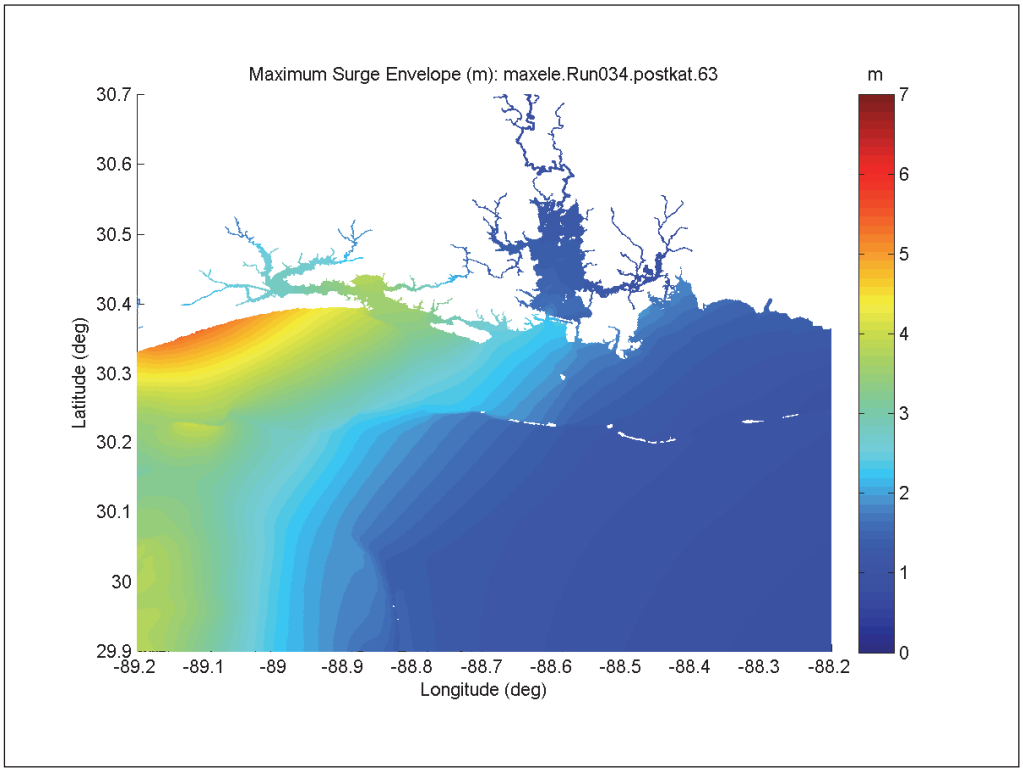

Figure F-10. Maximum surge envelope for Storm 034, Degraded condition.

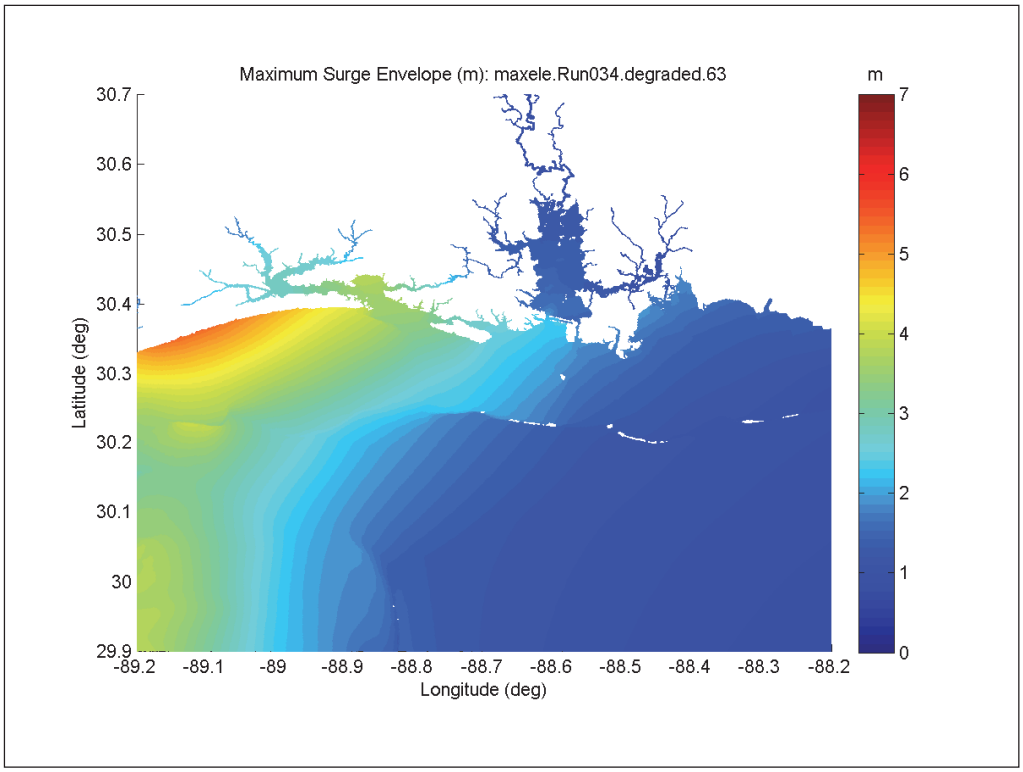

Figure F-11. Maximum surge envelope for Storm 034, Restored condition.

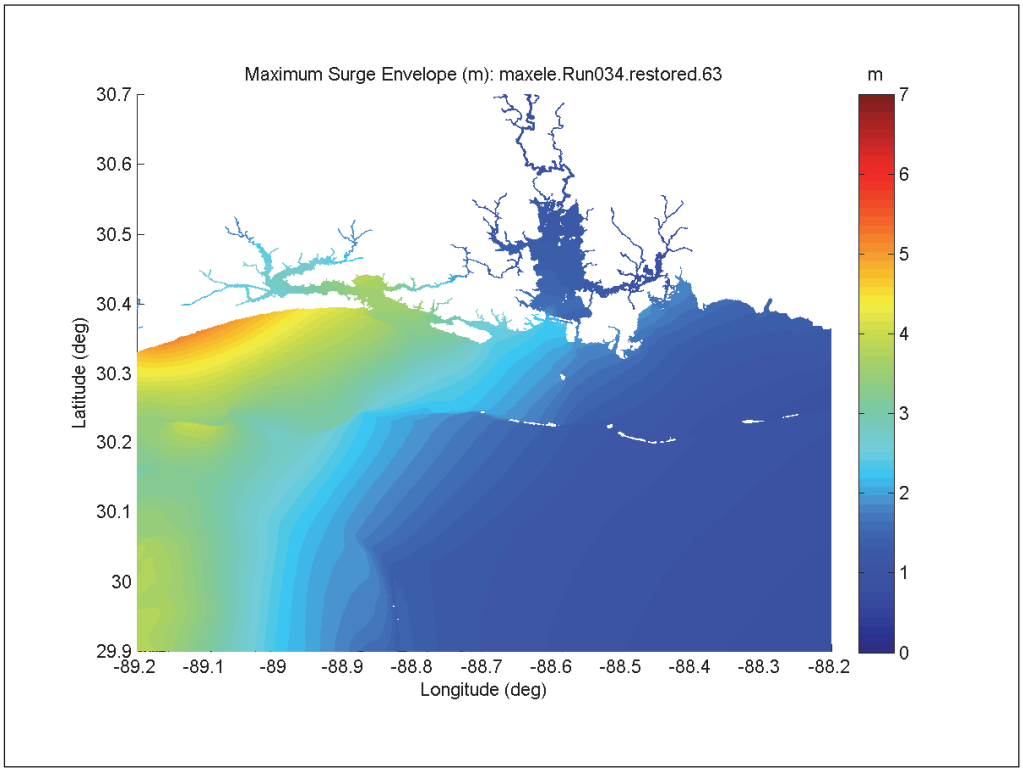

Figure F-12. Maximum surge envelope for Storm 034, Cumulative condition.

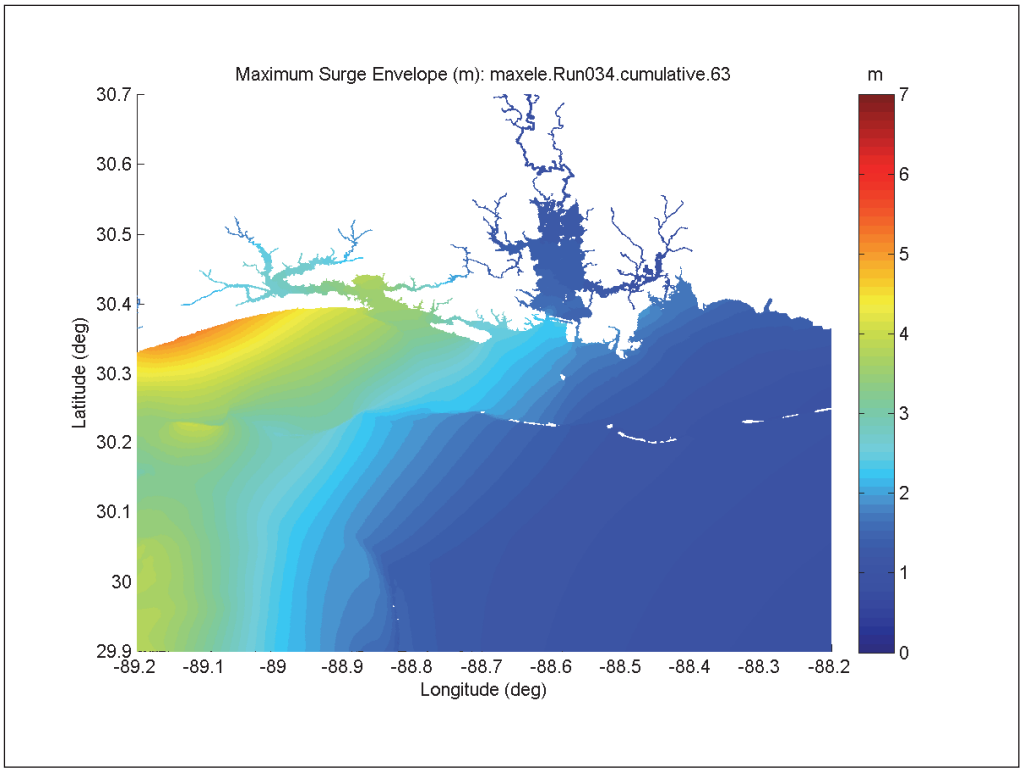

Figure F-13. Maximum surge envelope for Storm 059, Post-Katrina condition.

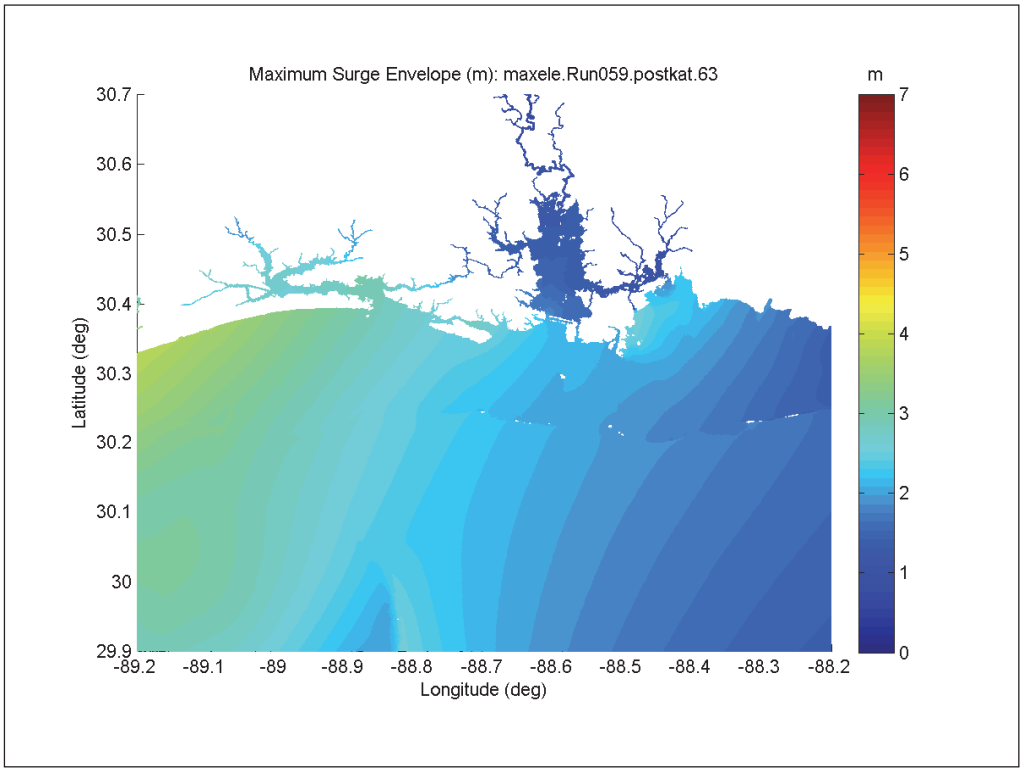

Figure F-14. Maximum surge envelope for Storm 059, Degraded condition.

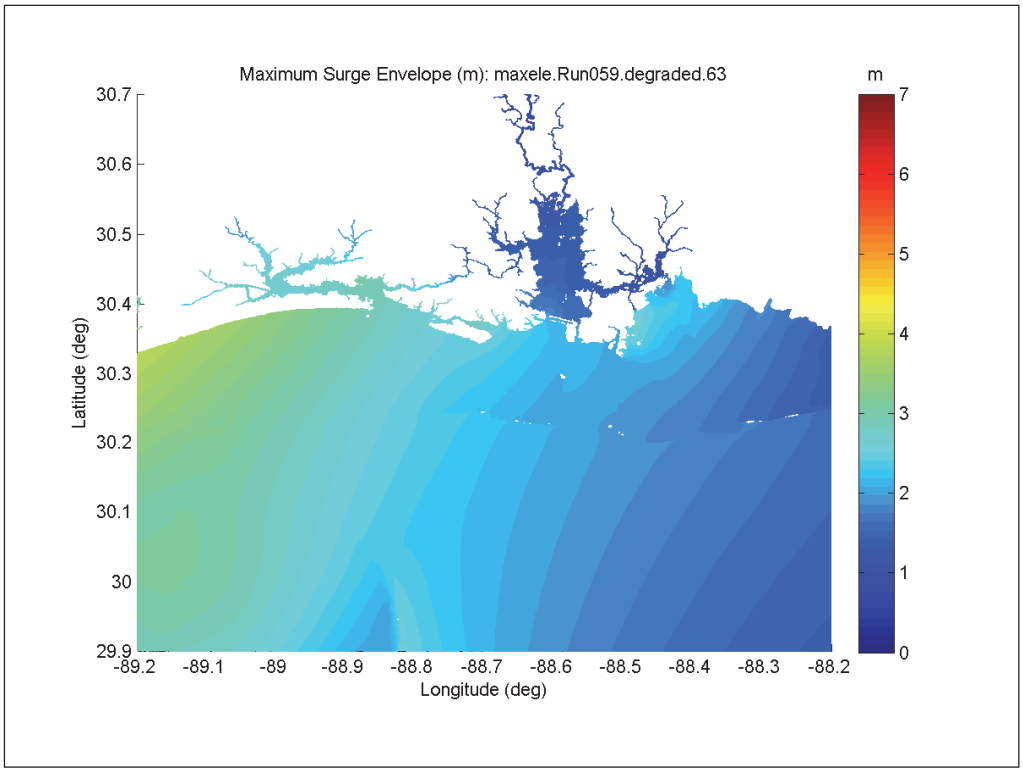

Figure F-15. Maximum surge Envelope for Storm 059, Restored condition.

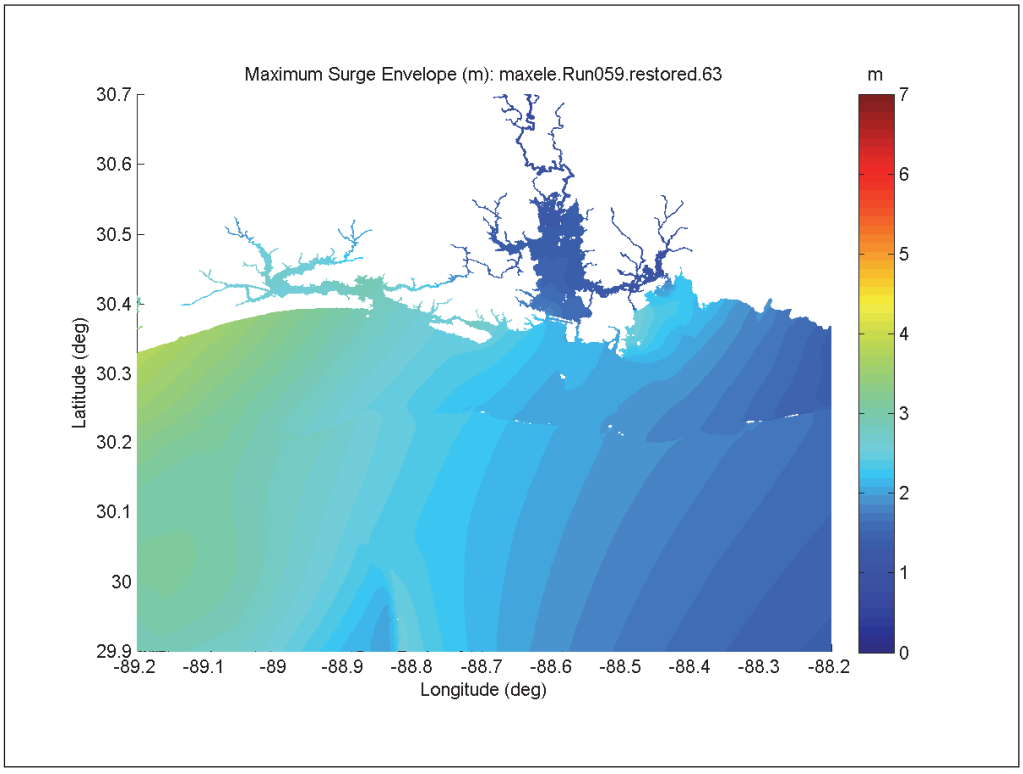

Figure F-16. Maximum surge envelope for Storm 059, Cumulative condition.

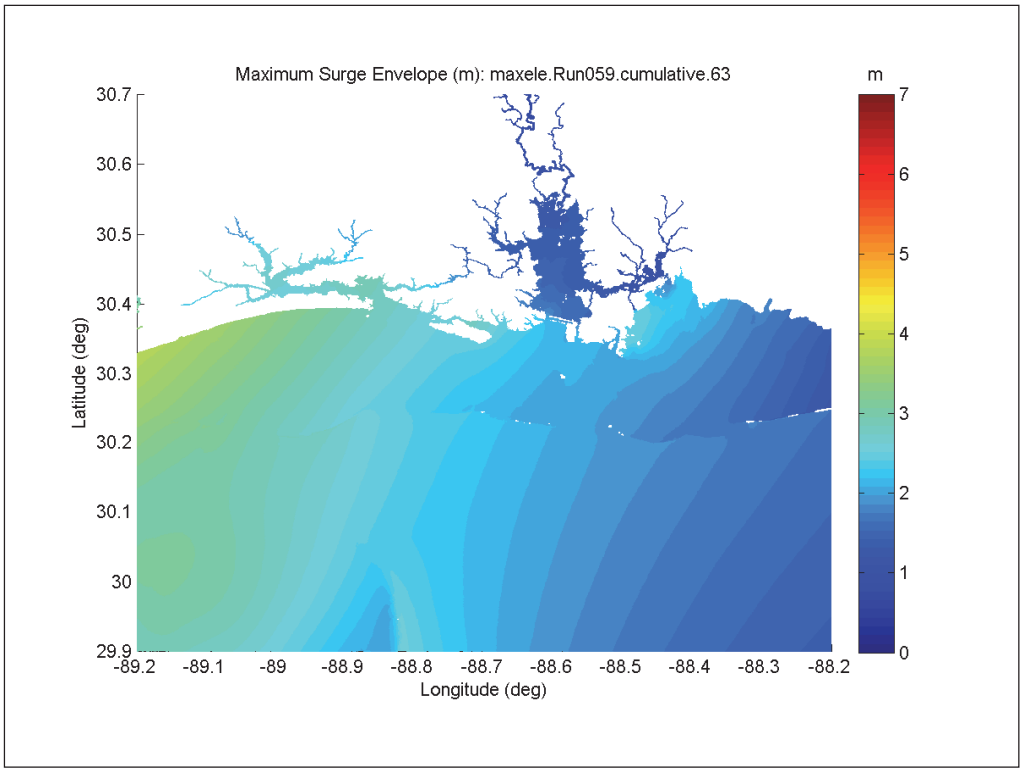

Figure F-17. Maximum surge envelope for Storm 060, Post-Katrina condition.

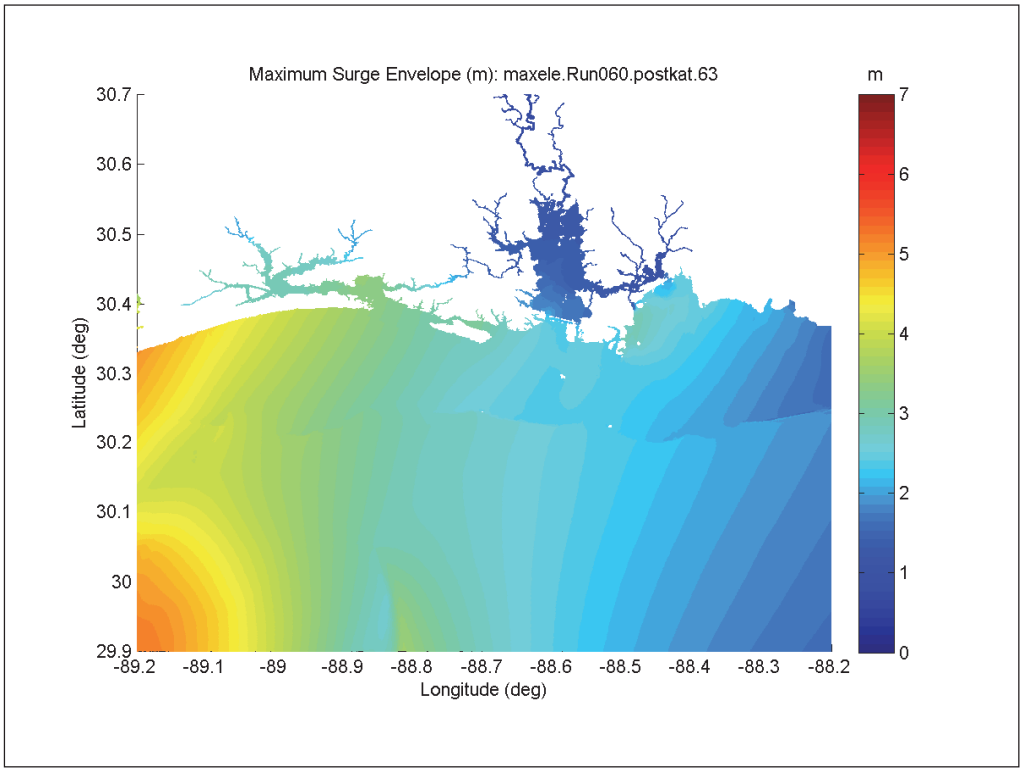

Figure F-18. Maximum surge envelope for Storm 060, Degraded condition.

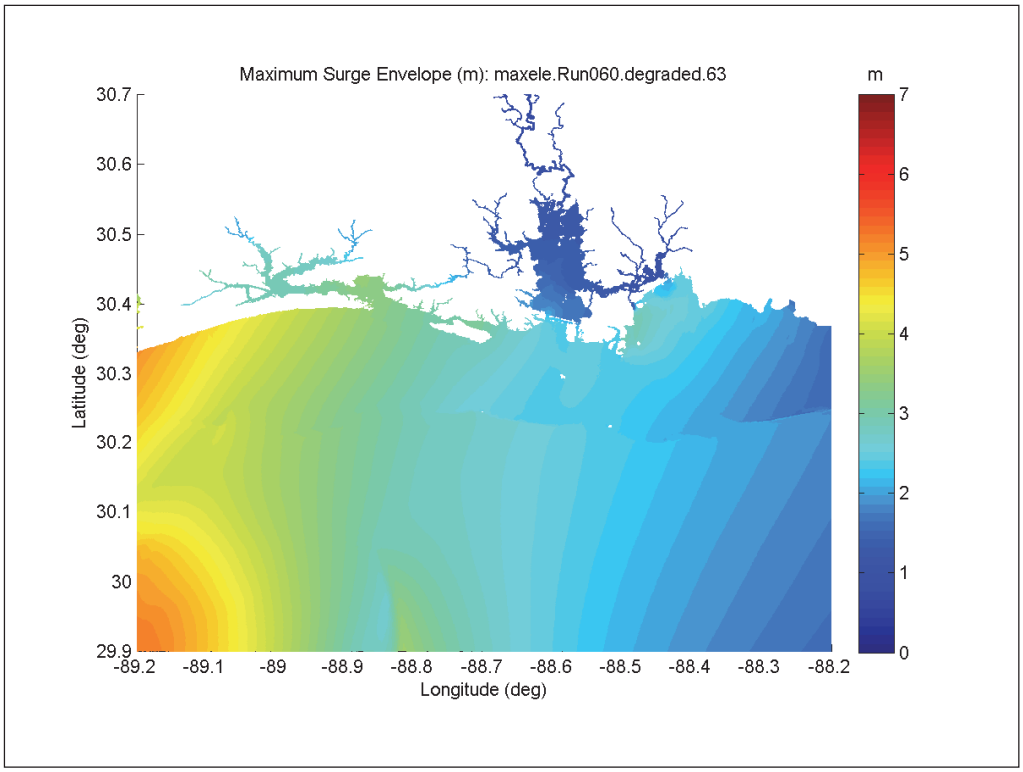

Figure F-19. Maximum surge envelope for Storm 060, Restored condition.

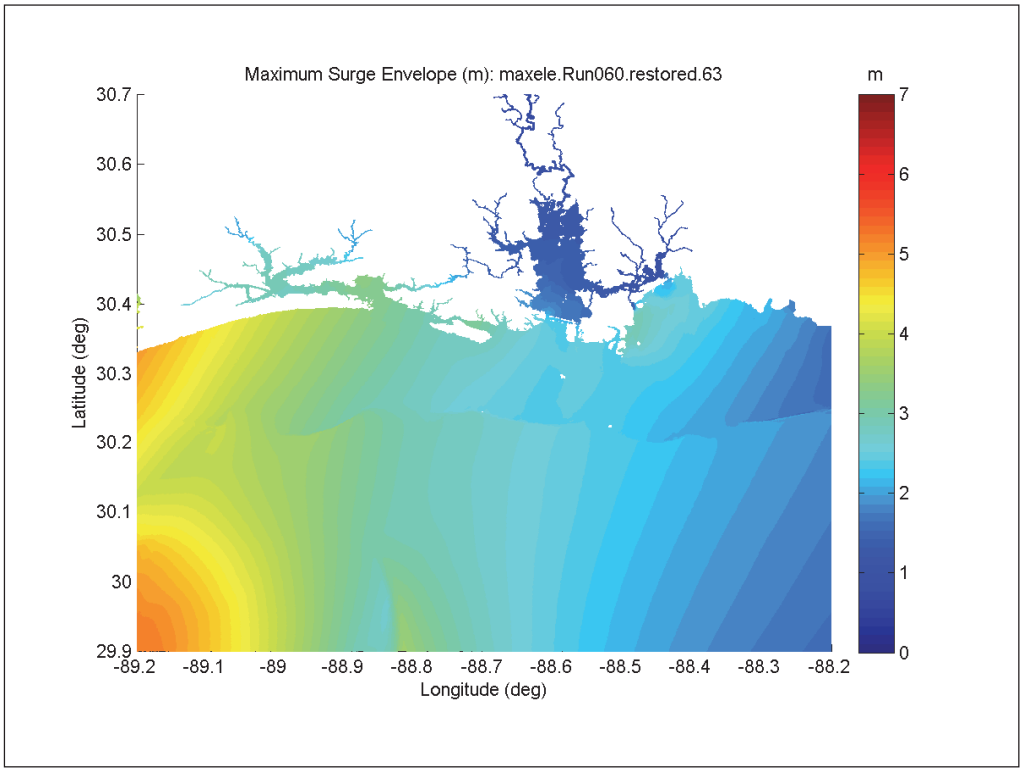

Figure F-20. Maximum surge envelope for Storm 060, Cumulative condition.

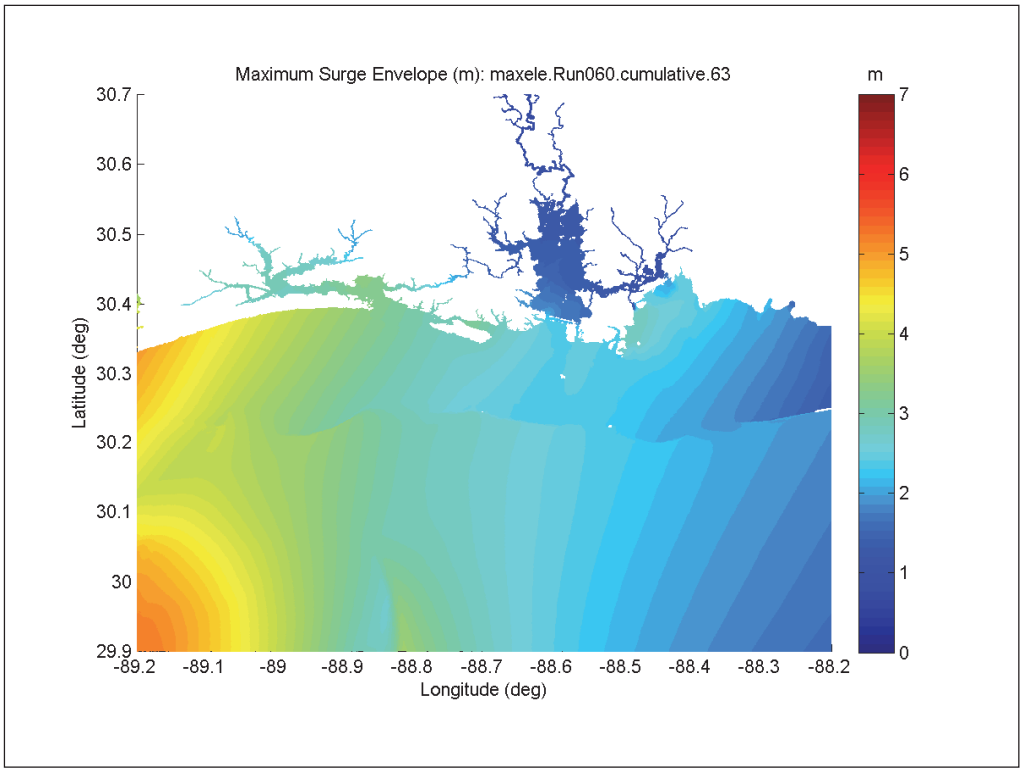

Figure F-21. Maximum surge envelope for Storm 088, Post-Katrina condition.

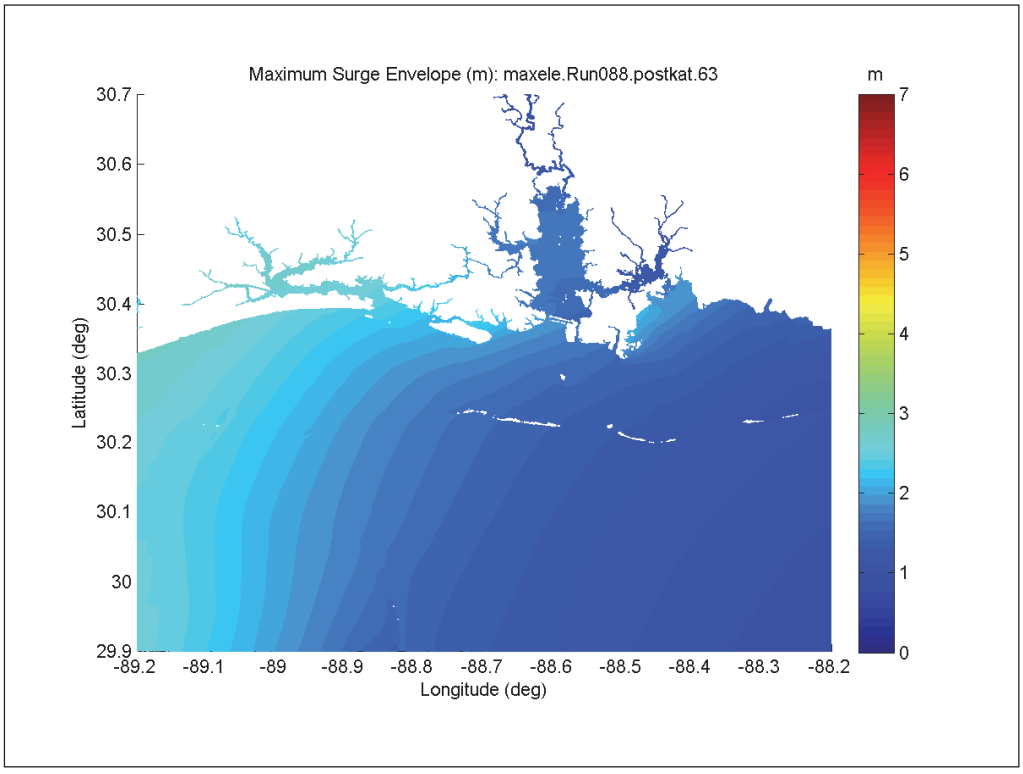

Figure F-22. Maximum surge envelope for Storm 088, Degraded condition.

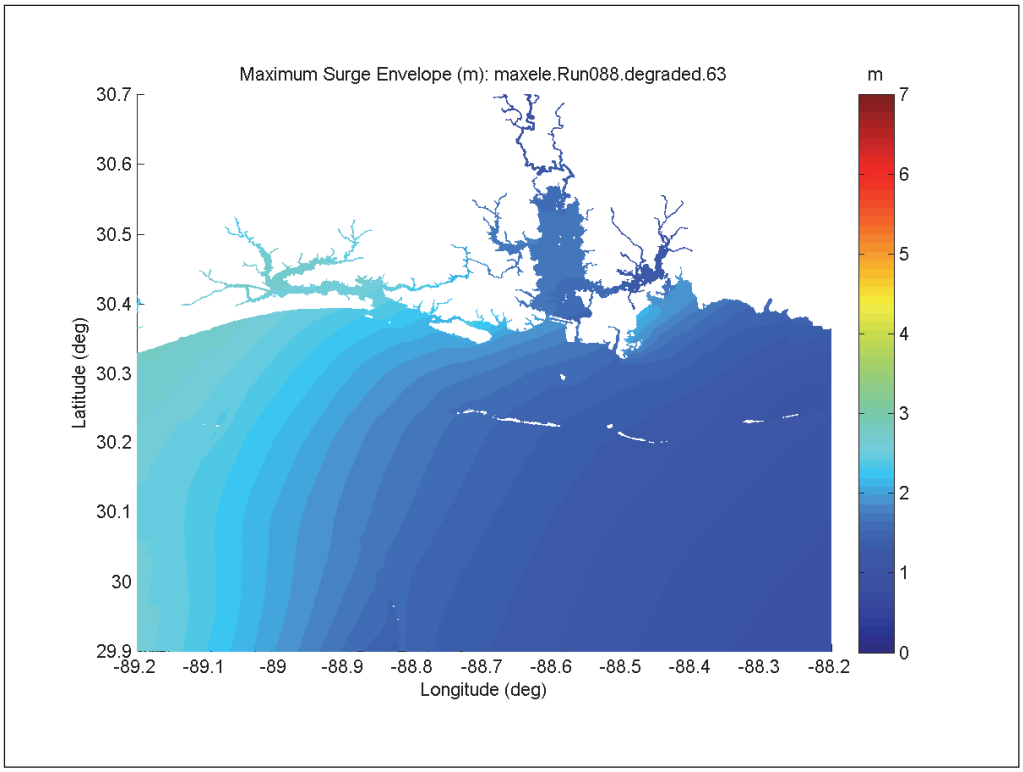

Figure F-23. Maximum surge envelope for Storm 088, Restored condition.

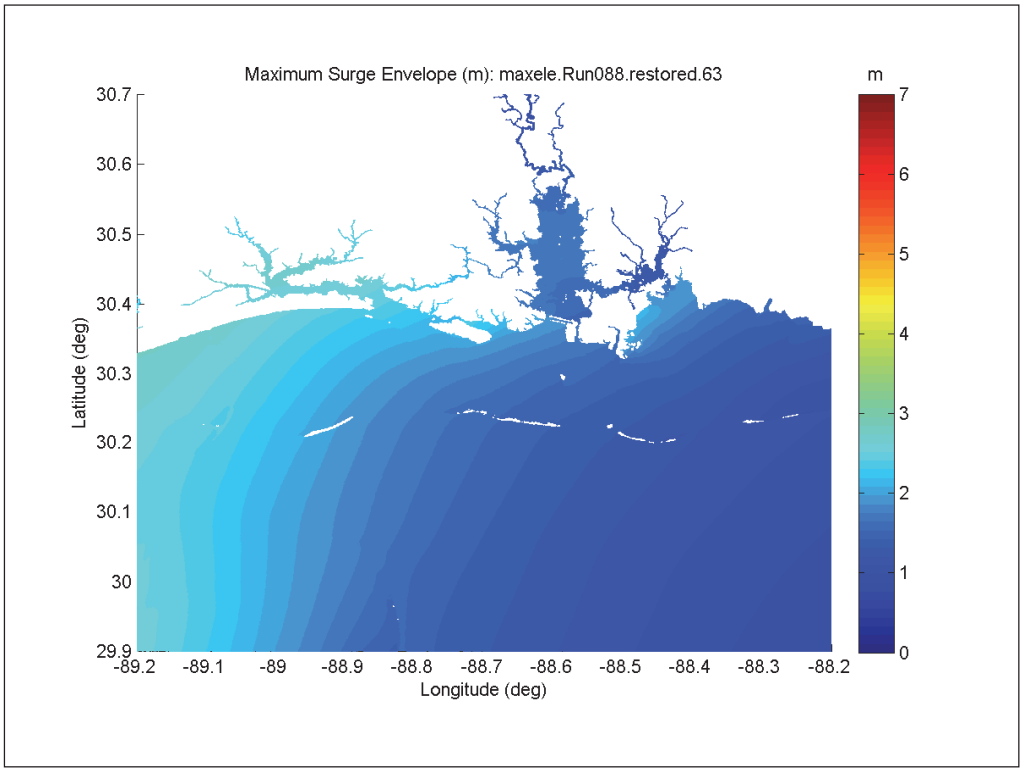

Figure F-24. Maximum surge envelope for Storm 088, Cumulative condition.

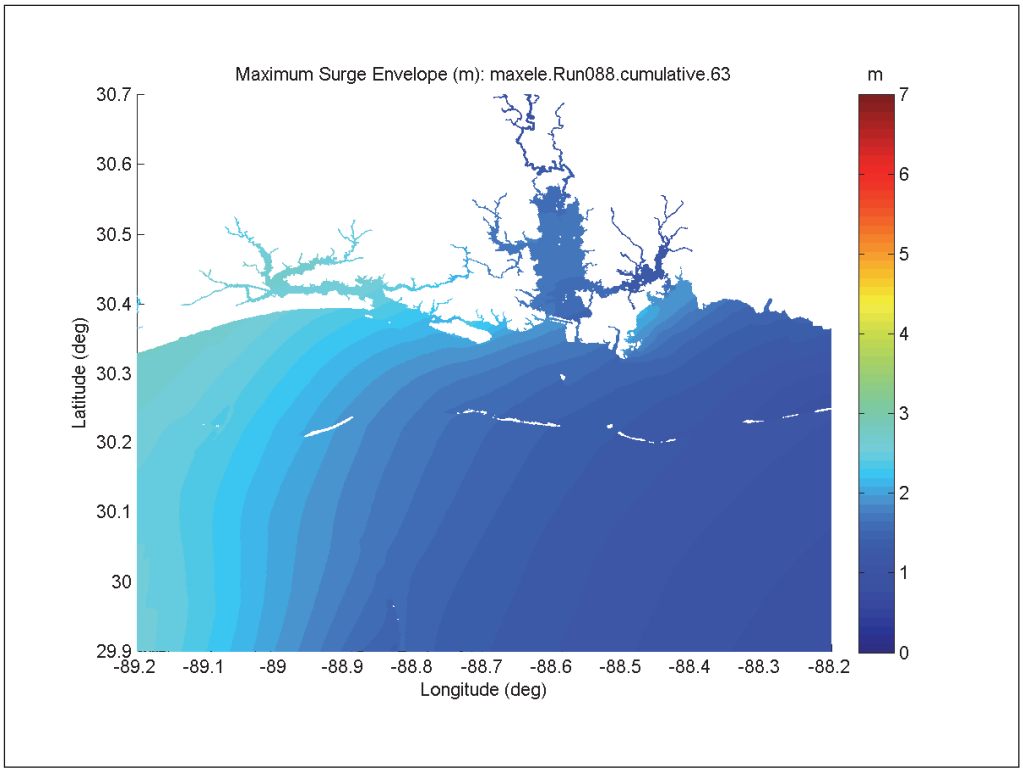

Figure F-25. Maximum surge envelope for Storm 089, Post-Katrina condition.

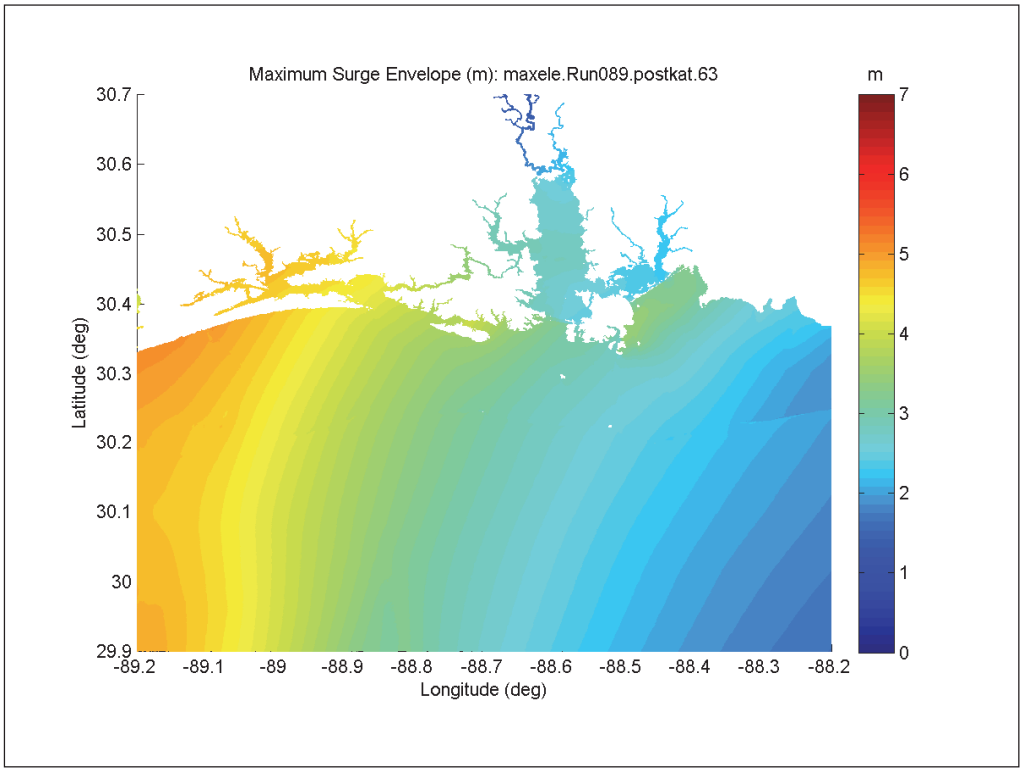

Figure F-26. Maximum surge envelope for Storm 089, Degraded condition.

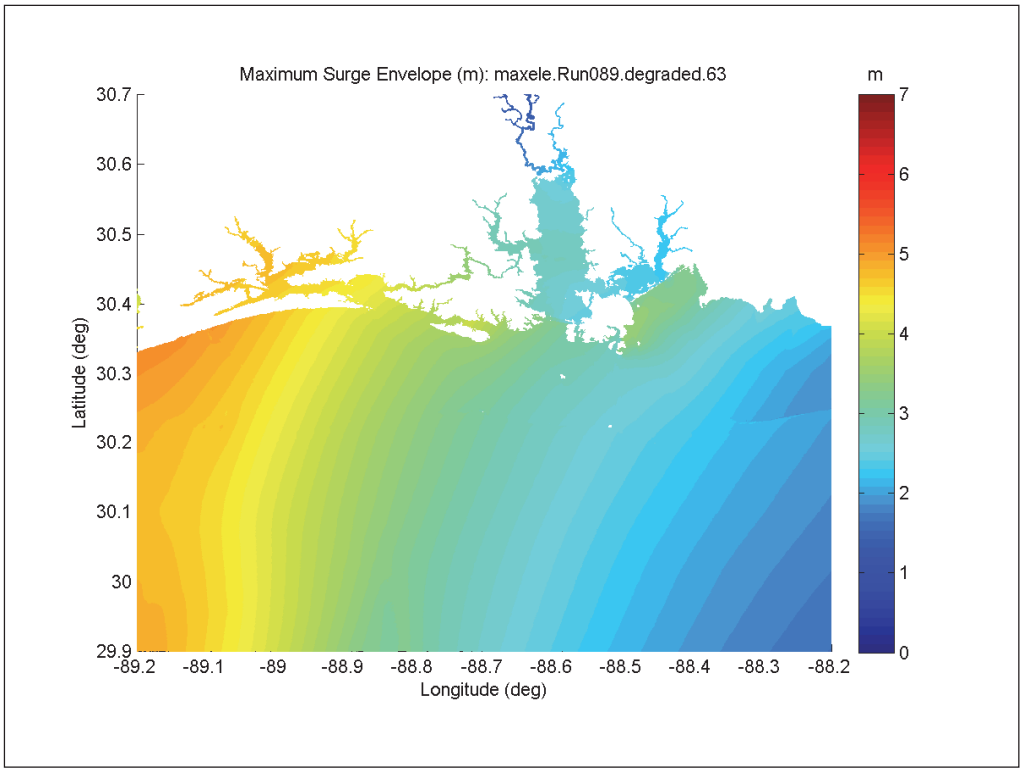

Figure F-27. Maximum surge envelope for Storm 089, Restored condition.

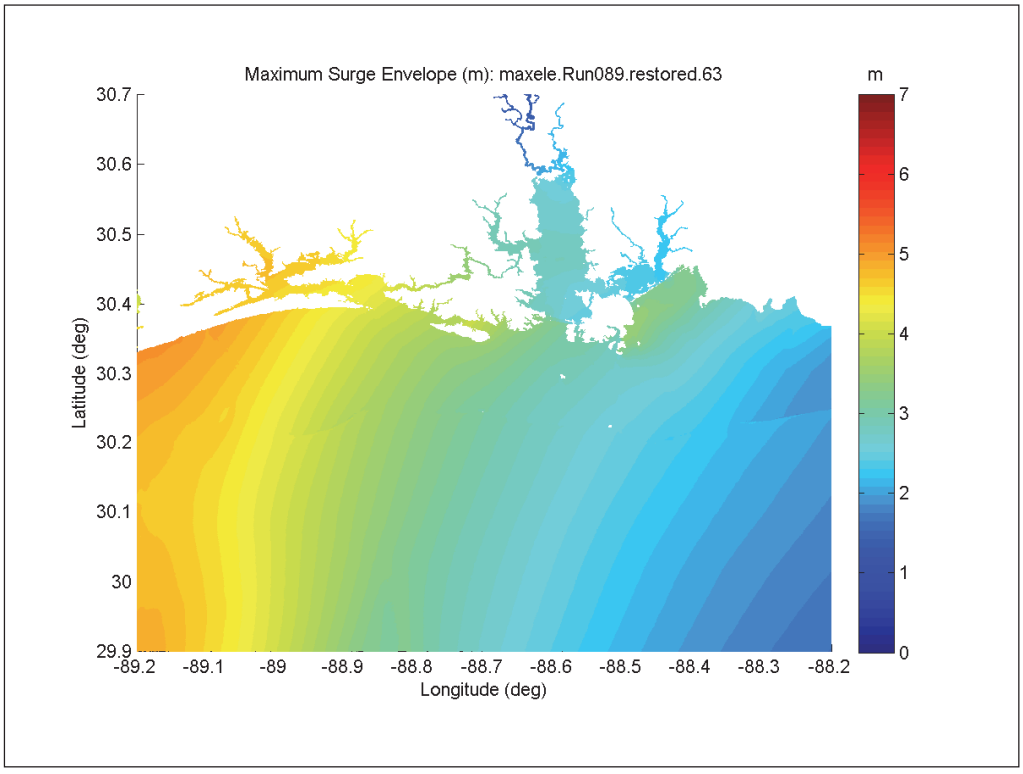

Figure F-28. Maximum surge envelope for Storm 089, Cumulative condition.

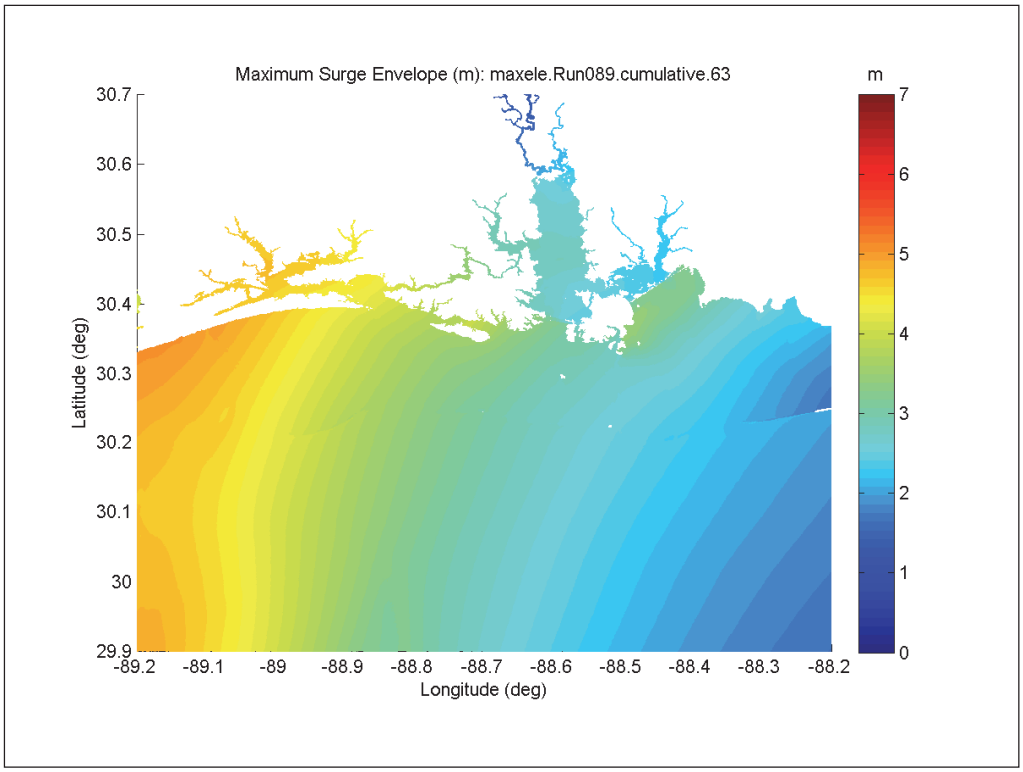

Figure F-29. Maximum surge envelope for Storm 104, Post-Katrina condition.

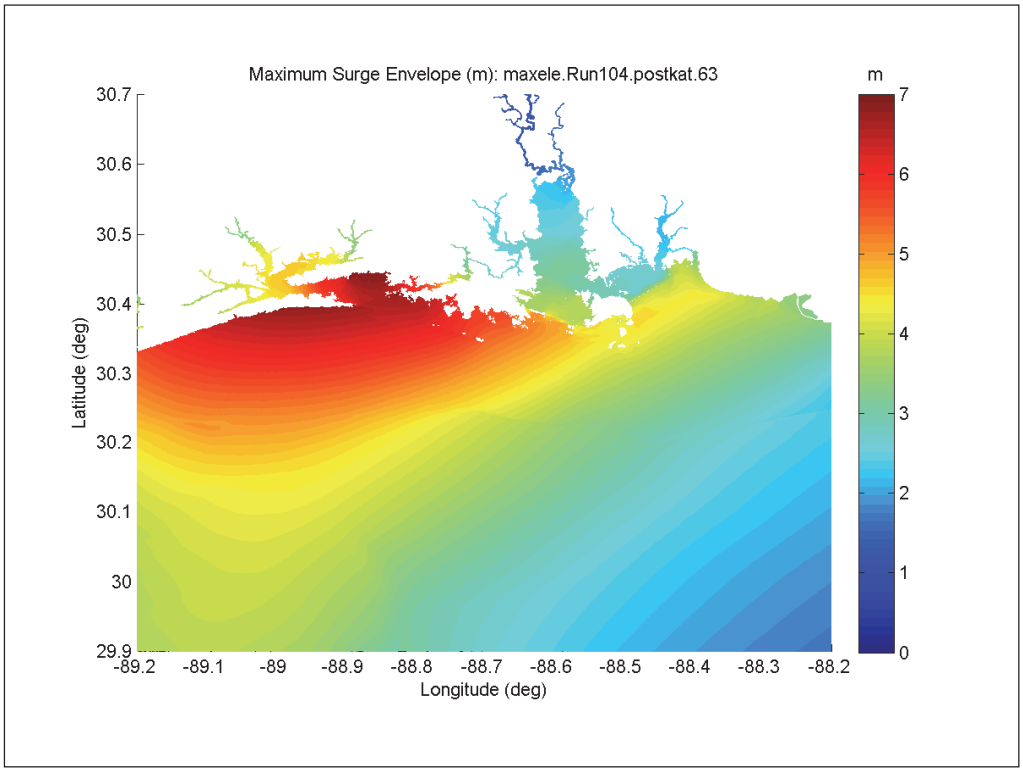

Figure F-30. Maximum surge envelope for Storm 104, Degraded condition.

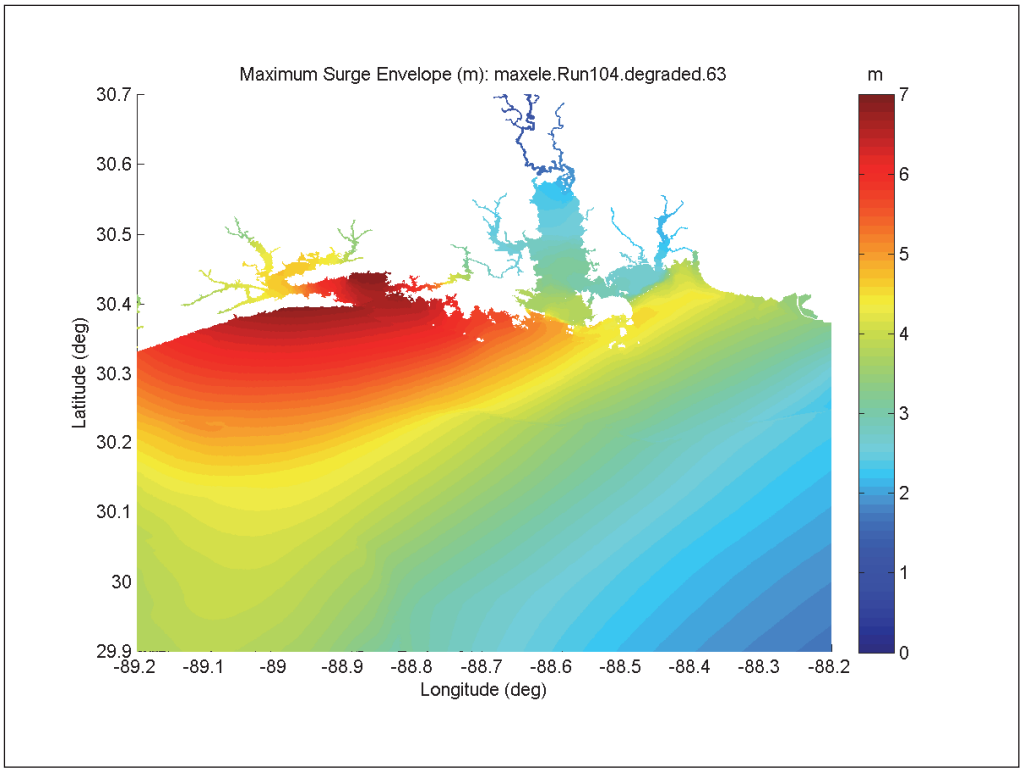

Figure F-31. Maximum surge envelope for Storm 104, Restored condition.

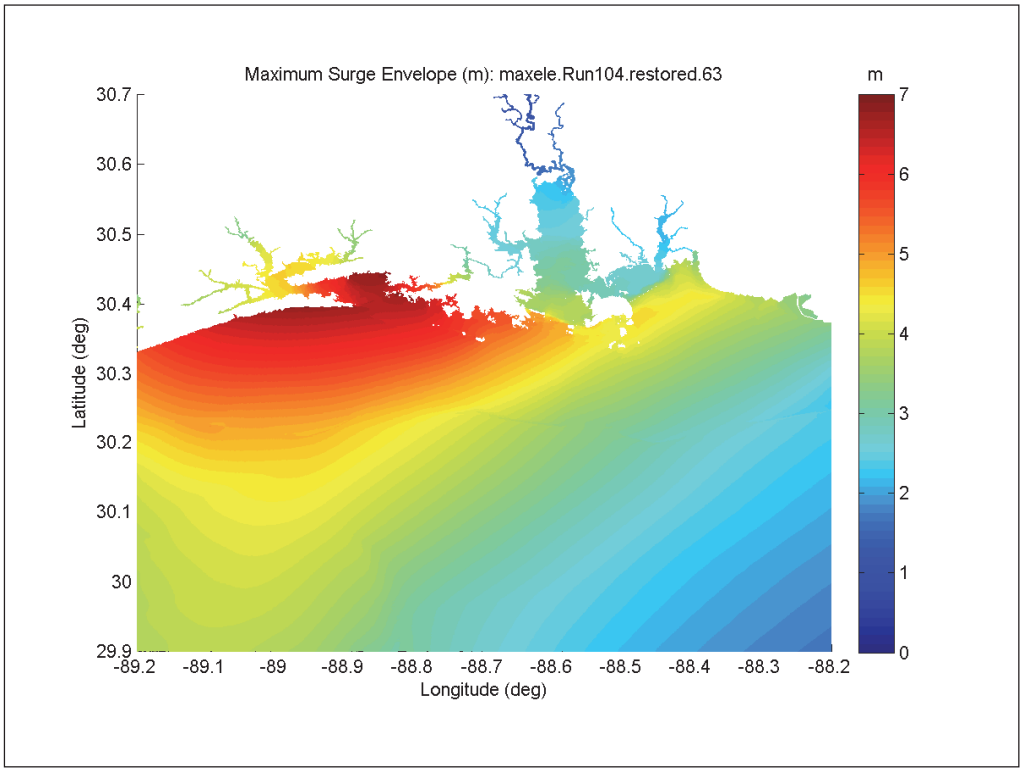

Figure F-32. Maximum surge envelope for Storm 104, Cumulative condition.

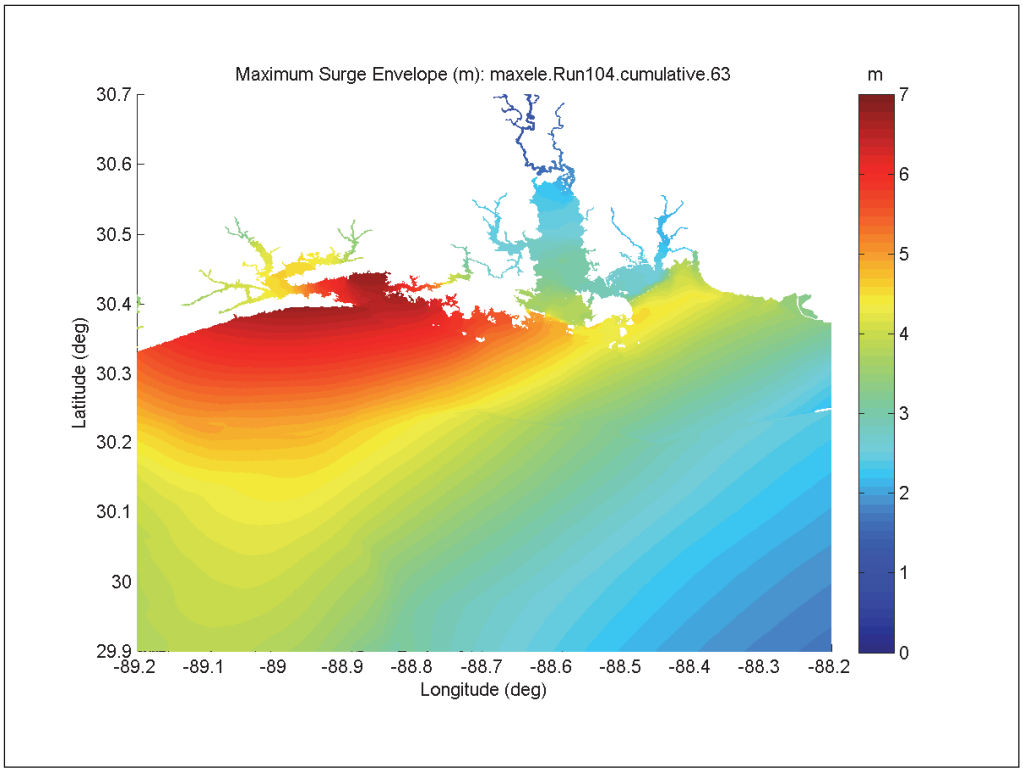

Figure F-33. Maximum surge envelope for Storm 133, Post-Katrina condition.

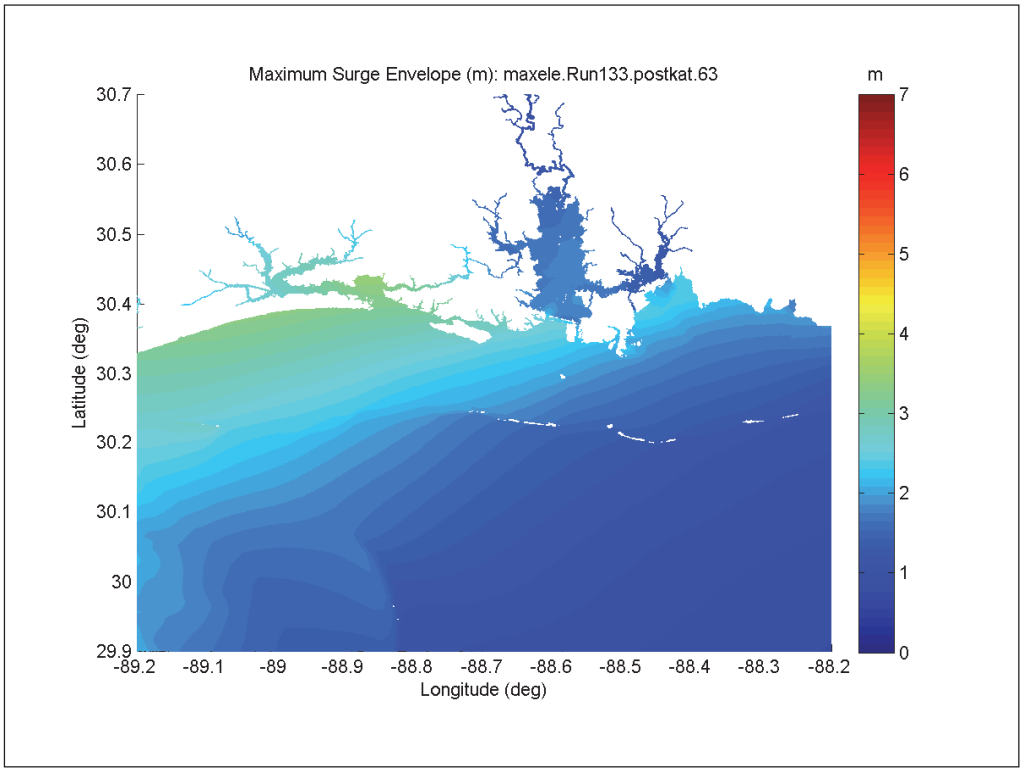

Figure F-34. Maximum surge envelope for Storm 133, Degraded condition.

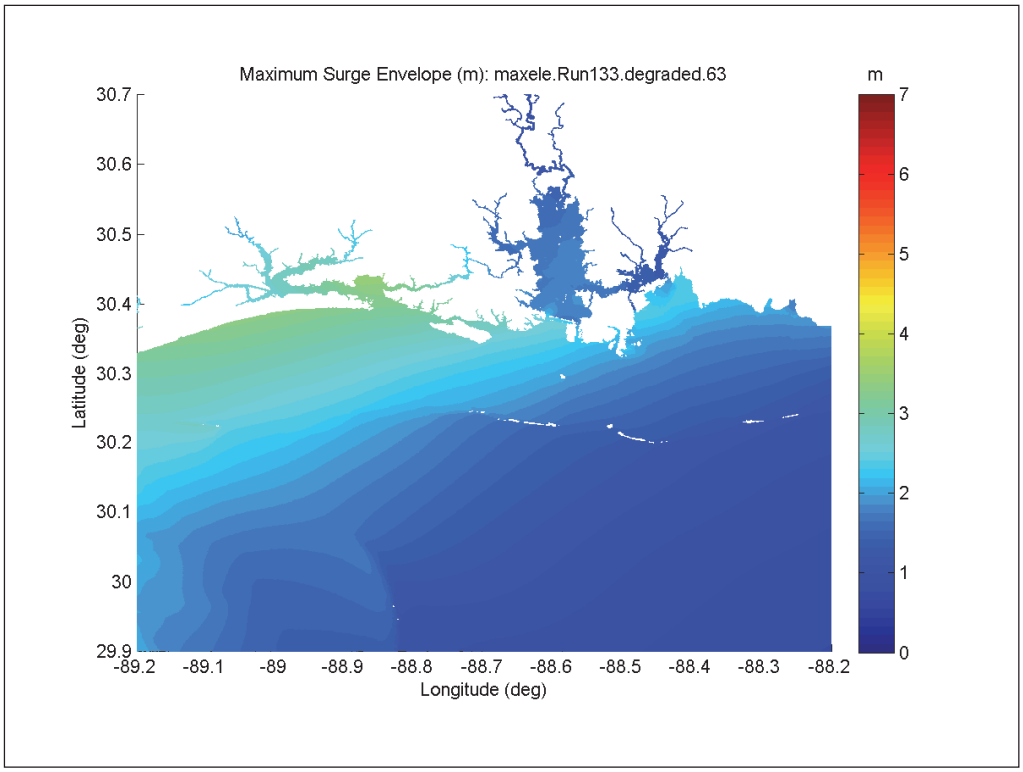

Figure F-35. Maximum surge envelope for Storm 133, Restored condition.

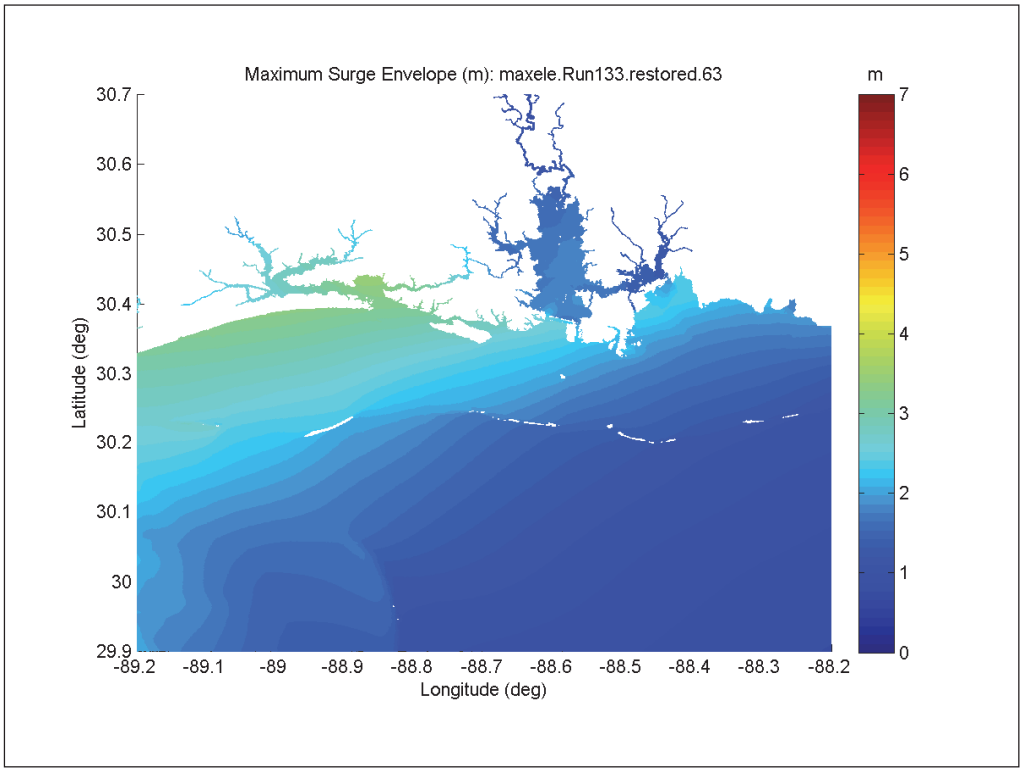

Figure F-36. Maximum surge envelope for Storm 133, Cumulative condition.

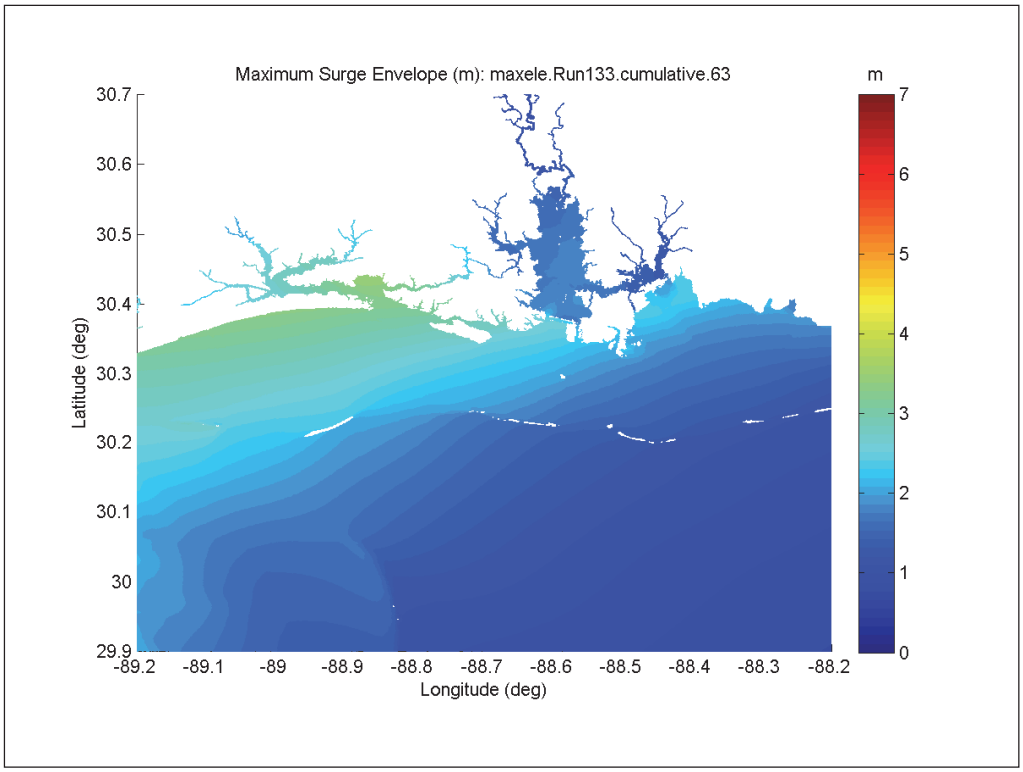

Figure F-37. Maximum surge envelope for Storm 134, Post-Katrina condition.

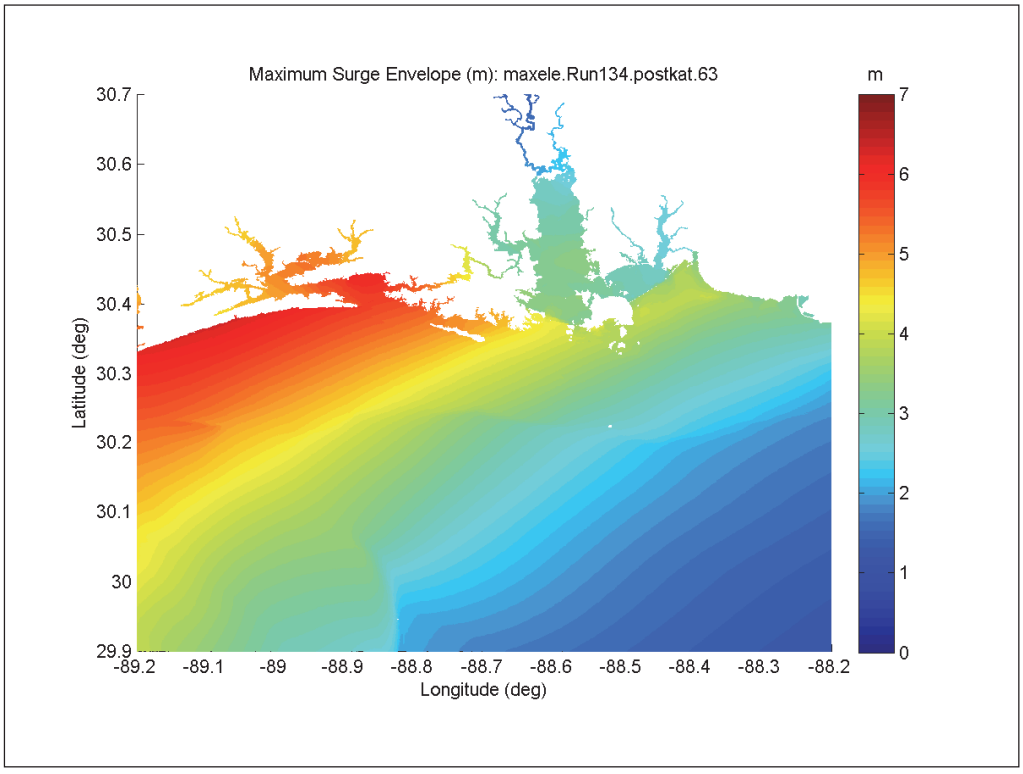

Figure F-38. Maximum surge envelope for Storm 134, Degraded condition.

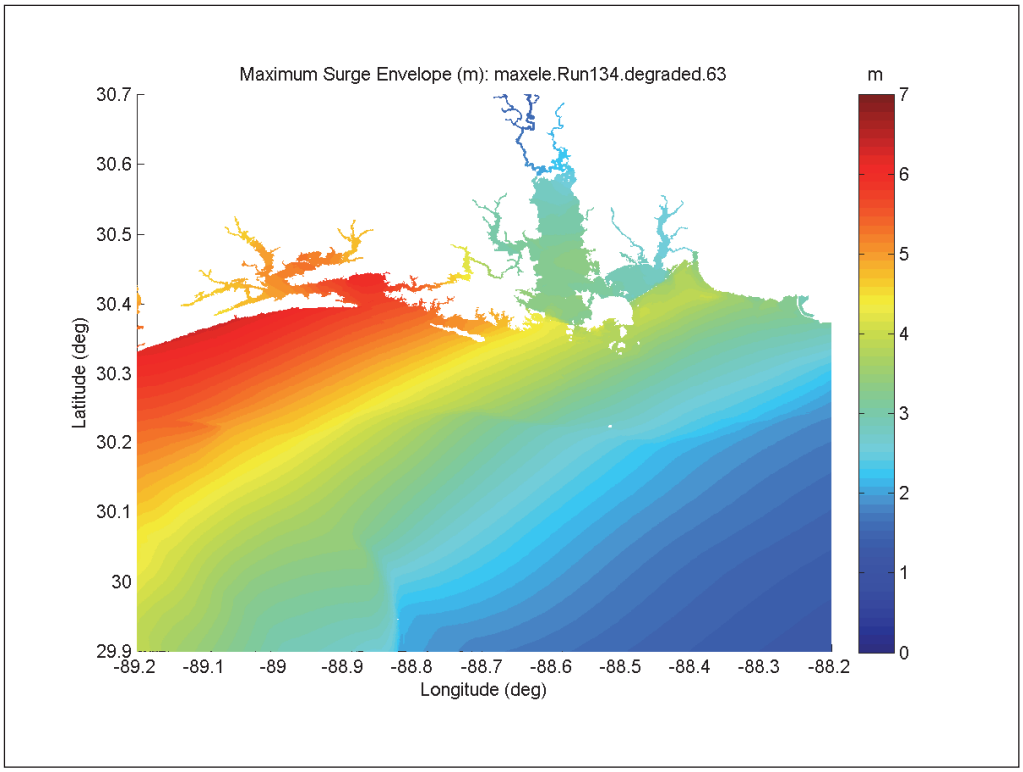

Figure F-39. Maximum surge envelope for Storm 134, Restored condition.

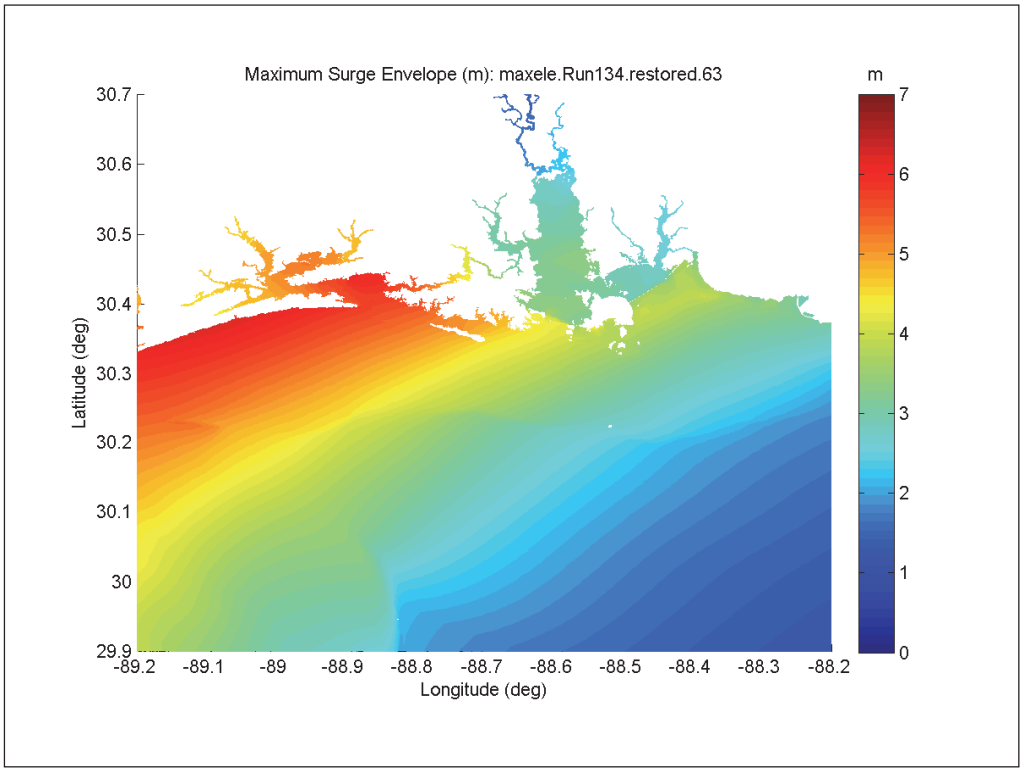

Figure F-40. Maximum surge envelope for Storm 134, Cumulative condition.

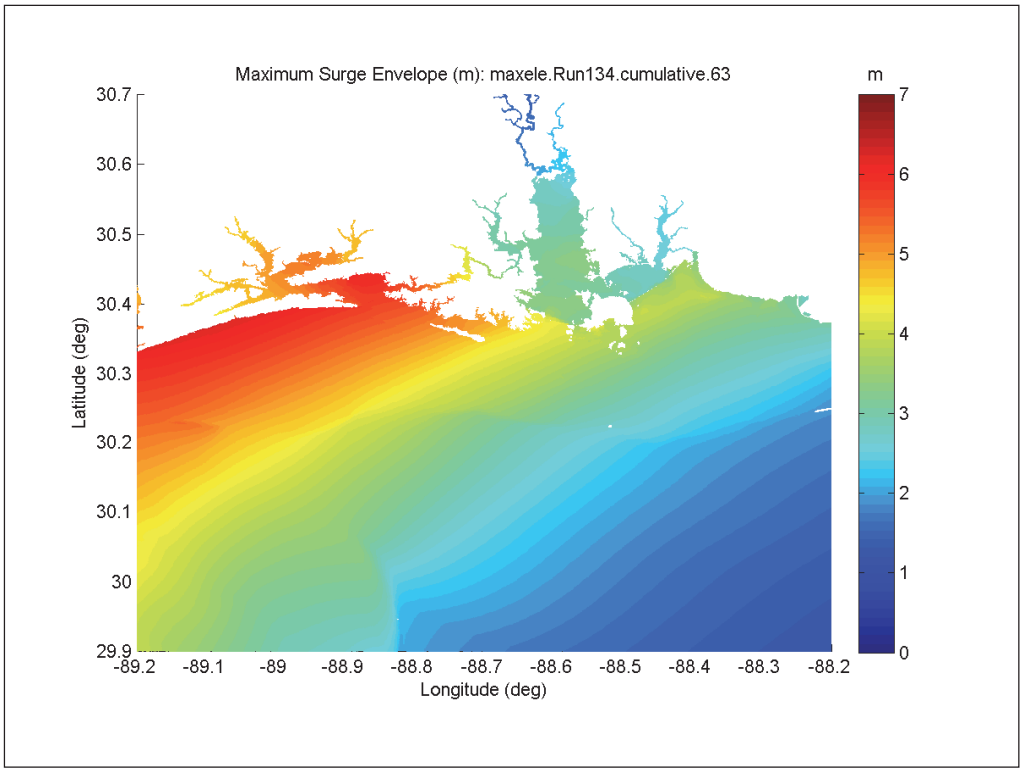

Figure F-41. Maximum surge envelope for Storm 823, Post-Katrina condition.

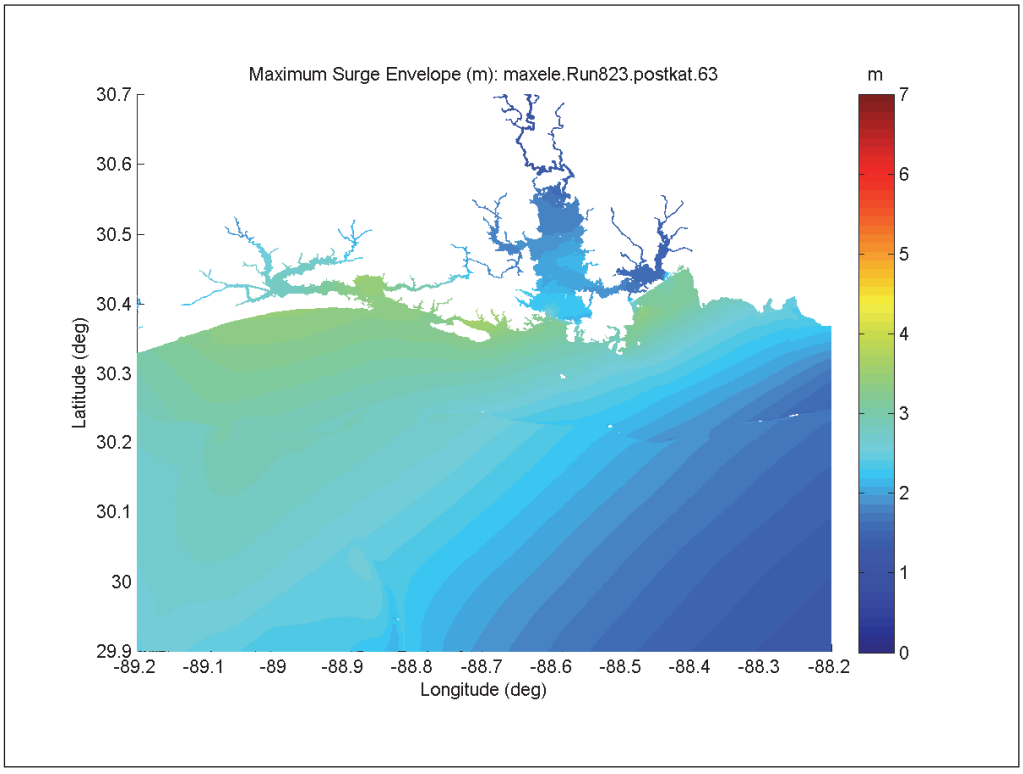

Figure F-42. Maximum surge envelope for Storm 823, Degraded condition.

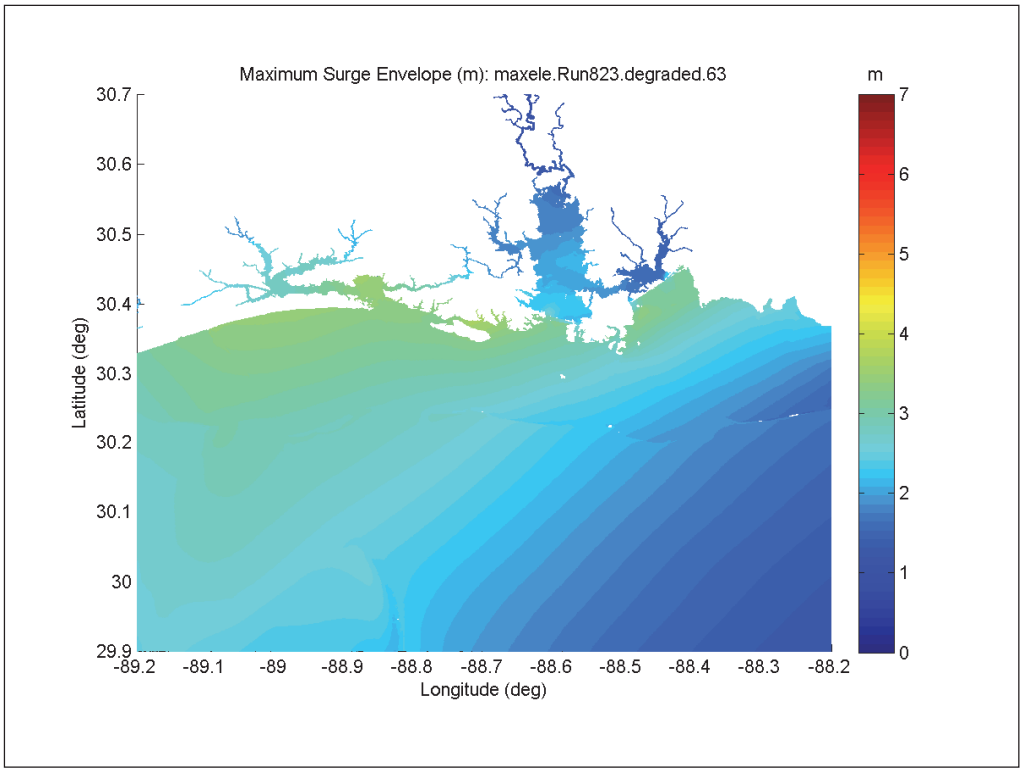

Figure F-43. Maximum surge envelope for Storm 823, Restored condition.

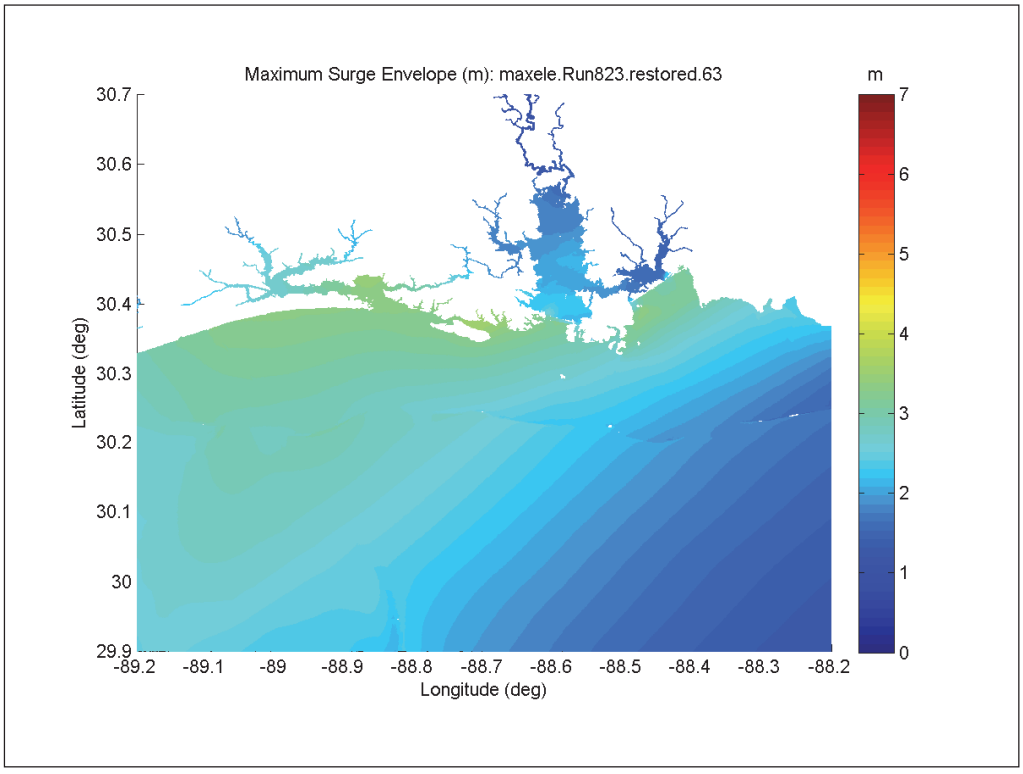

Figure F-44. Maximum surge envelope for Storm 823, Cumulative condition.

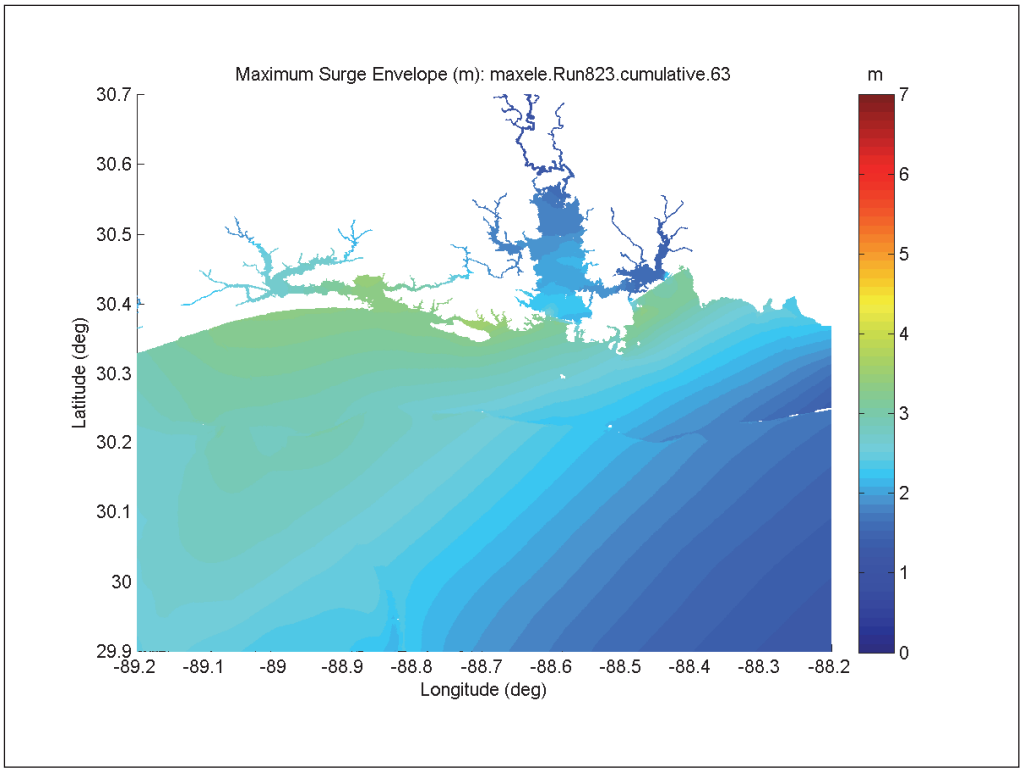

Figure F-45. Maximum surge envelope for Storm 825, Post-Katrina condition.

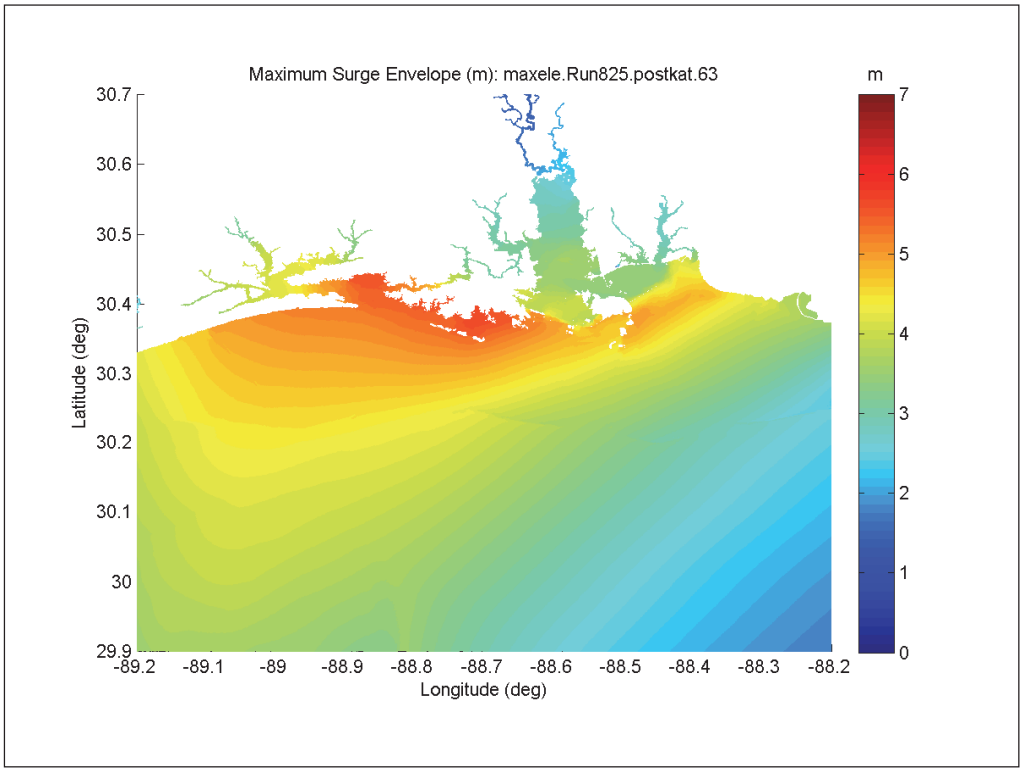

Figure F-46. Maximum surge envelope for Storm 825, Degraded condition.

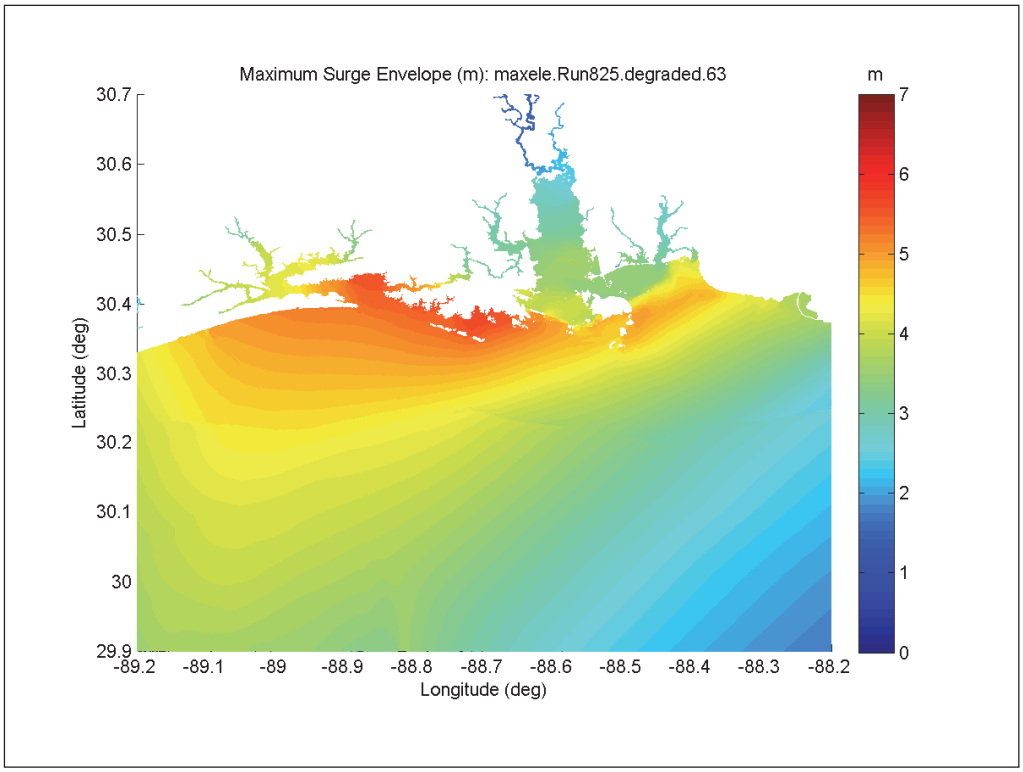

Figure F-47. Maximum surge envelope for Storm 825, Restored condition.

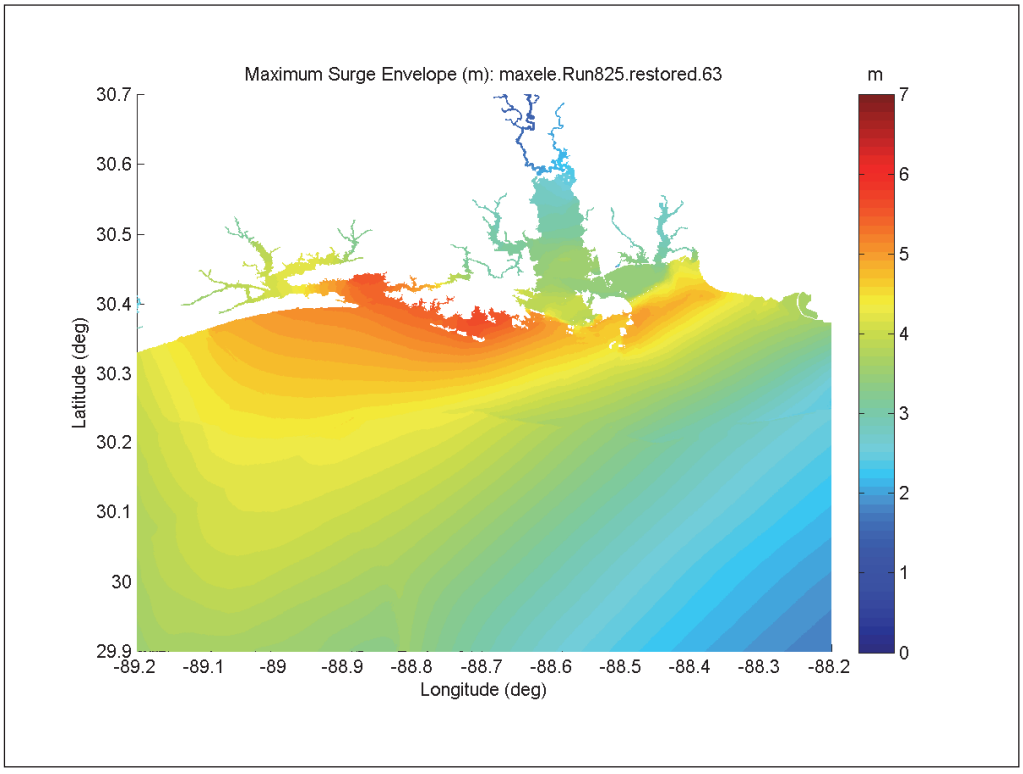

Figure F-48. Maximum surge envelope for Storm 825, Cumulative condition.

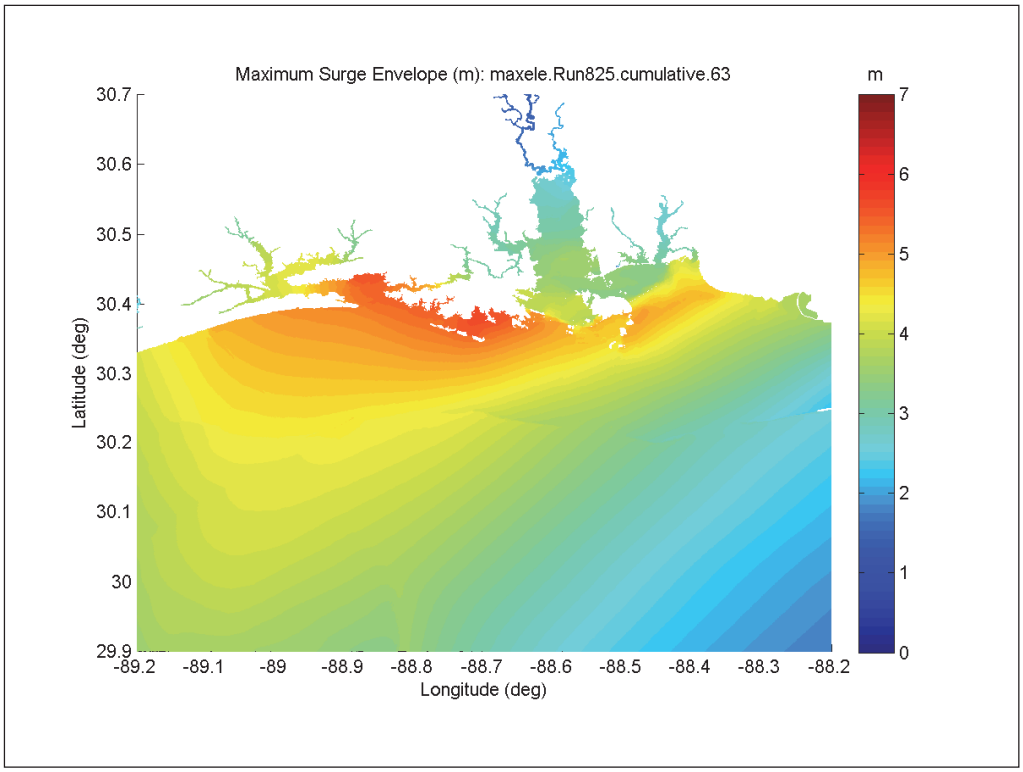

Figure F-49. Maximum surge envelope for Storm 827, Post-Katrina condition.

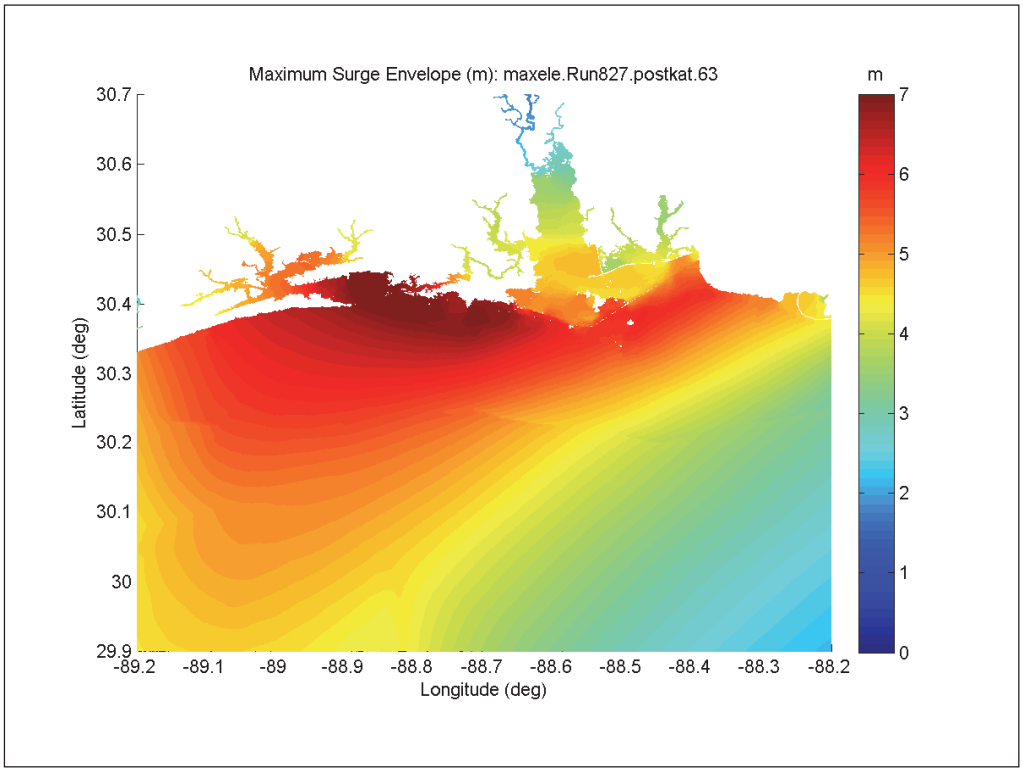

Figure F-50. Maximum surge envelope for Storm 827, Degraded condition.

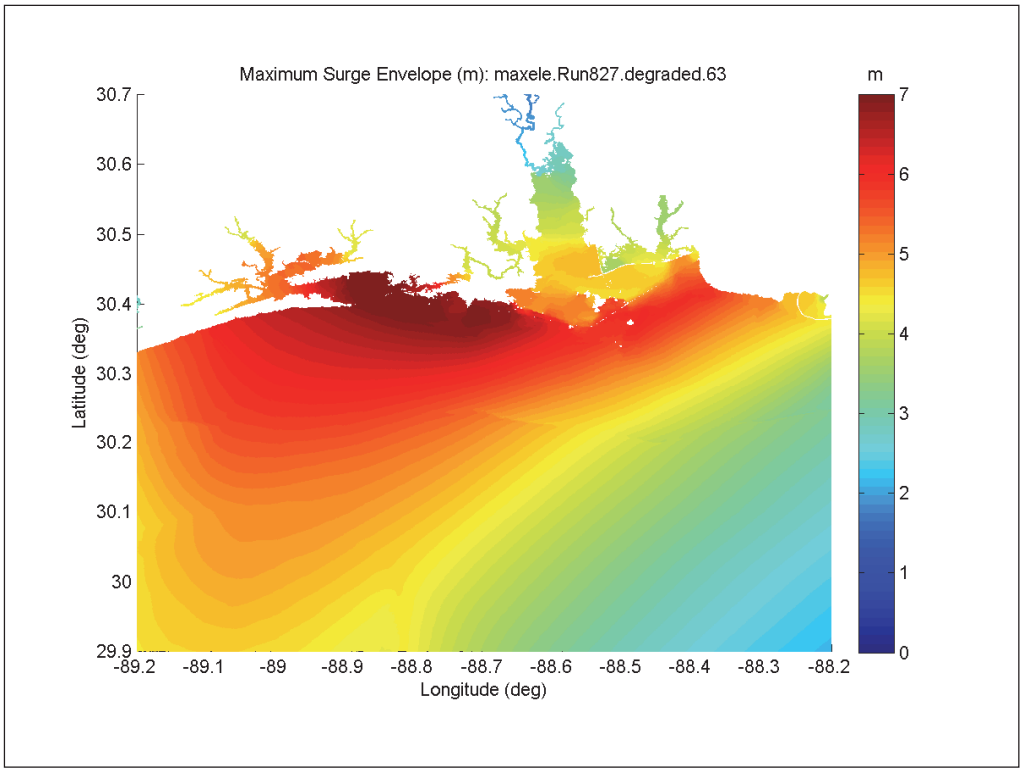

Figure F-51. Maximum surge envelope for Storm 827, Restored condition.

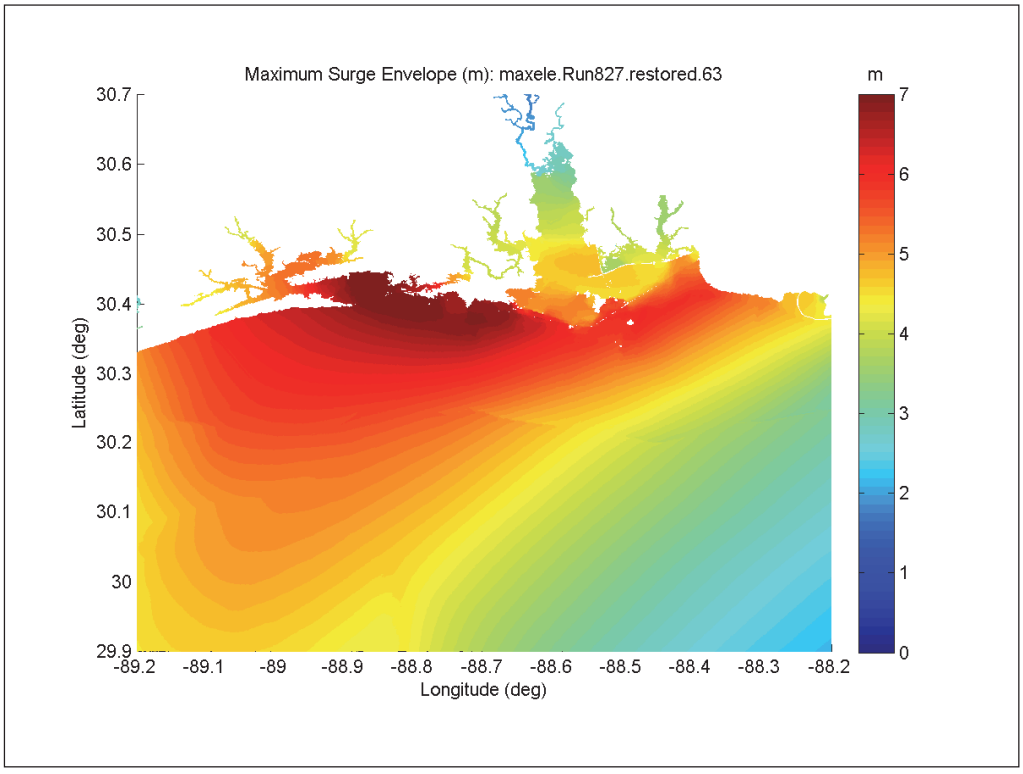

Figure F-52. Maximum surge envelope for Storm 827, Cumulative condition.

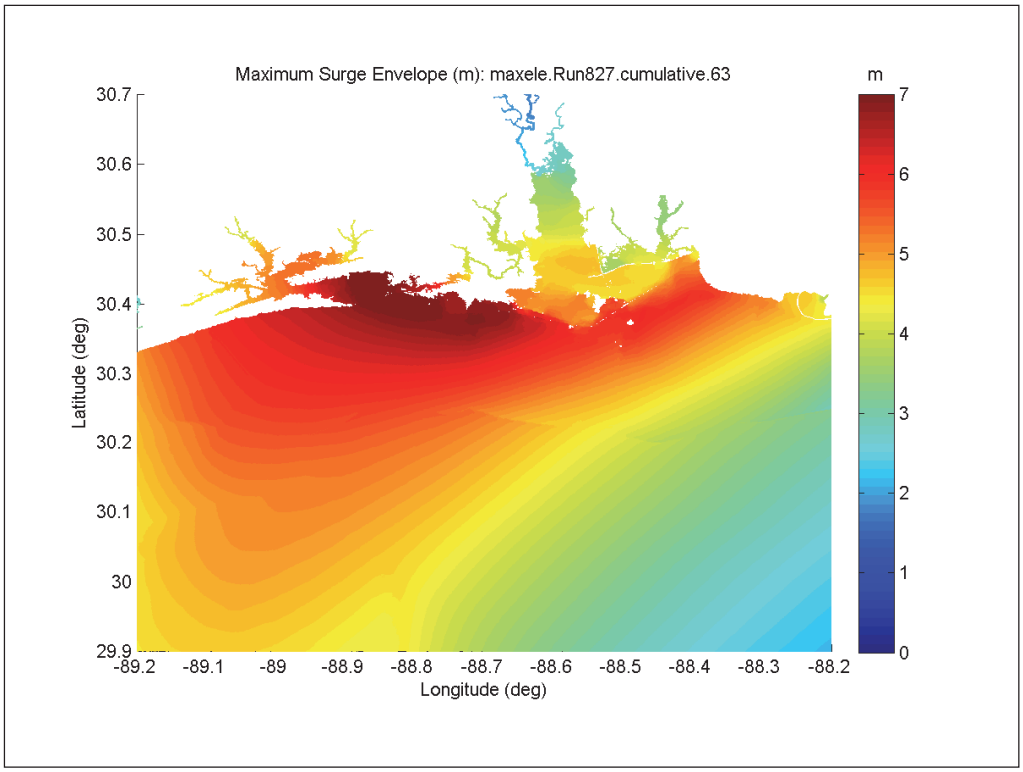

Figure F-53. Maximum surge envelope for Storm 851, Post-Katrina condition.

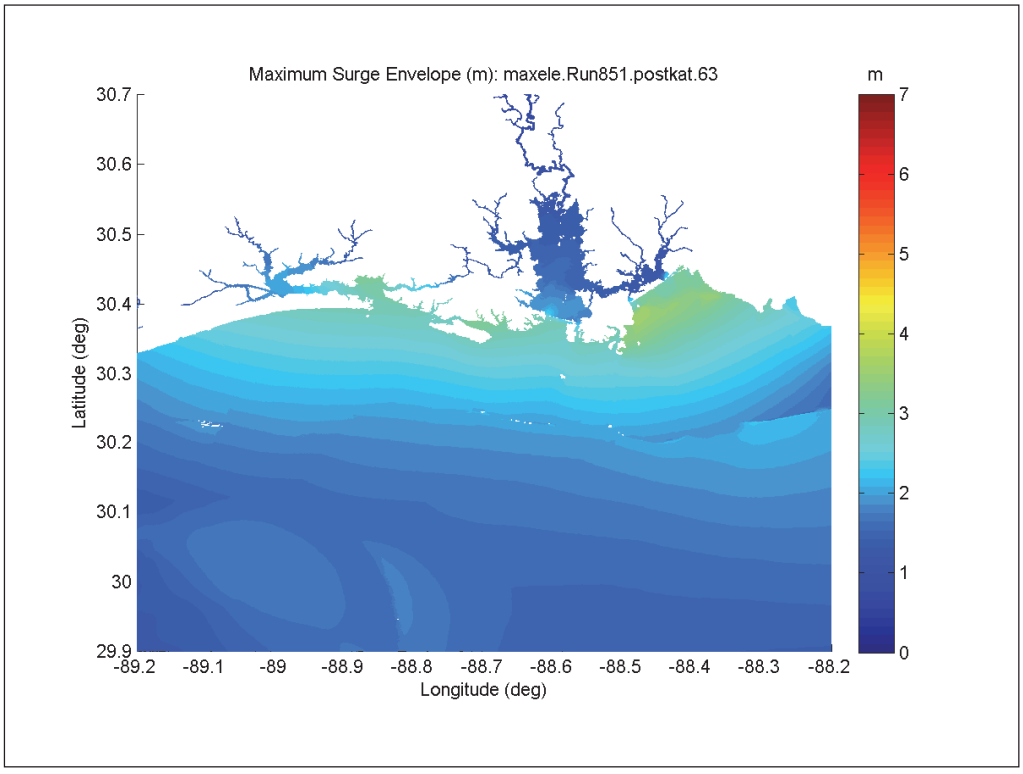

Figure F-54. Maximum surge envelope for Storm 851, Degraded condition.

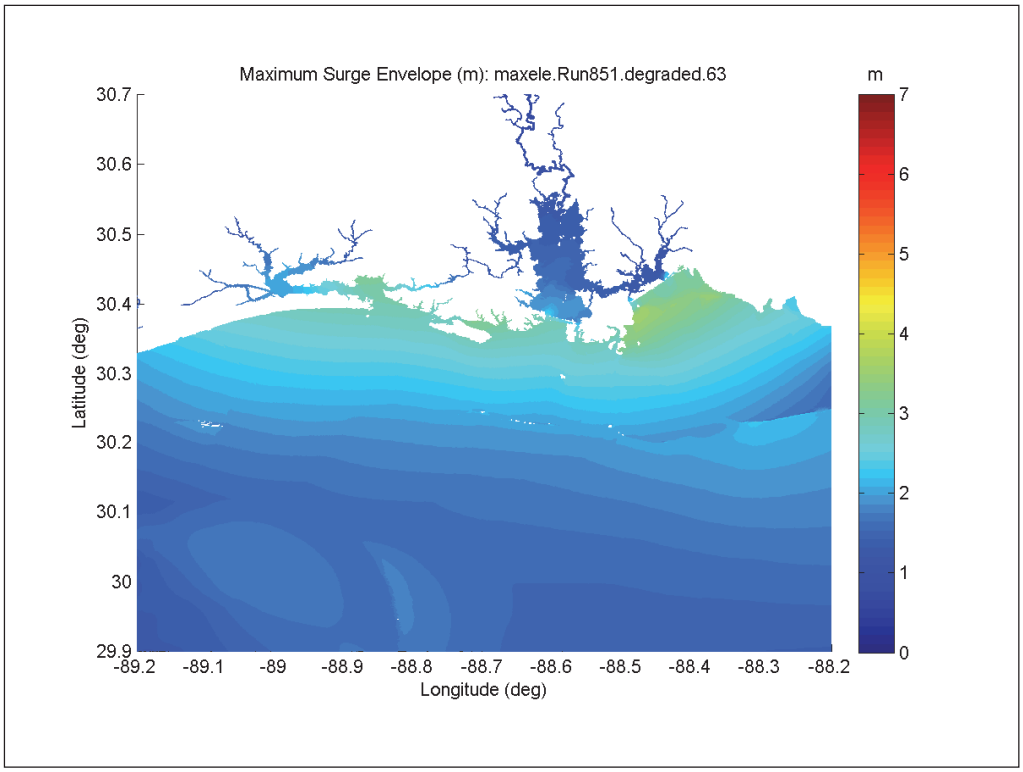

Figure F-55. Maximum surge envelope for Storm 851, Restored condition.

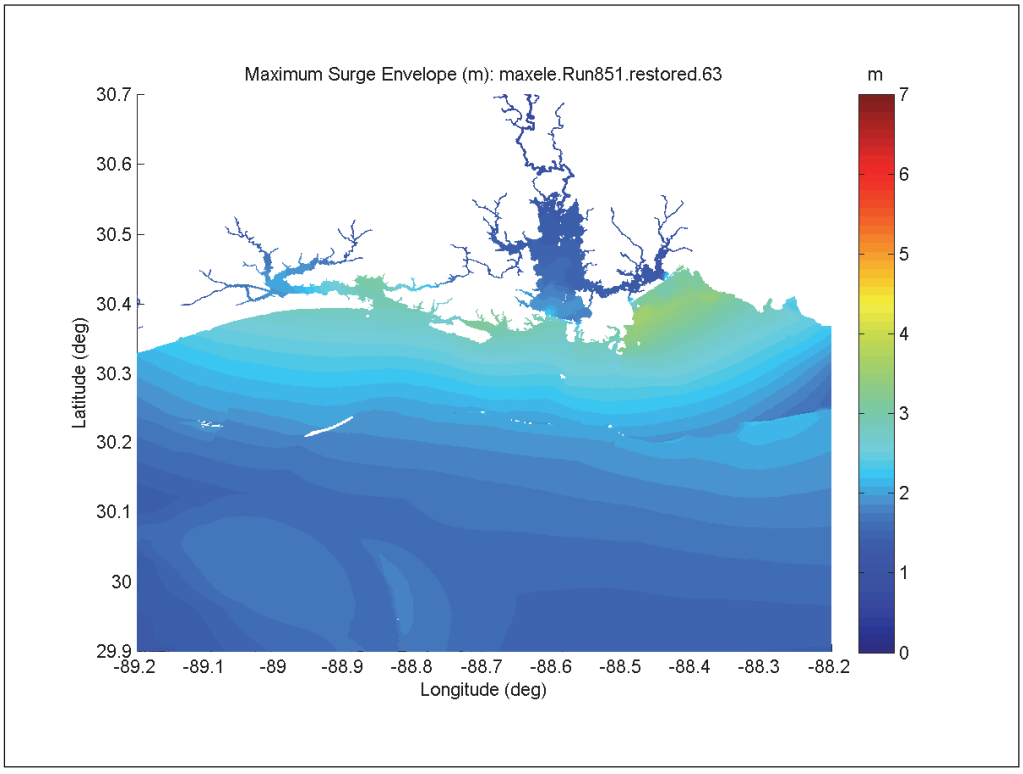

Figure F-56. Maximum surge envelope for Storm 851, Cumulative condition.

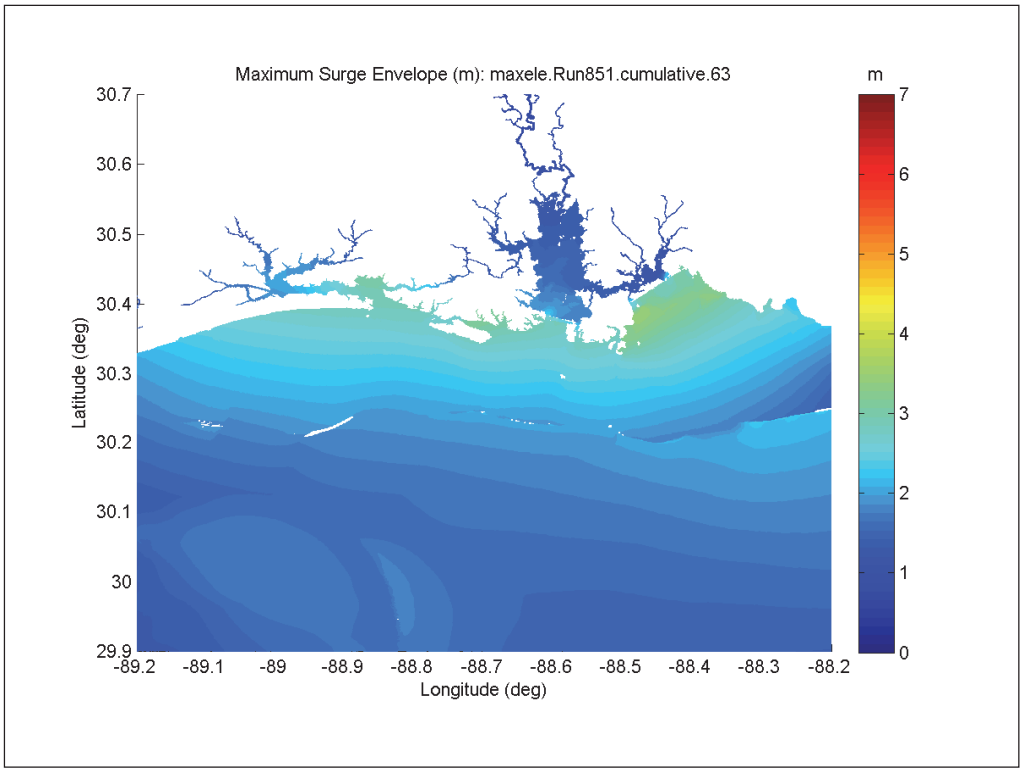

Figure F-57. Maximum surge envelope for Storm 852, Post-Katrina condition.

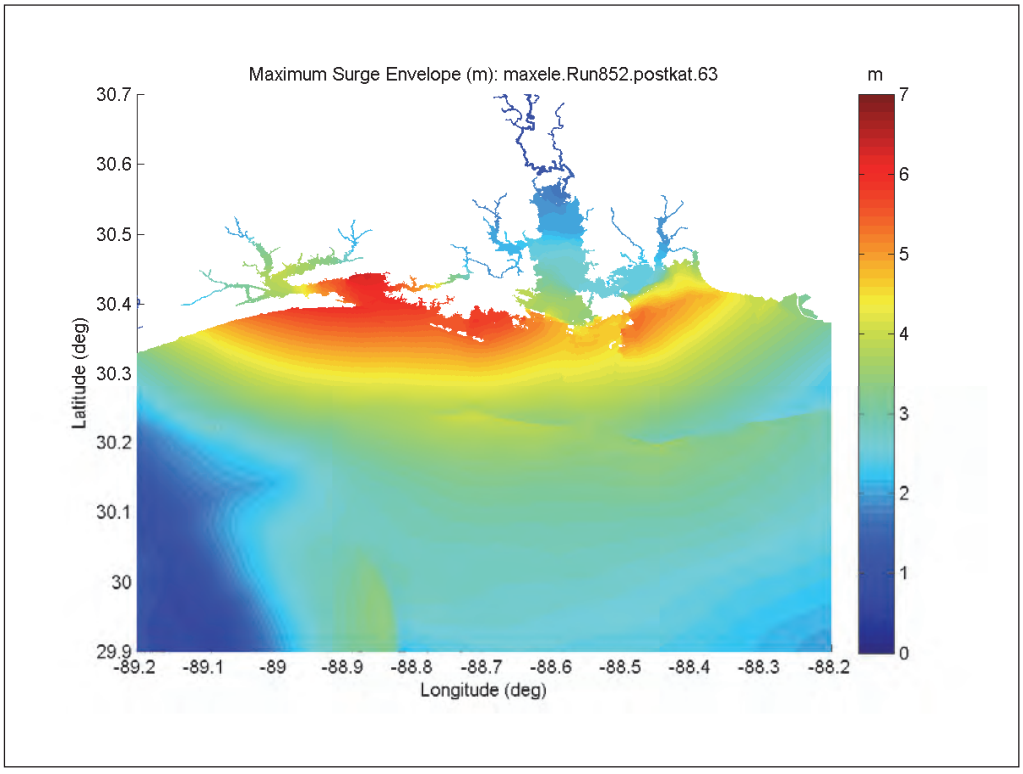

Figure F-58. Maximum surge envelope for Storm 852, Degraded condition.

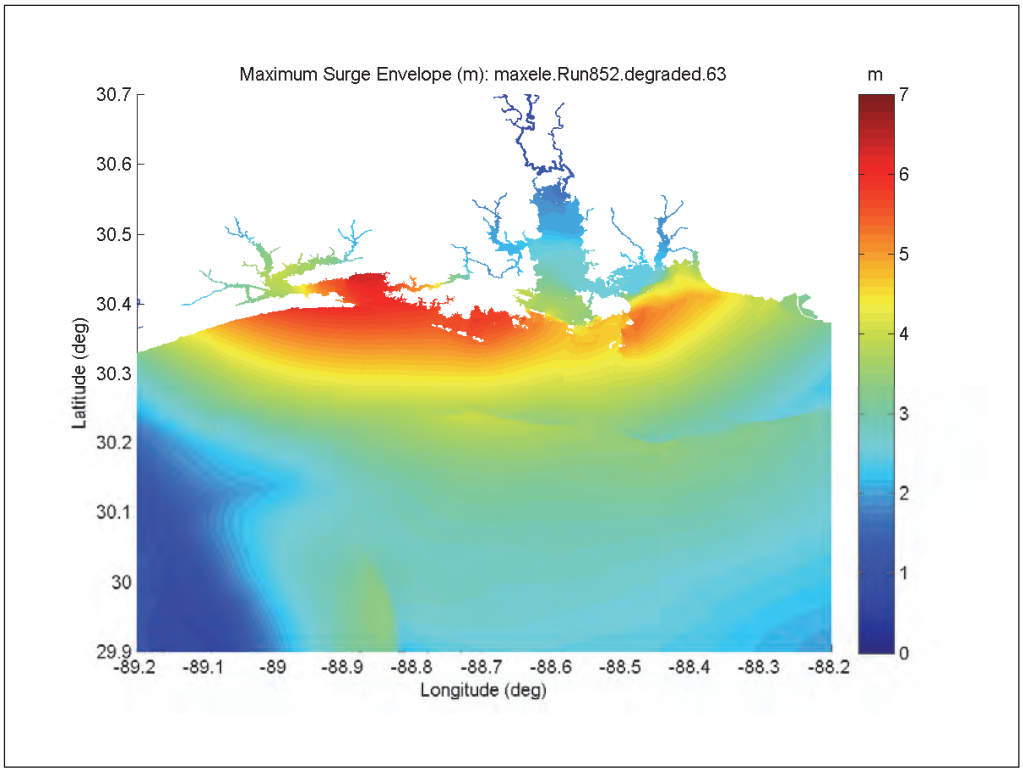

Figure F-59. Maximum surge envelope for Storm 852, Restored condition.

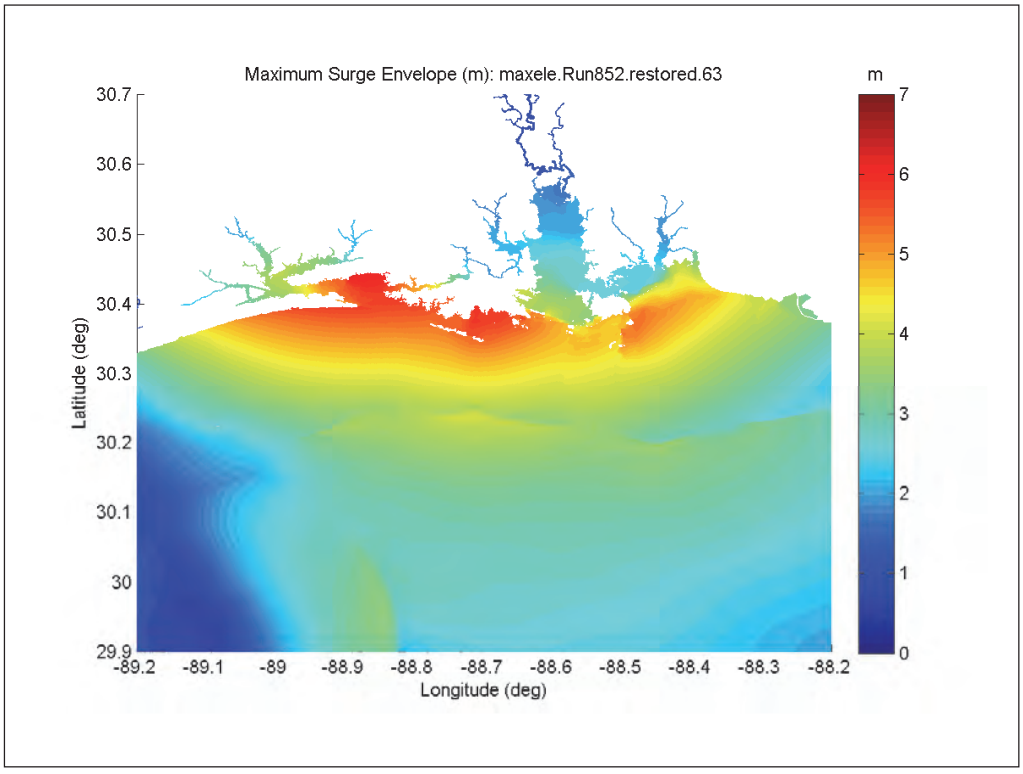

Figure F-60. Maximum surge envelope for Storm 852, Cumulative condition.

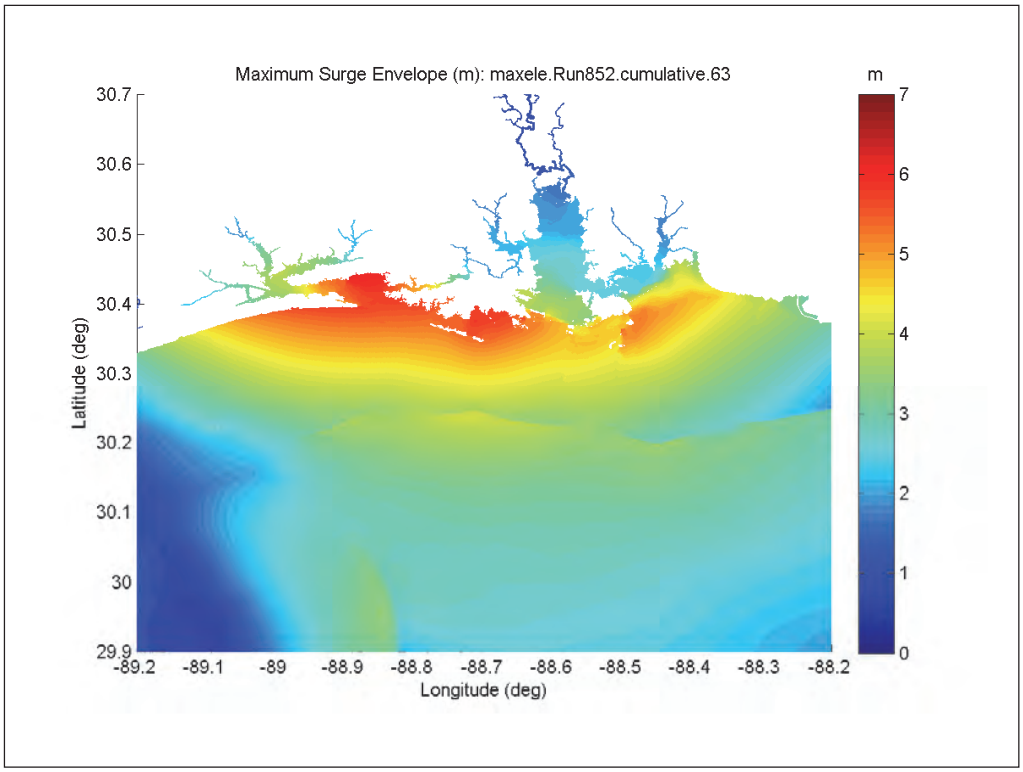

Appendix G: Nearshore Sediment Transport and Bathymetric Change Results for Existing Conditions and Restoration Scenarios

Notes

- There is no fill placement for the existing conditions, but the fill regions are indicated with dashed blue lines to facilitate comparison with the restoration scenarios (Figures G-1, G-8, and G-15 for the Alternative #1 Restoration scenarios and Figures G-43, G-45, and G-47 for the Alternative #2 Restoration).
- The fill regions for the restoration scenarios are indicated with solid blue lines to facilitate comparison (Figures G-2 through G-7, G-9 through G-14, and G-16 through G-21 for the Alternative #1 Restoration scenarios and Figures G-44, G-46, and G-48 for the Alternative #2 Restoration).
- The post-storm island footprint (NAVD = 0 m) contour is depicted as a black outline for reference for the existing conditions and the Alternative #1 Restoration scenarios (Figures G-22 through G-41), as well as the Alternative #2 Restoration (Figures G-49 through G-51).

Figure G-1. Existing conditions for Storm #1.

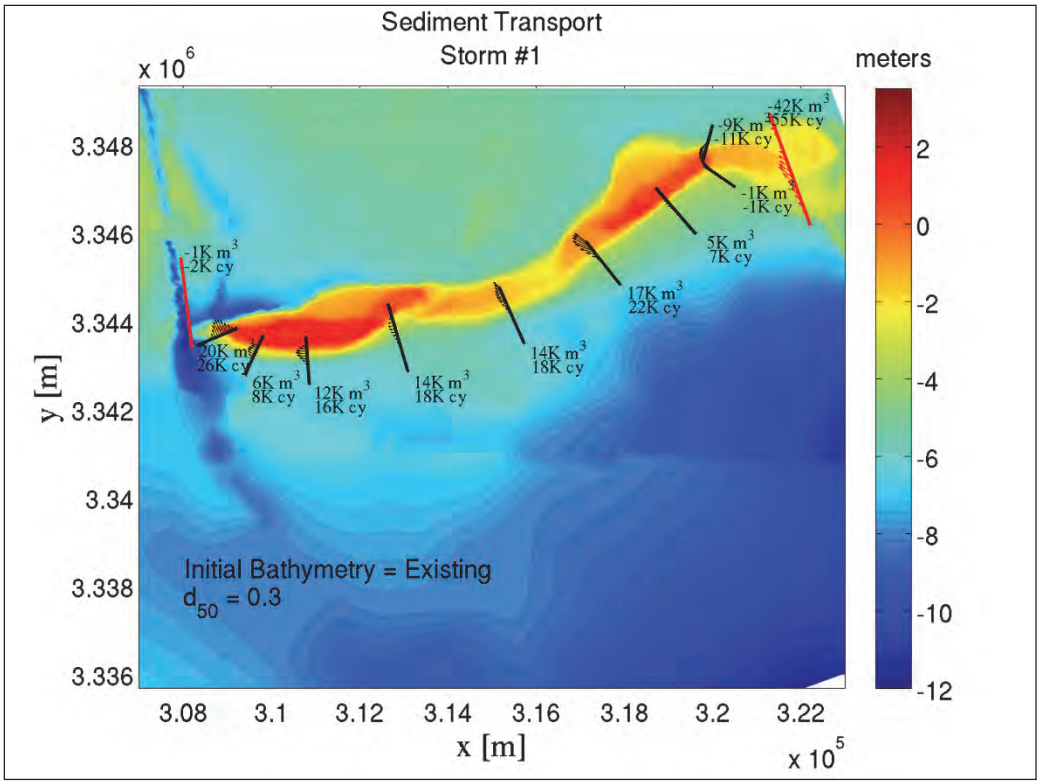

Figure G-2. Alternative #1 Restored conditions for Storm #1; Template A; With borrow pits.

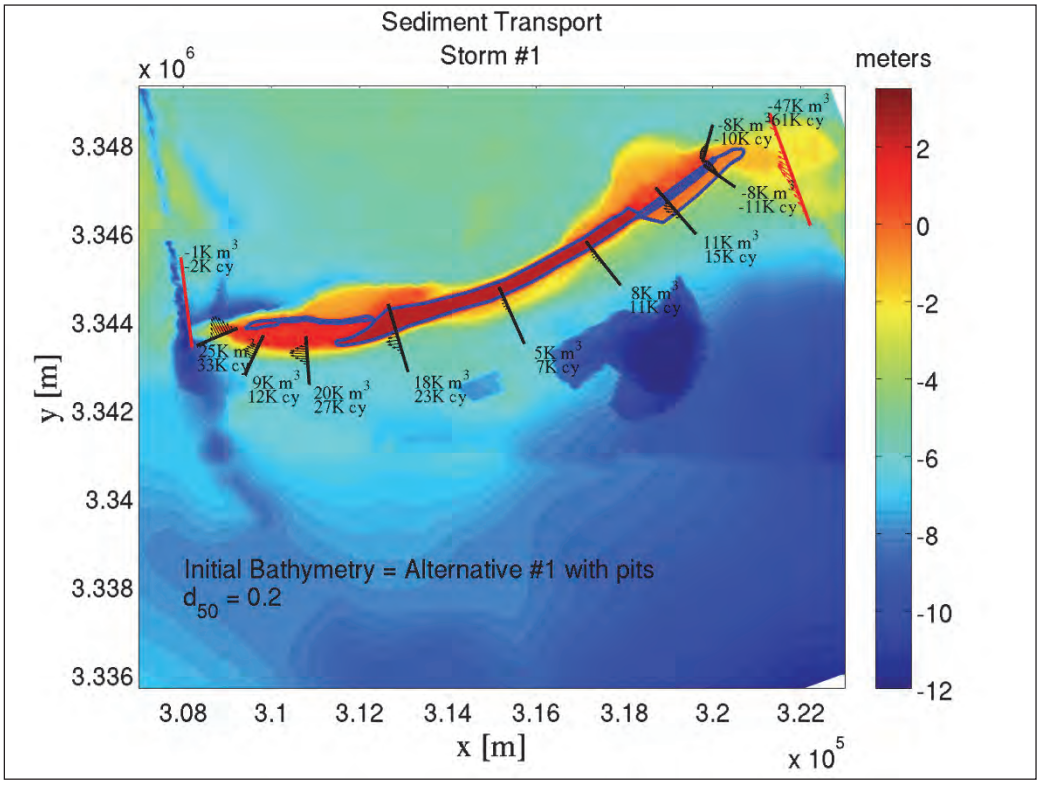

Figure G-3. Alternative #1 Restored conditions for Storm #1; Template B; With borrow pits.

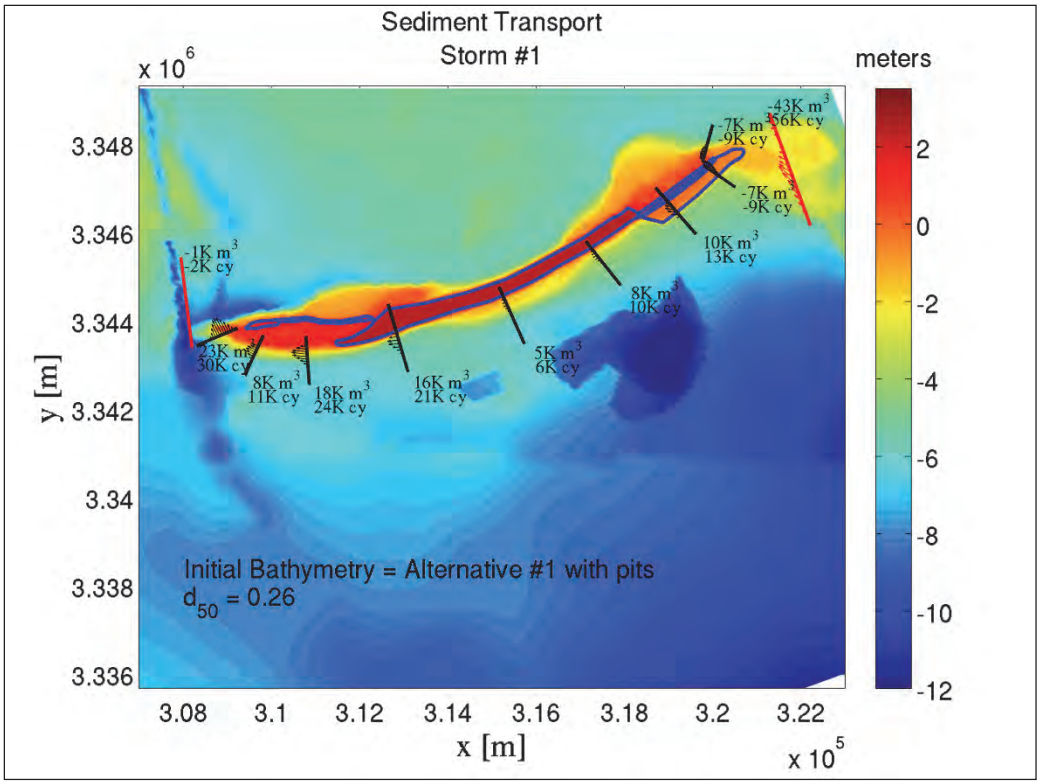

Figure G-4. Alternative #1 Restored conditions for Storm #1; Template C; With borrow pits.

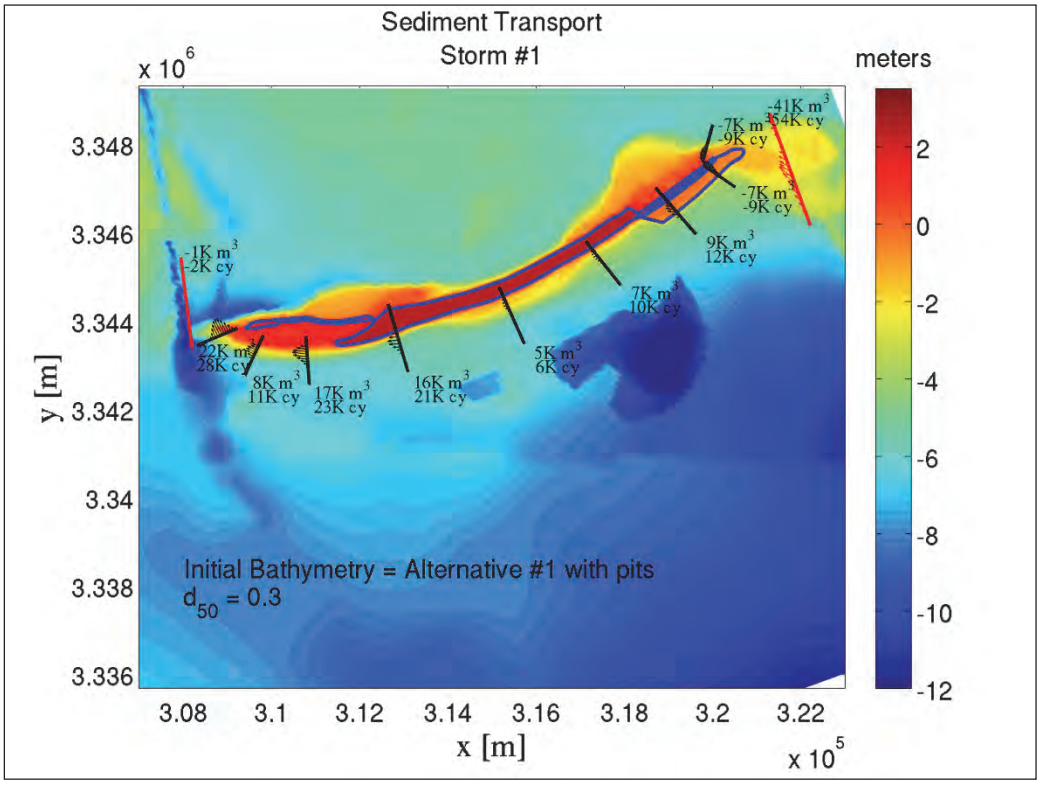

Figure G-5. Alternative #1 Restored conditions for Storm #1; Template A; Without borrow pits.

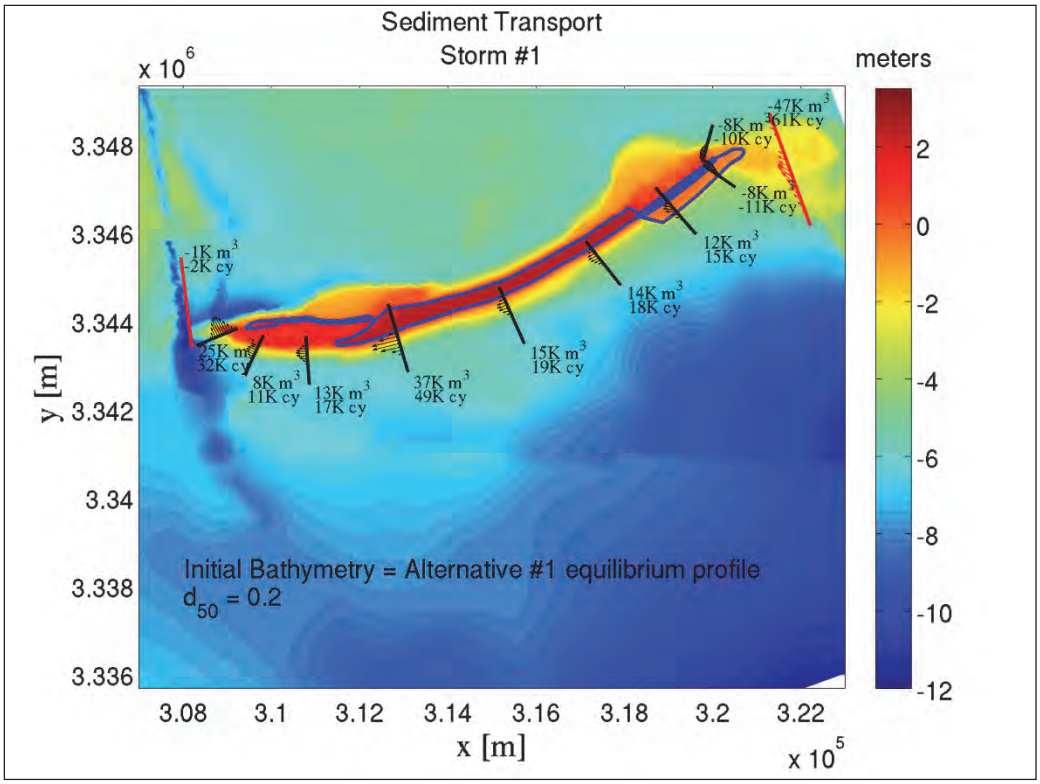

Figure G-6. Alternative #1 Restored conditions for Storm #1; Template B; Without borrow pits.

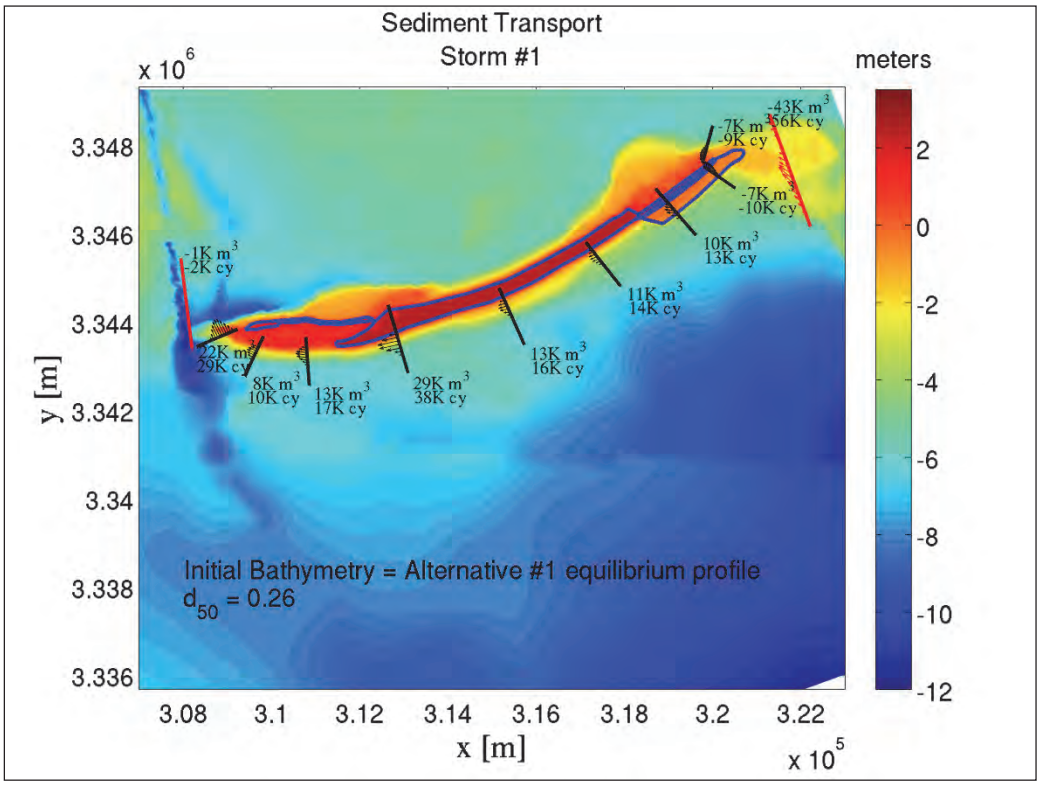

Figure G-7. Alternative #1 Restored conditions for Storm #1; Template C; Without borrow pits.

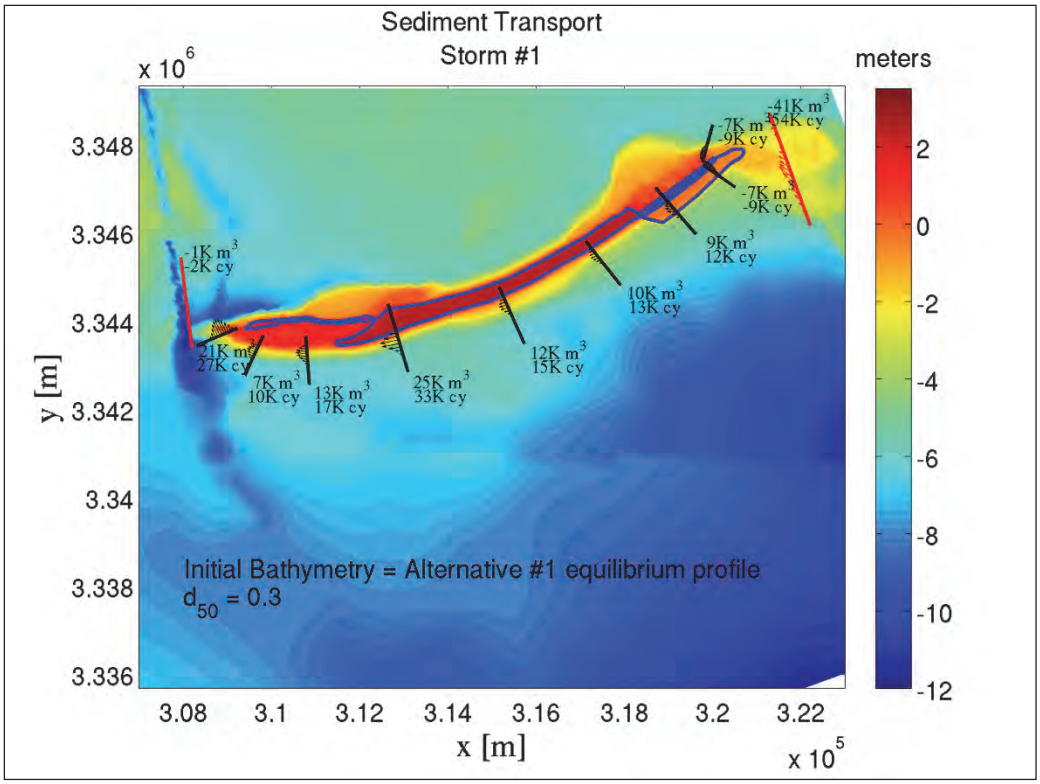

Figure G-8. Existing conditions for Storm #2.

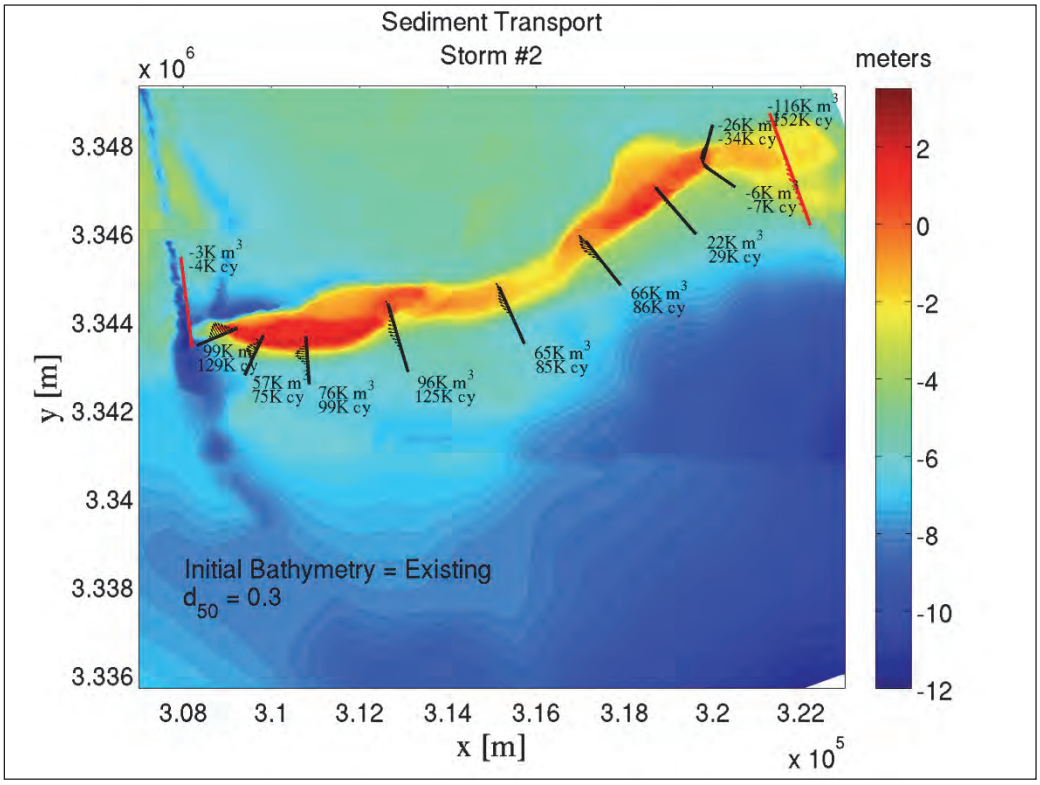

Figure G-9. Alternative #1 Restored conditions for Storm #2; Template A; With borrow pits.

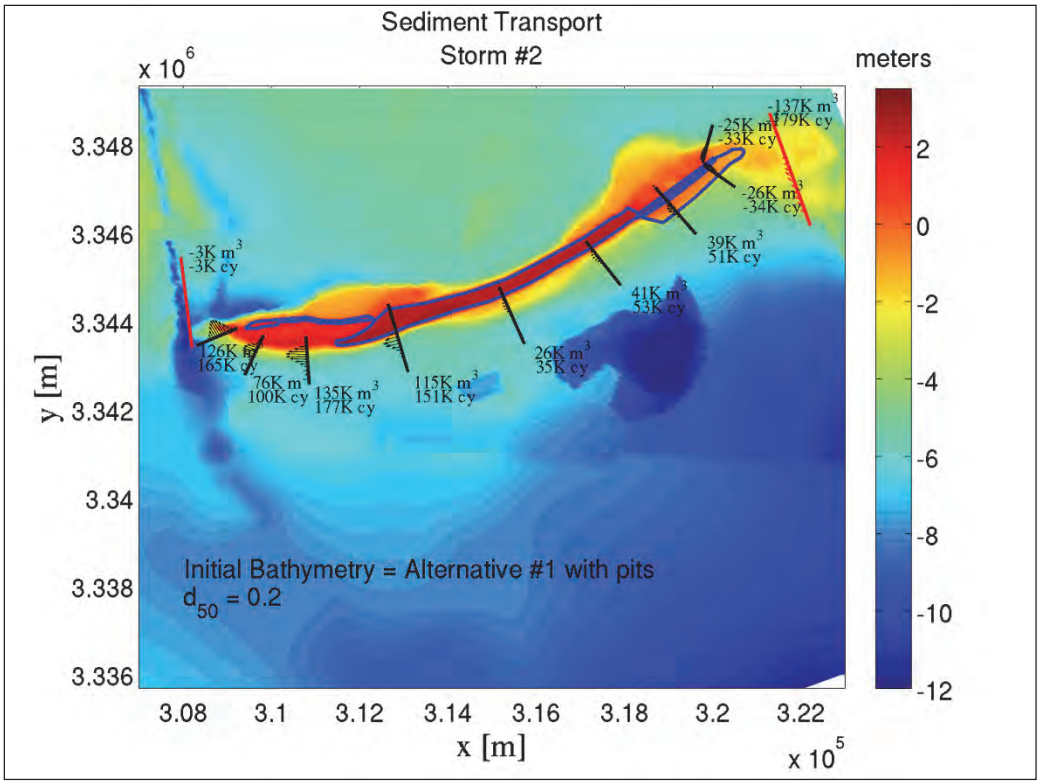

Figure G-10. Alternative #1 Restored conditions for Storm #2; Template B; With borrow pits.

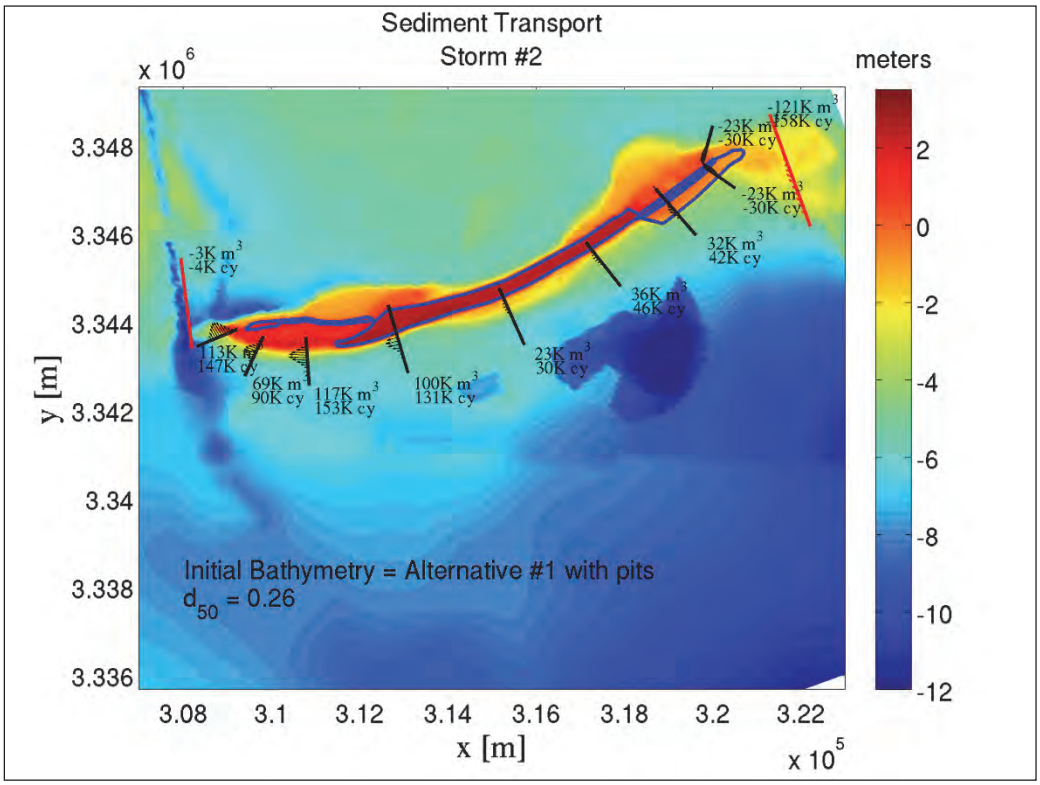

Figure G-11. Alternative #1 Restored conditions for Storm #2; Template C; With borrow pits.

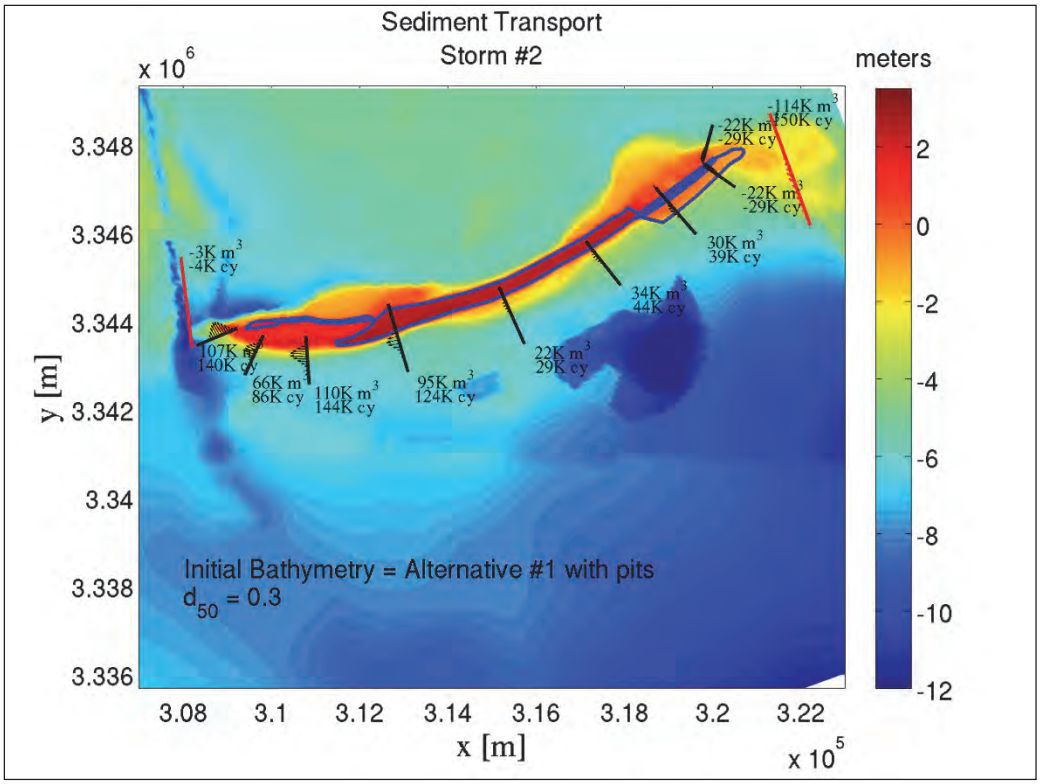

Figure G-12. Alternative #1 Restored conditions for Storm #2; Template A; Without borrow pits.

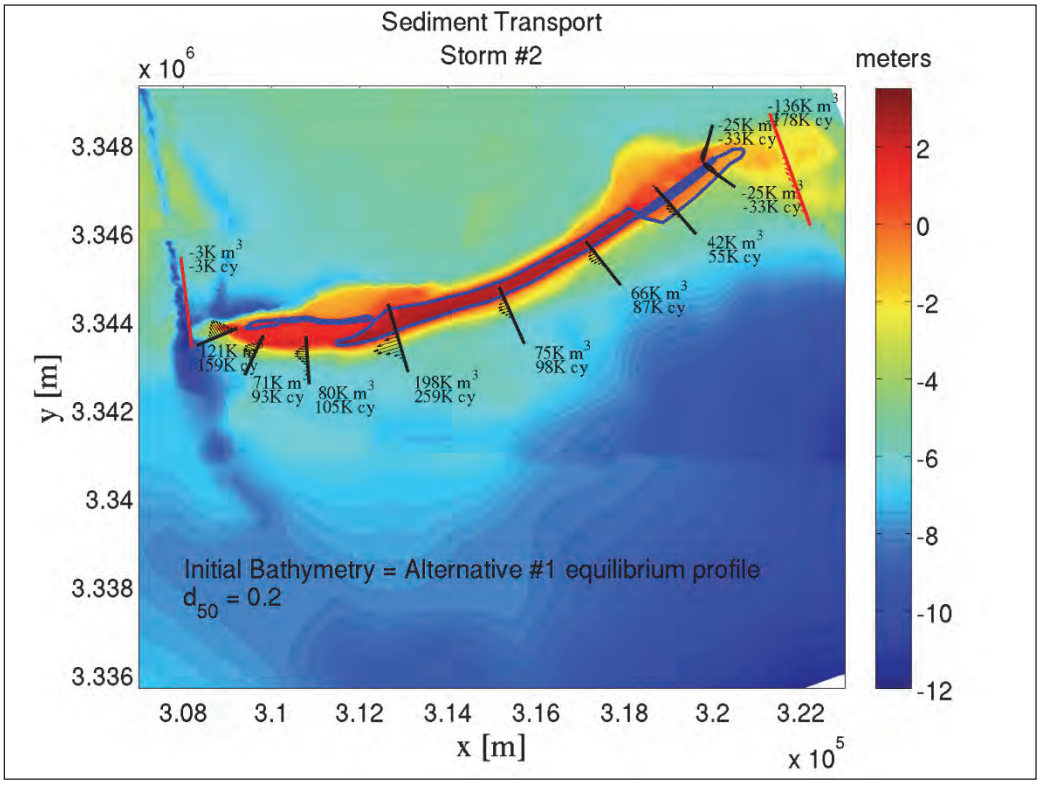

Figure G-13. Alternative #1 Restored conditions for Storm #2; Template B; Without borrow pits.

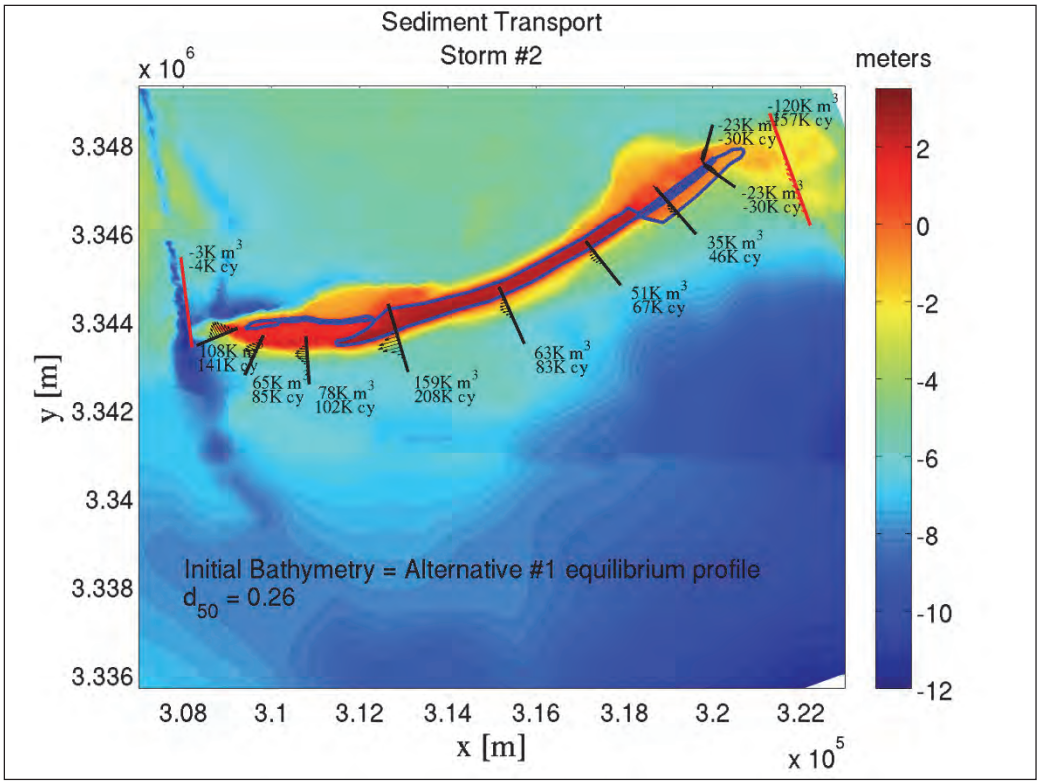

Figure G-14. Alternative #1 Restored conditions for Storm #2; Template C; Without borrow pits.

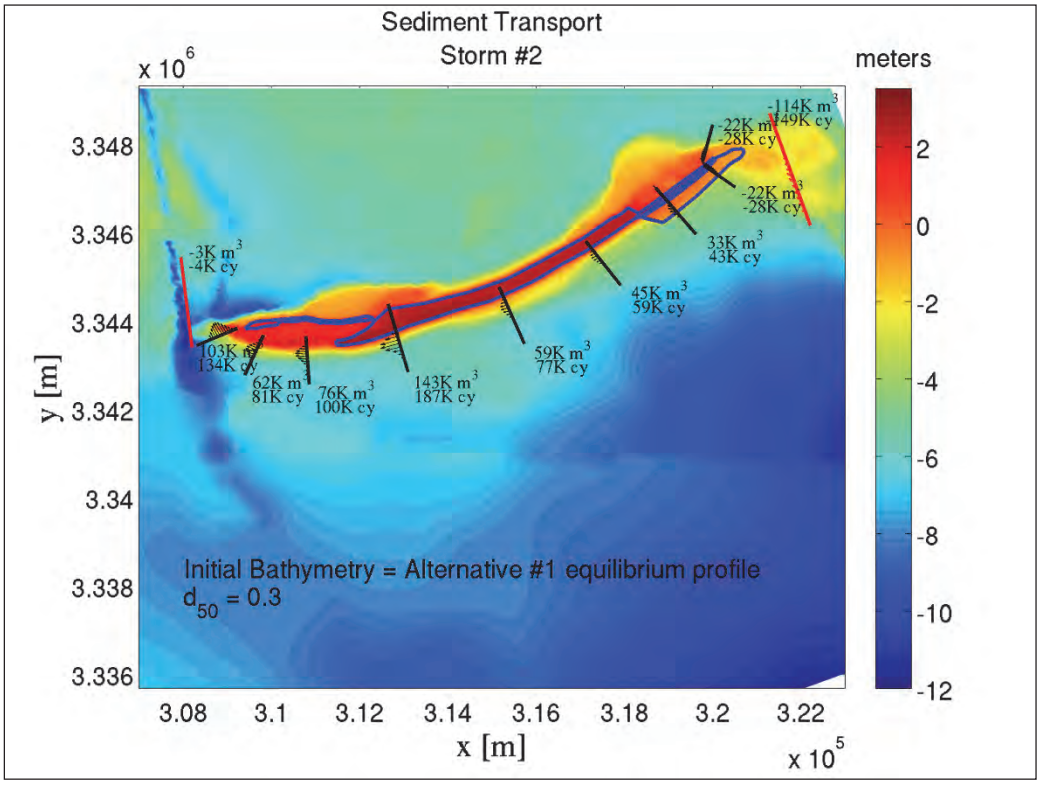

Figure G-15. Existing conditions for Storm #3.

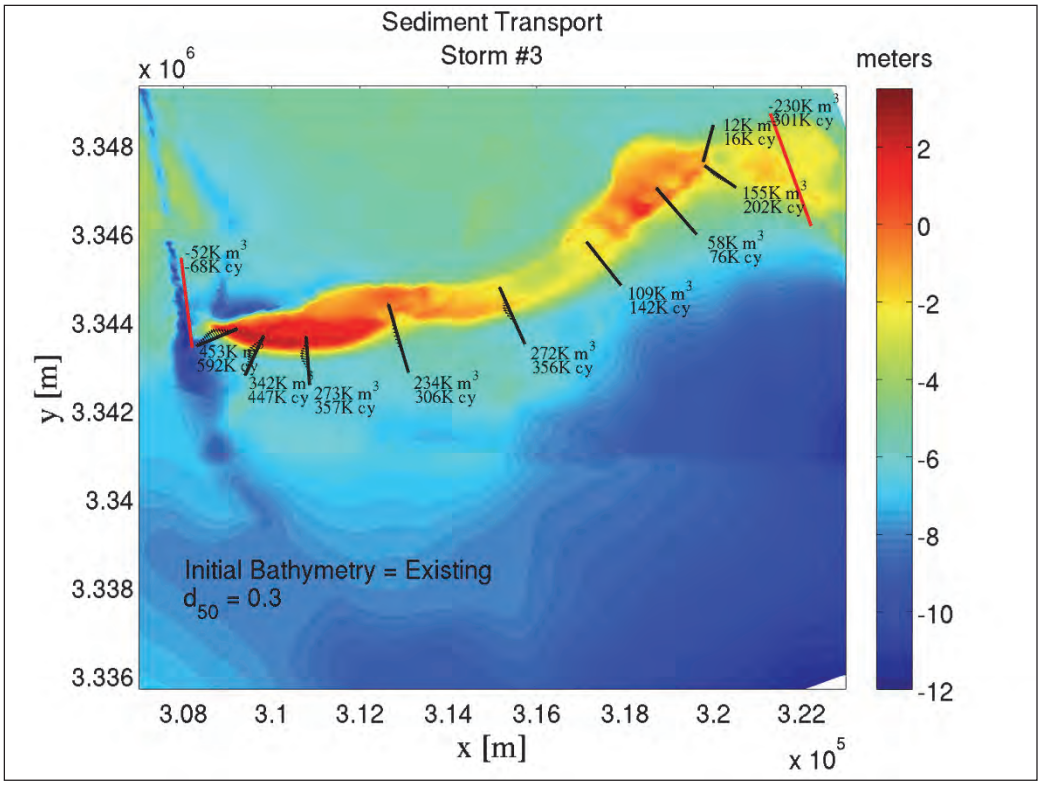

Figure G-16. Alternative #1 Restored conditions for Storm #3; Template A; With borrow pits.

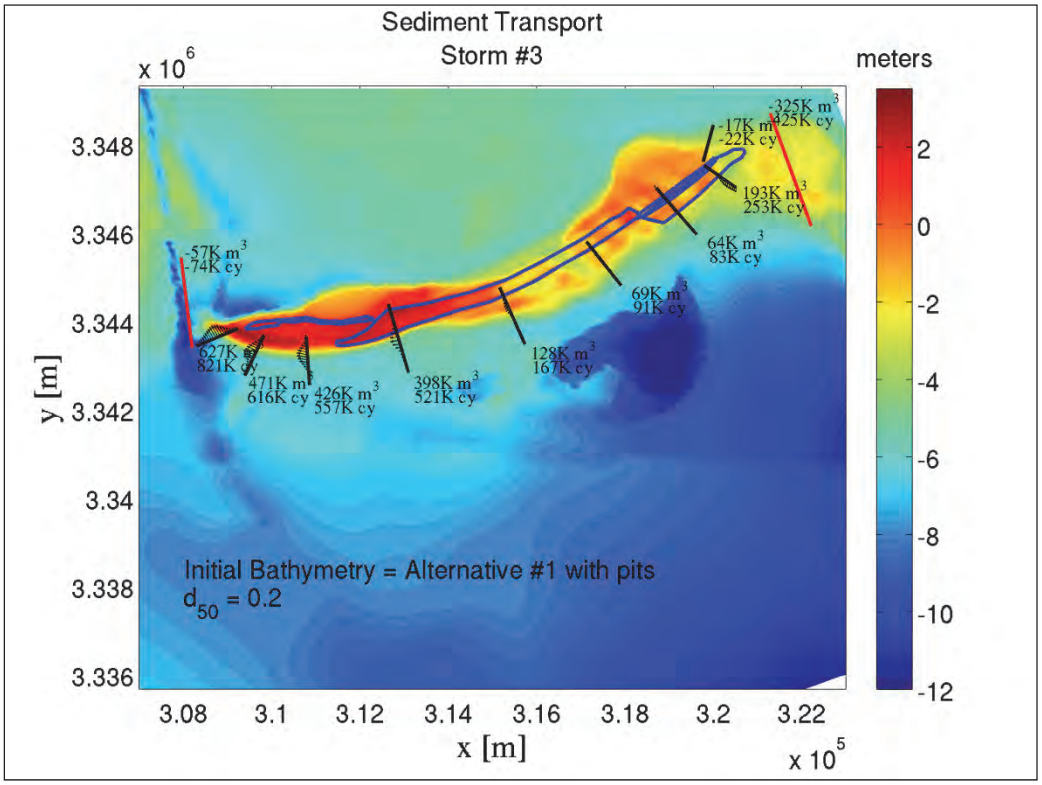

Figure G-17. Alternative #1 Restored conditions for Storm #3; Template B; With borrow pits.

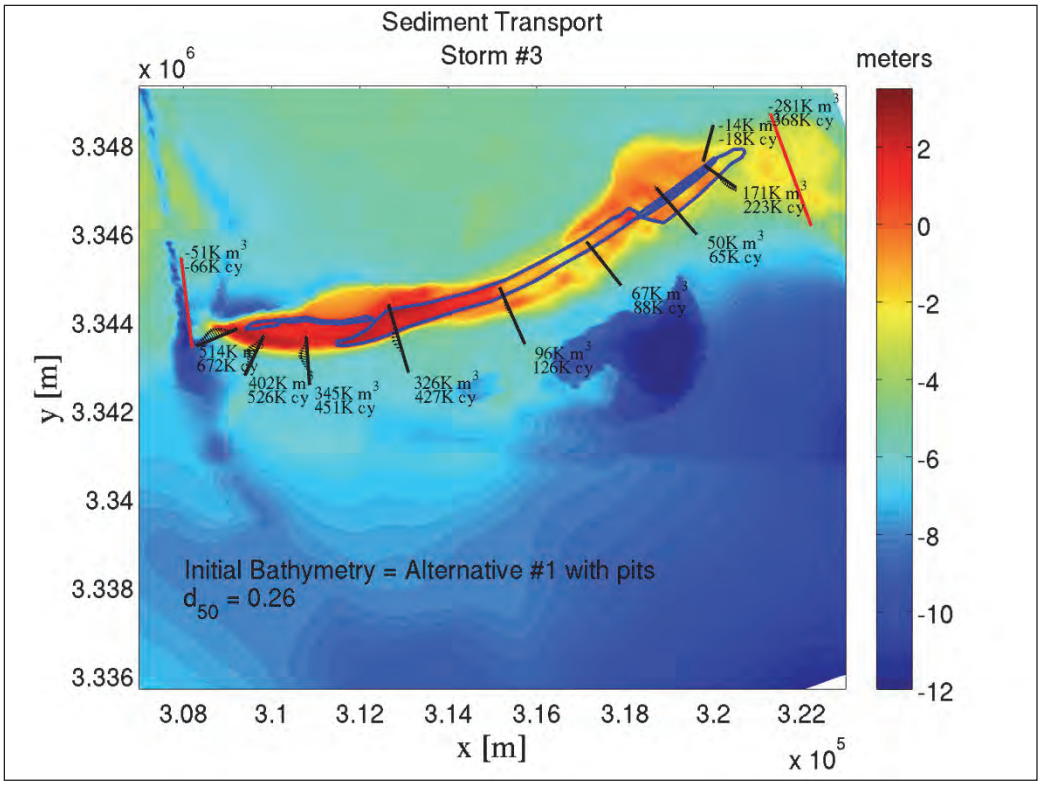

Figure G-18. Alternative #1 Restored conditions for Storm #3; Template C; With borrow pits.

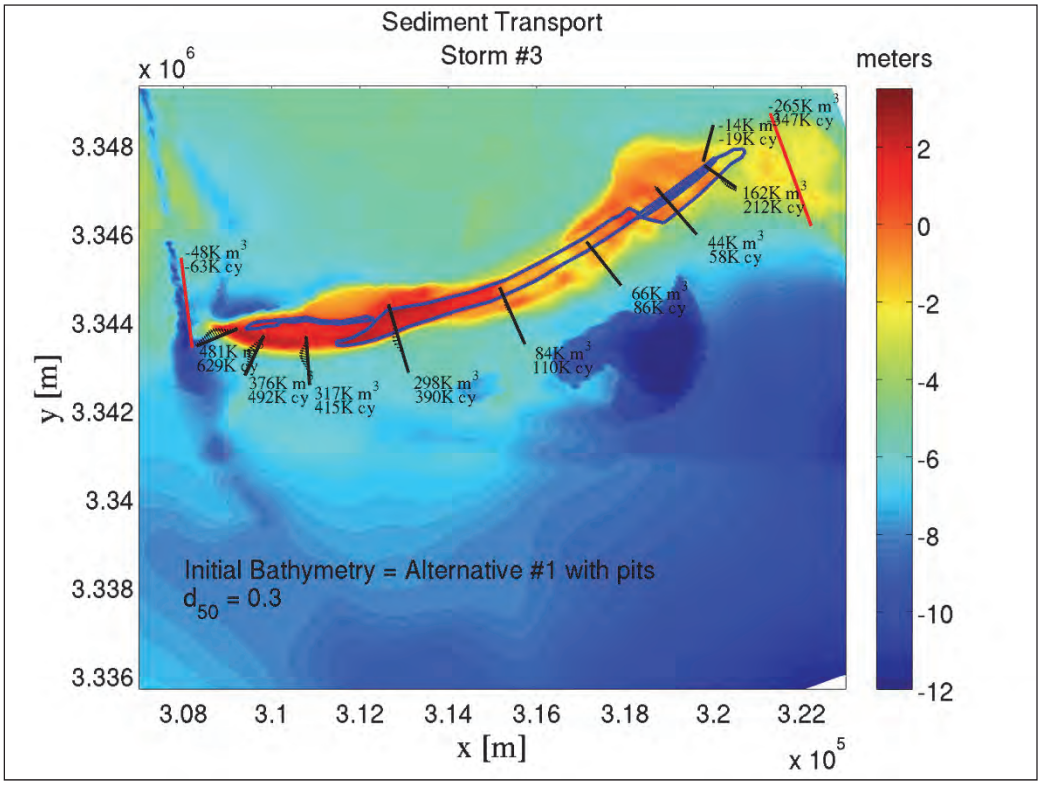

Figure G-19. Alternative #1 Restored conditions for Storm #3; Template A; Without borrow pits.

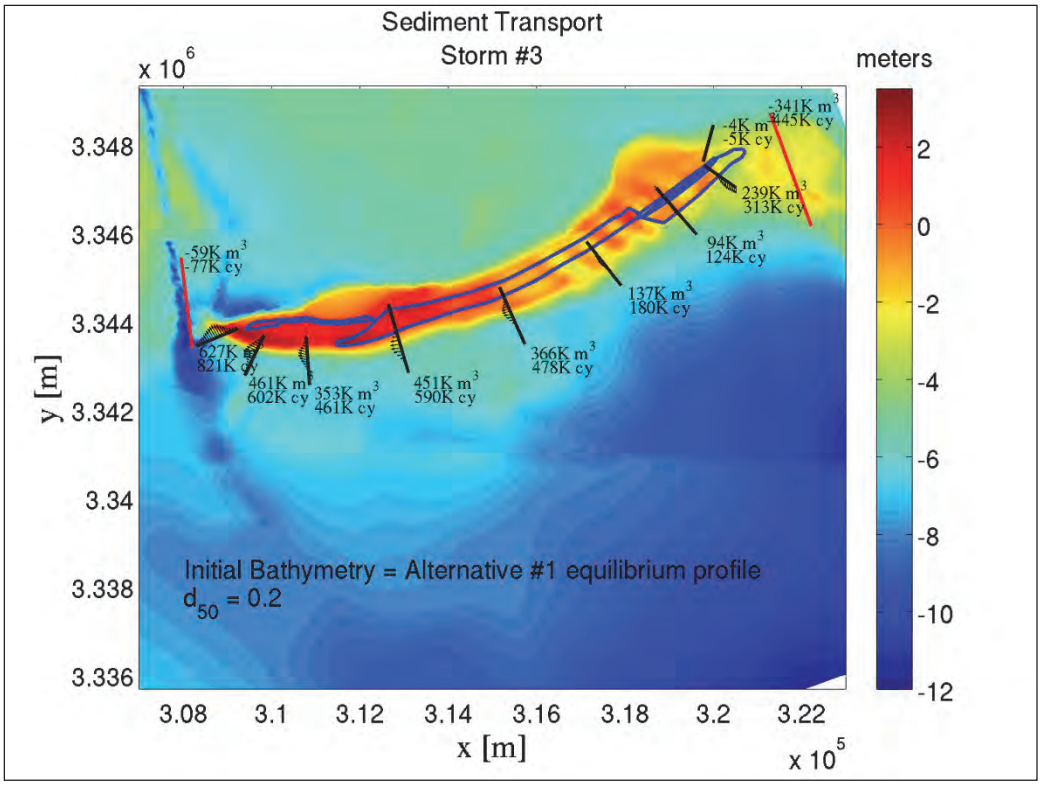

Figure G-20. Alternative #1 Restored conditions for Storm #3; Template B; Without borrow pits.

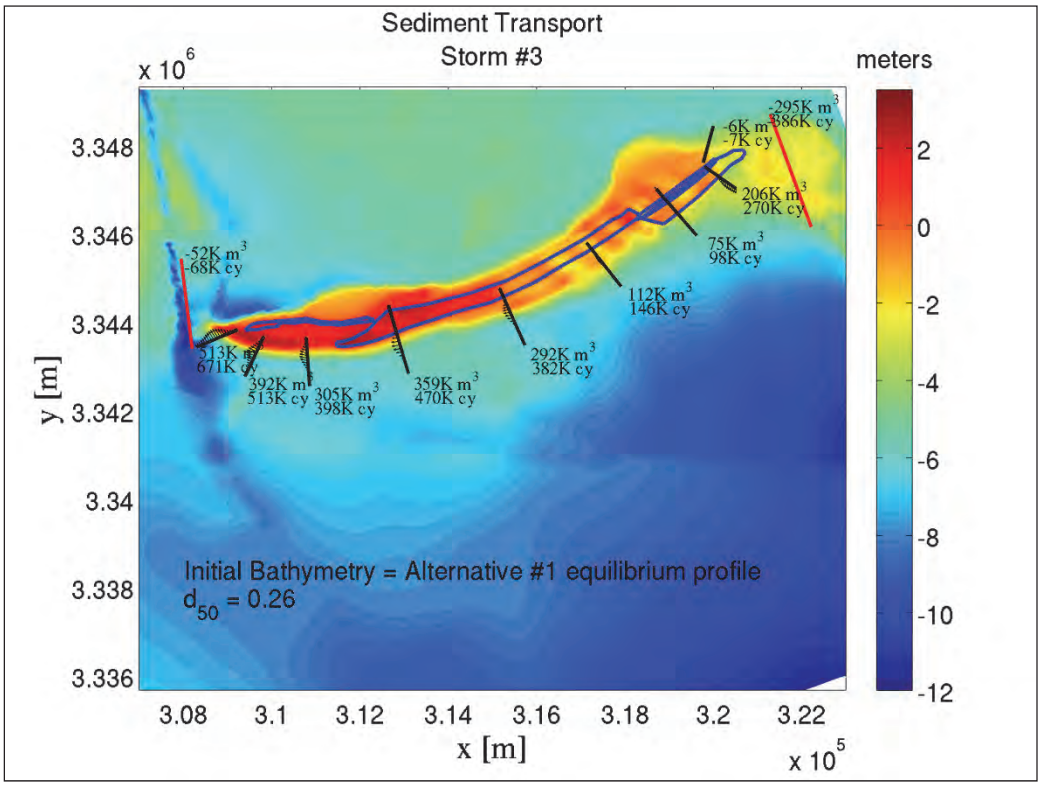

Figure G-21. Alternative #1 Restored conditions for Storm #3; Template C; Without borrow pits.

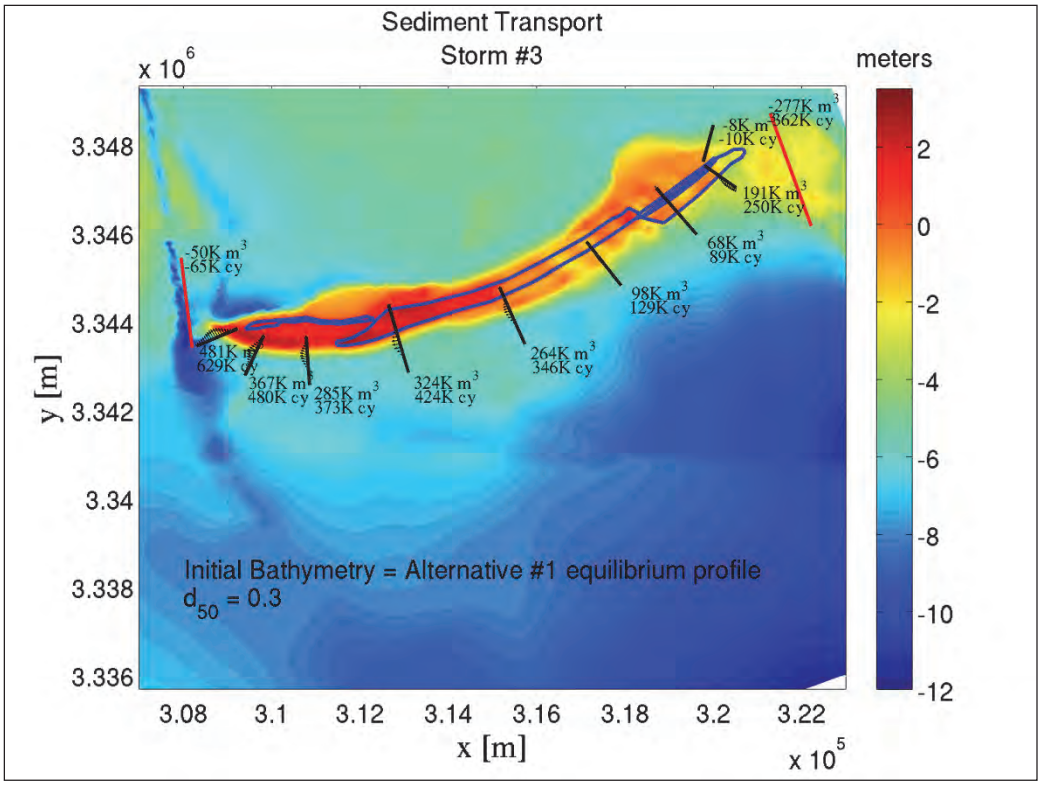

Figure G-22. Existing conditions for Storm #1.

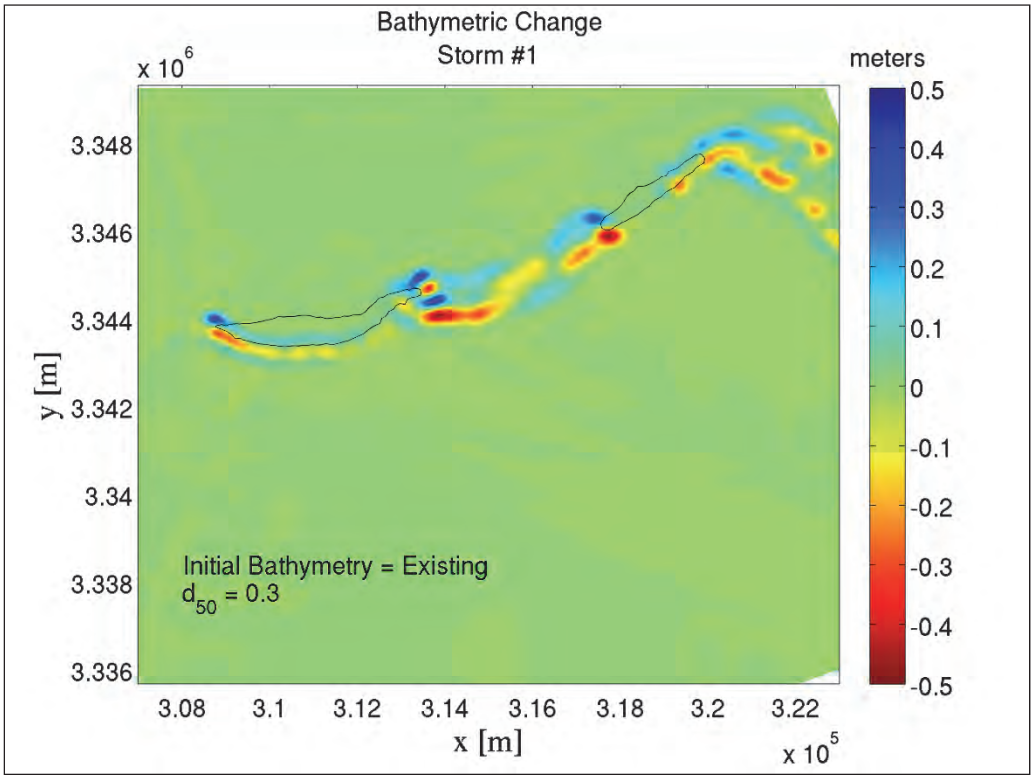

Figure G-23. Alternative #1 Restored conditions for Storm #1; Template A; With borrow pits.

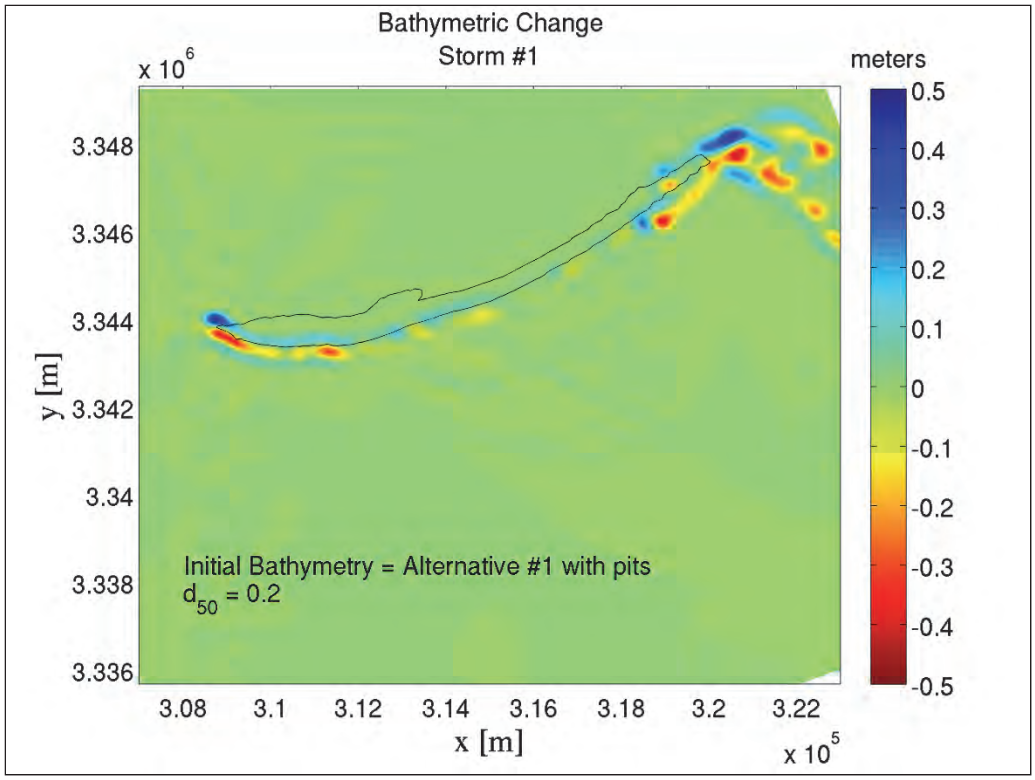

Figure G-24. Alternative #1 Restored conditions for Storm #1; Template B; With borrow pits.

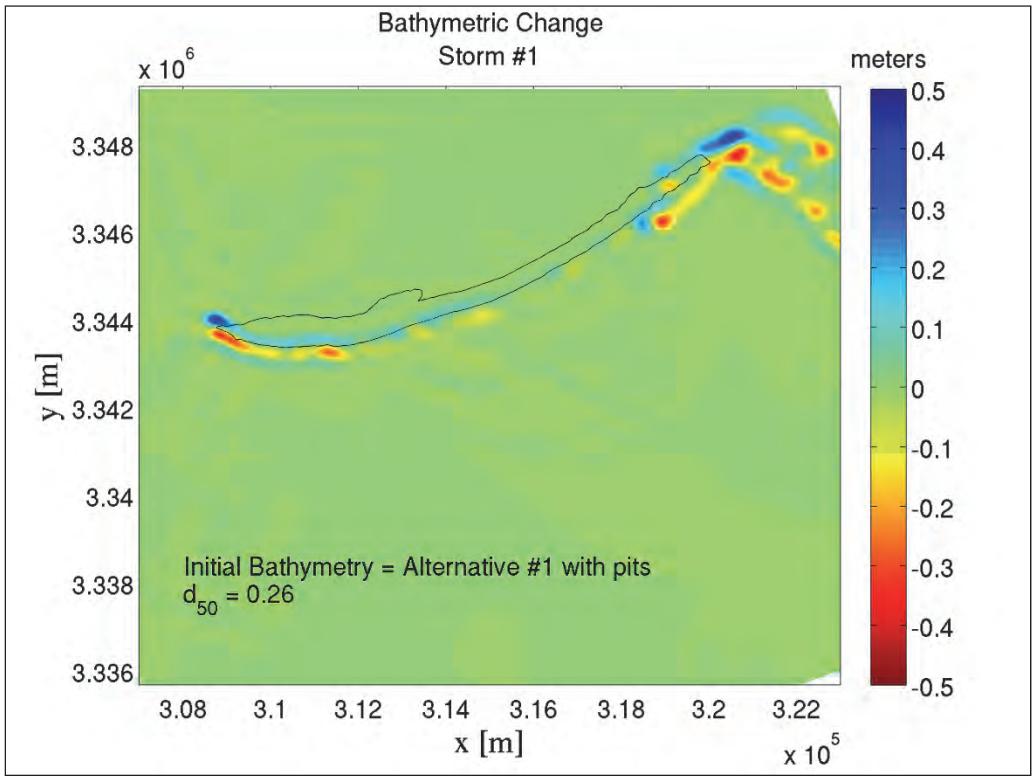

Figure G-25. Alternative #1 Restored conditions for Storm #1; Template C; With borrow pits.

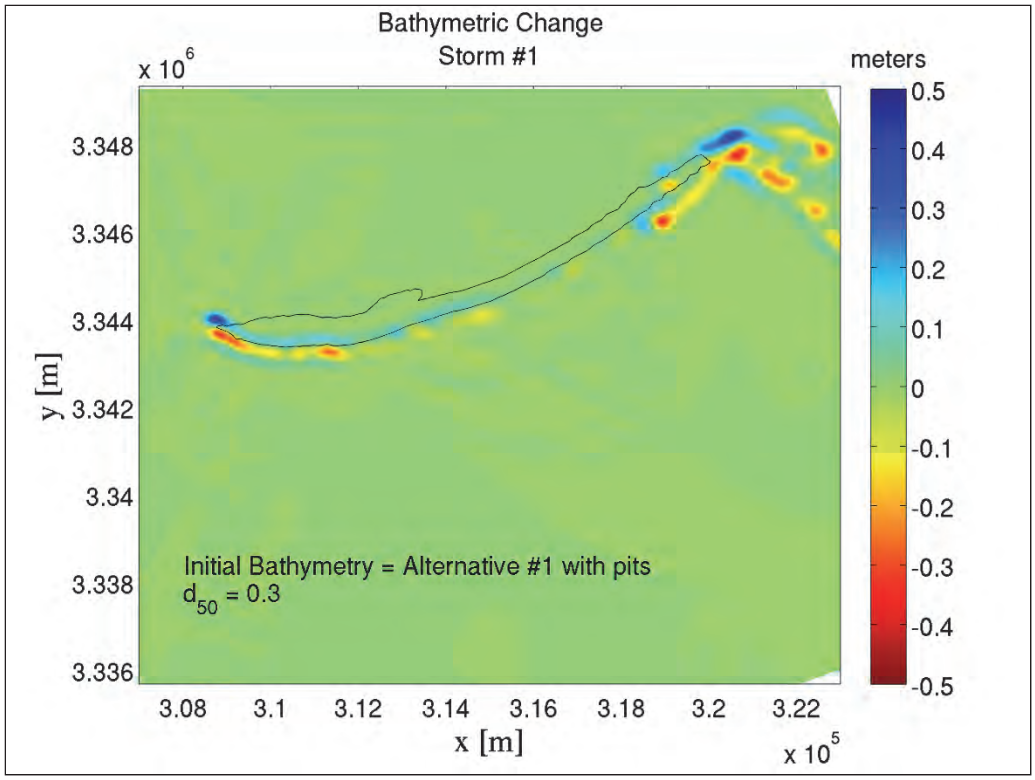

Figure G-26. Alternative #1 Restored conditions for Storm #1; Template A; Without borrow pits.

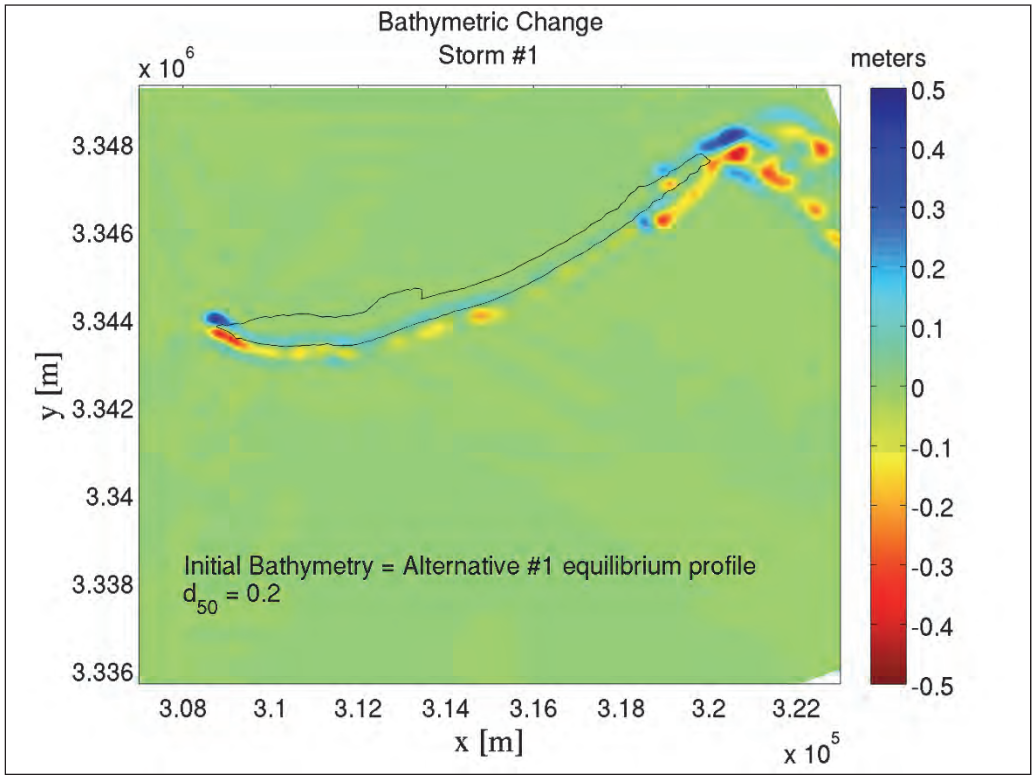

Figure G-27. Alternative #1 Restored conditions for Storm #1; Template B; Without borrow pits.

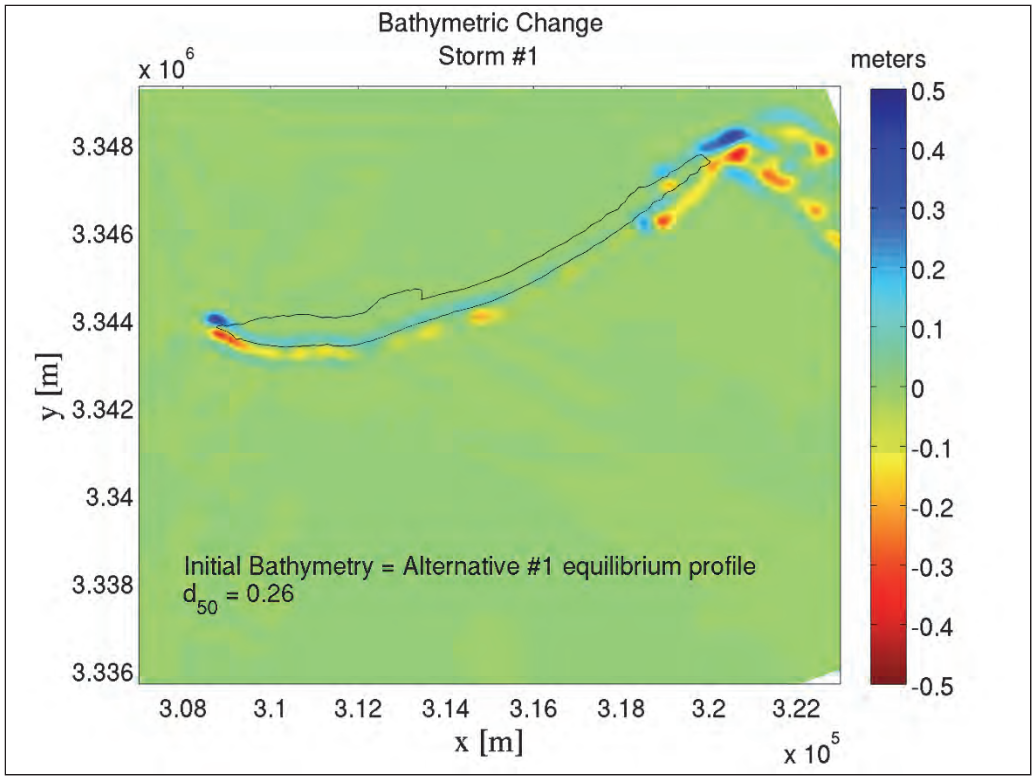

Figure G-28. Alternative #1 Restored conditions for Storm #1; Template C; Without borrow pits.

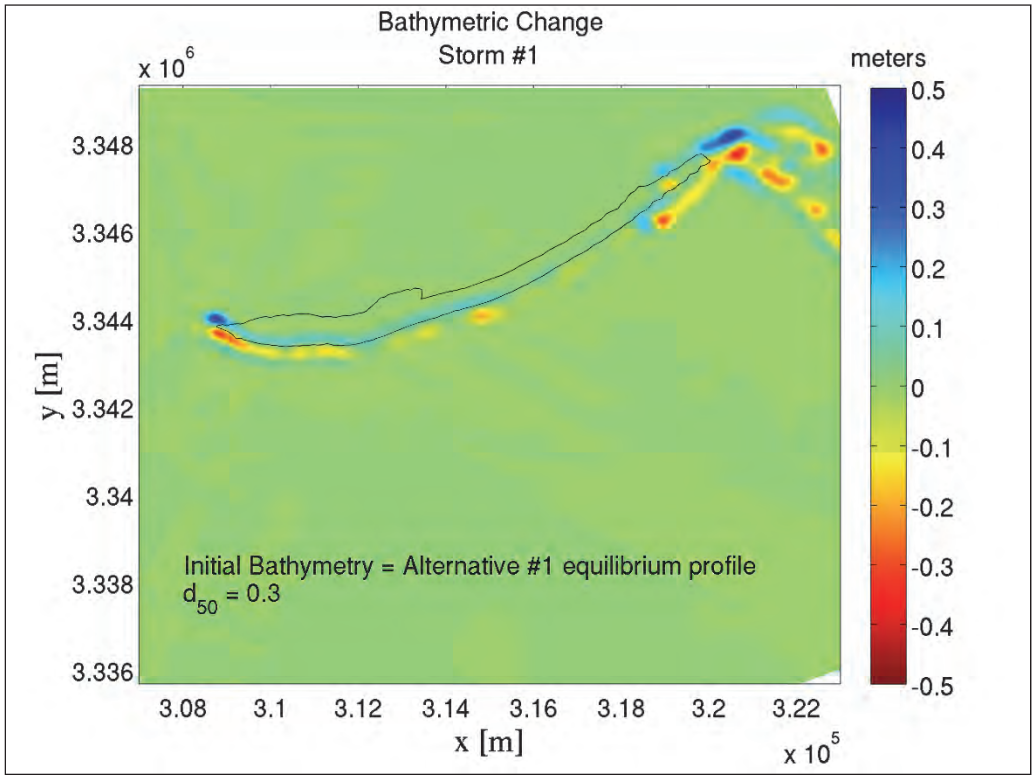

Figure G-29. Existing conditions for Storm #2.

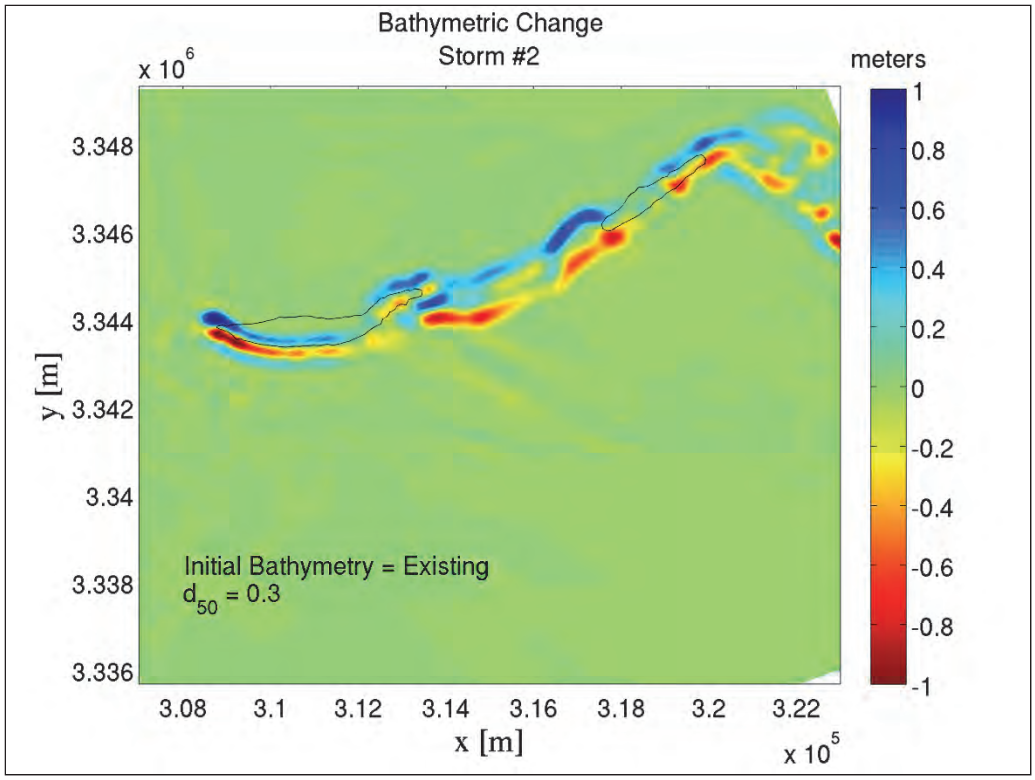

Figure G-30. Alternative #1 Restored conditions for Storm #2; Template A; With borrow pits.

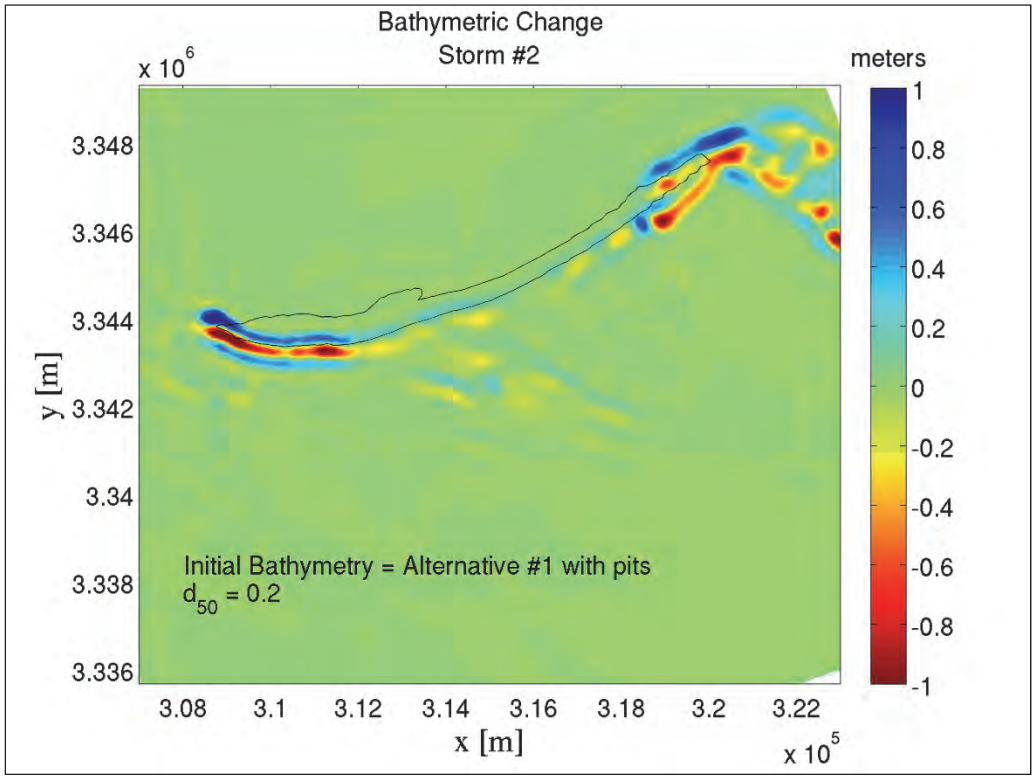

Figure G-31. Alternative #1 Restored conditions for Storm #2; Template B; With borrow pits.

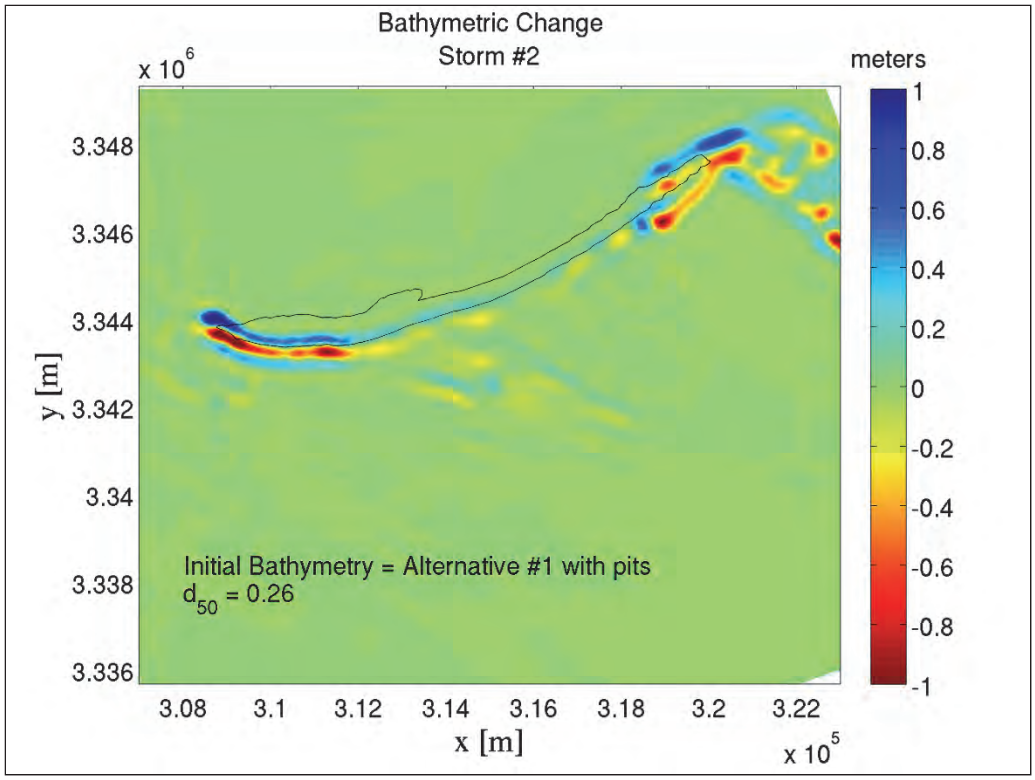

Figure G-32. Alternative #1 Restored conditions for Storm #2; Template C; With borrow pits.

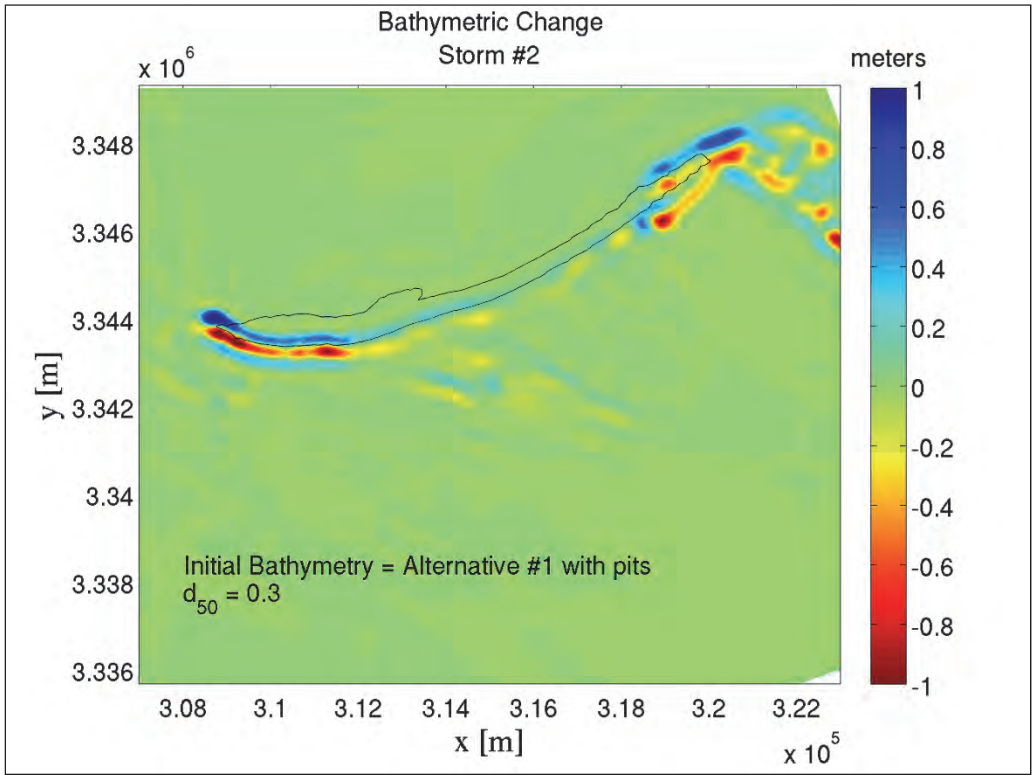

Figure G-33. Alternative #1 Restored conditions for Storm #2; Template A; Without borrow pits.

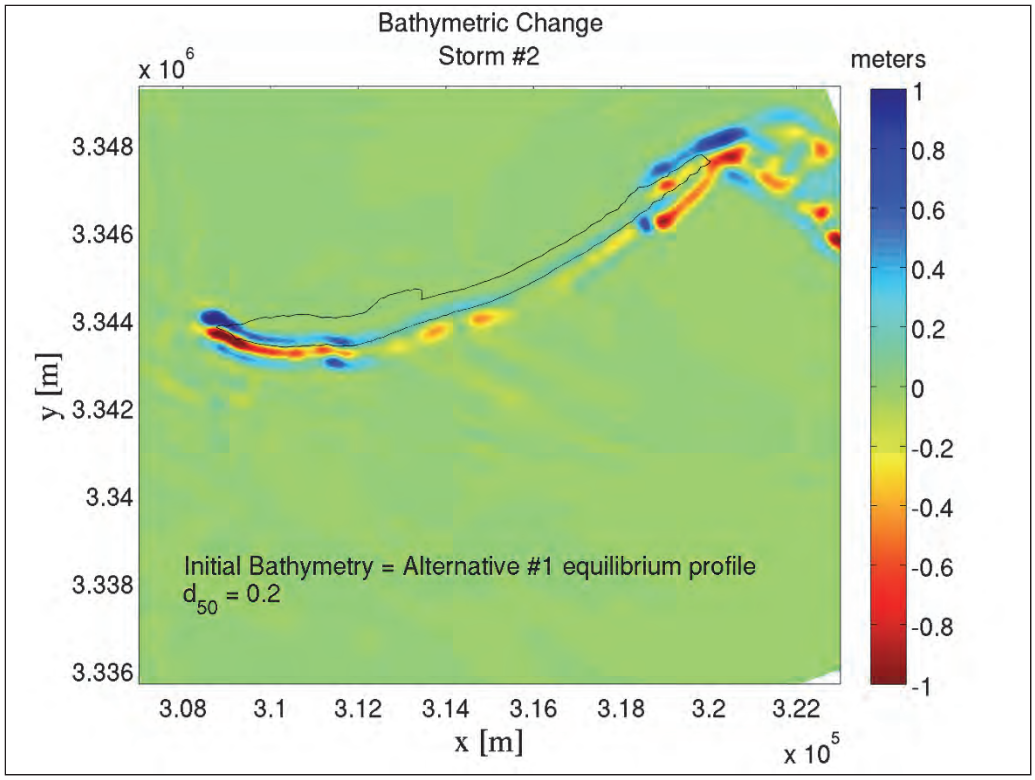

Figure G-34. Alternative #1 Restored conditions for Storm #2; Template B; Without borrow pits.

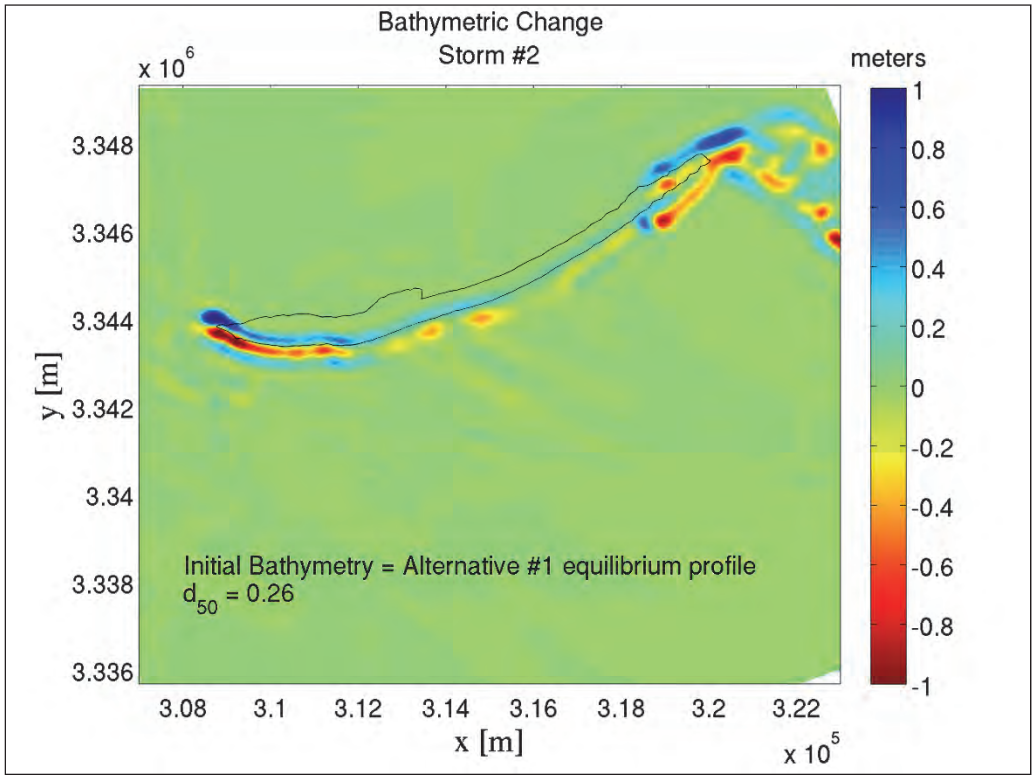

Figure G-35. Alternative #1 Restored conditions for Storm #2; Template C; Without borrow pits.

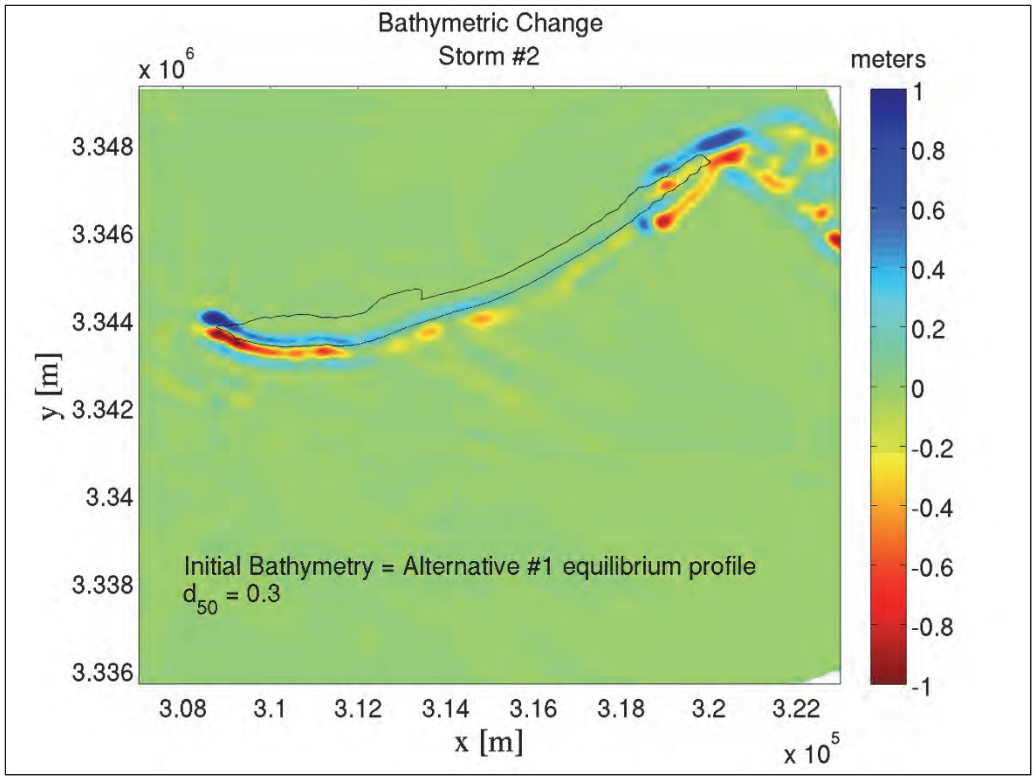

Figure G-36. Existing conditions for Storm #3.

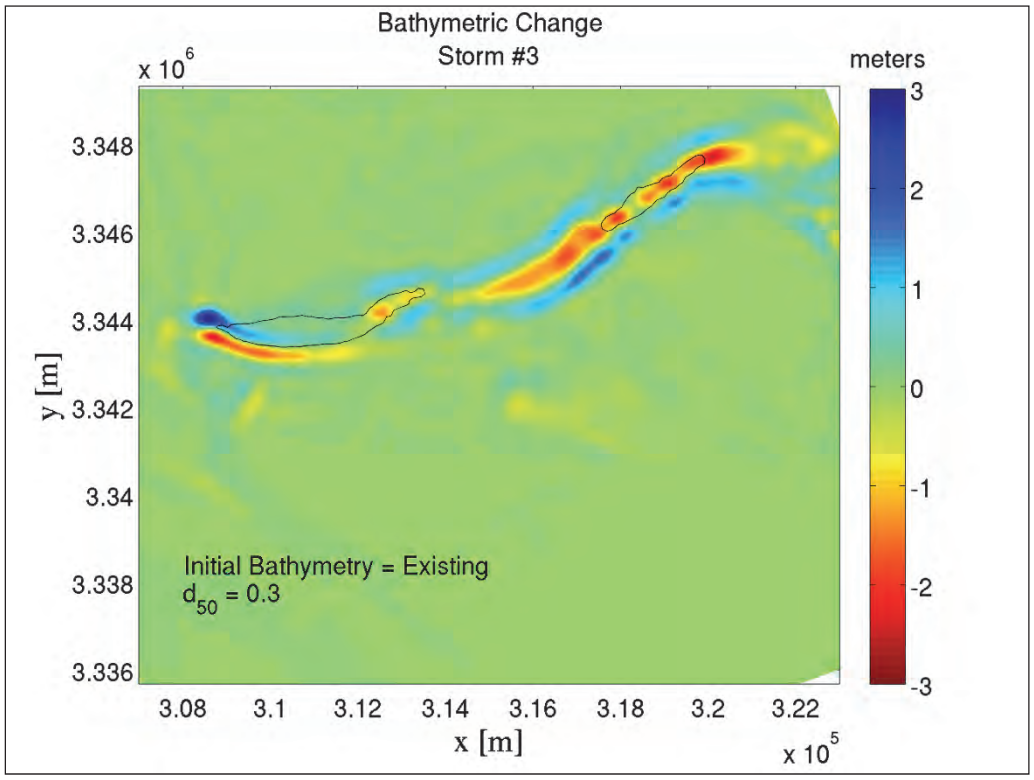

Figure G-37. Alternative #1 Restored conditions for Storm #3; Template A; With borrow pits.

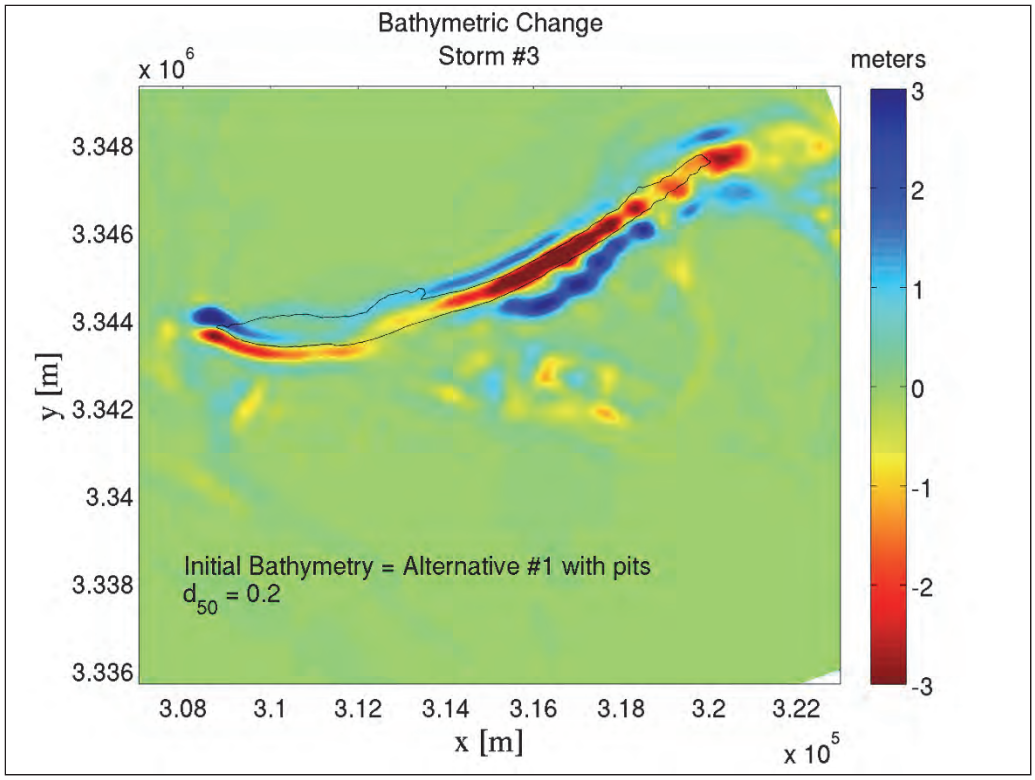

Figure G-38. Alternative #1 Restored conditions for Storm #3; Template B; With borrow pits.

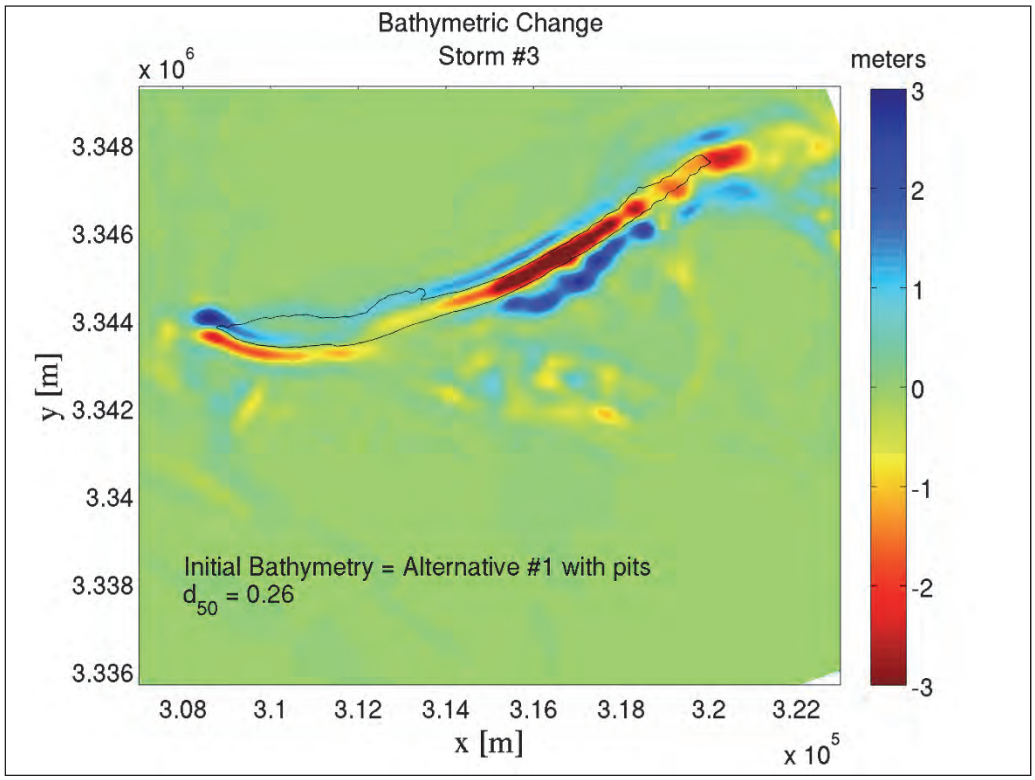

Figure G-39. Alternative #1 Restored conditions for Storm #3; Template C; With borrow pits.

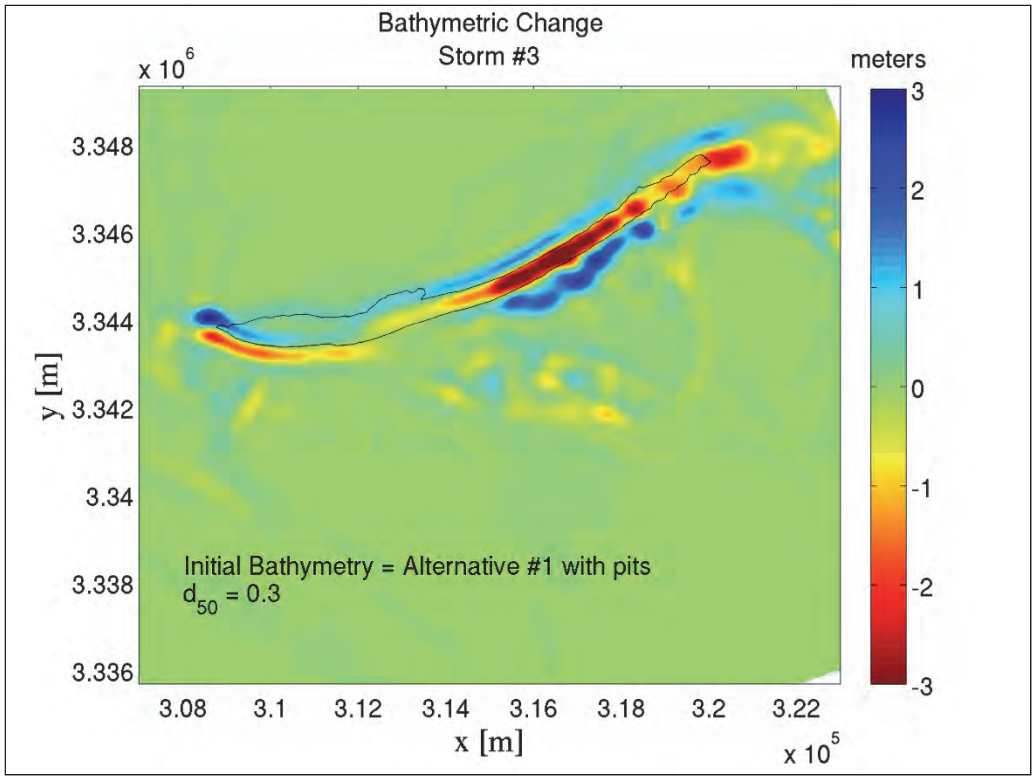

Figure G-40. Alternative #1 Restored conditions for Storm #3; Template A; Without borrow pits.

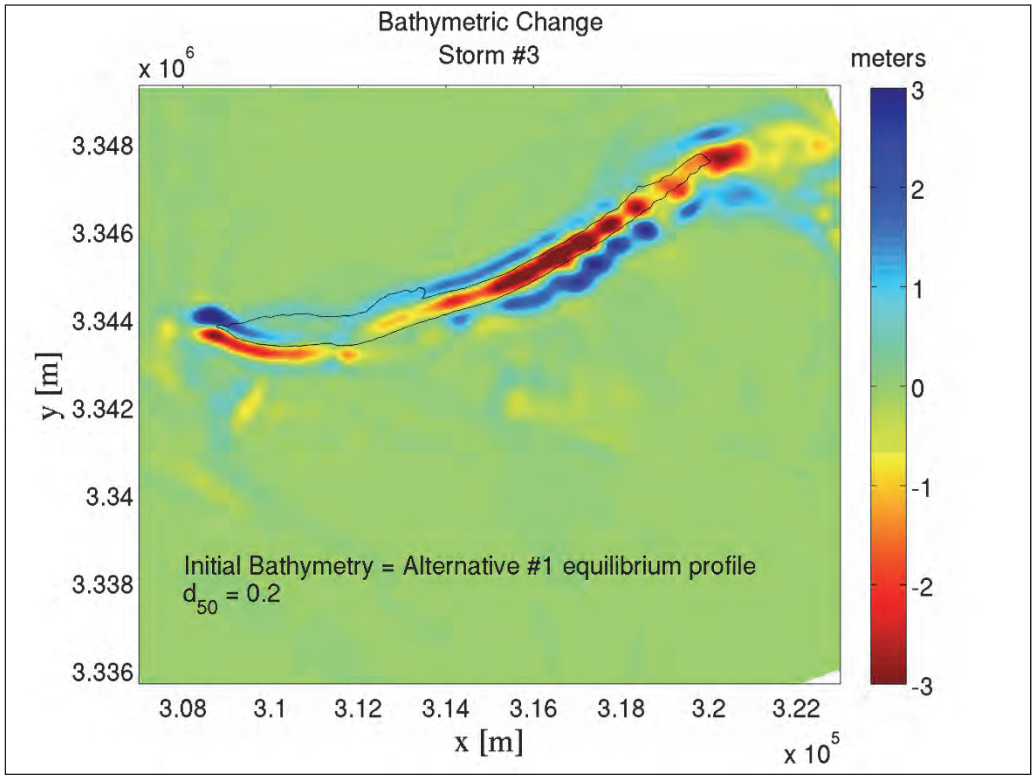

Figure G-41. Alternative #1 Restored conditions for Storm #3; Template B; Without borrow pits.

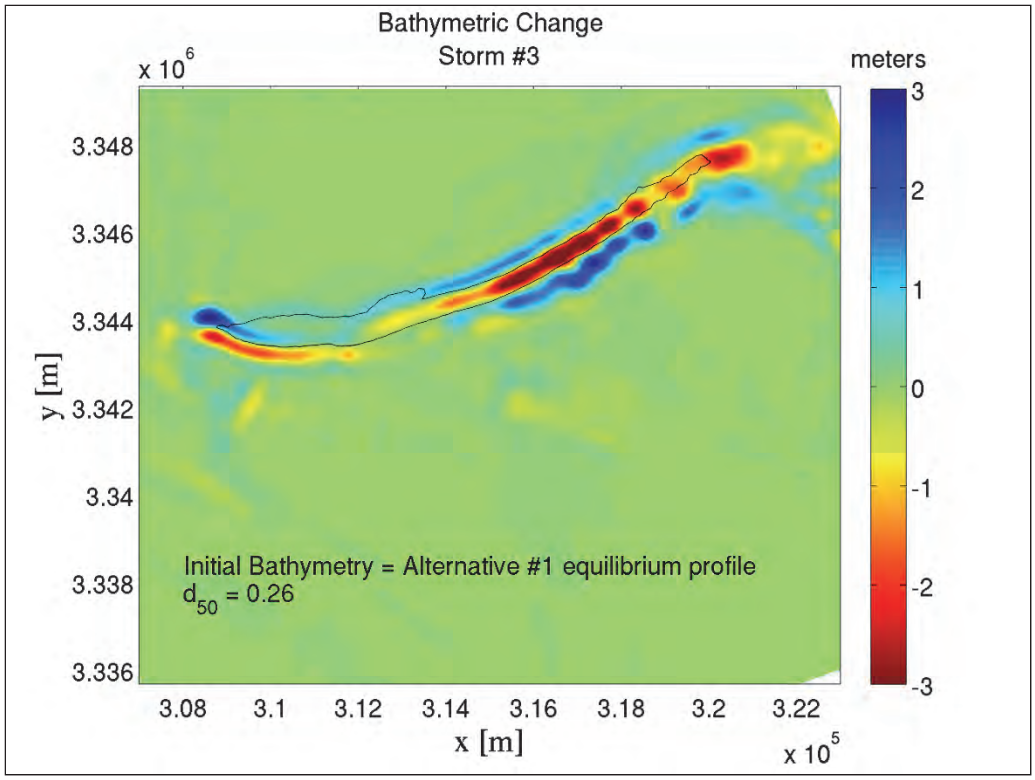

Figure G-42. Alternative #1 Restored conditions for Storm #3; Template C; Without borrow pits.

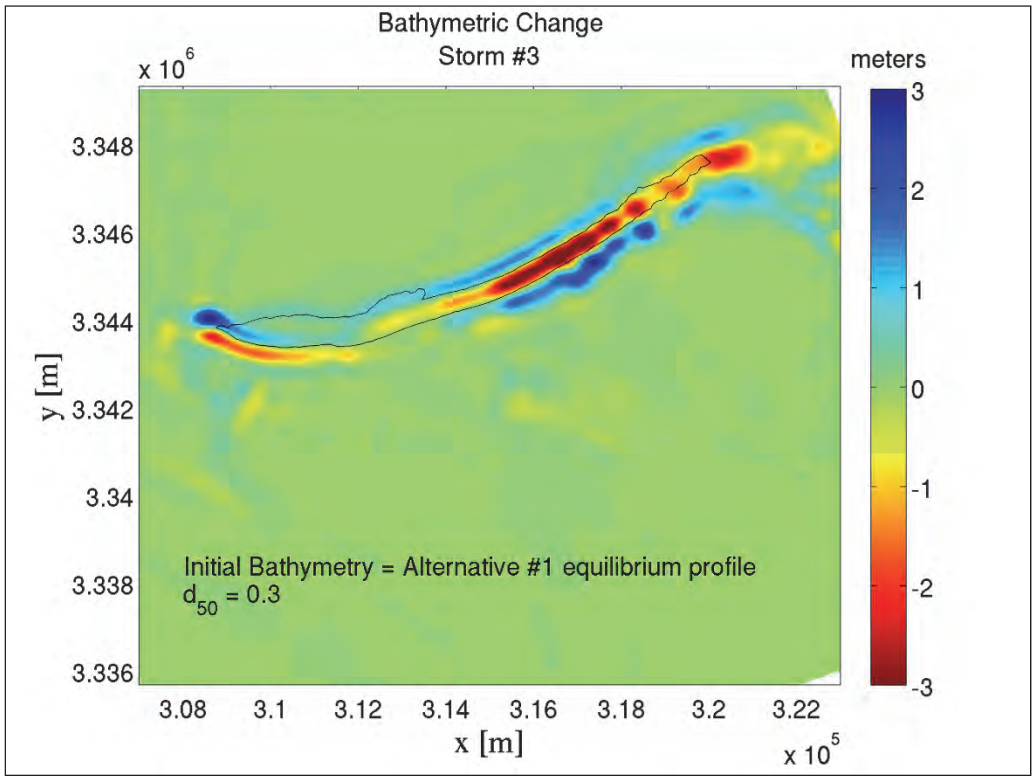

Figure G-43. Existing conditions for Storm #1.

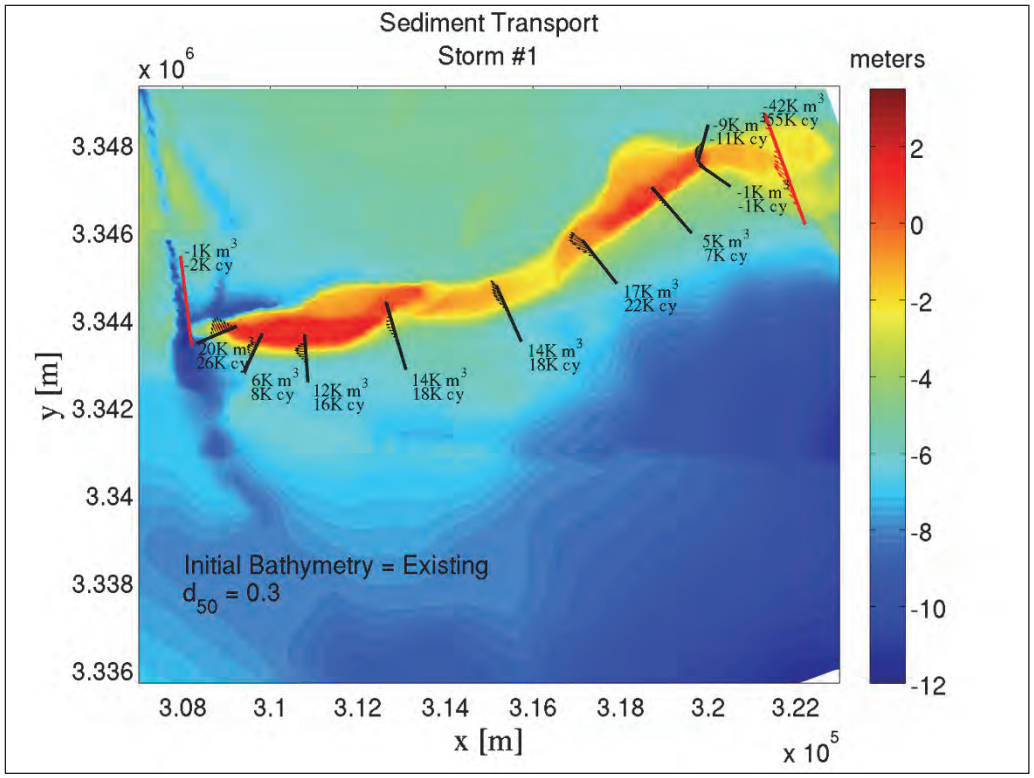

Figure G-44. Alternative #2 Restored conditions for Storm #1.

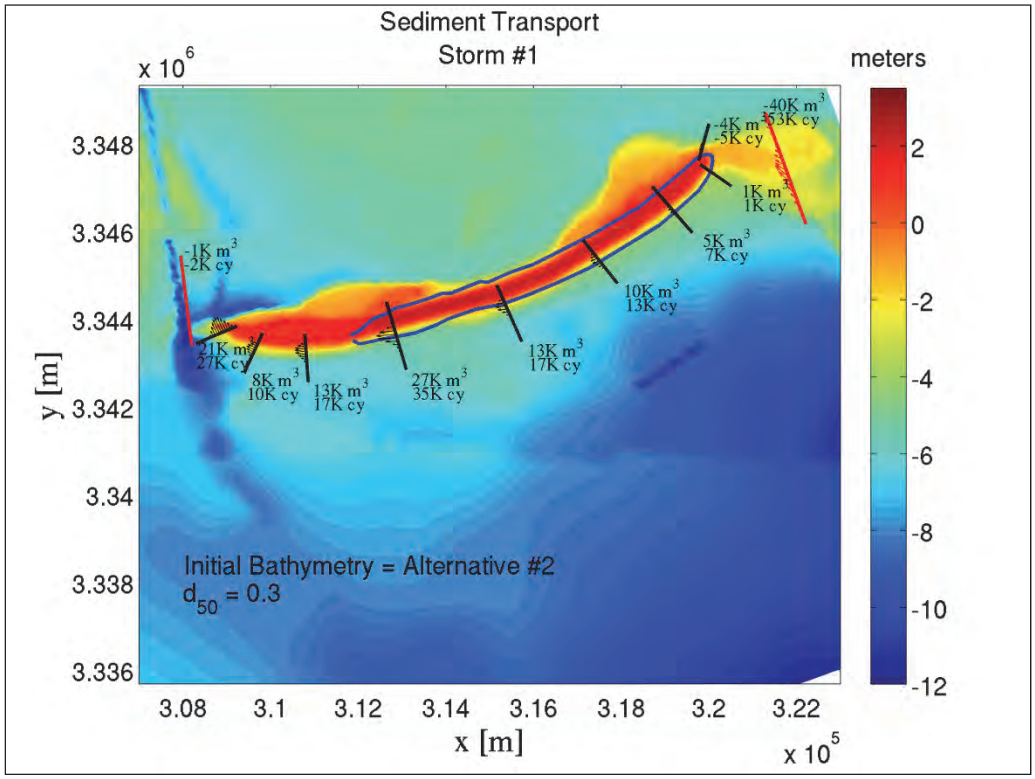

Figure G-45. Existing conditions for Storm #2.

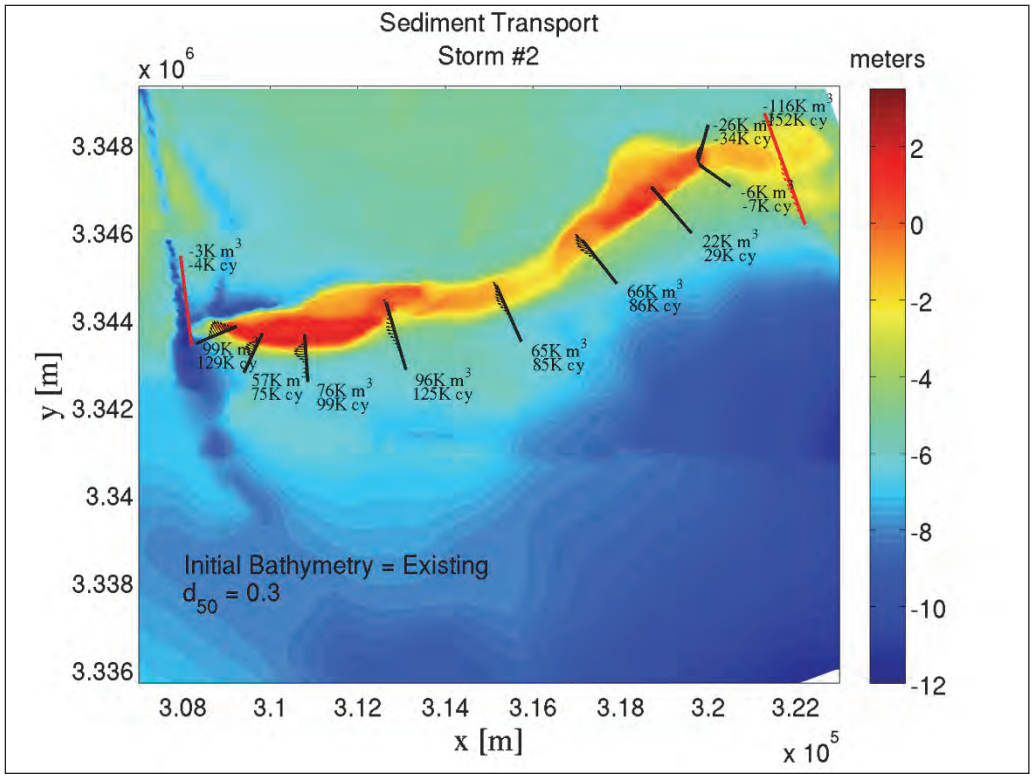

Figure G-46. Alternative #2 Restored conditions for Storm #2.

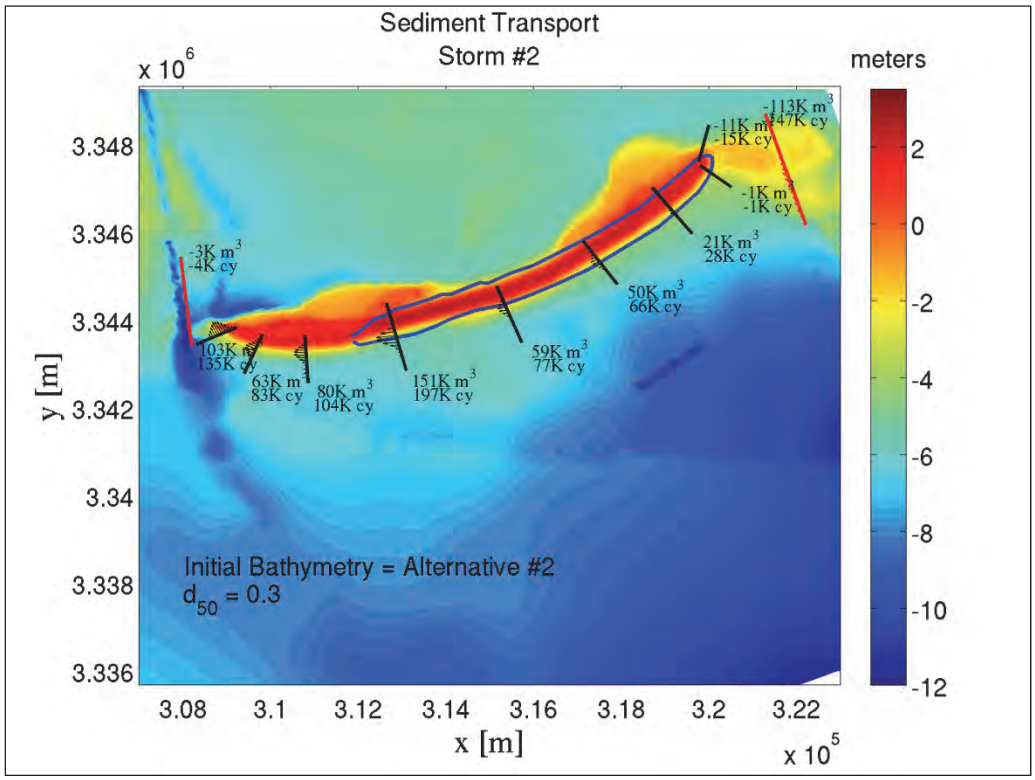

Figure G-47. Existing conditions for Storm #3.

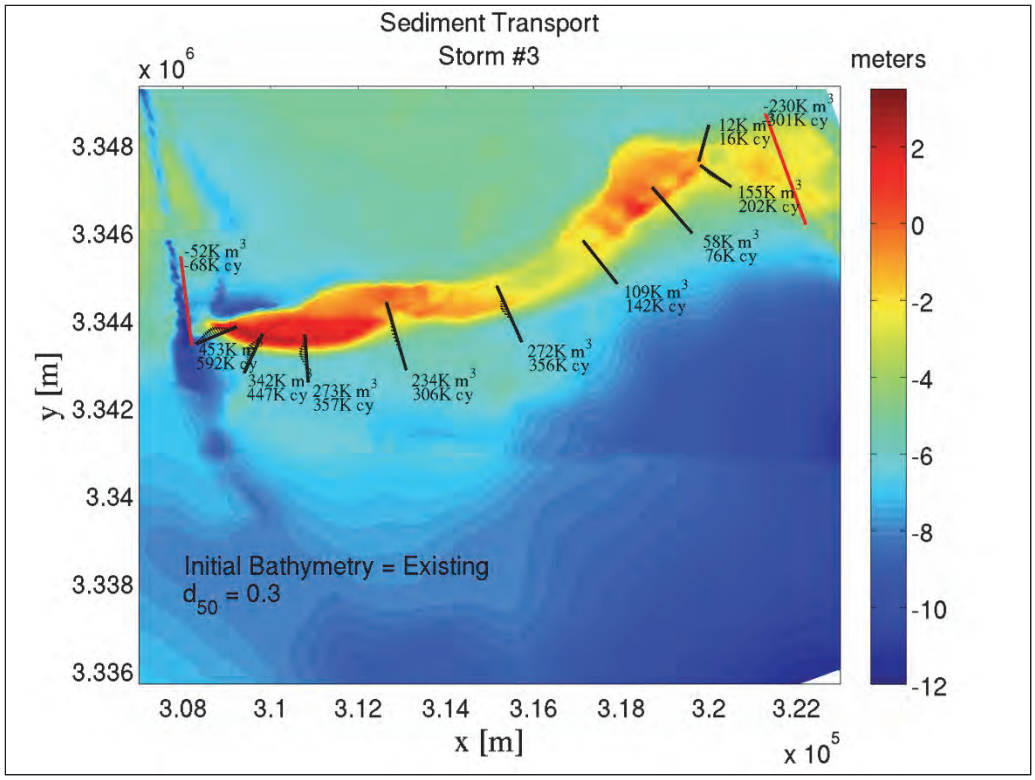

Figure G-48. Alternative #2 Restored conditions for Storm #3.

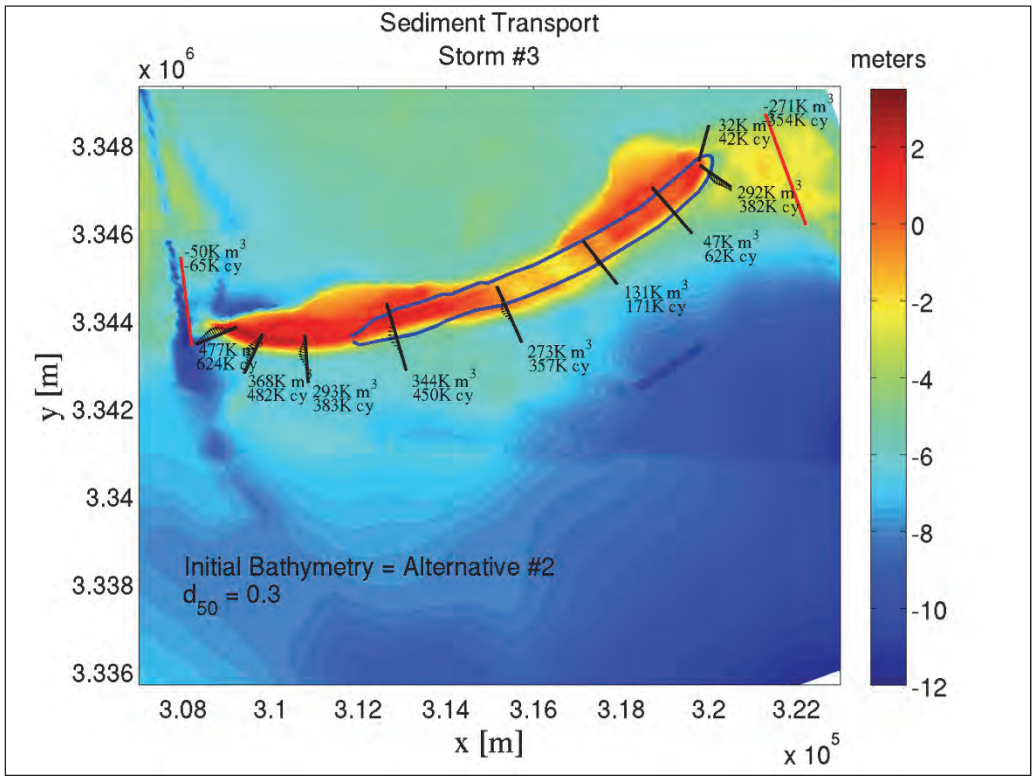

Figure G-49. Alternative #2 Restored conditions for Storm #1.

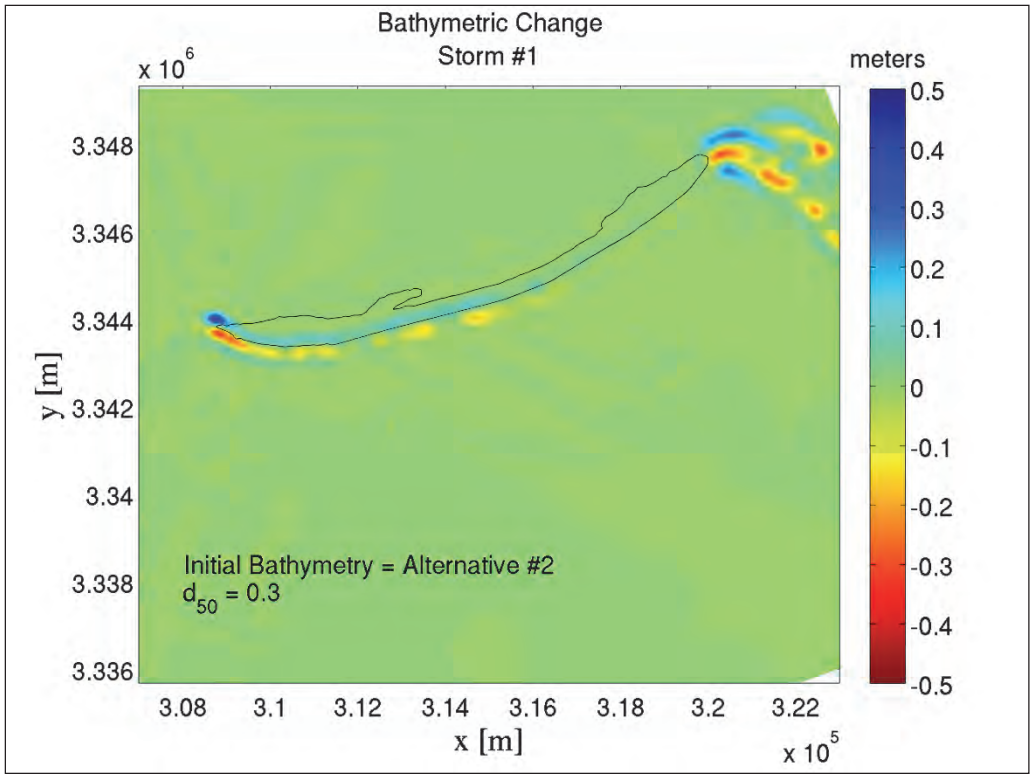

Figure G-50. Alternative #2 Restored conditions for Storm #2.

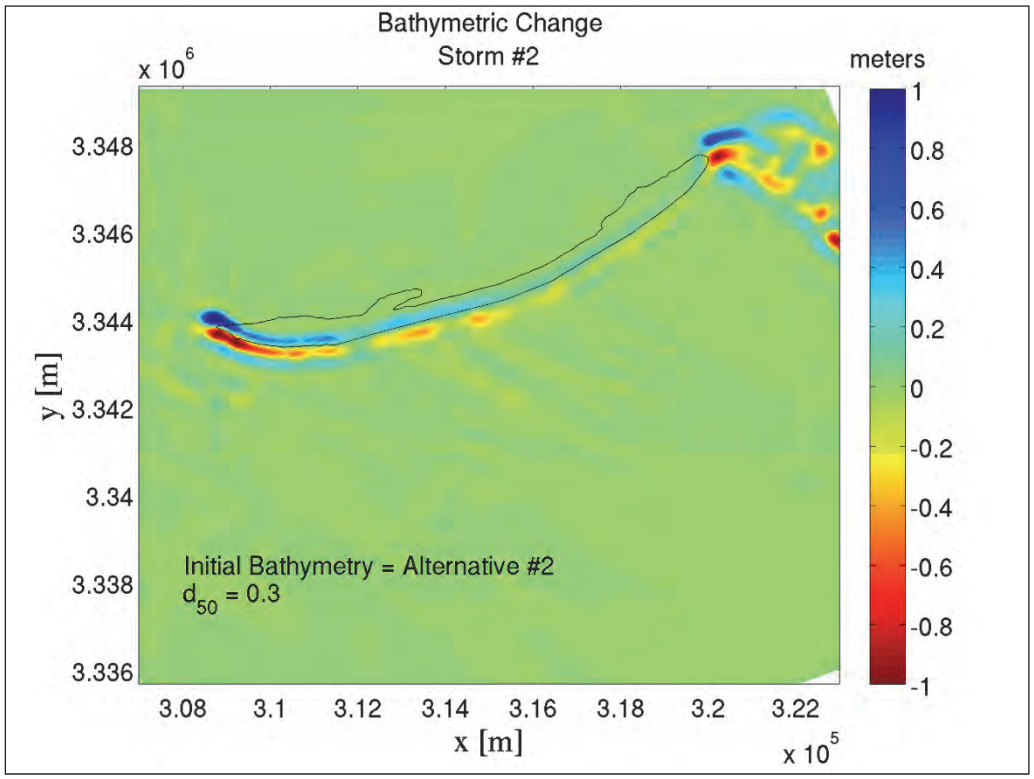

Figure G-51. Alternative #2 Restored conditions for Storm #3.

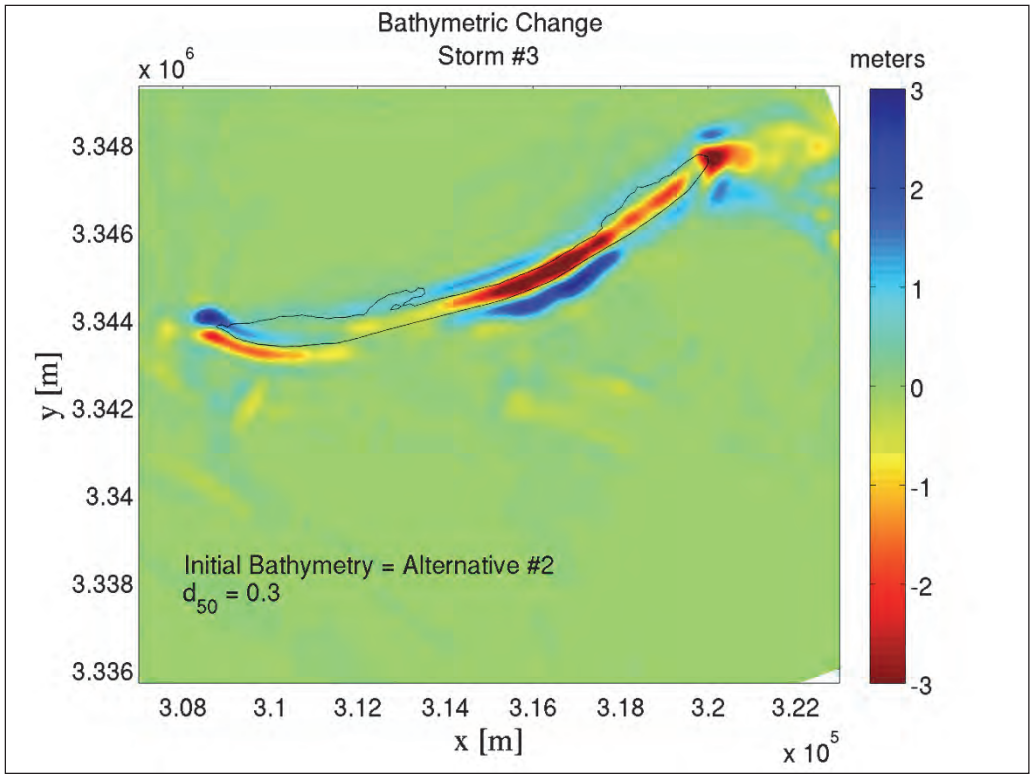

Appendix H: Nearshore Bathymetric Change Modeled Results for Existing Conditions and Restoration Scenarios

Note: The island footprint (NAVD = 0) contour is depicted as a black outline for reference.

Figure H-1. Existing conditions for Storm #1; d_{50} = 0.30 mm.

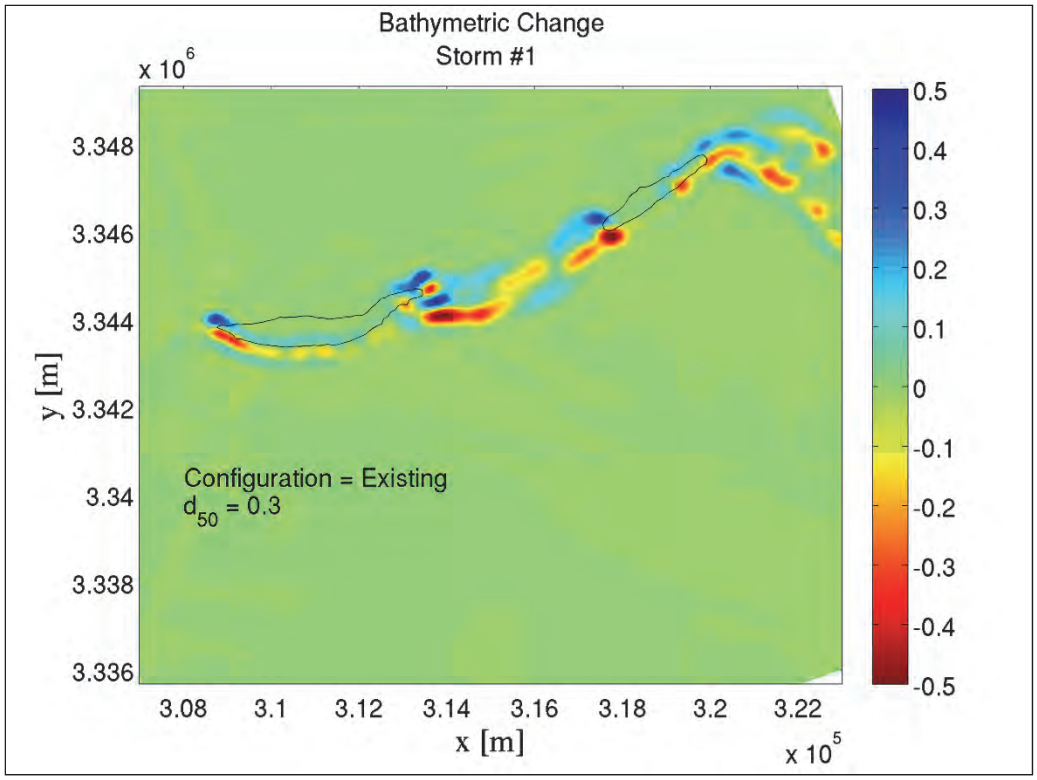

Figure H-2. Restored conditions for Storm #1; d_{50} = 0.20 mm (Template #1); With borrow pits.

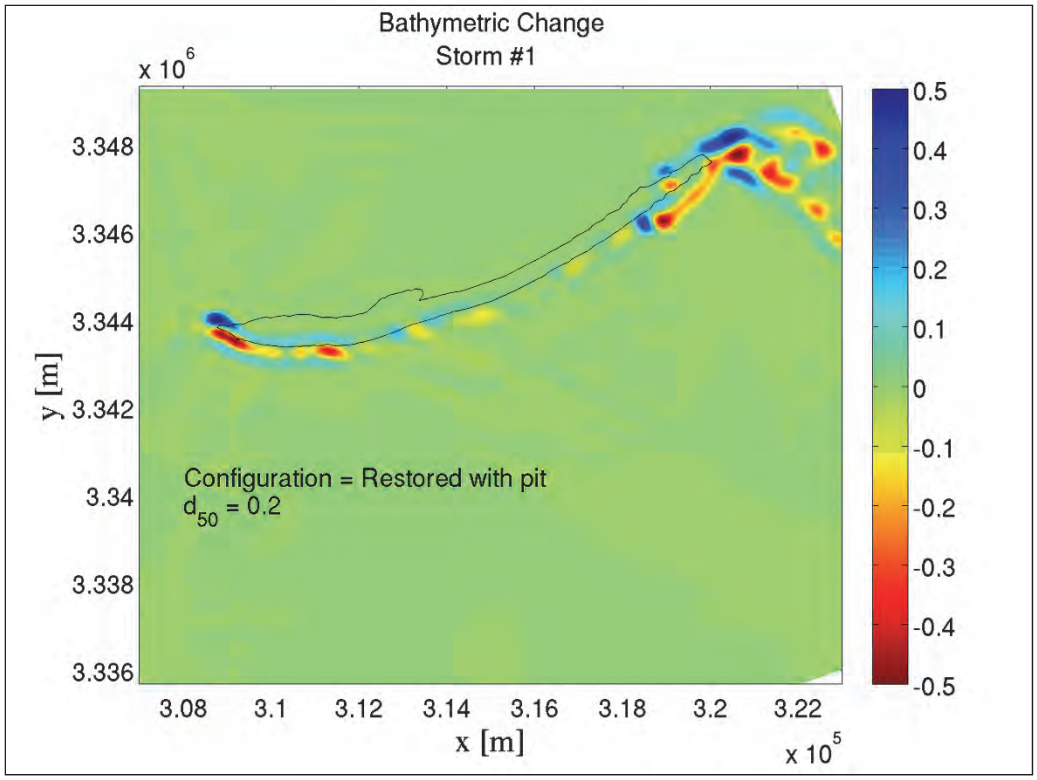

Figure H-3. Restored conditions for Storm #1; d50 = 0.26 mm (Template #2); With borrow pits.

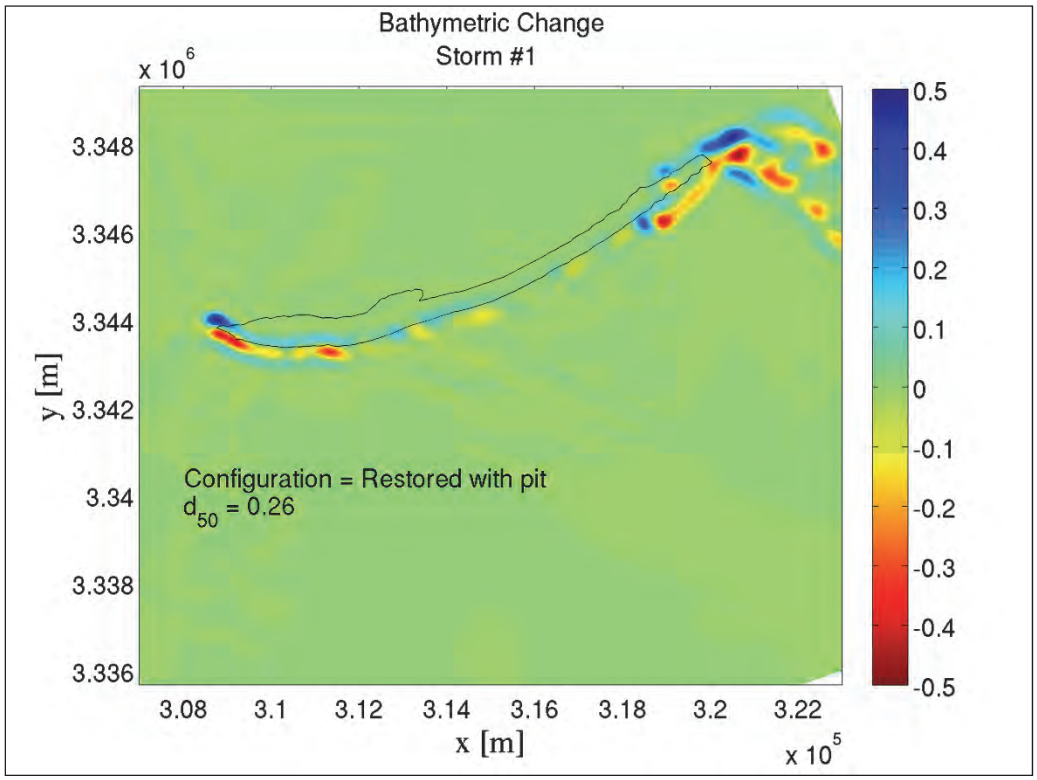

Figure H-4. Restored conditions for Storm #1; d_{50} = 0.30 mm (Template #3); With borrow pits.

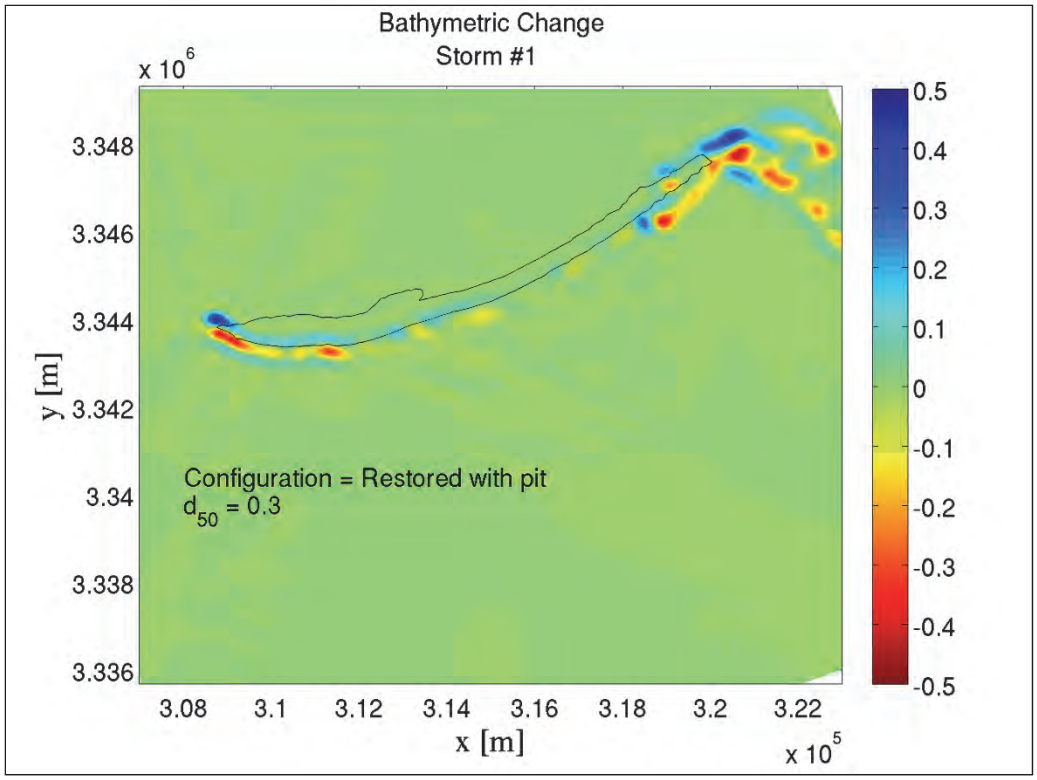

Figure H-5. Restored conditions for Storm #1; d_{50} = 0.20 mm (Template #1); Without borrow pits.

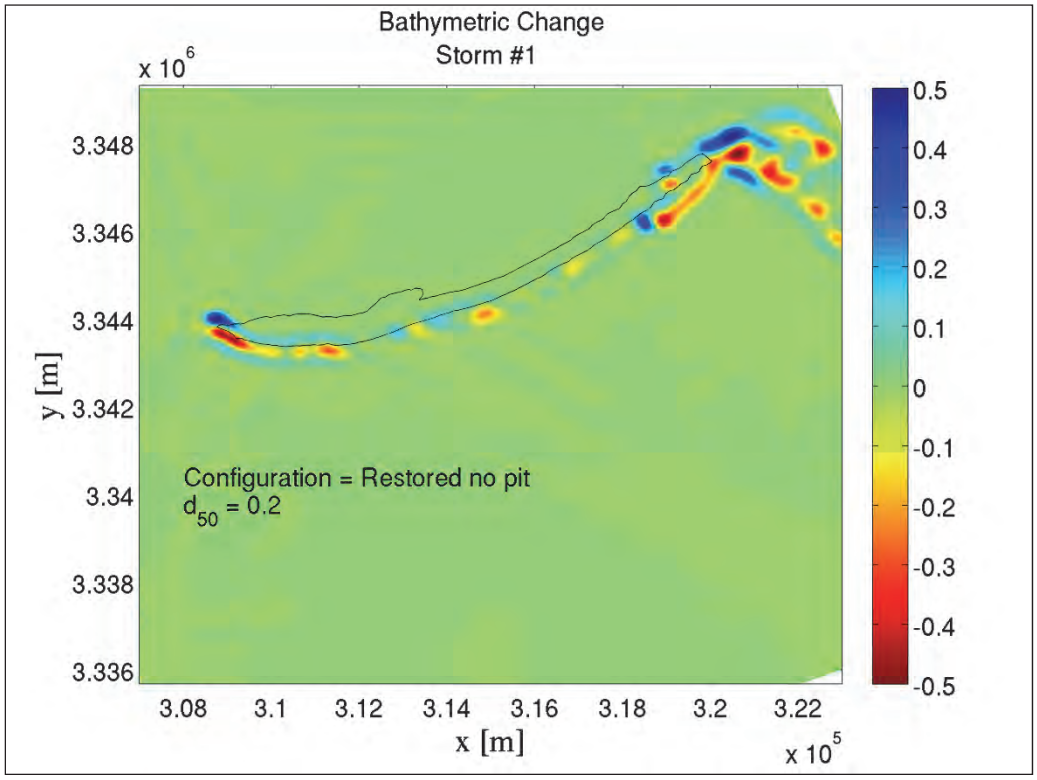

Figure H-6. Restored conditions for Storm #1; d_{50} = 0.26 mm (Template #2); Without borrow pits.

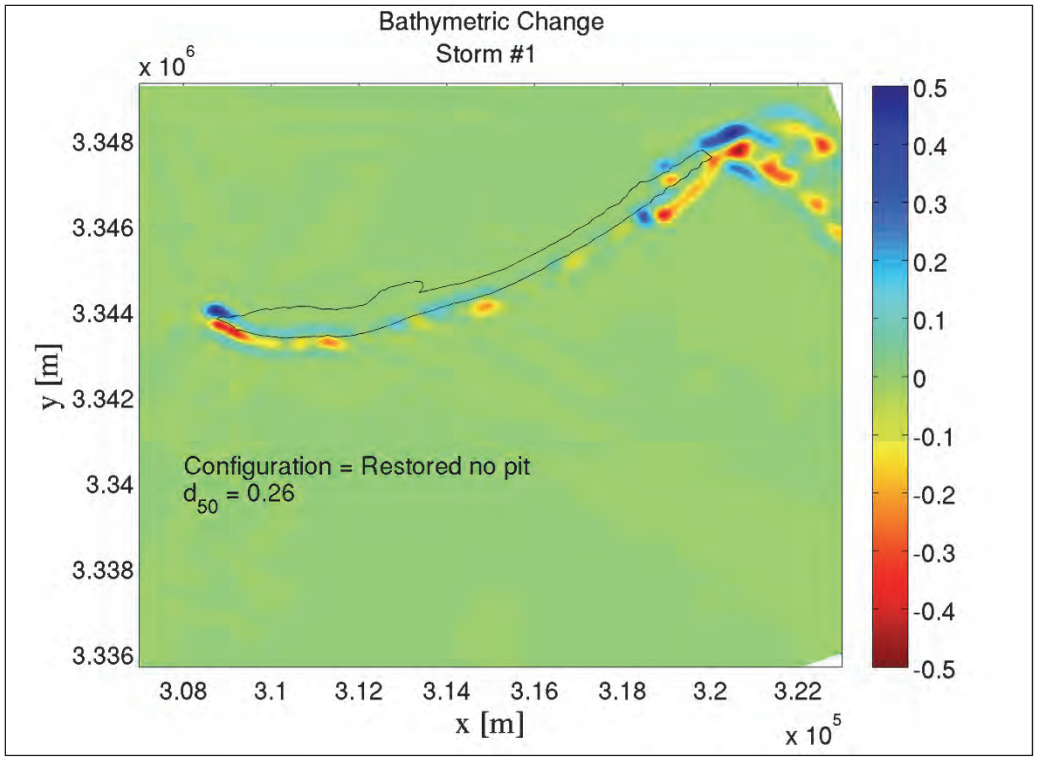

Figure H-7. Restored conditions for Storm #1; d_{50} = 0.30 mm (Template #3); Without borrow pits.

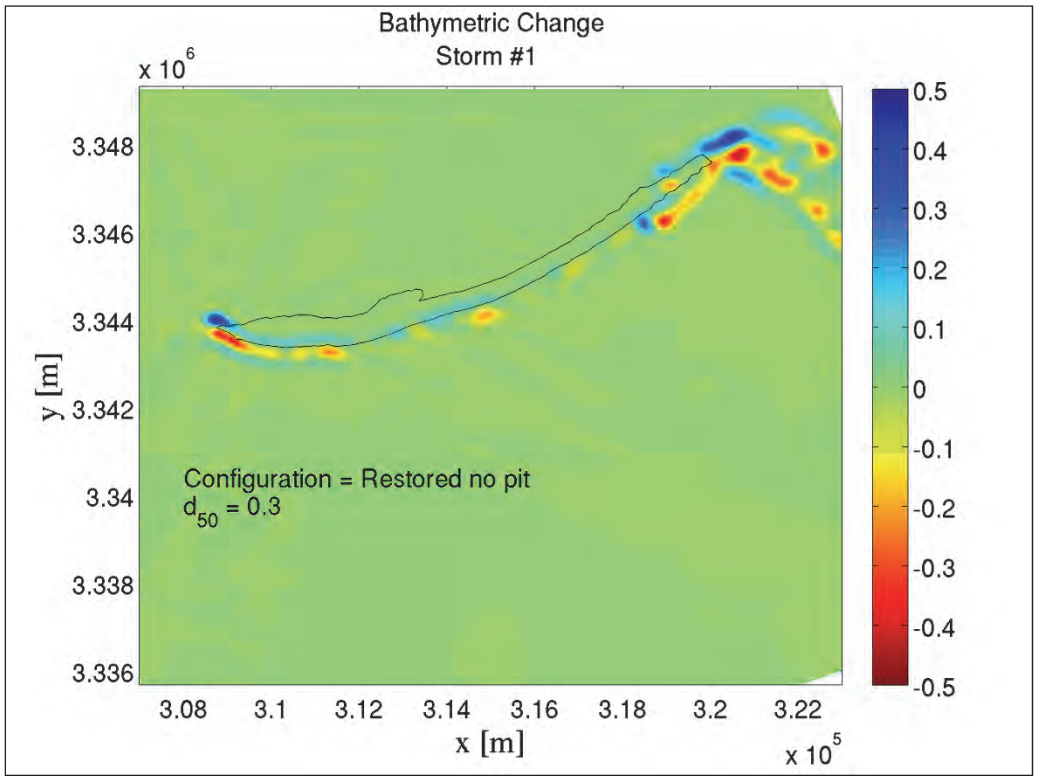

Figure H-8. Existing conditions for Storm #2; d_{50} = 0.30 mm.

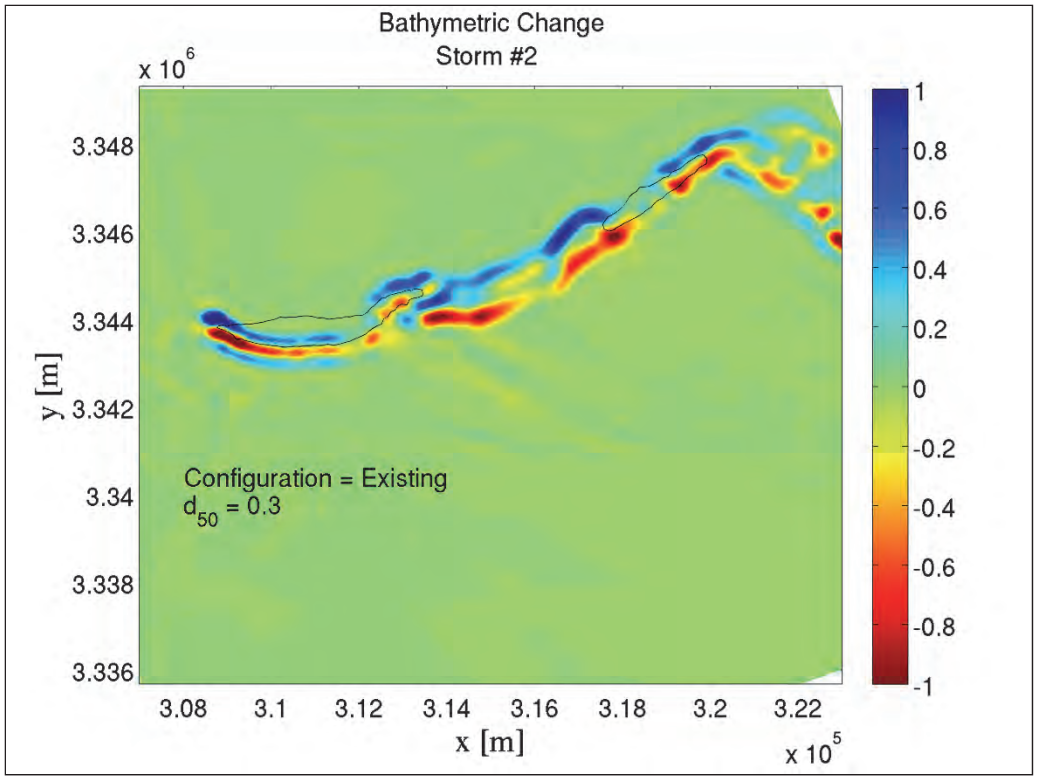

Figure H-9. Restored conditions for Storm #2; d_{50} = 0.20 mm (Template #1); With borrow pits.

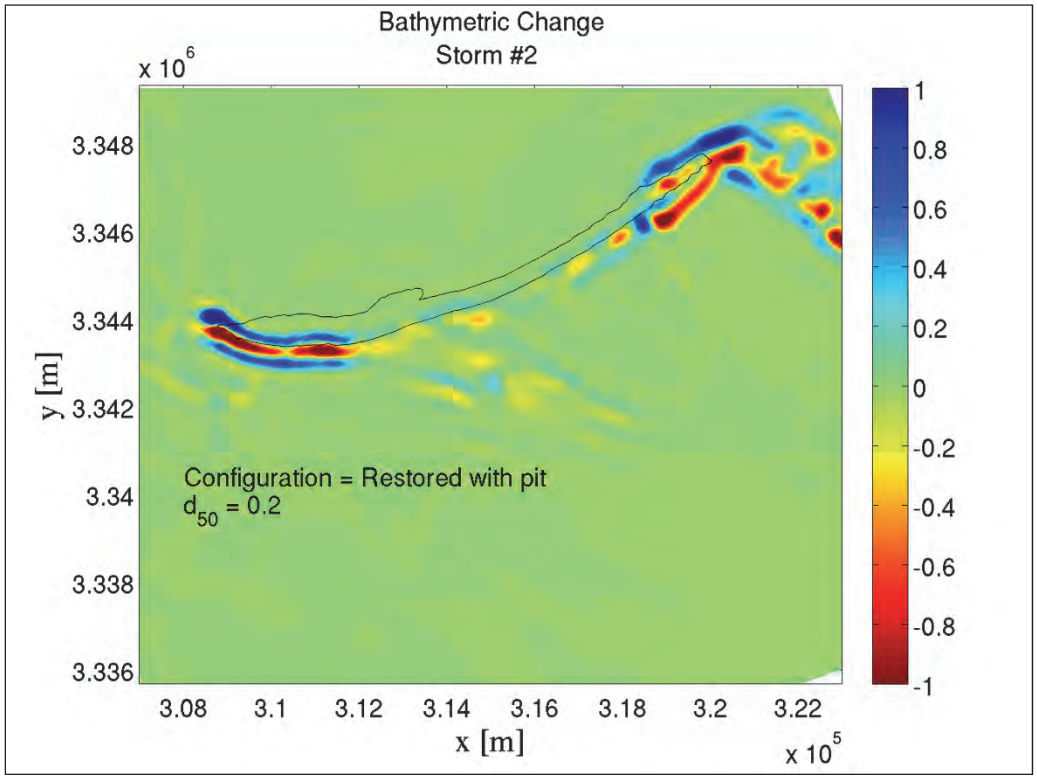

Figure H-10. Restored conditions for Storm #2; d_{50} = 0.26 mm (Template #2); With borrow pits.

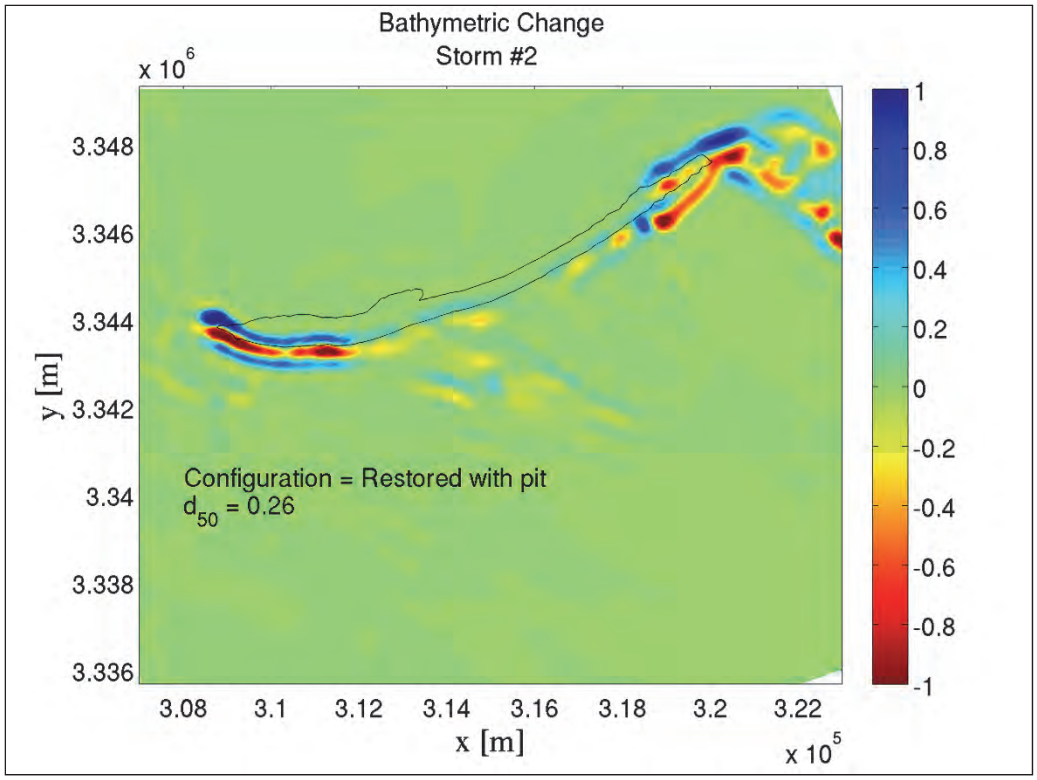

Figure H-11. Restored conditions for Storm #2; d_{50} = 0.30 mm (Template #3); With borrow pits.

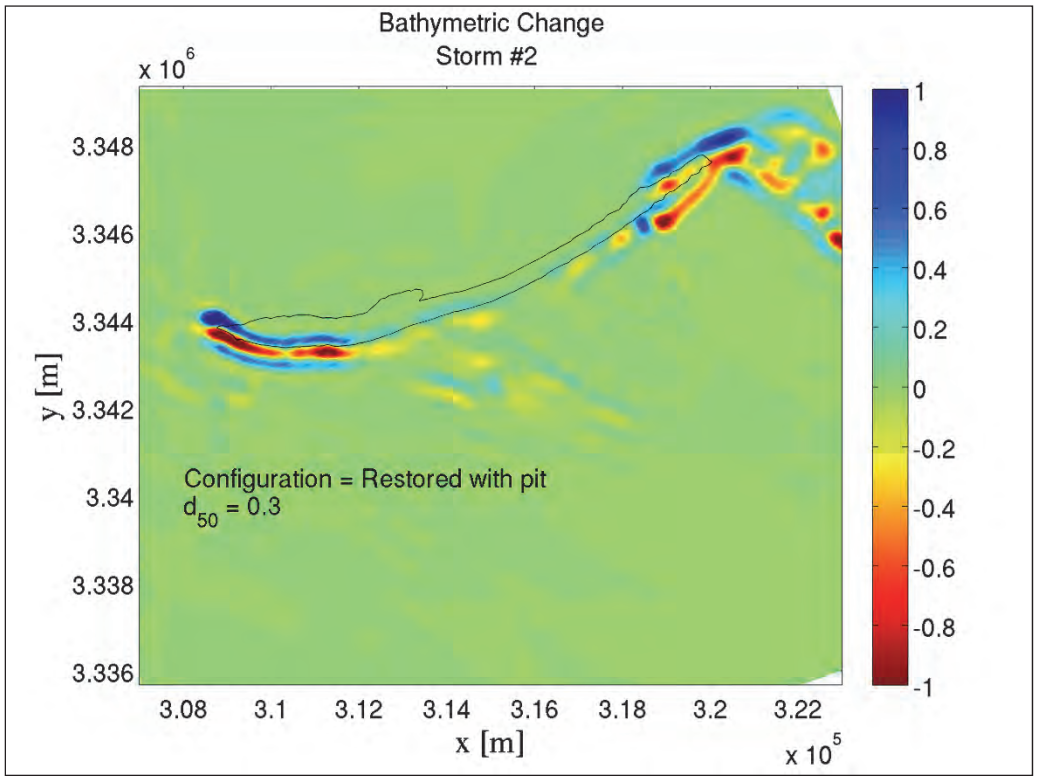

Figure H-12. Restored conditions for Storm #2; d_{50} = 0.20 mm (Template #1); Without borrow pits.

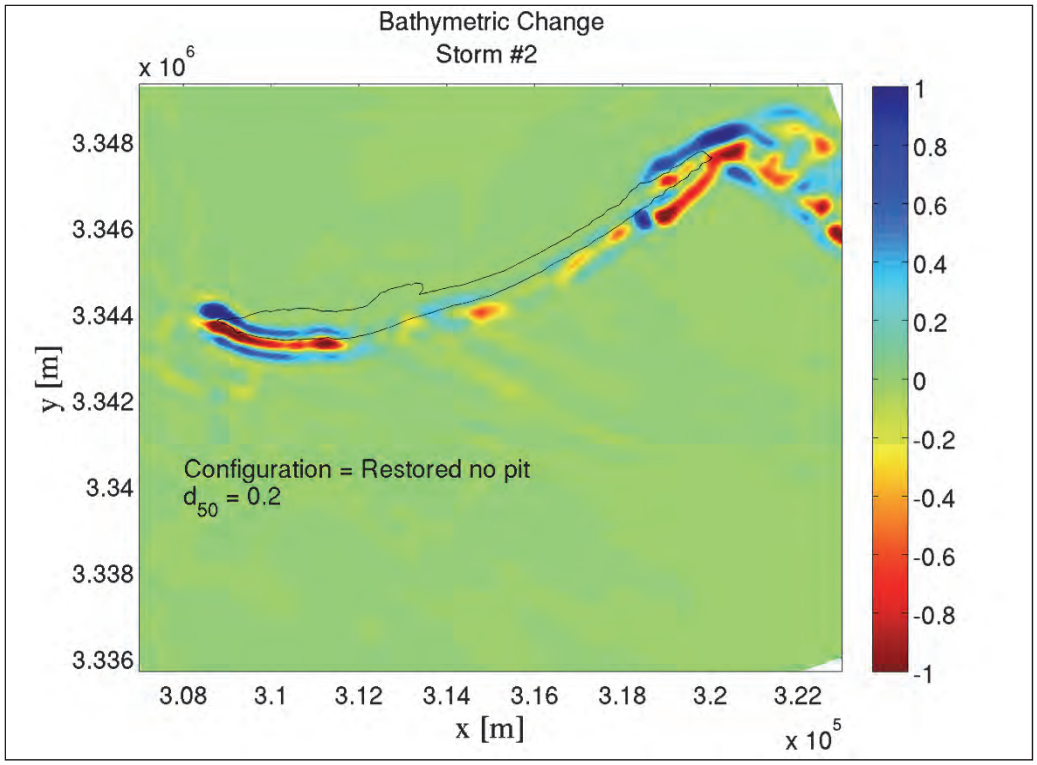

Figure H-13. Restored conditions for Storm #2; d_{50} = 0.26 mm (Template #2); Without borrow pits.

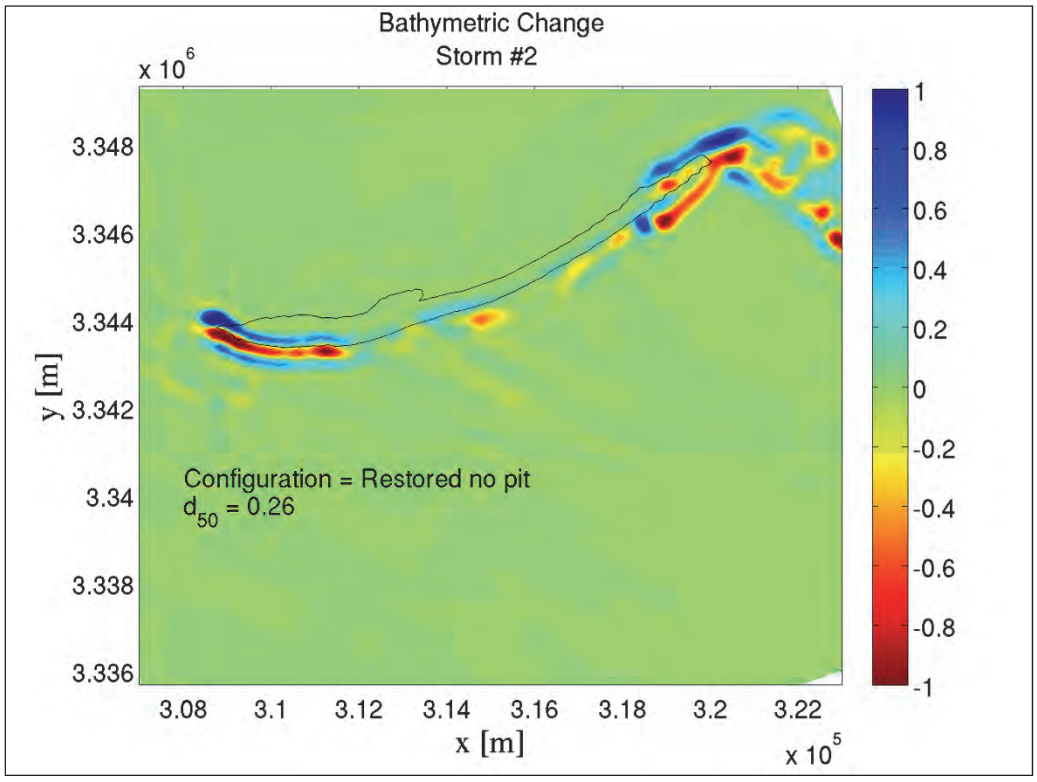

Figure H-14. Restored conditions for Storm #2; d_{50} = 0.30 mm (Template #3); Without borrow pits.

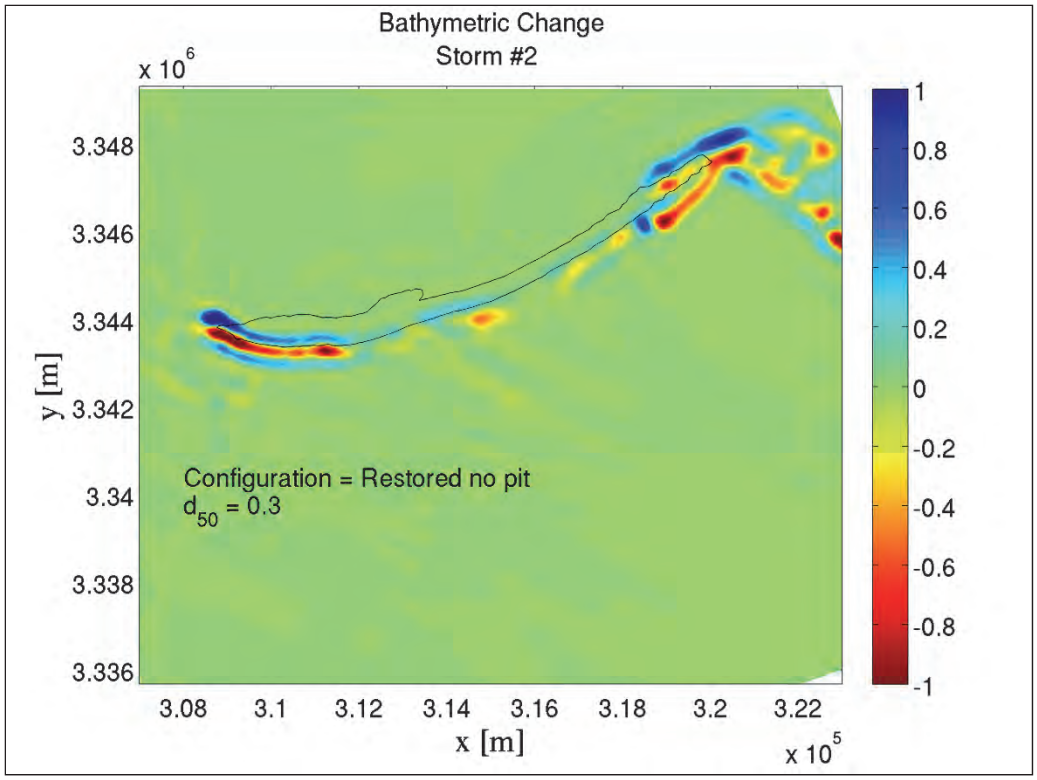

Appendix I: Nearshore Sediment Transport Modeled Results for Existing Conditions and Restoration Scenarios

Figure I-1. Existing conditions for Katrina; d_{50} = 0.30 mm.

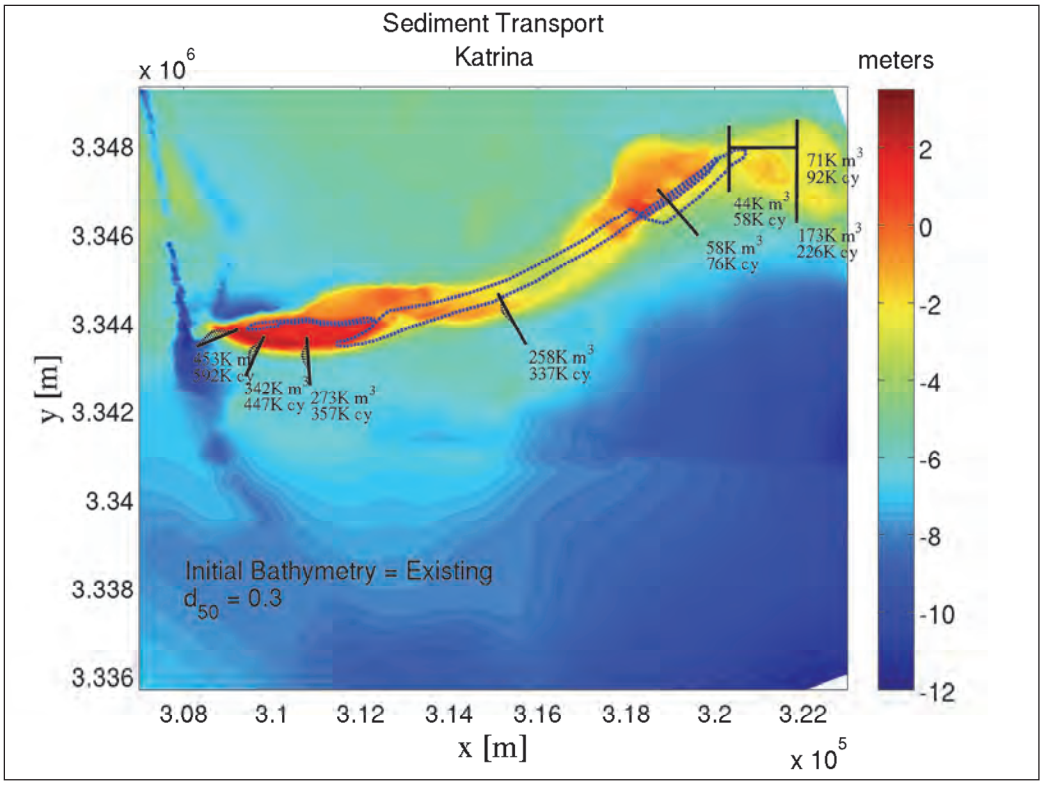

Figure I-2. Restored conditions for Katrina; d_{50} = 0.20 mm (Template #1); With borrow pits.

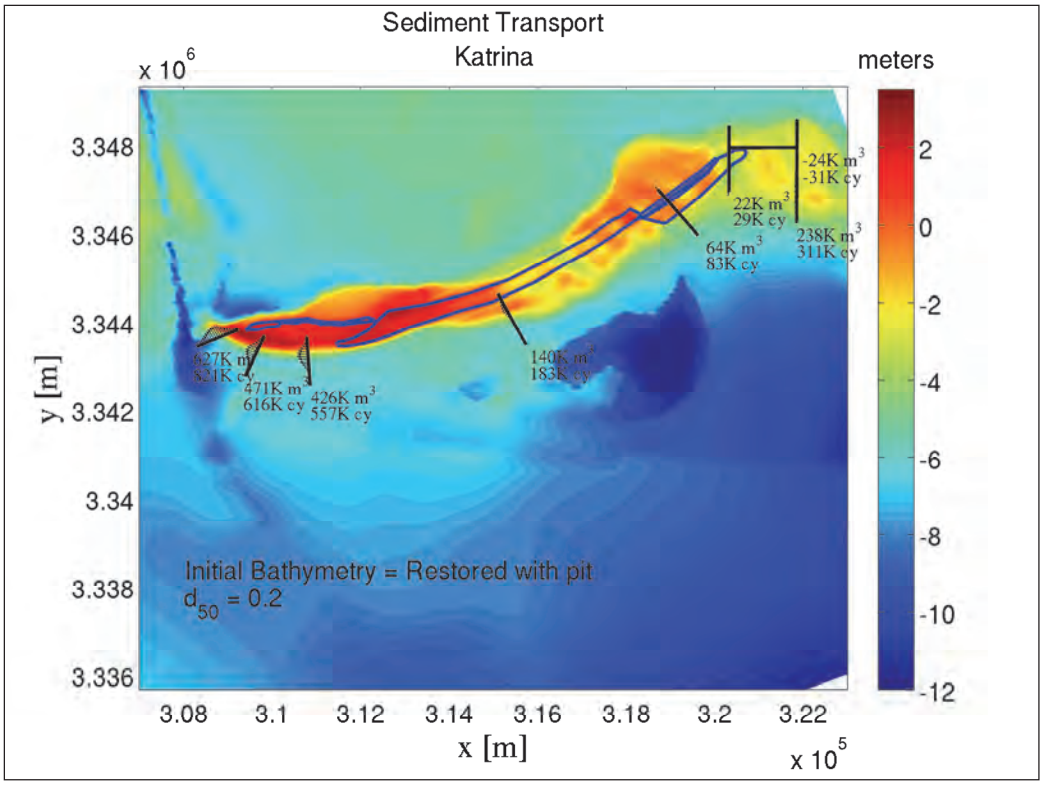

Figure I-3. Restored conditions for Katrina; d_{50} = 0.26 mm (Template #2); With borrow pits.

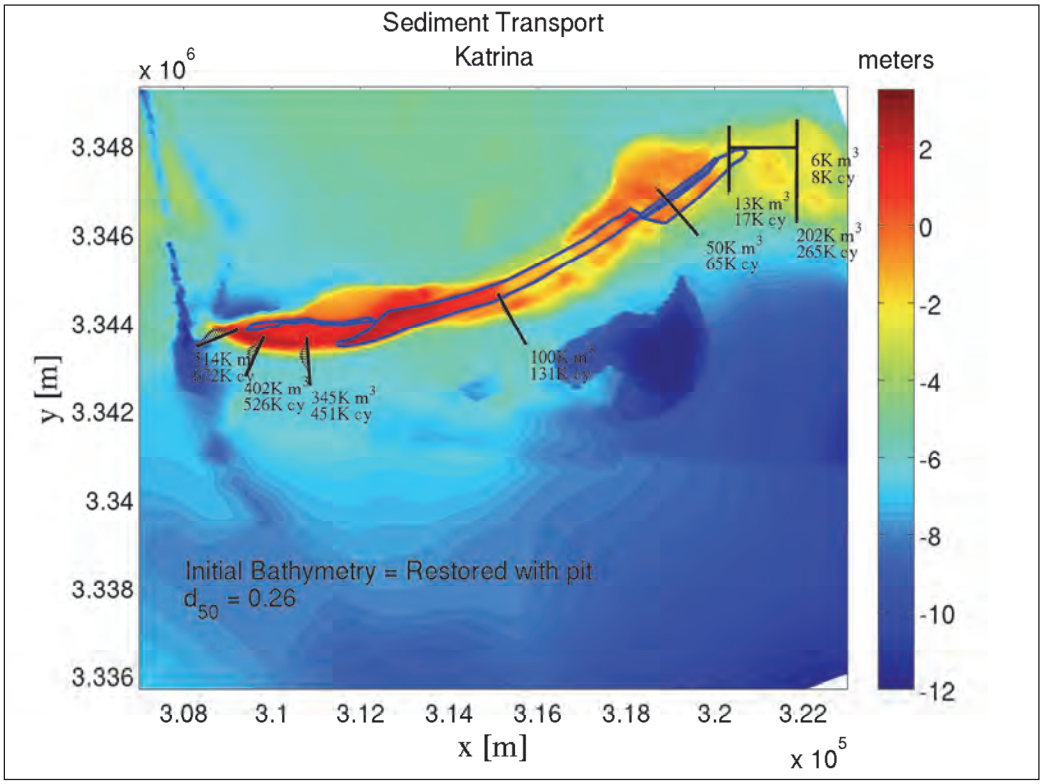

Figure I-4. Restored conditions for Katrina; d_{50} = 0.30 mm (Template #3); With borrow pits.

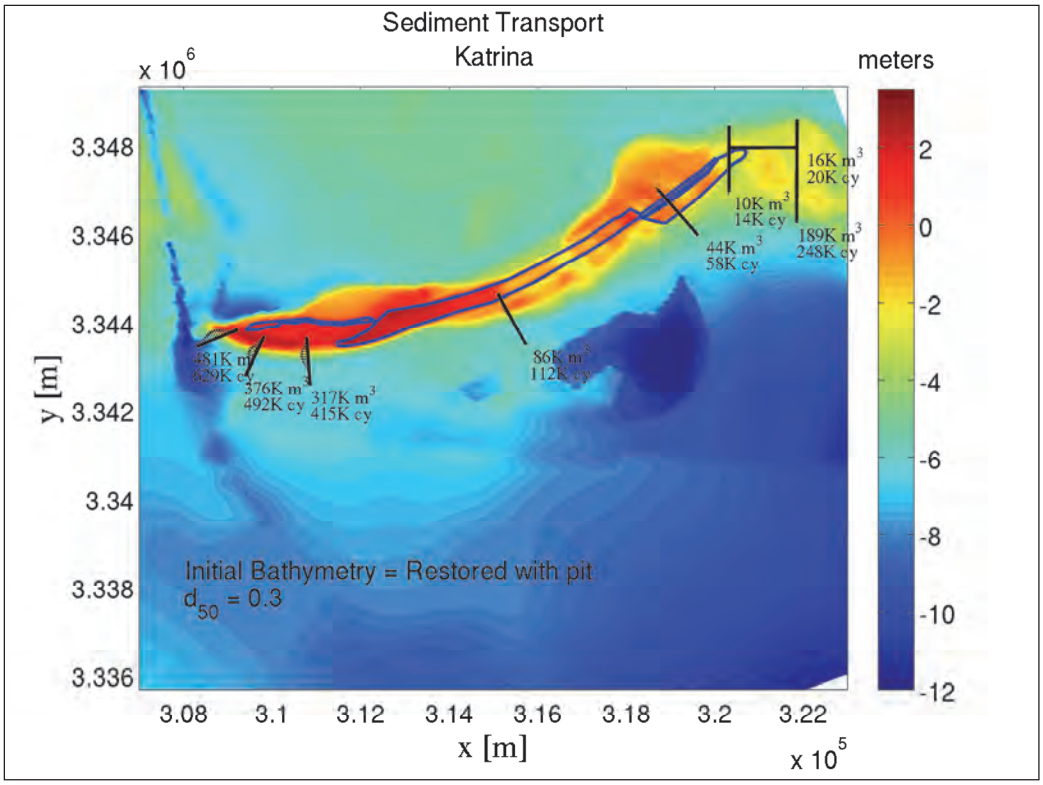

Figure I-5. Restored conditions for Katrina; d_{50} = 0.20 mm (Template #1); Without borrow pits.

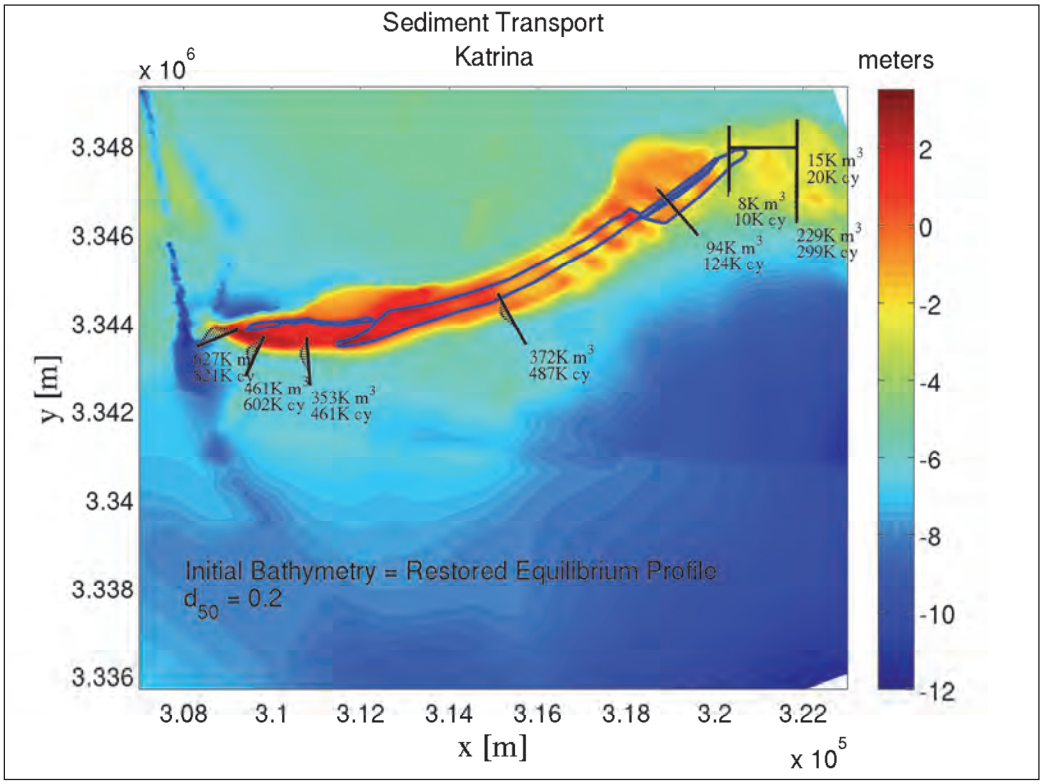

Figure I-6. Restored conditions for Katrina; d_{50} = 0.26 mm (Template #2); Without borrow pits.

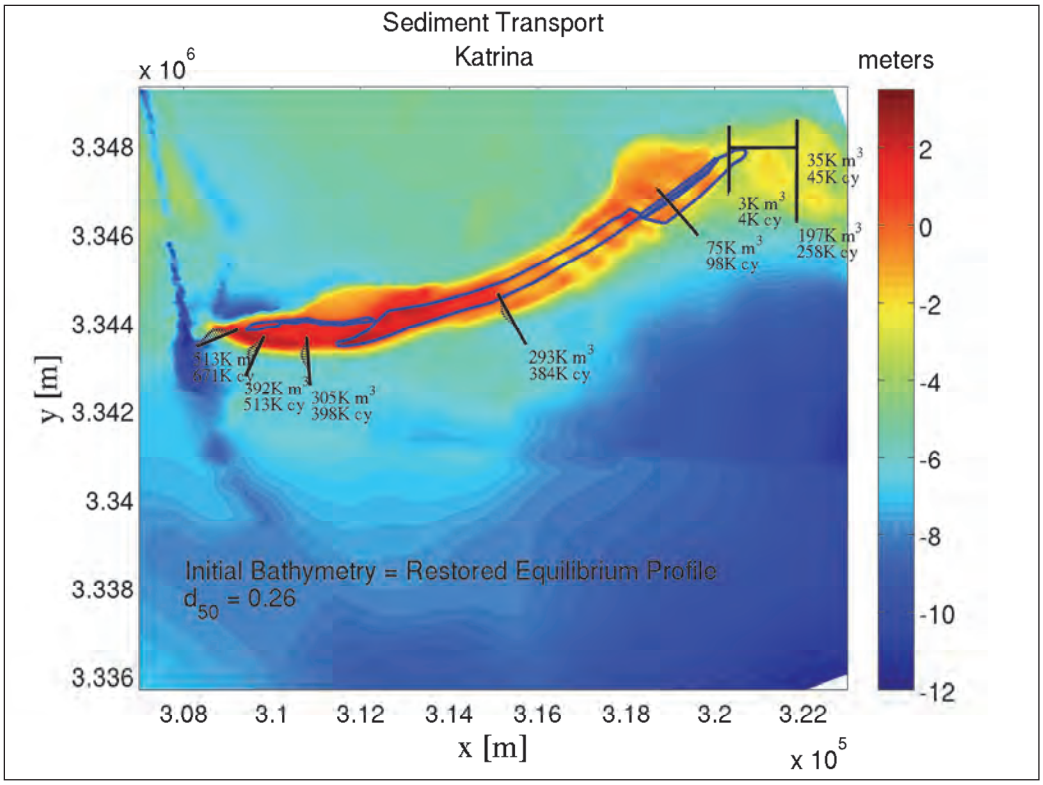

Figure I-7. Restored conditions for Katrina; d_{50} = 0.30 mm (Template #3); Without borrow pits.

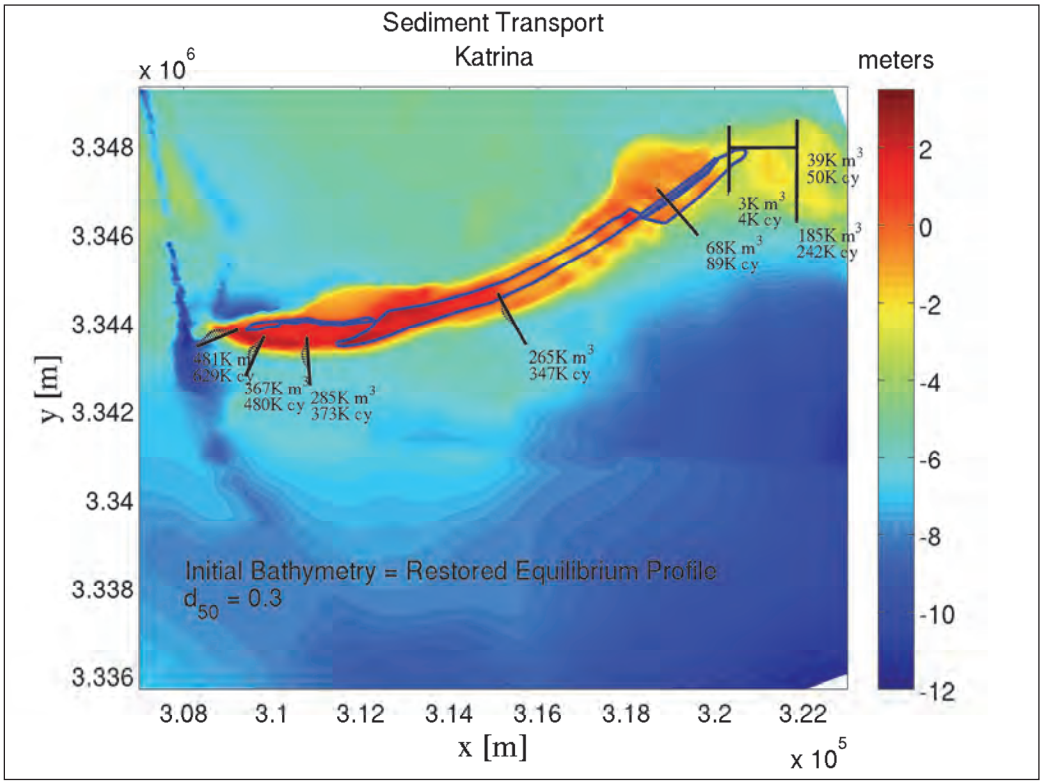

Appendix J: Nearshore Sediment Transport and Bathymetric Change Modeled Results for Existing Conditions and Alternative 3 Restoration Scenario

Note: The island footprint (NAVD = 0) contour is depicted as a black outline for reference in Figures J-7 through J-12.

Figure J-1. Existing conditions for Storm #1; d_{50} = 0.30 mm.

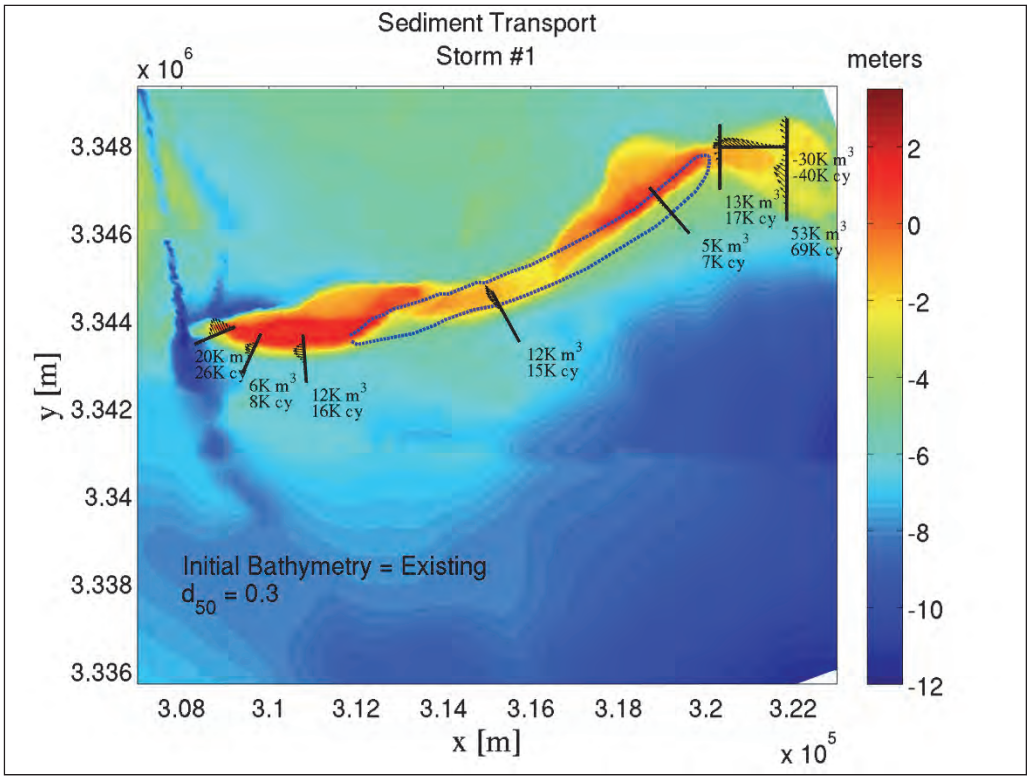

Figure J-2. Alternative 3 Restored conditions for Storm #1; d_{50} = 0.30 mm; With borrow pit.

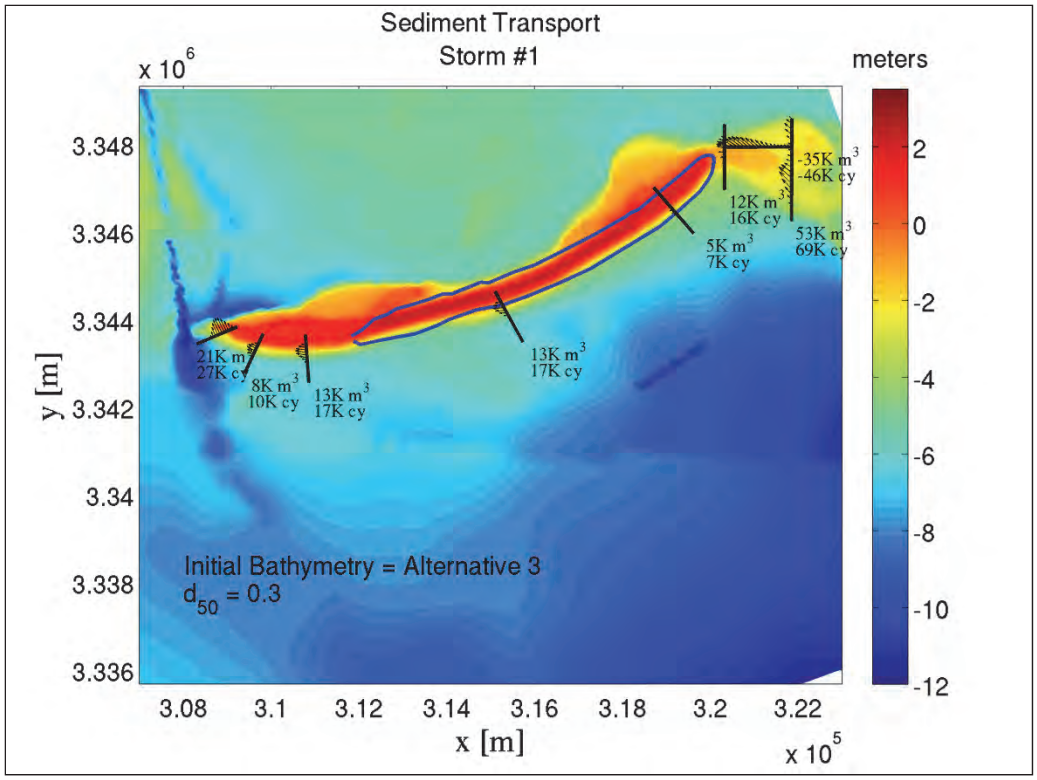

Figure J-3. Existing conditions for Storm #2; d_{50} = 0.30 mm.

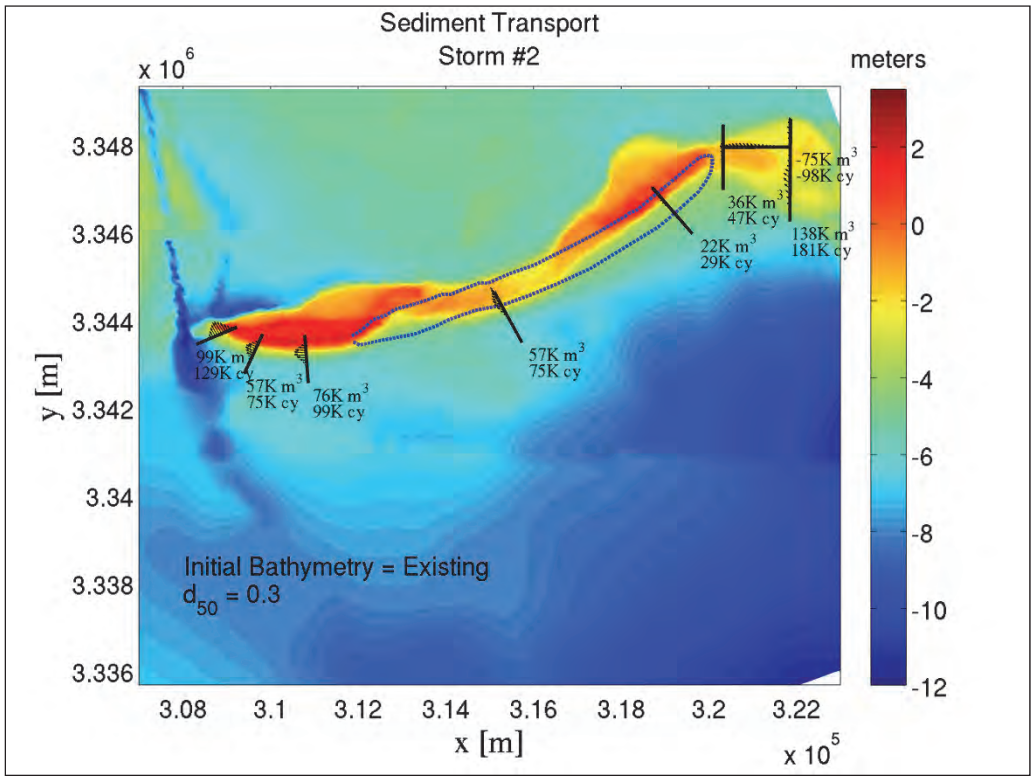

Figure J-4. Alternative 3 Restored conditions for Storm #2; d_{50} = 0.30 mm; With borrow pit.

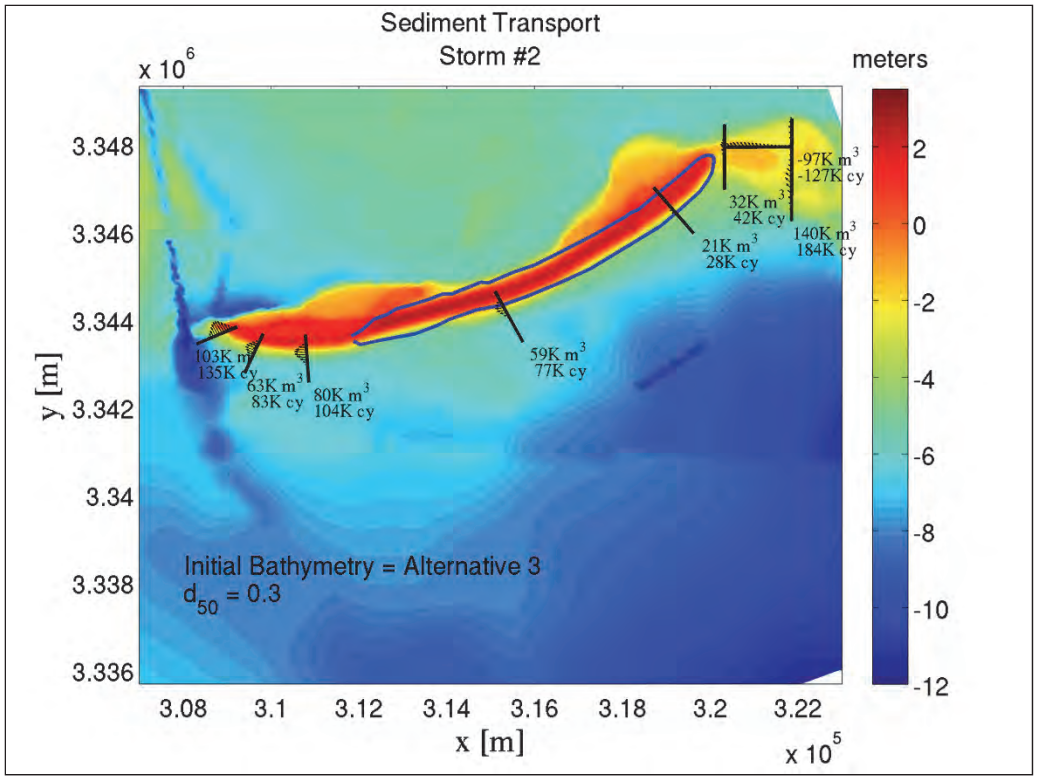

Figure J-5. Existing conditions for Storm #3; d_{50} = 0.30 mm.

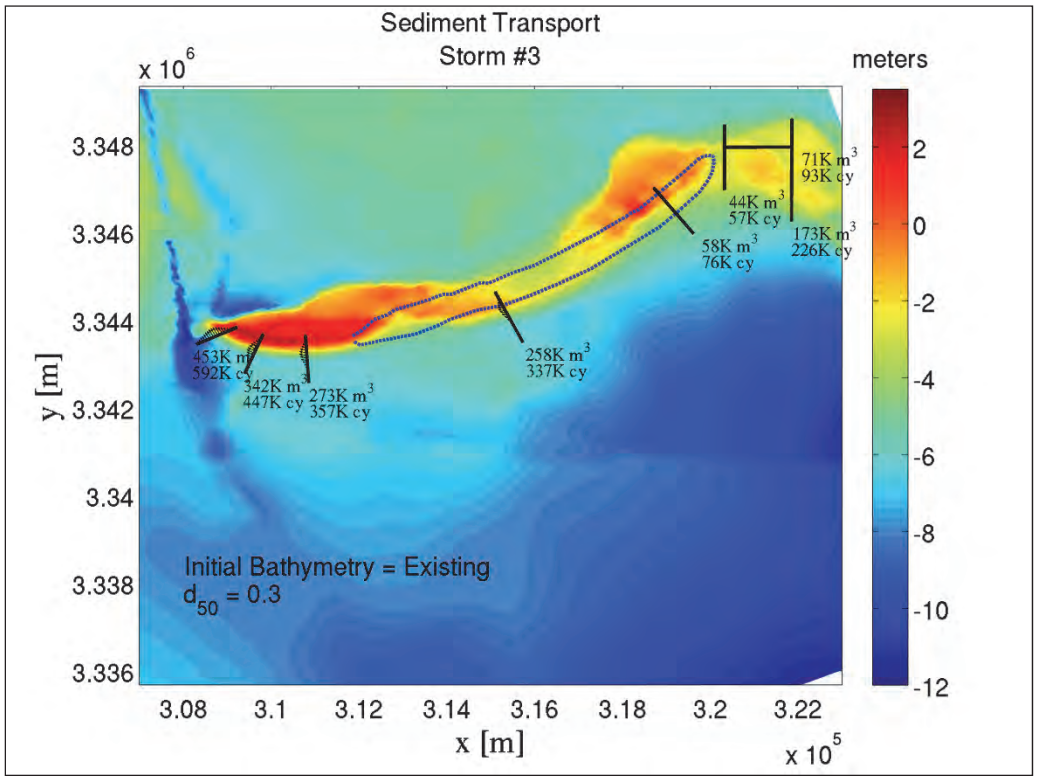

Figure J-6. Alternative 3 Restored conditions for Storm #3; d_{50} = 0.30 mm; With borrow pit.

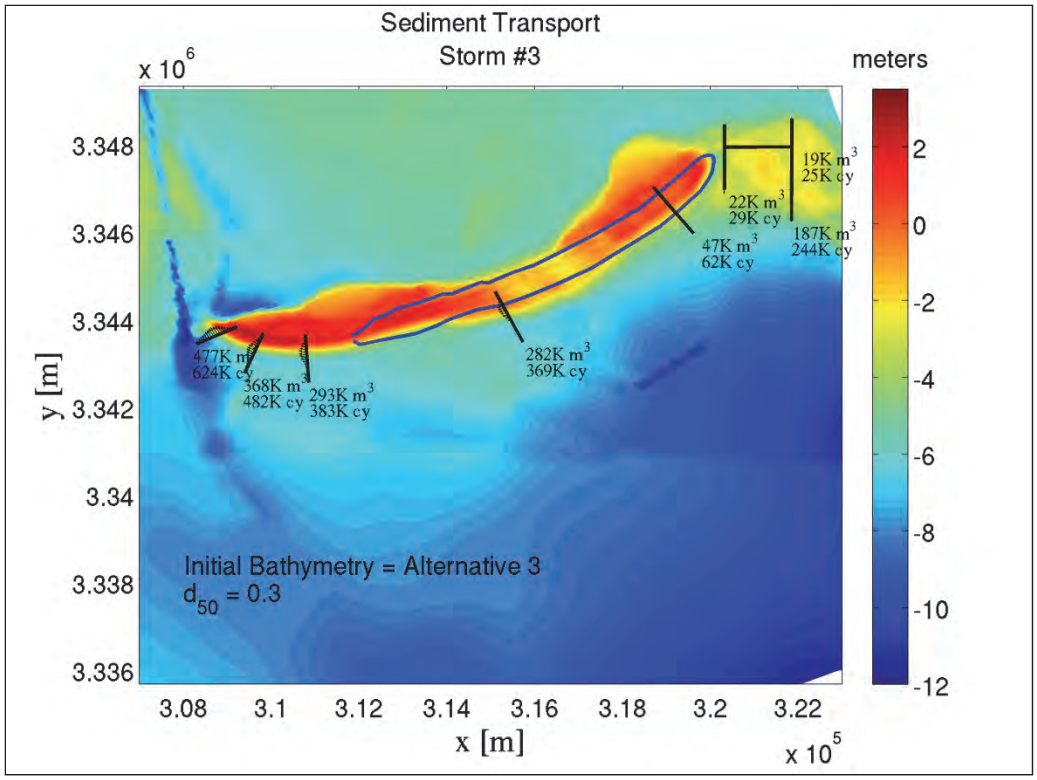

Figure J-7. Existing conditions for Storm #1; d_{50} = 0.30 mm.

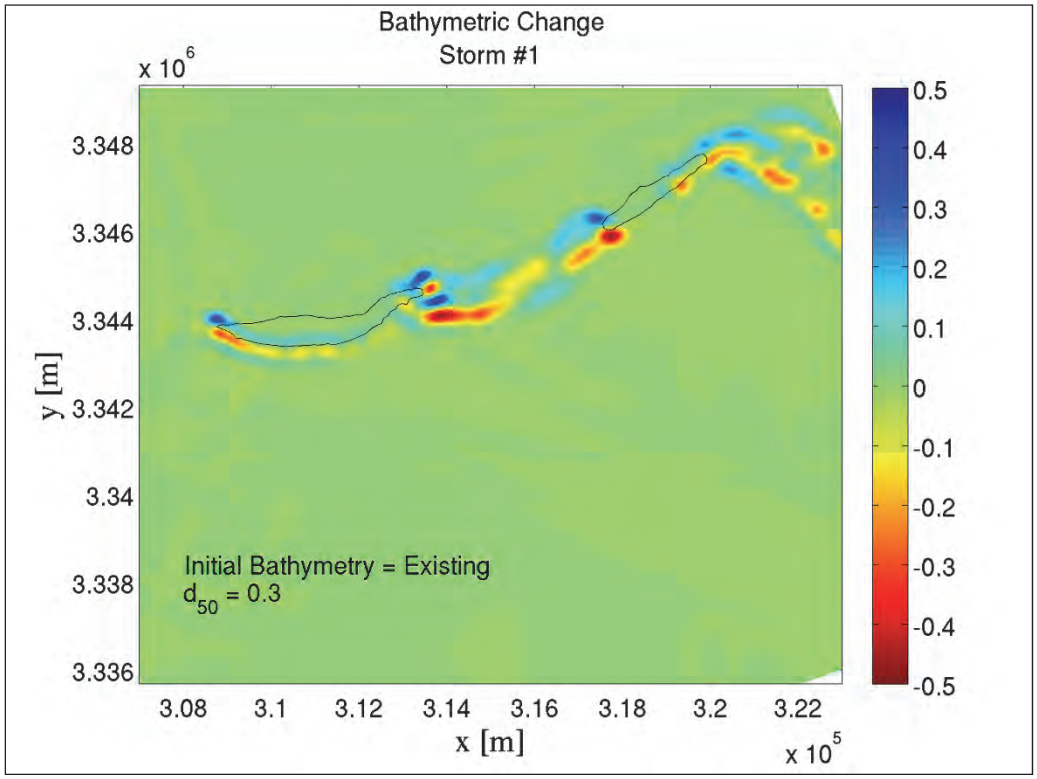

Figure J-8. Alternative 3 Restored conditions for Storm #1; d_{50} = 0.30 mm; With borrow pit.

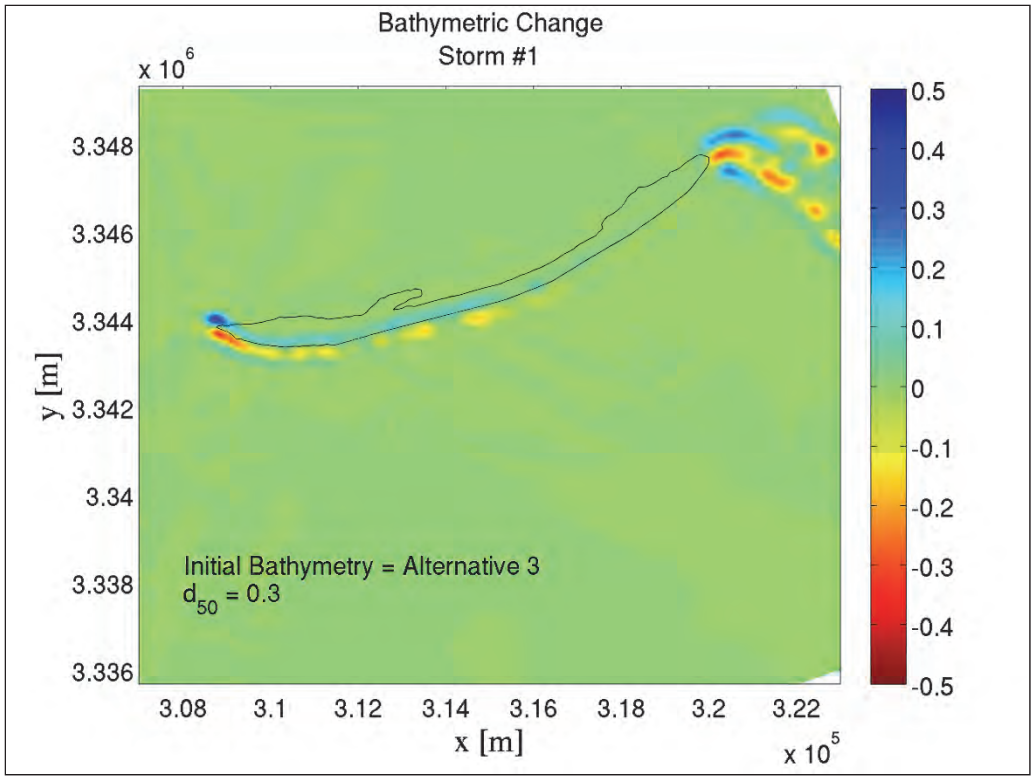

Figure J-9. Existing conditions for Storm #2; d_{50} = 0.30 mm.

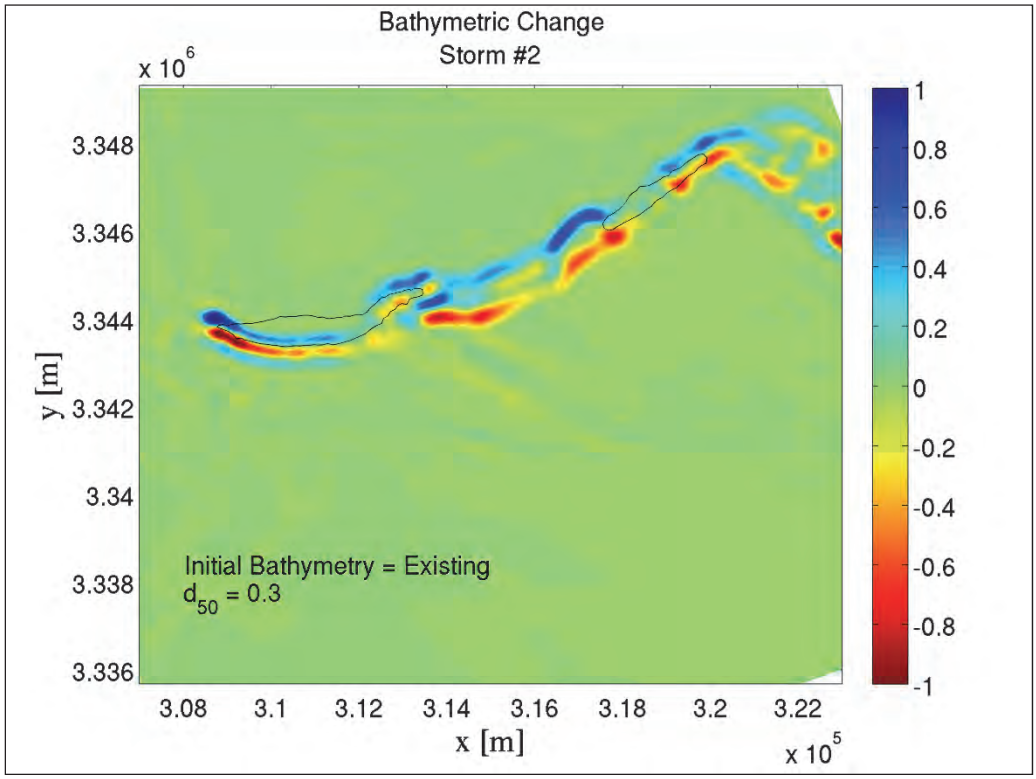

Figure J-10. Alternative 3 Restored conditions for Storm #2; d_{50} = 0.30 mm; With borrow pit.

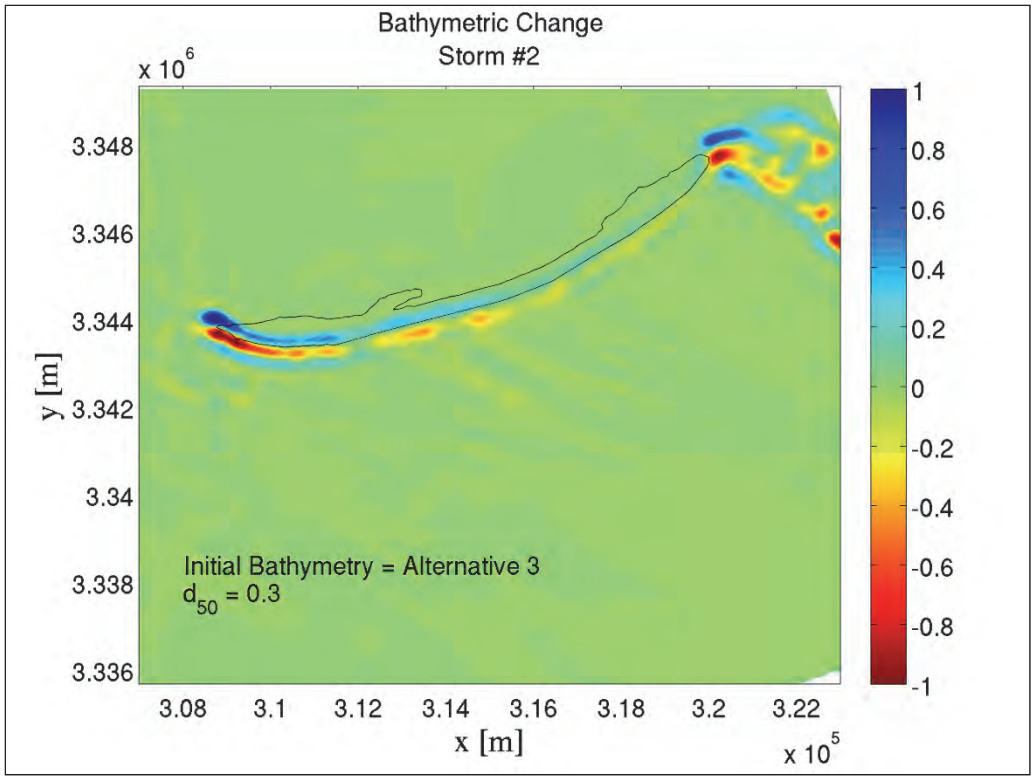

Figure J-11. Existing conditions for Storm #3; d_{50} = 0.30 mm.

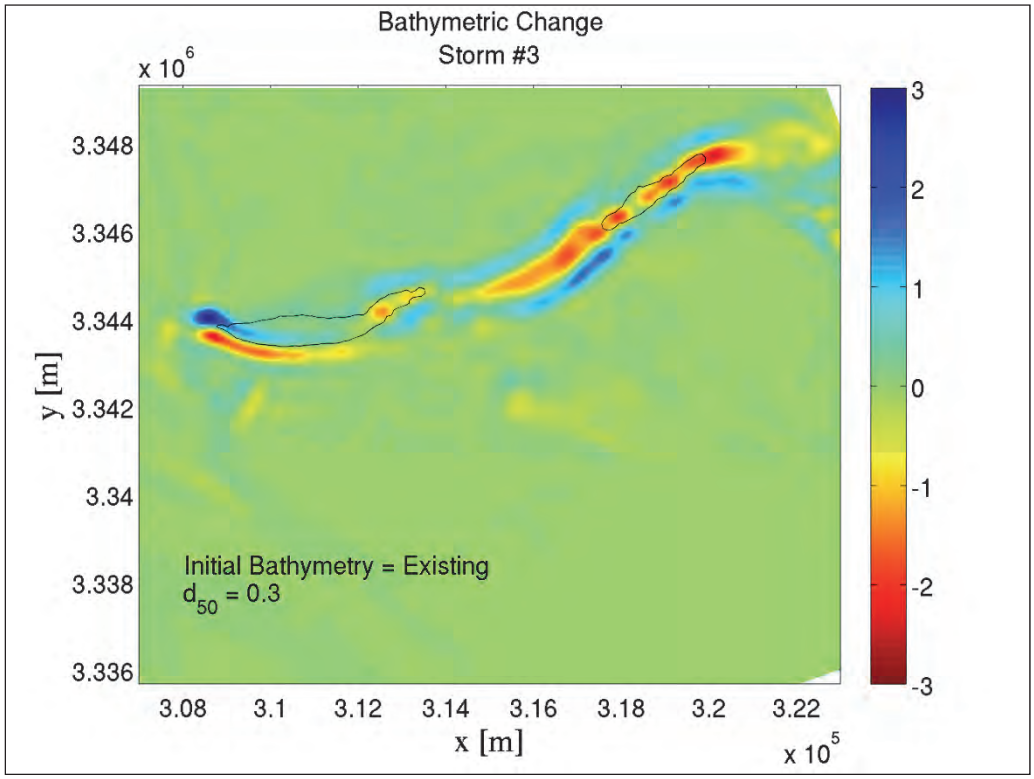

Figure J-12. Alternative 3 Restored conditions for Storm #3; d_{50} = 0.30 mm; With borrow pit.

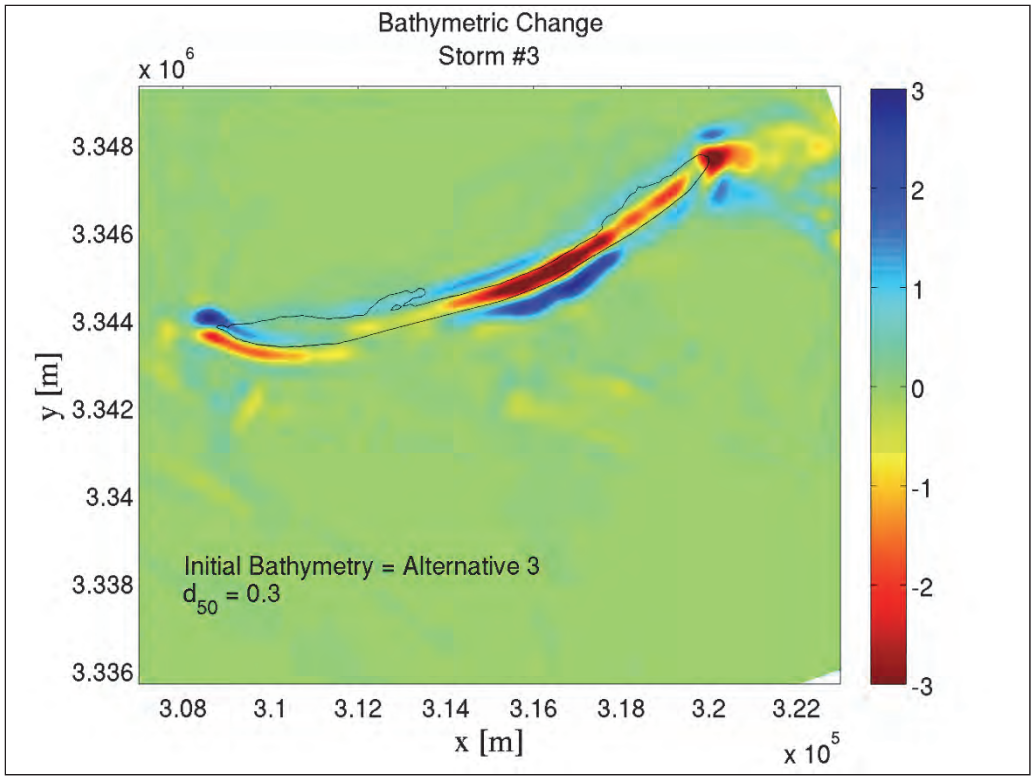

REPORT DOCUMENTATION PAGE

Form Approved
OMB No. 0704-0188

Public reporting burden for this collection of information is estimated to average 1 hour per response, including the time for reviewing instructions, searching existing data sources, gathering and maintaining the data needed, and completing and reviewing this collection of information. Send comments regarding this burden estimate or any other aspect of this collection of information, including suggestions for reducing this burden to Department of Defense, Washington Headquarters Services, Directorate for Information Operations and Reports (0704-0188), 1215 Jefferson Davis Highway, Suite 1204, Arlington, VA 22202-4302. Respondents should be aware that notwithstanding any other provision of law, no person shall be subject to any penalty for failing to comply with a collection of information if it does not display a currently valid OMB control number. **PLEASE DO NOT RETURN YOUR FORM TO THE ABOVE ADDRESS.**

1. REPORT DATE *(DD-MM-YYYY)*	2. REPORT TYPE	3. DATES COVERED *(From - To)*
May 2013	Final Report (TR)	

4. TITLE AND SUBTITLE

Mississippi Coastal Improvements Program; Evaluation of Barrier Island Restoration Efforts

5a. CONTRACT NUMBER

5b. GRANT NUMBER

5c. PROGRAM ELEMENT NUMBER

6. AUTHOR(S)
Ty V. Wamsley, Elizabeth S. Godsey, Barry W. Bunch, Raymond S. Chapman, Mark B. Gravens, Alison S. Grzegorzewski, Bradley D. Johnson, David B. King, Rusty L. Permenter, Dorothy H. Tillman, and Michael W. Tubman

5d. PROJECT NUMBER

5e. TASK NUMBER

5f. WORK UNIT NUMBER

7. PERFORMING ORGANIZATION NAME(S) AND ADDRESS(ES)

Coastal and Hydraulics Laboratory
US Army Engineer Research and Development Center
3909 Halls Ferry Road
Vicksburg, MS 39180

8. PERFORMING ORGANIZATION REPORT NUMBER

ERDC TR-13-12

9. SPONSORING / MONITORING AGENCY NAME(S) AND ADDRESS(ES)

US Army Corps of Engineer District, Mobile
109 Saint Joseph Street, Mobile Alabama 36602

10. SPONSOR/MONITOR'S ACRONYM(S)

11. SPONSOR/MONITOR'S REPORT NUMBER(S)

12. DISTRIBUTION / AVAILABILITY STATEMENT
Approved for public release; distribution is unlimited.

13. SUPPLEMENTARY NOTES

14. ABSTRACT

A comprehensive numerical modeling study was undertaken to support the barrier island restoration plan as part of the Mississippi Coastal Improvements Program. Hydrodynamic, wave, sediment transport, and water quality numerical modeling was conducted to evaluate the effect of Camille Cut closure on circulation and water quality of Mississippi Sound; the combined effect of Camille Cut and Katrina Cut closures on circulation and water quality of Mississippi Sound; reduction of storm wave energy at the mainland Mississippi coast as a result of closing Camille Cut; and optimization of nearshore placement of sand in the littoral zone. Water quality modeling of Mississippi Sound was conducted to determine potential impacts from proposed actions in the Ship Island area using the Curvilinear Hydrodynamic 3D model (CH3D) and the water quality model (CE-QUAL-ICM). Although water quality changes were observed for the alternatives modeled, the impact of Ship Island degradation or restoration does not significantly alter system wide circulation and water quality conditions. However, the condition of Ship Island has localized effects on circulation and water quality. The changes in storm wave energy at the mainland Mississippi coast as a result of Ship Island degradation and restoration were quantified through the application of an integrated coastal storm modeling system. Results indicate that the closure of Camille Cut and Ship Island restoration have the potential to reduce storm waves at the mainland coast. The C2SHORE model was applied to numerically predict the morphological response and sand fate for a selection of proposed alternatives. Results indicate that the Camille Cut restoration fill survives higher-frequency storms (such as the 1-yr and 10-yr events), but is breached during the lower-frequency 500-yr event modeled. Potential impacts of nearshore borrow areas were assessed with the spectral nearshore wave transformation model STWAVE and shoreline change model GENESIS. Scenarios included borrow areas offshore of Ship Island, Horn Island, and West Dauphin Island and were evaluated over a period of 20-years. The expected shoreline impacts are site-specific, with both prograding and eroding shoreline areas predicted.

15. SUBJECT TERMS
Borrow areas
Breach
Coastal Morphology
Hurricane
Water quality
Mississippi Sound
Shoreline erosion
Storm waves

16. SECURITY CLASSIFICATION OF:			17. LIMITATION OF ABSTRACT	18. NUMBER OF PAGES	19a. NAME OF RESPONSIBLE PERSON Ty V. Wamsley
a. REPORT	b. ABSTRACT	c. THIS PAGE			19b. TELEPHONE NUMBER *(include area code)*
Unclassified	Unclassified	Unclassified		515	601-634-2099

Standard Form 298 (Rev. 8-98)
Prescribed by ANSI Std. 239.18